Synthesis of Novel Nanophotocatalyst in Micro/Millifludic Supercritical Reactor

Prasaanth Ravi Anusuyadevi

université de BORDEAUX

THÈSE PRÉSENTÉE

POUR OBTENIR LE GRADE DE

DOCTEUR DE

L'UNIVERSITÉ DE BORDEAUX

ÉCOLE DOCTORALE DES SCIENCES CHIMIQUES

SPÉCIALITÉ : Physico-Chimie de la Matière Condensée

Par Prasaanth RAVI ANUSUYADEVI

Titre en français :

Synthèse de nouveaux nanophotocatalyseurs en millifluidique supercritique

Title in English:

Synthesis of novel nanophotocatalysts in millifluidic supercritical reactors

Sous la direction de : Samuel MARRE et Cyril AYMONIER

Soutenue prévue le 12 Décembre 2018

Membres du jury :

Mme. ROUGIER, Aline, Directeur de Recherche, ICMCB, Université de Bordeaux	Présidente
M. ABOU-HASSAN, Ali, Professeur associe, Sorbonne Université de Paris	Rapporteur
M. PAROLA, Stéphane Professeur, ENS, Université de Lyon	Rapporteur
Mme. SASSOYE, Capucine, Maitre de Conference, Sorbonne Université de Paris	Examinateur
M. AYMONIER, Cyril, Directeur de Recherche, ICMCB, Université de Bordeaux	Directeur de thèse
M. MARRE, Samuel, Chargé de Recherche, ICMCB, Université de Bordeaux	Directeur de thèse

Contents

Résumé de la thèse de doctorat en français 3

General Introduction 13

1. Heterogeneous nanophotocatalysts: synthetic approaches and applications 17

1.1. Introduction 21

1.2. Photocatalysis 23

1.2.1. Homogeneous photocatalysis 23

1.2.2. Heterogeneous photocatalysis 26

1.3. Heterogeneous photocatalytic systems 29

1.3.1. Types of photocatalytic semiconductor systems 29

1.3.2. Nano-binary photocatalysts 31

1.3.3. Ternary multi metallic photocatalytic materials 38

1.3.4. Solid solution photocatalysts 48

1.3.5. Nanocomposite photocatalysts 61

1.3.6. Conclusion of heterogeneous photocatalysts 80

1.4. Reactor design & implementation of photocatalysts in photochemical processes 81

1.4.1. Solid-Liquid (diphasic) & Solid-Liquid-Gas (triphasic) phase systems in heterogeneous photocatalysis 82

1.5. Conclusion and outcome of literature survey 88

2. Continuous synthesis of GaN nano-photocatalysts in supercritical millireactors 105

2.1. Gallium Nitride 109

2.1.1. Introduction 109

2.1.2. Properties and applications of GaN 110

2.1.3. Implementation of GaN in photon-conversion processes 112

2.1.4. Synthetic methodologies for GaN nanomaterials 113

2.1.5. Conclusion 116

2.2. Continuous synthesis of GaN QDs at supercritical conditions 117

2.2.1. Continuous synthesis of nanomaterials in supercritical fluids 117

2.2.2. Single source precursor introduction and its chemistry for obtaining GaN QDs 119

2.3. Continuous supercritical synthesis of GaN QDs using a co-flow configuration 122

2.3.1. Introduction 122

2.4. Simulation studies concerning the supercritical millireactors for GaN QDs production 129

2.5. Supercritical synthesis through a pre-heater setup 134

2.5.1. Introduction 134

2.5.2. Characterization of GaN QDs obtained from pre-heater supercritical millireactor 136

2.5.3. Conclusion 147

2.6. Application of GaN in heterogeneous photocatalysis 148

2.6.1. Introduction 148

2.6.2. Heterogeneous photocatalysis for the degradation of pollutants (organic dye) 148

2.6.3. Direct photocatalytic degradation of Methyl Orange using GaN QDS 150

2.6.4. Conclusion of the photocatalytic study 157

2.7. Conclusion 159

3. Continuous synthesis of visible light active $Ga_xIn_{1-x}N$ solid solution photocatalysts 171

3.1. Introduction 175

3.1.1. Motivation of the research work 175

3.1.2. Introduction to InGaN ternary materials 175

3.1.3. Synthetic methodologies and difficulties in attaining $Ga_xIn_{1-x}N$ ($0 \leq x \leq 1$) solid solution 177

3.1.4. Conclusion 179

3.2. Experimental Section 180

3.2.1. Introduction of the synthetic strategy developed for obtaining GaxIn1-xN ($0 \leq x \leq 1$) solid solutions 180

3.2.2. Continuous supercritical synthesis of the $Ga_xIn_{1-x}N$ ($0 \leq x \leq 1$) solid solution in toluene 181

3.2.3. Characterization of the $Ga_xIn_{1-x}N$ ($0 \leq x \leq 1$) solid solutions from supercritical toluene 184

3.2.4. Reasons for opting for dual solvent system 193

3.3. Tunability of $Ga_xIn_{1-x}N$ solid solution using toluene and methanol supercritical mixtures 195

3.3.1. Introduction to the synthesis 195

3.3.2. Characterization of $Ga_xIn_{1-x}N$ solid solution synthesized in toluene and methanol supercritical mixtures 195

3.3.3. Conclusion 215

3.4. Efficient trifluoromethylation of heteroarenes by visible light photoredox catalysis over $Ga_xIn_{1-x}N$ solid solutions semiconductor systems 216

3.4.1. Introduction 216

3.4.2. State-of-the-art methods for CF_3 incorporation or C-CF_3 bond formation 218

3.4.3. Photocatalyzed trifluoromethylation in batch mode using $Ga_{0.53}In_{0.47}N$ nanophotocatalysts ... 221

3.4.4. Continuous flow heterogeneous photocatalysis for direct radical trifluoromethylation of heteroarenes 227

3.4.5. Conclusion of photocatalytic studies 236

3.5. Conclusion 236

General Conclusion 245

Résumé de la thèse de doctorat en français

1. Introduction

L'économie mondiale a déjà commencé sa transition depuis les sources d'énergie conventionnelles vers celles non conventionnelles en raison de l'augmentation spectaculaire des émissions de CO_2 et de leur corrélation possible avec le changement climatique. La transposition se produit dans une phase rapide, non seulement dans le secteur de l'énergie, mais aussi dans les domaines de la chimie et du génie chimique. L'objectif final de ces stratégies est de limiter l'impact environnemental en développant des processus qui permettent une utilisation réduite des composés toxiques pour assurer un développement plus environnemental de l'humanité pour les générations à venir. La photochimie ou la photocatalyse sont des technologies durables qui convertissent l'énergie photonique abondamment disponible en énergie chimique utile. Ces procédés sont plus avantageux que la catalyse conventionnelle, car ils ne nécessitent pas d'activation thermique et limitent les effluents chimiques toxiques, qui sont principalement libérés par les systèmes employant la catalyse conventionnelle. Avec un développement rapide de la photochimie en flux au cours de la dernière décennie, plusieures réactions classiques ont pu être réalisées comme le couplage carbone-carbone (C - C), la réduction du dioxyde de carbone (CO_2), l'oxydation des composés toxiques, etc. *via* de nouveaux procédés photochimiques présentant moins de dangers, moins d'émissions d'effluents de déchets et aussi économiquement viables que la catalyse conventionnelle. Ces résultats ont alimenté la recherche dans ce domaine dans les différents domaines de la science et de l'ingénierie.

Mes recherches doctorales sont entièrement axées sur la conception, le développement et la synthèse de nouveaux nanophotocatalyseurs hétérogènes pour la réalisation de plusieurs réactions photochimiques par des méthodes optimisées énergétiquement. Ce travail a été réalisé dans le cadre du consortium 'Photo4Future' financé par le programme Horizon 2020 de recherche et d'innovation de l'Union européenne dans le cadre de l'accord de subvention Marie Sklodowska-Curie 641861. Le projet 'Photo4Future' vise spécifiquement la mise en œuvre de la lumière visible pour la réalisation de réactions de transformation chimique (réalisées en particulier dans les technologies d'assainissement de l'environnement), mais aussi dans l'activation de molécules organiques complexes se rapportant à la synthèse de produits chimiques à haute valeur ajoutée requise par les compagnies pharmaceutiques. Elle se focalise spécifiquement sur quatre domaines essentiels de la photochimie : (i) les études de nouvelles méthodes photocatalytiques dans les photoréacteurs à écoulement continu, (ii) le développement et la synthèse de photocatalyseurs hétérogènes, (iii) la modélisation, conception et fabrication de photoréacteurs et (iv) les investigations de la photocatalyse hétérogène par spectroscopie *in situ*. En tant que réseau de formation innovante (ITN), le projet 'Photo4Future' établit de façon concomitante un réseau de recherche entre les universités et les industries pour réaliser avec succès des modèles novateurs, des systèmes de réacteurs et des méthodes dans les quatre domaines clés de photochimie mentionnée ci-dessus.

Ce travail de thèse a été réalisé principalement à ICMCB, au CNRS et à l'Université de Bordeaux et des séjours de recherche ont été effectués à l'Université Technique d'Eindhoven (groupe de recherche de T. Nöel (NRG), département de génie chimique) et à l'Université de Cordoue (nano-scale Chimie et bio-groupe valorisation des déchets de masse, département de chimie organique, groupe de R. Luque). Les paragraphes qui suivent mettent en évidence l'importance de ces travaux de recherche dans les champs de recherche liés à la photocatalyse hétérogène.

L'ensemble du régime de la photocatalyse se divise en deux catégories : la photocatalyse homogène et hétérogène, où les deux types présentent le comportement fondamental du « piège à photons » et la conversion de l'énergie photonique en énergie chimique. Au cours des trois dernières décennies, des processus photocatalytiques hétérogènes utilisant des matériaux semi-conducteurs solides comme photocatalyseurs ont attiré l'attention croissante des scientifiques des matériaux et des ingénieurs chimistes. Ceci est principalement dû à la récupération facile des photocatalyseurs des milieux de réactions (par rapport aux photocatalyseurs homogènes) et aux bons taux de conversion / rendements chimiques obtenus, même après plusieurs cycles continus de recyclage. Le développement de photocatalyseurs « idéaux » semi-conducteurs, qui auraient la capacité de piéger une large gamme du spectre solaire en termes de longueur d'onde, tout en possédant la surface spécifique nécessaire pour effectuer plusieurs réactions photochimiques a connu un intérêt croissant. La photocatalyse hétérogène est un processus typique d'ingénierie en cascade qui se produit à la surface des photocatalyseurs. Elle implique le piégeage des photons, la conversion optoélectronique des photons en charges (électrons + trous), la séparation des charges, la migration des charges vers les réactifs adsorbés sur la surface des photocatalyseurs et enfin la désorption des produits de la surface.

Les nanomatériaux (en particulier les semi-conducteurs nanométriques ou quantum dots - QDs) peuvent fournir une surface élevée pour ces processus en cascade et sont devenus un domaine de recherche important dans le domaine de la photocatalyse hétérogène. Tout système photocatalytique doit répondre à trois critères indispensables : (i) une surface spécifique élevée, (ii) une capacité d'absorption lumineuse importante et (iii) une activité photocatalytique accrue. Comme les nanomatériaux remplissent facilement les deux premiers critères, la plupart des études se focalisent sur la conception et la synthèse des photocatalyseurs semi-conducteurs démontrant une activité photochimie importante.

Pour obtenir avec succès des photocatalyseurs hétérogènes nécessaires pour les applications photochimiques actuelles, j'ai d'abord réalisé un état de l'art sur les critères essentiels auxquels doivent répondre les systèmes photocatalytiques de pointe, ainsi que leurs stratégies de synthèse correspondantes. Cela a été fait en examinant les matériaux semi-conducteurs actuellement développés et leurs applications dans la photochimie. Cela a été fait pour la plupart des matériaux semi-conducteurs étudiés au cours des quatre dernières décennies. Une telle étude m'a amené à classer les divers matériaux semi-conducteurs disponibles dans quatre

familles différentes de photocatalyseurs hétérogènes, représentés schématiquement dans la Figure 1.

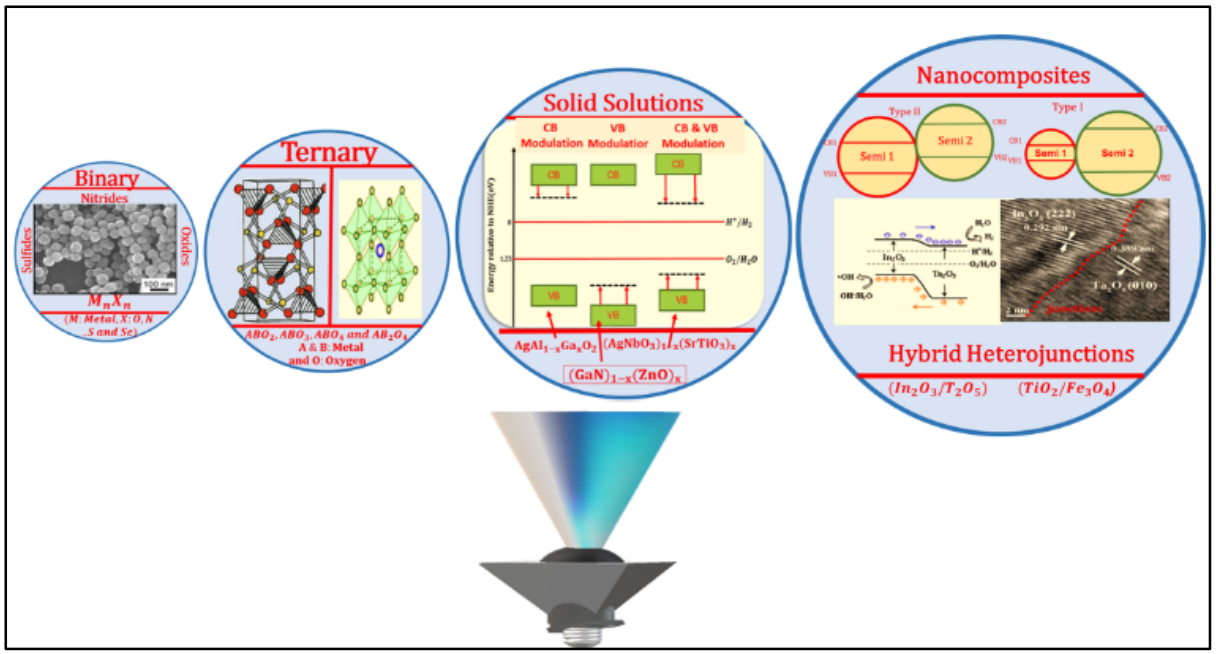

Figure 1. *Classification des photocatalyseurs semi-conducteurs en quatre familles différentes : (i) nanophotocatalyseurs binaires, (ii) nanophotocatalyseurs ternaires, (iii) solution solide de nanophotocatalyseurs et (iv) nanophotocatalyseurs composites.*

Ce travail de doctorat a consisté en la réalisation de nouveaux matériaux semi-conducteurs pour réaliser des réactions photochimiques ciblées par le projet « Photo4Future ». Le semi-conducteur de nitrure de gallium (GaN) a été choisi comme système principal dans cette étude de doctorat avec les nitrures du groupe III ($In_xGa_{1-x}N$), car ils présentent la propension à pouvoir former des photocatalyseurs semi-conducteurs appartenant aux quatre familles différentes de photocatalyseurs hétérogènes. Bien que GaN soit l'un des semi-conducteurs de troisième génération qui a été largement commercialisé dans les domaines électriques et optoélectroniques, son utilisation comme photocatalyseur n'a commencé que récemment. Le GaN possède de bonnes propriétés de transport d'électrons et présente une forte liaison atomique entre le gallium et l'azote (liaison covalente) formant un matériau semi-conducteur possédant une stabilité mécanique exaltée avec grande inertie chimique dans des environnements acides et basiques et même dans des environnements réactifs à haute température. Les prochaines sections détailleront la synthèse de nanophotocatalyseurs appartenant aux quatre familles mentionnées ci-dessus par le biais d'un milliréacteur supercritique à flux continu et leur mise en oeuvre efficace correspondante pour les réactions photochimiques.

2. Synthèse continue de nanophotocatalyseurs de GaN en milliréacteur supercritique

Dans ce travail de recherche, des QDs de GaN ont tout d'abord été synthétisés dans un milliréacteur tubulaire de manière continue et en conditions supercritiques au travers de la thermolyse d'un précurseur ($[Ga(N(CH_3)_2)_3$).

Dans une première partie, j'ai réalisé la synthèse de QDs de GaN au sein d'un système millifluidique en configuration « co-courant » (précurseur injecté dans un capillaire interne et solvant pur injecté dans un flux externe) dans l'hexane supercritique à 400°C et 150 bar. La performance de cette installation a été analysée ainsi que la durée de vie du réacteur et sa capacité à fonctionner avec des concentrations plus élevées en précurseurs ont également été examinées. Cette installation a présenté plusieurs inconvénients notamment le temps de vie du réacteur qui se bouchait après quelques synthèses. Les inconvénients associés à la configuration « co-courant » ont été identifiés par une étude utilisant la simulation numérique, ce qui a permis de déterminer la thermique du réacteur. Cette simulation a fourni un aperçu approfondi des champs de température et de densité au sein du milliréacteur supercritique. Les résultats de l'étude de simulation ont fourni l'aperçu complet du processus d'écoulement et l'influence de la stratégie d'injection sur le transfert de chaleur. Cela nous a permis d'étudier une nouvelle configuration d'injection basée sur un pré-chauffage du flux de solvant pour atteindre les températures de synthèse plus rapidement et éviter les phénomènes de bouchage. Les configurations de ces schémas d'injection « co-courant » et « pré-chauffage » sont représentées schématiquement dans la Figure 2.

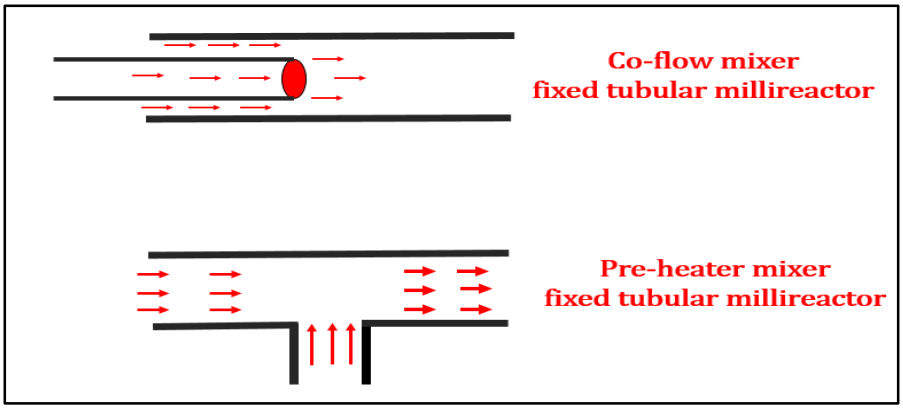

Figure 2. *Représentation schématique des configurations d'écoulement dans les mélangeurs « co-courant » et « pré-chauffeur ».*

Le milli-réacteur supercritique utilisant la configuration « pré-chauffeur » a permis de produire des QDs de GaN avec une reproductibilité accrue, tout en améliorant significativement la durée de vie du réacteur. Les QDs obtenus (400°C, 150 bar, 30s de temps de séjour) présentent des propriétés de confinement quantique, avec un déplacement des émissions de la luminescence vers le bleu d'environ 0,6 eV et 0,4 eV par rapport au bandgap du matériaux GaN « bulk » en phase cristalline cubique « zinc blend » et hexagonale « wurtzite », respectivement. Le spectre

d'absorption des QDs de GaN et son tracé en « Tauc plot » correspondant, sont représentés dans les figures 3 et 4. Ceci a permis de déterminer le bandgap des nanomatériaux synthétisés (3,8 eV).

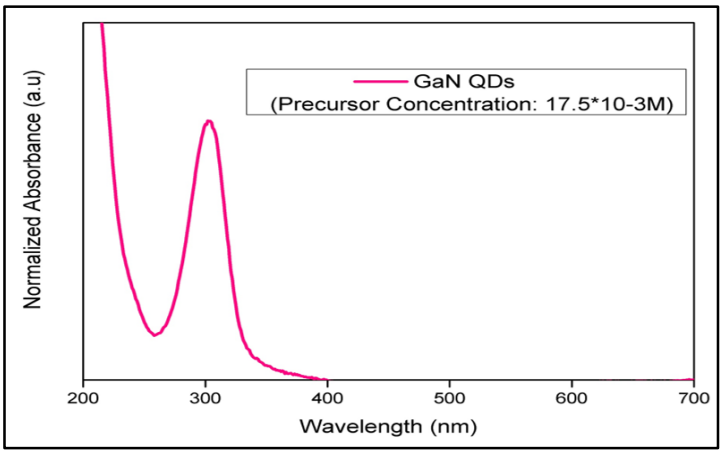

Figure 3. *Spectre d'absorption UV-visible des nanomatériaux de GaN synthétisés à partir de milliréacteur supercritique en configuration « pré-chauffeur » avec une concentration de précurseur de* $17.5 * 10^{-3} M$.

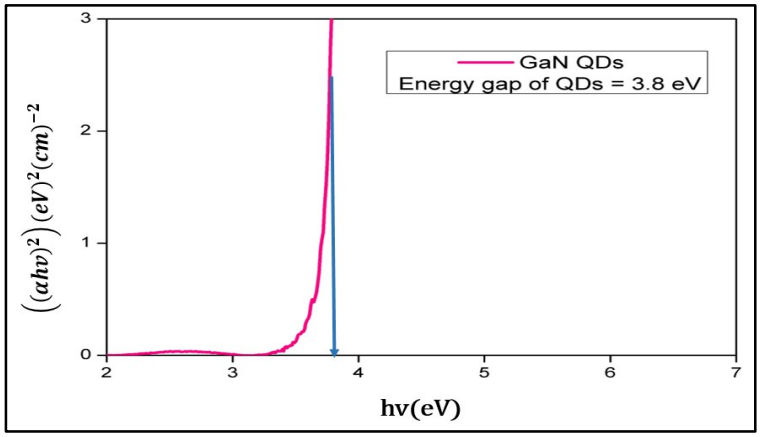

Figure 4. *Tauc plot des QDs de GaN calculé à partir du spectre d'absorption représenté dans la figure 3.*

En ce qui concerne la taille et la dispersion en taille des particules, par rapport à la technique de co-courant, les nanomatériaux de GaN obtenus avec le pré-chauffeur présentent à la fois des nanoparticules individuelles ainsi que des agrégats sphériques. Par ailleurs, jusqu'à 150 mg de GaN peuvent être synthétisés en continu avec le nouveau montage expérimental en une seule synthèse. Les QDs synthétisés ont ensuite été mis en œuvre avec succès dans une photoréaction catalysée (excitation photochimique directe) impliquant un procédé de dégradation photochimique d'un colorant azo organique (méthyl orange) sous lumière bleue (λ = 405 nm).

Les QDs de GaN synthétisés à partir du milliréacteur supercritique en configuration « pré-chauffeur » ont montré une efficacité élevée pour la dégradation du colorant « méthyle orange », présentant une efficacité de dégradation de 94% sous irradiation pendant une heure. Cette activité photocatalytique des QDs de GaN est 18 fois plus élevée que les nanophotocatalyseurs de TiO_2 (Degussa P25) disponibles dans le commerce (Figure 5). Cette étude a fourni une voie permettant d'utiliser efficacement l'irradiation en lumière bleue à travers des nanophotocatalyseurs binaires pour des réactions photochimiques impliquées dans les processus d'assainissement de l'environnement.

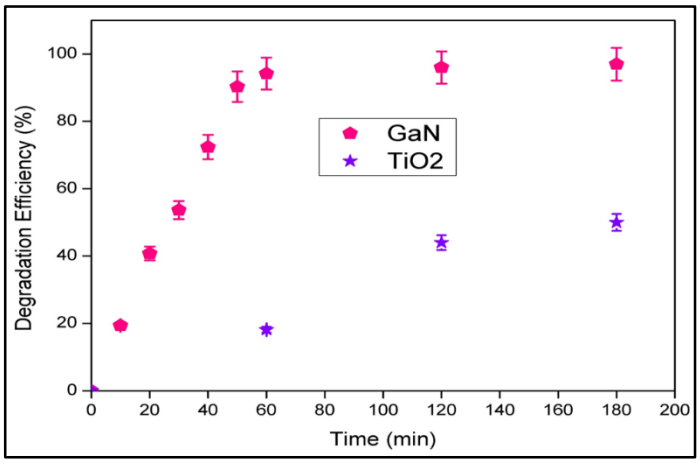

Figure 5. *Dégradation photocatalytique du colorant Methyle Orange (MO) avec les photocatalyseurs GaN ou TiO_2 ($MO = 8.3 * 10^{-5} M$, photocatalyseurs = 3 mg et durée de l'illumination = 180 min).*

3. Synthèse continue de nanophotocatalyseurs $Ga_xIn_{1-x}N$

Les nanophotocatalyseurs binaires à large bande comme les QDs de GaN ne possèdent pas le potentiel chimique nécessaire à la réalisation de réactions photocatalytiques hétérogènes sous irradiation en lumière visible, du fait de leur bandgap trop important. Afin d'élaborer des nanophotocatalyseurs permettant une photoréaction sensibilisée (processus de photoexcitation indirecte), un système de semi-conducteurs à bande étroite est nécessaire. Ceci peut être réalisé via la synthèse d'un système solution solide ternaire de $Ga_xIn_{1-x}N$. Jusqu'ici, dans le domaine de la science des matériaux, les nanoparticules de $Ga_xIn_{1-x}N$ ont été peu étudiées en raison de l'inadéquation des paramètres de maille entre GaN et InN, résultant la plupart du temps en des séparations de phase lorsque le taux d'indium dépasse 11%. Ce décalage des paramètres de maille découle des différences de rayon des cations de gallium et d'indium.

Dans ce travail de thèse, nous avons considéré la réaction entre des précurseurs de cupferronate d'indium et de gallium avec l'hexamethyldisilazane (HMDS), utilisé comme source d'azote pour la synthèse de QDs de $Ga_xIn_{1-x}N$ dans divers mélanges de solvants. Un nouveau milieu de synthèse à double solvants a été identifié, optimisé et mis en œuvre en flux continu dans un milliréacteur supercritique. Grâce à ce système à double solvant (toluène + méthanol), nous avons pu atteindre la solution solide complète de $Ga_xIn_{1-x}N$ ($0 < x < 1$) avec une ségrégation de phase très réduite. La composition des diverses solutions solides obtenues dans ce travail de recherche et les écarts de bandgap directs correspondant sont indiqués dans le tableau 1. Le diagramme schématique traçant l'évolution du bandgap en fonction de la composition de la solution solide de $Ga_xIn_{1-x}N$ est représenté dans la figure 6. Un maximum de 47mol% d'indium a été incorporé avec succès dans le réseau GaN pour la solution solide $Ga_xIn_{1-x}N$, sans aucune ségrégation de phase.

Tableau 1. *Valeurs des écarts d'énergie pour la solution solide GaxIn1-xN (x = 1, 0,77, 0,68, 0,53, 0,30, 0,22, 0,16 et 0) synthétisée à l'aide d'un mélange supercritique de toluène et de méthanol.*

S.No	$Ga_xIn_{1-x}N$ Solid solution	Energy gap (eV)
1	*GaN*	*3.43*
2	$Ga_{0.77}In_{0.23}N$	*3.24*
3	$Ga_{0.68}In_{0.32}N$	*2.99*
4	$Ga_{0.53}In_{0.47}N$	*2.62*
5	$Ga_{0.30}In_{0.70}N$	*2.48*
6	$Ga_{0.22}In_{0.78}N$	*2.12*
7	$Ga_{0.16}In_{0.84}N$	*1.97*
8	*InN*	*1.89*

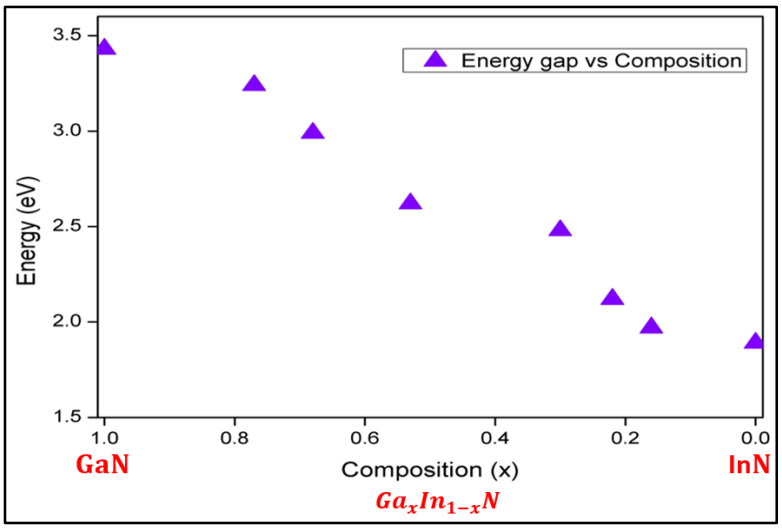

Figure 6. *Evolution du bandgap des nanomatériaux de $Ga_xIn_{1-x}N$ en fonction de la concentration d'indium, déterminé par la méthode du « Tauc plot ».*

Les QDs de $Ga_{0,53}In_{0,47}N$ synthétisés ont été utilisés ensuite avec succès en remplacement de des photocatalyseurs homogènes classiques (complexes de métaux de transition de type Ruthénium bypiridine) pour les réactions photochimiques de trifluorométhylation des hétéroarènes. Les hétéroarènes ont été choisis comme substrats réactifs modèles dans cette étude, car ils forment l'unité structurale fondamentale de plusieurs molécules de médicaments actuellement ciblées par l'industrie pharmaceutique. Les nanophotocatalyseurs GaInN ont montré une excellente activité en étant utilisés dans un montage photochimique fonctionnant en écoulement monophasique et/ou segmenté (gaz / liquide) sous irradiation en lumière visible. En particulier, un rendement RMN maximal de 80% a été atteint en 162 min (Figure 7).

Pour conclure, les nanophotocatalyseurs GaInN ont été utilisés avec succès pour la photocatalyse hétérogène (réaction de trifluorométhylation des arènes) dans les conditions d'écoulement au cours de ce travail de recherche. Par ailleurs, nous avons pu montrer que ces nanophotocatalyseurs hétérogènes peuvent être facilement récupérés en fin de réaction et qu'ils conservent un très bonne activité photocatalytique même après trois utilisations consécutives en écoulement (Figure 7).

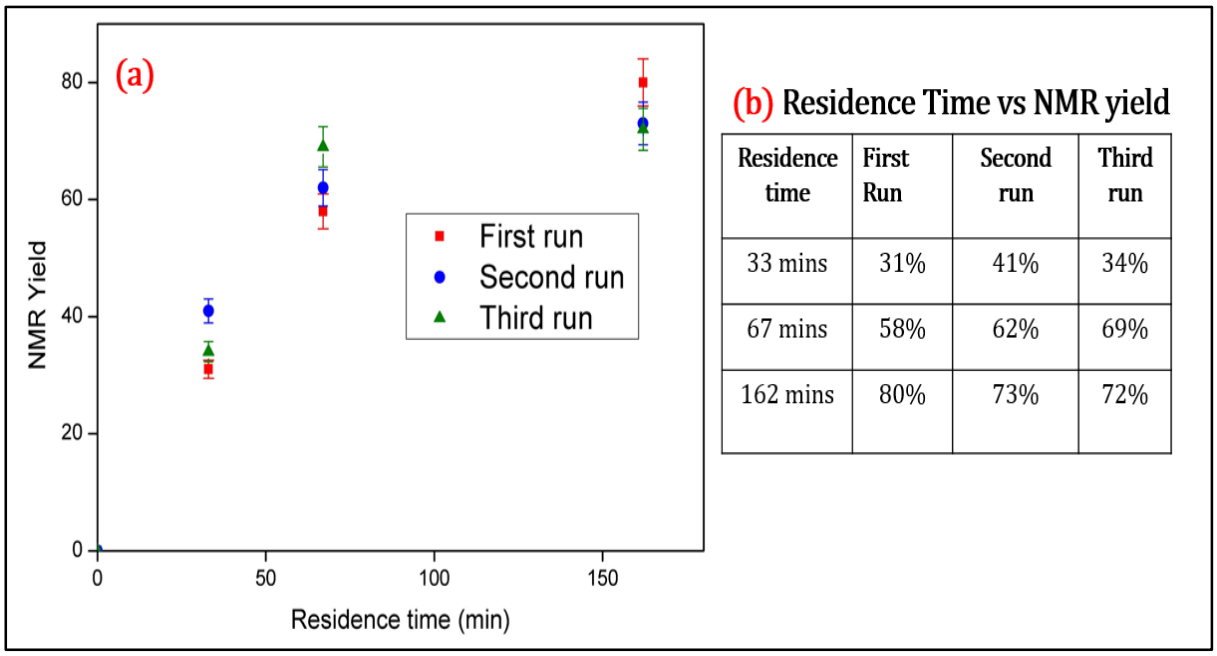

(b) Residence Time vs NMR yield

Residence time	First Run	Second run	Third run
33 mins	31%	41%	34%
67 mins	58%	62%	69%
162 mins	80%	73%	72%

Figure 7. *a. Evolution du rendement RMN pour la réaction photocatalytique de trifluorométhylation d'une arène en fonction du temps de résidence (RT) et comparaison de la recyclabilité des nanophotocatalyseurs GaInN après 3 utilisations ; b. tableau des valeurs correspondantes.*

4. Conclusion

Au cours de ce travail de thèse, plusieurs progrès ont été effectués dans la synthèse de nanophotocatalyseurs hétérogènes appartenant aux familles des matériaux nitrures binaires (GaN) et ternaires (GaInN) en utilisant les procédés de synthèse supercritiques continus. Ces nanophotocatalyseurs ont été efficacement mis en œuvre dans les processus de photocatalyse (photoexcitation directe - dégradation du Methyle Orange) et de photoréaction (photoexcitation indirecte – trifluorométhylation de composés arènes). Cette seconde application, couplée à la démonstration de la recyclabilité des nanophotocatalyseurs hétérogènes, ouvre de nombreuses perspectives pour les applications de photochimie. En effet, le développement de tels nanophotocatalyseurs hétérogènes doit permettre à terme de réduire efficacement les coûts de production en s'affranchissant des processus de purification post-synthèse nécessaires à l'élimination des photocatalyseurs homogènes classiques. Enfin, l'incorporation de groupements CF_3 dans les molécules pharmaceutiques a connu un intérêt croissant au cours des dernières années, afin d'augmenter le pouvoir d'action des molécules d'intérêt en réduisant significativement leur métabolisation par l'organisme.

General Introduction

Photochemistry or photocatalysis is a greener technology that converts abundantly available photonic energy into utilitarian chemical energy. It is highly advantageous than the conventional catalysis, as it relinquishes the thermal mode of activation and emancipates negligible toxic chemical effluents, which are predominantly released by the systems employing conventional catalysis. With rapid rise of flow photochemistry in the last decade, rendering currently requisite reactions like carbon-carbon (C-C) bond formation, carbon dioxide (CO_2) reduction, oxidation of toxic compounds, etc.; more hazardless, less emission of waste effluents and economical than conventional catalysis has fuelled research into this field by researchers across the several domains of science and engineering.

My doctoral research is fully focused on the design, development and synthesis of novel heterogeneous photocatalysts for myriad of photochemical reactions by optimum energy efficient methods. Which manifests under the 'Photo4Future' consortium funded by the European Union's Horizon 2020 research and innovation program under the Marie Sklodowska-Curie grant agreement No.641861. 'Photo4Future' targets specifically on the implementations of visible light for the chemical transformation reactions (realized in environmental remediation technologies), green activation of complex organic molecules pertaining to the synthesis of fine chemicals required by the pharmaceutical companies. It converges specifically on five essential areas of photochemistry: (i) Investigations of novel photocatalytic methodologies in continuous-flow photoreactors, (ii) development and synthesis of heterogeneous photocatalysts, (iii) modelling, design and fabrication of photo-microreactors, (iv) investigations of heterogeneous photocatalysis by in-situ spectroscopy and (v) opportunities for scalability and transport phenomenon of multiphase photocatalytic transformations. Being a part Innovative Training Network (ITN), 'Photo4Future' project concomitantly establishes a research network between universities and industries for successfully realizing the innovative models, reactor systems and methods in the five keys areas of photochemistry mentioned above.

This PhD study was carried out predominantly at ICMCB, CNRS and University of Bordeaux and secondments of research are done at Technical University of Eindhoven (Noel Research Group (NRG), Chemical Engineering department) and University of Cordoba (Nano-scale Chemistry & Bio-Mass waste valorisation group, Department of Organic Chemistry). The succeeding paragraphs briefs the importance of this research work in the heterogeneous photocatalytic fields.

The entire regime of photocatalysis diversifies itself into two categories: homogeneous and heterogeneous photocatalysis, where both kinds exhibit the fundamental behaviour of 'photon trap' and subsequent conversion of photonic energy into chemical energy. Over the past three decades, heterogeneous photocatalytic processes consisting of solid semiconductor materials used as photocatalysts have attracted increasing attention from the material scientists and the chemical engineers. This is primarily due to their propensity of facile separation from the product/unreacted streams and the exhibitence of requisite conversions and yields even after several continuous runs of recyclability. The switch of the current chemical processes from

non-renewable to renewable energy sources has triggered the outburst of research into the development of ideal semiconductor photocatalysts, which would have the ability to trap a wide range of natural (solar) / artificial photons and while possessing the superlative surface for performing several photochemical reactions. Heterogeneous photocatalysis is a typical cascaded engineering process occurring on the surface of photocatalysts. It involves photon entrapment, optoelectronic conversion of photons to charges (electrons + holes), charge separation, migration of charges to the reactants adsorbed on the surface of the photocatalysts and finally desorption of the products from the surface.

The nanomaterials (especially quantum confined semiconductors quantum dots - QDs) can provide high surface area for such cascaded surface processes and have become a prominent domain of research in the heterogeneous photocatalytic field. Any advanced photocatalytic system realized, should achieve the three indispensable criteria: (i) high specific surface area, (ii) enhanced light absorption capacity and (iii) increased photocatalytic activity. As the nanomaterials fulfils the first criteria easily, most of the studies concerning the design and synthesis of semiconductor photocatalysts in this research are primarily relied on the nanoscale domain.

To successfully procure heterogeneous photocatalysts required for the current developed/developing photochemical applications, I have classified the regime of nanophotocatalysts into four different families of heterogeneous photocatalysts:

I. Binary nanophotocatalysts

Highly quantum confined metal-oxides, sulfides and nitrides of the group II-VI & III-VI photocatalysts fall under this family. They heavily addressed in the flow hetero photochemistry due to their interesting optoelectronic, thermal and mechanical properties. Many of the photocatalysts of this group are commercially available and require development in its synthetic modes and surface tuning methodologies.

II. Ternary nanophotocatalysts

Ternary mutli-metallic materials consisting of two different metallic cations and a single anion. They possess all the properties and beneficial factors of binary materials but exhibit enhanced photocatalytic activity in many instance due to their dispersed valence band or conduction band, unlike binary nanophotocatalysts, their synthesis lies in the dormant phase due to the lack of cheap precursor and synthetic methodologies.

III. Solid solution nanophotocatalysts

Optical properties of semiconductor photocatalysts are tuned in this system through precise engineering of the band gap by combining two different semiconductor materials with different optical properties; this system involves co-synthesis of two semiconductors, where one semiconductor materials successfully fit in and distributes itself into the lattice of the host semiconductor. This system is famous for producing visible light active heterogeneous photocatalyst but an optimum balance is required between the requisite redox potential and visible light activity.

IV. Nanocomposite photocatalysts

This system involves the growth of a semiconductor material on another solid semiconductor photocatalysts resulting in type II heterojunction semiconductor. Usually core/shell systems are realized in this photocatalytic materials. This material is targeted achieving both ameliorated light absorption capacity and appropriate redox potentials for performing several photochemistries.

This PhD work is systematized in realizing the novel semiconductor materials confining to the regime of four different heterogeneous nanophotocatalytic families for successfully performing the photochemical reactions targeted by 'Photo4Future' project. The first chapter of this PhD thesis is dedicated to the review specifically anatomizing the various reported nanophotocatalysts' synthetic methodologies and their corresponding photochemical applications. This work completely explores the rationality behind the design of the semiconductor photocatalysts and motivation of their system for successfully carrying out the requisite photochemical reactions. The critical assessment carried out here briefly reports the synthetic modes of nanophotocatalysts belonging to the four different families of heterogeneous system, their reactive medium, precursors, reactive conditions (temperature, pressure, etc.). Finally concludes with the process setups and engineering techniques carried out for effective implementation of the as-synthesized photocatalysts in diverse photoreactors.

Following this intensive review, Gallium Nitride (GaN) semiconductor were opted as a base semiconductor system in this PhD study. Although GaN is one of the third generation semiconductor, which has been widely commercialized in the electrical and optoelectronic fields, its exploration as a photocatalyst has only started recently. GaN possesses enhanced electron transport property due to its superior drift velocity and exhibits strong atomic bonding between gallium and nitrogen (covalent bond) resulting in a semiconductor material possessing exalted mechanical stability along with great chemical inertness in harsh acidic and basic environments, even at high temperature reactive environments. The second chapter of this thesis deals with continuous synthesis of highly quantum confined GaN colloidal nanomaterials and subsequently targets its implementation in the environmental remediation photochemical reactions through direct photochemical excitation mode of heterogeneous photocatalysis.

The final chapter specifically targets in the continuous supercritical synthesis of highly visible light active semiconductor nanophotocatalysts to replace to the conventional, costly (economically non-viable), complex Tris(bipyridine)ruthenium(II) chloride ($[Ru(bpy)_3]Cl_2$) homogeneous photocatalysts used for the photocatalytic synthesis of efficient drug molecules with high biological activity. Ternary solid solution of GaN and InN nanomaterial was opted here to replace ruthenium complex catalysts, as GaN and InN (Indium Nitride), being a direct band gap semiconductor form a $Ga_xIn_{1-x}N$ solid solution, rendering an opportunity for utilizing photons across the entire visible range of the electromagnetic spectrum

Thanks to the funding provided by the Marie Sklodowska-Curie grant agreement through the 'Photo4future' project, which has successfully rendered me in developing novel heterogeneous photocatalytic materials for successful application in both water treatment (environmental

clean-up process) and efficient drug synthetic methodologies (as required by pharmaceutical industries).

Chapter 1

Heterogeneous nanophotocatalysts: synthetic approaches and applications

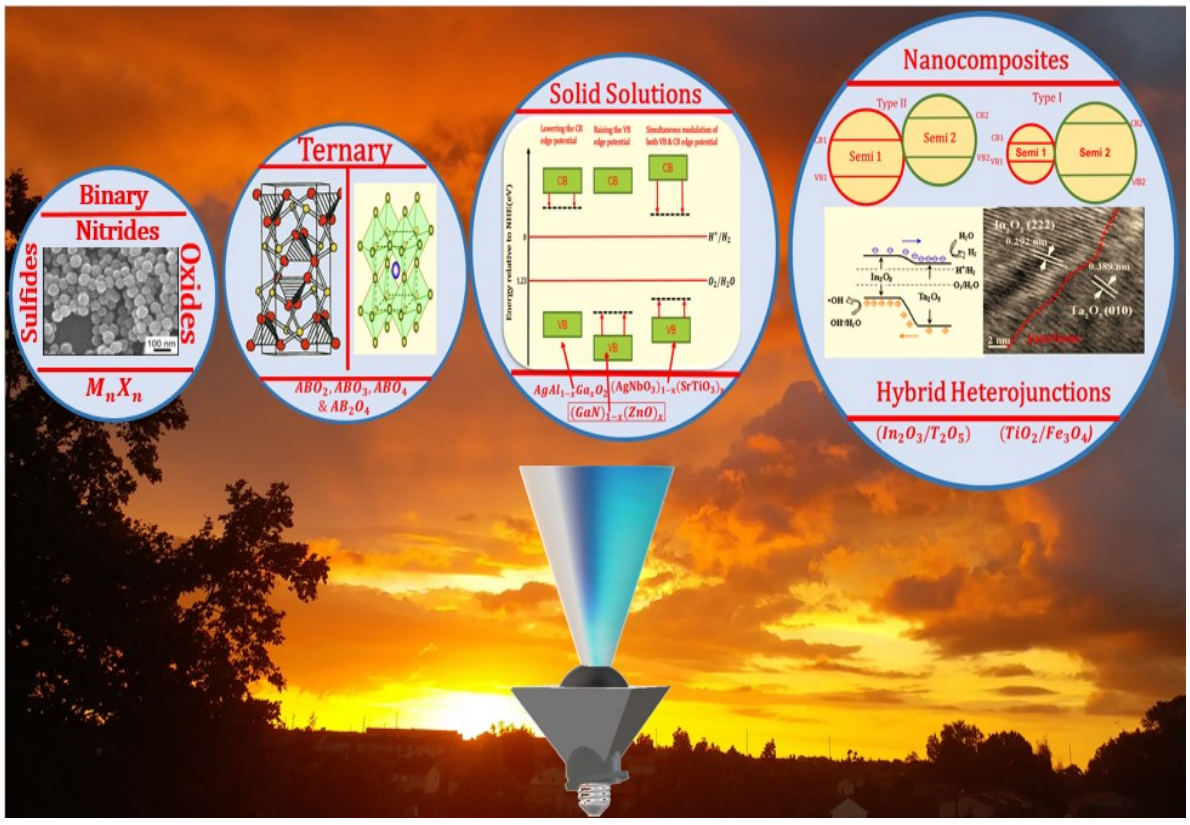

Contents

1. Heterogeneous nanophotocatalysts: synthetic approaches and applications 17

1.1. Introduction 21

1.2. Photocatalysis 23

1.2.1. Homogeneous photocatalysis 23

1.2.2. Heterogeneous photocatalysis 26

1.3. Heterogeneous photocatalytic systems 29

1.3.1. Types of photocatalytic semiconductor systems 29

1.3.2. Nano-binary photocatalysts 31

1.3.2.1. Oxide-binary photocatalysts 32

1.3.2.2. Chalcogenide-based binary photocatalysts 33

1.3.2.3. Nitride-based binary photocatalysts 35

1.3.3. Ternary multi metallic photocatalytic materials 38

1.3.3.1. Introduction 38

1.3.3.2. Ternary oxide photocatalysts 38

1.3.4. Solid solution photocatalysts 48

1.3.3.3. Solid solution through continuous modulation of CB 50

1.3.4.2. Solid solutions through modulation of VB 51

1.3.4.3. Solid solution through modulation of both CB and VB 53

1.3.4.4. Conclusion 58

1.3.5. Nanocomposite photocatalysts 61

1.3.5.1. Types of nanocomposite photocatalytic systems 61

1.3.5.2. Semiconductor-metal composite systems 62

1.3.5.3. Semiconductor-semiconductor composite systems 62

1.3.5.4. Considerations of semiconductor-semiconductor coupled nanocomposite photocatalytic systems 64

1.3.5.5. Nanocomposite semiconductor photocatalysts 65

1.3.6. Conclusion of heterogeneous photocatalysts 80

1.4. Reactor design & implementation of photocatalysts in photochemical processes 81

1.4.1. Solid-Liquid (diphasic) & Solid-Liquid-Gas (triphasic) phase systems in heterogeneous photocatalysis 82

1.5. Conclusion and outcome of literature survey 88

1.1. Introduction

The world economy has already started its shift from conventional energy sources to non-conventional ones due to the dramatic increase of CO_2 emission and the possible correlation with climate change. The transpose is happening in a rapid phase not only in the energy sector but also in the chemistry and the chemical engineering fields. The final objective of such strategies is to limit an environmental impact by developing processes, which allow the reduced use of toxic compounds for providing more sustained development of mankind for the next generations.

So far, the domain of renewable energy, indicates always its current inability to attain maximum efficiency compared to the non-renewable energies. Mimicking the naturally driven processes and implementing them for our daily use is one of the elementary way by which non-conventional energy sources can attain maximum utility. Photosynthesis is one such of novel natural process through which life on earth thrives by trapping solar energy and transforming it into chemical energy. Entrapment of solar light has diversified benefits in the form of photovoltaics (production electricity) and heat (thermal production) apart from the chemical energy production. Availability of solar energy is abundant in nature and duration of its accessibility is almost infinite in time scale with zero opportunity cost.

Analogous to the chlorophyll of leaves, several organic and inorganic materials have been developed in the last century, which traps the light at various energies of the electromagnetic spectrum. These materials imitate the three basic process of chlorophyll upon interaction with photons, which are: trapping of radiations, charge separation (creation of electrons and holes) and redox reactions by the separated charges. Such materials are called photocatalysts and they have been one of the mile stones for making efficient use of sunlight, for the complete shift to renewable domain especially in the energy and the synthetic fields.

Thanks to organic chemists and material scientists, several varieties of photocatalysts are currently available. The design and development of new types of photocatalytic materials are happening at a sporadic rate. Comprehensively, the available materials can be grouped into two different categories: (1) homogeneous and (2) heterogeneous photocatalysts. Within these two different domains, heterogeneous semiconductor-based photocatalysts have received increasing attention in the last 4 decades due to their many advantageous features, such as their recyclability and chemical stability, compared to their organic counterparts.

In this chapter, we have focused on the diverse heterogeneous photocatalysts reported so far in the scientific community. We have classified the reported heterogeneous photocatalysts into four different families, depending on (i) the increasing order of number of elements in the composition of semiconductor photocatalysts, (ii) the complexity of their morphology & band structure, (iii) the meticulous tuning of their optical band gap and finally, (iv) concomitant attainment of both light absorption capacity and enhanced photocatalytic activity.

The pattern of progression in the development of semiconductor materials within the perspective of ‘sensitized photoreaction’ has led us to classify them into four different families.

1. Binary nanophotocatalysts

Binary semiconductor materials composed of two different elements, metallic cation and non-metallic anion, which are explored as the initial class of photocatalysts, are reviewed in this section. For many binary photocatalysts the timeline of their exploration as photocatalysts has instigated several decades back. The current updated synthetic methodologies to produce them with enhanced surface properties and higher production rate are reported. Finally, the upcoming binary compounds, which are in the initial stages of exploration as photocatalysts are also reported in this section.

2. Ternary nanophotocatalysts

Following binary compounds, ternary semiconductors composed of two different metallic cations and a non-metallic anion fall as a succeeding set of photocatalysts, researched to a vast range in heterogeneous photocatalysis. Here the most imperative kinds of ternary photocatalysts, their upgraded synthetic techniques and the successful photochemistry achieved using them are reviewed.

3. Solid solution nanophotocatalysts

Reckoning of several benefits from sensitized photoreaction domain especially for environmental remediation and novel organic synthesis has led material scientists to design photocatalysts by combining two different binary compounds or ternary compounds resulting in solid solution materials which are usually synthesized to be active in the visible region. The three different kinds of band gap engineering strategies researched in the solid solution domain, for rendering them active as visible light photocatalysts, are reviewed in this portion.

4. Nanocomposite photocatalysts

Type II semiconductor heterojunction resulting in a nanocomposite material composed of two different compounds are identified as epitome of semiconductor photocatalysts in the current time span. Such novel examples of nanocomposites, with optimum balance of optical band gap and appropriate band edge potential for photocatalysis, are delineated in this unit.

The entire scheme of this chapter is designed in such way that, we will first deal with two broad kinds of photocatalysis carried out in the scientific community: homogeneous photocatalysis & heterogeneous photocatalysis. We will then move the trajectory of discussion more into heterogeneous photocatalysis explaining its two different modes of operation in the photocatalytic world:

- **Direct photochemical excitation or catalysed photoreaction.**
- **Indirect photochemical excitation or sensitized photoreaction.**

Among the two different processes of heterogeneous photocatalysis, extensive studies on semiconductor's implementation as photocatalyst were carried out in **'Indirect photochemical excitation'** domain. In such a novel sphere, in order to attain the efficient entrapment of photonic energy and good reaction kinetics, the novel semiconductor materials are continuously designed and developed to possess high surface area for photochemical reaction, appropriate band edge potentials, precise tuning of optical band gaps and visible light activity.

To conclude, the recent developments within the different families of heterogeneous photocatalysts, along with their photochemical applications and photoreactor systems, will be detailed in this chapter.

1.2. Photocatalysis

Photocatalysis is an intriguing chemical process in which the mode of activation of the catalyst takes place by photonic energy instead of thermal energy as in traditional methodology of catalysis. It is a phenomenon in which acceleration of a photoreaction takes place in the presence of a substance called photocatalyst. Speeding up of photoreaction occurs by the interaction of photocatalyst with reactive substrates in ground state or excited state. Predominantly, the term photocatalysis designates both the process, 'catalyzed photoreaction' and 'photosensitization'.

The process, where molecular transformations or alterations are happening in a molecule due to the interaction of electromagnetic radiation in an another molecule called sensitizer, is called photosensitization. This occurs when the light is absorbed by the sensitizer molecule (photocatalyst) and then it interacts with the reactive substance through energy or electron transfer. Analogously in catalyzed photoreaction, the light is absorbed by the reactive molecule(s). The photocatalyst speeds up the reaction by interacting with reactive substrate(s) either in ground or excited state and in some reactions even with the photoproducts resulting in an enhanced photoreaction. Photocatalysis on the whole refers to both the above mentioned diverse processes and is always defined in a wider language without any special indications to any one of the processes. The IUPAC definition of photocatalysis: "Change in the rate of a chemical reaction or its initiation under the action of ultraviolet, visible or infrared radiation in the presence of a substance—the photocatalyst—that absorbs light and is involved in the chemical transformation of the reaction partners" [1].

Like photocatalysis, the photocatalyst is also defined in a broad manner as a substance, which upon absorption of electromagnetic radiation (especially ultraviolet (UV), visible and infrared (IR) light), is able to chemically transform the reactants by interacting with them, in its excited state. The photocatalyst also regenerates itself after transforming the reactants into the products. The entire domain of photocatalyst diversifies itself into two different sections: homogeneous photocatalysts and heterogeneous photocatalysts. The chemical process implementing the homogeneous or heterogeneous photocatalyst is again termed as homogeneous or heterogeneous photocatalysis, respectively.

1.2.1. Homogeneous photocatalysis

When the reactants and the photocatalysts are present in the same phase, it can be termed as a homogenous photocatalytic system, as visualized in Figure 1.1. Initially, in the photocatalytic world, homogeneous systems were developed specifically for the removal of water pollutants, where the photocatalyst involves the generation of highly reactive species $OH^{\cdot}$ radicals. The common examples of such systems are: 1.H_2O_2/UV system, Ozone/UV and Photo-Fenton system [2, 3]. These systems are examples of Advance Oxidation Processes (AOPs), where oxidants like H_2O_2 and O_3 upon interaction with UV light were successful in releasing the $OH^{\cdot}$ radicals and oxidizing the pollutants which are soluble in water [4]. For the containments,

which are insoluble in water and dispersed, the Fenton's reagent (Fe^{2+}/H_2O_2) were found to be very successful in eliminating insoluble pollutants. Here hydroxyl radicals are produced by the reaction of ferrous salts and H_2O_2 [5]. The combination of the photons and Fenton's reagent (Photon-Fenton system) was more successful than the Fenton's reagent alone for the water purification of both soluble and insoluble pollutants due to the recycling of Fe^{2+} ions [6].

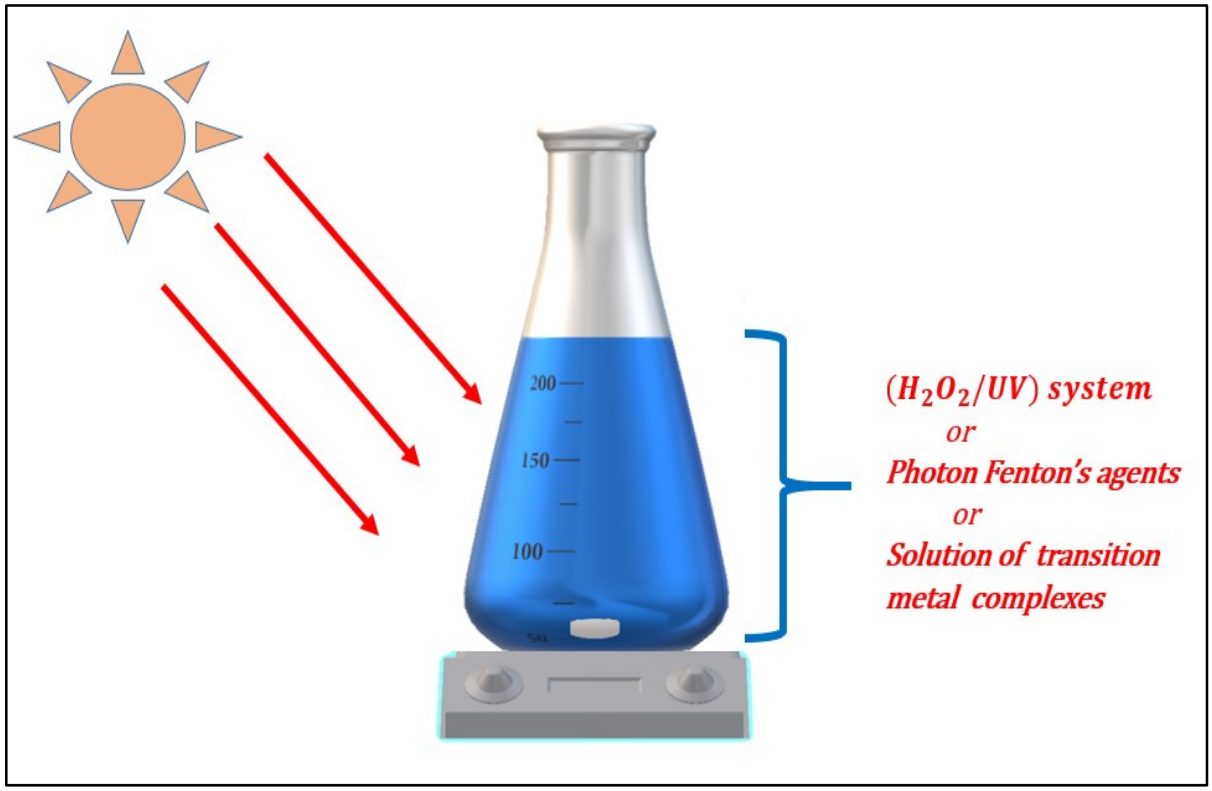

Figure 1.1. *A schematic depiction of a homogeneous photocatalytic system, where the photocatalyst exists in the same phase (liquid) as the reactant, for example: aqueous solution of [Ru(bpy)$_3$]Cl$_2$ (Tris(bipyridine)ruthenium(II) chloride).*

Most of the homogeneous systems are transition metal complexes, which in general possess a ligand co-ordinated to a metal ion (ML_n). Complexes of iron, copper and chromium have been reported for environmental remediation process (water purification) [7]. Besides, many transition metal complexes (ruthenium and iridium) have been reported for the synthesis of novel organic molecules by their ability to generate various radicals and activate many substrates [8]. As an example, visualization of such visible light active transition metal homogenous photocatalyst is depicted using polypyridyl complex of ruthenium, tris(2,2'-bipyridine) ruthenium(II) or $Ru(bpy)_3{}^{+2}$ shown in Figure 1.2-a.

In $Ru(bpy)_3{}^{+2}$, following the absorption of an electromagnetic radiation, a metal electron of the complex is excited to antibonding orbital on the ligand of the same complex, which results in the transfer of charge from the metal to ligand and the process is termed as Metal to Ligand Charge Transfer (MLCT). From this excited singlet state in the ligand, the electron undergoes rapid Intersystem Crossing (ISC) and reaches the lowest energy triplet state. Relaxation of the charge from the lowest energy triplet state to singlet ground state is quantum mechanically

restricted due to forbidden spin transition (relaxation from triplet to ground state). Due to which, the rate of relaxation of the excited state is slowed down resulting in an increased lifetime of the excited states (1100 ns for $Ru(bpy)_3^{+2}$), which is highly required for efficient photocatalytic activity [9 – 12].

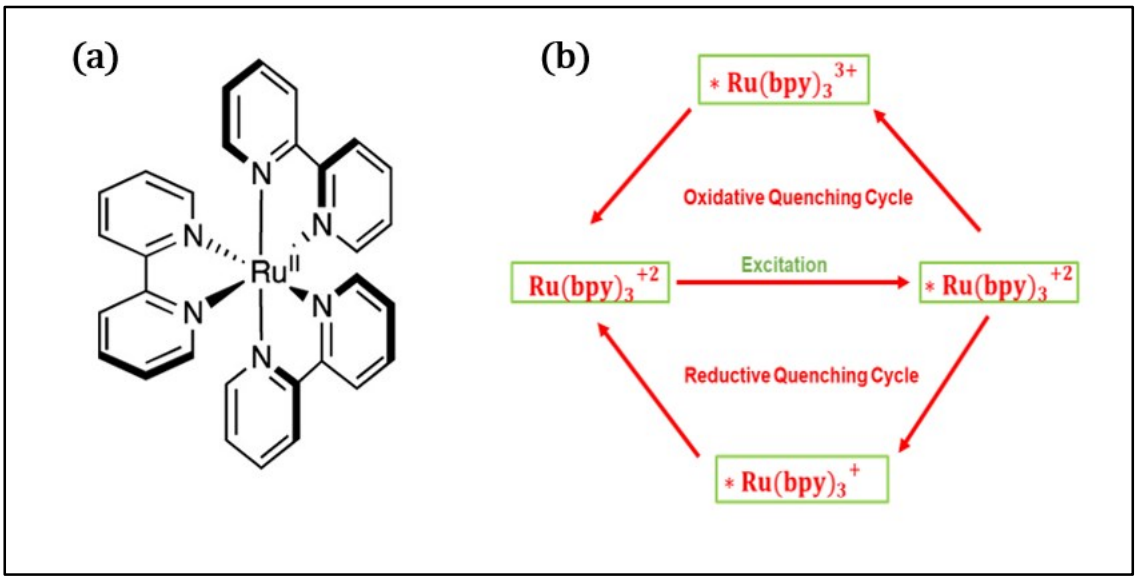

Figure 1.2. *a. Homogeneous photocatalyst: Ruthenium polypyridyl complex [8]; visible light active, absorption at 452nm; b. Photocatalytic cycle of homogeneous Ruthenium complex system.*

The complex, upon excitation, can proceed either via an oxidative or a reductive quenching cycle depending on the electron acceptors or donors present in the reactive medium under illumination of visible light. The excited photocatalyst $*Ru(bpy)_3^{+2}$ behaves as an oxidant in the reductive quenching cycle and as a reductant in the oxidative quenching cycle. The simple scheme representing the corresponding oxidative and reductive quenching cycle of $Ru(bpy)_3^{+2}$ complex upon excitation is depicted in Figure 1.2-b, as a typical example of transition metal complex homogeneous system. Conjunction of visible light activity, extended lifetime of photo excited states with successful engagement of bimolecular electron transfer process with various reactive substrates for $Ru(bpy)_3^{+2}$ and other complexes [9] have successfully rendered the above mentioned complexes as an enhanced homogeneous photoredox catalysts for photocatalytic water splitting reactions [13, 14] and carbon dioxide photo reduction to methane [15]. These complexes have also successfully procured the prosperous implementation of photocatalytic C-C bond formation: [2+2] cycloaddition [16] and direct asymmetric alkylation of aldehydes [16]. Similarly, the $Ru(bpy)_3^{+2}$ complexes have also attained buoyantly C-C bond construction through photocatalytic reductive dehalogenation of alkyl halides strategy [16].

The commercialization of such advantageous homogeneous photocatalyst for exploiting its enormous photocatalytic applications for our daily use was highly debilitated by the pitfall it possesses. Since in homogeneous photocatalysis, reactants, products and photocatalysts are present in the same phase, recovery of the photocatalysts from the reactive medium is very

difficult and is a highly energy exhaustive process. Certain well developed mass transfer operations involved in the recovery of the photocatalyst may even tend to damage or deactivate the photocatalyst. Another major pitfall of homogeneous photocatalysts, is its fragile stability at harsh photocatalytic conditions (high basic & acidic environments) [17]. Finally, such homogeneous photocatalysts exhibit high production cost compared to the commercially available semiconductor photocatalysts. These limitations are solved using heterogeneous photocatalytic systems, which will be dealt more in detail in the upcoming sections.

1.2.2.Heterogeneous photocatalysis

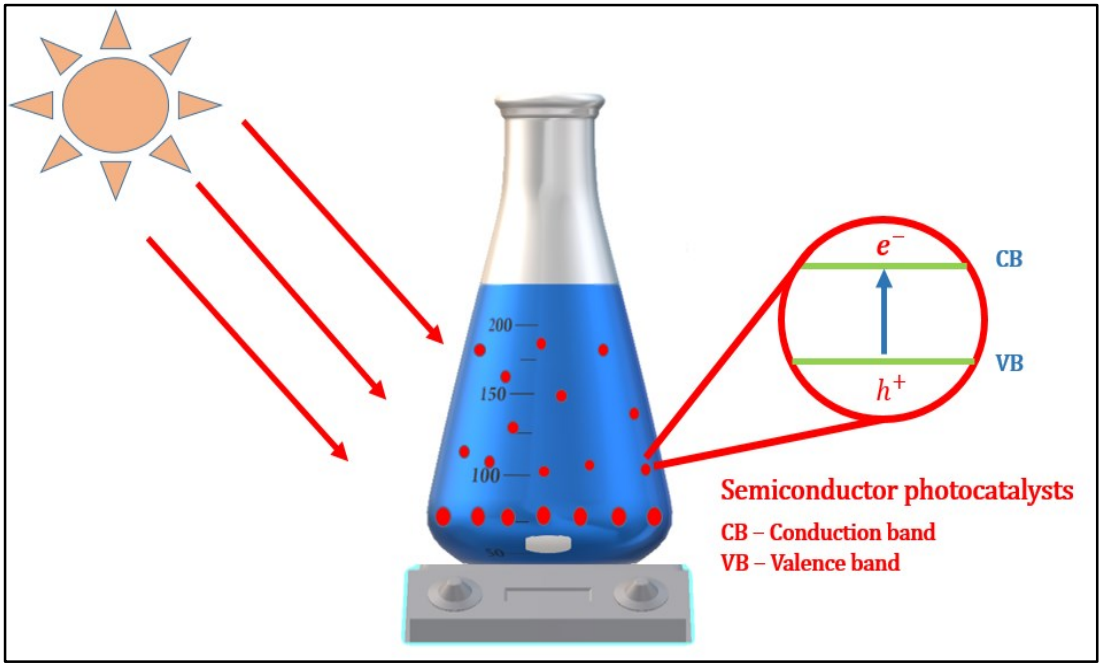

Figure 1.3. *Schematic depiction of a heterogeneous photocatalytic (semiconductor) system, semiconductor particles are dispersed in liquid phase.*

When the reactant molecules and the photocatalysts are present in different phases, the system can be termed as a heterogeneous photocatalytic system. Heterogeneous system consists of a solid semiconductor material(s) dispersed in the liquid or gas phase, where the semiconductor serves as photocatalyst and the photochemical reactions take place on the surface of the semiconductor material, as visualized in Figure 1.3. Heterogeneous photocatalysis is a classical area of science involving the combination of different phases. It is a polyphasic system, where different phases are working together in co-operation during the process [18]. Basically, the two main phases present in heterogeneous system are (i) the solid (semiconductor material) and (ii) the fluid phase (liquid-solvent or reactant and/or gas-reductant or oxidant). The photons activate the semiconductor material or the substrate and produce the charges for the reactions to occur. The photon flux is considered as “special phase” and it is designated as an “electromagnetic phase” [19]. A simple depiction of charge generation and surface bound photoredox reactions in semiconductor heterogeneous photocatalysis is portrayed in Figures 1.4 and 1.5.

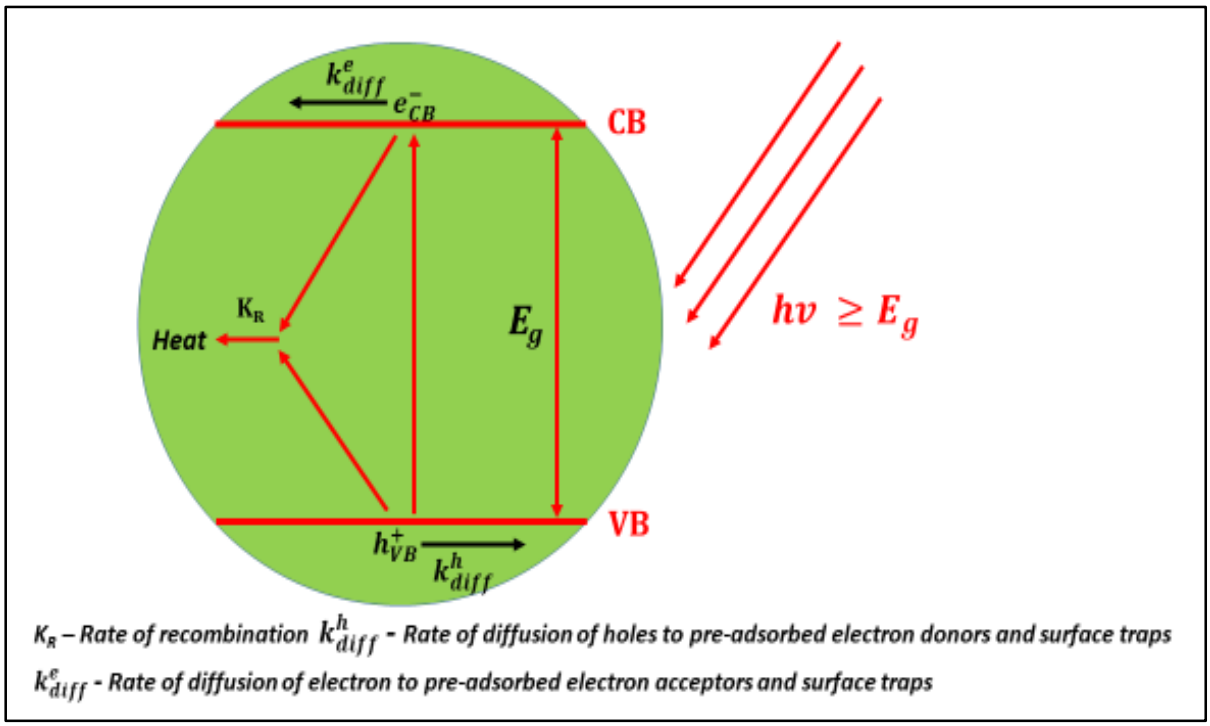

Figure 1.4. *Photophysical events in a spherical semiconductor particle upon excitation with photons possessing energy higher than its band gap.*

Semiconductor materials do not possess continuous energy levels as present in metals. They exhibit a band gap (E_g) between a top level of filled Valence Band (VB) and bottom of the empty Conduction Band (CB). When exposed to photons possessing energy (hv) higher than the band gap of semiconductor ($hv \geq E_g$), electron is promoted from the VB to CB, generating a hole in the VB, as depicted in Figure 1.4. The separated charge carriers undergo several routes upon excitation. Due to the presence of non-passivated surface states, the charges migrate to the surface of the semiconductor upon separation due to excitation. At the surface, the migrated electrons can reduce the acceptor molecules, the holes can oxidize the donor molecules pre-adsorbed on the surface, as depicted in Figure 1.5. The rate of charge transfers to the adsorbed species depends specifically on the position of the valence and conduction band edges and the redox energy levels of the adsorbed species. Parallel to these charge transfer events, the separate charge carriers can also recombine within the bulk of semiconductor (volume recombination) or on the surface of the semiconductor, resulting in heat dissipation. Therefore, heterogeneous photocatalysis is an exothermic process, where the charge transfer from the semiconductor to the adsorbed species is a continuous process upon the absorption of light with energy higher than the band gap of semiconductor [20].

The efficiency of heterogeneous photocatalysis can be quantified by quantum yield (Φ), expressed as:

$$\Phi = \frac{rate\ of\ product\ formation\ (mole\ s^{-1})}{rate\ of\ photon\ absorption\ (einstein\ s^{-1})} \quad (1.1)$$

In the equation (1.1), the rate of product formation is directly proportional to the rate of charges transferred to the reactant species adsorbed on the semiconductor surface (k_{CT}). Meanwhile,

the rate of photon absorption is proportional to the sum of the rates of recombination of charge carriers (k_R) and charge transfer to the reactant species (k_{CT}), as:

$$\Phi \propto {k_{CT}}/{(k_{CT} + k_R)} \tag{1.2}$$

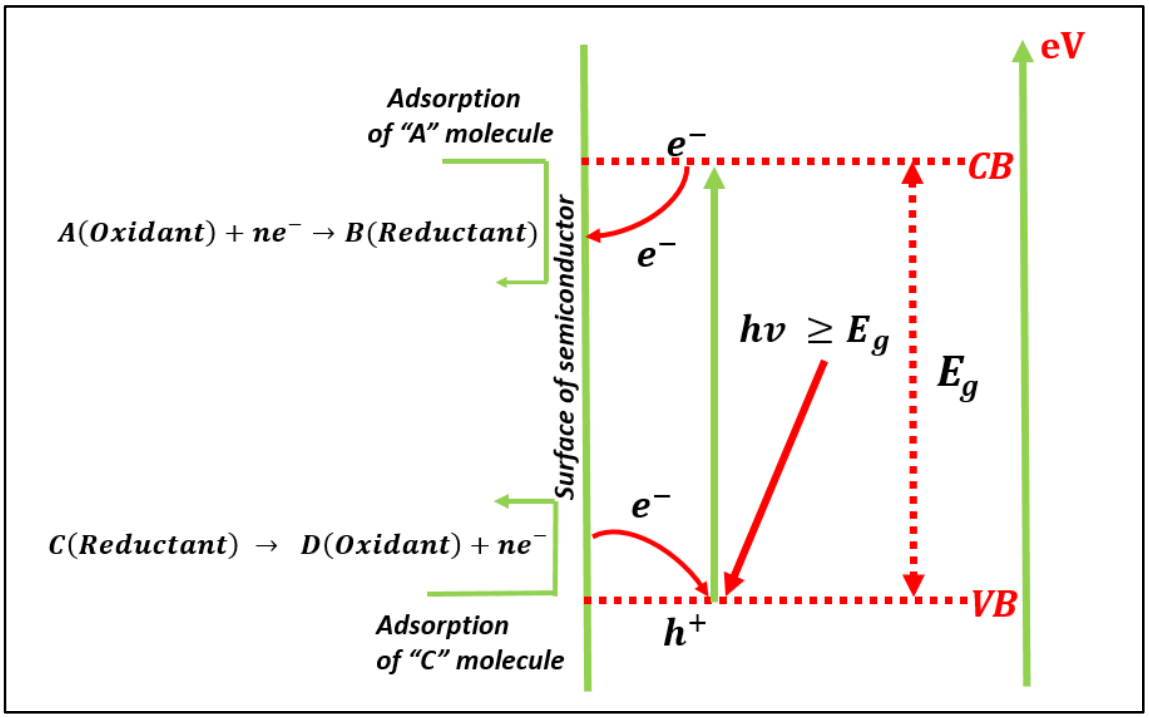

Figure 1.5. *Photochemical reactions on the surface of semiconductor particle upon excitation with photons possessing energy higher than its band gap.*

Heterogeneous photocatalytic system can be further classified into two different categories depending on whether excitation takes place on the photocatalyst or on the adsorbed substrate:

Indirect photochemical excitation or sensitized photoreaction

When the excitation takes place within the semiconductor material and charge transfer occurs from the excited semiconductor to the ground state of the adsorbed species as described above, it is called indirect photochemical excitation or sensitized photoreaction.

Direct photochemical excitation or catalysed photoreaction

When the excitation occurs on the adsorbed reactants on the semiconductor surface, which then transfer the charges to the catalyst substrates, it is called direct photochemical reaction or catalysed photoreaction [21].

In general, in heterogeneous photocatalysis regime, the report of direct photochemical excitation system is very rare due to its extremely low efficiency compared to the sensitized photoreaction. Limited amount of articles is found for direct photochemical system [22 – 24]. Therefore, in this chapter all the heterogeneous photocatalysis examples refer to indirect

photochemical reactions only. If any examples of direct photochemical reaction arise, they will be mentioned specifically.

1.3. Heterogeneous photocatalytic systems

Heterogeneous photocatalysis can be regarded as a cascaded engineering which involves various processes like optoelectronic conversion, charge transfer occurring on the surface/interface and finally downstream process of separation and recycling of the photocatalyst. Thus, whenever a photocatalytic system is desired to be made into commercial use, the above mentioned process should be optimized and incorporated into the desired photocatalytic system. Hence, the need of commercialization requires the optimization of the photocatalytic system, which leads to the development of advanced photocatalytic semiconductors such as solid solutions and hetero-composite compounds, mostly composite nanostructures.

1.3.1. Types of photocatalytic semiconductor systems

The growing demand of energy production from our contemporary sources and simultaneous repercussions to environment from waste of such sources have pushed the researchers to develop highly efficient systems for photocatalytic processes. The main application concerns the degradation of pollutants, the synthesis of organic compounds (especially drugs in pharmaceutical industry) and carbon dioxide conversion to useful fuels. Therefore, material scientists have developed semiconductor materials to transpose the several novel viable photochemical reactions from homogeneous to heterogeneous systems. As a result, numerous novel semiconductors have been widely researched and reported as effective photocatalysts in the past decades.

Most of the review articles reported so far in this field, have mainly focused on reporting the applications of the well-known Titania (TiO_2) photocatalyst along with the mechanism and fundamental reasoning for its high photocatalytic performance [20, 25]. Some other reviews have focused on reporting the fundamental aspects of particular applications using heterogeneous photocatalysts such as: dye degradation, removal of aqueous pollutants [26], [27], hydrogen production [28]. The other reviews reported concern the fundamental understanding of semiconductor band bending and its influence in heterogeneous photocatalysis [21], bridging of homogeneous and heterogeneous photocatalysts through coordination chemistry for novel performances [29] and strategies involving modifications of semiconductors for improving the selectivity of heterogeneous photocatalysis [30]. To date, there has been no review consolidating the different semiconductor systems and the rationale behind their design or indicating the particular photochemical reactions for which their performance was higher compared to other semiconductors, along with the type of photoreactor systems in which the photocatalysts are implemented.

As material scientist, the rationale behind this chapter is to give an overview of the various existing semiconductor materials and to segregate them into different families of photocatalytic systems. Obviously, we did not aim to address all the semiconductors here, but rather focusing on the most efficient ones. Concurrently, I report the current updated synthetic methodologies

for obtaining such novel semiconductors and I provide a description of the polyphasic photocatalytic reactor system in which they have been implemented.

Since 1972, when Honda and Fujishima observed the photosensitization effect of single titania crystal for photoelectrochemical water splitting under UV light [31], many semiconductors have been explored for photocatalysis. Simultaneously, the explored semiconductors were modified to alter the redox potentials for performing particular photoreactions like the synthesis of powdered Fe (Iron)-doped TiO_2 for the photocatalytic decomposition of water [32]. Charge separation kinetics were increased in such systems due to the transfer of photo-induced electron from the semiconductor to the noble metal. Recombination lifetime of electron-hole pairs in excited semiconductor materials was also reduced by other transition metal doping [33]. The excitation wavelength range of particular semiconductors was altered into wider range by dye sensitization or by the synthesis of nanocomposites. All these strategies can be visualized in Figure 1.6.

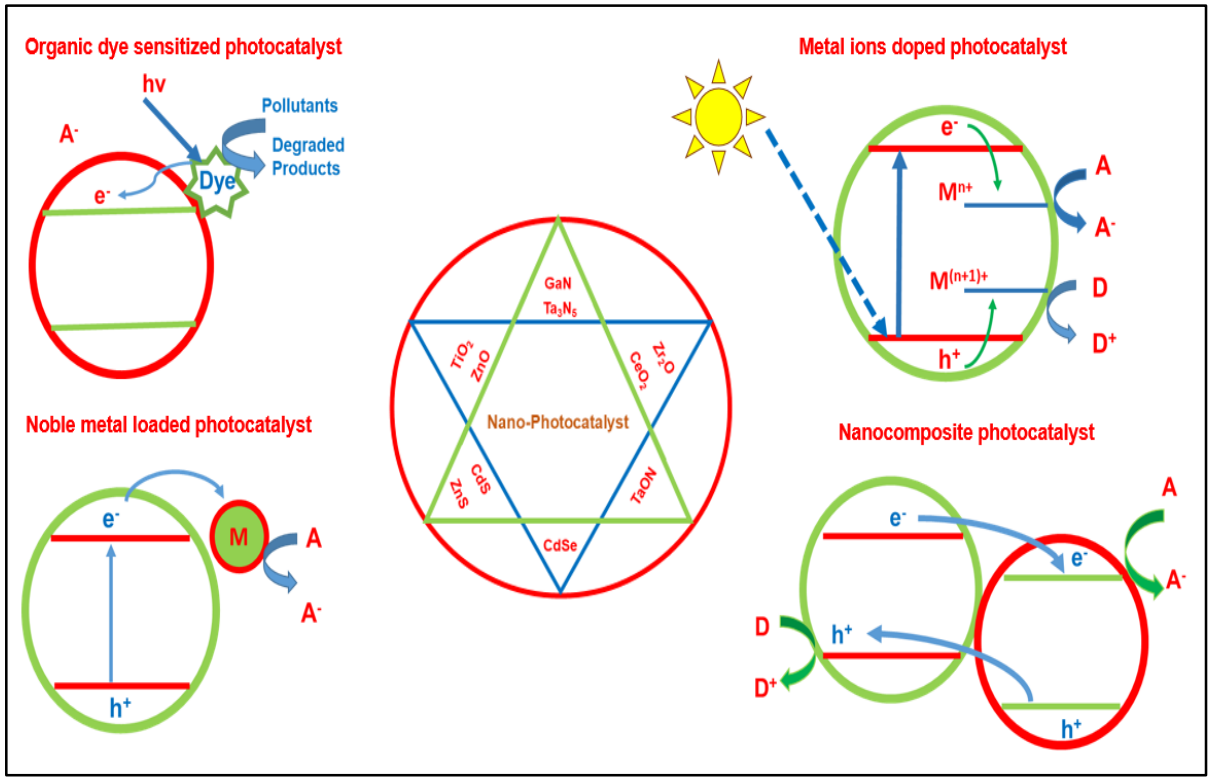

Figure 1.6. *Various strategies to engineer the band gap of semiconductor photocatalysts.*

In the past decades the strategies for modifying the semiconductors to perform different photochemistries or rendering them active in the visible region remained the same, but the attempt was carried out in a wider range of semiconductors, including the titania. In the recent times, many synthetic methodologies were reported for these modifications, which yielded photocatalysts with better catalytic performances. These novel semiconductor systems and their synthetic strategies are addressed here. As mentioned previously we have classified the photocatalytic materials in four diverse categories, which are detailed in the next sections.

1.3.2. Nano-binary photocatalysts

Among the inorganic semiconductors, the metallic-oxides/ sulfides of group II-VI & III-VI were the initially explored as binary semiconductors in heterogeneous photocatalysis due to their interesting optoelectronic properties. TiO_2, ZnO, ZrO_2, ZnS and CdS are among those binary semiconductors, which are researched for the past three to four decades with much attention due to their great performance for degrading various environmental pollutants in heterogeneous photocatalysis. The improvement of mechanical, chemical, optical and catalytic properties of binary semiconductors in the nanodomain has consistently pushed researchers for developing synthetic methodologies for these semiconductors. The developed methods have targeted for obtaining monodispersed particles with well-defined surface properties. Since heterogeneous photocatalysis is a surface phenomenon, the efficiency of the photochemical reaction is always function of the available surface area and phase purity of the surfaces. Through synthetic methodologies, the photocatalytic enhancement of binary semiconductors is attained by playing with the operating parameters to achieve monodispersed, structurally well-defined samples with good optical and catalytic properties.

The synthetic approaches for obtaining highly quantum confined nanomaterials with enhanced surface properties for heterogeneous photocatalysis were flourishingly furnished in the three different categories of binary semiconductors: oxides, chalcogenides and nitrides, as described in Figure 1.7. I discuss hereafter, some examples of binary photocatalytic materials along with their synthetic approaches and applications. The intrinsic attributes of the synthetic conditions and nature of the nanomaterial synthesised as a result of such reactive domains are summarized in Table 1.1.

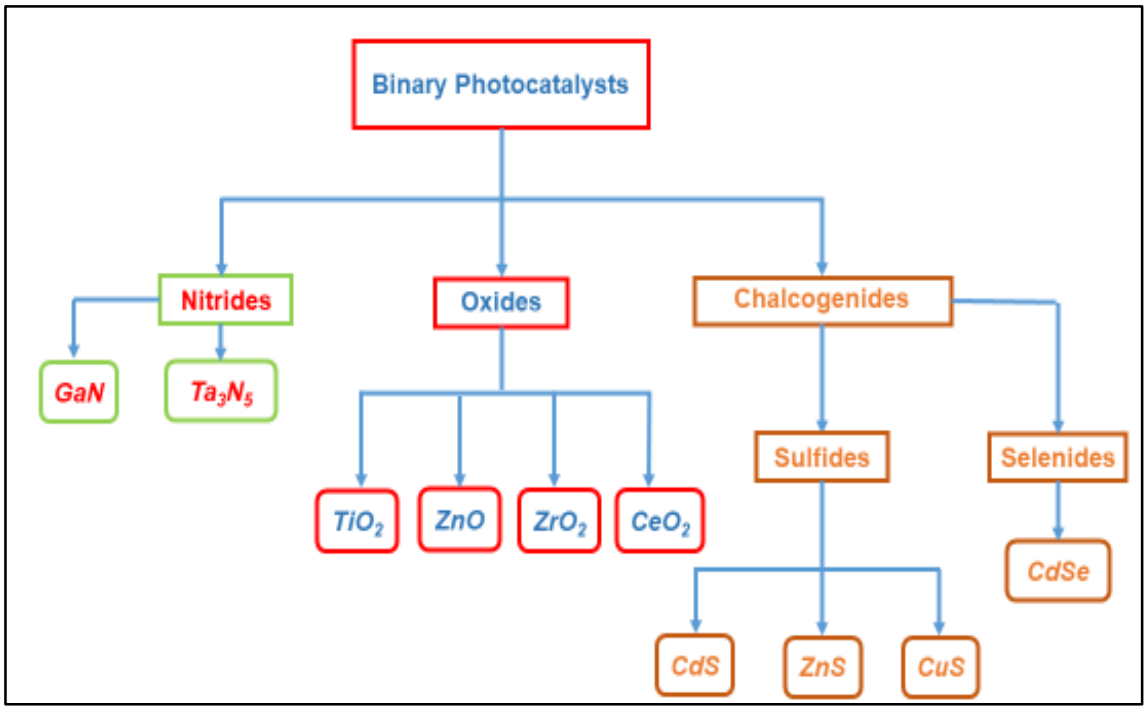

Figure 1.7. *Overview of binary semiconductor photocatalysts reported in this chapter.*

1.3.2.1. Oxide-binary photocatalysts

Teoh *et al*. synthesized TiO_2 nanoparticles by flame pyrolysis method (Figures 1.8-a and 1.8-b, which exhibited higher activity for sucrose photo-mineralization than commercially available Degussa P25 [34]. Direct Flame Spray Pyrolysis (FSP) technique yielded nanomaterials with well managed specific surface area, and morphology and high purity of crystallite phases without the requirement of post treatment techniques (precipitations and centrifugations, etc.). Here, different particle sizes were obtained by varying the flow rate of the precursors to the flame spray reactor, portrayed in Figure 1.8-a. Very recently, they have published a detailed review reporting the successful attempt of FSP techniques for synthesizing other binary nanophotocatalysts (ZnO, WO_3, etc.), doped binary semiconductors, noble metal loaded systems and mixed complex metal oxide nanocomposites [35].

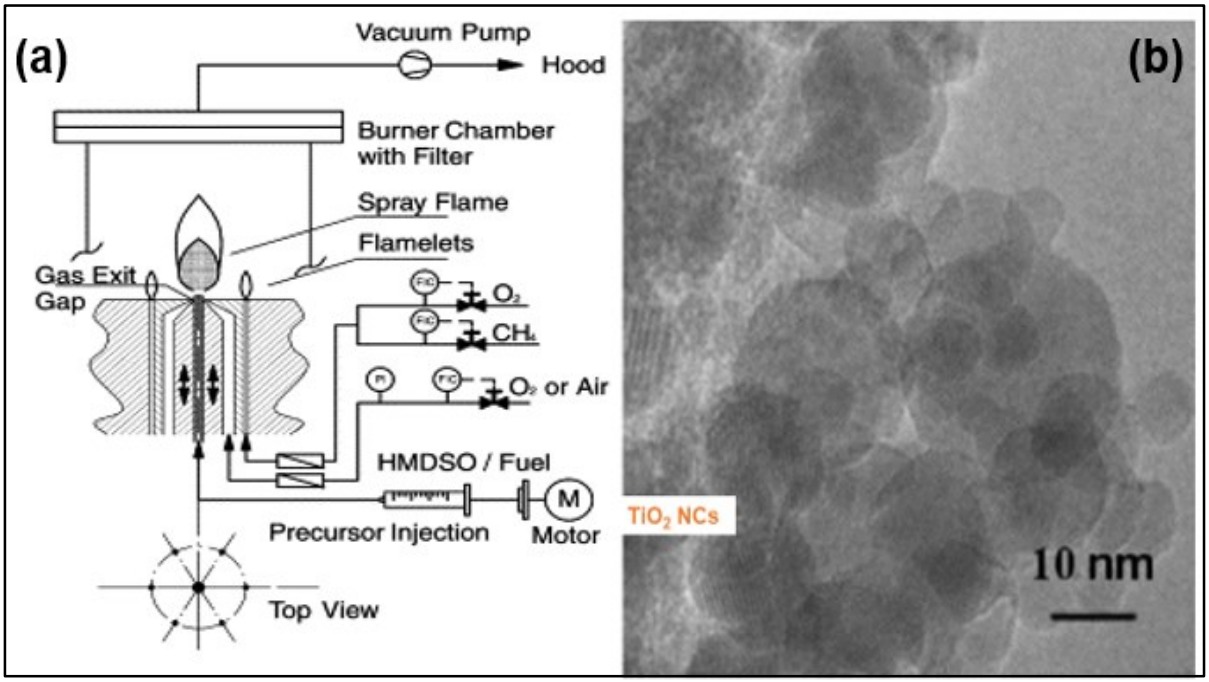

Figure 1.8. *a. Flame spray reactor utilised for the continuous synthesis of TiO_2 photocatalyst [36] more active than the commercial Degussa P25 synthesized by flame aerosol technique; b. HR-TEM image of TiO_2 nanocrystals (NCs) synthesized using the flame spray reactor [34].*

Among the binary semiconductors, zirconia especially nano-zirconia outperforms several binary photocatalysts for pollutants removal processes. Due to its high negative conduction band edge potential and different optical band gaps depending on the crystalline phase [37]. The wide band gap corresponds to 3.8 eV, 4.11 eV and 4.51 eV for cubic, tetragonal and monoclinic phases [38], respectively. The synthetic approach for obtaining peculiar nano-flower shaped zirconia (ZrO_2) for enhanced photocatalytic dye degradation compared to the ZrO_2 nanoparticles was reported by Zhanxia *et al*. They successfully synthesized stratified 3D-flower like nanostructures with 2D building block, see Figure 1.9-a. Their precursor selection (ZOS - zirconium oxide sulphate and sodium acetate) and the considered synthetic strategy

(hydrothermal + calcination) furnished the required flower-like nanostructures. Such an approach enabled the researchers to play with the morphology of nanostructures through pH control of the solution. The as-obtained nano flower-shaped ZrO_2 (with less surface area than the ZrO_2 nanoparticles) exhibited enhanced photocatalytic dye degradation performance compared to the tetragonal ZrO_2 nanoparticles with higher surface area due to their superior absorbance of photons in the UV-VIS region, depicted in the absorption spectrum of Figure 1.9-b. The enhanced absorption behaviour stems from the specially exposed facets (100) of the petals present in the graded nano-flower structures [39].

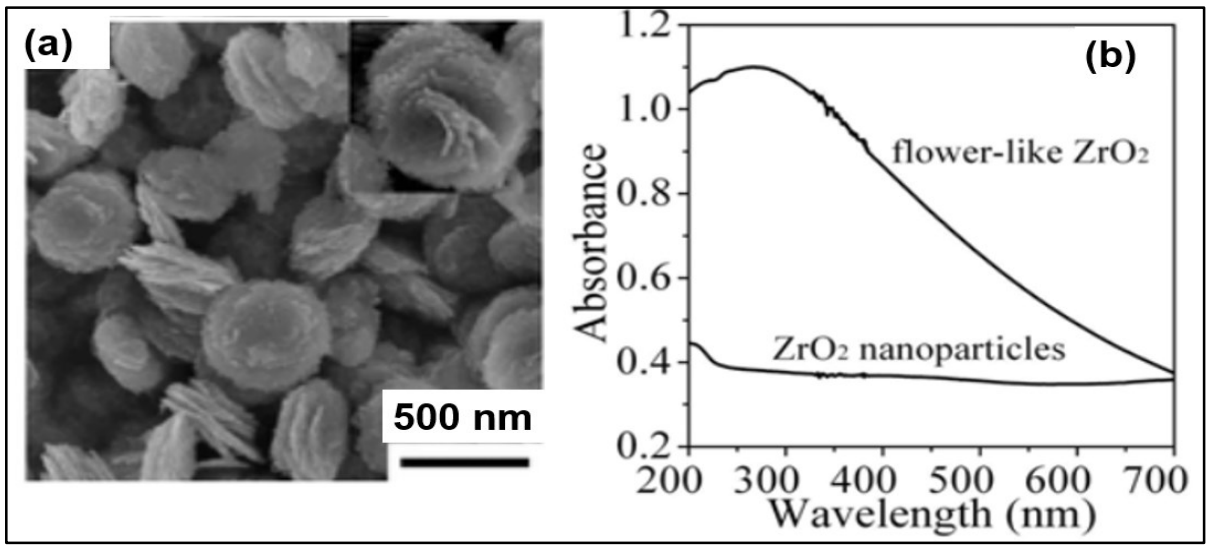

Figure 1.9. *a. FE-SEM image of nano flower shaped ZrO_2; b. UV-VIS absorption spectrum depicting the enhanced absorption behaviour of the flower shaped nanostructure of ZrO_2 compared to its nanoparticles [39].*

In the field of photocatalytic environmental remediation, similar to TiO_2 nano-photocatalysts, zinc oxide (ZnO) was also one of the most important binary oxide semiconductor explored in their nano-sized form for heterogeneous photocatalytic applications (particularly in water waste treatment) [40]. Additionally, within the oxide-based binary photocatalysts studied so far, CeO_2 possess high dielectric constant in its nano-size, which makes it as a promising binary oxide photocatalyst for purification of wastewater containing dye molecules [41, 42].The photochemistry explored so far, for both ZnO and CeO_2, are summarized in Table 1.1, were carried out on the nanomaterials synthesized in batch mode by hydrothermal process or by simple precipitation techniques. However, thanks to the rapid development of supercritical fluids in continuous processes, the synthesis of high quality ZnO and CeO_2 nanoparticles (NPs), was successfully attained by our group in the present decade [43, 44].

1.3.2.2. Chalcogenide-based binary photocatalysts

Across the realm of implementation of binary semiconductors in various heterogeneous photocatalytic applications, binary chalcogenides were assessed on equal intensity as binary oxide semiconductors. ZnS and CdS binary chalcogenides were tremendously studied in the past four decades for their successful application not only in environmental purification photochemistry but also for reduction of carbon dioxide, aldehydes, water splitting and

reductive dehalogenation of benzene derivatives. Especially, ZnS was focused a lot, due to its largest energy band gap of about 3.6 eV (among the binary chalcogenides of group II-VI [45]) and its facile phase control of ZnS nanocrystals [46]. Lately, a simple and robust production of ZnS nanoporous nanoparticles (NPNPs) *via* facile solution phase thermal decomposition technique carried out in the presence of N-vinylpyrrolidinone (PVP), was reported by Jin-Song Hu *et al*. Large scale produced ZnS photocatalysts outperformed commercial TiO_2 in degrading eosin B dye [47]. Interestingly, this ZnS NPNPs photocatalyst do not require any post treatment process as required by continuously synthesized ZnS photocatalyst for improving its activity [48]. The higher photocatalytic activity of ZnS NPNPs stems from their highly monodispersed, spherically uniform shaped. Where each sphere of ZnS were aggregates of hexagonal ZnS Nanocrystals (NCs) of 3 - 5 nm, formed as a result of self-assembly process. ZnS NPNPs of spherical shape and their aggregrates of small ZnS NCs are depicted in Figure 1.10.

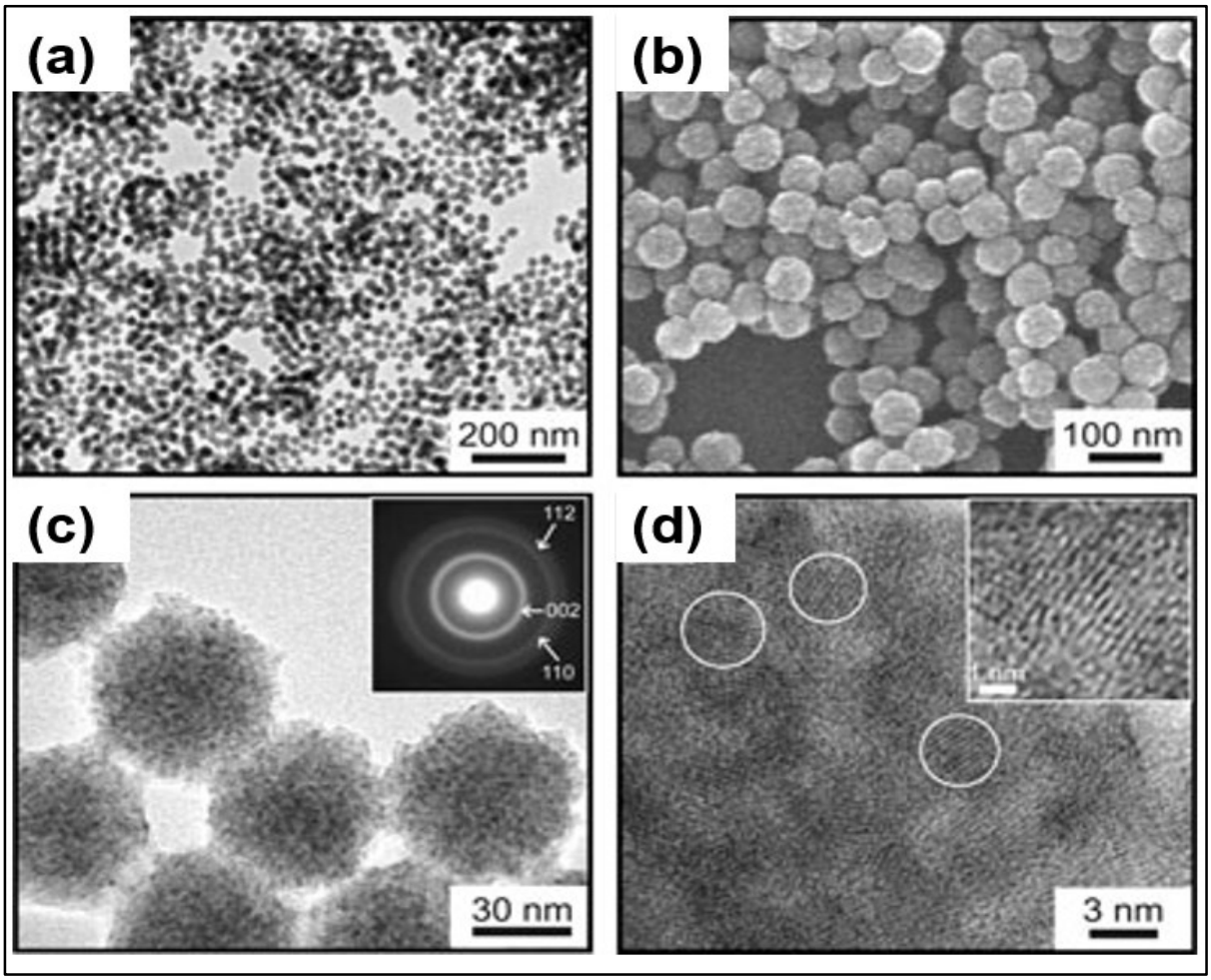

Figure 1.10. *a. TEM image of ZnS NPNPs; b. SEM image of spherical nanoporous ZnS; c. HR-TEM of ZnS NPNPs with electron diffraction of nanostructure in the inset of the figure; d. HR-TEM image depicting the lattice fringes of ZnS NCs, which undergoes self-assembly process to form the nanoporous ZnS spheres [47].*

Analogously, the synthesis of nano-hollow spherical cadmium sulfide (CdS) and hollow nanoporous copper sulfide (CuS) photocatalysts were reported by Man Luo *et al.* [49] and Wence Xu *et al.* [50], respectively. Latterly, a thermal sulfidation technique was introduced by

Dengwei Jing *et al.*, to obtain stable CdS nano photocatalyst against both oxidation and photocorrosion. This novel technique replaced the traditional old methodology of precipitation and subsequent heat treatment used for obtaining CdS nanomaterial, in which the resultant material suffered from severe photocorrosion due to oxidation of photogenerated holes during the heterogeneous photocatalysis. The thermal sulfidation technique lowered the phase transformation and crystallization temperature of CdS compared to the traditional synthetic methodologies. CdS nanomaterials obtained through this this novel process, possess nano-step arrangement on their surface. As a result of which they exhibit enhanced photocatalytic hydrogen evolution compared to the CdS samples prepared by conventional techniques [51]. In heterogeneous photocatalysis, CdS was profoundly studied for the hydrogen evolution process from the water splitting reaction under visible light due to its narrow band gap of about 2.38 eV and higher negative conduction potential than the reduction potential of H_2O/H_2 [49, 51]. Similarly, cadmium selenide (CdSe) (binary selenide semiconductor) was also acutely implemented for photocatalytic hydrogen evolution from water, even though it has a very narrow bulk band gap (1.74 eV). Enhanced photocatalysis of CdSe for hydrogen production stems from its strong quantum confinement behaviour, where precise control of size of CdSe NCs tunes the energy band gaps, providing the appropriate band edge (redox) potentials for photocatalysis. Recently, a strong relationship between the photocatalytic hydrogen production and various sizes of CdSe NCs (1.75 - 4.81 nm) synthesized by solvothermal method, due to strong quantum confinement, was reported by Holmes *et al.* [52].

1.3.2.3. Nitride-based binary photocatalysts

Compared to binary oxides and chalcogenides, the exploration of binary nitrides as photocatalysts has emerged only in the last two decades. Gallium nitride (GaN) exploration as a photocatalyst started after its immense success in sensing fields, due to high mechanical strength and chemical stability (at various pH) compared to binary oxide and chalcogenide-based semiconductors [53]. Very recently, the synthesis of GaN nanowires, which exhibit higher photocatalytic degradation of organic dyes compared to the photocatalytic activity of sub-micron GaN dot arrays and thin films, was reported by Jung *et al.* [54]. Tantalum nitride (Ta_3N_5) is an interesting, auspicious, binary nitride photocatalyst for solar water splitting reaction due to its band gap 2.1 eV and suitable band edge potentials [55 – 57]. For the degradation of dye (methylene blue) under visible light, it exhibits higher photocatalytic activity than visible light active nitrogen doped titania nanomaterials [58]. Khine Ma *et al.* developed a novel synthetic strategy, where they coupled alkali metal treated tantalum oxide precursor with ammonolysis process yielding highly crystallized Ta_3N_5 nanomaterials, which exhibit a six times higher photocatalytic activity for water oxidation reaction compared to Ta_3N_5 nanomaterials synthesized by other techniques [59]. In conclusion, I have briefly exposed in this section some examples of binary semiconductor photocatalytic materials. For traditional photocatalysts, the synthetic methodologies have been developed rapidly and now novel, continuous synthetic techniques are available to synthesize nanophotocatalysts at very high yield, as seen in the cases of TiO_2 or ZnO. Concerning the unconventional binary photocatalysts like GaN, CuS, etc., the synthetic methodologies developed specially to tune their photocatalytic activity are not deeply researched like the conventional ones because their

exploration as photocatalyst started only in the last two decades. Regarding their implementation in heterogeneous photocatalysis, their limit of application worked optimally well for degradation of organic dyes from textiles industries in the realm of photocatalytic environmental remediation and water splitting reactions in the presence of huge amount of sacrificial agents. The efficient photocatalytic degradation/demineralization of various organic toxic substrates apart from dyes was successfully carried out by ternary semiconductor photocatalysts due to their befitting band edge potential, diverse bandgaps and also due to their intrinsic surface properties.

Table 1.1. *Summary of binary semiconductor photocatalysts synthetic strategies with the background of photochemical reaction studied. (PC: binary semiconductor photocatalysts).*

PC	Synthetic methods	Precursors	Size of PC	Photochemistry studied	Illumination source	Reactor setup	Ref
TiO_2	Flame spray pyrolysis	$Ti[OCH(CH_3)_2]_4$, C_8H_{10} and CH_3CN.	11 - 21 nm (3.1 - 3.3 eV)	Mineralization of sucrose	Blue Lamp (15 W) λ = 300 - 400 nm λ_{max} = 350 nm	Spiral slurry flow photoreactor	[34]
ZnO	Precipitation and calcination	$Zn(OAc)_2$, PEG and $(NH_4)_2CO_3$.	20 nm	Degradation of methyl orange	UV lamp λ = 250 - 400 nm	Hollow cylindrical batch reactor	[40]
ZrO_2	Hydrothermal route, followed by calcination	Zirconium sulphate and sodium acetate.	Flowers with diameter 400 nm and petal thickness about 20 nm.	Degradation of rhodamine B	300 W High pressure mercury lamp (λ > 365 nm)	Cylindrical vessel with inner irradiation system	[39]
ZnS	Solution phase thermal decompositio n route	Zinc Acetate, thiourea, ethylene glycol and poly(N-vinyl-2-pyrrolidone)	About 60 nm (3.6eV)	Degradation of eosin B	125 W high pressure mercury lamp	Cylindrical pyrex glass	[60]
CdS	Thermal sulfidation process	Cadmium acetate and dry H_2S gas	100 - 300 nm (2.38 eV)	Photocatalytic hydrogen evolution	350 W Xenon lamp (λ > 430 nm)	Pyrex vessel with side irradiation	[51]
CdSe	Solvothermal method	Cadmium perchlorate, 2-Mercaptoethanol (MCE) and sodium hydrogen selenide	1.75 - 4.81 nm (3.11 - 1.89 eV)	Photocatalytic hydrogen production from water splitting reaction	300 W Xenon arc Lamp (λ > 320 nm)	Borosilicate glass flask	[52]
CeO_2	Hydrothermal reaction followed by calcination	$CeCl_2$ and NH_4OH	15 - 36 nm (4.16 eV)	Degradation of amido black and acridine orange.	250 W high pressure mercury lamp, UV range.	Glass vessel	[61]
GaN	Metal-organic chemical vapour deposition (MOVCD)	Trimethyl gallium (TMGa) and ammonia.	Nanowire of diameter: 20 - 50 nm, length of about 4 - 6 μm (3.4 eV)	Decolouration of Orange II	200 W Mercury lamp with filter cut off light shorter than 300 nm	Batch reactor	[54]
Ta_3N_5	Alkali metal treatment coupled with ammonlysis	Ta_2O_5, NaCl, Na_2O_3, KCl, K_2CO_3 and NH_3 gas	Average size 80 nm (2.1eV)	Photocatalytic oxygen evolution from water oxidation reaction	300 W Xenon lamp (λ > 420 nm)	Pyrex vessel with top irradiation type arrangement	[59]
CuS	Chemical dealloying method	Ti-Cu amorphous ribbon and H_2SO_4	Nanoporous globular clusters with 500 nm size and thickness 40 nm (1.6 - 1.7 eV)	Photo degeneration of methylene blue and methyl orange	500 W xenon lamp, illumination intensity was 0.01 W cm−2	Quartz cell	[50]

1.3.3. Ternary multi metallic photocatalytic materials

1.3.3.1. Introduction

In this section, we focus on ternary oxide and chalcogenide semiconductors, which consist of two different metallic cations and a single anion. These have been investigated a lot in the heterogeneous photocatalytic field because of their ability to carry out many indispensable reactions compared to binary semiconductors. Concurrently, they possess high stability among the diverse semiconductor photocatalytic materials. The semiconductor photocatalysts reviewed in this section can be grouped into different categories according to their composition, their molecular formula (ABO types for ternary oxides) and their crystalline structure, as depicted in Figure 1.11.

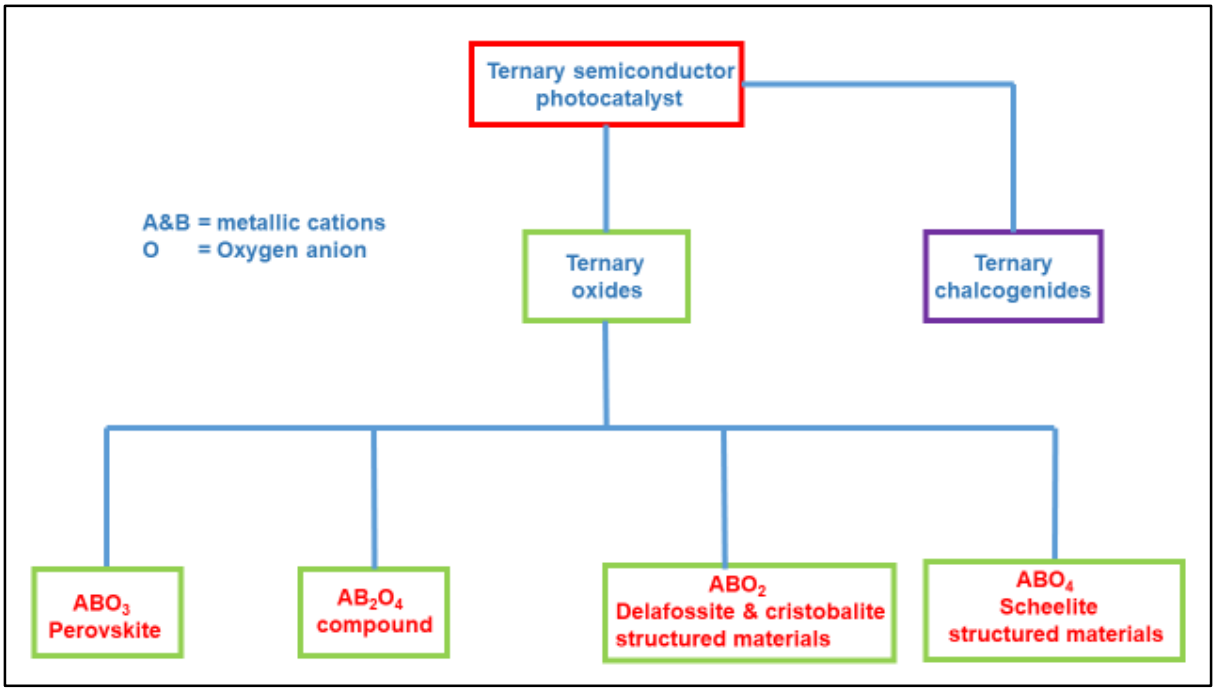

Figure 1.11. *Classification of ternary semiconductor photocatalysts reported in the field of photocatalysis.*

1.3.3.2. Ternary oxide photocatalysts

1.3.3.2.1. Perovskites photocatalysts (ABO_3 types)

We described hereafter few examples of the ternary perovskite oxide group semiconductor photocatalysts, with a general formula ABO_3, which are the most propitious photocatalysts. Here the terms A & B refer to different metallic cations. Predominantly, the 'A' cation is either alkali or alkaline or rare earth metal element, whereas the 'B' cation is regularly a transition metal element. An ideal perovskite oxide semiconductor has a cubic crystal structure, where typically the 'B' cation is much smaller than the 'A' cation. ABO_3 structure can be perceived in such a way that oxygen anion is coordinated with four 'A' cation, two 'B' cation, with the site of the 'B' cation positioned in the centre of the unit cell, as depicted in Figure 1.12-a. Another way by which the ABO_3 structure can be perceived is with 'A' site cation in the centre, as depicted in Figure 1.12-b. In this three dimensional correlated framework, the 'A' cation is

12-fold coordinated and 'B' is 6-fold coordinated with oxygen atoms. The three dimensional structure is constructed from the BO_6 octahedra network constituting the corner position with A cation positioned in the centre of the framework [62 – 64].

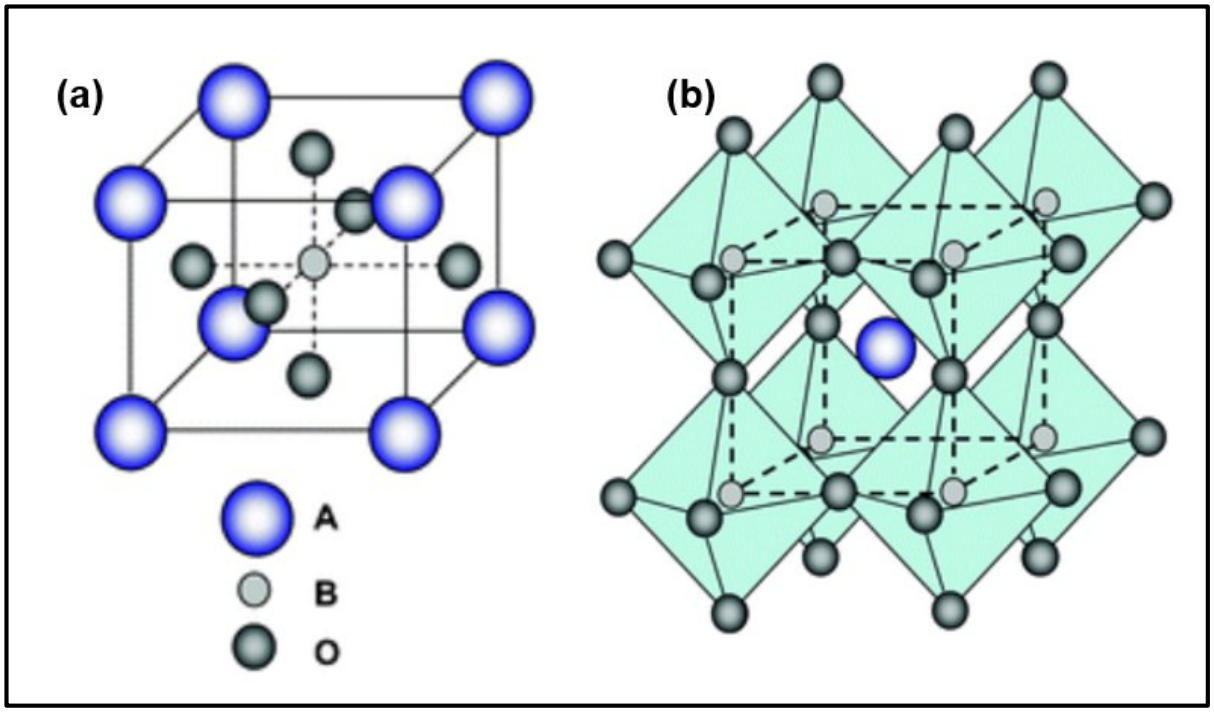

Figure 1.12. *a. Crystal structure of perovskite oxide (ABO_3) semiconductor photocatalysts with the B cation in the centre of the unit cell [63]; b. An ideal perovskite ABO_3 structure with BO_6 octahedra constituting the corner position of the framework with A cation at the centre [63].*

Titanate, tantalate and niobate-based perovskite oxide photocatalysts synthetic methodologies are consistently studied and new methods are proposed to enhance their individual photocatalytic activity by tuning both the surface area and the surface properties in the nanosized domain. Strontium titanate ($SrTiO_3$) finds immense application in heterogeneous photocatalysis and thermoelectric fields because of the easy capacity to precisely tune its physical and chemical properties, depending on its composition [65]. The tunability of $SrTiO_3$ manifests to such an extent that, it can be facilely converted into n-type semiconductor at room temperature by effortless electronation or doping strategies. In the field of heterogeneous photocatalysis, $SrTiO_3$ possessing a wide band gap of 3.2 eV [66], works effectively for absolute demineralization of organic pollutants under UV irradiation [67, 68]. It also exhibits enhanced water splitting reaction with metal co-catalyst on its surface [66, 69]. Notably, photocatalytic ammonia production and decomposition was also reported using $SrTiO_3$ as a photocatalyst [70]. The traditional solid state synthetic methods for obtaining $SrTiO_3$ nanomaterial photocatalysts suffer from polydispersed size distributions and reduced specific surface area. In the last decade, this synthetic process was replaced by hydrothermal, sol-gel and co-precipitation methods [68, 71]. Chen *et al.* reported that $SrTiO_3$ synthesized by the sol-gel technique exhibited enhanced degradation of nitric oxide (NO) (92% in 45 minutes) under UV irradiation [72].

In the standpoint of photon energy conversion process, the photocatalytic water decomposition into hydrogen and oxygen molecules was addressed by several researches. Unlike titanates, tantalates (alkali and alkaline earth tantalates) ternary oxide semiconductors exhibited photocatalytic water splitting activity without any co-catalyst or sacrificial agents in the water system. Alkali tantalates ($LiTaO_3$, $NaTaO_3$, $KTaO_3$) consist of perovskite's crystal structure, where TaO_6 octahedra constitute the corner position of the crystal framework. Tantalates exhibit photocatalytic activity without the addition of a reduction co-catalyst (NiO or Pt) or an oxidation co-catalyst (IrO_2 or MnO_x) because of their advantages: a higher conduction band edge of tantalates than the reduction potential of water (CB consists of Ta 5d orbitals and VB consists of O 2p orbitals), CB edge potential of tantalates is more negative than the reductive co-catalyst band edge potential and similarly VB edge potential is more positive than the oxidation band edge potential. Lastly, due to their high delocalization of exciton energy caused by the corner sharing crystal arrangement [73, 74].

Among the various tantalate ternary oxide semiconductors, lithium tantalate ($LiTaO_3$) exhibits the highest activity for water splitting under UV light without co-catalyst loading due to its wide band gap of (4.6 - 4.7 eV). Very recently, the conventional synthetic methods for $LiTaO_3$ (solid state synthesis, spray drying methods and polymerizable complex method) yielding large particles with small surface area have been replaced by solution based solvothermal and hydrothermal routes. Takasugi *et al.* synthesized $LiTaO_3$ by both the solvothermal and hydrothermal routes in 2015. They reported that $LiTaO_3$ obtained by their solvothermal route exhibits highly enhanced H_2 production rate (600 $\mu mol.h^{-1}$) compared to the activity of $LiTaO_3$ obtained from their hydrothermal route, which gave very low H_2 production rate (8 $\mu mol.h^{-1}$). High surface area (23.7 $m^2.g^{-1}$) and very small particle size (10 – 30 nm) were the reasons for better performance of $LiTaO_3$ obtained from solvothermal route [75].

Sodium tantalate ($NaTaO_3$), oppositely to $LiTaO_3$, exhibits low activity for water splitting compared to other tantalates ternary semiconductors without co-catalyst loading. However, NiO loaded $NaTaO_3$ exhibits the highest activity for water splitting among the co-catalyst loaded tantalates semiconductor. The study of co-catalyst loaded $NaTaO_3$ system led to the development of lanthanide (La) doped NiO/$NaTaO_3$ highly active photocatalytic systems, which yielded H_2 evolution at the rate of 5.9 $mmol.h^{-1}$ under UV irradiation [76]. Regarding the synthetic development of $NaTaO_3$ nanomaterial photocatalysts, nanopowders of $NaTaO_3$ with orthorhombic phase are obtained from their traditional solid state synthetic route. They possess a direct band gap of 4.1 eV and exhibit low activity for water splitting. By switching from conventional solid state to sol-gel technique, $NaTaO_3$ with monoclinic phase possessing an indirect band gap (3.9 eV) with high density of states near the band edges, due to which $NaTaO_3$ nanomaterials exhibit high activity compared to solid state synthesized $NaTaO_3$ [77]. He *et al.* synthesized $NaTaO_3$ (3.96 eV) nanopowders through a hydrothermal route, which exhibits high photoactivity under UV light for both gas (photo-degradation of formaldehyde, complete degradation within 35 minutes of irradiation) and liquid (photo-degradation of rhodamine B (RhB), complete degradation within 3 hours of irradiation) phase reaction [78]. Finally, among the alkali tantalates, potassium tantalate ($KaTaO_3$) was found to be a compelling replacement for binary TiO_2 photocatalyst for performing many diverse photochemical reactions due to its more negative CB edge potential (Ta 5d) than the titanates

(Ti 3d) and niobates (Nb 4d). $KaTaO_3$ (3.7 eV) synthesized by conventional solid state reaction displays activity for photocatalytic reduction of carbon dioxide with hydrogen as a reductant [79]. Bajorowicz *et al.* in 2014 reported the hydrothermal synthesis of a $KaTaO_3$ nanomaterial photocatalyst, which exhibits high photocatalytic activity in both liquid (degradation of phenol: 30% in 1 h) and gas phase (degradation of toluene: 64% in 1 h) compared to binary CdS and molybdenum disulfide (MoS_2) photocatalysts [80].

Another example of ternary oxide perovskite photocatalyst is silver niobate ($AgNbO_3$) (2.8 eV), which is photocatalytically active in the visible light [81]. The interesting properties of $AgNbO_3$ stems from its filled valence band composed of Ag 4d orbitals, which is far below the oxidation potential of water and therefore was used to produce H_2 or O_2 from water under visible light irradiation, in the presence of sacrificial agents [82 – 84]. It possesses excellent optical and electrical properties, which are conventionally used in several applications such as microwave communication, microelectronic technologies and heterogeneous photocatalysis [81]. Arney *et al.* reported the replacement of conventional synthetic solid state route of $AgNbO_3$ nano photocatalyst by molten salt flux synthetic route. This newly developed flux method resulted in nanophotocatalyst, which disclosed enhanced photocatalytic activity for H_2 generation (5.9 $\mu mol.g^{-1}.h^{-1}$) from aqueous methanol solution under visible light compared to the activity displayed by $AgNbO_3$ photocatalyst synthesized by solid state route (3.4 $\mu mol.g^{-1}.h^{-1}$) [82].

1.3.3.2.2. Ternary oxide (AB_2O_4 types) photocatalysts

The second type of interesting ternary oxide semiconductor photocatalysts elucidated here have a general formula AB_2O_4 (MIn_2O_4 where M = Ca or Sr or Ba). These alkali earth metal-based ternary oxides contain p-block Indium (In) metal with a d^{10} configuration. Such p-block metal containing ternary oxides have evinced to form a new set of photocatalyst compared to the conventional binary/ternary oxide photocatalysts containing d^0 configuration transition metal ions (Ta, Nb and Ti). The three photocatalysts of the group MIn_2O_4 demonstrated the photocatalytic degradation of organic dyes under visible light [85 – 87]. They also successfully manifested the decomposition of pure water into hydrogen and oxygen when loaded with ruthenium (IV) oxide (RuO_2) co-catalyst [88 – 90]. Among the three types of MIn_2O_4 photocatalysts, the order of photocatalytic activity is $CaIn_2O_4 > SrIn_2O_4 > BaIn_2O_4$ for both dye degradation and water splitting reaction. As the size of the ionic radii increases in the MIn_2O_4 system (Ca to Sr to Ba) the crystal structure changes due to the change in the lattice parameters. $CaIn_2O_4$ and $SrIn_2O_4$ possess similar structure with uniform arrangement of distorted InO_6 octahedra network, which favours enhanced charge transfer to the surface upon photoexcitation, whereas $BaIn_2O_4$ photocatalyst consists of several kinds of InO_x polyhedra network (mixture of InO_6 octahedra and InO_5 hexahedra network), which is unfavourable for charge transfer due to irregular tunnelling of charge carriers upon excitation. Within $CaIn_2O_4$ and $SrIn_2O_4$ photocatalysts, $CaIn_2O_4$ exhibits higher activity irrespective of similar crystal structure, due to the more positive oxidation potential. Even though the CB and VB of both $CaIn_2O_4$ and $SrIn_2O_4$ consists of O 2p and In 5s orbitals, respectively, the VB of $CaIn_2O_4$ photocatalyst has higher oxidative nature due to higher ionic core potential of the 'Ca' ion. Currently, the synthesis of the $CaIn_2O_4$ photocatalyst by conventional techniques is replaced

by novel methods to attain different shapes in the nanodomain, to implement its activity for diverse photochemistries. Ding *et al.* reported a novel solution-combustion synthetic route for producing $CaIn_2O_4$ nanorods with large surface area and high crystallinity. The as-synthesized $CaIn_2O_4$ nanorods exhibited 66% photocatalytic mineralization of toluene in gas phase within 360 minutes of irradiation under visible light, which is four times higher than the activity disclosed by $CaIn_2O_4$ nanomaterial synthesized by traditional Solid State Reaction (SSR) route. Similarly, platinum (Pt) dispersed $CaIn_2O_4$ nanorods unveiled from water splitting reaction, hydrogen generation rate of 1.23 $\mu mol.h^{-1}.g^{-1}$, which is 24 times higher than the photocatalytic activity displayed by Pt dispersed $CaIn_2O_4$ (synthesized by SSR route) [91]. When considering the MIn_2O_4 photocatalytic systems, researchers have rigorously searched for ternary oxides containing metal ions (Ag^+ and Bi^{3+}) with $d^{10}/d^{10}s^2$ configuration, as they possessed short energy band gap for visible light activity.

1.3.3.2.3. Ternary oxides (ABO_2 types) photocatalysts

The third category of ternary oxide semiconductor photocatalysts discussed here, possess visible light activity and are silver containing group III oxides, with molecular formula $AgMO_2$ (M = Al, Ga, In) [92 – 95]. This family includes: α-$AgGaO_2$ (2.38 eV), α-$AgInO_2$ (1.90 eV), β-$AgGaO_2$ (2.18eV) and β-$AgAlO_2$ (2.95 eV) which are indirect band gap semiconductors. They are active under visible light radiations. 'α' refers to the delafossite structure and 'β' to the cristobalite-related structure. Maruyama *et al.* reported the use of a cation-exchange technique for the synthesis of the above silver family of ternary indirect band gap semiconductors and Ouyang *et al.* performed the photocatalytic evaluation of four different ternary oxides (α-$AgGaO_2$, α-$AgInO_2$ β$AgGaO_2$ and β-$AgAlO_2$) by studying the gas phase photocatalytic decomposition of isopropanol under visible light [94, 96]. Cationic exchange reaction occurs between the silver nitrate ($AgNO_3$) precursor and sodium oxide complex precursor, $NaMO_2$ (where M = Ga or Al or In). The hierarchical order of photocatalytic activity was found to be α-$AgGaO_2$ > β-$AgAlO_2$ > β$AgGaO_2$ > α-$AgInO_2$.

In these semiconductors, the crystal structure and optical band gap of the semiconductor photocatalysts stand as the key properties influencing the photocatalytic activity. $AgGaO_2$ nanomaterial photocatalysts possessing delafossite crystal structure exhibits the highest activity (88.8 $ppm.h^{-1}$ of acetone produced from photocatalytic isopropanol decomposition) compared to other silver containing ternary oxide semiconductors of $AgMO_2$ family. Delafossite crystal structure exists as two different polytypes: 3-R (Rhombedral) and 2-H (Hexagonal), as depicted in Figure 1.13-a and 1.13-b. $AgGaO_2$ and $AgInO_2$ synthesized here were crystallized in the 3-R polytype form. In both the polytypes of delafossite structure, one bonding layer is formed by O-A-O (O – oxygen, A – silver cation) dumbbell layers. These dumbbell layers are interleaved with BO_6 octahedra blocks, which can be visualized in the Figure 1.13-a and 1.13-b. These two individual layers act as separate paths for electrons (BO_6 layers) and hole conduction (O-A-O dumbbell layer) upon excitation by photons. Importantly, each oxygen atom of the delafossite structure forms tetrahedron OB_3A block, where the tetrahedron block favours the hole conduction.

The repulsion existing between the oxygen anion in the dumbbell (O-A-O) bonds, shortens the bond distance between the 'A' cation and the oxygen anion, which increases the interaction

between the metallic (A) cation and the oxygen anion. As a result of which highly dispersed VB is formed in such crystal structure. Such a dispersed VB leads to a semiconductor possessing reduced effective mass of the holes with higher mobility of holes. Such enhanced mobility of holes results in increased separation of charges upon excitation, thereby increasing the photocatalytic activity. This novel dispersed valence band characteristic is not seen in cristobalite structure (β-$AgAlO_2$ and β-$AgGaO_2$), which explains the reasons for lower photocatalytic activity (5.3 $ppm.h^{-1}$ and 2.2 $ppm.h^{-1}$ of acetone produced, respectively) compared to α-$AgGaO_2$. The very low photocatalytic activity of α-$AgInO_2$ (1.3 $ppm.h^{-1}$ of acetone production) for isopropanol decomposition can be solely attributed to its very low band gap (1.9 eV), not possessing appropriating band edge potentials for oxidation [96].

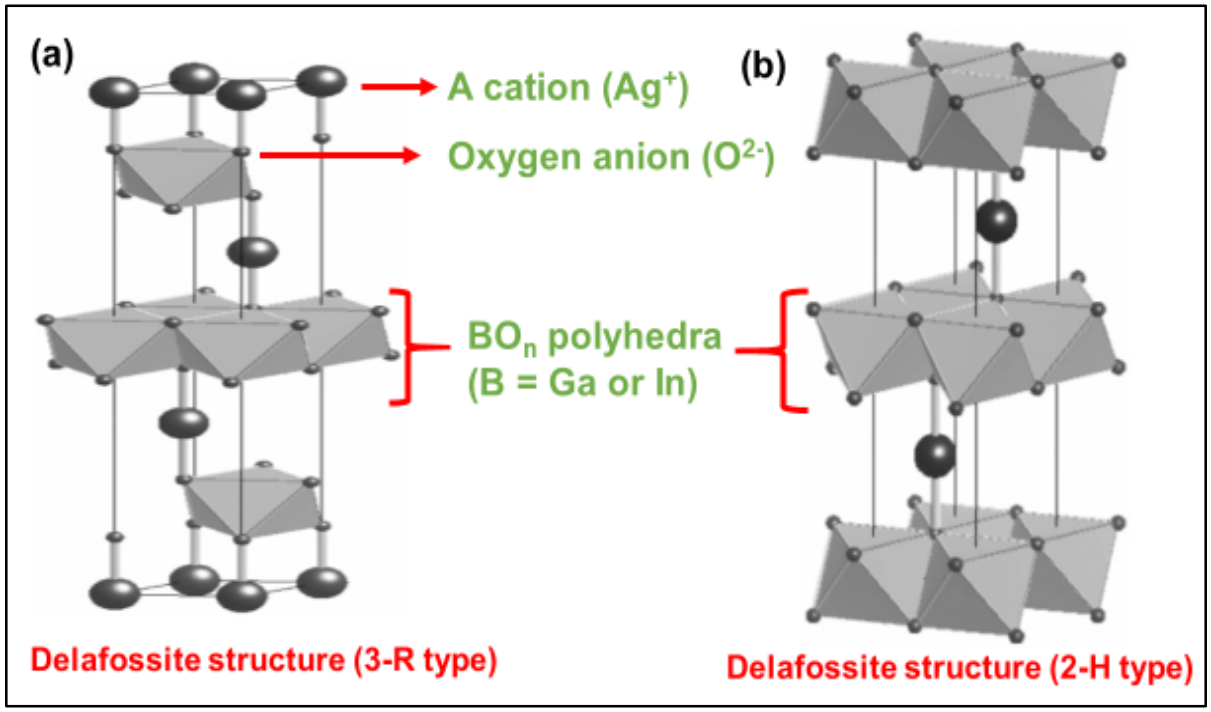

Figure 1.13. *a. 3-R polytype of delafossite crystal structure; b. 2-H polytype of delafossite crystal structure (redrawn based on the images [94]).*

1.3.3.2.4. Ternary oxides (ABO_4 types) photocatalysts

Bismuth vanadate $BiVO_4$ (2.4 eV), is yet another visible light active ternary oxide photocatalyst, which grabbed the attention of researchers for its polymorphic nature and interesting ferroelastic and ion conductive properties. Such fascinating properties strongly depends on the crystalline structure of $BiVO_4$. The three polymorphic form of $BiVO_4$ are: scheelite-monoclinic (SM), scheelite-tetragonal (ST) and zircon-tetragonal (ZT) [97 – 99]. Among the various crystalline forms of BiVO4, SM systems exhibit the highest photocatalytic O_2 evolution from aqueous silver nitrate solution and photocatalytic degradation of endocrine compounds especially alkylphenol groups under visible light irradiation [100 – 102]. Even though SM-$BiVO_4$ and ST-$BiVO_4$ semiconductor possess the same scheelite crystal structure, SM structure outperforms ST in heterogeneous photocatalysis. In the SM-$BiVO_4$ crystal structure, a variety of bond length between Bi-O atoms are observed, which are not seen in ST-

$BiVO_4$ compound. The presence of different bond lengths of Bi-O atoms leads to distortion of the crystal structure caused by the lone pairs of $6s^2$ of Bi^{3+} cations. Specifically, within the SM-$BiVO_4$ compound, VO_4^{3-} tetrahedrons are distorted, which can be visualized in Figure 1.14-a. Such distortion has a profound effect on the electronic structure of the semiconductor. In $BiVO_4$ ternary semiconductors, the VB is composed of Bi 6s and O 2p orbitals and CB is composed of V 3d orbitals. Due to the distortion of SM structure, the overlap of VB orbitals occurs. The extent of O 2p and Bi 6s orbitals overlap increases with the increase of the extent of distortion in the crystal structure. The increase in VB orbitals overlap results in the increase of charge separation kinetics upon photoexcitation, due to the delocalization of electrons and holes, resulting in enhanced migration of holes to the surface of the semiconductor, thus ultimately increasing the photocatalytic activity. Such enhanced migration of holes is absent in ST-$BiVO_4$ (Figure 1.14-b) semiconductor due to the absence of distortion in the scheelite crystal structure [97, 103].

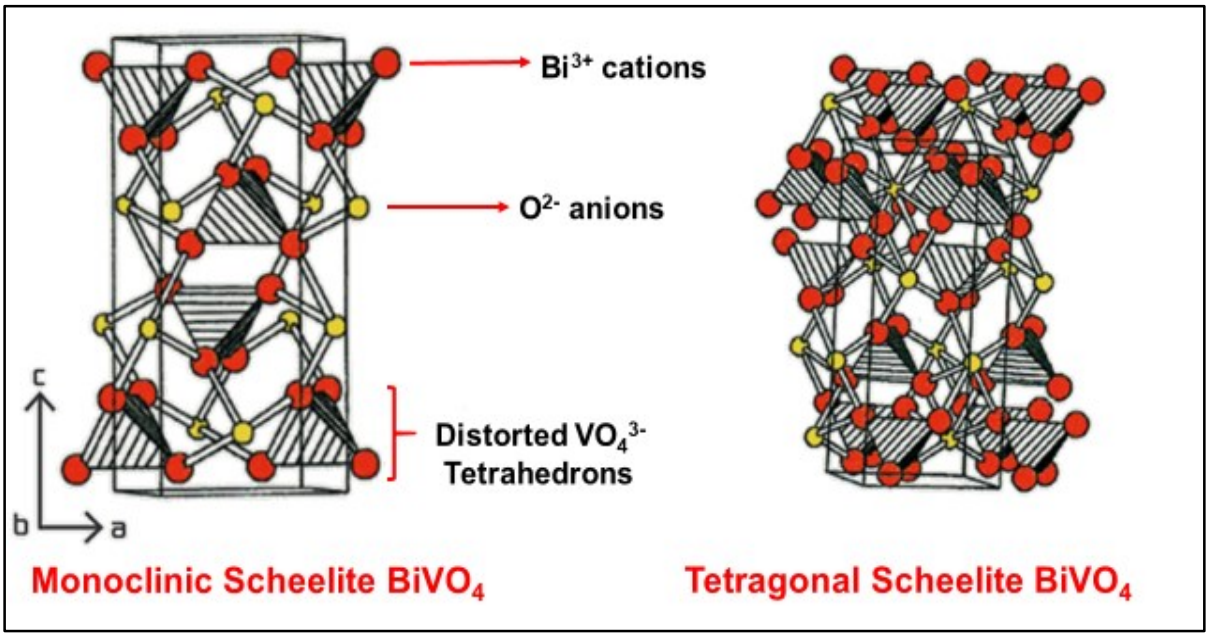

Figure 1.14. *a. Monoclinic scheelite (SM) structure of $BiVO_4$ compound; b. Tetragonal scheelite (ST) structure of $BiVO_4$ compound [104].*

Conventionally, such novel SM-$BiVO_4$ photocatalysts are synthesized by solid state reaction at high temperature, which results in nanomaterials possessing surface defects, which was detrimental for heterogeneous photocatalysis. Lately Kudo *et al.* replaced the conventional route by room temperature aqueous process, which resulted in nanomaterials with well-defined crystallinity [102]. Recently, Yu *et al*. reported the hydrothermal route for synthesizing SM-$BiVO_4$ with enhanced surface texture and morphology compared to the nanomaterials synthesized by aqueous process route. In the reported novel route of hydrothermal synthesis, they successfully deployed the methodology for varying the photocatalytic activity for O_2 evolution from aqueous silver nitrate solution, by varying the pH of the synthetic medium of the photocatalyst. The variation of the pH (1, 4 and 9) of the synthetic medium successfully varied the electronic band gap (2.39, 2.46 and 2.47 eV), thus influencing the activity of heterogeneous photocatalysis [103].

1.3.3.2.5. Ternary chalcogenide photocatalysts

Besides ternary oxides, ternary chalcogenides of the type AB_xC_y (where A = Cu, Ag, Zn or Cd; B = Ga or In; C = S or Se or Te; x, y =integer) possess excellent optical and electrical properties and have found their successful implementation in solar cells, optoelectronic devices and heterogeneous photocatalysis [105 – 107]. Among these highly functional chalcogenides, ternary semiconductors of the group I-III-VI (silver-indium-sulfide ($AgInS_2$) and copper-gallium-sulfide ($CuGaS_2$), have been highly explored in heterogeneous photocatalytic studies and other optical fields. Due to their negligible toxicity, their high absorption coefficient and their visible light activity (short energy band gap) for many novel reactions [108 – 113].

Visible light active $AgInS_2$ ternary photocatalyst was traditionally synthesized by solvothermal route, hot press method, spray pyrolysis technique and thermal decomposition of single source precursors [107, 114 – 116]. Such synthetic approaches suffer from several disadvantages due to the extreme process conditions (long reaction time, high temperature and pressure) and several secondary pollutions caused by the waste streams of the synthetic processes. Recently, solving the above mentioned issues, Luo *et al.* reported the synthesis of $AgInS_2$ in one pot aqueous media without the use of catalyst, template or any organic solvent. This novel aqueous route was economically viable, environmentally benign and gave ternary $AgInS_2$ nanomaterials with high synthesis reproducibility and mono-dispersity. The as-synthesized $AgInS_2$ (2.04 eV) photocatalysts displayed propitious photocatalytic activity of degrading Rhodamine-B (RhB) (>80% of dye degradation in 100 minutes) under visible light [117].

Similarly, for the case of copper-gallium-sulfide ($CuGaS_2$) ternary chalcogenide photocatalyst, the conventional synthetic methodologies are hydrothermal, solvothermal and hot injection route [118 – 121]. These suffered from several drawbacks like the production of polydispersed samples or the difficulties of large scale production. Regulacio *et al.* resolved the drawbacks by introducing a facile non-injection route for synthesizing $CuGaS_2$ nanomaterials. The as-reported synthetic method possesses, several advantages like high reproducibility, mass production of the samples and convenient control of the synthetic domain. The as-synthesized $CuGaS_2$ (2.52 eV) nano-photocatalyst exhibits promising photocatalytic activity for RhB dye degradation (63% of dye was degraded in 270 minutes) under visible light irradiation [122].

Unlike binary semiconductor photocatalysts, none of the ternary semiconductors photocatalysts are commercialized so far, even though they possess certain advantageous photocatalytic properties for performing many indispensable photochemistries. The main reason for their non-commercialization stems from the lack of development in the synthetic approaches to meet economical needs. So far, the reported novel ternary photocatalysts have not been attempted in continuous synthetic process. Although continuous, scalable supercritical processes for the synthesis of ternary materials have been developed in our research group. The ternary semiconductors synthesized by our supercritical processes have not been explored in the heterogeneous photocatalytic field [123, 124]. The successful attainment of visible light active photocatalyst was possible by ternary semiconductor fabrication, which can perform multitudinous photochemistry. The main and the biggest limitation of ternary semiconductors is that the precise increment or decrement of band edge potential depending on the particular redox potential of photochemistry addressed, it is not possible by fabricating ternary

semiconductor photocatalysts by various synthetic methodologies. Such precise engineering of band edge potentials is achieved in solid solution photocatalysts, which will be addressed in the next section. Table 1.2 summarizes some examples of the synthesis and details the photocatalytic processes of ternary semiconductors studied so far.

Table 1.2. *Summary of nano-ternary semiconductor photocatalysts synthetic strategies with the background of photochemical reactions studied (TC: Ternary semiconductor photocatalysts).*

TC	Synthetic methods	Precursors	Size of TC	Photochemical reaction	Illumination source	Photoreactor	Ref
$SrTiO_3$	Sol-gel method	Strontium nitrate, citric acid, deionized water, butyl titanate and glycol.	20 - 40 nm **(3.2 eV)**	Degradation of nitrogen oxides (NO_x)	UV light (20 W)	Glass reactor inside mirror box	[72]
$LiTaO_3$	Hydrothermal and solvothermal methods	$TaCl_5$, $LiOH.H_2O$, H_2O_2, NH_3, methanol and acetone.	Hydrothermal yields nanorods with 20 nm diameter and length of 2 - 10 µm. Solvothermal yields nanoparticles of 10 - 50 nm **(4.6 - 4.7 eV).**	Water splitting reaction	450 W high pressure mercury lamp, UV light source.	Inner radiation cell made up of quartz	[75]
$NaTaO_3$	Hydrothermal method	Ta_2O_5, NaOH and deionized water.	About 200 nm **(3.96 eV)**	Decomposition of gaseous formaldehyde and rhodamine B solution under UV irradiation	8 W Bactericidal Lamp, ($\lambda >$ 254 nm, 2.5 mW/cm^2)	Cylindrical quartz cell	[78]
$KTaO_3$	Hydrothermal method	KOH, Ta_2O_5, deionized water and ethanol .	200 - 1000 nm **(3.4 eV)**	Degradation of phenol in liquid phase Degradation of toluene in gas phase	1000 W Xenon lamp 25 LEDs, 63 mw per diode and λ_{max} = 375 nm	Reactor with quartz window Flat stainless steel reactor with quartz window	[80]
$AgNbO_3$	Molten salt flux synthesis method	Ag_2O, Nb_2O_5 and Na_2SO_4	100 - 5000 nm **(2.75 - 2.81 eV)**	H_2 production from aqueous methanol solution	External 400 W Xenon arc-lamp equipped with a long pass cut off filter ($\lambda >$ 420 nm)	Outer irradiation type fused-silica reaction cell with a volume 90 mL	[82]
$CaIn_2O_4$	Combustion synthesis	Calcium nitrate, indium nitrate and glycine.	Approximately 90 nm	Decomposition of methylene blue , toluene oxidation and water decomposition	300 W Xenon arc lamp fitted with UV cut off filter	Pyrex glass cell	[91]
α-$AgGaO_2$	Cation exchange method	$NaGaO_2$, $AgNO_3$ and KNO_3	200 -1000 nm **(2.4 eV)**	Decomposition of isopropanol (IPA) under UV or visible light.	Xenon lamp with glass filters	Glass vessel with a quartz lid	[96]
$BiVO_4$	Hydrothermal method	NH_4VO_3, $Bi(NO_3)_3.5H_2O$ and HNO_3.	49 - 490 nm **(2.39 - 2.47 eV)**	O_2 evolution from an aqueous solution of $AgNO_3$ under visible light irradiation.	300 W Xenon lamp with cut off filter for visible light ($\lambda >$ 420 nm)	Closed gas circulation system fitted with Pyrex made reaction cell	[125]
$AgInS_2$	One step aqueous route	Silver nitrate, indium acetate, sodium sulfide and L-glutathione	3.0 ± 0.3 nm **(2.04 eV)**	Degradation of rhodamine-B (RhB) under visible irradiation.	500 W mercury lamp	Quartz cell	[117]
$CuGaS_2$	Colloidal synthesis method using hot injection technique	Copper(II) and gallium(III) diethyl dithio carbamate.	Nanorods with length of about 189 nm and width of about 8 nm **(2.52 eV)**	Degradation of RhB	500 W Halolite lamp ($\lambda >$ 430 nm)	Glass vial	[122]

1.3.4. Solid solution photocatalysts

The optical properties of semiconductor photocatalysts are fundamentally the manifestation of their inherent electronic structure, such as the transition from the VB to the CB. In case of wide bandgap binary photocatalysts, their optical gap circumscribes many redox potentials but their implementation is limited, due to their activity in the UV region. Oppositely, certain ternary photocatalysts possess narrow band gap active in the visible region but doesn't have appropriate band edge potentials for performing diverse photochemistries. In both cases (binary and ternary), an inherent electronic structure does not regulate an optimum balance between the visible light activity and the required redox potential.

In the evolution of semiconductor heterogeneous photocatalysis field, binary photocatalysts are rendered active in the visible (solar) light by doping the semiconductor with metallic cations or non-metallic anions [33, 126, 127]. Incorporation of such dopants not only extend the optical response of wide band gap photocatalysts into the solar range, but also acts as trap centres for electrons and holes upon excitation, thereby increasing the charge separation kinetics and thus leading to higher photocatalytic activity [128, 129]. Comparably, retardation of electron-hole recombination upon excitation was observed when co-catalysts like Platinum (Pt), Gold (Au) and silver (Ag) are loaded on the surface of the binary or ternary photocatalysts. These co-catalyst possess large work function and form Schottky barrier on the photocatalyst interface, leading to increased charge separation kinetics and thus enhancing the photocatalytic activity [130 – 132]. Here, co-catalysts (noble-metal nanoparticles) behave as a depot for the commuting photogenerated electrons from the semiconductor photocatalyst.

Besides these positive effects, doped semiconductors suffer from huge setback like thermal instability of the doped nanomaterials and low photocatalytic activity under UV irradiation. The dopant material increases the photocatalytic activity (by trapping the charges) only when an optimum amount is incorporated into the semiconductor. Beyond the optimum concentration, they behave as recombination centres for electrons and holes leading to a decrease of the photocatalytic activity. They require highly expensive synthetic techniques like ion implantation, sputtering, and plasma-enhanced chemical vapour deposition routes [128, 133]. Whereas for co-catalysts (noble-metals) loaded systems, the metal centres retard electron-hole recombination only till they are charged. However, immediately on getting negatively charged, they attract the holes and form recombination centres, which are detrimental to heterogeneous photocatalysis [134].

Meticulous modulation of energy band gap through the fabrication of solid solution semiconductors had disentangled the above problems of electron-hole recombination in doped and loaded semiconductor photocatalysts. The formulation of solid solution photocatalysts is done by combining a wide band gap binary/ ternary semiconductor with very narrow band gap binary/ternary semiconductor, for example: ZnS-CdS [135]. The resultant solid solution ($Zn_{1-x}Cd_xS$ ($0.2 \leq x \leq 1$)) not only possesses an activity under visible light radiation but also maintains suitable band edge potentials for performing the required photochemistry.

According to IUPAC, a solid solution is defined as, *"a crystal containing a second constituent, which fits into and is distributed in the lattice of the host crystal. (The term `Solid Solution' is*

not referred for amorphous materials)" [136]. The fabrication of solid solutions is attained by precise engineering of both the electronic structure of a compound and its crystal structure. Apart from the band gap position, the other properties which one has to consider while synthesizing the solid solutions are: (1) the similarities in the crystal structure of the two end members from which the solid solution is made, (2) the electronegativity and the valence state of the compounds [137]. For a visible light active photocatalyst, good stability under light irradiation and excellent visible light absorption are the crucial properties. Photocatalysts are highly stable when the bottom of the CB is more negative than the potential of O_2/O_2^-. Hence, the stability is ensured by choosing the appropriate semiconductors for fabricating solid solution photocatalysts. The synthetic methods of certain important solid solution photocatalysts are discussed in this section. We particularly focus on the solid solutions synthesized by combining two or three different semiconductors, where the fabrication results in giving visible light active compounds. The various solid solution photocatalysts reviewed here can be divided into three different categories, depending on the strategy applied for obtaining the solid solution:

1. Solid solution through continuous modulation of CB,
2. Solid solutions through continuous modulation of VB,
3. Solid solution through continuous modulation of both CB and VB.

A schematic representation of attainment of visible light activity (narrowing of band gap) through the three different strategies of band gap engineering can be visualized in Figure 1.15. These three categories of solid solution photocatalysts are discussed hereafter.

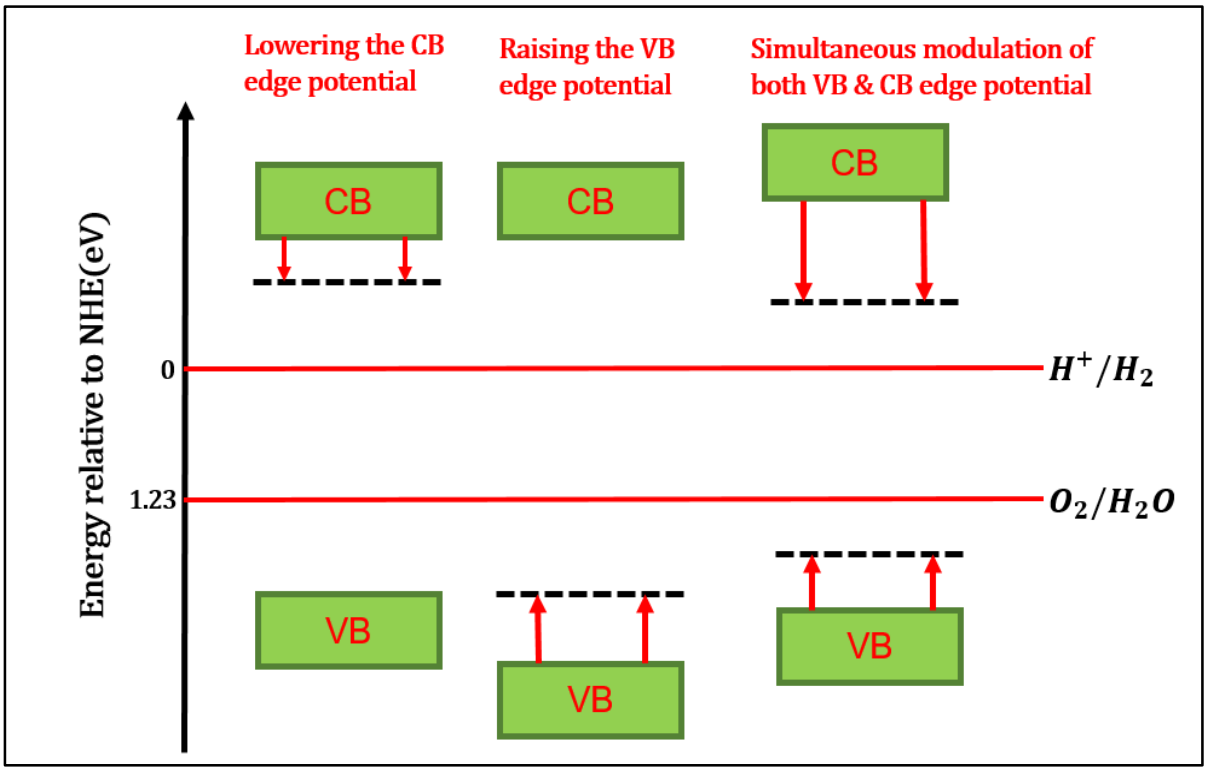

Figure 1.15. *Different modes of band gap engineering through which an optimum balance between visible light activity and redox potential of band edge potential are maintained.*

1.3.3.3. Solid solution through continuous modulation of CB

Silver (Ag) based oxide photocatalysts have grabbed a lot of attention in the heterogeneous photocatalytic field due to their interesting valence band, which is composed of hybridized Ag 4d and O 2p orbitals. These fascinating oxide semiconductors of the family $AgMO_2$ (M = Al, Ga, In) were extensively reviewed in the ternary section of photocatalysts. The solid solution photocatalysts fabricated with $AgMO_2$ ternary oxides can effortlessly extend into the entire region of visible spectrum and can still retain the VB potential, thus possessing strong oxidizing potential for photocatalytic decomposition of various organic compounds. Within the family of $AgMO_2$ ternary photocatalysts, β-$AgAlO_2$ was the first developed photocatalyst, which exhibits low activity in the visible region due to its wide band gap (2.8 eV) [93] or (2.95 eV) [96].

Ouyang *et al.* improved the photocatalytic activity of β-$AgAlO_2$ ternary photocatalyst for decomposition of isopropanol under visible light, through continuously tuning the conduction band edge of β-$AgAlO_2$ semiconductor by combining it with narrow band gap β-$AgGaO_2$ (2.18 eV) semiconductor, resulting in a novel β-$AgAl_{1-x}Ga_xO_2$ solid solution photocatalyst [138]. They synthesized β-$AgAl_{1-x}Ga_xO_2$ solid solution through a two-step (sol-gel followed by cation exchange) method, which exhibited a homogeneous crystal system with orthorhombic symmetry belonging to the family of cristobalite structure. The linear band gap variation of the solid solution with respect to composition, observed in UV-VIS absorption spectrum is depicted in Figure 1.16-a. It clearly indicates that continuous solid solution through precise tuning of CB was obtained in the system. The resultant solid solution β-$AgAl_{1-x}Ga_xO_2$ ($0 \leq x \leq 1$) exhibits photocatalytic activity, which largely depends on its composition. Among the various compositions, β-$AgAl_{0.6}Ga_{0.4}O_2$ semiconductor (2.58 eV) exhibits the highest photocatalytic activity for isopropanol photo-degradation. The photocatalytic production rate of acetone (photo-decomposed product of isopropanol) by β-$AgAl_{0.6}Ga_{0.4}O_2$ photocatalyst was 35 and 63 times higher than its end components β-$AgAlO_2$ and β-$AgGaO_2$, respectively.

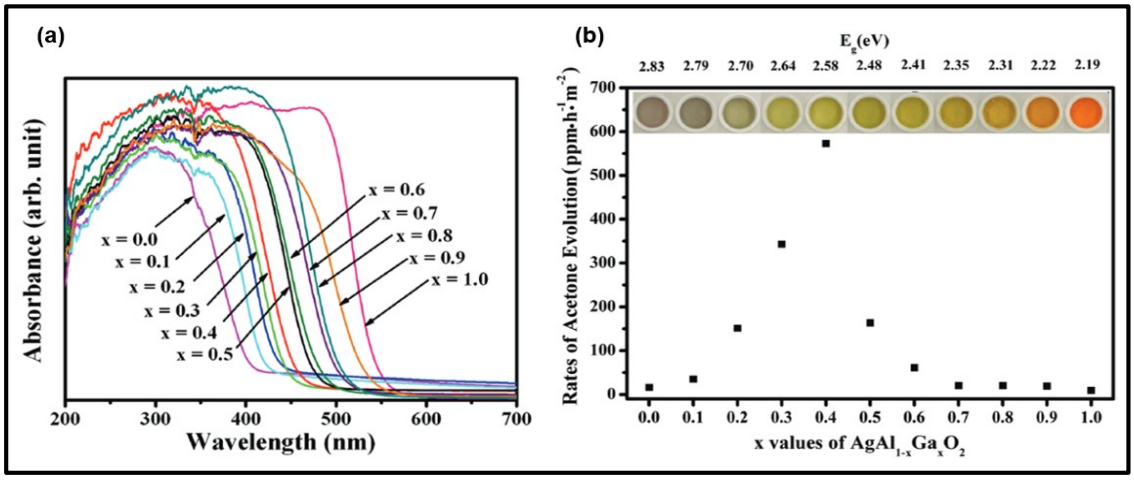

Figure 1.16. *a. β-$AgAl_{1-x}Ga_xO$ solid solution fabricated from β-$AgAlO_2$ and β-$AgGaO_2$ ternary oxide semiconductors by precise tuning CB from 2.83 eV to 2.19 eV; b. Depiction of color of the various compositions of the solid solution along with their corresponding acetone evolution rate vs the band gap of the solid solution photocatalysts [138].*

The color of the various compositions of the solid solutions and the acetone evolution rate with respect to the band gaps of continuously CB modulated solid solution is depicted in Figure 1.16-b [138].

1.3.4.2. Solid solutions through modulation of VB

Prerequisites of any visible light active photocatalyst are (i) the stability under visible light irradiation and (ii) satisfactory absorption property. Niobium containing perovskite oxide photocatalysts were extensively explored in heterogeneous photocatalysis, since they suffice the requirement of intensified stability, as their CB edge potential is far more negative than the potential of O_2/O_2^- [83, 139]. Silver niobate ($AgNbO_3$) is one such perovskite photocatalyst, which exhibits enough stability under visible light irradiation and possesses narrow band gap (2.79 eV) due to the hybridized VB composed of Ag 4d and O 2p orbitals. $AgNbO_3$ exhibits visible light active photocatalytic activity for producing O_2 from silver nitrate solution but it doesn't own enough oxidation potential for decomposing several organic compounds. Li *et al.* improved the photo-oxidizing ability of $AgNbO_3$ photocatalyst by combing it with $NaNbO_3$ (3.4 eV) perovskite semiconductor, resulting in a $(AgNbO_3)_x(NaNbO_3)_{1-x}$ $(0 \leq x \leq 1)$ solid solution photocatalyst. They synthesized the solid solution through conventional solid state synthesis route. As the $NaNbO_3$ content is increased, the absorption band edge of solid solution is blue shifted, resulting in the widening of the optical band gap. The CB edge potential of both $AgNbO_3$ and $NaNbO_3$ are pinned at the same level (-0.4 eV vs NHE) [83]. As the solid solution is formed with increasing $NaNbO_3$ content, the top of the VB is continuously modulated, shifting the VB top from $AgNbO_3$ (+2.39 eV) to VB top of $NaNbO_3$ (+3 eV), indicating that the oxidation potential of the solid solution is more positive than the one of $AgNbO_3$. Among the continuous range of solid solution, $(AgNbO_3)_{0.6}(NaNbO_3)_{0.4}$ exhibits the highest photocatalytic activity for 2-propanol (IPA) decomposition under visible light irradiation, where the activity is three times higher than the one of the $AgNbO_3$ photocatalyst. As the ionic radius of Na (1.18 Å) is smaller than Ag (1.28 Å), the formation of solid solution results in reduced lattice parameters, leading to decrement of particle size and an increase of the surface area compared to $AgNbo_3$ photocatalyst [140].

Similar kind of continuous VB modulation without CB alteration was reported on the solid solution formed through the synthesis of binary photocatalysts (GaN and ZnO) [141]. Such d^{10}-(oxy) nitride solid solution was fabricated from d^{10} oxide photocatalyst (ZnO). Indeed, the CB bottom of the d^{10} oxide semiconductor is composed of hybridized s & p metallic cation, leading to large dispersion of CB, resulting in the increased mobility of the photogenerated electron, thus intensifying the photocatalytic activity. GaN was chosen as another constituent of the solid solution, as N 2p orbitals possess higher potential energy than O 2p orbitals and also possess similar CB, like ZnO. Such system was designed for overall water splitting reaction under visible light, as it suffices the requirements of narrow band gap below 3 eV, possesses appropriate band edge for water splitting and exhibits good stability under photocatalysis. GaN (3.4 eV) contains the required band edge potential for water splitting, but is active under UV light only. The fabrication of $(Ga_{1-x}Zn_x)(N_{1-x}O_x)$ solid solution with ZnO (3.2 eV) results in the upliftment of the VB, leading to narrow band gap solid solution. The upraise of VB potential without any changes to the CB was hypothesized due to the repulsion existing

between O 2p and Zn 3d orbitals [142]. DFT calculations performed by Kazuhiko Maeda *et al.* have confirmed that the bottom of the CB is composed of only Ga 4s & 4p orbitals, whereas the top of VB is composed of N 2p orbital followed by Zn 3d & O 2p, which falls in agreement with the theoretical calculations performed on this system by Jensen *et al.* and Huang *et al.* [143, 144]. A schematic representation of the above described CB and VB of solid solution and variation of band gap with increment of ZnO content is depicted in Figures 1.17-a and 1.17-b.

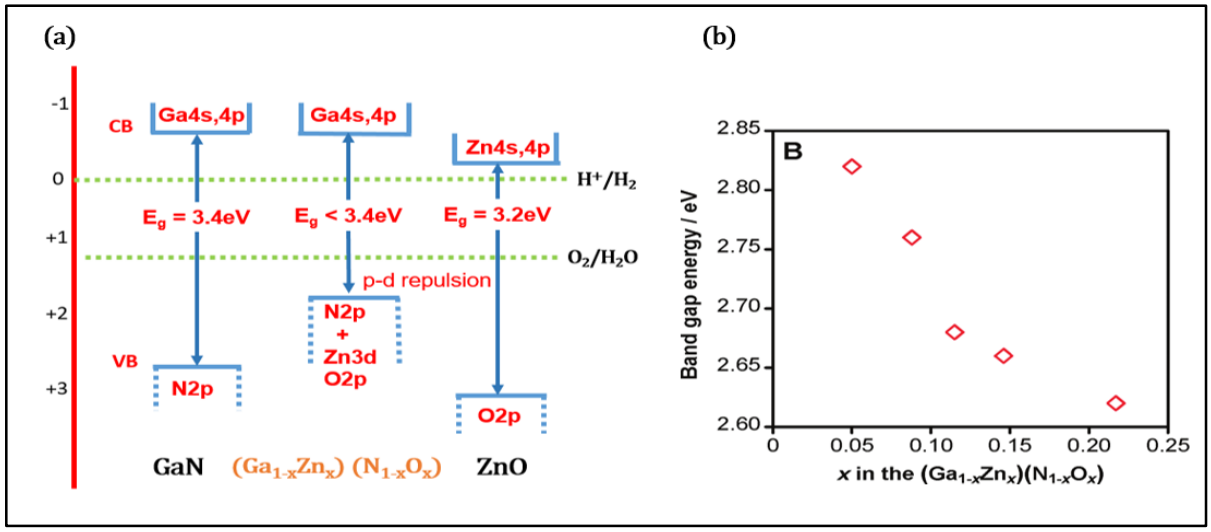

Figure 1.17. *a. Schematic description of band structures of GaN, ZnO and* $(Ga_{1-x}Zn_x)$ $(N_{1-x}O_x)$ *solid solution (redrawn based on the article [142]); b. Variation of the band gap with respect to ZnO content in the solid solution [142].*

Maeda *et al.* reported the synthesis of $(Ga_{1-x}Zn_x)(N_{1-x}O_x)$ through nitridation of oxide precursors (Ga_2O_3 & ZnO) at high temperature (> 1123 K) under ammonia flow. The as-synthesized solid solution exhibited negligible activity for water splitting, but when loaded with co-catalyst like 1 wt% Rh (Rhodium) and 1.5 wt% Cr (Chromium) on $(Ga_{1-x}Zn_x)(N_{1-x}O_x)$ solid solution with very low Zn quantity (Zn/Ga = 0.14), enhanced photocatalytic H_2 and O_2 production of 360 µmol.h^{-1} and 162 µmol.h^{-1} was observed, respectively [142]. The conventional nitridation method suffered from several drawbacks like long nitridation time, higher temperatures (> 1123 K) and large particles in micron scale. Recently, Sumithra & Anitha *et al.* replaced the conventional nitridation by solution combustion method, which yields to particles in the nanoscale (40 nm); the resultant $(Ga_{1-x}Zn_x)(N_{1-x}O_x)$ possesses high zinc content (Zn/Ga = 20, 30 and 40). The solid solution with (Zn/Ga = 20) exhibits good activity in water splitting under visible light without the aid of co-catalyst, with apparent quantum yield of H_2 production at 0.048% [145]. Eventhough the above described VB modulated solid solution has various advantages, a rigorous development of synthetic methodologies is required for this system to attain the continuous modulation of VB and to study its effect on various photochemistries apart from water splitting reactions.

1.3.4.3. Solid solution through modulation of both CB and VB

Simultaneous regulation of equilibrium between absorption extension into visible region and both oxidative & reductive abilities of photocatalysts is attained in solid solution photocatalysts, fabricated through synchronous precise tuning of both VB and CB. Due to the favourable inclination of partial substitution of comprehensive metallic cations and valences at the position of A and B elements in ABO_3 structured perovskites. They stand as propitious materials for the fabrication of solid solution through simultaneous engineering of both VB and CB.

Wang et *al.* performed the precise tuning of both CB and VB by forming a $(AgNbO_3)_{1-x}(SrTiO_3)_x$ solid solution between visible active $AgNbO_3$ (450 nm) and UV active $SrTiO_3$ (380 nm) perovskites. They synthesized a solid solution through solid state reaction method, where the resultant solid solution's CB is composed of hybridized Nb 4d and Ti 3d orbitals. As the Nb 4d is more positive than the Ti 3d, an increase of $AgNbO_3$ content brings the bottom of CB band downwards. Similarly, the VB of this solid solution is composed of hybridized Ag 4d and O 2p: where Ag 4d being more positive than O 2p, it pushes the top of VB upwards, thus favouring activity in the visible region with optimum balance between the redox potentials. The presence of such hybridized CB and VB in the solid solution with continuous dispersion favors enhanced charge carrier transportation upon excitation, thus leading to increased photocatalytic activity. The solid solution obtained here exhibited continuous modulated CB and VB for the composition ($0 \leq x < 0.95$) and discontinuous CB and VB for the composition ($0.95 \leq x \leq 1$), due to very low concentration of the other constituents of the solid solution. A schematic representation of continuous modulated CB and VB and discontinuous interbands (dopant levels) are depicted in the Figure 1.18. Among the continuous range of $(AgNbO_3)_{1-x}(SrTiO_3)_x$ photocatalysts, $(AgNbO_3)_{0.75}(SrTiO_3)_{0.25}$ exhibits the highest photocatalytic activity for O_2 production from silver nitrate solution of about 162 μmol.h^{-1}, with apparent quantum efficiency of about 16.4% under visible light radiation.

The same photocatalyst exhibited high activity for Isopropanol (IPA) decomposition, where it completely demineralized IPA to CO_2 within 22 hours under visible light irradiation [146]. As the $(AgNbO_3)_{0.75}(SrTiO_3)_{0.25}$ solid solution possessed the optimum equilibrium between the visible light absorption and reductive/oxidative potentials, it exhibited higher photocatalytic activity than the two end members and other composition of the solid solution photocatalysts.

Ternary semiconductors possessing scheelite crystal structure have found to be active photocatalysts for H_2 and O_2 evolution from aqueous solutions containing sacrificial agents [97, 147, 148] (see section (3.3) on ternary photocatalysts). Calcium molybdate ($CaMoO_4$), a ternary oxide of the molybdate family exhibits scheelite crystal structure and manifests its application in heterogeneous photocatalysis, photoluminescence and microwave applications. The divalent ions present in the scheelite-type molybdate semiconductors can be indisputably substituted with other metallic ions resulting in an abundant families of solid solution photocatalysts.

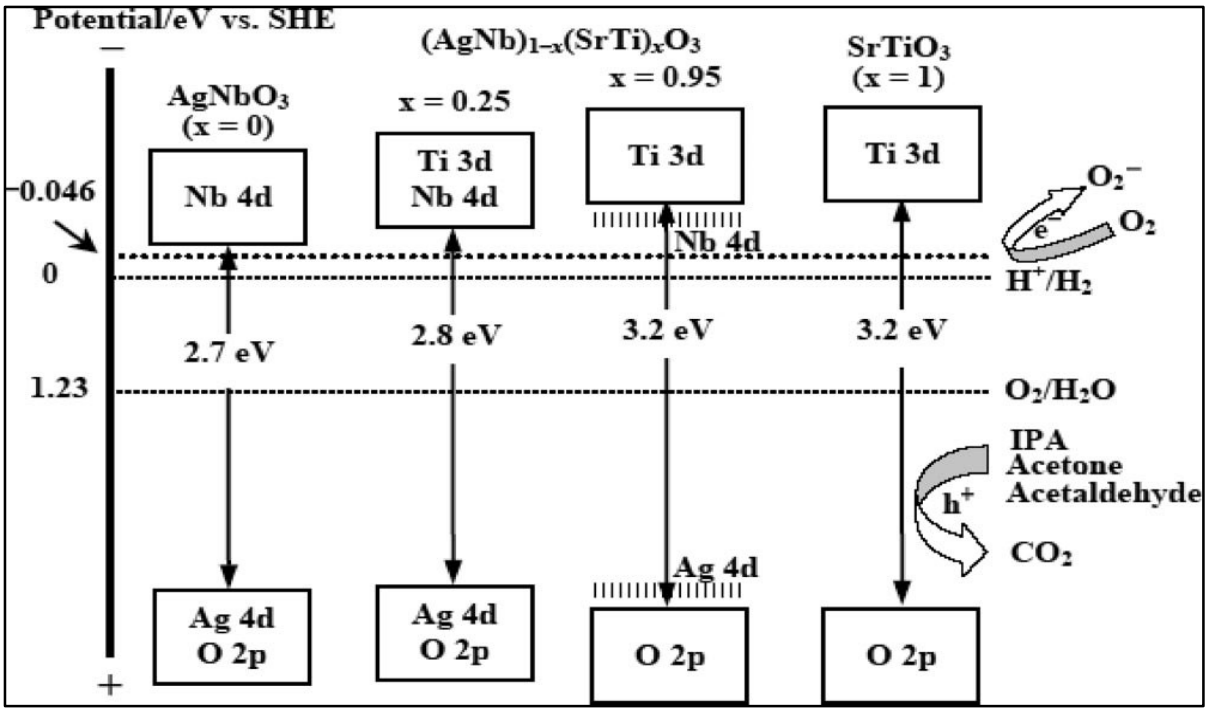

Figure 1.18. *Schematic depiction of the continuous modulation of CB and VB in* $(AgNbO_3)_{1-x}(SrTiO_3)_x$ *(0.25 < x < 0.95) and the discontinuous interbands (dopant levels) in the composition (0.95 ≤ x ≤ 1) [146].*

Yao *et al.* synthesized Scheelite-Tetragonal (ST) $Ca_{1-x}Bi_xV_xMo_{1-x}O_4$ ($x = 0 - 1$), solid solution photocatalysts through solid state route by combining ST-$CaMoO_4$ (3.64 eV) with Scheelite-Monoclinic (SM) $BiVO_4$ (2.34 eV). $Ca_{1-x}Bi_xV_xMo_{1-x}O_4$ solid solutions' absorption band edge is monotonically red shifted towards the visible region as the $BiVO_4$ content is increased in the solid solution and no discontinuous interbands were observed in this solid solution. The CB bottom is composed of hybridized Mo 4d and V 3d and the top of the VB is composed of hybridized Bi 6s and O 2p. The band edge potential of the solid solution is located between the end constituents and is precisely engineered by varying the ratio between $BiVO_4$ and $CaMoO_4$. Apart from the ideal balance between the reductive/oxidative potentials and visible light absorption, the hybridized CB and VB promote faster charge transfer due to their dispersed nature and increase the photocatalytic activity. This phenomenon is observed more in solid solution than in ternary or binary photocatalysts. Among the continuous range of solid solution photocatalysts synthesized, $Ca_{0.2}Bi_{0.8}V_{0.8}Mo_{0.2}O_4$ exhibits the highest activity for photocatalytic O_2 production (100 μmol.h^{-1}) from silver nitrate solution at apparent quantum efficiency of 10% compared to that of $BiVO_4$ (33.8 μmol.h^{-1}) at quantum efficiency of 2.7% under visible light irradiation [149].

1.3.4.3.1. Chalcogenide-based solid solutions

Chalcogenide solid solution photocatalysts, especially sulfides, are always fabricated by continuous tuning of both CB and VB, where a wide band gap material is combined with a low band gap semiconductor. Sulfide semiconductors have addressed several heterogeneous

photocatalytic reactions due to their suitable band edge position and their energy gap for photocatalytic H_2 production under visible light [150, 151]. Even if binary sulfides like cadmium sulfide (CdS) were found to be moderate photocatalysts for H_2 production (see section (3.2.1.2) chalcogenide-based binary photocatalysts), they suffer from quick recombinations of photogenerated charge carriers and photo-corrosion under visible light activity, which limits their use at large scale [152].

The formulation of highly crystalline solid solutions combining wide band gap zinc sulfide (ZnS) with CdS, solves the photo-stability issues of CdS under visible light. The synthesis of $Cd_xZn_{1-x}S$ $(0 < x < 1)$ solid solutions was achieved through several techniques like: co-precipitation [153, 154], cation-exchange [155] and hydrothermal methods [156, 157]. These conventional techniques exhibit several drawbacks. For instance, the final elemental composition of solid solutions deviate heavily from the initial stoichiometric amount taken for synthesis in co-precipitation techniques [153].

Similarly, the attainment of minimal control over band structure was adversed in cation exchange route, while hydrothermal method required long reaction time for obtaining highly crystallized solid solution photocatalysts. In 2013, Li *et al.* replaced the conventional synthetic routes with facile thermolysis route for obtaining highly crystalline $Cd_xZn_{1-x}S$ $(0 < x < 1)$ solid solution nanoparticles [158]. Their synthetic route consists of the thermolysis of a single source precursor (complex Zinc –Cadmium -Thiourea), where the formation rate of solid solutions occurred in small time scale (30 minutes).

The as-synthesized solid solutions $Cd_xZn_{1-x}S$ were found to be aggregates of small crystallized nanoparticles (average size = 10 nm), as depicted schematically in Figure 1.19. The continuous red shift of steep absorption band edge, with increasing CdS content, confirmed the precise engineering of the CB and VB in this solid solutions obtained by this thermolysis method. The absorption spectrum and equivalent color of $Cd_xZn_{1-x}S$ $(0 < x < 1)$ solid solutions are depicted in the Figure 1.19-c.

Among the different ranges of $Cd_xZn_{1-x}S$ $(0 < x < 1)$ (2.3 - 3.10 eV) solid solutions, $Cd_{0.5}Zn_{0.5}S$ (2.45 eV) possesses the superlative balance between the CB and VB potentials and the visible light absorption ability exhibited the maximum photocatalytic H_2 production (7.42 $mmol.h^{-1}.g^{-1}$) from water with sacrificial agents (Na_2S & Na_2SO_3) without the aid of co-catalysts (Pt). This photocatalytic activity exceeds the activities of CdS and ZnS by 24 and 54 times, respectively. Additionally, it is much higher than the activity displayed by co-catalyst (Pt) loaded CdS photocatalysts. A schematic representation of the CB and VB tuning with respect to composition and visible light active H_2 production rate for the $Cd_xZn_{1-x}S$ solid solutions and Pt-CdS photocatalysts is depicted in Figures 1.19-d and 1.19-e.

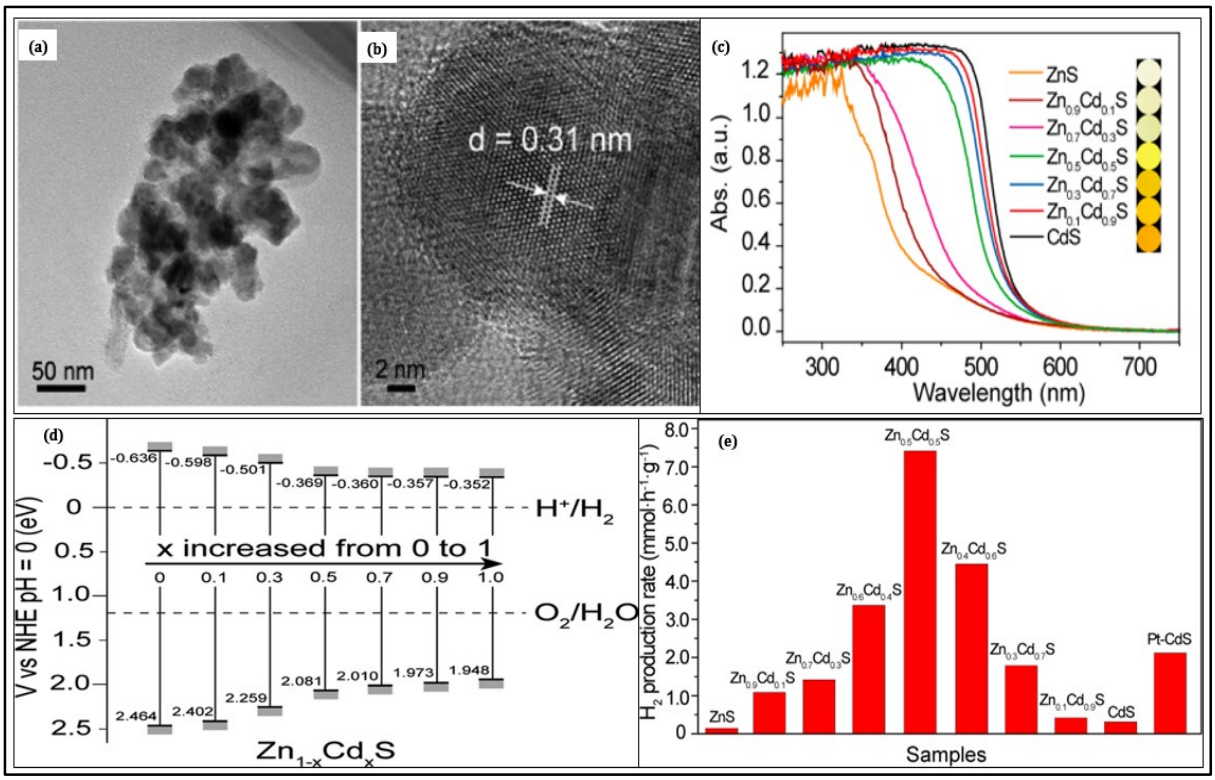

Figure 1.19. *a. TEM image of $Zn_{0.5}Cd_{0.5}S$ solid solution, average diameter of aggregates (50 - 100 nm); b. HR-TEM image of $Zn_{0.5}Cd_{0.5}S$ solid solution, diameter of each NP is about 10 nm; c. UV-VIS diffuse reflectance spectra of $Cd_xZn_{1-x}S$ solid solutions (x = 0, 0.3, 0.5, 0.7 and 0.9) [158]; d. Band gap variation with respect to composition; e. H_2 production rate with respect to composition in $Cd_xZn_{1-x}S$ solid solutions [158].*

Nevertheless, $Cd_xZn_{1-x}S$ solid solution systems carry some limitations. When the value of 'x' is very low, the band gap is very wide, resulting in low activity under visible light. When the value of 'x' is high the CB edge potential is very low resulting in negligible photoactivity without the loading of a co-catalyst (Pt) [151]. Conflicting to CdS, ZnS is a wide band gap photocatalyst. It is therefore incapable to produce H_2 (water splitting) under visible light. However, Kudo *et al.* reported that through an aqueous (precipitation) route, copper (Cu) can be incorporated into the ZnS lattice, resulting in a $Zn_xCu_{1-x}S$ $(0 \leq x \leq 1)$ solid solution. In such systems, for a low quantity of Cu, highly visible light active $Zn_{0.957}Cu_{0.043}S$ (2.5 eV) solid solution was obtained. The copper metal was opted here for the formulation of solid solution because of the similar ionic radii of Zn (0.60 Å) and Cu (0.63 Å) in four-coordination states. The exhibitence of a good photocatalytic H_2 production (450 µmol.h^{-1}) by $Zn_{0.957}Cu_{0.043}S$ solid solution from aqueous Na_2SO_3 solution, at an apparent quantum yield of 3.7% under visible light without the aid of co-catalyst (Pt), have confirmed that incorporation of copper into the ZnS lattice has tuned the VB to certain extent for visible light activity without altering the reduction potential edge of ZnS [159]. The red shifted absorption spectrum of $Zn_{0.957}Cu_{0.043}S$ solid solution with steep absorption edge has confirmed that the solid solution was formed, instead of mixture of CuS and ZnS.

The origin of visible light activity in such systems due to the transitions from the donor levels of Cu to the CB of ZnS had led researches to include Cu in $Cd_xZn_{1-x}S$ solid solution through various synthetic techniques, resulting in a novel $Cd_xCu_yZn_{1-x-y}S$ solid solution, where the precise modulation of VB and CB of ZnS are achieved through the incorporation of Cu and Cd elements at very low value of 'x' and 'y'. Liu *et al.* synthesized the $Cd_xCu_yZn_{1-x-y}S$ solid solutions through a co-precipitation technique, where the $Cd_{0.1}Cu_{0.01}Zn_{0.89}S$ (2.33 eV) solid solution exhibited maximum photocatalytic activity (350 μmol.h^{-1}) for H_2 production at an apparent quantum yield of 9.6%, compared to $Cd_{0.1}Zn_{0.9}S$ (2.66 eV) and $Zn_{0.99}Cu_{0.01}S$ (2.5 eV) solid solution photocatalytic H_2 production of about 96.8 μmol.h^{-1} and 12.5 μmol.h^{-1}, respectively from the aqueous solution of Na_2SO_3 and Na_2S under visible light irradiation [160].

The ternary semiconductor materials of the group I-III-VI_2 (I = Cu, Ag; III = Al, Ga, In; VI_2 = S, Se, Te), especially $CuInS_2$, have received increasing attention as a new class of materials in the field of solar cells and also for solar driven H_2 production from water splitting reactions [161]. Many solid solution photocatalysts have been made by combining ternary of group I-III-VI_2 and ZnS material possessing the same crystal structure. In ternary sulfide semiconductors such as $AgInS_2$ or $CuInS_2$, the VBs are composed of d-states of Ag or Cu assorted with p-states of sulphur [162, 163]. These results in VBs far more negative than VBs of ZnS or CdS. Such feature is highly needed for visible light activity as VB is precisely tuned by monovalent cations of Ag or Cu in $AgInS_2$ or $CuInS_2$. Precise tuning of CB is also achieved through Indium ions, when ZnS is combined with either $AgInS_2$ or $CuInS_2$, as illustrated in Figure 1.20.

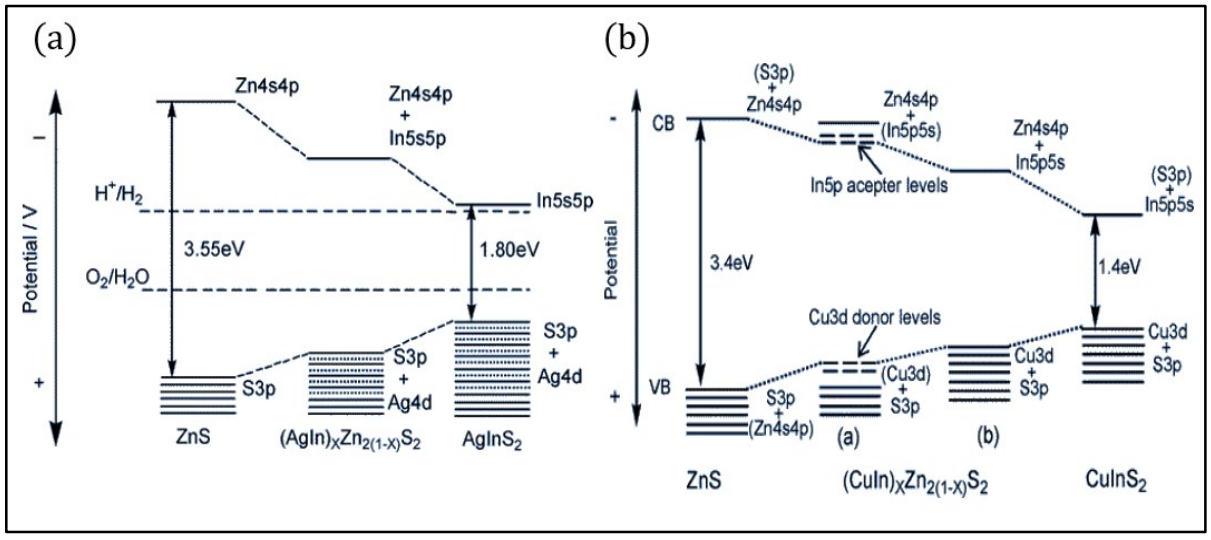

Figure 1.20. *a. Band gap modulation in $(AgIn)_x Zn_{2(1-x)}S_2$[164]; b. Band gap engineering attained in $(CuIn)_xZn_{2(1-x)}S_2$ solid solutions [165].*

Tsuji *et al.* reported the synthesis of $(AgIn)_xZn_{2(1-x)}S_2$ $(0 \leq x \leq 1)$ (3.55 - 1.8 eV) solid solutions through the heat treatment of complex greyish Ag-In-Zn sulfide precursor, prepared through the bubbling of H_2S in a mixture of metallic nitrate salts. Here, they attempted several different heat treatment strategies through which the photocatalytic activity of the resultant

solid solutions was improved. $(AgIn)_{0.22}Zn_{1.58}S_2$ (2.33 eV) solid solution synthesized through heat treatment under N_2 flow exhibited photocatalytic activity for H_2 production (72 μmol.h^{-1}) from aqueous solution of K_2SO_3 and Na_2S under visible light irradiation. The same solid solution synthesized through heat treatment under sealed quartz ampule tube without N_2 flow gave a higher photocatalytic activity for H_2 production (328 μmol.h^{-1}). The photocatalytic activity was 4.5 times higher than the solid solution synthesized by N_2 flow, as the newly proposed heat treatment methodology prevented the volatilization of metallic cations during the synthesis. When loading 3 wt% of co-catalyst (Pt) on the $(AgIn)_{0.22}Zn_{1.58}S_2$ (synthesized by heat treatment in sealed quartz tube), the photocatalytic rate for H_2 production under visible light was further enhanced by a factor of three (944 μmol.h^{-1}), with the highest apparent quantum yield of 20% [164].

Subsequently in the following years, the same research group (Tsuji *et al.* & Kudo *et al.*) employed the above newly modified heat treatment process (1123 K for 5 h) in sealed quartz tube for the synthesis of $(CuIn)_xZn_{2(1-x)}S_2$ $(O \leq x \leq 1)$ (3.5 -1.4 eV) solid solution photocatalysts. For very low $CuInS_2$ content (x < 0.05), discontinuous discrete energy levels were formed in the system, as depicted in Figure (1.20.b). Above this composition (x > 0.05), continuous VB was formed and monotonous red shift to visible region occurred with the increase in the value of 'x'. Among the solid solutions synthesized, $(CuIn)_{0.09}Zn_{1.82}S_2$ exhibited moderate photocatalytic activity for H_2 production (7 μmol.h^{-1}) from aqueous solution containing sacrificial agents (K_2SO_3) under visible light irradiation. The same solid solution photocatalyst, when loaded with 0.5 wt% of co-catalysts (Pt), displayed the highest photocatalytic activity for H_2 production (684 μmol.h^{-1}) with an apparent quantum yield of 12.5% [165].

Tsuji *et al.* & Kudo *et al.* developed the heat treatment technique for solid solution synthesis further. They reduced the heat treatment temperature from 1123 K to 873 K and increased the heat treatment duration of complex single source solid solution precursor from 5 to 20 h. To synthesize ZnS-$CuInS_2$-$AgInS_2$ solid solutions and compare its photocatalytic ability with respect to ZnS-$CuInS_2$ and ZnS-$AgInS_2$ solid solution photocatalysts. Prior to the photocatalytic study all three different solid solution photocatalysts were loaded with 0.75 wt% of co-catalysts (Ru) on their surfaces to boost up the photocatalytic effect. The $(CuAg)_{0.15}In_{0.3}Zn_{1.4}S_2$ solid solution with the aid of co-catalysts (Ru) exhibited higher photocatalytic activity for H_2 production (2.3 mmol.h^{-1}) from aqueous solution containing sacrificial agents (K_2SO_3 & Na_2S) than the activity exhibited by $(CuIn)_{0.09}Zn_{1.82}S_2$ and $(AgIn)_{0.22}Zn_{1.56}S_2$ solid solution photocatalysts [166].

1.3.4.4. Conclusion

In conclusion, solid solution photocatalysts can exhibit very high activity under visible/UV irradiation as optimum balance between required redox potentials and absorption band edge is successfully engineered. The main drawback or limiting step in the synthesis of solid solution photocatalysts are (i) the precursor preparation step and (ii) the cost of the single source precursor available to synthesize the required solid solution. The product yield of the so far developed batch protocols for solid solution synthesis is very low. The implementation for flow

synthesis of solid solution photocatalysts is still in the dormant phase and very rare solid solution materials are synthesized through continuous flow techniques. An overview of the synthetic methodologies and the synthesis conditions along with the heterogeneous photochemical system is reported in Table (1.3).

Table 1.3. *Overview of the synthetic methodologies, conditions and precursor used in the synthesis for solid solution materials along with their heterogeneous photocatalytic system is reported (SS: Solid solution semiconductor photocatalysts).*

SS	Synthetic methods	Precursors	Photochemical reaction	Illumination source	Reactor setup	Ref
β-$AgAl_{1-x}Ga_xO_2$ ($0 \leq x \leq 1$) **(2.19 - 2.8 eV)**	Cation exchange method	CH_3COONa, $Al(NO_3)_3.9H_2O$, $Ga(NO_3)_3.nH_2O$ and $AgNO_3$.	Decomposition of IPA first into acetone and then to CO_2 under visible light.	300 W Xenon arc lamp, ($400 < \lambda <$ 500 nm) Blue LED lamps	500 mL reactor equipped with a Pyrex glass lid as window	[138]
$(AgNbO_3)_{1-x}$ $(NaNbO_3)_x$ ($0 \leq x \leq 1$) **(2.79 - 3.4 eV)**	Solid State reaction method	Ag_2O, Na_2CO_3 and Nb_2O_5	Decomposition of IPA into acetone and CO_2 under visible light.	Blue Light Emitting LEDs (BLEDs) with light intensity of 0.01 $mWcm^{-2}$ (λ = 400 - 550 nm)	Glass reactor of volume 500 mL	[140]
$(Ga_{1-x}Zn_x)$ $(N_{1-x}O_x)$ With and without RuO_2 loading. **(2.6 – 2.8 eV)**	Nitridation of powdered precursor mixture	Ga_2O_3, ZnO and NH_3 gas	For water splitting reaction using visible light.	High pressure mercury lamp 450 W	Pyrex inner irradiation type reaction vessel	[142]
$(AgNbO_3)_{1-x}$ $(SrTiO_3)_x$ ($0 \leq x \leq 1$) **(2.7 - 3.2 eV)**	Solid state reaction method	Ag_2O, $SrCO_3$, Nb_2O_5 and TiO_2	O_2 evolution from silver nitrate solution and decomposition of IPA.	300 W Xenon arc lamp with cut off filter to obtain visible light ($\lambda \geq$ 410 nm)	Closed gas circulation system containing Pyrex glass vessel, with a flat side window for light irradiation	[146]
$Ca_{1-x}Bi_xV_xMo_{1-x}O_4$ **(2.34 - 3.64 eV)**	Solid state reaction method	$CaCO_3$, Bi_2O_3, V_2O_5 and MoO_3	O_2 evolution from $AgNO_3$ solution	300 W Xenon lamp with cut off filter attached providing visible light ($\lambda \geq$ 420 nm)	Closed Gas circulation system with side window attached Pyrex cell.	[149]
$Cd_xZn_{1-x}S$ ($0 < x < 1$) **(2.3 - 3.10 eV)**	Thermolysis of zinc-cadmium-thiourea (Zn-Cd-Tu) complex	Thiourea, $Zn(AC)_2.2H_2O$ and $Cd(AC)_2.2H_2O$	Visible light driven H_2 production from aqueous solution containing sacrificial agents.	350 W Xenon arc lamp with UV cut off filter, $\lambda \geq$ 400 nm	10 mL Pyrex flask, with openings of flask are sealed with silicone rubber septums	[158]
$Cd_xCu_yZn_{1-x-y}S$ **$Cd_{0.1}Cu_{0.01}Z_{0.89}S$ (2.33eV)**	Co-precipitation method	$Zn(NO_3)_2$, $Cu(NO_3)_2$, $Cd(NO_3)_2$ and Na_2S	H_2 from aqueous solution under visible light containing sacrificial agents	350 W Xenon lamp with optical filter ($\lambda \geq$ 430 nm)	Side window fixed Pyrex cell	[160]
$(AgIn)_xZn_{2(1-x)}S_2$ ($0 \leq x \leq 1$) **(1.8 - 3.3 eV)**	Heat treatment of Ag-In-Zn sulfide complex precursor	$AgNO_3$, $In(NO_3).3.9H_2O$ and $Zn(NO_3)_2.6H_2O$	H_2 Evolution from aqueous solution containing sacrificial agents.	Solar Simulator (AM 1.5) and 300 W Xenon lamp	Gas closed circulation system with a side or top window Pyrex cell	[164]
$(CuIn)_xZn_{2(1-x)}S_2$ ($0 \leq x \leq 1$) **(1.8 - 3.55 eV)** Pt or Ru loaded as Co-Catalyst on the solid solution	Heat treatment of Cu-In-Zn sulfide complex precursor. Photo deposition method.	$Zn(NO_3).6H_2O$, $In(NO_3).3.6H_2O$ and $CuCl_2$. H_2PtCl_6. $6H_2O$ and $RuCl_3.nH_2O$.	H_2 evolution form aqueous solution containing sacrificial agents.	300 W Xenon lamp with a cut off filter ($\lambda \geq$ 420 nm)	Gas closed circulation system fitted Pyrex cell, with window for illumination fixed to the sides of the Pyrex cell	[165]
ZnS-$CuInS_2$-$AgInS_2$ Ru Co-catalyst	Heat treatment. Co-catalysts loaded by photo-deposition method.	$Zn(NO_3).6H_2O$, $AgNO_3$, $In(NO_3).3.6H_2O$ and $CuCl_2.2H_2O$ $(NH_4)_2RuCl_6$	H_2 evolution from an aqueous solution containing sulphide and sulphite sacrificial agents.	300 W Xenon lamp with cut off filter for emission at $\lambda \geq$ 420 nm	Closed gas circulation fixed Pyrex cell	[166]

1.3.5. Nanocomposite photocatalysts

An advanced photocatalytic system consists of materials which have to exhibit two critical features: (i) an ameliorated light absorption capacity and (ii) an enhanced photocatalytic performance. These crucial features provide the insights for developing composite photocatalysts by coupling two or three different materials together. The pairing of these materials is based on the energy exchange between materials possessing different electronic structures. In these composite materials, either one of the two or three materials combined can absorb the light individually, thus effectively increasing the total photonic energy absorbed. At the same time, a careful consideration of electronic structures of the coupled materials promotes effective separation of the photogenerated electrons and holes resulting in enhanced photocatalytic performances [137, 167]. In this section, we will describe the different nanocomposite systems realized as novel photocatalysts in heterogeneous photocatalysis. In details more rationale behind their design, synthetic methodology and photochemistry in which they are implemented will be addressed.

1.3.5.1. Types of nanocomposite photocatalytic systems

Composite nanostructures are usually composed of semiconductor-metal or semiconductor-semiconductor nanostructured systems. In semiconductor-metal composite systems noble metals such as Pt, Au, Pd, Rh, Ni, Cu and Ag are loaded on the surface of the semiconductor material (for example TiO_2), resulting in improving the photocatalytic efficiency (see section (3.4) solid solution photocatalysts). The various kind of nanocomposite systems are systematically illustrated in the Figure 1.21.

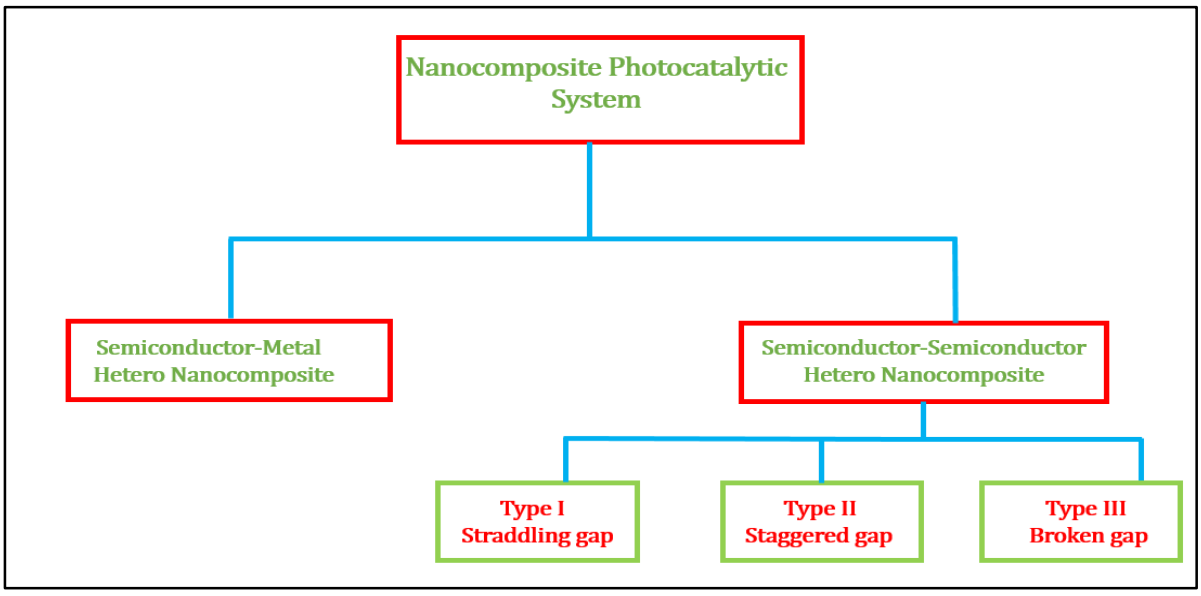

Figure 1.21. *Schematic illustration of the various types of hetero-composite systems.*

1.3.5.2. Semiconductor-metal composite systems

Arrangement or design of metal-composite systems is depicted in Figure 1.22. The enhancement of the photocatalytic activity happens because these metals loaded act as reservoirs for the photogenerated electrons. When the fermi level (E_F) of the metal loaded is below the CB potential of the semiconductor material, the photogenerated electrons of the semiconductor upon photonic excitation are transferred to the metal particles loaded and the holes remain within the semiconductor material. Therefore, both can be used to carry out the reduction and oxidation reactions, respectively. Thus, metals possessing suitable work function compared to semiconductor materials can prevent/reduce electron hole recombinations. The metal-semiconductor composites facilitate the charge transfer process, as schematically depicted in Figure 1.22. and improve the charge carrier separation efficiency, thus ultimately resulting in the increase of photocatalytic performances [168, 169].

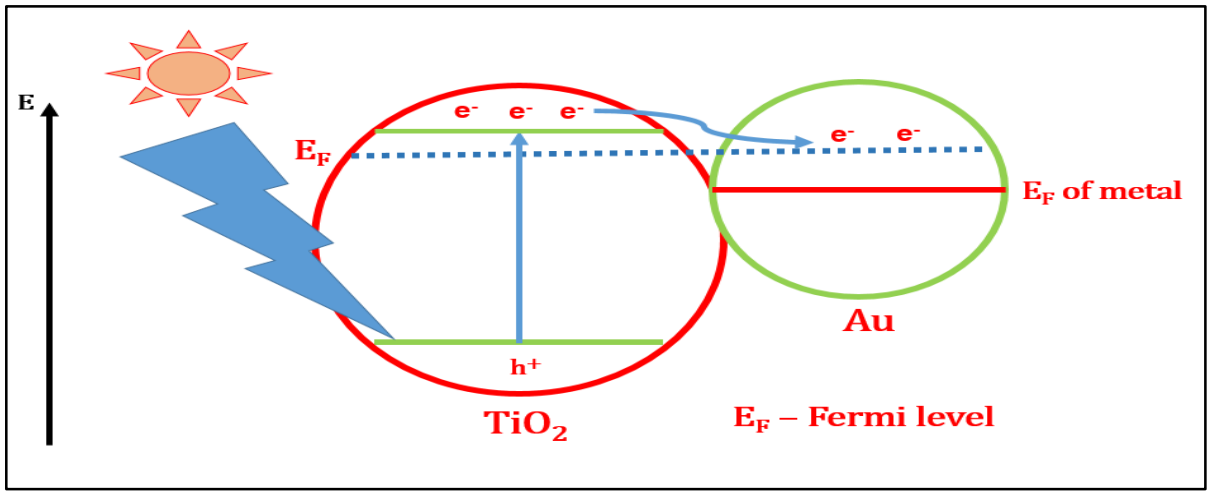

Figure 1.22. *Basic schematic representation of semiconductor-metal nanocomposite systems, drawn based on Au loaded TiO_2 photocatalytic system [168].*

1.3.5.3. Semiconductor-semiconductor composite systems

Unlike the semiconductor-metal composite systems, the semiconductor-semiconductor (SC-SC) coupled systems, where both materials individually absorb the photonic radiations, can result in harvesting more photonic energy. Thus, the first crucial requirement of enhanced light absorption is satisfied by this system. Whenever a semiconductor is coupled to different semiconductor materials, it results in three kinds of heterojunctions depending on the respective position of energy levels of each semiconductor: (i) straddling gap (Type I), (ii) staggered gap (Type II) and (iii) broken gap (type III). These three kinds of heterojunctions are depicted in Figure 1.23.

Within the three kinds of heterojunctions semiconductors, the type II hetero-composite system is the most desirable one for photocatalysis. The difference in chemical potential (arising from the appropriate position of band edge potentials, VB & CB of semiconductor 2 > VB & CB of semiconductor 1) between the two different semiconductors in Type II system results in band bending at the interface of the semiconductors. Band bending phenomenon instigates an

electric field, which drives the electrons and holes of the semiconductors upon photoexcitation in the opposite direction, leading to spatial separation of photon generated charge carriers and senhancing their photocatalytic activity [170, 171].

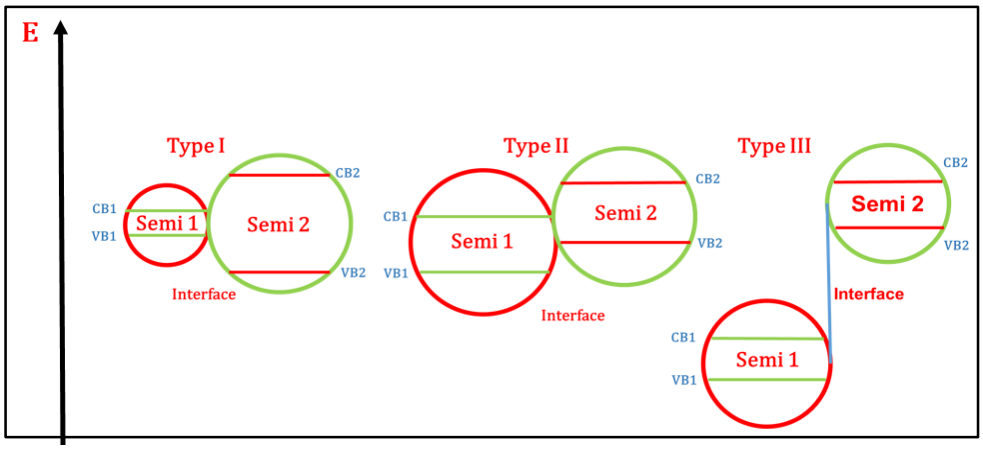

Figure 1.23. *Schematic representation of energy band gap diagram of three kinds of semiconductor heterojunction.*

Usually, these kind of systems are designed in such way that it results in possessing enhanced light absorption and efficient charge separation. To have an enhanced light absorption, the composite materials are generally composed of one semiconductor which is active in the UV region, for example TiO_2 or ZnO, while the other material is active in the visible region, for example CdS, CdSe, etc. The mechanism of charge transfer occurring in these systems, where efficient separation of charges occurs, is clearly demonstrated in Figure 1.24.

When the above composite materials are activated using the UV radiation, both the band gaps are excited, electrons migrate from the CB 2 to CB 1, holes migrate from the VB 1 to VB 2, thus resulting in efficient separation of charge carriers. In the case of visible light excitation, only the narrow band gap material is excited, the electrons from CB 2 migrate to CB 1 and holes remain within the VB 2, resulting in efficient charge separation. Here, irrespective of the electromagnetic irradiation (UV or visible) photo-generation and charge separation can be attained in the Type II system. From here onwards, I will focus typically in the SC-SC coupled nanocomposite system as it satisfies the two essential criteria of an advanced photocatalytic system.

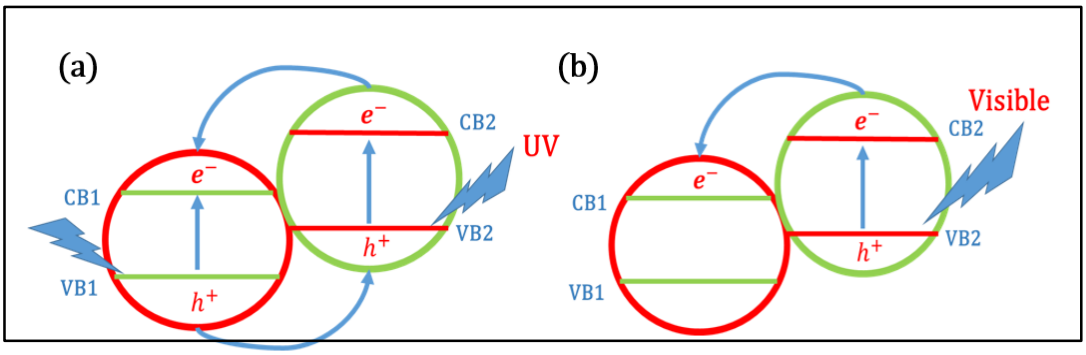

Figure 1.24. *Band gap diagram of Type II heterojunction illustrating the photo-generation of charge carriers and efficient separation of them upon (a) UV excitation and (b) visible light excitation.*

1.3.5.4. Considerations of semiconductor-semiconductor coupled nanocomposite photocatalytic systems

Even though these composite systems show enhanced photocatalytic performances, there are several essential factors to be considered during their design and their synthesis.

1.3.5.4.1. Importance of material amount ratio (semiconductor 1/semiconductor 2)

The synergistic absorption of light by both the semiconductors in the heterojunction provides the combined system to absorb photons with energies higher than their individual band gaps. Therefore, the light absorption limit of these composite materials is determined by the band gap of the narrower semiconductor, which is generally active in the visible region. Thus, it can be clearly seen that absorption intensity of the composite material can be increased by increasing the amount of narrow band gap material. Nevertheless, this doesn't increase necessarily the photocatalytic performance of the composite system, as it is seen in several composite samples, like AgI-BiOI composite systems. The reduced photocatalytic performance and increased light absorption intensity upon increment of AgI (narrow band gap) is due to the increase in the excessive number of trapping sites upon the increase of the AgI content [172]. Thus, it is very important to determine the optimal composition of both the semiconductors in such systems so that appropriate balance between the intensity of light absorption and photocatalytic performance can be maintained.

1.3.5.4.2. Importance of interfaces

In semiconductor-semiconductor nanocomposite systems, there is possibility for the occurrence of defects due to the lattice mismatch at the materials interface. These defects can trap the photogenerated electrons or holes leading to recombination. This prevents the use of photogenerated electrons and holes for reduction or oxidation reaction, respectively. Oppositely, the lattice mismatch can lead to an electric field at the interface between the two materials, which separates the charges further leading to higher photocatalytic activity. Thus, the quality of the heterogeneous interface stands to be another crucial factor affecting the photocatalytic performance [170]. In order to obtain high quality interface with less number of defects, high temperature annealing is usually employed in the synthetic methodologies. Apart from the annealing step itself, the annealing temperature is critical and determines the quality of the interface, which ultimately affects the photocatalytic performances, as simplified in the case of Bi_2O_3 - $SrTiO_3$ [173]. The quality of the heterojunction interfaces in various nanocomposites can also be improved by sedulous selection of the synthetic methods.

1.3.5.4.3. p-n type junction composite systems

Apart from the heterojunction composites mentioned above, which are basically made up of n-type semiconductor materials, there also exists another type of heterojunction composite material, which is formed by coupling n-type and p-type semiconductor materials thus resulting in heterojunction called p-n type junction. This is an exceptional kind of heterojunction, which possesses the previously mentioned advantages of composite systems: increased light absorption limit and effective charge carrier separation. In addition to these advantageous

properties, this p-n type junction possesses a supplementary internal electric field at the interface formed between the two semiconductor materials. This internal electric field further improves the charge separation efficiency in the composite materials and ultimately enhances the photocatalytic performance of the p-n junction type composite systems. Specifically, in the reported p-n junction composites photocatalysts, the photocatalytic reductive activity is higher than the reductive activities of its individual constituents but the photocatalytic oxidative activity is lower than that of its constituent materials. This is because, at equilibrium, when an internal electric field is formed at the interface of the p-n junction composite material, the p-type becomes negatively charged and n-type becomes positively charged. Upon excitation, the holes start moving towards the negative side and electrons towards the positive side, where the p-type semiconductor behaves as a hole trap and scavengers, which is unfavourable for photocatalytic oxidation reactions. These nanocomposites include for instance Cu_2O/TiO_2, NiO/TiO_2, p-ZnO/n-TiO_2 $CuBi_2O_4/Bi_2WO_6$, Cu_2O/In_2O_3, etc.[174 – 178].

1.3.5.5. Nanocomposite semiconductor photocatalysts

In this section, we report some of the most developed and researched nanocomposite photocatalytic systems. The synthetic methods used to produce such photocatalysts are also discussed.

1.3.5.5.1. TiO_2-based nanocomposite photocatalysts

TiO_2 has been tremendously researched for several decades due to its very high oxidation efficiency in photocatalysis, high photo-stability and low cost [179]. Still, TiO_2 application is hindered due to its wide band gap (3.2 eV) for anatase (polymorph of TiO_2), requiring ultraviolet irradiation ($\lambda < 380$ nm) for photocatalytic activation [180]. On the other hand, cadmium sulfide (CdS) is a relatively narrow band gap material (2.4 eV), extensively researched and modified (see section (3.4) solid solution photocatalyst) for photocatalytic H_2 production from water splitting reactions under visible light irradiation. CdS alone, exhibits poor photocatalytic performance for H_2 production, mainly due to the rapid recombination of electrons and holes upon excitation; secondarily, due to its low photo-stability in aqueous solutions. There are various strategies available to increase the photocatalytic efficiency of CdS. One solution consists in facilitating charge separation in CdS by coupling it to a wide band gap semiconductor material like TiO_2, ZnO, etc.

The growth of CdS on TiO_2 results in the TiO_2/CdS type II heterojunction, where upon excitation by visible light, causes photo-generation of electrons and holes in CdS. Electrons from CB of CdS are transferred to CB of TiO_2 and holes remain within CdS resulting in efficient charge separation, which ultimately provides the increase in the photocatalytic efficiency [181]. In the heterogeneous photocatalytic domain, different kinds of TiO_2/CdS nanocomposites have been synthesized through different techniques, such as: (i) CdS QDs sensitized in ordered mesoporous titania through ion-exchange route [181] and (ii) CdS nanoparticles coated on TiO_2 nanotubes through wet chemical methods [181]. Recently, Duong Vu *et al.* reported a novel non-noble co-catalyst loaded TiO_2/CdS nanocomposites ($Ni - TiO_2/CdS$) [182]. This nanocomposite system consists of TiO_2 nanorods, nanoparticles of CdS and Ni clusters. They synthesized capped TiO_2 through a solvothermal route and controlled the

length of the nanorods through the aid of surfactants. On these nanorods, CdS NPs were grown though colloidal synthesis, resulting in hybrid TiO_2/CdS nanocomposites. Subsequently, co-catalyst (Ni) clusters were selectively deposited on the nanocomposites through a photodepositon route. A schematic illustration of the synthesis of $(Ni - TiO_2/CdS)$ nanocomposite photocatalytic systems is depicted in the Figure 1.25-a.

The as-synthesized novel nanocomposite $(Ni - TiO_2/CdS)$ photocatalytic systems exhibited maximum photocatalytic activity for H_2 production (151.35 µmol.g^{-1}) from aqueous solution containing sacrificial agent (ethanol), compared to the activity of CdS (3.465 µmol.g^{-1}) under visible light irradiation. Such a highly enhanced photocatalytic activity (44 times higher than CdS) is attained in this nanocomposite system due to the enhancement of charge separation upon photoexcitation. The schematic illustration of the charge transfers from CdS to TiO_2 nanorods and then co-catalyst is depicted in Figure 1.25-b. Apart from traditional nanocomposite photocatalysts fabricated by coupling UV (wide band gap) and visible light (narrow band gap) active semiconductors, nanocomposites synthesized by combining two wide band gap semiconductors were also found to be active under visible light irradiation.

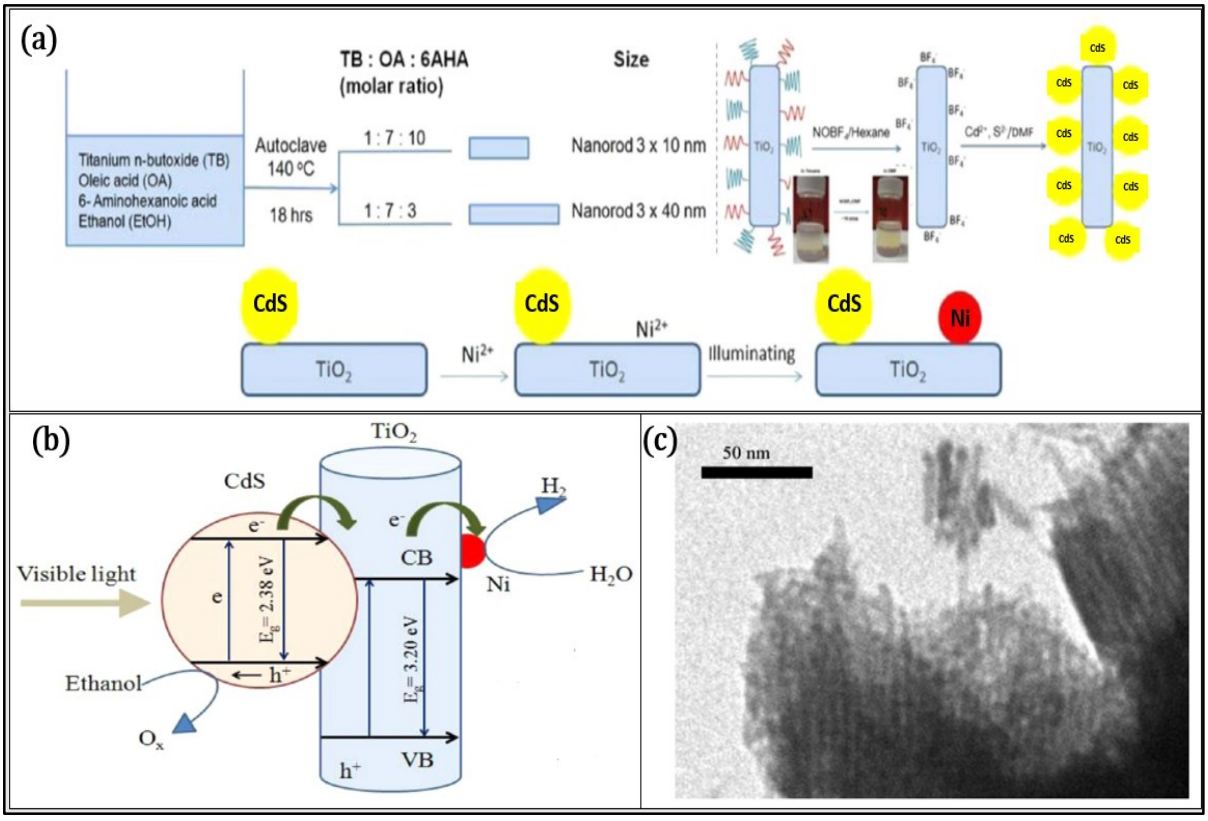

Figure 1.25. *a. Illustration of synthetic methodology for obtaining Ni-TiO_2/CdS photocatalysts [182]; b. Charge transfer pathway in Ni-TiO_2/CdS nanocomposite photocatalysts upon visible light irradiation for H_2 production from aqueous ethanol solution [182]; c. TEM image of TiO_2 nanorods [182].*

Their visible light activity is due to the introduction of impurity and defect levels in the forbidden gap of the nanocomposite semiconductor system. TiO_2/ZnO nanocomposite is an example of the above mentioned visible light active photocatalysts, formed by combining two wide band gap UV active semiconductors (TiO_2 (3.32 eV) and ZnO (3.37 eV)). Zhang *et al.*

synthesized TiO_2/ZnO nanocomposites through a two-step method consisting of homogeneous hydrolysis and low temperature crystallization. They claimed the absorption red shift of the TiO_2/ZnO nanocomposite system into the visible region is due to the introduction of dopant energy levels in the TiO_2 forbidden band gaps by the Zn^{2+} cations [183]. Importantly, TiO_2/ZnO nanocomposites exhibited photocatalytic efficiency higher than the two individual semiconductors. The TiO_2/ZnO composite system is successfully synthesized through a hydrothermal, a spin coating and an atomic layer deposition technique, where these strategies were found to be economically unfavourable in the long run [184 – 186]. Hussein *et al.* synthesized mesoporous coupled TiO_2/ZnO nanocomposites with varying composition (TiO_2:ZnO) through facile and cheap sol-gel route. The as-synthesized nanocomposites with 30 and 50 wt% of ZnO coupled with TiO_2 exhibit the highest photocatalytic activity for H_2 production (770 μmol.g^{-1} and 739 μmol.g^{-1}, respectively) from aqueous solution containing methanol as an electron acceptor, under UV irradiation compared to the activity of commercially available TiO_2, Degussa P25 (356 μmol.g^{-1}) [187]. Very recently, Prasannalakshmi *et al.* reported the synthesis of rod shaped TiO_2/ZnO nanocomposites through a sol-gel method, which exhibited the highest activity for the photocatalytic degradation of organic dyes (Brilliant Green (BG) and Methylene Blue(MB)) under solar irradiation [188].

Similarly to the TiO_2/ZnO system, TiO_2/ZnS photocatalyst is yet another interesting visible light active system, even though it is composed of two different UV active semiconductors: TiO_2 (3.2 eV) and ZnS (3.6 eV). The visible light activity is due to formation of new energy levels within the forbidden band gap of TiO_2, resulting from sulphur doping of the titania surface, when the composite is fabricated. Štengl *et al.* synthesized spherical agglomerate of TiO_2/ZnS nanocomposite consisting of alternate nanosized titania and sphalerite crystalline islands through homogeneous hydrolysis route. The resultant TiO_2/ZnS (2.9 eV) nanocomposite exhibited the highest activity for photocatalytic degradation of Orange II dye under visible irradiation (λ = 400 nm) (degradation constant for nanocomposite, k = 0.0069 min^{-1}), compared to the activities of commercially available Degussa P25 (3.1 eV) (k = 0.0022 min^{-1}) and pure anatase (3.2 eV) (k = 0.0009 min^{-1}). The increased activity of the nanocomposite compared to the individual bulk semiconductors is mainly due to the reduced charge transfer resistance and secondly due to increased surface area [189]. N. Shanmugam *et al.* synthesized nanoparticles of TiO_2 and TiO_2/ZnS nanocomposite through a facile sol-gel method, where the TiO_2/ZnS system exhibited enhanced activity for degradation of organic dyes (Brilliant Green (BG) and Methylene Blue(MB)) under solar irradiation compared to TiO_2 nanoparticles due to reduced band gap energy and the increased charge separation kinetics through type II heterojunction [190].

1.3.5.5.2. ZnO-based nanocomposite photocatalysts

In the heterogeneous photocatalytic field for environmental remediation applications, especially for wastewater treatment systems, the nano binary TiO_2 (3.2 eV) and ZnO (3.37 eV) photocatalysts have been substantially studied due to their appropriate band edge potentials for performing pollutant removal photochemistries [190]. TiO_2 and ZnO in nanosize regime possesses certain advantageous features such as: (i) a high exciton binding energy of 60 meV

(correspondingly, TiO_2 has 4 meV), (ii) a high electron mobility of 200 $cm^2.V^{-1}.s^{-1}$ (correspondingly, TiO_2 has 30 $cm^2.V^{-1}.s^{-1}$), (iii) a facile adaptation of the structure, (iv) an anisotropic growth and (v) an ease of crystallization [191 – 196]. In spite of such distinct features, both ZnO and TiO_2 suffer from low photocatalytic efficiency due to higher rate of recombination of photo-induced electrons and holes compared to the rate of charge transfer to the surface bound redox reactions [197]. Furthermore, they exhibit very low visible light activity due to their wide band gap. The photocatalytic efficiency of ZnO can be improved by forming a type II heterojunction. Coupling a semiconductor to ZnO resulting in type II band offset are generally of two types. ZnO can either be coupled to a similar binary oxide wide band gap semiconductor, where the resultant nanocomposite possesses visible light activity and displays enhanced photocatalytic efficiency, as seen in the case of TiO_2/ZnO nanocomposite system. The second type of coupling involves growing of lattice matched photosensitizer inorganic crystals on ZnO surface, which ensures a maximum utility of visible light and an enhanced photocatalytic activity [198].

The sensitizers should possess a narrow band gap and an appropriate band edge potentials for the transfer of the photogenerated electrons from its CB to ZnO CB under visible light activity, leading to enhanced separation of charge carriers [199]. Among the various inorganic sensitizers, the coupling of In_2S_3 to ZnO is reported here, as In_2S_3 possesses a narrow band gap (2 - 2.3 eV) with higher carrier mobility and a good stability in photocatalytic reactions [200]. Khanchandani *et al.* reported the synthesis of ZnO/In_2S_3 core/shell nanorods array through a soft chemical approach consisting of a surface functionalization route by using citric acid as functionalization agent. Here, they synthesized ZnO nanorods and In_2S_3 NPs through a solvothermal method. Then, they successfully coated the ZnO nanorods with In_2S_3 through a surface functionalization route. The one dimensional ZnO nanorods structure is preferred here, as it provides an optimum geometrical structure for the effective transport of charge carriers and it reduces the charge recombination to a certain extent within the ZnO nanostructures [201]. ZnO/In_2S_3 nanorods morphology and characteristic length and thickness is depicted in Figure 1.26. The as-synthesized core/shell nanocomposite possesses a type II band offset, as its absorption band edge shifted to visible region (due to the incorporation of In_2S_3) and exhibits high photocatalytic activity (degradation constant, k =0.0174 min^{-1} for rhodamine (RhB) dye degradation under visible light irradiation), compared to ZnO nanorods (k = 0.00039 min^{-1}) and In_2S_3 NPs (k = 0.0042 min^{-1}). The enhanced photocatalytic activity of ZnO/In_2S_3 core/shell nanocomposites (56 times higher than the activity of ZnO nanorods and 5 times higher than In_2S_3 NPs) was due to the effectual separation of photo-induced charge carriers, attributed to the type II heterojunction formed between the two different semiconductors [202].

Apart from In_2S_3, among the inorganic sensitizers, CdS was used to form a type II heterojunction nanocomposite with ZnO, as CdS possessed a narrow band (2.4 eV) gap for visible light activation. Similar lattice constant to ZnO and high optical absorption coefficient. Khanchandani *et al.* applied the same surface functionalization route used for ZnO/In_2S_3 nanocomposites for the synthesis of ZnO/CdS nanorods core/shell array systems. Citric acid (CA) was used as the surface functionalization agent. By varying the CA amount, the shell thickness of CdS was successfully tuned. Here, they reported the influence of the shell

thickness on the photocatalytic activity of the nanocomposites [201]. The schematic illustration of the soft chemical approach consisting of surface functionalization route for the synthesis of ZnO/CdS core/shell nanocomposite is depicted in Figure 1.27.

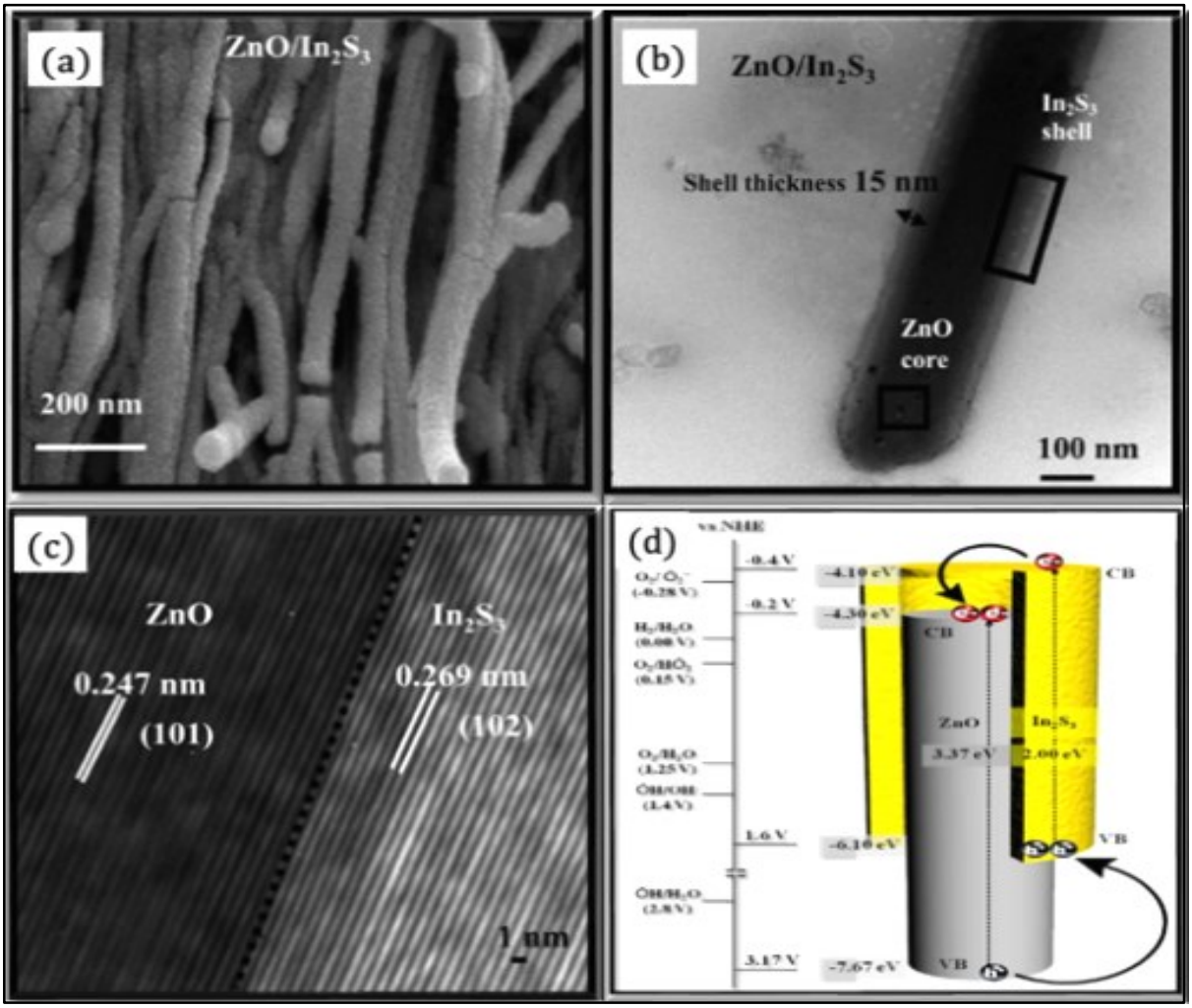

Figure 1.26. *a. FESEM image of ZnO/In_2S_3 core/shell nanorods arrays; b. and c. TEM and HR-TEM of ZnO/In_2S_3 core/shell nanocomposites; d. Schematic illustration of the charge transfer and separation in nanocomposite systems [202].*

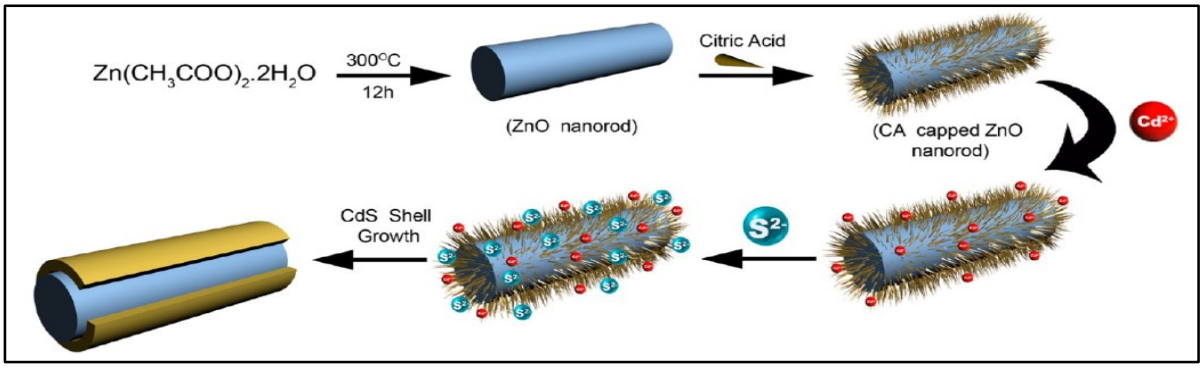

Figure 1.27. *Schematic depiction of the surface functionalization route used for the synthesis of ZnO/CdS core/shell nanocomposite [201].*

They synthesized ZnO/CdS nanorods core/shell nanocomposites with three different shell thickness: 10 nm, 20 nm and 30 nm. The absorption band edge of ZnO nanorods is red shifted to the visible region when they are coated with CdS shell. The monotonous red shift to the visible region increased with an increase in the shell thickness. Compared to the ZnO nanorods and the CdS NPs, the nanocomposites exhibited high activity for the photocatalytic degradation of RhB under simulated solar radiation. The enhanced photocatalytic activity is due to the reduced rate of recombination of charge carriers because of type II heterojunction. Within the nanocomposites with varying shell thickness, the ZnO/CdS system with maximum shell thickness exhibited the highest photocatalytic activity due to an extended absorption in the visible region. The degradation rate constant, (k (min^{-1})) of ZnO nanorods, CdS NPs, ZnO/CdS (10 nm shell thickness), ZnO/CdS (20 nm shell thickness) and ZnO/CdS (30 nm shell thickness) are 0.011, 0.0035, 0.019, 0.025 and 0.039 min^{-1}, respectively.

1.3.5.5.3. SnO_2-based nanocomposite photocatalysts

In the trajectory of application of heterogeneous photocatalysis for environmental clean-up, several semiconductor photocatalysts are developed for the removal of toxic and harmful chemicals released by industries. Within the regime of nanocomposite photocatalytic systems, nano binary wide band gap, n-type tin(IV) oxide (SnO_2) appeared as a favourable semiconductor to which any active semiconductor photocatalysts (suffering from low quantum efficiency due to faster recombination of electrons and holes) can be coupled for generating a type II heterojunction, thus enhancing the photocatalytic efficiency. SnO_2 manifests itself as an ideal constituent in nanocomposite system due to its wide band gap (3.6 eV) and its CB edge potential (E_{CB} = 0 V vs NHE, at pH = 7) which is lower than the CB potential of most of the semiconductors used in photocatalytic organic mineralization/degradation. Additionally, another distinct advantage of SnO_2 is that it is cheaply available, possesses excellent chemical stability, high optical transparency in the visible range (97%) and good electrical properties [203 – 207]. Wang *et al.* fabricated SnO_2/TiO_2 nanocomposites by hydrothermally growing SnO_2 on TiO_2 nanofibers (synthesized by electrospinning technique) [203]. In contrast to two-step synthesis (electrospinning + hydrothermal) of SnO_2/TiO_2 nanocomposites, Zhang *et al.* synthesized SnO_2/ZnO hetero-nanocomposites through direct electron spinning technique [208]. Both the SnO_2/TiO_2 and SnO_2/ZnO hetero nanocomposites exhibited high photocatalytic activity for the degradation of RhB under UV light, compared to the activities of their individual constituent semiconductors.

Concerning the visible light active nanocomposites fabricated from SnO_2 material, iron oxide (α-Fe_2O_3) nanomaterial is frequently coupled to SnO_2 and studied in the heterojunction nanocomposites domain for applications in photocatalysis, gas and liquid sensors [209 – 212]. α-Fe_2O_3 is a n-type semiconductor with a narrow band gap (2.2 eV) exhibiting poor photocatalytic performances due to small diffusion length of holes (2 - 4 nm). The efficient separation of photogenerated charges are observed when α-Fe_2O_3 is coupled with SnO_2. Kang *et al.* synthesized necklace-like hierarchical SnO_2/Fe_2O_3 nanocomposites through a chemical vapour deposition route (CVD), where they have grown hierarchically Fe_2O_3 hexagonal disk on nanocable consisting of SnO_2 as core and epitaxial Fe_2O_3 as shell. SEM images of such a hierarchical SnO_2/Fe_2O_3 nanocomposite system is depicted in Figures 1.28-a and 1.28-b. The

as-synthesized novel hierarchical SnO_2/Fe_2O_3 system exhibits high photocatalytic activity (complete degradation in 2.5 h) for the degradation of methylene blue (MB) under visible light, compared to the pure SnO_2 (synthesized by CVD, exhibits 83% degradation within 2.5 h) and commercially available Fe_2O_3 (58% degradation of MB within 2.5 h) [213]. Xia *et al.* synthesized a non-core/shell SnO_2/Fe_2O_3 nanocomposite system through a co-precipitation technique, where the resultant composite exhibited exalted activity for the degradation of acid blue 62 dye under visible irradiation. These SnO_2/Fe_2O_3 nanocomposites degraded 98% of the dye within one hour, which is 3.6 times higher than the activity exhibited (27% degradation of dye in one hour) by commercially available titania (Degussa P25) photocatalyst [209].

SnO_2/SnS_2 is yet another visible light active nanocomposite system developed and studied especially for the environmental clean-up implementations of photocatalysis. Tin sulfide (SnS_2) is a n-type narrow band gap semiconductor (2.18 - 2.44 eV), it stands as an ideal compound for dye sensitization studies due to the absence of surface states associated with dangling bonds.

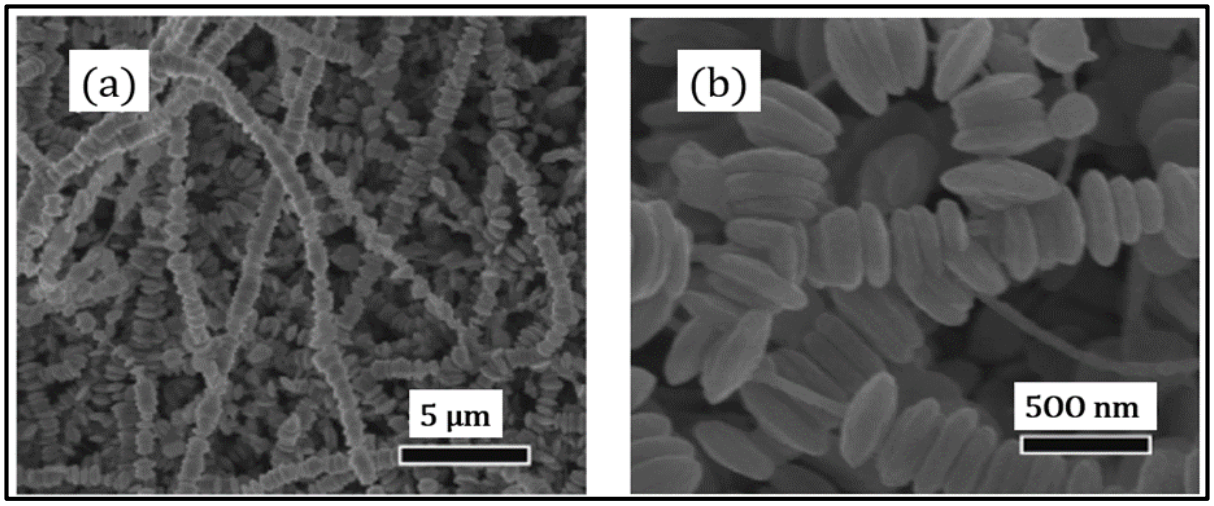

Figure 1.28. *a. and b. SEM image of hierarchical SnO_2/Fe_2O_3 nanocomposite synthesized by CVD technique [213].*

These dangling bonds act as traps for the photogenerated electrons [214]. It serves as a competent photocatalyst in the visible light region due to its thermal, oxidative stability in air and stable existence without corrosion in acidic and neutral solutions [215]. Generally, SnS_2 is coupled to wide band semiconductor with favourable band edge potentials for obtaining type II heterojunction photocatalysts. Yang *et al.* synthesized SnS_2/TiO_2 nanocomposites by growing SnS_2 on commercial titania through *insitu* synthetic methodologies. The resultant nanocomposite exhibited enhanced activity for degradation of Methyl Orange (MO) under UV light irradiation compared to the SnS_2 and the TiO_2 [216]. Yong Cai Zhang *et al.* synthesized non-core/shell type SnS_2/SnO_2 nanocomposite system with a strong interface contact through *insitu* oxidation of SnS_2 under hydrothermal conditions (in the presence of H_2O_2). The resultant nanocomposite is depicted in Figures 1.29-a and 1.29-b. By varying the duration of oxidation and the amount of H_2O_2, the amount of SnO_2 in the nanocomposite was successfully varied.

The as resultant SnS_2/SnO_2 (18.1 wt% of SnO_2) exhibited high photocatalytic activity (degradation constant, k = 9.260 min^{-1}) for Methyl Orange (MO) degradation under visible light, compared to the activity of SnS_2 (k = 5.941 min^{-1}) (synthesized by hydrothermal reactions) and physical mixture of SnS_2/SnO_2 (7.094 min^{-1}) [217].

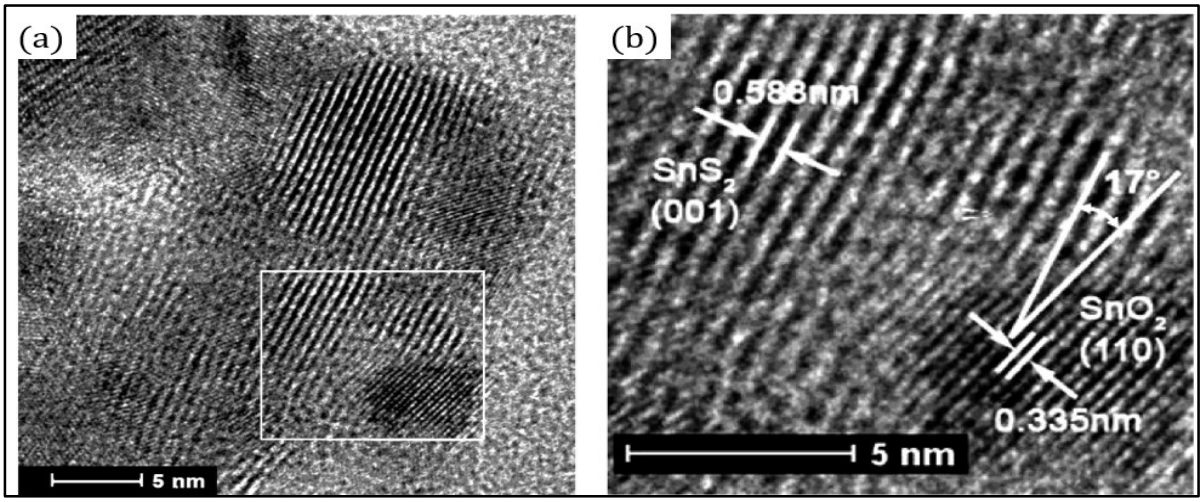

Figure 1.29. *a. HR-TEM of SnS_2/SnO_2 (18.1 mass% of SnO_2); b. Enlargement of the interface observed [217].*

1.3.5.5.4. Magnetically separable nanocomposite photocatalysts (Fe_3O_4-based systems)

Magnetically separable photocatalytic materials have received a tremendous attention for environmental remediation process like the removal of organic pollutants from wastewater. These photocatalytic materials with magnetic supports or magnetic materials coupled to semiconductors forming a nanocomposite system, can be easily separated from the liquid phase by applying an external magnetic field. This allows overcoming the limitations associated with other separation techniques, resulting in high recovery and reusability of the photocatalysts [218]. These magnetically active photocatalysts can be easily designed in composite systems by combining a magnetically active material with a photocatalytic active material. So far, most of the researchers focused their attention on the TiO_2/Fe_3O_4 composite system.

Donia Beydoun *et al.* synthesized TiO_2/Fe_3O_4 nanocomposite system by coating titania on Fe_3O_4 (magnetite) particles through the sol-gel technique [218]. The as-synthesized (TiO_2/Fe_3O_4) nanocomposite system exhibited very low photocatalytic performance compared to the single phase TiO_2, mainly due to the formation of type I heterojunction between the two materials instead of favourable type II. This leads to enhanced recombination of electrons and holes instead of separation and results in very low activity. Additionally, TiO_2/Fe_3O_4 nanocomposite system was not stable under UV irradiation and suffered from severe photodissolution of the magnetic phase. The photodissolution is due to the direct contact between the TiO_2 and the magnetic phase. The photogenerated electrons from the titania reduces the metallic iron of the magnetic phase, which leads to photodissolution. To prevent

dissolution and to improve the photocatalytic activity of the titania-magnetic system, Beydoun *et al.* introduced a passive SiO_2 layer onto the titania-magnetic system resulting in $TiO_2/SiO_2/Fe_3O_4$ nanocomposites. This system exhibited higher enhanced photocatalytic activity than the previously reported TiO_2/Fe_3O_4 nanocomposite system and single phase titania for photooxidation of sucrose. Unfortunately, this possessed several limitations. Indeed, in order to attain maximum separation of charges within the photocatalyst, the insulation layer (SiO_2) and photoactive layer(TiO_2) should be thin. The reduction of the thickness of these two layers leads to reduced photocatalytic activity [219].

Importantly, iron oxide undergoes phase transition, when subjected to heat treatment at high temperature (400°C). This phase transition leads to a loss of the magnetic properties. Since most of the above nanocomposites are synthesized through a sol-gel process, the heat treatment is required. Therefore it is always difficult to attain highly photoactive titania-magnetic nanocomposites with enhanced magnetic properties [220]. The essential criteria for attaining highly photocatalytic active magnetic nanocomposite systems using Fe_3O_4 (0.1 eV) semiconductor, are through the construction of special structure of the nanocomposite or development of special kind of interface phase junction (insertion of an insulation layer) between the magnetic materials and the active photocatalysts. In contrast to the core/shell type of TiO_2/Fe_3O_4 nanocomposite system, Zhang *et al.* synthesized a $Fe_3O_4/BiOCl$ nanocomposite system though colloidal synthesis, where BiOCl (Bismuth oxychloride) flakes are inlaid with Fe_3O_4 NPs. The as-obtained coupled structure of $Fe_3O_4/BiOCl$ exhibited similar photocatalytic activity for degradation of Rhodamine (RhB) dye under visible light, compared to the activity of BiOCl nanoflakes. Here, facile separation of photocatalysts was achieved using the external magnetic field and the recycled catalysts maintained their photocatalytic activity even after five consecutive runs. In this particular system, the photocatalytic activity of BiOCl is reserved after combining with magnetic semiconductor, due to the special kind of coupled heterostructures, where the rate of charge transfer to redox reactions is higher than the rate of recombination, even though the nanocomposite possesses type I heterojunction [221]. The schematic illustration of such a coupled structure and core/shell structure of the $Fe_3O_4/BiOCl$ nanocomposite along with the corresponding TEM images is depicted in Figures 1.30 and 1.31.

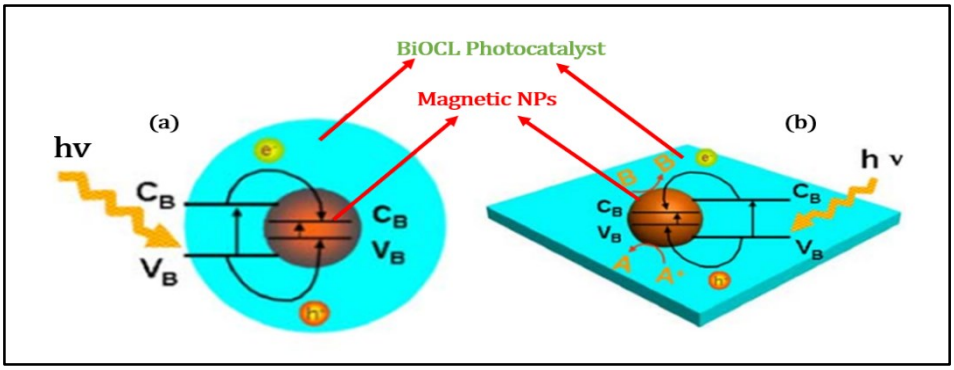

Figure 1.30. *a. Schematic illustration of core/shell $Fe_3O_4/BiOCl$ nanocomposites with charge transfer route; b. Coupled structure of $Fe_3O_4/BiOCl$ nanocomposites, where Fe_3O_4 NPs are inlaid in the BiOCl nanoflakes [221].*

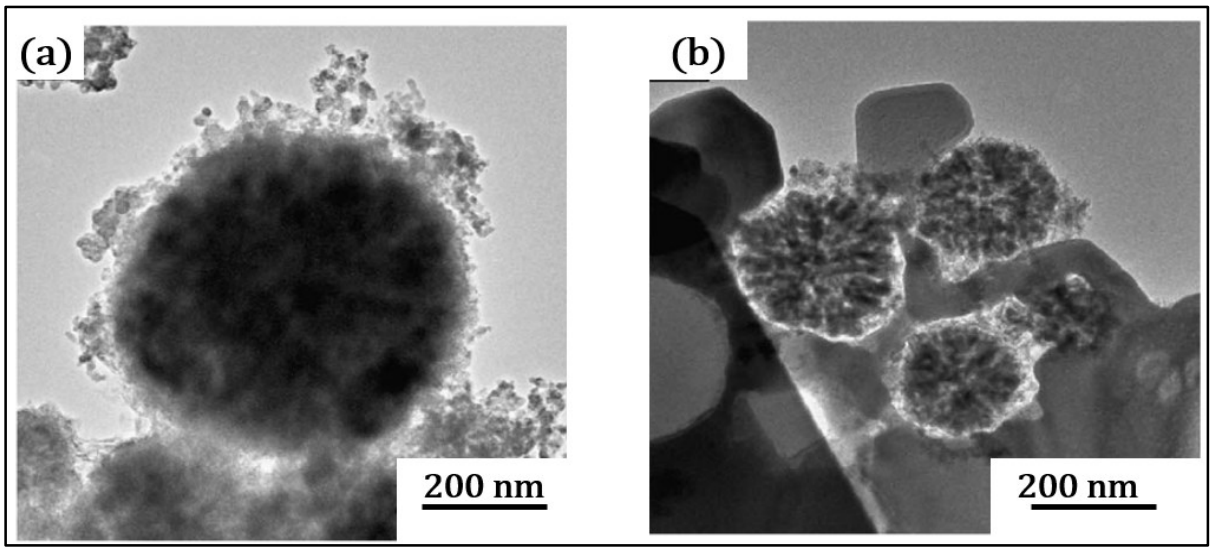

Figure 1.31. *a. TEM image of core/shell $Fe_3O_4/BiOCl$ nanocomposite; b. TEM image of coupled $Fe_3O_4/BiOCl$ nanocomposites [221].*

1.3.5.5.5. Chalcogenide nanocomposite photocatalysts (CdS/ZnS systems)

In the implementation of heterogeneous photocatalysis in wastewater treatments, diverse photocatalysts have been developed constantly to tackle several toxic compounds. Especially, the diverse phenolic compounds, which possesses enhanced stability and bio-accumulation properties [222 – 224]. Similar to TiO_2/Fe_3O_4 nanocomposites possessing type I heterojunction, CdS/ZnS nanocomposites is another hybrid heterostructures with type I phase junction studied in heterogeneous photocatalysis field. This nanocomposite was successfully obtained through synthetic methods like: (i) Metal organic chemical vapour deposition (MOCVD) [225, 226] and (ii) wet chemical methods consisting of surface functionalization route [227, 228]. Wang *et al.* synthesized 1-D (Dimensional) CdS/ZnS nanocomposites with nanowire morphologies through a two-step mild solution method consisting of solvothermal reactions. This synthetic strategy didn't require any pre-treatment of the surface of the core (CdS) to introduce any functional groups prior to shell growth. The as-synthesized CdS/ZnS core/shell nanowires exhibit good photocatalytic activity for the degradation of 4-chlorophenol (4CP) (89% of 4CP was degraded in 12 h) under visible light compared to the activity of CdS nanowires (74% degradation in 12 h) and anatase-TiO_2 (30% degradation in 12 h of irradiation). Additionally, the CdS/ZnS core/shell system exhibited maximum photocatalytic activity for the degradation of Methylene Blue (MB) dye under visible light irradiation (complete degradation in 6 h of irradiation) compared to the uncoated CdS nanowires (63% of degradation in 6 h) and anatase-TiO_2 (67.9% degradation in 6 h) [229]. Eventhough this CdS/ZnS core/shell system possesses type I heterojunction, it exhibits enhanced photocatalytic activity because of the passivation of surface states in the CdS cores by the ZnS shell, which acts as surface traps for the photogenerated charge carriers. SEM images revealing the morphology of CdS/ZnS core/shell nanowires are depicted in Figure 1.32.

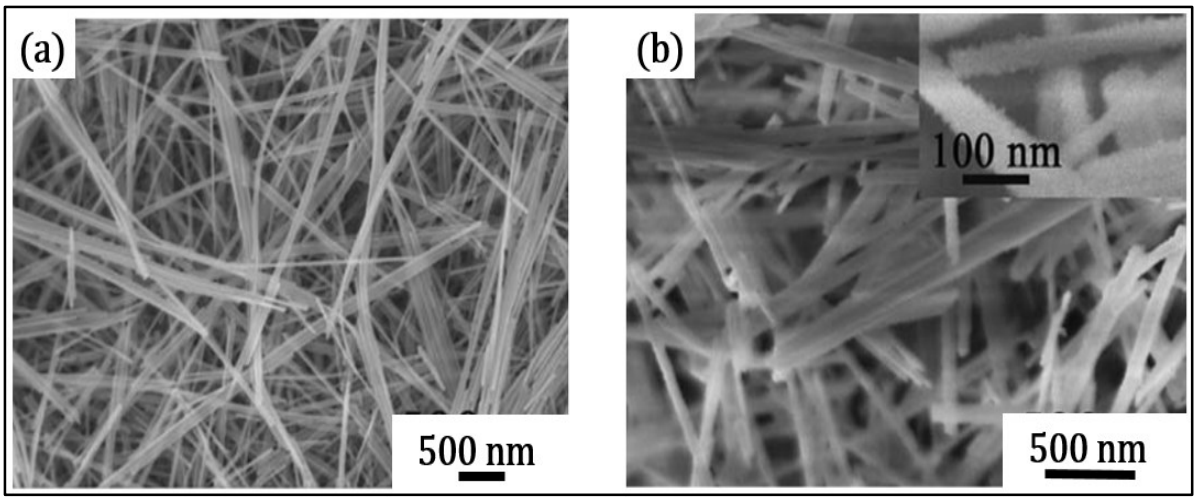

Figure 1.32. *a. SEM image of CdS nanowires with 45 nm diameter; b. SEM of CdS/ZnS core/shell nanocomposites with 60 nm diameter and shell thickness of 5 - 10 nm. The inset figure depicts the surface of the shell, which consists of ZnS NPs [229].*

1.3.5.5.6. Mesoporous In_2O_3/Ta_2O_5 nanocomposite systems

Mesoporous semiconductor photocatalysts exhibit fascinating mass transport properties. Intrinsically, they possess large surface area, thin walls and good light harvesting capabilities. Potentially, they stand has ideal candidates for photocatalytic hydrogen production from water splitting reactions. Takahara *et al*. synthesized mesoporous Ta_2O_5 through a ligand-assisted templating method, which exhibited photocatalytic activity for overall water decomposition. In contrast to mesoporous Ta_2O_5 materials, highly crystallized Ta_2O_5 materials exhibited negligible H_2 production and no O_2 production was observed. The high photocatalytic activity is due to the efficient migration of electrons and holes through the thin walls of mesoporous Ta_2O_5, where the rate of migration of photogenerated charge carriers is higher in mesoporous Ta_2O_5 than the migration occurring in the highly crystallized Ta_2O_5 samples, from the lattice to the surface [230]. Eventhough the mesoporous structure possesses such large features, it is highly limited because of the collapse of the porous structure and the decrease of its surface area during the template removal process, due to its very low thermal stability. Such limitation is resolved by the introduction of second component into the mesoporous structure [231].

Xu *et al.* synthesized mesoporous heterostructured In_2O_3/T_2O_5 nanocomposites through a one-step sol-gel process using Pluronic (P123), triblock copolymer surfactant, as structural directing agent. The incorporation of In_2O_3 (2.7 eV) [232] into the mesoporous Ta_2O_5 (3.9 - 4 eV) [232] resulted in the formation of a type II heterojunction with reduced band gap energy, rendering the photocatalyst active in the visible region. Subsequently, the thermal stability of the mesoporous Ta_2O_5 was greatly enhanced after the formation of nanocomposite. The as-synthesized mesoporous In_2O_3/T_2O_5 exhibited photocatalytic activity for the H_2 generation (189 $\mu mol.h^{-1}.g^{-1}$) from aqueous methanol solution under simulated solar irradiation, compared to the activity of non-porous In_2O_3/T_2O_5 nanocomposite synthesized without the template (54 $\mu mol.h^{-1}.g^{-1}$) and pure crystalline Ta_2O_5 (84 $\mu mol.h^{-1}.g^{-1}$). The high photocatalytic activity of

the mesoporous In_2O_3/T_2O_5 system is primarily due to the efficient separation of photogenerated electrons and holes due to the type II junction formation.

Compared to non-mesoporous In_2O_3/T_2O_5 nanocomposites, mesoporous systems exhibit high activity due to their large surface area, which provides more active sites for H_2 production. The photogenerated electrons and holes have to travel short distance in the mesoporous structure due to very thin walls, which is not observed in the other two photocatalysts [233]. Xu *et al.* and Guan *et al.* further investigated the three dimensional mesoporous In_2O_3/T_2O_5 nanocomposite systems as a function of the wt% of In_2O_3 incorporation and the calcination temperature employed in the heat treatment. They revealed that at the interface of the mesoporous In_2O_3/T_2O_5, a doping thin layer is formed due to the substitution of In^{3+} by Ta^{+5} resulting in the formation of a p-type conduction.

Contrastingly, the doping of Ta^{5+} in In_2O_3, results in the formation of n-type conduction. Thus a p-n junction type II heterostructure is formed in this mesoporous composite system, which favors the photocatalytic activity. The heterojunction area in the nanocomposite increases with an increasing amount of In_2O_3. The maximum area of heterojunction was attained for 20 wt% of In_2O_3, beyond which the heterojunction area decreases and the photocatalytic performance decreases. Still, the mesoporous nanocomposites with varying In_2O_3 (wt%) possess higher activity than the pure crystalline Ta_2O_5 photocatalysts. The mesoporous In_2O_3/T_2O_5 nanocomposites with 20 wt% of In_2O_3 was synthesized at varying calcination temperatures (450, 550, 650, 750°C). An increase of the calcination temperature from 450°C results in the surface area and pore volume decreases. The complete destruction of the mesoporous structure is observed at 750°C, leading to the formation of crystallized nanocomposites with very low photocatalytic activity. They confirmed that the onset of destruction of the mesoporous structure started from 650°C, below 650°C the three dimensional novel structure was retained [234]. A schematic illustration of the charge transfer process in this mesoporous nanocomposites and the HR-TEM image of the interface junction region between two material in In_2O_3/T_2O_5 mesoporous nanocomposite is depicted in Figure 1.33.

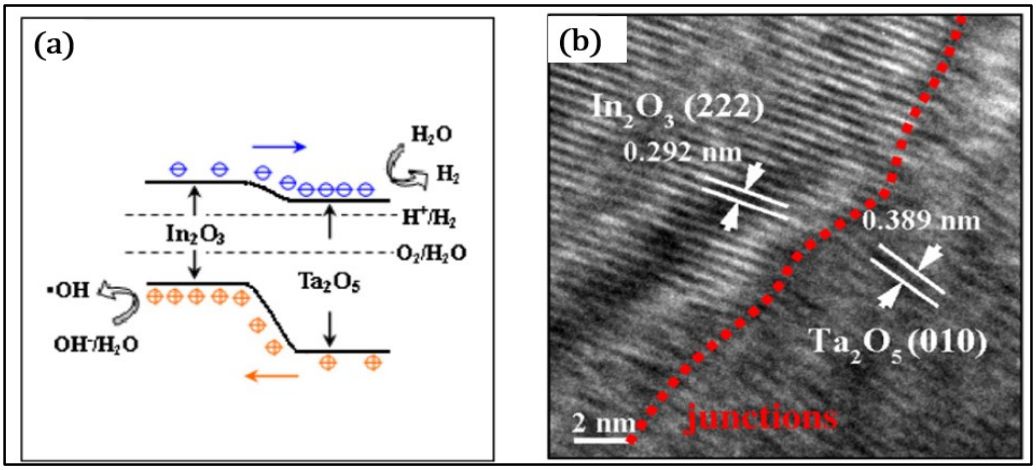

Figure 1.33. *a. Schematic description of charge transfer route in mesoporous* In_2O_3/T_2O_5 *nanocomposites with type II heterojunction; b. HR-TEM image of the interface region between* In_2O_3 *and* Ta_2O_5 *materials in the* In_2O_3/T_2O_5 *nanocomposites (with 20wt%* In_2O_3*) calcined at 750°C [234].*

1.3.5.5.7. Conclusion

Unlike the synthesis of solid solutions or binary and ternary photocatalysts, the synthesis of nanocomposites generally requires in two consecutive steps. The first step involves the synthesis of the base semiconductor material and the second step involves the growth of the different semiconductor material on the base compound. The transformation of two a consecutive steps process into a direct single step method is now been researched vigorously in the field of photocatalysis, in order to tune the interface of the two different semiconductor materials to enhance the photocatalytic activity. The exploration of the influence of the interface on the charge transfer and on the recombination rate is also deeply studied to elucidate the reason for the variation of photocatalytic performance with respect to the lattice strain and mismatch for different nanocomposite systems. The nanocomposite system synthesis can be considered as the terminal part of the construction of advanced photocatalytic systems. Here, it mostly involves surface passivation (removal trap states) core and creation of type II heterojunction for efficient charge separation. Table 1.4 gives some examples of photocatalytic nanocomposite systems along with their photochemistry applications.

Table 4. *Summary of synthetic methodologies, precursors and dimensions of nanocomposite photocatalysts reviewed here along with their corresponding photochemical applications are listed (NCs: Nanocomposites).*

NCs	Synthetic methods	Precursors	Size of the nanomaterials	Photochemical reaction	Illumination source	Reactor setup	Ref
TiO_2 nanorods TiO_2/CdS Ni-TiO_2/CdS	Capped TiO_2 synthesized through Solvothermal method Colloidal Synthesis of TiO_2/CdS Ni-TiO_2/CdS synthesis by photodeposition method	Titanium n-butoxide (TB), Oleic acid (OA),6-Aminohexaonic acid and Ethanol $NOBF_4$-capped-TiO_2, cadmium acetate dihydrate and thioamide. $Ni(NO_3)_2$	10-40 nm TiO_2/CdS nanoparticles aggregate to form hollow nanospheres with uniform diameter of around 150 nm.	H_2 generation were carried out under visible light irradiation ($\lambda >$ 420 nm)	320 W xenon lamp with a 420 nm cut off filter	Septum sealed gas vials with a 420 nm cut off filter	[182]
TiO_2/ZnO	Sol-gel method	Titanium(IV) n-butoxide and zinc nitrate hexahydrate	6-14 nm	H_2 evolution from an aqueous media containing methanol	300 W xenon lamp with filter, illumination source (240 nm $< \lambda <$ 400 nm)	5 mL semi batch reactor attached with UV filter and light source	[187]
TiO_2/ZnS	Homogeneous hydrolysis	Titanium oxo-sulphate, zinc sulphate and thioacetamide	Spherical agglomerates consisting of alternate anatase (approx. 6 nm) sphalerite crystalline islands (approx. 15 nm)	Degradation of Orange II dye	Florescent lamp (254 nm, 365 nm and 400 nm) with 8 W power	Quartz tube with stainless steel cover	[189]
ZnO nanorods In_2S_3 NPs ZnO/In_2S_3 core/shell nanorods arrays	Solvothermal method Surface functionalization route	Zinc acetate di-hydrate, citric acid, $In(NO_3)_3.5H_2O$ and $Na_2S.9H_2O$.	Average diameter of ZnO nanorods 100 ± 6 nm and average length of ZnO nanorods of about 500 - 600 nm. Thickness of In_2S_3 shell is 15 ± 2 nm.	Degradation of RhB dye.	500 W Xenon Lamp with cut off filter ($\lambda \geq$ 420 nm)	Beaker with top covered with glass plate	[202]
ZnO nanorods and CdS NPs ZnO/CdS nanorods core/shell arrays	Solvothermal method Surface functionalization route	Zinc acetate di-hydrate, cadmium chloride, thiourea, citric acid, and ethylene glycol.	Average diameter of ZnO nanorods 100 nm and CdS shell thickness (10 – 30 nm)	Degradation of RhB under simulated solar irradiation	No information mentioned in the article	Glass beaker immersed in ice-cold water bath	[201]
SnO_2/Fe_2O_3	Co-precipitation	$SnCl_4.5H_2O$, $FeCl_3.6H_2O$, deionized water and ammonia	6 - 24 nm	Degradation of acid blue 62.	1000 W Xenon lamp with a cut off filter to remove light below 400 nm	Quartz jacketed photoreactor	[209]

SnS_2 SnS_2/SnO_2	Hydrothermal synthesis For NCs: In situ oxidation of SnS_2 NPs under hydrothermal conditions	Precursors for SnS_2 nanoparticles are $SnCl_4.5H_2O$ and thioacetamide and acetic acid. For NCs: SnS_2 and H_2O_2	12 - 26 nm	Degradation of methyl orange (MO)	1000 W Xenon lamp ($\lambda > 420$ nm)	Photoreactor consisting of two layer Pyrex bottles with water circulation at the middle of the bottles.	[217]
Fe_3O_4 NPs $Fe_3O_4/BiOCl$	Colloidal synthesis Colloidal synthesis	For NPs: $FeCl_3.6H_2O$, $FeCl_3.7H_2O$, ammonium hydroxide, deionized water and oleic acid. For NCs: $Bi(NO_3)_3$, HNO_3, Fe_3O_4 NPs, $NH_3.H_2O$, chloroform, SDS and deionized water.	Fe_3O_4 NPs of size 7- 10 nm have aggregated on large BiOCl flakes of size 200 - 500 nm.	Degradation of RhB dye.	500 W Xenon lamp with cut off filter ($\lambda \geq 420$ nm)	No info mentioned in the article	[221]
CdS Nanowires 1D CdS/ZnS core/shell NCs	Solvothermal method Solvothermal Method	For nanowires: $Cd(S_2CNEt_2)_2$ prepared by precipitation of $CdCl_2$ and NaS_2CNEt_2. For NCs: CdS nanowires, ethanol, $Zn(CH_3COO)_2.2H_2O$ and $(NH_2)_2CS$	Dia of about 45 nm and length of about several μm. Shell was composed of ZnS NPs with diameter of about 4 nm.	Degradation of methylene blue and 4-chlorophenol (4CP) under visible light were carried out separately.	300 W Xenon lamp with a cut off filter ($\lambda > 420$ nm)	Jacketed quartz reactor	[229]
In_2O_3/Ta_2O_5	Sol-gel process	$Ta(OC_2H_5)_5$, HCL, $In(NO_3)_3.nH_2O$ and (Pluronic P123) triblock copolymer surfactant	Average pore diameter of the NCs is 5.9 nm	H_2 production from aqueous methanol solution.	300 W Xenon lamp was used as a simulated sunlight	External irradiated Pyrex cell with closed gas circulation system	[233]

1.3.6. Conclusion of heterogeneous photocatalysts

The so far, up-to-date developed semiconductor materials within the four different families of heterogeneous photocatalysts is reported in this section. From this review it is obvious that synthesis of these advanced materials is still procured in the batch system and their complete transpose into the continuous synthetic regime is hindered by several factors. One among them is the precursor availability, especially single source precursors and the inability of the currently developed continuous systems for attaining the requisite surface properties of the coupled/alloy semiconductors material in nanosize. Thus appropriate selection of the precursor and the efficient design of the continuous flow reactor is the need of the hour for efficiently transforming the synthesis of some notable novel solid solutions and nanocomposites photocatalysts into the continuous flow regime.

The up-coming sections in this chapter will elucidate the effective implementation of the as-synthesized nanophotocatalysts (belonging to the four different families of heterogeneous photocatalysts) in photoreactor setups. These sections will typically target in detailing the various factors considered in the design of the photoreactors for achieving effective illumination of the semiconductor nanophotocatalysts coupled with the simultaneous enhancement of mass and heat transfers of the heterogeneous processes. The succeeding chapters in this PhD thesis will specifically targets in the effective synthesis of novel nanophotocatalysts within each different family of the heterogeneous photocatalysts and finally unravels the implementation of the as-synthesized nanophotocatalysts by targeting the corresponding specific application for which the photocatalytic material was rationalized and synthesized.

1.4. Reactor design & implementation of photocatalysts in photochemical processes

The heterogeneous photocatalysis is a polyphasic system involving the interaction between different phases (solid and fluid: liquid or gas), through mass transfer (adsorption) upon mixing and charge transfer (redox reactions) upon exposure to electromagnetic phase (light). Therefore, the geometrical organization and geometry of a reactor for heterogeneous photocatalysis depends extensively on the photochemistry/reaction engineering (applications) to which the system is subjected and the source of electromagnetic radiations. The geometrical design of the reaction vessel and the appropriate choice of such photocatalytic reactors is based on the composition of the polyphasic (heterogeneous photocatalytic) system (solid-gas, solid-liquid and solid-liquid-gas) and the specific area in which the photocatalytic application is carried out.

The design of the photoreactor is always targeted to achieve high photocatalytic activity by ensuring efficient illumination of the solid photocatalytic material under the defined photocatalytic conditions. The organization or placement of the radiation source aims at optimizing the use of the photons within the reactor's space and concurrently resulting in a system possessing enhanced mass and heat transfer rates for attaining higher photocatalytic activity with the novely designed semiconductor photocatalysts. In this section, we targeted the report of the various photocatalytic reactors successfully used in the heterogeneous photocatalytic field by classifying the photocatalytic applications into different multiphasic systems. The composition and chemistry of the phases involved in such systems determines the compatible materials for the construction of the photoreactor. I systematically detail the incorporation and the efficient utilization of solid semiconductor photocatalysts in such photoreactors [18, 235 – 237].

The different multiphasic systems employed in heterogeneous photocatalysis are:

- Solid-Gas (organic/inorganic) system,
- Solid-Liquid system,
- Solid-Liquid-Gas system.

Around 80-90% of the photochemical reactions realized in the heterogeneous photocatalytic field falls under the categories of solid-liquid (diphasic) and solid-gas-liquid (triphasic) systems. The remaining 10 - 20% that constitutes the solid-gas systems are photochemical reactions constituting the degradation of pollutants (especially organic compounds). Since the research work focused in my thesis deals more with former case, the subsequent section will focus only on the solid-liquid and solid-gas-liquid phase systems. The details about the solid-gas phase and the illustration of various photoreactors manifesting under this section is provided in the annexure of this doctoral thesis.

1.4.1. Solid-Liquid (diphasic) & Solid-Liquid-Gas (triphasic) phase systems in heterogeneous photocatalysis

In both solid-liquid (diphasic) and solid-liquid-gas (triphasic) systems, the effective utilization of photocatalysts are achieved by two different methods: suspension and immobilization. In the former system, the photocatalytic material is suspended in the liquid phase with the help of magnetic stirring, toroidal or non-toroidal or agitation promoted by gas molecules. This suspension of the photocatalytic materials in liquid phase (aqueous or non-aqueous) is called "slurry system". In the immobilized system; the photocatalysts are bonded to inert surfaces, either through a physical or a chemical bonding. Comparing the slurry and the immobilized photocatalytic reactor systems, the slurry reactors are highly advantageous due to the attainment of the high photocatalytic activity. This enhanced behaviour of slurry systems is due to the intrinsic furnishing of high total surface area of photocatalysts per unit volume. Even though the slurry system is highly economical for both fabrication and operation, its major and only limitation is the requirement for downstream separation of the photocatalytic materials from the product/liquid stream [238].

In heterogeneous photocatalysis, the water splitting reactions carried out in closed air-tight batch slurry reactors can be regarded as solid-liquid phases systems. These batch reactors are made up of Pyrex, quartz or plexiglas materials and the suspension is achieved through magnetic stirring. The orientation of the photon source is basically through internal or external irradiation. Takasugi *et al*. reported an inner irradiation slurry reactor made up of quartz material for water splitting reaction, the photon source being provided by 450 W high pressure mercury lamp [75]. Arney *et al*. reported an externally irradiated slurry reactor made up of fused silica material for H_2 production from water splitting. A 400 W Xenon arc lamp equipped with IR water filter and cooler was used as a photon source [82]. Priya & Kanmani *et al*. developed a two different novel batch slurry (BG) and batch slurry recycle reactor fitted with continuous supply of inert gas (BRRwCG) for water splitting reaction under solar irradiation. Both the reactor materials were made up of plexiglas, as it is transparent to the solar spectrum wavelength (290 - 700 nm). The photocatalytic material was successfully suspended in BG through magnetic stirring. Analogously, in BRRwCG, the suspension was achieved through continuous bubbling of the reactant solution by an inert gas. Simultaneously, a part of the reactant solution was recirculated using a peristaltic pump. The catalyst composition in both reactors was kept the same and it was found that BRRwCG exhibited higher photocatalytic activity than BG due to the enhanced mass transfer and photon distribution [239].

After water splitting reaction involving the conversion of photon energy to chemical energy, the photocatalytic oxidation (degradation) of organic dyes is the most studied process in the field of heterogeneous photocatalysis. According to the world bank study, around 17-20% of water pollution is due to the textile and dyeing industries. Within these dyes released into the atmosphere, more than 50% of the dyes are azo-dyes, whose treatment by anaerobic or any other methods results in the formation of toxic compounds (like aromatic amine) [240]. Thus, heterogeneous photocatalysis is a cheap and greener technique for completely mineralizing

these dyes materials. These solid-liquid-gas phase photocatalytic processes are carried out in batch slurry reactors made up of quartz or Pyrex. The suspension of photocatalytic particles is achieved by magnetic stirring and the system is continuously purged with oxygen or air [39, 47].

In order achieve higher throughput of wastewater treatment, continuous operation is necessary. Slurry rectors or photocatalytic suspended systems suffer from severe limitation of photon and mass transfer when they are upscale to achieve higher throughput. Additionally, a downstream process is required for the separation of the photocatalysts from the product stream. McCullagh *et al.* developed a novel continuous flow slurry reactor for the degradation of methylene blue (MB) dye under UV irradiation [241, 242]. This system coupled the usage of 'Drum Reactor' design and pelletized titania photocatalytic particles. They employed the commercially available Hombikat pellet titania catalyst, which feed the system from downstream processing of separating the photocatalysts from liquid phase.

The photocatalytic reactor consists of rotating cylindrical vessels stacked one upon another and connected in series. Each cylindrical vessel has a unique arrangement of serially connected baffles on its inner side. The cylinders containing these baffles during the continuous heterogeneous photocatalytic operation are rotated continuously due to which the baffles separate the photocatalysts from liquid stream and provide enhanced suspension. The direction of rotation of the cylinders is perpendicular to the propagation light source and this provides enhanced illumination of the suspended pelletized titania photocatalysts. This entire reactor setup is constructed using 'Perspex' material, which provides high penetration of photons leading to higher energy utilization. The schematic representation of this novel drum-kind of continuous slurry reactor is depicted in Figure 1.34.

However, this reactor arrangement suffers from the attrition of pellet particles, which leads to a reduction in size of the particles and the smaller particles are unseparated by the rotatory action and are carried away by the product stream. Other strategies have been developed in order to avoid the attrition of photocatalytic particles and to achieve enhanced separation without the need of downstream processes in the continuous flow operation of solid-gas-liquid systems. Especially for the treatment of wastewater streams at higher throughput (photocatalytic oxidation of dyes).

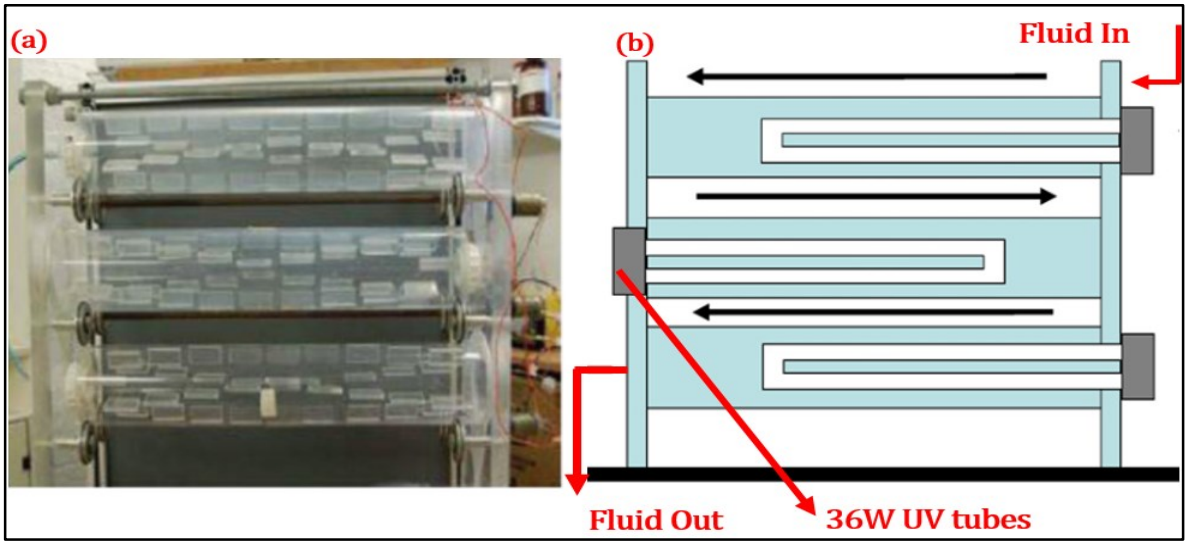

Figure 1.34. *a. Representation of continuous flow photocatalytic slurry reactors designed in a drum reactor fashion; b. A schematic representation of photocatalytic reactor shown in Figure 1.34-a with fluid flow direction [242].*

These strategies considered the use of immobilized photocatalytic reactors. The photocatalytic particles employed in these systems are immobilized on inert surfaces by either physical or chemical bonding, which prevents the need of downstream processing for separating the photocatalytic particles. Behnajady *et al.* reported a continuous flow tubular photocatalytic reactor with immobilized photocatalysts for the degradation of Acid Red 27 (AR27) (an anionic monoazo dye) [243]. Here, the commercially available TiO_2 (Degussa P25) was immobilized on a glass plate. The immobilization was carried out using a heat attachment method. The continuous flow tubular photoreactor consists of four quartz tubes connected in series through polyethylene tubes. The P25-TiO_2 loaded glass tubes were inserted in each quartz tube. The photocatalytic reactor was illuminated using a low pressure mercury lamp, which was positioned in front of the quartz tubes. A schematic depiction of this continuous flow system is shown in Figure 1.35.

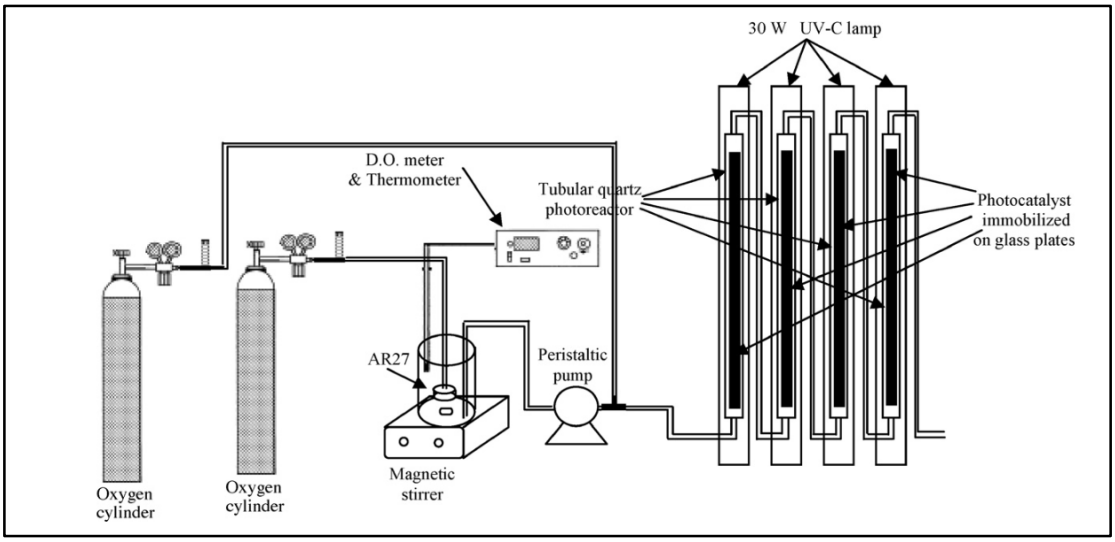

Figure 1.35. *Scheme of the continuous flow tubular photocatalytic reactor with immobilized titania photocatalysts on glass inert surface [243].*

Li *et al.* reported the use of a Double Cylindrical Shell (DCS) photoreactor with an immobilized monolayer of TiO_2 coated on silica gel beads [244]. The design of this photoreactor was very much similar to the annular reactor. It consists of two concentric cylindrical columns, where the exterior column is made up of plexiglass materials and the interior tube is a quartz tube. The photoreactor is irradiated internally with a UV black lamp. Inserted axially on the inner side of the quartz tube. The exterior region of the quartz tube consists of a monolayer of immobilized TiO_2 glass beads. The exterior region of the plexiglass tube is covered with an aluminium foil to reflect the UV light back into the reaction region, as depicted in Figure 1.36. This reactor was use for the degradation of methyl orange (MO) and rhodamine B (RhB).

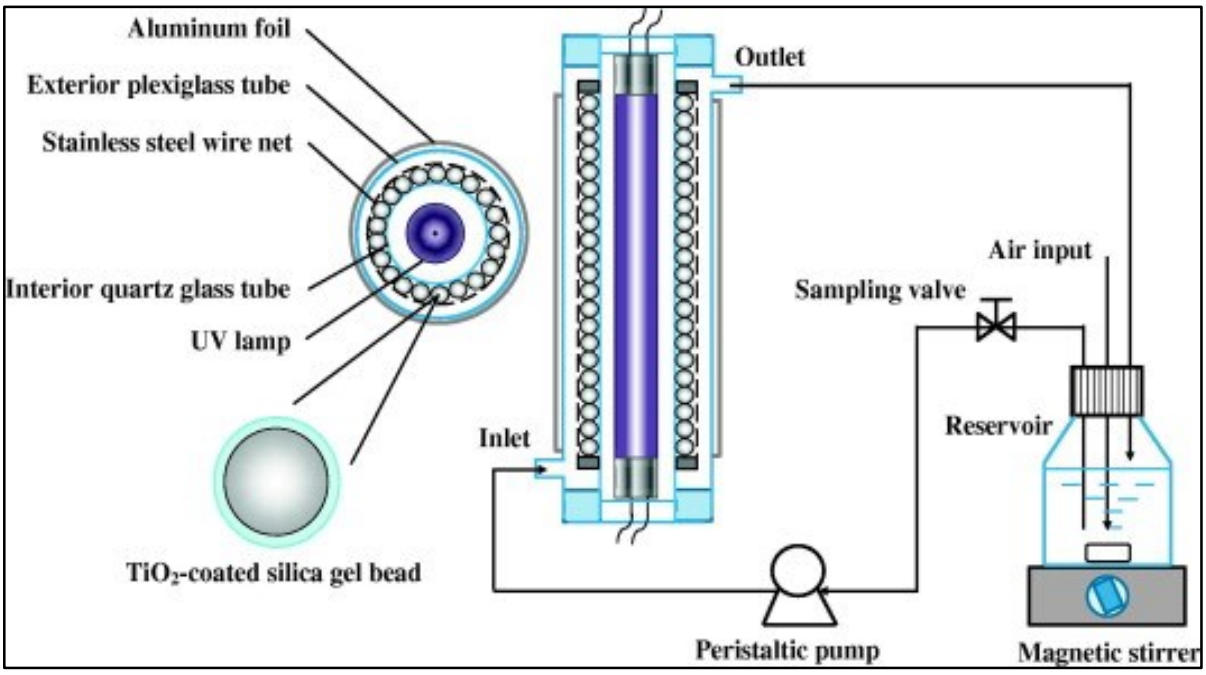

Figure 1.36. *A schematic representation of DCS photoreactor with a monolayer of immobilized TiO_2 coated silica gel beads [244].*

The other notable immobilized photocatalytic reactors reported for the wastewater treatment involving the degradation of dye was a labyrinth bubble photoreactor, reported by Xiao-gang *et al*. In this system, a TiO_2 photocatalyst was immobilized on quartz glass particles and a labyrinth fluid flow arrangement was achieved by the arrangement of parallel baffle plates within the reaction vessel [245].

Even though there are several notable systems developed in immobilized photocatalytic reactors for wastewater treatment process. Their implementation in large scale remains complicated. The complex design of the irradiation source, according to the requisite length of the upscale system have limited the researches from developing these systems further. Currently, the search for novel photoreactors and for effective utilization of the photocatalysts have pushed the scientists more into the microreactor fabrication and design. These microreactors provide enhanced mass transfer compared to the conventionally mentioned immobilized photocatalytic reactors, due to the higher surface-to-volume ratio achieved as a result of their small dimensions [246, 247]. Simultaneously, they provide the opportunity for

low catalysts loading, enhanced heat transfers and homogeneous photon distribution [248]. Recently, Vasconcellos *et al.* immobilized the commercially available TiO_2 photocatalysts on inert PDMS support, resulting in the fabrication of an immobilized micro-photocatalytic reactor for the degradation of methylene blue (MB) and RhB under UV-LED irradiation [248].

Concerning the slurry reactors, there is currently a rapid research effort to replace the mechanically attained suspension by air or reactive gas agitation attained suspension. These systems are given a lot of preference now a day because of the rapid development of microreactor, which leads to low catalysts loading. Similarly, advanced progress in the downstream separation equipments have also motivated researchers for such a continuous flow slurry reactor without any immobilization. Very recently, Rakhshaee *et al.* designed a novel Plug Flow Reactor (PFR) in which nano hematite (α-Fe_2O_3) photocatalysts was successfully suspended in the liquid phase with air promoted suspension [249]. A scheme of the as-designed reactor is depicted in Figure 1.37. In this system the nano photocatalysts are successfully suspended in the solution with the help of upward motion of air bubbles. These suspended nanoparticles tend to form a nanofilm between the airbubbles and the wall of the reactor, resulting in higher photocatalytic activity due to enhaced mass transfer and photon absorption. A scheme of the flow stress within this novel PFR along with nanophotocatalytic film formed between the bubble and the wall is depicted in Figure 1.38.

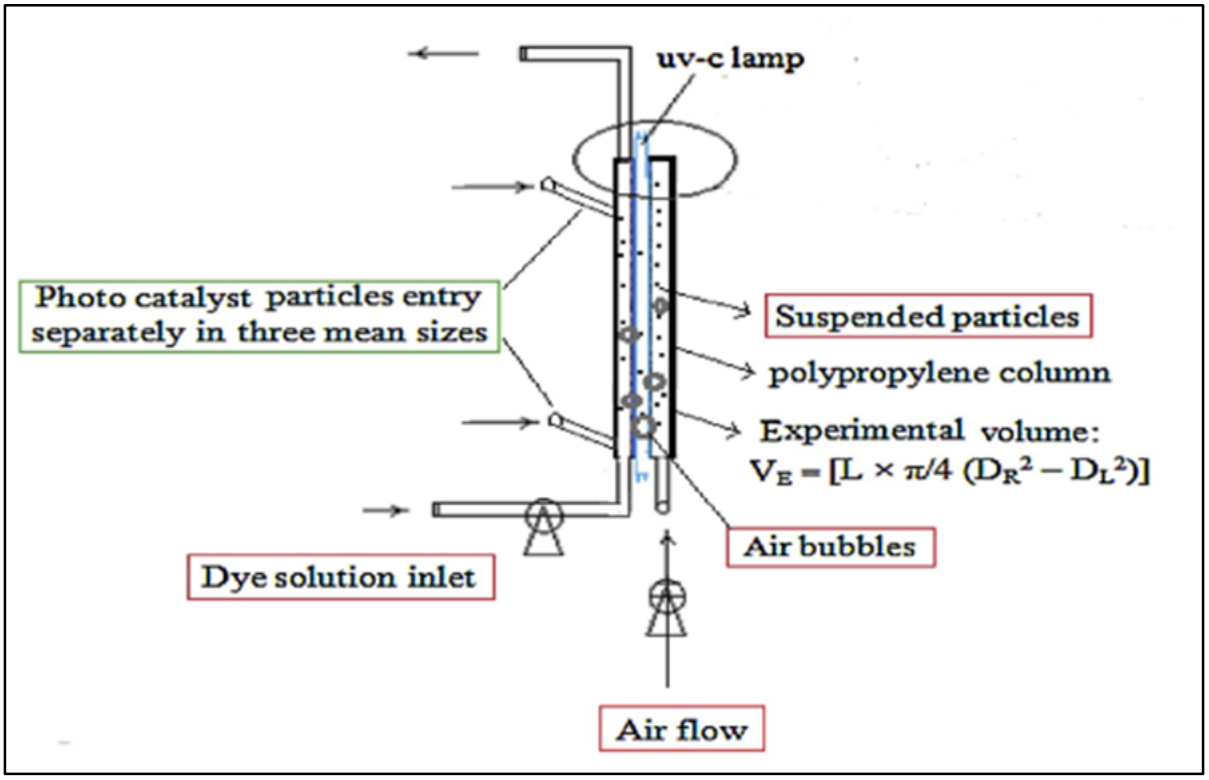

Figure 1.37. *A schematic depiction of novel PFR (column length 30cm) with air promoted suspension and internal irradaition [249].*

This PFR exhibits enhanced photocatalytic activity for the degradation of several dyes, such as: methylene blue (MB), bismarck brown Y (BB), rhodamine B (RhB) and malachite green (MG), compared to the conventional packed bed reactors. Finally, gas promoted suspension is

far more advantageous and would provide further enhanced photocatalytic activity for water treatment processes, when implemented in microreactor channels.

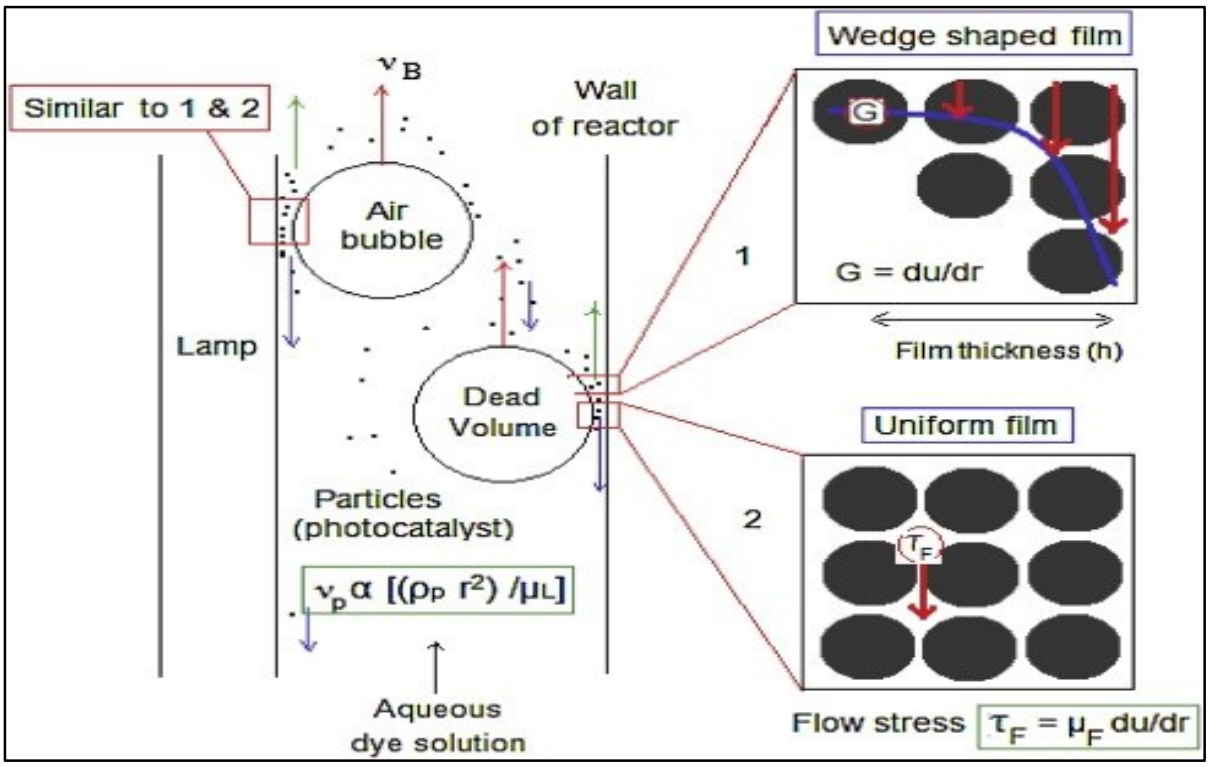

Figure 1.38. *A schematic representation of velocity gradient existing in the film between the wall raising air bubble [249].*

1.5. Conclusion and outcome of literature survey

This literature review was classified into two different sections. The first section was completely focused on the heterogeneous photocatalysts with band gap engineering and surface optimization carried out on several semiconductor materials through various synthetic methods. In this section, the various semiconductor photocatalysts researched so far in the heterogeneous photocatalysis field have been briefly reviewed and have been segregated into four different types depending on their composition, crystalline nature and conjunction of different semiconductors.

First, the developed synthetic strategies have been mentioned along with the rationale applied behind the design of the synthetic methodologies and their advantageous features compared to conventional synthetic methods. Secondly, the choice of the semiconductors considered to produce novel advanced photocatalysts have been explained for each different cases of solid solutions and nanocomposite systems. A brief summary of heterogeneous photocatalytic systems, type of photoreactors and illumination ranges was provided for each individual semiconductor materials addressed in the four different families of photocatalysts.

The second portion of the review focused on the efficient utilization of photocatalysts through various photocatalytic reactor systems. In this section, several photocatalytic reactors developed to enhance both photon and mass transfer operations were detailed.

From this literature review, it became very obvious that the synthetic strategies reported so far for different advanced photocatalytic system have hardly attempted continuous synthetic approaches, thus preventing from their application at large scales. The exploration of supercritical fluids synthesized semiconductor nanomaterials have not been explored as photocatalysts for any photochemical reactions. Additionally, the various developed photocatalytic reactors have been primarily focused in utilizing the commercially available TiO_2 (Degussa, P25) for performing photochemical reactions. Only very few studies have been carried out in efficiently incorporating other novel photocatalysts into these photocatalytic reactor systems.

Hence, based on this literature survey, the following scientific study was carried out in my doctoral research. The research work mainly focussed on synthesizing photocatalytic nanomaterials using continuous supercritical techniques. Any novel heterogeneous photocatalysis process requires semiconductor materials in the nano size with well-defined surface properties. Thanks to low viscosity and the high diffusivity of supercritical conditions, monodispersed and quantum confined particles have been successfully reported in continuous supercritical fluid processes. Hence, the advantageous supercritical fluids synthetic strategies will be used for obtaining novel semiconductor photocatalysts in this PhD study.

Gallium nitride (GaN), a nitride-based binary semiconductor material is rigid, displays chemical stability in both acidic and basic conditions and prolonged stability even on exposure to high temperature for long period of time. Additionally, along with its beneficial electrical properties, it disposes itself as an optimum semiconductor material for heterogeneous

photocatalysis. In this doctoral thesis, GaN was opted as a based semiconductor material for heterogeneous photocatalytic process due to its reliable properties for stable operation of the various photochemical reactions. GaN quantum dots binary photocatalysts will be synthesized and consecutively implemented in the visible light promoted catalyzed photoreaction for the degradation of azo dyes, whose applications falls in the region of waste water treatment. Supplementarily, a new synthetic strategy developed for the synthesis of GaN/TiO_2 nanocomposite photocatalysts was proposed. Post-synthetic strategies will be carried out for effectively implementing the nanocomposites in photoreactor systems for future photocatalytic work. The details of the synthetic protocol and their corresponding photochemistry, photoreactor setup and process conditions will be analysed elaborately in the succeeding chapters.

Since the entire research domain of Photo4Future targets on the efficient utilization of visible light for various photochemical reactions. This PhD work later concentrates on the development of visible light active heterogeneous photocatalysts (which is not the case of GaN) for novel and commercially requisite photochemical reactions. Correspondingly, nitrides-based solid solution semiconductors satisfy this primary goal of visible light activity through the formation of solid solution semiconductor photocatalysts, in particular $Ga_xIn_{1-x}N$.

$Ga_xIn_{1-x}N$ solid solution photocatalysts will be synthesized continuously in flow supercritical millireactor and was implemented for conventional photosensitized reaction for the synthesis of drug molecules with high bioavailability under visible light irradiation such as trifluoromethylation reaction of heteroarenes. In this purpose, $Ga_xIn_{1-x}N$ ($0 \leq x \leq 1$) solid solutions is opted here as it provides the propensity to utilize the photonic energy ranging all across the visible spectrum.

References

[1] A. Hosseinnia, M. Keyanpour-rad, and M. Pazouki, "Photo-catalytic Degradation of Organic Dyes with Different Chromophores by Synthesized Nanosize TiO 2 Particles," *World Appl. Sci. J.*, vol. 8, no. 11, pp. 1327–1332, 2010.

[2] I. T. Peternel, N. Koprivanac, A. M. L. Božić, and H. M. Kušić, "Comparative study of UV/TiO2, UV/ZnO and photo-Fenton processes for the organic reactive dye degradation in aqueous solution," *J. Hazard. Mater.*, vol. 148, no. 1–2, pp. 477–484, 2007.

[3] C. H. Wu and C. L. Chang, "Decolorization of Reactive Red 2 by advanced oxidation processes: Comparative studies of homogeneous and heterogeneous systems," *J. Hazard. Mater.*, vol. 128, no. 2–3, pp. 265–272, 2006.

[4] Y. S. Shen, Y. Ku, and K. C. Lee, "The effect of light absorbance on the decomposition of chlorophenols by ultraviolet radiation and u.v./H2O2processes," *Water Res.*, vol. 29, no. 3, pp. 907–914, 1995.

[5] C. L. Hsueh, Y. H. Huang, C. C. Wang, and C. Y. Chen, "Degradation of azo dyes using low iron concentration of Fenton and Fenton-like system," *Chemosphere*, vol. 58, no. 10, pp. 1409–1414, 2005.

[6] R. Bauer and H. Fallmann, "The photo-Fenton oxidation—a cheap and efficient wastewater treatment method," *Res. Chem. Intermed.*, vol. 23, no. 4, pp. 341–354, 1997.

[7] P. Cieśla, P. Kocot, P. Mytych, and Z. Stasicka, "Homogeneous photocatalysis by transition metal complexes in the environment," *J. Mol. Catal. A Chem.*, vol. 224, no. 1–2, pp. 17–33, 2004.

[8] C. K. Prier, D. A. Rankic, and D. W. C. MacMillan, "Visible Light Photoredox Catalysis with Transition Metal Complexes: Applications in Organic Synthesis," *Chem. Rev.*, vol. 113, no. 7, pp. 5322–5363, 2013.

[9] A. Juris, V. Balzani, P. Belser, and A. von Zelewsky, "Characterization of the Excited State Properties of Some New Photosensitizers of the Ruthenium (Polypyridine) Family," *Helv. Chim. Acta*, vol. 64, no. 7, pp. 2175–2182, 1981.

[10] J. K. McCusker, "Femtosecond Absorption Spectroscopy of Transition Metal Charge-Transfer Complexes," *Acc. Chem. Res.*, vol. 36, no. 12, pp. 876–887, 2003.

[11] K. Kalyanasundaram, "Photophysics, photochemistry and solar energy conversion with tris(bipyridyl)ruthenium(II) and its analogues," *Coord. Chem. Rev.*, vol. 46, no. C, pp. 159–244, 1982.

[12] A. Juris, V. Balzani, F. Barigelletti, S. Campagna, P. Belser, and A. von Zelewsky, "Ru(II) polypyridine complexes: photophysics, photochemistry, eletrochemistry, and chemiluminescence," *Coord. Chem. Rev.*, vol. 84, no. C, pp. 85–277, 1988.

[13] M. Gratzel, "Artificial Photosynthesis: Water Cleavage into Hydrogen and Oxygen by Visible Light," *Acc. Chem. Res.*, vol. 14, no. 12, pp. 376–384, 1981.

[14] T. J. Meyer, "Chemical Approaches to Artificial Photosynthesis," *Acc. Chem. Res.*, vol. 22, no. 5, pp. 163–170, 1989.

[15] H. Takeda and O. Ishitani, "Development of efficient photocatalytic systems for CO2 reduction using mononuclear and multinuclear metal complexes based on mechanistic studies," *Coord. Chem. Rev.*, vol. 254, no. 3–4, pp. 346–354, 2010.

[16] M. a Ischay, M. E. Anzovino, J. Du, and T. P. Yoon, "Efficient Visible Light Photocatalysis of [2 + 2] Enone Cycloadditions Efficient Visible Light Photocatalysis of [2 + 2] Enone Cycloadditions," vol. 130, no. September, pp. 12886–12887, 2008.

[17] B. Dawoud, E. Amer, and D. Gross, “Experimental investigation of an adsorptive thermal energy storage,” *Int. J. energy Res.*, vol. 31, no. August 2007, pp. 135–147, 2007.

[18] J. M. Herrmann, “Heterogeneous photocatalysis: an emerging discipline involving multiphase systems,” *Catal. Today*, vol. 24, no. 1–2, pp. 157–164, 1995.

[19] D. Chen, M. Sivakumar, and A. K. Ray, “Heterogeneous Photocatalysis in Environmental Remedia tion,” *Dev. Chem. Eng. Miner. Process*, vol. 8, no. (5/6), pp. 505–550, 2000.

[20] A. L. Linsebigler, G. Lu, and J. T. Yates, “Photocatalysis on TiO2Surfaces: Principles, Mechanisms, and Selected Results,” *Chem. Rev.*, vol. 95, no. 3, pp. 735–758, 1995.

[21] Z. Zhang and J. T. Yates, “Band bending in semiconductors: Chemical and physical consequences at surfaces and interfaces,” *Chem. Rev.*, vol. 112, no. 10, pp. 5520–5551, 2012.

[22] F. Chen, Y. Xie, J. Zhao, and G. Lu, “Photocatalytic degradation of dyes on a magnetically separated photocatalyst under visible and UV irradiation,” *Chemosphere*, vol. 44, no. 5, pp. 1159–1168, 2001.

[23] C. Galindo, P. Jacques, and A. Kalt, “Photodegradation of the aminoazobenzene acid orange 52 by three advanced oxidation processes: UV/H2O2, UV/TiO2 and VIS/TiO2,” *J. Photochem. Photobiol. A Chem.*, vol. 130, no. 1, pp. 35–47, 2000.

[24] Y. Ma and J.-N. Yao, “Photodegradation of Rhodamine B catalyzed by Ti02 thin films,” *J. Photoc+Fmistry Photobiol. AChemistry J. Photochem. Photobiol. A Chem.*, vol. 116, no. 7 ml, pp. 167–170, 1998.

[25] J. Schneider *et al.*, “Understanding TiO_2 Photocatalysis: Mechanisms and Materials,” *Chem. Rev.*, vol. 114, no. 19, pp. 9919–9986, 2014.

[26] M. A. Rauf and S. S. Ashraf, “Fundamental principles and application of heterogeneous photocatalytic degradation of dyes in solution,” *Chem. Eng. J.*, vol. 151, no. 1–3, pp. 10–18, 2009.

[27] J.-M. Herrmann, “Heterogeneous photocatalysis: fundamentals and applications to the removal of various types of aqueous pollutants,” *Catal. Today*, vol. 53, no. 1, pp. 115–129, Oct. 1999.

[28] I. D. and C. Z. Canan Acar, “A review on selected heterogeneous photocatalysts for hydrogen production,” *Int. J. ENERGY Res.*, vol. 31, no. August 2007, pp. 135–147, 2014.

[29] C. Gao, J. Wang, H. Xu, and Y. Xiong, “Coordination chemistry in the design of heterogeneous photocatalysts,” *Chem. Soc. Rev.*, vol. 46, no. 10, pp. 2799–2823, 2017.

[30] J. Kou, C. Lu, J. Wang, Y. Chen, Z. Xu, and R. S. Varma, “Selectivity Enhancement in Heterogeneous Photocatalytic Transformations,” *Chem. Rev.*, vol. 117, no. 3, pp. 1445–1514, 2017.

[31] A. Fujishima and K. Honda, “Electrochemical photolysis of water at a semiconductor electrode,” *Nature*, vol. 238, no. 5358, pp. 37–38, 1972.

[32] G. N. Schrauzer and T. D. Guth, “Photolysis of Water and Photoreduction of Nitrogen on Titanium Dioxide1,” *J. Am. Chem. Soc.*, vol. 99, no. 22, pp. 7189–7193, 1977.

[33] W. Choi, A. Termin, and M. R. Hoffmann, “The Role of Metal Ion Dopants in Quantum-Sized TiO2: Correlation between Photoreactivity and Charge Carrier Recombination Dynamics,” *J. Phys. Chem.*, vol. 98, no. 51, pp. 13669–13679, Dec. 1994.

[34] W. Y. Teoh, L. Mädler, D. Beydoun, S. E. Pratsinis, and R. Amal, “Direct (one-step) synthesis of TiO2and Pt/TiO2nanoparticles for photocatalytic mineralisation of sucrose,” *Chem. Eng. Sci.*, vol. 60, no. 21, pp. 5852–5861, 2005.

[35] W. Y. Teoh, “A perspective on the flame spray synthesis of photocatalyst nanoparticles,” *Materials (Basel).*, vol. 6, no. 8, pp. 3194–3212, 2013.

[36] L. Mädler, H. K. Kammler, R. Mueller, and S. E. Pratsinis, “Controlled synthesis of nanostructured particles by flame spray pyrolysis,” *J. Aerosol Sci.*, vol. 33, no. 2, pp. 369–389, 2002.

[37] S. Basahel, T. Ali, M. Mokhtar, and K. Narasimharao, “Influence of crystal structure of nanosized ZrO2 on photocatalytic degradation of methyl orange,” *Nanoscale Res. Lett.*, vol. 10, no. 1, pp. 1–13, 2015.

[38] K. City, “Electronic structures of three phases of zirconium oxide,” vol. 150, pp. 19–24, 1988.

[39] Z. Shu, X. Jiao, and D. Chen, “Synthesis and photocatalytic properties of flower-like zirconia nanostructures,” *CrystEngComm*, vol. 14, no. 3, pp. 1122–1127, 2012.

[40] R. Y. Hong *et al.*, “Synthesis, surface modification and photocatalytic property of ZnO nanoparticles,” *Powder Technol.*, vol. 189, no. 3, pp. 426–432, 2009.

[41] Y. Zhai, S. Zhang, and H. Pang, “Preparation, characterization and photocatalytic activity of CeO2nanocrystalline using ammonium bicarbonate as precipitant,” *Mater. Lett.*, vol. 61, no. 8–9, pp. 1863–1866, 2007.

[42] S. B. Khan, M. Faisal, M. M. Rahman, and A. Jamal, “Exploration of CeO2nanoparticles as a chemi-sensor and photo-catalyst for environmental applications,” *Sci. Total Environ.*, vol. 409, no. 15, pp. 2987–2992, 2011.

[43] Y. Roig, S. Marre, T. Cardinal, and C. Aymonier, “Synthesis of exciton luminescent ZnO nanocrystals using continuous supercritical microfluidics,” *Angew. Chemie - Int. Ed.*, vol. 50, no. 50, pp. 12071–12074, 2011.

[44] C. Slostowski, S. Marre, J. M. Bassat, and C. Aymonier, “Synthesis of cerium oxide-based nanostructures in near- and supercritical fluids,” *J. Supercrit. Fluids*, vol. 84, pp. 89–97, 2013.

[45] E. Monroy, F. Omnès, and F. Calle, “Wide-bandgap semiconductor ultraviolet photodetectors,” *Semicond. Sci. Technol.*, vol. 18, no. 4, 2003.

[46] I. A. Banerjee, L. Yu, and H. Matsui, “Room-temperature wurtzite ZnS nanocrystal growth on Zn finger-like peptide nanotubes by controlling their unfolding peptide structures,” *J. Am. Chem. Soc.*, vol. 127, no. 46, pp. 16002–16003, 2005.

[47] J.-S. Hu *et al.*, “Mass Production and High Photocatalytic Activity of ZnS Nanoporous Nanoparticles,” *Angew. Chemie Int. Ed.*, vol. 44, no. 8, pp. 1269–1273, 2005.

[48] S. L. and H. Z. and M. T. Swihart, “Spray pyrolysis synthesis of ZnS nanoparticles from a single-source precursor,” *Nanotechnology*, vol. 20, no. 23, p. 235603, 2009.

[49] M. Luo, Y. Liu, J. Hu, H. Liu, and J. Li, “One-Pot Synthesis of CdS and Ni-Doped CdS Hollow Spheres with Enhanced Photocatalytic Activity and Durability,” *ACS Appl. Mater. Interfaces*, vol. 4, no. 3, pp. 1813–1821, Mar. 2012.

[50] W. Xu *et al.*, “Nanoporous CuS with excellent photocatalytic property,” *Sci. Rep.*, vol. 5, pp. 1–11, 2015.

[51] D. Jing and L. Guo, “A Novel Method for the Preparation of a Highly Stable and Active CdS Photocatalyst with a Special Surface Nanostructure,” *J. Phys. Chem. B*, vol. 110, no. 23, pp. 11139–11145, Jun. 2006.

[52] M. A. Holmes, T. K. Townsend, and F. E. Osterloh, “Quantum confinement controlled photocatalytic water splitting by suspended CdSe nanocrystals,” *Chem. Commun.*, vol. 48, no. 3, pp. 371–373, 2012.

[53] I. Yonenaga, “Thermo-mechanical stability of wide-bandgap semiconductors: High temperature hardness of SiC, AlN, GaN, ZnO and ZnSe,” *Phys. B Condens. Matter*, vol. 308–310, pp. 1150–1152, 2001.

[54] and G.-C. Y. Hye Seong Jung, Young Joon Hong, Yirui Li, Jeonghui Cho, Yong-Jin Kim, “Photocatalysis Using GaN Nanowires,” vol. 2, no. 4, pp. 1–21, 2008.

[55] M. Tabata *et al.*, "Modified Ta3N5 powder as a photocatalyst for O 2 evolution in a two-step water splitting system with an iodate/iodide shuttle redox mediator under visible light," *Langmuir*, vol. 26, no. 12, pp. 9161–9165, 2010.

[56] W. J. Chun *et al.*, "Conduction and valence band positions of Ta2O5, TaOn, and Ta3N5 by UPS and electrochemical methods," *J. Phys. Chem. B*, vol. 107, no. 8, pp. 1798–1803, 2003.

[57] G. Hitoki, A. Ishikawa, T. Takata, J. N. Kondo, M. Hara, and K. Domen, "Ta3N5 as a Novel Visible Light-Driven Photocatalyst (λ<600 nm)," *Chem. Lett.*, no. 7, pp. 736–736, 2002.

[58] Q. Zhang and L. Gao, "Ta3N5 Nanoparticles with Enhanced Photocatalytic Efficiency under Visible Light Irradiation," *Langmuir*, vol. 20, no. 22, pp. 9821–9827, Oct. 2004.

[59] S. S. K. Ma, T. Hisatomi, K. Maeda, Y. Moriya, and K. Domen, "Enhanced Water Oxidation on Ta3N5 Photocatalysts by Modification with Alkaline Metal Salts," *J. Am. Chem. Soc.*, vol. 134, no. 49, pp. 19993–19996, Dec. 2012.

[60] J. S. Hu *et al.*, "Mass production and high photocatalytic activity of ZnS nanoporous nanoparticles," *Angew. Chemie - Int. Ed.*, vol. 44, no. 8, pp. 1269–1273, 2005.

[61] S. B. Khan, M. Faisal, M. M. Rahman, and A. Jamal, "Exploration of CeO2 nanoparticles as a chemi-sensor and photo-catalyst for environmental applications," *Sci. Total Environ.*, vol. 409, no. 15, pp. 2987–2992, Jul. 2011.

[62] M. A. Peña and J. L. G. Fierro, "Chemical structures and performance of perovskite oxides," *Chem. Rev.*, vol. 101, no. 7, pp. 1981–2017, 2001.

[63] K. Zhang *et al.*, "Research progress and materials selection guidelines on mixed conducting perovskite-type ceramic membranes for oxygen production," *RSC Adv.*, vol. 1, no. 9, pp. 1661–1676, 2011.

[64] G. Zhang, G. Liu, L. Wang, and J. T. S. Irvine, "Inorganic perovskite photocatalysts for solar energy utilization," *Chem. Soc. Rev.*, vol. 45, no. 21, pp. 5951–5984, 2016.

[65] K. Fujinami, K. Katagiri, J. Kamiya, T. Hamanaka, and K. Koumoto, "Sub-10 nm strontium titanate nanocubes highly dispersed in non-polar organic solvents," *Nanoscale*, vol. 2, no. 10, pp. 2080–2083, 2010.

[66] T. Ohno, T. Tsubota, Y. Nakamura, and K. Sayama, "Preparation of S, C cation-codoped SrTiO3and its photocatalytic activity under visible light," *Appl. Catal. A Gen.*, vol. 288, no. 1–2, pp. 74–79, 2005.

[67] S. Ahuja and T. R. N. Kutty, "Nanoparticles of SrTiO3prepared by gel to crystallite conversion and their photocatalytic activity in the mineralization of phenol," *J. Photochem. Photobiol. A Chem.*, vol. 97, no. 1–2, pp. 99–107, 1996.

[68] X. Wei *et al.*, "Single-crystal-like mesoporous SrTiO3 spheres with enhanced photocatalytic performance," *J. Am. Ceram. Soc.*, vol. 93, no. 5, pp. 1297–1305, 2010.

[69] K. Domen, A. Kudo, and T. Onishi, "Mechanism of photocatalytic decomposition of water into H2 and O2 over NiOSrTiO3," *J. Catal.*, vol. 102, no. 1, pp. 92–98, 1986.

[70] Q. Li, K. Domen, S. Naito, T. Onishi, and K. Tamaru, "Photocatalytic synthesis and photodecomposition of ammonia over SrTiO3 and BaTiO3 based catalysts.," *Chem. Lett.*, vol. 2, no. 3, pp. 321–324, 1983.

[71] D. K. LEE, I.-S. CHO, D. K. YIM, J.-H. NOH, K. S. HONG, and D.-W. KIM, "Synthesis and photoactivity of hetero-nanostructured $SrTiO_3$," *J. Ceram. Soc. Japan*, vol. 118, no. 1382, pp. 876–880, 2010.

[72] L. Chen, S. Zhang, L. Wang, D. Xue, and S. Yin, "Preparation and photocatalytic properties of strontium titanate powders via sol–gel process," *J. Cryst. Growth*, vol. 311, no. 3, pp. 746–748, Jan. 2009.

[73] A. Kudo, “Photocatalyst Materials for Water Splitting,” *Catal. Surv. from Asia*, vol. 7, no. 1, pp. 31–38, 2003.

[74] H. Kato and A. Kudo, “Water splitting into H2 and O2 on alkali tantalate photocatalysts ATaO3 (A = Li, Na, and K),” *J. Phys. Chem. B*, vol. 105, no. 19, pp. 4285–4292, 2001.

[75] S. Takasugi, K. Tomita, M. Iwaoka, H. Kato, and M. Kakihana, “The hydrothermal and solvothermal synthesis of LiTaO3photocatalyst: Suppressing the deterioration of the water splitting activity without using a cocatalyst,” *Int. J. Hydrogen Energy*, vol. 40, no. 16, pp. 5638–5643, 2015.

[76] A. Kudo and H. Kato, “Effect of lanthanide-doping into NaTaO3 photocatalysts for efficient water splitting,” *Chem. Phys. Lett.*, vol. 331, no. 5–6, pp. 373–377, 2000.

[77] C. C. Hu and H. Teng, “Influence of structural features on the photocatalytic activity of NaTaO3powders from different synthesis methods,” *Appl. Catal. A Gen.*, vol. 331, no. 1, pp. 44–50, 2007.

[78] Y. He, Y. Zhu, and N. Wu, “Synthesis of nanosized NaTaO3in low temperature and its photocatalytic performance,” *J. Solid State Chem.*, vol. 177, no. 11, pp. 3868–3872, 2004.

[79] K. Teramura, S. ichi Okuoka, H. Tsuneoka, T. Shishido, and T. Tanaka, “Photocatalytic reduction of CO2using H2as reductant over ATaO3photocatalysts (A = Li, Na, K),” *Appl. Catal. B Environ.*, vol. 96, no. 3–4, pp. 565–568, 2010.

[80] B. Bajorowicz, A. Cybula, M. J. Winiarski, T. Klimczuk, and A. Zaleska, “Surface properties and photocatalytic activity of KTaO3, CdS, MoS2semiconductors and their binary and ternary semiconductor composites,” *Molecules*, vol. 19, no. 9, pp. 15339–15360, 2014.

[81] G. Li *et al.*, “Synthesis and visible light photocatalytic property of polyhedron-shaped AgNbO3,” *Dalt. Trans.*, no. 40, pp. 8519–8524, 2009.

[82] D. Arney, C. Hardy, B. Greve, and P. A. Maggard, “Flux synthesis of AgNbO3: Effect of particle surfaces and sizes on photocatalytic activity,” *J. Photochem. Photobiol. A Chem.*, vol. 214, no. 1, pp. 54–60, Jul. 2010.

[83] H. Kato, H. Kobayashi, and A. Kudo, “Role of Ag+ in the band structures and photocatalytic properties of AgMO3 (M: Ta and Nb) with the perovskite structure,” *J. Phys. Chem. B*, vol. 106, no. 48, pp. 12441–12447, 2002.

[84] A. Kudo, “Development of photocatalyst materials for water splitting,” *Int. J. Hydrogen Energy*, vol. 31, no. 2, pp. 197–202, 2006.

[85] J. Tang, Z. Zou, M. Katagiri, T. Kako, and J. Ye, “Photocatalytic degradation of MB on MIn2O4(M = alkali earth metal) under visible light: Effects of crystal and electronic structure on the photocatalytic activity,” *Catal. Today*, vol. 93–95, pp. 885–889, 2004.

[86] Y. Zhang, R. Selvaraj, M. Sillanpää, Y. Kim, and C.-W. Tai, “Coprecipitates Synthesis of $CaIn_2O_4$ and Its Photocatalytic Degradation of Methylene Blue by Visible Light Irradiation,” *Ind. Eng. Chem. Res.*, vol. 53, no. 29, pp. 11720–11726, 2014.

[87] J. Tang, Z. Zou, J. Yin, and J. Ye, “Photocatalytic degradation of methylene blue on CaIn2O4under visible light irradiation,” *Chem. Phys. Lett.*, vol. 382, no. 1–2, pp. 175–179, 2003.

[88] J. Sato, N. Saito, H. Nishiyama, and Y. Inoue, “Photocatalytic Activity for Water Decomposition of Indates with Octahedrally Coordinated d10 Configuration. I. Influences of Preparation Conditions on Activity,” *J. Phys. Chem. B*, vol. 107, no. 31, pp. 7965–7969, Aug. 2003.

[89] J. Sato, N. Saito, H. Nishiyama, and Y. Inoue, “New photocatalyst group for water decomposition of RuO2-loaded p-block metal (In, Sn, and Sb) oxides with d10configuration,” *J. Phys. Chem. B*, vol. 105, no. 26, pp. 6061–6063, 2001.

[90] J. Sato, N. Saito, H. Nishiyama, and Y. Inoue, "Photocatalytic Activity for Water Decomposition of Indates with Octahedrally Coordinated d ^{10} Configuration. I. Influences of Preparation Conditions on Activity," *J. Phys. Chem. B*, vol. 107, no. 31, pp. 7965–7969, 2003.

[91] J. Ding, S. Sun, J. Bao, Z. Luo, and C. Gao, "Synthesis of CaIn2O4 Rods and Its Photocatalytic Performance Under Visible-light Irradiation," *Catal. Letters*, vol. 130, no. 1–2, pp. 147–153, 2009.

[92] Y. Maruyama, H. Irie, and K. Hashimoto, "Visible Light Sensitive Photocatalyst, Delafossite Structured α-AgGaO2," *J. Phys. Chem. B*, vol. 110, no. 46, pp. 23274–23278, Nov. 2006.

[93] S. Ouyang, H. Zhang, D. Li, T. Yu, J. Ye, and Z. Zou, "Electronic structure and photocatalytic characterization of a novel photocatalyst AgAlO2," *J. Phys. Chem. B*, vol. 110, no. 24, pp. 11677–11682, 2006.

[94] Y. Maruyama, H. Irie, and K. Hashimoto, "Visible light sensitive photocatalyst, delafossite structured α-AgGaO2," *J. Phys. Chem. B*, vol. 110, no. 46, pp. 23274–23278, 2006.

[95] S. Ouyang, Z. Li, Z. Ouyang, T. Yu, J. Ye, and Z. Zou, "Correlation of crystal structures, electronic structures, and photocatalytic properties in a series of Ag-based oxides: AgAlO2, AgCrO2, and Ag2CrO4," *J. Phys. Chem. C*, vol. 112, no. 8, pp. 3134–3141, 2008.

[96] S. Ouyang, N. Kikugawa, D. Chen, Z. Zou, and J. Ye, "A Systematical Study on Photocatalytic Properties of AgMO $_2$ (M = Al, Ga, In): Effects of Chemical Compositions, Crystal Structures, and Electronic Structures," *J. Phys. Chem. C*, vol. 113, no. 4, pp. 1560–1566, 2009.

[97] S. Tokunaga, H. Kato, and A. Kudo, "Selective preparation of monoclinic and tetragonal BiVO4with scheelite structure and their photocatalytic properties," *Chem. Mater.*, vol. 13, no. 12, pp. 4624–4628, 2001.

[98] J. D. Bierlein and A. W. Sleight, "Ferroelasticity in BiVO4," *Solid State Commun.*, vol. 16, no. 1, pp. 69–70, 1975.

[99] P. R. Bodart, "Orientation of electric üeld gradient and chemical shift," vol. 226, pp. 223–226, 1999.

[100] S. Kohtani, J. Hiro, N. Yamamoto, A. Kudo, K. Tokumura, and R. Nakagaki, "Adsorptive and photocatalytic properties of Ag-loaded BiVO4 on the degradation of 4-n-alkylphenols under visible light irradiation," *Catal. Commun.*, vol. 6, no. 3, pp. 185–189, 2005.

[101] S. Kohtani *et al.*, "Photodegradation of 4-alkylphenols using BiVO4photocatalyst under irradiation with visible light from a solar simulator," *Appl. Catal. B Environ.*, vol. 46, no. 3, pp. 573–586, 2003.

[102] A. Kudo, K. Omori, and H. Kato, "A novel aqueous process for preparation of crystal form-controlled and highly crystalline BiVO4 powder from layered vanadates at room temperature and its photocatalytic and photophysical properties," *J. Am. Chem. Soc.*, vol. 121, no. 49, pp. 11459–11467, 1999.

[103] J. Yu and A. Kudo, "Effects of Structural Variation on the Photocatalytic Performance of Hydrothermally Synthesized BiVO4," *Adv. Funct. Mater.*, vol. 16, no. 16, pp. 2163–2169, 2006.

[104] B. S. Schwarz, H. Wirth, and O. Schmidt-park, "Rich yellow," pp. 26–31, 2016.

[105] B. B. Kale, J. O. Baeg, S. M. Lee, H. Chang, S. J. Moon, and C. W. Lee, "CdIn2S4nanotubes and 'marigold' nanostructures: A visible-light photocatalyst," *Adv. Funct. Mater.*, vol. 16, no. 10, pp. 1349–1354, 2006.

[106] Z. Chen *et al.*, "Photocatalytic Degradation of Dyes by ZnIn $_2$ S $_4$ Microspheres under Visible Light Irradiation," *J. Phys. Chem. C*, vol. 113, no. 11, pp. 4433–4440, 2009.

[107] W. Du, X. Qian, J. Yin, and Q. Gong, "Shape- and phase-controlled synthesis of monodisperse, single-crystalline ternary chalcogenide colloids through a convenient solution synthesis strategy," *Chem. - A*

Eur. J., vol. 13, no. 31, pp. 8840–8846, 2007.

[108] I. Tsuji, H. Kato, and A. Kudo, "Visible-Light-Induced H2 Evolution from an Aqueous Solution Containing Sulfide and Sulfite over a ZnS–CuInS2–AgInS2 Solid-Solution Photocatalyst," *Angew. Chemie Int. Ed.*, vol. 44, no. 23, pp. 3565–3568, 2005.

[109] M. Nanu, J. Schoonman, and A. Goossens, "Nanocomposite three-dimensional solar cells obtained by chemical spray deposition," *Nano Lett.*, vol. 5, no. 9, pp. 1716–1719, 2005.

[110] "Photocatalytic Hydrogen Evolution on ZnS−CuInS2−AgInS2 Solid Solution Photocatalysts with Wide Visible Light Absorption Bands.pdf." .

[111] S. C. Erwin and I. Žutić, "Tailoring ferromagnetic chalcopyrites," *Nat. Mater.*, vol. 3, no. 6, pp. 410–414, 2004.

[112] D. Aldakov, A. Lefrançois, and P. Reiss, "Ternary and quaternary metal chalcogenide nanocrystals: Synthesis, properties and applications," *J. Mater. Chem. C*, vol. 1, no. 24, pp. 3756–3776, 2013.

[113] H. Zhong, Z. Bai, and B. Zou, "Tuning the luminescence properties of colloidal I-III-VI semiconductor nanocrystals for optoelectronics and biotechnology applications," *J. Phys. Chem. Lett.*, vol. 3, no. 21, pp. 3167–3175, 2012.

[114] K. Yoshino, H. Komaki, T. Kakeno, Y. Akaki, and T. Ikari, "Growth and characterization of p-type AgInS2crystals," *J. Phys. Chem. Solids*, vol. 64, no. 9–10, pp. 1839–1842, 2003.

[115] L. Tian, H. I. Elim, W. Ji, and J. J. Vittal, "One-pot synthesis and third-order nonlinear optical properties of AgInS2 nanocrystals," *Chem. Commun.*, no. 41, pp. 4276–4278, 2006.

[116] Z. Aissa, T. Ben Nasrallah, M. Amlouk, J. C. Bernède, and S. Belgacem, "Some physical investigations on AgInS2sprayed thin films," *Sol. Energy Mater. Sol. Cells*, vol. 90, no. 7–8, pp. 1136–1146, 2006.

[117] Z. Luo, H. Zhang, J. Huang, and X. Zhong, "One-step synthesis of water-soluble AgInS2and ZnS-AgInS2composite nanocrystals and their photocatalytic activities," *J. Colloid Interface Sci.*, vol. 377, no. 1, pp. 27–33, 2012.

[118] Z. Zhuang, X. Lu, Q. Peng, and Y. Li, "A facile 'dispersion-decomposition' route to metal sulfide nanocrystals," *Chem. - A Eur. J.*, vol. 17, no. 37, pp. 10445–10452, 2011.

[119] J. Q. Hu, B. Deng, C. R. Wang, K. B. Tang, and Y. T. Qian, "Hydrothermal preparation of CuGaS2 crystallites with different morphologies," *Solid State Commun.*, vol. 121, no. 9–10, pp. 493–496, 2002.

[120] Q. Lu, J. Hu, K. Tang, Y. Qian, G. Zhou, and X. Liu, "Synthesis of nanocrystalline CuMS2 (M = In or Ga) through a solvothermal process," *Inorg. Chem.*, vol. 39, no. 7, pp. 1606–1607, 2000.

[121] Y. H. A. Wang, X. Zhang, N. Bao, B. Lin, and A. Gupta, "Synthesis of shape-controlled monodisperse wurtzite CuInxGa1-xS2semiconductor nanocrystals with tunable band gap," *J. Am. Chem. Soc.*, vol. 133, no. 29, pp. 11072–11075, 2011.

[122] M. D. Regulacio, C. Ye, S. H. Lim, Y. Zheng, Q. H. Xu, and M. Y. Han, "Facile noninjection synthesis and photocatalytic properties of wurtzite-phase CuGaS2nanocrystals with elongated morphologies," *CrystEngComm*, vol. 15, no. 26, pp. 5214–5217, 2013.

[123] G. Philippot *et al.*, "Continuous BaTi<inf>1-y</inf>Zr<inf>y</inf>O<inf>3</inf> (0≤y≤1) nanocrystals synthesis in supercritical fluids for nanostructured lead-free ferroelectric ceramics," *Mater. Des.*, vol. 86, pp. 354–360, 2015.

[124] G. Philippot, C. Elissalde, M. Maglione, and C. Aymonier, "Supercritical fluid technology: A reliable process for high quality BaTiO3based nanomaterials," *Adv. Powder Technol.*, vol. 25, no. 5, pp. 1415–1429, 2014.

[125] J. Yu and A. Kudo, “Effects of structural variation on the photocatalytic performance of hydrothermally synthesized BiVO4,” *Adv. Funct. Mater.*, vol. 16, no. 16, pp. 2163–2169, 2006.

[126] H. Wang and J. P. Lewis, “Second-generation photocatalytic materials: Anion-doped TiO2,” *J. Phys. Condens. Matter*, vol. 18, no. 2, pp. 421–434, 2006.

[127] C. M. Teh and A. R. Mohamed, “Roles of titanium dioxide and ion-doped titanium dioxide on photocatalytic degradation of organic pollutants (phenolic compounds and dyes) in aqueous solutions: A review,” *J. Alloys Compd.*, vol. 509, no. 5, pp. 1648–1660, 2011.

[128] H. Dong *et al.*, “An overview on limitations of TiO<inf>2</inf>-based particles for photocatalytic degradation of organic pollutants and the corresponding countermeasures,” *Water Res.*, vol. 79, pp. 128–146, 2015.

[129] A. Fujishima, X. Zhang, and D. A. Tryk, “TiO2photocatalysis and related surface phenomena,” *Surf. Sci. Rep.*, vol. 63, no. 12, pp. 515–582, 2008.

[130] H. Tran, J. Scott, K. Chiang, and R. Amal, “Clarifying the role of silver deposits on titania for the photocatalytic mineralisation of organic compounds,” *J. Photochem. Photobiol. A Chem.*, vol. 183, no. 1–2, pp. 41–52, 2006.

[131] E. Kowalska, H. Remita, C. Colbeau-Justin, J. Hupka, and J. Belloni, “Modification of titanium dioxide with platinum ions and clusters: Application in photocatalysis,” *J. Phys. Chem. C*, vol. 112, no. 4, pp. 1124–1131, 2008.

[132] V. Subramanian, E. Wolf, and P. V. Kamat, “Semiconductor-metal composite nanostructures. To what extent do metal nanoparticles improve the photocatalytic activity of TiO2films?,” *J. Phys. Chem. B*, vol. 105, no. 46, pp. 11439–11446, 2001.

[133] J. Zhang, Y. Wu, M. Xing, S. A. K. Leghari, and S. Sajjad, “Development of modified N doped TiO2 photocatalyst with metals, nonmetals and metal oxides,” *Energy Environ. Sci.*, vol. 3, no. 6, pp. 715–726, 2010.

[134] R. Daghrir, P. Drogui, and D. Robert, “Modified TiO2 for environmental photocatalytic applications: A review,” *Ind. Eng. Chem. Res.*, vol. 52, no. 10, pp. 3581–3599, 2013.

[135] Z. Mei *et al.*, “Hexagonal Zn1-xCdxS ($0.2 \leq x \leq 1$) solid solution photocatalysts for H2generation from water,” *Catal. Sci. Technol.*, vol. 7, no. 4, pp. 982–987, 2017.

[136] IUPAC, “Compendium of Chemical Terminology 2nd ed. (the ‘Gold Book’),” *Blackwell Sci. Publ. Oxford*, p. 1670, 2014.

[137] Z. Wang *et al.*, “Progress on extending the light absorption spectra of photocatalysts,” *Phys. Chem. Chem. Phys.*, vol. 16, no. 7, pp. 2758–2774, 2014.

[138] S. Ouyang and J. Ye, “β-AgAl1-xGaxO2 Solid-Solution Photocatalysts: Continuous Modulation of Electronic Structure toward High-Performance Visible-Light Photoactivity,” *J. Am. Chem. Soc.*, vol. 133, no. 20, pp. 7757–7763, May 2011.

[139] D. E. Scaife, “Oxide semiconductors in photoelectrochemical conversion of solar energy,” *Sol. Energy*, vol. 25, no. 1, pp. 41–54, 1980.

[140] G. Li, T. Kako, D. Wang, Z. Zou, and J. Ye, “Composition dependence of the photophysical and photocatalytic properties of (AgNbO3)1-x(NaNbO3)xsolid solutions,” *J. Solid State Chem.*, vol. 180, no. 10, pp. 2845–2850, 2007.

[141] K. Maeda *et al.*, “GaN:ZnO Solid Solution as a Photocatalyst for Visible-Light-Driven Overall Water Splitting,” *J. Am. Chem. Soc.*, vol. 127, no. 23, pp. 8286–8287, Jun. 2005.

[142] K. Maeda and K. Domen, “Solid Solution of GaN and ZnO as a Stable Photocatalyst for Overall Water Splitting under Visible Light,” *Chem. Mater.*, vol. 22, no. 3, pp. 612–623, Feb. 2010.

[143] L. L. Jensen, J. T. Muckerman, and M. D. Newton, “First-principles studies of the structural and electronic properties of the (Ga1-xZnx)(N1-xOx) solid solution photocatalyst,” *J. Phys. Chem. C*, vol. 112, no. 9, pp. 3439–3446, 2008.

[144] T. Hirai *et al.*, “Origin of Visible Light Absorption in GaN-Rich (Ga 1 - x Zn x)(N 1 - x O x) Photocatalysts,” *J. Phys. Chem. C*, vol. 111, no. 51, pp. 18853–18855, 2007.

[145] S. S. Menon, R. Anitha, B. Gupta, K. Baskar, and S. Singh, “Synthesis of GaN:ZnO solid solution by solution combustion method and characterization for photocatalytic application,” vol. 50025, no. 2016, p. 50025, 2016.

[146] D. Wang, T. Kako, and J. Ye, “New Series of Solid-Solution Semiconductors $(AgNbO_3)_{1-x}(SrTiO_3)_x$ with Modulated Band Structure and Enhanced Visible-Light Photocatalytic Activity,” *J. Phys. Chem. C*, vol. 113, no. 9, pp. 3785–3792, 2009.

[147] K. Hideki, M. Naoko and K. Akihido, “Photophysical and Photocatalytic Properties of Molybates and Tungstates with a Scheelite Structure,” *Chem. Letters*, vol. 33, no. 9, pp. 1216–1217, 2004.

[148] A. Kudo, K. Ueda, H. Kato, and I. Mikami, “Photocatalytic O2 evolution under visible light irradiation on BiVO4 in aqueous AgNO3 solution,” *Catal. Letters*, vol. 53, no. 3, pp. 229–230, 1998.

[149] W. Yao and J. Ye, “Photophysical and Photocatalytic Properties of Ca1-xBixVxMo1-xO4 Solid Solutions,” *J. Phys. Chem. B*, vol. 110, no. 23, pp. 11188–11195, Jun. 2006.

[150] J. Zhang, J. Yu, Y. Zhang, Q. Li, and J. R. Gong, “Visible Light Photocatalytic H2-Production Activity of CuS/ZnS Porous Nanosheets Based on Photoinduced Interfacial Charge Transfer,” *Nano Lett.*, vol. 11, no. 11, pp. 4774–4779, Nov. 2011.

[151] J. F. Reber and M. Rusek, “Photochemical hydrogen production with platinized suspensions of cadmium sulfide and cadmium zinc sulfide modified by silver sulfide,” *J. Phys. Chem.*, vol. 90, no. 5, pp. 824–834, Feb. 1986.

[152] M. Matsumura, S. Furukawa, Y. Saho, and H. Tsubomura, “Cadmium sulfide photocatalyzed hydrogen production from aqueous solutions of sulfite: Effect of crystal structure and preparation method of the catalyst,” *J. Phys. Chem.*, vol. 89, no. 8, pp. 1327–1329, 1985.

[153] C. Xing, Y. Zhang, W. Yan, and L. Guo, “Band structure-controlled solid solution of Cd1 - xZnxS photocatalyst for hydrogen production by water splitting,” *Int. J. Hydrogen Energy*, vol. 31, no. 14, pp. 2018–2024, 2006.

[154] F. del Valle *et al.*, “Influence of Zn concentration in the activity of Cd1-xZnxS solid solutions for water splitting under visible light,” *Catal. Today*, vol. 143, no. 1–2, pp. 51–56, 2009.

[155] J. Yu, J. Zhang, and M. Jaroniec, “Preparation and enhanced visible-light photocatalytic H2-production activity of CdS quantum dots-sensitized Zn1−xCdxS solid solution,” *Green Chem.*, vol. 12, no. 9, pp. 1611–1614, 2010.

[156] Q. Nie, Q. Yuan, Q. Wang, and Z. Xu, “In situ synthesis of Zn x Cd 1− x S nanorod by a hydrothermal route,” *Journal of materials science*, vol. 39, no. 16. pp. 5611–5612, 2004.

[157] J. Yu, B. Yang, and B. Cheng, “Noble-metal-free carbon nanotube-Cd0.1Zn0.9S composites for high visible-light photocatalytic H2-production performance,” *Nanoscale*, vol. 4, no. 8, pp. 2670–2677, 2012.

[158] Q. Li *et al.*, “Zn1–xCdxS Solid Solutions with Controlled Bandgap and Enhanced Visible-Light Photocatalytic H2-Production Activity,” *ACS Catal.*, vol. 3, no. 5, pp. 882–889, May 2013.

[159] A. Kudo and M. Sekizawa, “Photocatalytic H2 evolution under visible light irradiation on Zn1-x Cu x S solid solution,” *Catal. Letters*, vol. 58, no. 4, pp. 241–243, 1999.

[160] G. Liu, L. Zhao, L. Ma, and L. Guo, “Photocatalytic H2 evolution under visible light irradiation on a novel CdxCuyZn1−x−yS catalyst,” *Catal. Commun.*, vol. 9, no. 1, pp. 126–130, Jan. 2008.

[161] J. Klaer *et al.*, “Efficient thin-film solar cells prepared by a sequential process,” *Semicond. Sci. Technol.*, vol. 13, no. 12, pp. 1456–1458, Dec. 1998.

[162] S. N. Rashkeev and W. R. L. Lambrecht, “Second-harmonic generation of I-III-${\mathrm{VI}}_{2}$ chalcopyrite semiconductors: Effects of chemical substitutions,” *Phys. Rev. B*, vol. 63, no. 16, p. 165212, Apr. 2001.

[163] A. A. Lavrentiev, B. V. Gabrel’yan, and I. Y. Nikiforov, “Chemical binding in ternary chalcogenides AIBIIICVI2,” *J. Struct. Chem.*, vol. 41, no. 3, pp. 418–426, 2000.

[164] I. Tsuji, H. Kato, H. Kobayashi, and A. Kudo, “Photocatalytic H2 Evolution Reaction from Aqueous Solutions over Band Structure-Controlled (AgIn)xZn2(1-x)S2 Solid Solution Photocatalysts with Visible-Light Response and Their Surface Nanostructures,” *J. Am. Chem. Soc.*, vol. 126, no. 41, pp. 13406–13413, Oct. 2004.

[165] I. Tsuji, H. Kato, H. Kobayashi, and A. Kudo, “Photocatalytic H2 Evolution under Visible-Light Irradiation over Band-Structure-Controlled (CuIn)xZn2(1-x)S2 Solid Solutions,” *J. Phys. Chem. B*, vol. 109, no. 15, pp. 7323–7329, Apr. 2005.

[166] I. Tsuji, H. Kato, and A. Kudo, “Visible-Light-Induced H2 Evolution from an Aqueous Solution Containing Sulfide and Sulfite over a ZnS-CuInS2-AgInS2 Solid-Solution Photocatalyst,” *Angew. Chemie Int. Ed.*, vol. 44, no. 23, pp. 3565–3568, 2005.

[167] H. Tong, S. Ouyang, Y. Bi, N. Umezawa, M. Oshikiri, and J. Ye, “Nano-photocatalytic Materials: Possibilities and Challenges,” *Adv. Mater.*, vol. 24, no. 2, pp. 229–251, 2012.

[168] P. V Kamat, “Meeting the Clean Energy Demand: Nanostructure Architectures for Solar Energy Conversion,” *J. Phys. Chem. C*, vol. 111, no. 7, pp. 2834–2860, Feb. 2007.

[169] C.-H. Liao, C.-W. Huang, and J. C. S. Wu, “Hydrogen Production from Semiconductor-based Photocatalysis via Water Splitting,” *Catalysts*, vol. 2, no. 4, pp. 490–516, 2012.

[170] Y. Wang, Q. Wang, X. Zhan, F. Wang, M. Safdar, and J. He, “Visible light driven type II heterostructures and their enhanced photocatalysis properties: A review,” *Nanoscale*, vol. 5, no. 18, pp. 8326–8339, 2013.

[171] H. McDaniel, P. E. Heil, C. L. Tsai, K. Kim, and M. Shim, “Integration of type II nanorod heterostructures into photovoltaics,” *ACS Nano*, vol. 5, no. 9, pp. 7677–7683, 2011.

[172] H. Cheng, B. Huang, Y. Dai, X. Qin, and X. Zhang, “One-Step Synthesis of the Nanostructured AgI/BiOI Composites with Highly Enhanced Visible-Light Photocatalytic Performances,” *Langmuir*, vol. 26, no. 9, pp. 6618–6624, May 2010.

[173] H. Zhang *et al.*, “Preparation, characterization and photocatalytic activity of polycrystalline Bi2O3/SrTiO3 composite powders,” *J. Phys. Chem. Solids*, vol. 67, no. 12, pp. 2501–2505, Dec. 2006.

[174] L. Huang, F. Peng, H. Wang, H. Yu, and Z. Li, “Preparation and characterization of Cu2O/TiO2 nano–nano heterostructure photocatalysts,” *Catal. Commun.*, vol. 10, no. 14, pp. 1839–1843, Aug. 2009.

[175] C. Shifu, Z. Sujuan, L. Wei, and Z. Wei, “Preparation and activity evaluation of p-n junction photocatalyst NiO/TiO2,” *J. Hazard. Mater.*, vol. 155, no. 1–2, pp. 320–326, 2008.

[176] H. Road, “J. Bandara* and H. C. Weerasinghe,” vol. 5, no. 4, pp. 305–314, 2005.

[177] L. Wei, C. Shifu, Z. Huaye, and Y. Xiaoling, “Preparation, characterisation of p-n heterojunction

photocatalyst CuBi2O4/Bi2WO6 and its photocatalytic activities," *J. Exp. Nanosci.*, vol. 6, no. 2, pp. 102–120, 2011.

[178] L. Wei and C. Shifu, "Preparation and Characterization of p-n Heterojunction Photocatalyst Cu[sub 2]O/In[sub 2]O[sub 3] and its Photocatalytic Activity under Visible and UV Light Irradiation," *J. Electrochem. Soc.*, vol. 157, no. 11, p. H1029, 2010.

[179] X. Chen and S. S. Mao, "Titanium Dioxide Nanomaterials: Synthesis, Properties, Modifications, and Applications," *Chem. Rev.*, vol. 107, no. 7, pp. 2891–2959, Jul. 2007.

[180] J. L. Gole, J. D. Stout, C. Burda, Y. Lou, and X. Chen, "Highly Efficient Formation of Visible Light Tunable TiO2-xNx Photocatalysts and Their Transformation at the Nanoscale," *J. Phys. Chem. B*, vol. 108, no. 4, pp. 1230–1240, Jan. 2004.

[181] K. R. Gopidas, M. Bohorquez, and P. V. Kamat, "Photophysical and photochemical aspects of coupled semiconductors: charge-transfer processes in colloidal cadmium sulfide-titania and cadmium sulfide-silver(I) iodide systems," *J. Phys. Chem.*, vol. 94, no. 16, pp. 6435–6440, 1990.

[182] T. T. D. Vu, F. Mighri, A. Ajji, and T.-O. Do, "Synthesis of Titanium Dioxide/Cadmium Sulfide Nanosphere Particles for Photocatalyst Applications," *Ind. Eng. Chem. Res.*, vol. 53, no. 10, pp. 3888–3897, Mar. 2014.

[183] M. Zhang, T. An, X. Liu, X. Hu, G. Sheng, and J. Fu, "Preparation of a high-activity ZnO/TiO2photocatalyst via homogeneous hydrolysis method with low temperature crystallization," *Mater. Lett.*, vol. 64, no. 17, pp. 1883–1886, 2010.

[184] Y. Gu *et al.*, "Optical and microstructural properties of ZnO/TiO2 nanolaminates prepared by atomic layer deposition.," *Nanoscale Res. Lett.*, vol. 8, no. 1, p. 107, 2013.

[185] R. Liu, H. Ye, X. Xiong, and H. Liu, "Fabrication of TiO2/ZnO composite nanofibers by electrospinning and their photocatalytic property," *Mater. Chem. Phys.*, vol. 121, no. 3, pp. 432–439, 2010.

[186] T. Potlog, V. Botnariuc, S. Raevschi, M. Dobromir, and D. Luca, *3rd International Conference on Nanotechnologies and Biomedical Engineering*, vol. 55. 2016.

[187] A. M. Hussein *et al.*, "Mesoporous coupled ZnO/TiO2 photocatalyst nanocomposites for hydrogen generation," *J. Renew. Sustain. Energy*, vol. 5, no. 3, pp. 1–13, 2013.

[188] P. Prasannalakshmi and N. Shanmugam, "Fabrication of TiO2/ZnO nanocomposites for solar energy driven photocatalysis," *Mater. Sci. Semicond. Process.*, vol. 61, no. December 2016, pp. 114–124, 2017.

[189] V. Štengl, S. Bakardjieva, N. Murafa, V. Houšková, and K. Lang, "Visible-light photocatalytic activity of TiO2/ZnS nanocomposites prepared by homogeneous hydrolysis," *Microporous Mesoporous Mater.*, vol. 110, no. 2–3, pp. 370–378, 2008.

[190] P. Prasannalakshmi and N. Shanmugam, "Fabrication of TiO2/ZnS nanocomposites for solar energy mediated photocatalytic application," *Spectrochim. Acta - Part A Mol. Biomol. Spectrosc.*, vol. 175, pp. 1–10, 2017.

[191] E. M. Kaidashev *et al.*, "High electron mobility of epitaxial ZnO thin films on c-plane sapphire grown by multistep pulsed-laser deposition," *Appl. Phys. Lett.*, vol. 82, no. 22, pp. 3901–3903, 2003.

[192] K. L. Chopra and S. R. Das, "Photoelectrochemical Cells," *Thin Film Sol. Cells*, vol. 414, no. November, pp. 457–481, 1983.

[193] J. B. Asbury, Y. Wang, and T. Lian, "Multiple-Exponential Electron Injection in Ru(dcbpy) 2 (SCN) 2 Sensitized ZnO Nanocrystalline Thin Films," *J. Phys. Chem. B*, vol. 103, no. 32, pp. 6643–6647, 1999.

[194] Q. Shen, X. Zhao, S. Zhou, W. Hou, and J. J. Zhu, "ZnO/CdS hierarchical nanospheres for

photoelectrochemical sensing of Cu2+," *J. Phys. Chem. C*, vol. 115, no. 36, pp. 17958–17964, 2011.

[195] T. P. Chou, Q. Zhang, G. E. Fryxell, and G. Cao, "Hierarchically structured ZnO film for dye-sensitized solar cells with enhanced energy conversion efficiency," *Adv. Mater.*, vol. 19, no. 18, pp. 2588–2592, 2007.

[196] Q. Zhang, T. P. Chou, B. Russo, S. A. Jenekhe, and G. Cao, "Aggregation of ZnO nanocrystallites for high conversion efficiency in dye-sensitized solar cells," *Angew. Chemie - Int. Ed.*, vol. 47, no. 13, pp. 2402–2406, 2008.

[197] T. Xu, L. Zhang, H. Cheng, and Y. Zhu, "Significantly enhanced photocatalytic performance of ZnO via graphene hybridization and the mechanism study," *Appl. Catal. B Environ.*, vol. 101, no. 3–4, pp. 382–387, 2011.

[198] J. Nayak, H. Lohani, and T. K. Bera, "Observation of catalytic properties of CdS-ZnO composite nanorods synthesized by aqueous chemical growth technique," *Curr. Appl. Phys.*, vol. 11, no. 1, pp. 93–97, 2011.

[199] H. Zhou, Y. Qu, T. Zeid, and X. Duan, "Towards highly efficient photocatalysts using semiconductor nanoarchitectures," *Energy Environ. Sci.*, vol. 5, no. 5, pp. 6732–6743, 2012.

[200] X. Gan, X. Li, X. Gao, J. Qiu, and F. Zhuge, "TiO $_2$ nanorod arrays functionalized with In $_2$ S $_3$ shell layer by a low-cost route for solar energy conversion," *Nanotechnology*, vol. 22, no. 30, p. 305601, Jul. 2011.

[201] M. Guo, P. Diao, X. Wang, and S. Cai, "The effect of hydrothermal growth temperature on preparation and photoelectrochemical performance of ZnO nanorod array films," *J. Solid State Chem.*, vol. 178, no. 10, pp. 3210–3215, 2005.

[202] S. Khanchandani, S. Kundu, A. Patra, and A. K. Ganguli, "Band Gap Tuning of ZnO/In2S3 Core/Shell Nanorod Arrays for Enhanced Visible-Light-Driven Photocatalysis," *J. Phys. Chem. C*, vol. 117, no. 11, pp. 5558–5567, Mar. 2013.

[203] C. Wang, C. Shao, X. Zhang, and Y. Liu, "SnO2 nanostructures-tio2 nanofibers heterostructures: Controlled fabrication and high photocatalytic properties," *Inorg. Chem.*, vol. 48, no. 15, pp. 7261–7268, 2009.

[204] S. Wu, H. Cao, S. Yin, X. Liu, and X. Zhang, "Amino acid-assisted hydrothermal synthesis and photocatalysis of SnO 2 nanocrystals," *J. Phys. Chem. C*, vol. 113, no. 41, pp. 17893–17898, 2009.

[205] Q. Kuang, C. Lao, Z. L. Wang, Z. Xie, and L. Zheng, "High-Sensitivity Humidity Sensor Based on a Single SnO $_2$ Nanowire," *J. Am. Chem. Soc.*, vol. 129, no. 19, pp. 6070–6071, 2007.

[206] C. Wang, Y. Zhou, M. Ge, X. Xu, Z. Zhang, and J. Z. Jiang, "Large-Scale Synthesis of SnO $_2$ Nanosheets with High Lithium Storage Capacity," *J. Am. Chem. Soc.*, vol. 132, no. 1, pp. 46–47, 2010.

[207] M. Law, H. Kind, B. Messer, F. Kim, and P. Yang, "Photochemical Sensing of NO_2 with SnO_2 Nanoribbon Nanosensors at Room Temperature," *Angew. Chemie Int. Ed.*, vol. 41, no. 13, pp. 2405–2408, 2002.

[208] Z. Zhang *et al.*, "Electrospun Nanofibers of ZnO−SnO2 Heterojunction with High Photocatalytic Activity," *J. Phys. Chem. C*, vol. 114, no. 17, pp. 7920–7925, May 2010.

[209] H. Xia, H. Zhuang, T. Zhang, and D. Xiao, "Visible-light-activated nanocomposite photocatalyst of Fe2O3/SnO2," *Mater. Lett.*, vol. 62, no. 6–7, pp. 1126–1128, Mar. 2008.

[210] N. Hayashi *et al.*, "Microscopic studies of a SnO2/α-Fe2O3architectural nanocomposite using Mössbauer spectroscopic and magnetic measurements," *J. Solid State Chem.*, vol. 181, no. 12, pp. 3283–3286, 2008.

[211] M. Rumyantseva *et al.*, "Nanocomposites SnO2/Fe2O3: Sensor and catalytic properties," *Sensors Actuators, B Chem.*, vol. 118, no. 1–2, pp. 208–214, 2006.

[212] Y.-J. Chen, C.-L. Zhu, L.-J. Wang, P. Gao, M.-S. Cao, and X.-L. Shi, "Synthesis and enhanced ethanol sensing characteristics of α-Fe $_2$ O $_3$ / SnO $_2$ core–shell nanorods," *Nanotechnology*, vol. 20, no. 4, p. 45502, Jan. 2009.

[213] J. Kang, Q. Kuang, Z. X. Xie, and L. S. Zheng, "Fabrication of the SnO2/α-Fe2O3 hierarchical heterostructure and its enhanced photocatalytic property," *J. Phys. Chem. C*, vol. 115, no. 16, pp. 7874–7879, 2011.

[214] N. Takeda and B. A. Parkinson, "Adsorption morphology, light absorption, and sensitization yields for squaraine dyes on SnS2 surfaces," *J. Am. Chem. Soc.*, vol. 125, no. 18, pp. 5559–5571, 2003.

[215] Y. C. Zhang, Z. N. Du, S. Y. Li, and M. Zhang, "Novel synthesis and high visible light photocatalytic activity of SnS2 nanoflakes from SnCl2·2H2O and S powders," *Appl. Catal. B Environ.*, vol. 95, no. 1–2, pp. 153–159, Mar. 2010.

[216] C. Yang, W. Wang, Z. Shan, and F. Huang, "Preparation and photocatalytic activity of high-efficiency visible-light-responsive photocatalyst SnSx/TiO2," *J. Solid State Chem.*, vol. 182, no. 4, pp. 807–812, Apr. 2009.

[217] Y. C. Zhang, Z. N. Du, K. W. Li, M. Zhang, and D. D. Dionysiou, "High-performance visible-light-driven SnS2/SnO2nanocomposite photocatalyst prepared via in situ hydrothermal oxidation of SnS2nanoparticles," *ACS Appl. Mater. Interfaces*, vol. 3, no. 5, pp. 1528–1537, 2011.

[218] D. Beydoun, R. Amal, G. K.-C. Low, and S. McEvoy, "Novel Photocatalyst: Titania-Coated Magnetite. Activity and Photodissolution," *J. Phys. Chem. B*, vol. 104, no. 18, pp. 4387–4396, 2000.

[219] S. Watson, J. Scott, D. Beydoun, and R. Amal, "Studies on the preparation of magnetic photocatalysts," *J. Nanoparticle Res.*, vol. 7, no. 6, pp. 691–705, 2005.

[220] S. Xu, W. Shangguan, J. Yuan, J. Shi, and M. Chen, "Preparations and photocatalytic degradation of methyl orange in water on magnetically separable Bi12TiO20 supported on nickel ferrite," *Sci. Technol. Adv. Mater.*, vol. 8, no. 1–2, pp. 40–46, 2007.

[221] L. Zhang, W. Wang, L. Zhou, M. Shang, and S. Sun, "Fe3O4coupled BiOCl: A highly efficient magnetic photocatalyst," *Appl. Catal. B Environ.*, vol. 90, no. 3–4, pp. 458–462, 2009.

[222] X. Shen, L. Zhu, G. Liu, H. Yu, and H. Tang, "Enhanced Photocatalytic Degradation and Selective Removal of Nitrophenols by Using Surface Molecular Imprinted Titania," *Environ. Sci. Technol.*, vol. 42, no. 5, pp. 1687–1692, 2008.

[223] L. Keith and W. Telliard, "ES&T Special Report: Priority pollutants: I-a perspective view," *Environ. Sci. Technol.*, vol. 13, no. 4, pp. 416–423, 1979.

[224] X. Shen, L. Zhu, J. Li, and H. Tang, "Synthesis of molecular imprinted polymer coated photocatalysts with high selectivity," *Chem. Commun.*, no. 11, pp. 1163–1165, 2007.

[225] Y. J. Hsu, S. Y. Lu, and Y. F. Lin, "One-step preparation of coaxial CdS-ZnS and Cd1-xZnxS-ZnS nanowires," *Adv. Funct. Mater.*, vol. 15, no. 8, pp. 1350–1357, 2005.

[226] Y. Hsu and S. Lu, "One-step preparation of coaxial CdS – ZnS nanowires {," *Society*, no. July, pp. 2102–2103, 2004.

[227] M. R. Kim, Y. M. Kang, and D. J. Jang, "Synthesis and characterization of highly luminescent CdS@ZnS core-shell nanorods," *J. Phys. Chem. C*, vol. 111, no. 50, pp. 18507–18511, 2007.

[228] A. Datta, S. K. Panda, and S. Chaudhuri, "Synthesis and optical and electrical properties of CdS/ZnS core/shell nanorods," *J. Phys. Chem. C*, vol. 111, no. 46, pp. 17260–17264, 2007.

[229] L. Wang, H. Wei, Y. Fan, X. Liu, and J. Zhan, "Synthesis, Optical Properties, and Photocatalytic Activity

of One-Dimensional CdS@ZnS Core-Shell Nanocomposites," *Nanoscale Res. Lett.*, vol. 4, no. 6, pp. 558–564, 2009.

[230] Y. Takahara, J. N. Kondo, T. Takata, D. Lu, and K. Domen, "Mesoporous tantalum oxide. 1. Characterization and photocatalytic activity for the overall water decomposition," *Chem. Mater.*, vol. 13, no. 4, pp. 1194–1199, 2001.

[231] J. H. Pan and W. I. Lee, "Preparation of highly ordered cubic mesoporous WO3/TiO 2 films and their photocatalytic properties," *Chem. Mater.*, vol. 18, no. 3, pp. 847–853, 2006.

[232] F. E. Osterloh, "Inorganic Materials as Catalysts for Photoelectrochemical Splitting of Water," *Chem. Mater.*, vol. 20, p. 35, 2008.

[233] L. Xu, J. Guan, L. Gao, and Z. Sun, "Preparation of heterostructured mesoporous In2O3/Ta2O5 nanocomposites with enhanced photocatalytic activity for hydrogen evolution," *Catal. Commun.*, vol. 12, no. 6, pp. 548–552, Feb. 2011.

[234] L. Xu, J. Guan, W. Shi, and L. Liu, "Heterostructured mesoporous In2O3/Ta2O5composite photocatalysts for hydrogen evolution: Impacts of In2O3content and calcination temperature," *J. Colloid Interface Sci.*, vol. 377, no. 1, pp. 160–168, 2012.

[235] L.-N. He, R. D. Rogers, D. Su, P. Tundo, and Z. Conrad Zhang, *Green Chemistry and Sustainable Technology*. 2014.

[236] M. Bouchy and O. Zahraa, "Photocatalytic reactors," *Int. J. Photoenergy*, vol. 5, no. 3, pp. 191–197, 2003.

[237] A. E. Cassano, C. A. Martin, R. J. Brandi, and O. M. Alfano, "Photoreactor Analysis and Design: Fundamentals and Applications," *Ind. Eng. Chem. Res.*, vol. 34, no. 7, pp. 2155–2201, 1995.

[238] D. Arney, C. Hardy, B. Greve, and P. A. Maggard, "Flux synthesis of AgNbO3: Effect of particle surfaces and sizes on photocatalytic activity," *J. Photochem. Photobiol. A Chem.*, vol. 214, no. 1, pp. 54–60, 2010.

[239] R. Priya and S. Kanmani, "Batch slurry photocatalytic reactors for the generation of hydrogen from sulfide and sulfite waste streams under solar irradiation," *Sol. Energy*, vol. 83, no. 10, pp. 1802–1805, 2009.

[240] A. Ajmal, I. Majeed, R. N. Malik, H. Idriss, and M. A. Nadeem, "Principles and mechanisms of photocatalytic dye degradation on TiO $_2$ based photocatalysts: a comparative overview," *RSC Adv.*, vol. 4, no. 70, pp. 37003–37026, 2014.

[241] M. Lazar, S. Varghese, and S. Nair, "Photocatalytic Water Treatment by Titanium Dioxide: Recent Updates," *Catalysts*, vol. 2, no. 4, pp. 572–601, 2012.

[242] C. McCullagh, P. K. J. Robertson, M. Adams, P. M. Pollard, and A. Mohammed, "Development of a slurry continuous flow reactor for photocatalytic treatment of industrial waste water," *J. Photochem. Photobiol. A Chem.*, vol. 211, no. 1, pp. 42–46, 2010.

[243] M. A. Behnajady, N. Modirshahla, N. Daneshvar, and M. Rabbani, "Photocatalytic degradation of an azo dye in a tubular continuous-flow photoreactor with immobilized TiO2on glass plates," *Chem. Eng. J.*, vol. 127, no. 1–3, pp. 167–176, 2007.

[244] D. Li *et al.*, "A novel double-cylindrical-shell photoreactor immobilized with monolayer TiO2-coated silica gel beads for photocatalytic degradation of Rhodamine B and Methyl Orange in aqueous solution," *Sep. Purif. Technol.*, vol. 123, pp. 130–138, 2014.

[245] X. gang Hao, H. hui Li, Z. lin Zhang, C. mai Fan, S. bin Liu, and Y. ping Sun, "Modeling and experimentation of a novel labyrinth bubble photoreactor for degradation of organic pollutant," *Chem. Eng. Res. Des.*, vol. 87, no. 12, pp. 1604–1611, 2009.

[246] Y. Su, N. J. W. Straathof, V. Hessel, and T. Noël, "Photochemical transformations accelerated in

continuous-flow reactors: Basic concepts and applications," *Chem. - A Eur. J.*, vol. 20, no. 34, pp. 10562–10589, 2014.

[247] T. Van Gerven, G. Mul, J. Moulijn, and A. Stankiewicz, "A review of intensification of photocatalytic processes," *Chem. Eng. Process. Process Intensif.*, vol. 46, no. 9 SPEC. ISS., pp. 781–789, 2007.

[248] K. S. Elvira, X. C. i Solvas, R. C. R. Wootton, and A. J. deMello, "The past, present and potential for microfluidic reactor technology in chemical synthesis," *Nat. Chem.*, vol. 5, p. 905, Oct. 2013.

[249] R. Rakhshaee and J. Darvazeh, "Studying role of air bubbles on suspension of hematite particles with three size ranges in plug flow reactor to improve dyes photo degradation compared to conventional packed bed photo reactors," *J. Hazard. Mater.*, vol. 356, no. January, pp. 61–72, 2018.

Chapter 2

Continuous synthesis of GaN nano-photocatalysts in supercritical millireactors

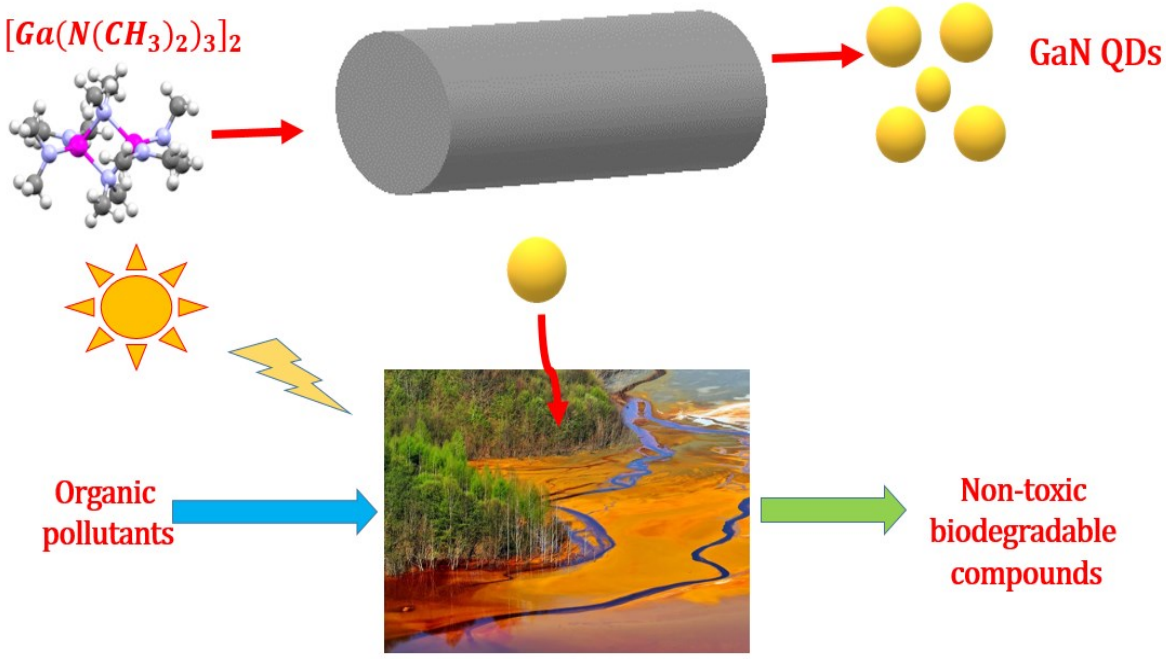

Contents

2. Continuous synthesis of GaN nano-photocatalysts in supercritical millireactors 105

2.1. Gallium Nitride 109
2.1.1. Introduction 109
2.1.2. Properties and applications of GaN 110
2.1.3. Implementation of GaN in photon-conversion processes 112
2.1.4. Synthetic methodologies for GaN nanomaterials 113
2.1.5. Conclusion 116

2.2. Continuous synthesis of GaN QDs at supercritical conditions 117
2.2.1. Continuous synthesis of nanomaterials in supercritical fluids 117
2.2.2. Single source precursor introduction and its chemistry for obtaining GaN QDs 119

2.3. Continuous supercritical synthesis of GaN QDs using a co-flow configuration 122
2.3.1. Introduction 122

2.4. Simulation studies concerning the supercritical millireactor for GaN QDs production. 129

2.5. Supercritical synthesis through a pre-heater setup 134
2.5.1. Introduction 134
2.5.2. Characterization of GaN QDs obtained from pre-heater supercritical millireactor 136
2.5.3. Conclusion 147

2.6. Application of GaN in heterogeneous photocatalysis 148
2.6.1. Introduction 148
2.6.2. Heterogeneous photocatalysis for the degradation of pollutants (organic dye) 148
2.6.3. Direct photocatalytic degradation of Methyl Orange using GaN QDS 150
2.6.4. Conclusion of the photocatalytic study 157

2.7. Conclusion 159

2.1. Gallium Nitride

2.1.1.Introduction

Gallium Nitride (GaN) is a direct, binary, wide band gap semiconductor of group III-V compounds. The three polymorphs of GaN are: (i) the wurtzite structure with a hexagonal symmetry, (ii) the zinc blende structure with a cubic symmetry and (iii) the rocksalt structure with a cubic symmetry.

GaN crystallizes often in the wurtzite-hexagonal phase (α-GaN) and it is the thermodynamically most stable phase with a band energy gap of 3.39 eV [1] and the corresponding crystal structure of this stable phase is depicted in Figure 2.1 [2]. The crystallization of GaN in zinc blende-cubic phase (β-GaN) is rarely noticed especially in GaN film synthesis process with a band gap of 3.2 eV [3, 4]. The rocksalt-cubic phase was observed only at ultra-high pressure conditions (> 37 GPa) [5].

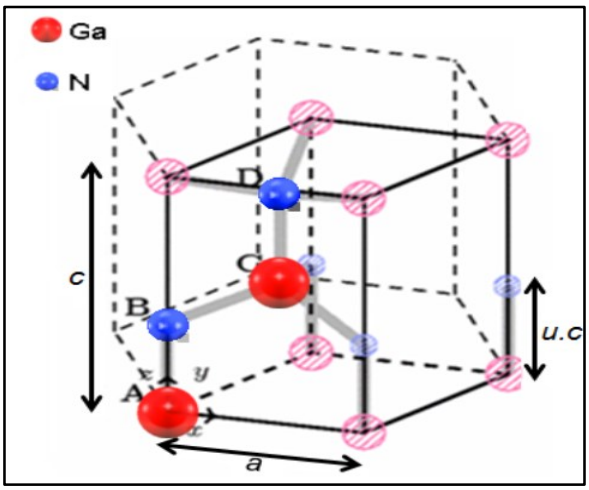

Figure 2.1. *Wurtzite crystal structure of GaN with hexagonal symmetry [2].*

On releasing the pressure GaN returned back completely to wurtzite phase from rocksalt phase structure [5]. Finally, among these three polymorphs the wurtzite-hexagonal GaN is the most stable form and crystallizes often at ambient conditions, whereas zinc-blende and rocksalt with cubic symmetry are metastable phases. The rocksalt GaN is a fascinating metastable phase, which possesses ionic bonding between gallium and nitrogen, while the wurtzite and zinc blende possess both covalent and ionic bonding between its constituent elements, with more prominence for covalent bonding [6]. The co-existence of these three crystallite phases was observed in GaN materials synthesized through wet chemical synthetic methods (benzene thermal process) [7]

2.1.2. Properties and applications of GaN

GaN being one of the third generation semiconductor, it has been widely applied in many fields. The areas of the GaN applications are primarily focused and even commercialized in the electronic, optoelectronic and sensor fields. These devices, which have used GaN as their integral component, have primarily targeted in implementing GaN wurtzite and GaN zinc blende material for devices, which require GaN in film form [8]. The applications mentioned here are only based on these two crystallized forms of GaN. The key properties which enable the application of GaN crystals in various devices are mentioned below along with their corresponding devices (notable properties are also indicated in Table 2.1). GaN has excellent electron transport properties due to the large saturated electron drift velocity of the GaN wurtzite phase [9] and the zinc blende cubic phase possess higher drift velocity than the wurtzite phase [10]. These GaN crystals exhibit remarkable differences in their electron and phonon dispersions, ultimately leading to different drift velocity values.

GaN is intrinsically a n-type semiconductor. P-type GaN is achieved initially only by magnesium (Mg) doping through low-energy electron beam irradiation (LEEBI) treatment [11]. Several other techniques like metal organic chemical vapour deposition (MOCVD), molecular beam epitaxy (MBE) and reactive molecular beam epitaxy have been developed for attaining p-type Mg doped GaN [12]. Even though such p-type GaN are obtained, achieving enhanced high p-type conductivity in GaN or in other group III nitrides are extremely difficult due to 'unipolar' or 'asymmetric' doping problem. The reasons for such doping problems are due to: (i) low dopant solubility, (ii) hydrogen passivation, (iii) low valence band maximum of GaN and (iv) high defect ionization energies [13 – 15]. Among these issues, the problems associated with the low solubility and the hydrogen passivation are solved by non-equilibrium semiconductor growth environment and high annealing treatment of the sample. Nevertheless, the fundamental problem associated with increasing the activation energy of p-type doped GaN is still unsolved. This is particularly attributed to the VB nature of GaN semiconductor. The VB consists of nitrogen (N) 2p orbitals, which are strongly electronegative and have a deep 2p atomic orbital. This results in a relatively deep acceptor energy, which cannot be activated by thermal activation mode. So far, Mg stands to be an ideal and only promising material for achieving p-type GaN [12]. Currently, the scientific world is using several strategies to solve the various issues associated with p-type semiconductor fabrication of GaN (like increment of VB maximum through co-doping, etc.) and other group III nitrides [16].

The enhanced electron transport property due to superior drift velocity, high dielectric breakdown field, strong atomic bonding between gallium and nitrogen (covalent bond), high melting point, inherent exalted chemical and mechanical stability of GaN, has rendered the implementation of the GaN in fabrication of high power & temperature electronic devices like high electron mobility transistor (HEMT) [18, 19]. Besides GaN is rigid, exhibits chemical inertness in both acidic and basic environments and prolonged stability at high temperature. Thanks to these attributes, the nano structural GaN based transistors have been successfully fabricated in sensor devices applied to biological fields for detecting pH, chloride ion, glucose, specific biomarkers (abnormal enzymes, low molecular weight proteins or antigens) in liquid (blood, saliva or urine) gas samples (exhaled air) and solid (tissues) samples analysed [20, 21].

Gas & liquid sensors fabricated using GaN nano-thick/thin films or nanoparticles have been successfully realized in industrial, lab or commercial areas for sensing combustible gases, volatile organic compounds, ammonia, hydrogen sulfide, ethanol and water molecules [22 – 28].

Table 2.1. *Thermal and electrical properties of GaN wurtzite and zinc blende crystal structures*.

Electrical and Thermal properties	GaN Wurtzite (WZ)	GaN Zinc Blende (ZB)	Reference
Band gap (eV)	**3.39**	**3.2**	[28]
Breakdown field (V cm^{-1})	$\sim 5 * 10^6$	$\sim 5 * 10^6$	[28]
Mobility of electrons (V^{-1} cm^2 s^{-1})	≤ 1000	≤ 1000	[28]
Mobility of holes (V^{-1} cm^2 s^{-1})	≤ 200	≤ 350	[28]
Electron thermal velocity (m s^{-1})	$2.6 * 10^5$	$3.2 * 10^5$	[28]
Hole thermal velocity (m s^{-1})	$9.4 * 10^4$	$9.5 * 10^4$	[28]
Melting point (°C)	**2500**	**2500**	[28]
Thermal conductivity (W cm^{-1} $°C^{-1}$)	**1.3**	**1.3**	[28]

The direct large energy band gap of GaN, the ability to precisely engineer the direct optical gap of solid solutions of GaN, formed in conjunction with other group III nitrides (InN (1.95 eV) and AlN (6.28 eV)) [29] has driven the realization of commercial optoelectronic devices based on GaN. These optoelectronic devices are: (i) UV, blue and green Light Emitting Diodes (LEDs), (ii) Laser Diodes (LDs) (violet LDs), (iii) photodetectors and (iv) active luminescent layer in Field Emission Displays (FEDs) [24, 29 – 37]. These devices have been commercialized. Currently, various nanostructures of GaN realized successfully in these devices were: single crystalline GaN nanowires and nanotubes used as propitious materials for LEDs and UV nanolasers [35, 38 – 41]. Besides high power electronic & optoelectronic devices mentioned above, the essential supplementary devices based on GaN are high resolution printers, high density CD ROM storage systems, acoustic-optic & piezo-electric modulators and high temperature piezo/pyro-electronic sensors [8, 42]

2.1.3.Implementation of GaN in photon-conversion processes

GaN with appropriate band gap potentials was first employed in photon to chemical energy conversion process for the production of hydrogen from water splitting reactions through photoelectrochemical cells. The insolubility of GaN in various alkalis and acids at ambient temperature conditions, resistance to corrosion even in aqueous solution, coupled with its other beneficial properties (rigidness, thermal stability or electrical properties) were the real motivation for the exploration of GaN in photon conversion process [43]. The study of GaN in photoelectrochemical cells for hydrogen generation was started only in 2005 after the successful realization of the heterogeneous photocatalytic water splitting using GaN photocatalysts [44 – 46]. Currently, GaN nanowires were successfully used in these photoelectrochemical cells with a maximum incident photon to current conversion efficiency of about 15-18% [47].

The exploration of GaN and also other group III nitrides in heterogeneous photocatalytic fields still lies in the dormant phase. The so far reported heterogeneous photocatalysis using GaN semiconductor has not even attained a minor fraction of the extent to which titanium dioxide (TiO_2)-based photocatalytic systems have been exploited for various photochemistries in the past several decades [48]. GaN semiconductor heterogeneous photocatalysis studies have focused only on the conventional photocatalysis (indirect photochemical excitation or sensitized photoreaction). Within this conventional photocatalytic system, GaN-based nanocomposite systems (p-type GaN/InGaN heterostructures with nanowire morphology) were employed for photocatalytic hydrogen production from water splitting under visible light irradiation [49]. Both hydrogen production from water splitting and CO_2 reduction were successfully achieved with noble metal loaded GaN nanowires under UV irradiation [50]. GaN nanowires, GaN thin films or sub-micron dot arrays were investigated for Orange II dye degradation under UV irradiation [51]. Nanocomposites of GaN semiconductor were even used for degrading organic pollutant, Cresol Red (CR) [52].

So far, no study has been carried out on GaN semiconductor for photochemical reaction involving catalyzed photoreaction (direct photochemical excitation). This chapter focuses on carrying out this particular catalyzed photoreaction for the degradation of organic pollutants. GaN was opted, as a predominant photocatalyst in this doctoral research due to its highly beneficial features like: (i) chemical stability in both acidic and alkaline conditions, (ii) thermal stability and its innate ability to dissipate large amount of heat, (iii) availability of redox potentials for carrying out multitude of reactions (degradation of organic pollutant, water splitting or CO_2 reduction) and (iv) ability to precisely engineer its band gap to render it active in the visible region through solid solution formation [50]. A schematic depiction of GaN's band edge potential vs NHE and complete optical range from UV to visible, which can be successfully achieved through solid solution with indium nitride (InN) as shown in Figure 2.2.

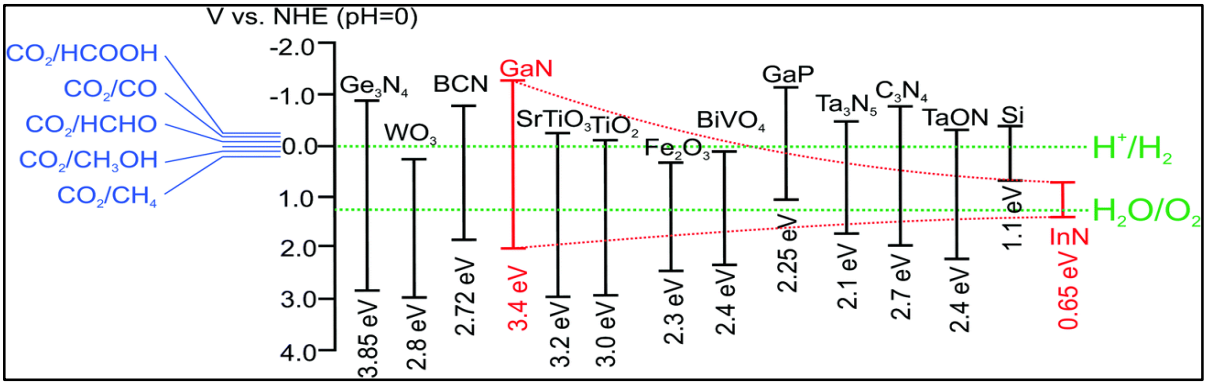

Figure 2.2. *A Schematic depiction displaying the band edge potentials of GaN and the absolute optical range from UV to visible, which can be achieved through solid solution formation between GaN and InN [53].*

2.1.4. Synthetic methodologies for GaN nanomaterials

The wide spectrum of applications involving the GaN semiconductor was realized through materials in the nano-size domain, where the small size (nano) occurs in either one or two or three dimensions. These low dimensional nanomaterials are nanowires, nanotubes, nanorods, nanobelts and nanocrystals/nanoparticles, etc. Among them nanoparticles with size less than the Bohr exciton radius (2.5 nm [54] or 2.8 nm [55, 56]) are interesting due to the quantum confinement effects. Indeed, these nanoparticles exhibit size dependent quantization effect, where electrons and holes are confined in three dimensions. This leads to a discretization of band gaps. Nanoparticles exhibiting the above quantization effects are also called quantum dots (QDs). Apart from these highly fascinating nanomaterials, whose properties are different from the bulk materials, certain applications employing GaN semiconductor are also realized through GaN in thin film. So far, in the scientific domain for GaN (third generation semiconductor) several synthetic methodologies have been reported for attaining the above mentioned unique morphologies with well-defined requisite properties for the particular applications in which they are implemented. The most notable or the key important synthetic methodologies for each of these particular GaN morphologies are listed here:

1. *GaN thin films* were synthesized through Metal Organic Chemical Vapour Deposition (MOCVD) [57], low cost electrochemical deposition technique [58] and Ammonobasic Reactive Sublimation (ARS) method [59],

2. *GaN nanorods* were successfully attained through Chemical Vapour Deposition (CVD) [60], Reactive Molecular Beam Epitaxy (RMBE) [61], carbon nanotube confined reaction between gallium oxide vapour and ammonia gas [62] and through pyrolyzing the mixture of tris(dimethyl amido)-gallium(III) and ferrocene under ammonia atomsphere [63],

3. *GaN nanotubes* were obtained through gold (Au) catalyzed-MOCVD technique [64] and halide vapour phase epitaxy (HVPE) [65],

4. *GaN nanobelts* were accomplished through catalysts (nickel (Ni) and boron trioxide (B_2O_3)) assisted CVD reaction between a mixture of gallium (Ga), gallium(III) oxide (Ga_2O_3) and ammonia [66]. Also through non-catalytically and continuous two step thermal ammoniation technique [67],

5. *GaN nanowires* were grown on catalysts free substrates through thermal chemical vapour deposition (TCVD) route [68] and also through catalysts free physical vapour deposition route (PVD) method [69],

6. *GaN nanocrystals* were prepared by the calcination of gallium(III) nitrate ($Ga(NO_3)_3$) powder in a continuous flow ammonia with a temperature range of 500 - 1050°C [70]. Similarly, GaN nanocrystals were prepared through a two-step combustion process consisting of (i) hydrothermal process for the conversion of Ga_2O_3 to $Ga(NO_3)_3$, followed by subsequent (ii) calcination (950 - 1050°C) route under ammonia atomsphere [71]. Analogously, the synthesis of GaN nanocrystals at room temperature was successfully attained through sol-gel process [72] and also by metathesis reaction between gallium halide and lithium nitride in the presence of diethyl ether [73],

7. *GaN QDs* were synthesized recently by Dimos *et al.* through pyrolysis of tris(dimethylamido)-gallium(III) (single source) precursor under continuous flow ammonia in ordered silica mesoporous silica (MCM-41) host matrix at 365°C for 4 hours [74]. Just a couple of year back, our research group successfully attempted the thermos/ammonolysis of single source precursor (tris (dimethyl amido)-gallium(III)) in continuous flow tubular reactor in supercritical cyclohexane conditions and also in supercritical ammonia-hexane mixture. This setup resulted in the production of GaN QDs with 22 s residence time [75].

Generally, nanostructured photocatalysts are highly preferred in heterogeneous photocatalysis process due to their high surface to volume ratio. Since the redox reactions happen on the surface of the photocatalysts, the surface to volume ratio is a crucial factor for determining the photocatalytic activity in that process. Among the diverse nanostructured materials (mentioned above), QDs have attracted lot of interest in the heterogeneous photocatalytic field due to their *enhanced surface to volume ratio and quantum confinement effect* in three dimensions. The various beneficial features of QDs offer for heterogeneous photocatalysis are [76]:

1. The physical dimensions of nanomaterials provide more surface area for reactant adsorption and ultimately resulting in enhanced photocatalytic activity,

2. As the particle size goes below the Bohr exciton radius, a strong quantum confinement occurs resulting in materials possessing different optical and electronic (mostly enhanced) properties than their bulk counterparts,

3. In heterogeneous photocatalysis, for QDs photocatalysts, *the transportation length of electrons or holes* from the inner bulk of the particle to the surface reaction site is short. As a result of which, *the migration rate of electrons or holes is higher, ending up in providing higher photocatalytic activity* than their corresponding bulk counterparts,

4. Due to their small size, a precise tuning of surface chemistry of the QDs can be easily performed. Currently synthetic methodologies are available for precise shell growth on QD's surface leading to core/shell hetero-nanocomposite photocatalysts or solid solution photocatalysts depending on the materials chosen for shell growth.

Due to these advantageous properties, GaN QDs were opted in this research work. Additionally, this particular chapter focuses on catalyzed photoreaction (direct photochemical excitation) involving degradation of toxic organic pollutants (dye molecules). QDs are interesting materials for such applications for the following reasons:

- In the catalyzed photoreaction process, where the dye molecules are excited and electrons are injected into the semiconductor materials, band bending phenomenon is taking place at the interface between the QDs and the dye molecule. This interface plays a critical role in influencing the charge or energy transfer between the excited dye molecule and the semiconductor surface, eventually influencing the photocatalytic activity,

- In case of n-type semiconductor, upward band bending occurs and the electrons from the LUMO of the dye molecule is transferred easily into the semiconductor and migrate immediately towards to the inner bulk of the semiconductor, as depicted in Figure 2.3-a.

- Oppositely, in case of p-type semiconductor, which results in downward band bending, the electric fields prevent the migration of the electron into the bulk of semiconductor due to the opposite electric field and make the electrons to accumulate on the surface of the semiconductor, as depicted in Figure 2.3-b. These accumulated electrons recombine with the HOMO of the dye molecules ultimately resulting in the quenching of the excitation process, resulting in very low photocatalytic activity.

In our case, I am targeting the synthesis of GaN QDs, which is intrinsically a n-type semiconductor. Thus, such system successfully achieves the first condition of facile migration of electrons from the excited dye to the semiconductor surface.

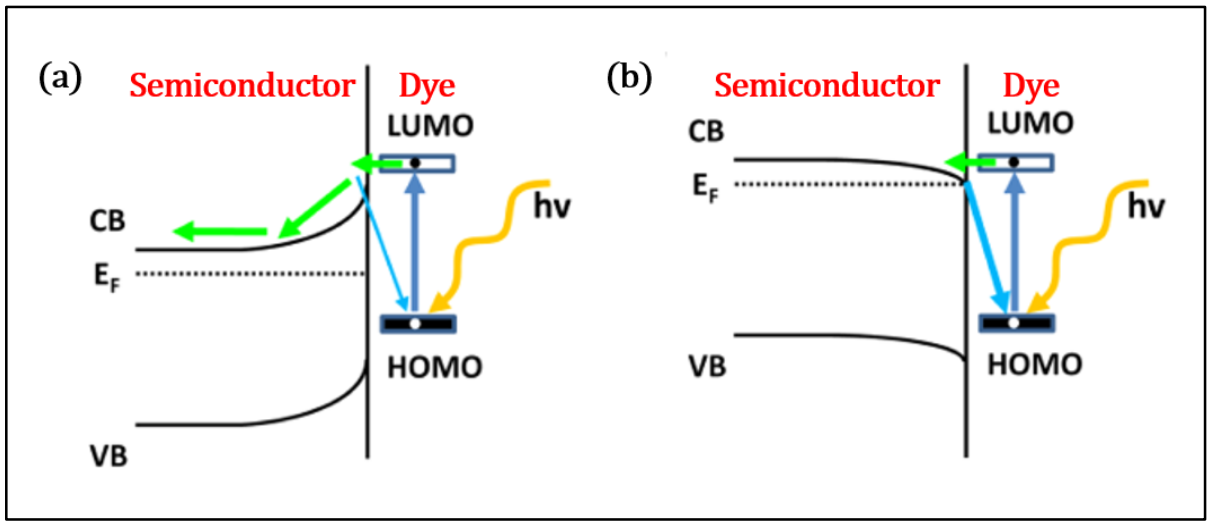

Figure 2.3. *a. A schematic depiction of band bending at semiconductor-molecule (dye) interface in direct photochemical excitation system for n-type semiconductor with upward band bending; b. p-type semiconductor with downward band bending [77].*

2.1.5. Conclusion

To conclude, GaN QDs will be employed in this study for degradation of the organic pollutants in heterogeneous photocatalytic study through the direct photochemical excitation process. To perform such a photocatalytic study, the synthesis of GaN QDs will be carried out with a continuous supercritical tubular millireactor through the thermolysis of a single source tris(dimethylamido)-gallium(III) precursor. The more specific details about this single source precursor chemistry and the reasons for opting the supercritical medium for this continuous synthesis strategy will be described in the upcoming sections of this chapter.

Regarding the synthesis of GaN QDs, a new supercritical reactor system (pre-heater) was developed for achieving the stable, high yield continuous production of GaN QDs.

The last section of the chapter will focus on the heterogeneous photocatalysis for the degradation of organic pollutant (azo dye) under visible light activity. I will also detail some reasoning for the better performance of our GaN QDs compared to the commercially available Degussa P25, TiO_2 photocatalytic nanomaterials.

2.2. Continuous synthesis of GaN QDs at supercritical conditions

2.2.1. Continuous synthesis of nanomaterials in supercritical fluids

Within the realm of bottom up methodology, Supercritical Fluids (SCFs) medium have been successfully implemented as reactive media for synthesizing various nanomaterials, especially semiconductors.

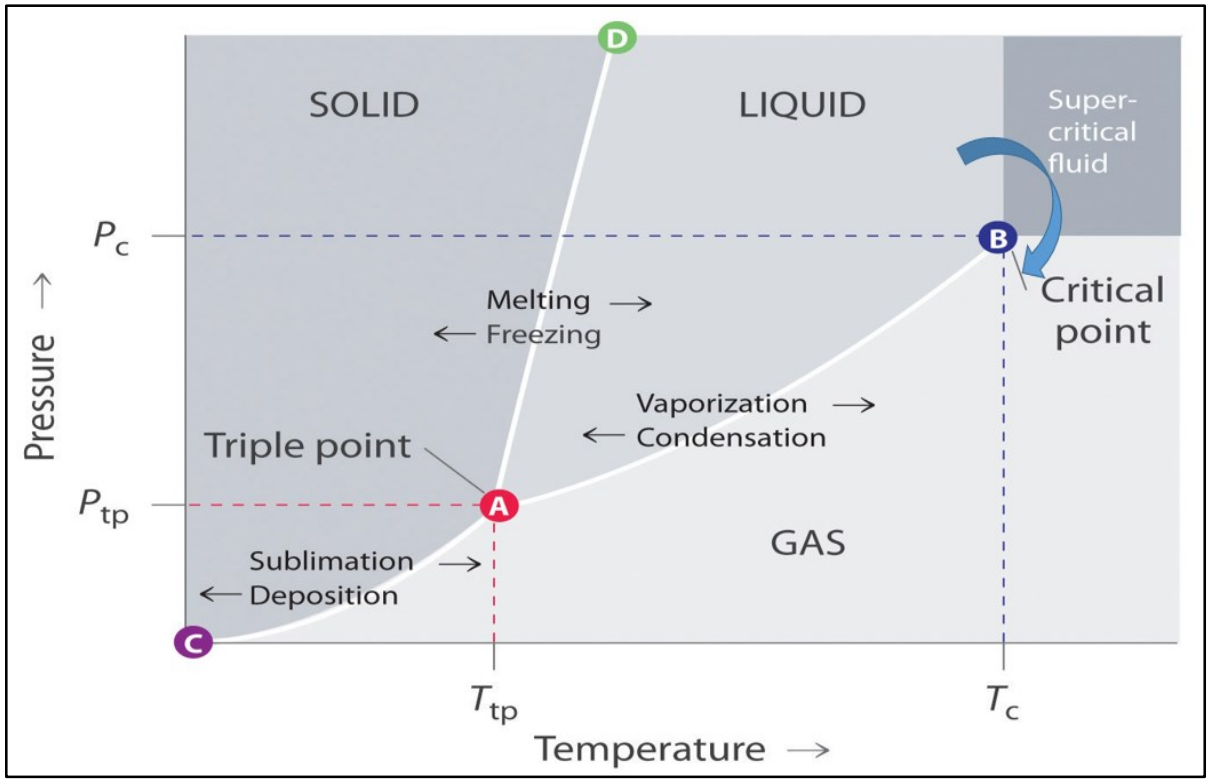

Figure 2.4. *Schematic depiction of a phase diagram (pressure vs temperature) for a substance, exhibiting three phases-solid, liquid and gas, importantly a supercritical region. The line connecting the points A and C is the vapour pressure curve of solid phase, line between A and B represents the vapour pressure curve of the liquid phase. Line between A and D represents the equilibrium existing between the solid and liquid phase. All these three equilibrium lines intersect at the triple point (A) (diagram redrawn based on the book [78]).*

SCFs was highly captivating for material scientist due to the facile control and tunability of the solvent properties along with their other interesting properties. A compound is termed as a 'supercritical' fluid, when it is used at a temperature and pressure higher than the critical temperature (T_c) and critical pressure (P_c) of that particular compound [79], which can be visualized in the schematic depcition in Figure 2.4. At the critical point, the density of both gas and liquid phases becomes equal, resulting in the disappearence of the gas-liquid interface. Microscopically at this region, the fluctuations of density occur at the scale of light wavelength (hundreds of nanometres) resulting in scattering the light (cloud point). This phenomenon is

called the critical opalescence [80]. Simultaneously, macroscopically at these critical conditions, the compressibility of the fluid tends to infinity.

The interesting aspect of the SCFs is their innate ability to shift from liquid to gas properties without intersecting the gas-liquid equilibrium curve, as depicted by the arrow in Figure 2.4, meaning without experiencing any phase transition. Thus, SCFs are hybrid media possessing physicochemical properties intermediate between liquids and gases. The SCFs exhibit liquid like density and the overall density of SCFs manifest in the range of 20 - 80% of their liquid density, furnishing them to be optimally dense as liquid solvents for dissolving various precursors for synthesizing nanomaterials. Simultaneously, SCFs exhibit gas-like viscosity behaviour, their overall viscosity of SCFs falls around 5 - 10% of their liquid state, which favors better mixing of the reactive precursors in the continuous phase and eliminates the mass transfer limitations typically of the liquid phase due to the increase of diffusion coefficient of molecules. Importantly, SCFs properties can be precisely controlled by variations of temperature and pressure. These reasons, along with other notable features, faster thermal and diffusion processes, higher reaction rate in time duration of short seconds to minutes, have made SCFs optimal media for nanomaterials production [80]. In my research work, the continuous production of GaN QDs is carried out in tubular millireactor, adopting SCFs reactive medium. They offer very narrow residence time distribution (RTD) compared to the conventional liquid phase continuous processes.

In Chemical Engineering sciences, many reactions are switched from batch to flow reactors. The rise of 'Flow Chemistry' in many domains of chemical reactions offers enhanced heat transfer, elevated mixing, higher reproducibility and the ability to work in secure environment even though intense pressure and temperature are needed [81 – 83]. In the paradigm shift of batch to flow reactors, regarding the nanomaterial synthesis, the important factors to be considered are: residence time, flow rate, Reynolds number, etc. In a monophasic flow at laminar conditions in a channel, fluid encounters a parabolic velocity profile. Specifying that the velocity of the fluid in contact with surface of the channel (walls) is zero and velocity is maximum for the fluid in the middle of channel. The dispersion effect is seen due to the non-constant velocity in the radial direction, leading to residence time distribution (RTD).

All materials nucleating and growing inside the flow channels will not spend the same time within reactor channels [84]. The RTD becomes narrower as the viscosity of the fluid is reduced. Hence, for synthesizing highly quantum confined semiconductors with high monodispersity in flow reactors, narrow RTDs is the prerequisite. Fluids with high diffusivity fulfil such conditions, enabling the flow device to yield high quality (monodisperse) nanomaterials. SCF are such fluid with high diffusivity and low viscosity as mentioned before satisfies the condition of obtaining narrow RTD. Since SCFs have very low viscosity, they provide very low pressure drop even at higher flow rates. Hence, coupling of flow reactors with SCFs offers material scientist an improved control of the synthetic parameters (temperature, pressure and residence time), leading to controlled synthesis of nanomaterials with narrow size distribution in a reproducible and scalable way. Based on the above mentioned advantages, I have selected continuous SCFs synthesis in this PhD study to synthesize nanophotocatalysts. The next section will detail the chemistry behind GaN synthesis from single source precursor.

2.2.2. Single source precursor introduction and its chemistry for obtaining GaN QDs

One of the main reason for the persistent focus of researchers on the group III nitrides is the availability of single source precursors in the form of amido compounds of gallium, indium and aluminium. Amido complexes exhibit substantial propensity to oligomerize through the formation of strong metal-nitrogen bridges. Regarding the GaN synthesis, there are several types of monoamides, diamides and triamides of gallium as single source precursors are available. Among the diverse complexes, homoleptic amido compound belonging to triamide class of gallium with the form $[M(NR_2)_3]$ are chosen in this research work [85, 86].

Tris(dimethylamido)-gallium(III) with molecular formula $C_{12}H_{36}Ga_2N_6$ or $[Ga(N(CH_3)_2)_3]_2$, was the homoleptic amido complex opted as precursor here. This homoleptic metal amido compound exhibits facile solution reactions and can generate GaN nanocrystalline materials depending on the synthetic protocol. The schematic 2D and 3D representation of this homoleptic amido complex compound is depicted in Figures 2.4-a and 2.4-b.

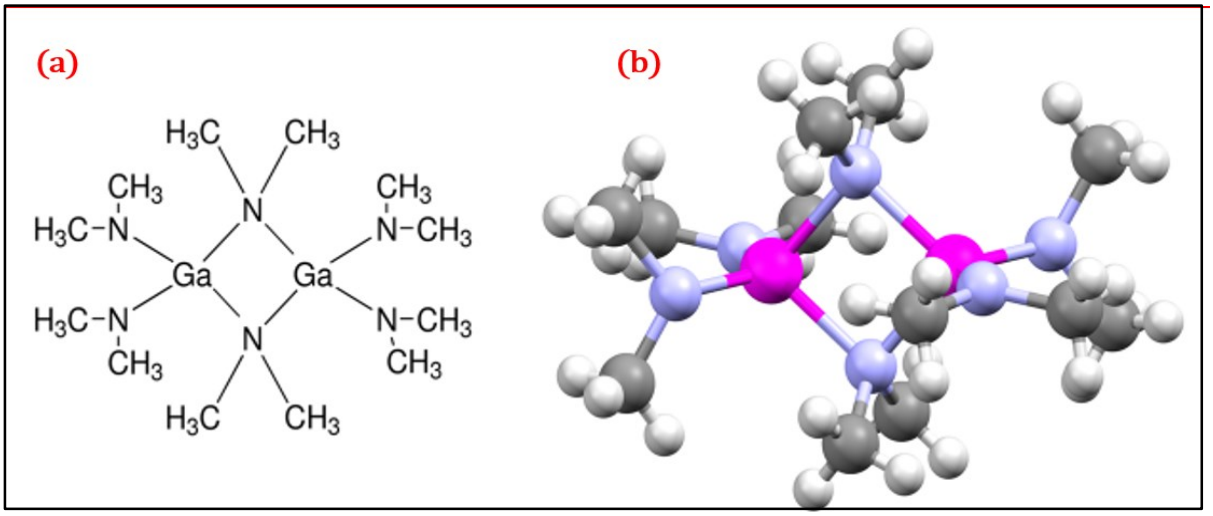

Figure 2.4. *a. Schematic depiction of* $[Ga(N(CH_3)_2)_3]_2$ *precursor [87]; b. Corresponding three dimensional structure of* $[Ga(N(CH_3)_2)_3]_2$ *, adapted and re-drawn from reference [88], where pink color balls represent the gallium atoms, violet for nitrogen, grey or light black for carbon and small whitish balls for hydrogen atoms, respectively.*

Homoleptic amido complexes are highly beneficial precursors for producing their corresponding nitride semiconductor materials. This feature stems from their ability to banish NH_3 molecules from their complexes through a stepwise deamination process at relatively low temperature. Several researchers in the past decades have successfully attempted the synthesis of GaN nanomaterials from $[Ga(N(CH_3)_2)_3]_2$ single source precursor in batch process, as summarized in Figure 2.5. In this pictorial representation the numbers within the blue circles represent the various reaction routes attempted on $[Ga(N(CH_3)_2)_3]_2$ precursor to clinch the requisite GaN nanocrystalline materials. These numbers are denoted on the increasing order of years in which they are reported because the process got simplified as the years progressed.

In 1996, Janik, Wells *et al.* proposed a methodology for synthesizing polymeric gallium imide $\{Ga(NH)_{3/2}\}_n$ by reacting the $[Ga(N(CH_3)_2)_3]_2$ with liquid or gaseous ammonia at room temperature. This technique is represented by the Scheme 1 in the Figure 2.5. The resultant polymeric imide can eliminate the NH_3 molecules through pyrolysis either in vacuum or NH_3 atmosphere resulting in GaN nanocrystalline materials with a mixture of cubic and hexagonal crystalline phases [89]. In 1997, they reported a similar strategy for GaN nanomaterials where they performed the pyrolysis of polymeric imide in the reflux of TMHD (N, N, N', N'-Tetramethyl 1,6-hexanediamine) at "low" temperature (210°C). The resultant GaN nanocrystalline material possessed the similar mixture of cubic and hexagonal phases but the photoluminescence (PL) was enhanced compared to GaN obtained from the previous route. This strategy of pyrolysis in amine medium under reflux is depicted in the Scheme 2 of Figure 2.5.

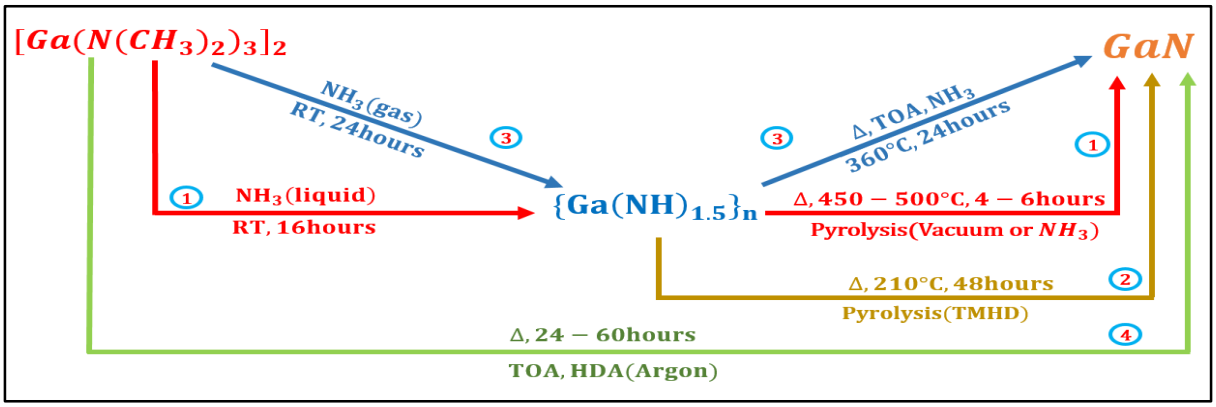

Figure 2.5. *Schematic summary of so far reported synthetic strategies utilizing* $[Ga(N(CH_3)_2)_3]_2$ *precursor for obtaining GaN nanomaterials.*

This work confirmed that the reactive medium plays a huge role in the surface passivation of defects, which ultimately increases the band edge emission [90].

These two synthetic methods offered poor control over the particle size. Quantum confined nanomaterials were not synthesized by these methods. In 1999 Micic *et al.* adopted the strategy used for obtaining group III-V phosphide QDs. They developed a slow heating technique for pyrolyzing the polymeric gallium imide compound in a coordinating mixture of trioctyl amine (TOA) and hexadecyl amine (HDA). An ammonia flow at ambient pressure was maintained during this heat treatment process and even when the reaction solution is cooled back to room temperature. The amine reactive environment ensured the hydrophobic capping of the small particles generated, resulting in producing small particles with good dispersion. Weak quantum confined GaN QDs were obtained in this synthetic strategy. Among the amine mixture of TDA & HDA, HDA can sterically hinder the surface of GaN and provides a dense capping of the GaN QDs [54]. This highly beneficial route for obtaining GaN QDs is depicted in the Scheme 3 of Figure 2.5.

Finally, in 2006, Pan *et al.* re-investigated the two step methodology of Scheme 3 in Figure 2.5. They successfully observed that GaN QDs can be easily realized by direct pyrolysis of the $[Ga(N(CH_3)_2)_3]_2$ precursor and *relinquished* the method for obtaining polymeric gallium

imide $\{Ga(NH)_{3/2}\}_n$. This was a key achievement in GaN QDs synthesis utilizing the homoleptic amido complex precursor, as it eliminates the usage of ammonia gas, which can be caustic and hazardous. In this novel synthetic route, they exhibited a single step pyrolysis of $[Ga(N(CH_3)_2)_3]_2$ directly to GaN QDs in argon atmosphere with precursor dissolved in amine mixture (TOA & HDA) [91], which is depicted in the Scheme 4 of Figure 2.5. This synthetic route resulted in providing GaN QDs with higher yield and enhanced control over the particle size, resulting much better confined effects compared to the GaN QDs synthesized by Micic *et al*.

All of the synthetic protocols summarized here are based on $[Ga(N(CH_3)_2)_3]_2$ precursor and were performed in batch reaction vessel, which involves severe limitations such as: (i) low heat & mass transfer, (ii) difficulty in handling the ammonia, (iii) difficulty in recovering the polymeric gallium imide intermediate precursor, (iv) limitations due to the reactor geometry and low throughput per synthesis, even though they generate GaN nanomaterials/QDs.

These limitations tender the synthetic process to be non-optimum for achieving GaN QDs. All of the batch methods for GaN generation from amido complex exhibits poor control over size distribution and most of the time results in polydispersed particles. Some approaches like repetitive centrifugation and redistribution were used in appropriate solvents to segregate the large-sized particles from quantum confined small particles. Nevertheless, the problems associated with heat & mass transfer and attaining higher throughput per synthesis can be solved by utilizing a continuous flow setup for GaN QDs synthesis. In particular, the critical requisites (monodispersed GaN QDs) are achieved by implementing the continuous flow process at supercritical conditions. The intrinsic nature of the supercritical medium and its highly beneficial features for attaining monodispersed population of nanomaterials and homogeneous residence time for all the reactants in the system are elaborated in detail in the next section. The chemistry for the thermolysis of $[Ga(N(CH_3)_2)_3]_2$ precursor in continuous flow supercritical tubular reactor targets in eliminating the usage of caustic and hazardous ammonia and amine compounds in the reaction medium. The development of new reactive medium without the implementation of amines is critical and ultimately required in this research work because amines provide the hydrophobic capping of the GaN QDs, that to dense capping in many cases due to less steric hindrance, which is not viable for our photocatalytic study involving degradation of dyes in aqueous medium. This new reactive medium development will also eliminate the post processing steps of removing /adding surface moieties from the GaN QDs.

2.3. Continuous supercritical synthesis of GaN QDs using a co-flow configuration

2.3.1. Introduction

This section of the chapter consists of three parts: (i) continuous supercritical synthesis of GaN QDs in co-flow mixer fixed supercritical setup, (ii) mathematical simulation study on co-flow mixer hinged system and pre-heater mixer hinged system and (iii) synthesis of GaN QDs through newly developed pre-heater mixer fixed supercritical setup.

To synopsize the research work concerning GaN QDs production, I have performed GaN QDs production in already reported co-flow based supercritical setup at higher throughput and more enhanced pressure and temperature control. The performance of this co-flow setup was analysed and reactor's lifetime and its ability to operate at higher concentration of precursor feed rate were also considered. The materials obtained from the co-flow technology were subjected to structural and chemical characterizations study and their corresponding results were analysed. This co-flow based setup suffered from several disadvantages like low reactor's life time and lack of facile operation of the system. Mathematical simulation on the energy balance and heat transfer rates for the attainment of supercritical conditions and thermolysis of amido complex precursor were performed on co-flow to elucidate its reasons for carrying several disadvantages. Based on the mathematical simulation results, a new supercritical reactor was fabricated with pre-heater mixer replacing the co-flow arrangement. The drawbacks of co-flow synthesis and the result of computational heat transfer stood as motivation for designing the pre-heater coupled SCF millireactor in my research work. The final section of this chapter are fully focused on the systematic evaluation of this pre-heater based supercritical millireactor and characterization of the GaN QDs produced by this system.

The synthesis of GaN QDs starting from Tris(dimethylamido)-gallium(III) precursor through a two-step ammonolysis & thermolysis route in supercritical hexane and ammonia mixture with the formation of intermediate polymeric gallium imide was first attempted using co-flow system developed by Giroire *et al.* [75]. The motive behind such an investigation was to ensure whether such a SCF milliflow device produces high reproducibility and enough throughput of nanomaterials.

The continuous flow setup involving supercritical medium consists of four prime components. They are: (i) injection system for the precursor solution and solvents (pumps), (ii) mixers for combining the various feeds or flow streams, (iii) reactor fitted with the heating system and a (iv) back pressure regulator (BPR). Residence time in the reactor is controlled or precisely tuned by varying the volume of the reactor, the flow rate of the pumps or the temperature and/or the pressure of the system. The schematic representation of process flow diagram of co-flow mixer based system fabricated in our lab for the GaN QDs production is depicted in Figure 2.6. Hereafter, I will detail out the various chemical compounds used for the GaN QDs production and the equipments employed for the fabrication of the overall co-flow based supercritical setup.

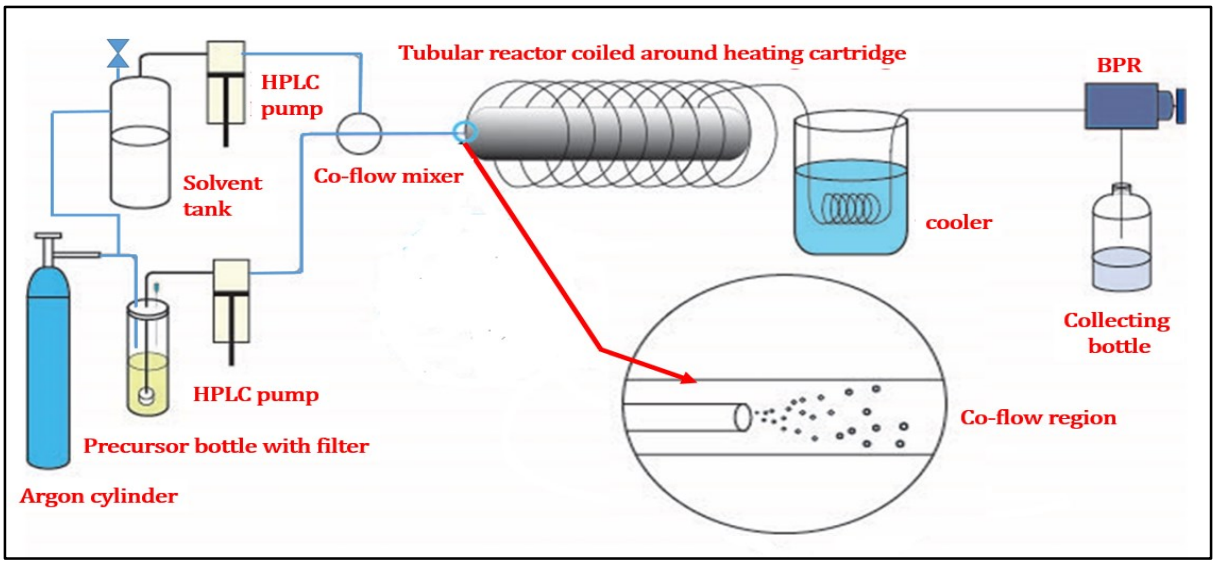

Figure 2.6. *A schematic representation of the continuous supercritical co-flow mixer based setup fabricated for GaN QDs production.*

2.3.1.1. Precursors & Solvent

Tris(dimethylamido)-gallium(III), 99.9% (metal basis) from Alfa-Aesar and cyclohexane anhydrous, 99.5% from Sigma-Aldrich were purchased and used without further purification or processing in the synthesis methodology. Solvent and precursors were received in inert gas filled, sealed packing's and were stored in argon circulated glove box to prevent water or oxygen contamination.

2.3.1.2. Reactor

The continuous flow tubular reactor as depicted in Figure 2.6, was made up of three-meter long, 1/16'' of an inch (1mm inner diameter) stainless steel tube. The reactor is fabricated by manually coiling the tube around a heating cartridge (Acim Jouanin, 800 W, 230 V). The total volume of the reactor was adjusted to 2.36 mL.

2.3.1.3. Description of the continuous flow reactor setup

In a typical experiment, the precursor solution and solvent are injected using JASCO (HPLC) high pressure pumps. The solvent is stored in specially designed solvent tank with tight rubber sealing and four-valve system for solvent suction and argon gas injection, the remaining valve acts as vent for the solvent tank, so that continuous flow of argon gas is maintained. Similarly, the precursor solution is stored in specially designed precursor bottle with a rubber sealing and four-valve system like the solvent bottle. The concurrent flow is established in the upstream section by positioning a 1/32'' of an inch stainless tube (400 µm inner diameter) within a (1 mm inner diameter) tube. This smaller diameter tube starts from the outlet of the precursor pump and enters within the 1 mm inner diameter tube, (forming a concentric tubing arrangement) ends exactly at the inlet section of the reactor, as depicted in Figure 2.6. This arrangement results in the creation of a co-flow region. The mixing of the co-flowing streams starts happening exactly at the entry of the tubular millireactor, which can be seen in Figure

2.6. The downstream section of the system consists of cylindrical water bath used for cooling the product stream and therefore quenching the reaction. The pressure within the continuous supercritical reactor is maintained at 150 bar using a back pressure regulator (BPR). Nanoparticles / QDs are obtained in solution at the outlet of the BPR.

2.3.1.4. Experimental Section

The synthesis of GaN QDs using co-flow setup was done at increasing concentration of the precursor solution to ensure whether the designed co-flow process setup yields GaN QDs which are reproducible in their properties and has higher throughput. The precursor solution is prepared carefully in the glovebox by dissolving the calculated quantity of amido gallium precursor in anhydrous cyclohexane. The first phase of synthesis was done in low concentration (0.025 M in the precursor bottle). The second phase of synthesis was attempted at a little bit higher concentration (0.035 M in the precursor bottle) so that higher throughput was aimed per synthesis.

The precursor solution and the co-current solvent are injected individually with two separated pumps at a flow rate of 1mL/min each, resulting in a residence time of 33 seconds. The injection was done at 400°C and 150 bar above the critical point of cyclohexane: T_c = 281 °C, P_c = 40.7 bar [92].

The conjunction of precursor solution with co-solvent furthers dilutes the precursor concentration in the millireactor. When the precursor solution combines with co-solvent, the concentration of the precursor in the millireactor becomes $12.5 * 10^{-3} M$. This concentration was chosen as minimum limit for the synthesis as it yielded small quantity (30 - 40 mg) of nanomaterials for characterization. The maximum theoretical yield which can be obtained is 41% (wt%). In order to obtain more quantity of particles for the photocatalytic applications or for extensive characterization, the concentration limit was pushed higher in the second phase of the synthesis to 0.035M in the precursor bottle leading to a concentration in the supercritical millireactor of $17.5 * 10^{-3} M$.

As the precursor is injected at supercritical conditions of cyclohexane (400°C and 150 bar) inside the millireactor, the subsequent thermolysis of the precursor and the supersaturation is attained. The nanomaterials nucleate due to high supersaturation reached and grow as they pass through the reactor regime. The as-synthesized nanomaterials are collected in the glass bottles (used as collection vials) and stored under argon.

2.3.1.5. Structural characterization of GaN QDs obtained from co-flow supercritical synthesis

In co-flow synthesis dark beige grey GaN particles were obtained. The as-synthesized particles in solution were centrifuged at 10,000 RPM for 10 minutes and the supernatant was removed and the particles were redispersed in fresh anhydrous cyclohexane. The centrifugation step was done twice, following which the particles are deposited on the silicon substrate with zero background and the X-ray powder diffraction study was performed. To determine the

characteristics of the crystallite phase, powder XRD analyses of GaN nanomaterials synthesized by co-flow technique at different concentrations of the precursor are plotted and illustrated in Figure 2.7.

The synthesis of GaN nanomaterials was carried out at two different precursor concentrations in the millireactor: $(i)\ 12.5 * 10^{-3}M$ and $(ii)\ 17.5 * 10^{-3}M$. The XRD pattern of the GaN nanomaterials synthesized at different concentrations are shown in Figure 2.7. The XRD pattern for the samples produced at the lower concentration ($12.5 * 10^{-3}M$) possessed a wider peak without any distinctive attributes. This XRD pattern cannot be satisfactory indexed to any one of the reference GaN peaks mentioned in Figure 2.7, comprehensively the featureless XRD spectrum indicates that it has mixture of cubic and hexagonal close packed crystal structures. Closer observation of unique broad peaks at 35° and 62° and sloppy bump from 40° indicates us that the resultant nanomaterials has more amount cubic phases in it, in additional to the hexagonal phase.

Higher precursor concentration ($17.5 * 10^{-3}M$) was taken while keeping all other synthetic conditions the same as before. The main target of this research is to investigate whether the co-flow system provides enhanced reproducibility and higher throughput. The study of phase two-synthesis was done using a new millireactor possessing the same volume and dimensions as used in phase-one, even the tubing and all other upstream and downstream equipments used were newly fabricated and was not used before. This revamp of system was done to ensure that none of the materials or reactor effluents of phase-one study pollutes the phase-two synthesis. The XRD pattern of GaN nanomaterials synthesized at higher concentration ($17.5 * 10^{-3}M$) is also displayed in Figure 2.7. Synthesis with higher concentration resulted in XRD pattern where the onset of distinguishing peak started at 30°C, and had a maximum intensity at 35°C. The wide peak from 30° to 40° was found to be similar to the normalized Gaussian curve; this kind of uniform curve was not seen in the XRD pattern of GaN nanomaterials synthesized at lower concentration in phase one synthesis.

Secondly, a large bump was seen in the pattern from 40° to 50° and minor protuberance was seen from 60° to 80°. This corresponding pattern was not satisfactorily fitted to any of the GaN reference peaks. Overall the crystallite phase of GaN was found to be a mixture of cubic and hexagonal phases. *These broad featureless peaks are characteristics of nanosized crystalline GaN domains*. The XRD pattern reported in Figure 2.7 for GaN nanomaterials synthesized at a concentration of $17.5 * 10^{-3}M$ of precursor in the millireactor, closely resembled the spectrum reported by several authors [73, 91, 93], where the GaN was synthesized in batch mode using different precursors at different conditions.

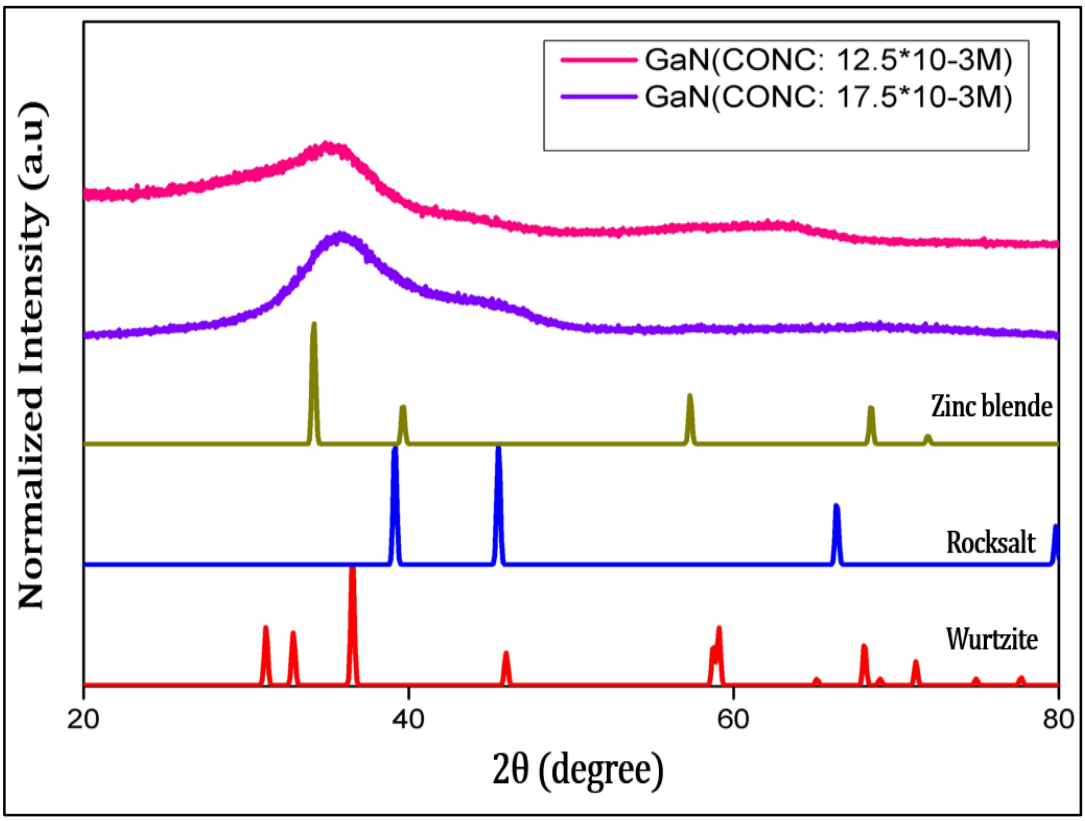

Figure 2.7. *XRD pattern of GaN nanomaterials synthesized in continuous co-flow, supercritical medium at different precursor concentrations in the milli reactor* ($(i)\ 12.5 * 10^{-3}M$ *and* $(ii)\ 17.5 * 10^{-3}M$).

Consecutive experiments of GaN synthesis was performed on co-flow system (at concentration $17.5 * 10^{-3}M$) to study the reproducibility of GaN nanomaterials synthesis. After each synthesis, the system was purged with fresh solvent, to collect as much particles from the rector or any particles retained in the BPR. In these experiments, the concentration of Tris(dimethyl)amido gallium precursor taken was $17.5 * 10^{-3}M$. After each synthesis, XRD study was performed on the particles subsequently.

The reproducibility of crystallite structures in GaN nanomaterials was attained in the first and second consecutive experiments but the reproducibility was not observed in the third and fourth continuous experiments. More importantly the reactor got clogged after completion of fourth experiment, a new reactor was fabricated for the next experiment. The similar trend of XRD pattern observed in Figure 2.7 was observed for 50 experiments of GaN co-flow synthesis, where the reactor got clogged at the end of the each 4^{th} experiment. In this study a total of seventeen millireactors were fabricated and the trend of crystallite phases in Figure 2.7 was repeatedly seen. This gave a very good conclusion that reproducibility of GaN nanomaterials with similar properties and reactor's lifetime was not ensured in co-flow methodology, for the direct pyrolysis of amido complex homoleptic precursor. All XRD pattern depicted in Figure 2.7 without any distinguishing peaks are characteristics of GaN material in the nanosized regime. This characterization alone wouldn't stand as a direct proof that material synthesised

are nanomaterials. The next characterization technique performed was TEM analysis to investigate the morphology and size of the nanomaterial synthesized.

The as-synthesized GaN nanomaterials in solution was centrifuged twice and the supernatant was removed. The particles were dried and subsequently re-dispersed in anhydrous ethanol solution and ultra-sonicated for few minutes (5 minutes' maximum). The resultant nanomaterials dispersed solution was drop casted on carbon (formvar) 200 mesh copper grid, mesh (for TEM characterization) and on lacey carbon covered 300 mesh copper grid (for HR-TEM study). The drop casting procedure was done in open atmosphere and the grids were dried for few minutes after drop casting, then loaded in the corresponding equipments for measurement.

TEM analysis was initially carried out on GaN nanomaterials synthesized at different concentrations of phase-one and phase-two synthesis ($(i)\ 12.5 * 10^{-3}M$ and $(ii)\ 17.5 * 10^{-3}M$). Irrespective of the concentration of precursors in the millireactors, the GaN nanomaterials from both the synthesis exhibited similar morphology and size. The global view of the GaN nanomaterial in the TEM analysis were islands of aggregates with especially spherical shaped contrasting aggregrates. These spherical aggregrates were in size range of 50 - 200 nm. Interestingly, some spherical shaped aggregrates were also observed within the island of large aggregrates in irregular morphologies. The closer zooming of these island of particle aggregates revealed small spherical aggregates with size form ranging from 30 - 60 nm. The observation of such highly aggregated particles mostly in spherical shape can be attributed to the absence of external surface stabilizing ligands in the nanomaterials' ensemble. The synthesis of these GaN nanomaterials was carried by direct pyrolysis of precursor alone without the addition of external surface passivating ligands. To understand the innate nature of these aggregate of different morphologies (spherical and non-spherical), to study the crystal structure and geometry of the GaN nanomaterials, HR-TEM characterization was performed.

When zooming further down into the spherical aggregrates under HR-TEM study, it was found that each spherical aggregrates were actually aggregrates of crystalline GaN nanomaterials with average size (diameter, since each coherent domains appears as spheres) of about 2.6 nm was observed (Bohr exciton radius of GaN, 2.5 nm [54]).

The investigation of each of these crystalline domains of GaN aggregated to form the big spheres, it was found that the entire ensemble of GaN nanomaterials was non-homogeneous mixture of hexagonal-wurtzite and cubic-zinc blende GaN particles. This means that there some particles crystallized with hexagonal geometry possessing wurtzite crystal structure and there is another set of particles crystallized in cubic symmetry with zinc blende crystal structure. Thanks to the d-spacing measurement, the values obtained can be indexed to the particular crystal plane of their corresponding crystal structure. This measurement is depicted in Figure 2.8, where more obviously d-spacing's (d =0.28 Å) corresponding to <100> plane of hexagonal wurtzite crystal structure of GaN, (d = 0.266 Å) <111> plane of cubic zinc blende is seen. All these information summarizes that GaN nanomaterials synthesized possesses a non-homogeneous mixture of GaN particles crystallized in wurtzite and zinc blende crystal structures.

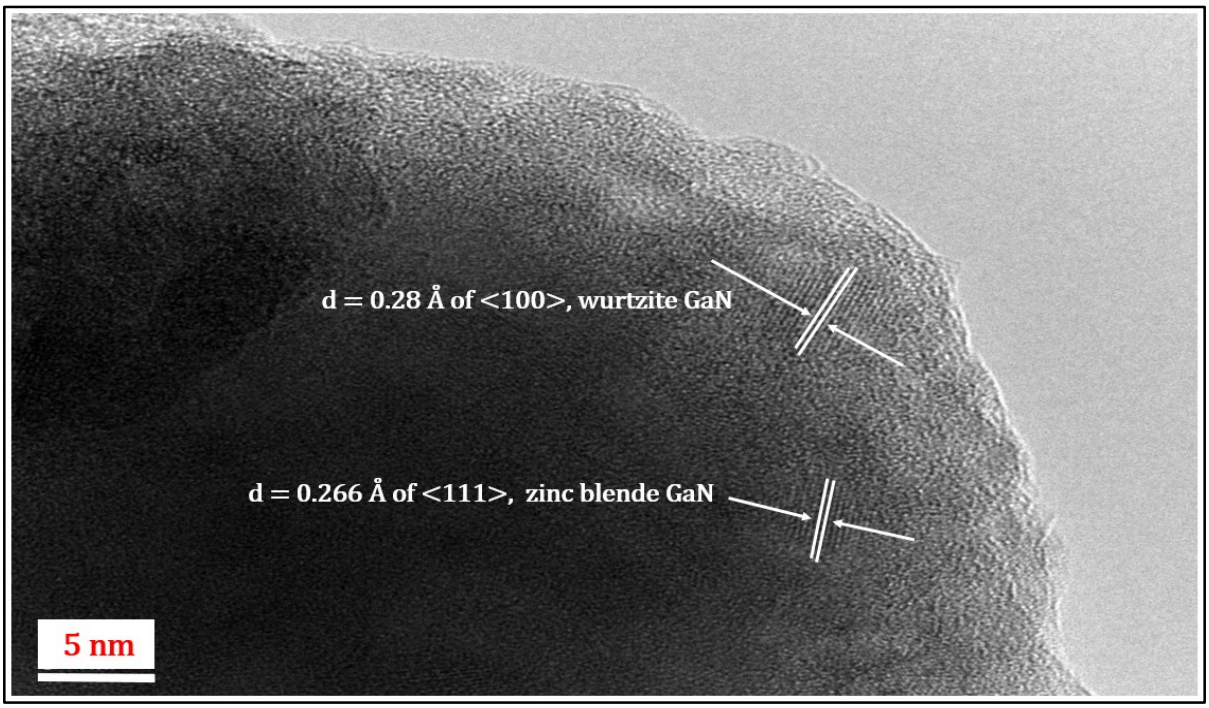

Figure 2.8. *HR-TEM image of GaN QDs synthesized by co-flow with precursor concentration* $17.5 * 10^{-3}M$.

2.3.1.6. Conclusion of co-flow synthesis

The continuous supercritical direct thermolysis of tris(dimethylamido)-gallium(III) in a co-flow setup at different concentrations ((i) $12.5 * 10^{-3}M$ and (ii) $17.5 * 10^{-3}M$) has yielded GaN nanomaterials. From a synthetic point of view, the co-flow technique was not an optimum one for synthesizing nanocrystalline of GaN continuously (yield ≤ 20%). The study using this setup has confirmed that the synthesis of GaN at different precursor concentrations resulted in the clogging of the reactor at the end of every fourth synthesis and the same trend was followed for repeated consecutive experiments with new millireactors.

In order to identify the drawback associated with co-flow setup and to develop a novel supercritical millireactor, simulation study was performed on the energy balance and heat transfer of the system. The details of such simulation and outcomes of the will be elucidated in the next section.

2.4. Simulation studies concerning the supercritical millireactors for GaN QDs production

The results of the study for co-flow supercritical synthesis based on confined nucleation have led me to identify the issues, which are preventing the co-flow from attaining high throughput and enhanced reactor lifetime. These are the important characteristics, which are essential prerequisites of continuous flow supercritical reactor.

The basic motive of the research in this section of the chapter is to perform 2D simulation on the experimentally employed co-flow mixer fixed supercritical millireactor and to propose an alternative design. The reasoning for performing this study is to understand the temperature field within the concurrent flow regime of the co-flow system. This simulation study is completely deployed on the Lagrangian-Eulerian model developed and studied by Erriguible *et al.* for supercritical fluids [94].

To simulate the continuous flow of cyclohexane in supercritical tubular millireactor, the flow was considered as compressible, non-isothermal and monophasic. The temperature distribution is obtained by solving a compressible set of equations. The temperature and density fields within the system are determined in the Lagrangian form through the divergence of velocity and heat flux and later the results are advected through the Eulerian form. The governing equations of this system that are solved by numerical analysis are the conservation of momentum and energy equations, given by Equations 2.1 and 2.2.

Conservation of momentum equation

$$\rho\left(\frac{\partial \mathbf{V}}{\partial t}+\mathbf{V}\cdot\nabla\mathbf{V}\right)=-\nabla\left(P^{0}-\delta t\left(\frac{1}{\chi_T}+\frac{\beta^{2}T}{\rho C_v\chi_T^{2}}\right)\nabla\cdot\mathbf{V}-\delta t\frac{\beta}{\rho C_v\chi_T}\nabla\cdot\mathbf{\Phi}\right)+\rho\,\mathrm{g} \qquad \textbf{(2.1)}$$
$$+\nabla\cdot\left(\mu\left(\nabla\mathbf{V}+\nabla^{t}\mathbf{V}-\frac{2}{3}\nabla\cdot\mathbf{V}\underline{\underline{\mathrm{I}}}\right)\right)$$

Energy conservation equation

$$\rho C_v\left(\frac{\partial T}{\partial t}+\mathbf{V}\cdot\nabla T\right)=-\nabla\cdot\mathbf{\Phi}-\frac{\beta T}{\chi_T}\nabla\cdot\mathbf{V} \qquad \textbf{(2.2)}$$

Where ρ = density, P = pressure, V = velocity, T = temperature, t = time, C_v = heat capacity at constant volume, χ_T = isothermal compressibility, β = thermal expansion co-efficient, μ = shear viscosity, λ = compression viscosity (second co-efficient of viscosity). The χ_T, β, C_v, λ and μ values are taken from the NIST database [92]. The codes written for solving the above equation numerically were done with a software specially developed at the I2M/TREFLE department. Numerical solution of the above two equations was approached based on the 'Finite volume Method' and 'Total Variation Diminishing (TVD)' methods for the discretization of mass conservation equation terms.

In this numerical modelling study along with the co-flow mixer fixed tubular millireactor, we have also considered a pre-heater fixed tubular millireactor reactor for this modelling studies. In the pre-heater system, the cold precursor solution at room temperature is mixed with pre-heated solvent and the combined mixture enters the reactor system, resulting in burst nucleation. This pre-heater based system was first introduced by Adschiri *et al*. for hydrothermal supercritical flow synthesis [95]. The configurations of these considered flow schemes corresponding to co-flow and pre-heater based system are schematically depicted in Figure 2.9.

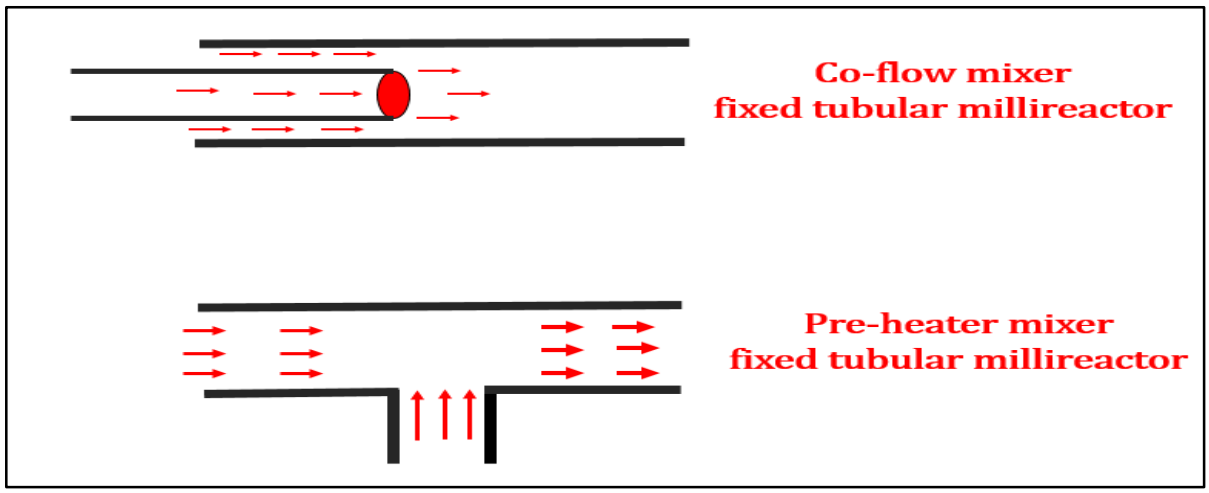

Figure 2.9. *A schematic depiction of flow configurations in considered co-flow mixer and pre-heater mixer fixed tubular millireactor systems for modelling studies.*

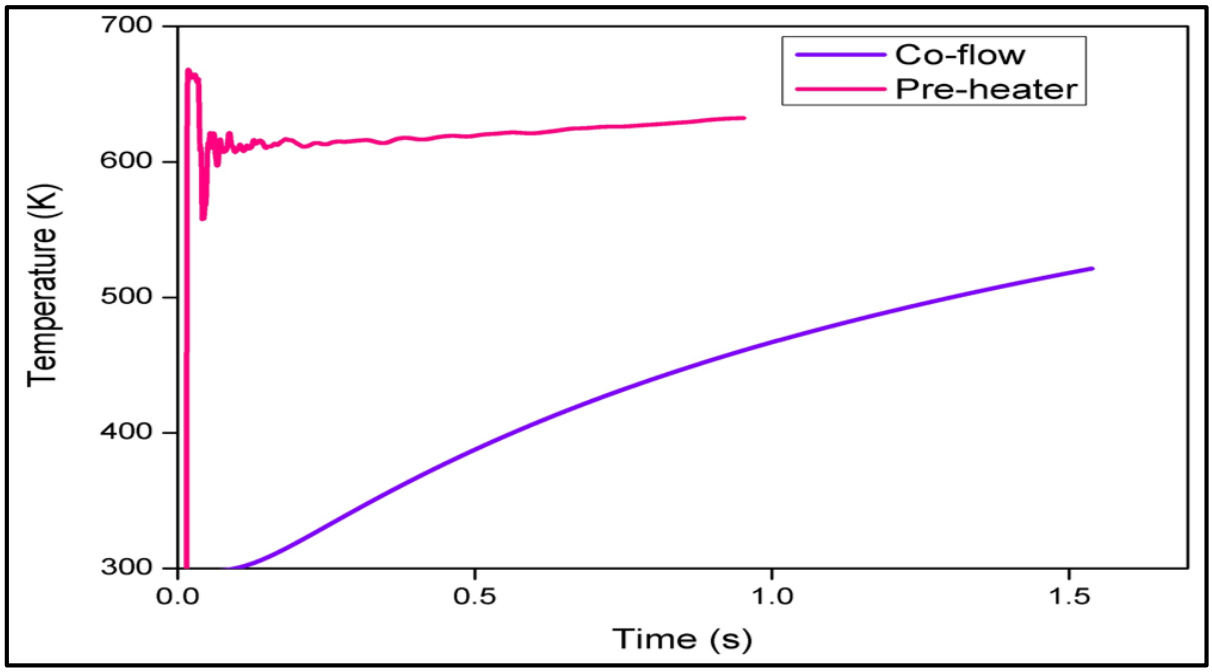

Figure 2.10. *Temperature vs time (simulation results) profile at the centre of the tubular reactor for cyclohexane flow in supercritical millireactors with co-flow or pre-heater mixer.*

It was found that among the two mixers compared, the maximum temperature (350 °C or 613 K) required for the system was immediately attained in the pre-heater mixer fixed system compared to the co-flow mixer. The numerical results of the temperature profile of these mixers are plotted and schematically illustrated in Figures 2.10 and 2.11.

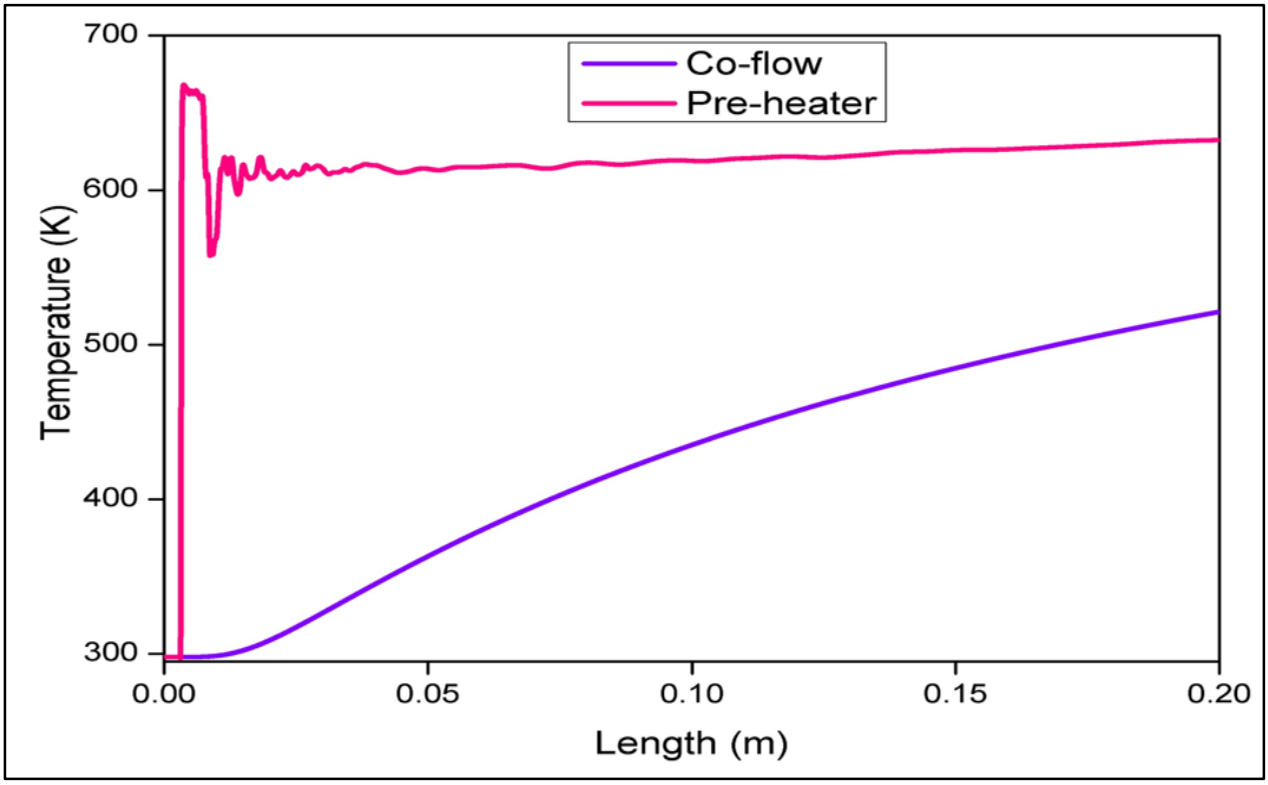

Figure 2.11. *Temperature vs reactor's length (simulation results) profile of cyclohexane continuous flow in supercritical millireactors with co-flow or pre-heater mixer.*

From Figure 2.10, temperature vs time profile, it is very obvious that the rate of temperature (requisite temperature, > 350°C) attainment in co-flow setup takes more time and procurement of temperature required for thermolysis happens not in the beginning of the reactor but after several centimetre length scale (approximately 500 - 600 cm) of the millireactor, as depicted in temperature vs reactor length profile in Figure 2.11.

The co-flow system consists of continuous flow of the precursor solution (precursor + cyclohexane) in the inner tube and co-current flow of cyclohexane solvent in the outer concentric tube as depicted visually in Figure 2.9. The combined solution of precursor solution and co-solvent doesn't reach both the requisite thermolysis temperature (340 °C or 613 K) and the critical temperature of cyclohexane (281.1 °C or 554.1 K) at onset of the tubular millireactor section. This effect is concluded from the heat transfer simulation results depicted in Figures 2.10 and 2.11. Due to the attainment of low temperature at the commencement of the millireactor compared to the requisite high temperature, the chemistry of the amido complex thermolysis reaction changes in the co-flow system.

In order to elucidate the chemistry in the co-flow system lets see the case of metal derivatives reported by Janik *et al*., where group 13 metal derivatives of the form $M(NR_2)_3$ (amides), (here R=H) undergoes a gradational deamination route at relatively lower temperature yielding the GaN product in the end [89], as shown in the Equation 2.3.

Contrastingly, in the homoleptic amido complex compounds, like the precursor ($[Ga(N(CH_3)_2)_3]_2$) studied in this research work, doesn't follow the same pattern shown in Equation 2.3. The tris(dimethylamido)-gallium(III) complex undergoes transamination reaction in the presence liquid or gaseous ammonia at room temperature to form polymeric gallium imide without the presence of any carbon atoms, as depicted in Figure 2.5. This polymeric precursor undergoes thermolysis at higher temperature from 350°C to 400°C.

Similarly, the complex tris(dimethylamido)-gallium(III) ($[Ga(N(CH_3)_2)_3]_2$) could directly undergo thermolysis without converting into polymeric amide compounds, when subjected to temperature range of 350 – 400°C.

$$Ga(NR_2)_3 \xrightarrow[-NH_3]{\Delta} Ga(NR_2)(NH) \xrightarrow[-1/2NH_3]{\Delta} Ga(NR)_{3/2} \xrightarrow[-1/2NH_3]{\Delta} GaN \qquad (2.3)$$

In our co-flow setup due to the not enough fast increase of temperature as depicted in Figures 2.10 and 2.11, the direct thermolysis of the amido complex to GaN is not attained on the first 250 cm of the millireactor. The temperature below the supercritical temperature of cyclohexane favors conversion of ($[Ga(N(CH_3)_2)_3]_2$) precursor to complex metal-organic groups, which deposit on the reactor walls during the first three consecutive continuous synthesis. It is because of this phenomenon that the co-flow arrangement gets clogged after 4th continuous synthesis irrespective of the concentration of the precursor in the millireactor.

In order to obtain GaN QDs with reproducibility and enhanced reactor's lifetime from the direct one step thermolysis of $[Ga(N(CH_3)_2)_3]_2$ precursor, a supercritical millireactor system with immediate high temperature attainment (> 350°C) is required, that too from the onset of the tubular millireactor inlet is particularly needed. As the such rapid temperature attainment provides the optimum reactive medium for direct thermolysis and formation of GaN material. From the simulation results, it was found that a pre-heater fixed tubular millireactor satisfies the conditions of immediate temperature attainment of 350°C at the onset of the reactor, thus manifesting itself as an optimum system for GaN QDs production.

Based on the numerical simulation results, 2D flow simulation in the pre-heater system was performed using MPI parallel (640000 nodes) programming to schematically depict the rapid attainment of high temperature (> 350 °C) in pre-heated fixed supercritical tubular millireactor system onset of the reactor, this corresponding simulation (pictorial) result is depicted in Figure 2.12.

Figure 2.12 represents the temperature of the fluid within the pre-heater mixer fixed system showing the immediate attainment of higher temperature (> 350 °C) at the onset of millireactor. In this arrangement, the precursor solution from the room temperature combines with the

preheated fluid (400 °C) exactly at the onset of tubular reactor. This sort of conjunction, engineers the ability of pre-heater fixed system to attain immediately the required temperature (> 350 °C and 400 °C after 5 s) for direct thermolysis of $[Ga(N(CH_3)_2)_3]_2$ precursor to GaN material without forming any complexes of metal organics. To conclude, the pre-heater mixer based system should be more optimum and viable system for GaN QDs production compared to the co-flow based system.

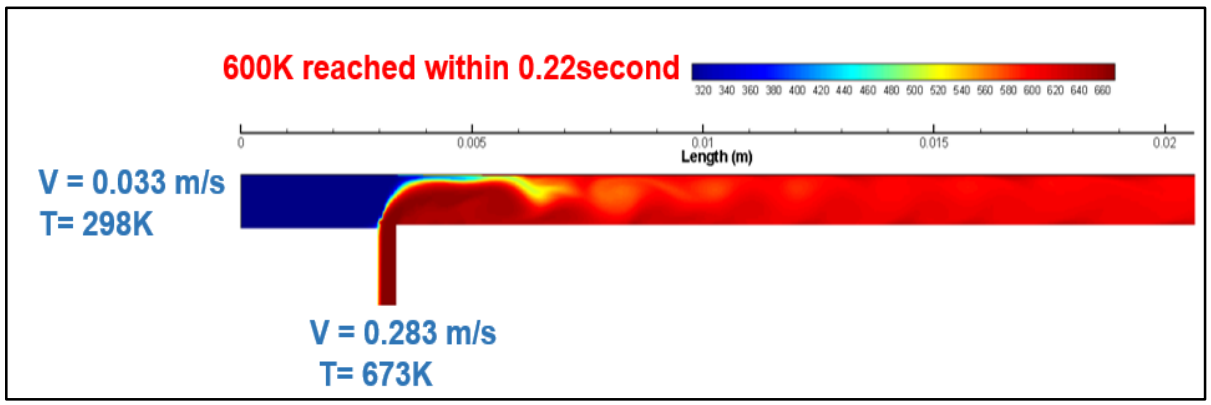

Figure 2.12. *Two-dimensional flow simulation of cyclohexane in supercritical millireactor with pre-heater (mixer) fixed arrangement.*

The next section of the chapter focus on describing, fabricating and experimenting the novel pre-heater supercritical millireactor for GaN QDs production. The characterisation and study of GaN QDs produced from the pre-heater system is performed in view of photocatalytic applications and simultaneously, the supercritical millireactors' performance and lifetime is also estimated.

2.5. Supercritical synthesis through a pre-heater setup

2.5.1. Introduction

To design an optimal system for the direct thermolysis of $[Ga(N(CH_3)_2)_3]_2$ precursor with a swift attainment of thermolyzing temperature (> 350°C) is required within the inception of the millireactor. An instantaneous attainment of high temperature is possible in pre-heater setup, which was confirmed using simulation studies as depicted in Figures 2.10, 2.11 and 2.12. The prime focus of this study is to systematically analyse the experimental high throughput of the pre-heater setup with enhanced reactor's lifetime for GaN nanomaterials synthesis. Consecutively, the materials have been characterized (morphology, size and optical properties).

2.5.1.1. Precursor and solvent

Tris(dimethylamido)-gallium(III) ($[Ga(N(CH_3)_2)_3]_2$), 99.9% (metal basis) from Alfa-Aesar and cyclohexane anhydrous, 99.5% from Sigma-Aldrich were used in this synthesis. The solvents and precursors were received in inert gas filled, sealed packing's and were stored in an argon circulated glove box to prevent water and oxygen contamination. Both chemicals were used directly for synthesis without any further purification or treatment.

2.5.1.2. Process equipment description

The process setup used here is depicted in Figure 2.13. The flow reactor was made up of three-meter long 1/16'' of an inch (1 mm inner diameter) stainless steel tube. The reactor is fabricated by manually coiling the tube around a heating cartridge (Acim Jouanin, 800 W, 230 V). The total volume of the reactor corresponds to 2.36 mL. The pre-heater, which belongs to the upstream of the process is fabricated from one-meter long 1/32''of an inch (400 µm inner diameter) stainless steel tube, through manual coiling like the tubular reactor. In the upstream of the process, the precursor solution and the solvent through the pre-heater were injected using the two separated JASCO high pressure pumps. The solvent is stored in a specially designed solvent tank with tight rubber sealing, four-valve system for suction and for maintaining argon atmosphere. Similarly, the precursor solution is stored in specially designed precursor bottle with a rubber sealing and four-valve system like the solvent tank.

The 400°C heated anhydrous cyclohexane from the pre-heater outlet is mixed with precursor solution at room temperature in a T-shaped mixer, from which the hot diluted fluid mixture (precursor solution + preheated solvent) enters the tubular reactor. The downstream section of the process setup consists of a cylindrical water bath used for cooling the product stream and quenching the reaction. The pressure within the continuous supercritical reactor is maintained at 150 bar using a back pressure regulator (BPR).

2.5.1.3. Experimental section

The synthesis of GaN QDs through the direct thermolysis of $[Ga(N(CH_3)_2)_3]_2$ precursor was carried out using the pre-heater hinged supercritical continuous flow millireactor, schematically depicted in Figure 2.13.

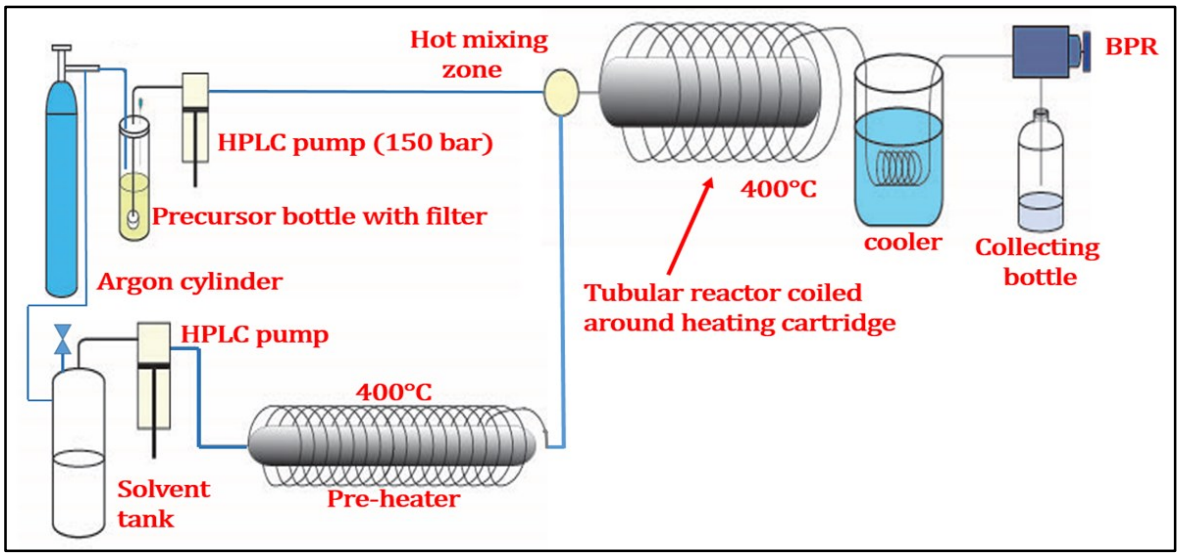

Figure 2.13. *Schematic representation of the continuous supercritical pre-heater hinged tubular millireactor fabricated for GaN QDs production.*

The reactor and the pre-heater were operated at 400°C and 150 bar. The precursor solution was prepared inside the glove box by adding 500 mg of homoleptic amido complex precursor to 35 mL of anhydrous cyclohexane solvent, in a specially designed precursor bottle, as mentioned before. The amount was taken in such way that precursor concentration in precursor bottle was 0.035 M. The injection of the precursor solution was done at 1mL/min and the preheated cyclohexane solution at 1mL/min resulting in a residence time of 33 s. Hence the concentration attained in the millireactor was 0.0175 M. The injected precursor solution at room temperature mixes with the preheated anhydrous cyclohexane solution enters the reactor to reach rapidly the thermolyzing temperature (> 350°C) immediately within milliseconds, confirmed from the simulation results, depicted in Figures 2.10, 2.11 and 2.12. Light beige grey particles in solution are obtained in the collection bottle during the continuous synthesis, which was slightly whitish than the particles in solution obtained with the co-flow technique. The collection bottle is purged with argon gas during and also after synthesis, to store the particles in argon atmosphere till it is used for further characterization.

In total, around 30 individual continuous flow syntheses of GaN QDs were performed using the pre-heater technique, with precursor concentration of 0.017 M in the reactor without clogging (Reactor's lifetime was increased). Besides, the throughput of particle obtained per synthesis was (100 – 150 mg) much higher than the co-flow technique (< 100 mg) and throughput of GaN QDs production was similar in all the experiments performed using the pre-heater setup. Approximately per day through continuous synthesis using the pre-heater system 300 – 450 mg of GaN QDs was synthesized.

2.5.2. Characterization of GaN QDs obtained from pre-heater supercritical millireactor

2.5.2.1. Structural characterization

The GaN particles obtained were transferred to a centrifuging vial and centrifuged at 10,000 RPM for 10 minutes. The centrifugation procedure was carried out twice, after each centrifugation, the supernatant was removed and the particles were redispersed in fresh anhydrous cyclohexane solvent. The solvent was dried and the particles were deposited on a silicon substrate with zero background before the powder x-ray diffraction was performed. A schematic representation of the obtained powder X-ray diffraction pattern is plotted and illustrated with standard XRD reference of GaN in Figure 2.14.

The obtained diffraction pattern distinctly designates that GaN nanomaterials display wider peak similar to a normal Gaussian curve in the region 30 - 40°, without any other distinctive peaks. This is a conventional characteristic XRD pattern often displayed by nanocrystalline GaN [73, 91, 93]. Comparative study of the obtained diffraction pattern with reference peaks was carried out, as depicted in Figure 2.14, the analysis stipulates that the GaN nanomaterials synthesized here contains a mixture of particles crystallized in hexagonal and cubic crystal structures. The XRD pattern has a uniform wider peak with maximum intensity at 35.68°. This wider Gaussian portion cannot be satisfactorily indexed to one particular crystal structure but it could be due to the combination of intensities arising from the various crystal structures of GaN nanomaterials. Therefore, it can be concluded that the as-synthesized GaN QDs are a mixture of GaN nanomaterials crystallized in cubic/ hexagonal crystal structures. The aslant protuberance seen from 40° - 50° region, emerges from the cubic NaCl crystal structured particles present in the nanomaterials' ensemble.

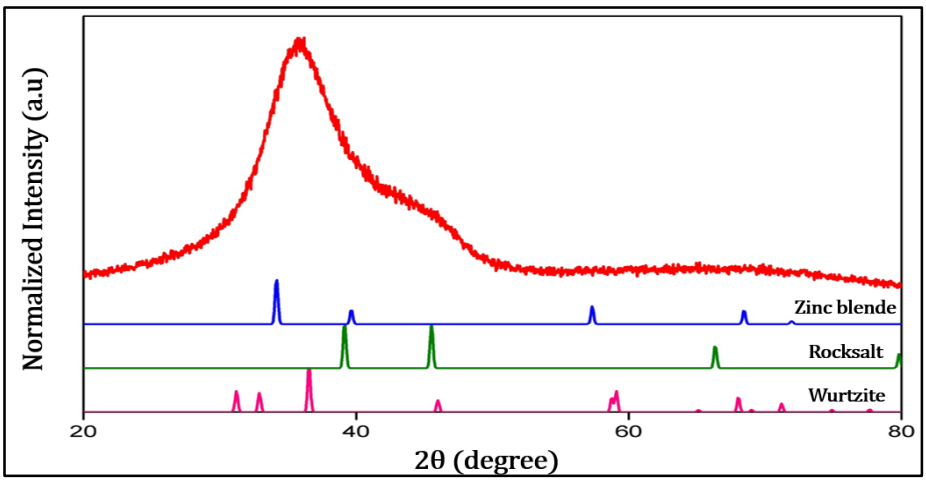

Figure 2.14. *Powder XRD pattern of GaN nanomaterials synthesized in pre-heater hinged supercritical tubular millireactor (with precursor concentration* $17.5 * 10^{-3} M$ *inside the millireactor, illustrated along with standard reference spectrum of GaN material with different crystal structures.*

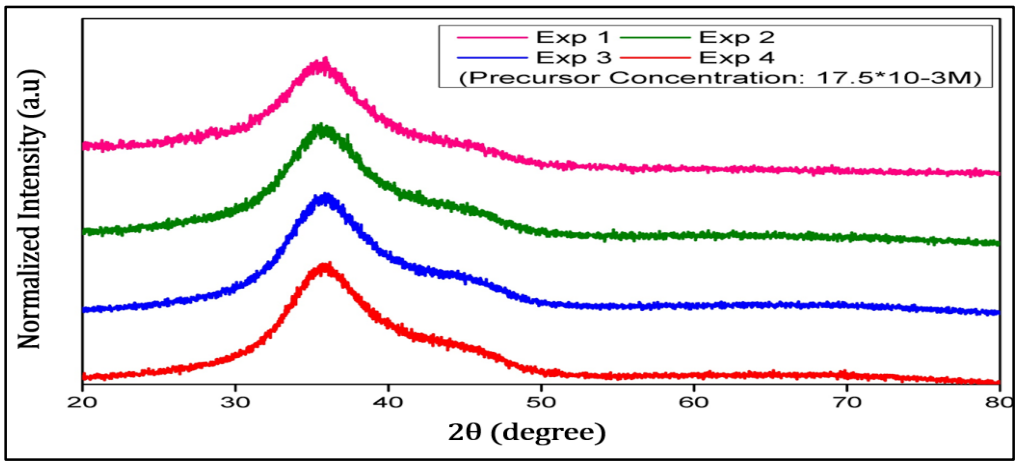

Figure 2.15. *XRD pattern of GaN nanomaterials obtained from each individual continuous flow experiments using pre-heater based supercritical millireactor. The concentration of precursor ($17.5 * 10^{-3} M$ inside the millireactor) was maintained the same in all the individual experiment carried out in pre-heater setup.*

The consistency of crystallite phases from GaN nanomaterials synthesized, in each individual synthesis was also studied, this was done to infer the reproducibility of the process. The results concluded that pre-heater flow reactor yielded the exact same crystallite phases of nanomaterials in each of the individual flow synthesis. The reproducibility of crystallite phases can be visualized in Figure 2.15, where the pattern of GaN nanomaterials obtained from each individual flow synthesis using pre-heater flow system are depicted.

The morphology and size distribution of the GaN nanomaterials are studied using the transmission electron microscopy (TEM) technique. The synthesized nanomaterials are dispersed in ethanol solution and are further ultra-sonicated for few minutes. The resultant solution is drop casted on carbon (formvar) covered 200 mesh copper grid for TEM analysis. The drop casted grids are dried in open air before the microscopy analysis, and then used directly. The schematic pictorial representation of obtained TEM images are depicted in Figures 2.16-a and 2.16-b. The particle size distribution is also measured for GaN QDs and schematically illustrated in Figure 2.16-d.

The TEM images obtained for the GaN nanomaterials synthesized in the pre-heater supercritical millireactor with precursor concentration $17.5 * 10^{-3}$M are depicted in the Figures 2.16-a and 2.16-b. From these images, GaN nanomaterials existed as two distinct set of particles. The former one is obviously the big spherical aggregates. The later distinct ones are distinctive set of dispersed particles in the size range below 5 nm, these smaller and widely dispersed particles are obviously seen in all images of the Figure 2.16.

These distinctive set of dispersed GaN nanoparticles are observed only from the GaN nanomaterials synthesized using the pre-heater based supercritical millireactor and not seen in the co-flow technique, where only island of aggregates were seen. The size of the spherical aggregrates observed in both the image of Figures 2.16-a and 2.16-b were in the range of 110 - 243 nm. The number of spherical aggregates observed in these TEM images were actually much less than the aggregates observed with the co-flow synthesis. In many parts of TEM

images, additionally in several TEM images more of distinctive dispersed smaller particles were seen. These particles were below 5 nm with a maximum size of 4.4 nm and a minimum size of 1.3 nm (average size of these particles were 2.85 ± 0.71 nm).

The Bohr exciton radius of bulk GaN at room temperature was reported by certain authors as 2.5 nm [54], although others have reported the value to be 2.8 nm [55, 56]. As the sizes of the low dimensional GaN nanoparticles observed in the TEM images were below the Bohr exciton diameter, we can confirm that GaN QDs have been produced from the supercritical synthesis using the pre-heater setup. The size distribution of these low dimensional GaN QDs in the form histogram have been depicted in Figure 2.16-d. For this size distribution analysis, a sum of 100 nanoparticles were analysed and most of the particles were in the size range of 2.5 – 3.5 nm (65 particles). Another key important factor to be observed in these TEM images of GaN nanoparticles is that spherical aggregates were also present in the sample. These high dimensional spheres were studied using HR-TEM.

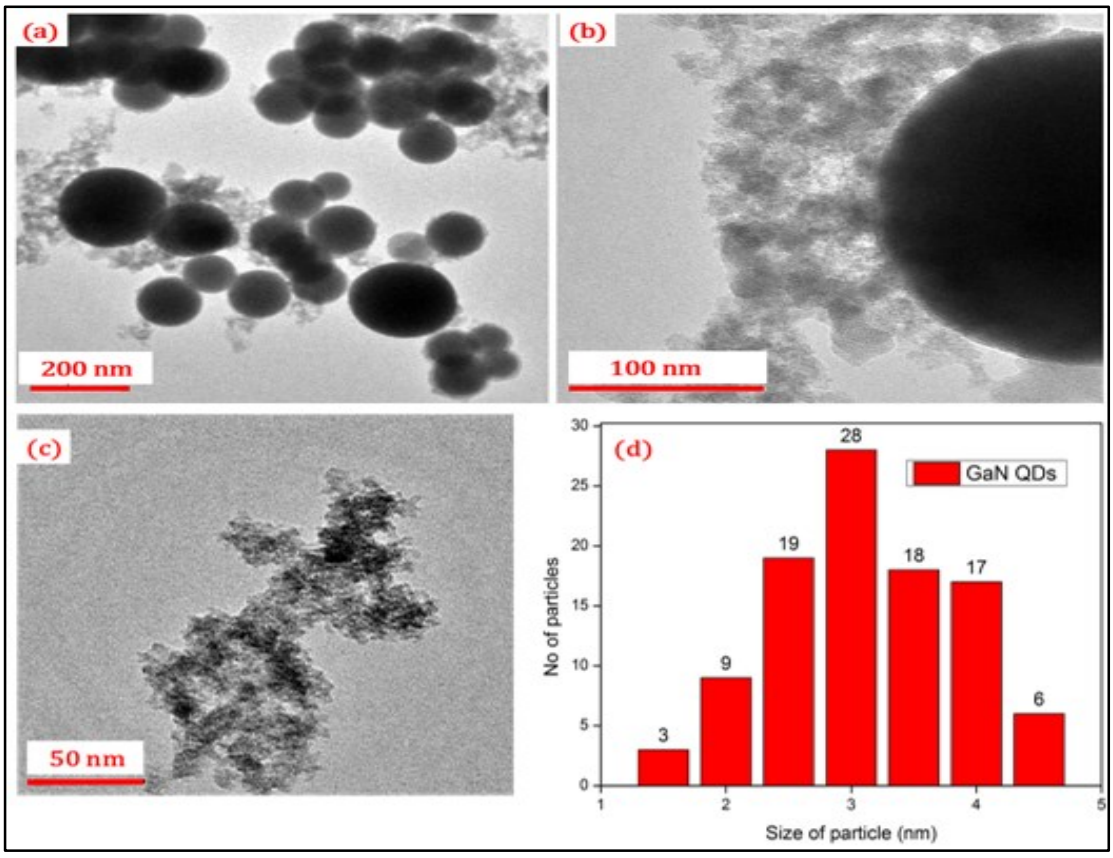

Figure 2.16. *a and b. TEM images of GaN QDs synthesized using the pre-heater hinged supercritical millireactor with precursor concentration of* $17.5 * 10^{-3} M$ *in the tubular millireactor; c. TEM images depicting the dispersed aggregate of low dimensional GaN nanoparticles; d. The nanoparticle size distribution histogram of low dimensional particles observed in the TEM study of GaN nanomaterials analysed in Figure (2.16.c).*

In order to prepare the samples for HR-TEM study, the particles were dispersed in ethanol solvent and ultrasonicated for a maximum of five minutes. The resultant dispersion is drop casted on LACEY carbon covered 300 mesh copper grid and dried in open atomsphere. The obtained images were schematically depicted in Figures 2.17-a and 2.17-b.

As for TEM, similar structures (spherical aggregates and dispersed small dimensional particles) were seen in the HR-TEM images. Spherical aggregates of size maximum up to 372 nm were seen. The size range of these spheres was 60 – 372 nm. The spheres ranging from 60 - 80 nm were predominantly more in numbers than the bigger spheres, as depicted in Figures 2.17-a and 2.17-b. Further zooming deep into these spherical aggregates allows for observing their innate nature. Within these spheres, coherent crystalline domains of GaN nanomaterials were seen. Crystalline domains corresponding to hexagonal-wurtzite and cubic-NaCl were present. This observation agrees well with the aslant protuberance seen within the 40° - 50° region of the XRD pattern of Figure 2.14, which corresponds to crystallite phases of cubic-NaCl (rocksalt) GaN material. The observed crystalline domains and the calculated d-spacing were schematically indicated in Figures 2.18-a and 2.18-b.

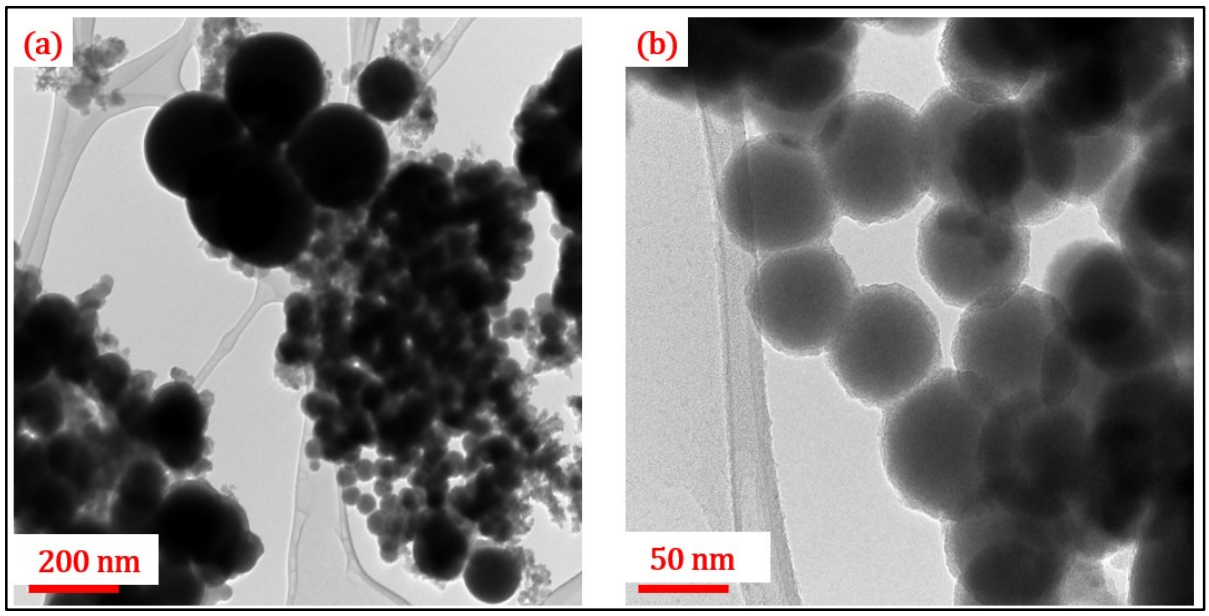

Figure 2.17. *a and b. HR-TEM images of GaN nanomaterials synthesized using the pre-heater hinged supercritical millireactor with precursor concentration of* $17.5 * 10^{-3} M$ *in the millireactor.*

In the Figure 2.18-a, the identified d-spacing values depends on the lattice fringes taken into consideration. In Figure 2.18-a, d-spacing of GaN hexagonal wurtzite corresponding to the (101) plane and GaN cubic rocksalt corresponding to the (200) plane were identified. In Figure 2.18-b d-spacing values of the (100) plane of GaN wurtzite hexagonal crystal structure and the (200) plane of rocksalt crystal structure were seen. The observation of this random mixture of crystallite planes corresponding to cubic and hexagonal crystal structures of GaN indicates that GaN nanomaterials produced consists of a mixture of GaN hexagonal and cubic crystal structures. It is worth noticing that GaN nanomaterials with cubic rocksalt crystal structure have been seen here, whereas cubic zinc blende with hexagonal wurtzite structures were only

observed in the particles synthesized from co-flow setup. Finally, in this HR-TEM characterization study, lattice fringes were observed only on the different places of spherical aggregrate, no lattice fringes were observed for the dispersed small particles (1 - 5 nm).
Using HR-TEM, elemental mapping was carried out. The main objective of such a study is to quantitatively visualize the spatial distribution of elements within the nanomaterials and specially to attain an overview of the elements bounded to the surface of the nanomaterials. As these GaN nanomaterials will be implemented as heterogeneous photocatalysts, where surface bound redox reactions are going to be carried out, information of surface elements will be highly helpful in understanding the mechanism of photochemical reactions.

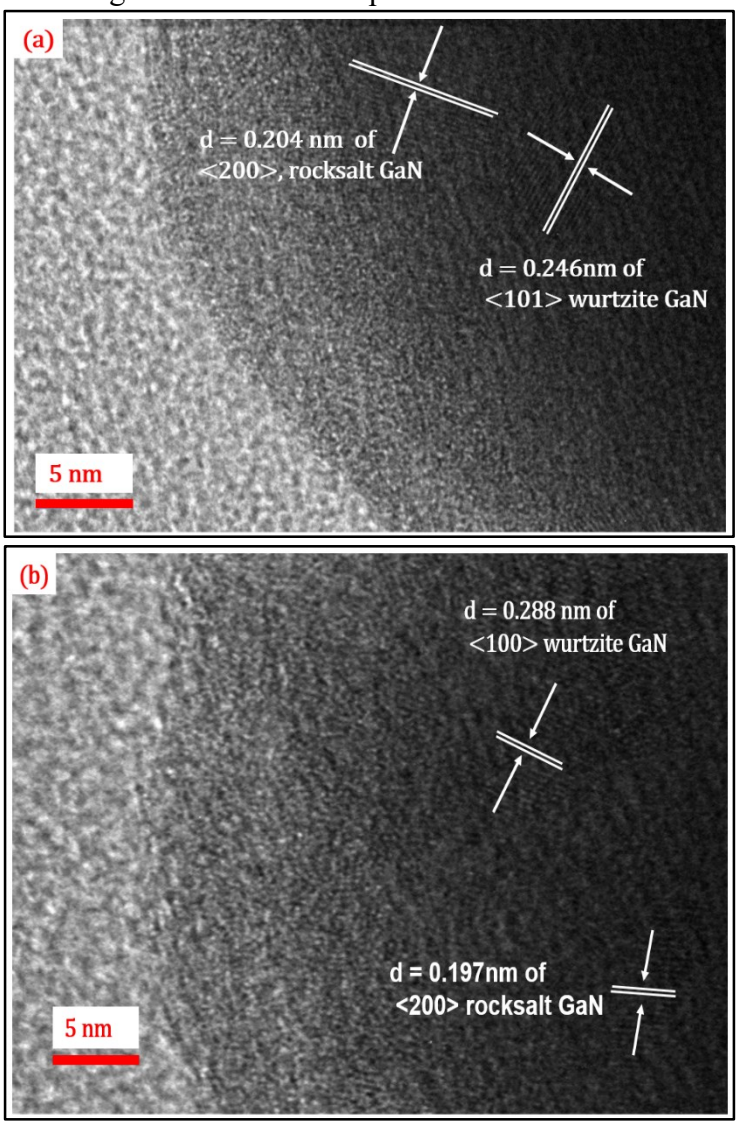

Figure 2.18. *a and b. HR-TEM image of GaN QDs, where crystallized domains of GaN cubic-NaCl and wurtzite hexagonal structures were seen. Here GaN QDs was synthesized using pre-heater system with a precursor concentration of* $17.5 * 10^{-3} M$ *in the millireactor.*

The elemental mapping of the GaN nanomaterials is obtained through Energy Dispersive X-Ray Spectroscopy (EDS). The obtained elemental mapping image is depicted in Figure 2.19.

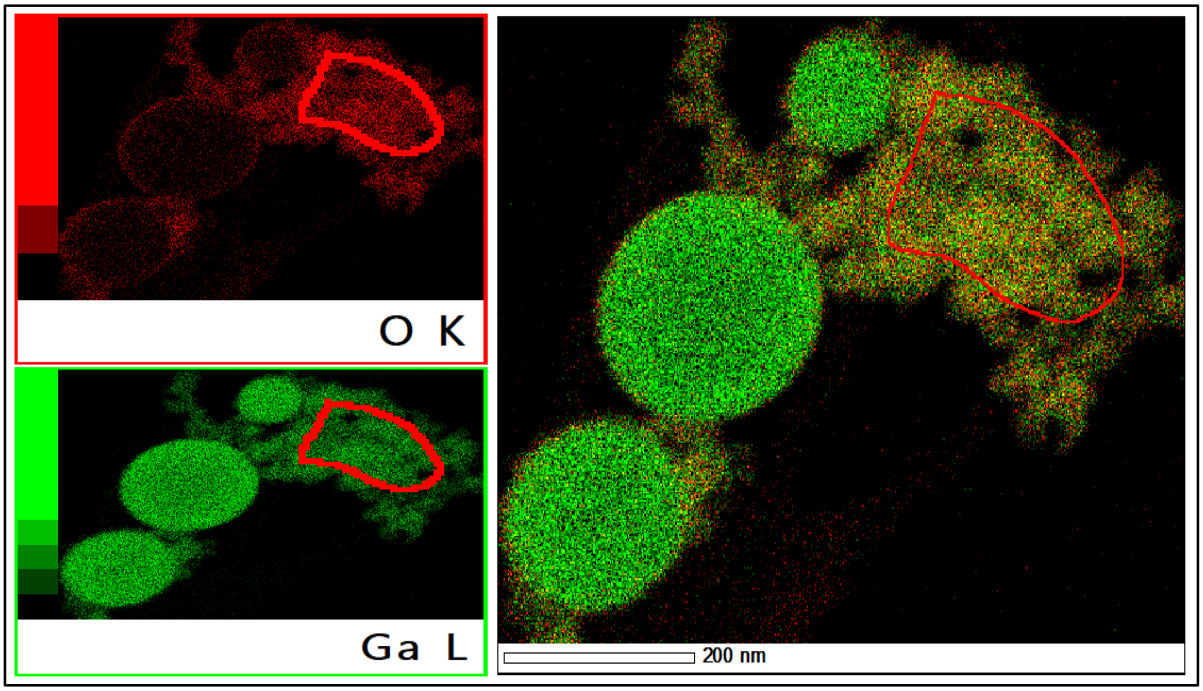

Figure 2.19. *Elemental mapping of GaN nanomaterials synthesized through the pre-heater fixed supercritical millireactor, obtained through EDS technique, where the red imaging corresponds to the oxygen and green to the gallium atoms.*

From the elemental mapping analysis obtained by EDS technique, it became very obvious that the surface of the GaN nanomaterials ensemble possessed oxygen atoms. These oxygen atoms are physically or chemically bonded to the surface of these nanomaterials, when being exposed to open atmosphere during the sample preparation. The presence of these oxygen impurities indicates that they are many non-passivated dangling orbitals or bonds are present on the surface of the GaN nanomaterials, which can therefore be occupied by oxygen atoms. These non-passivated sites could be mostly due to nitrogen vacancies. Since the nitrogen signal in elemental mapping analysis is weak and not accurate, it is not being displayed in Figure 2.19. In order to elucidate the nature of GaN QDs surface more accurately and to reveal the level of impurity and the bonding present within the inside of the GaN nanomaterials, XPS and surface etched XPS analysis were carried out.

2.5.2.2. Surface characterization

The surface chemistry of the GaN QDs was characterized by XPS (X-Ray Photoelectron Spectroscopy). To perform XPS analysis under ultra-high vacuum, the samples were recovered from the dispersed solution and dried for several hours at ambient conditions. The recorded XPS survey of the GaN nanomaterials synthesized by pre-heater supercritical millireactor with precursor concentration of $17.5 * 10^{-3}$M in the millireactor is depicted in Figure 2.20.

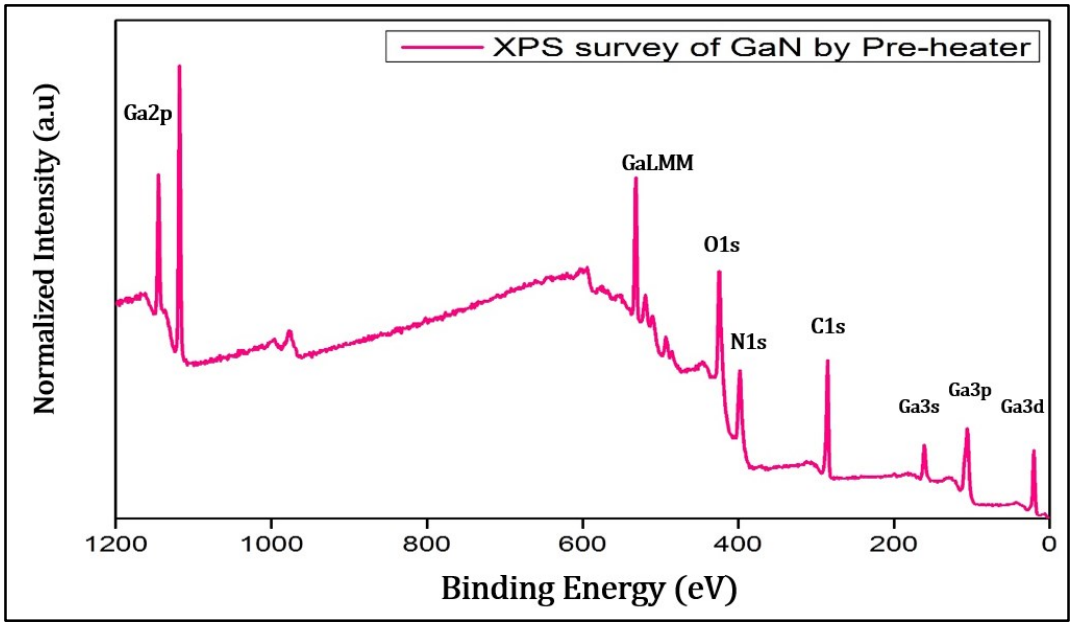

Figure 2.20. *XPS survey of the GaN QDs synthesized by the pre-heater supercritical millireactor with precursor concentration of* $17.5 * 10^{-3} M$.

The recorded XPS survey depicted in Figure 2.20 shows the presence of Ga, O and C chemical elements, in addition to nitrogen.

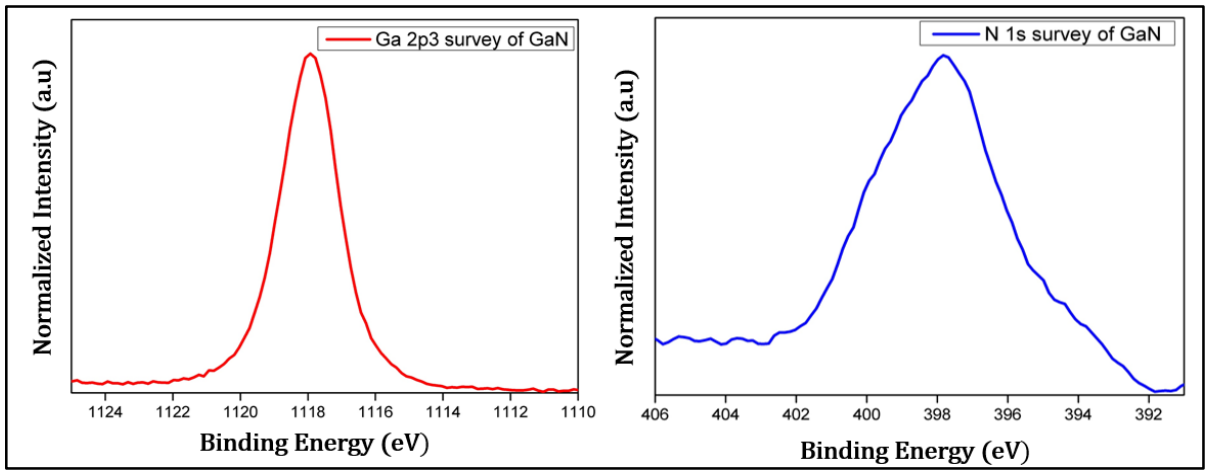

Figure 2.21. *a and b. Ga 2p3 and N 1s XPS spectra of the surface of GaN nanomaterials.*

The $Ga\ 2p_{3/2}$ maximum peak at 1117.9 eV (see Figure 2.21-a) reveals some Ga_2O_3 bonding. As $N\ 1s$ is overlapped with the $Ga\ LM1$ Auger line (see Figure 2.21-b), no conclusion concerning the presence of nitrogen can be directly drawn. Carbon and oxygen are due to the contamination of the nanomaterials when exposed to atmosphere and mainly due to post processing of the nanomaterials (centrifugation, dipersion in fresh solvent, etc.).

In order to reveal the sub-surface nature of the GaN nanomaterials, depth profiling was carried out to etch the contaminated top layers. Etching was performed using an argon ion gun sputtering at low energy. The sputtering rate was approximatively 0.2 nm/s. At each interval

of 30 s, the etching was stopped and high resolution photoelectron spectra were recorded. In the Ga 2p3 sputtered spectra (Figure 2.22-a), the appearance of low energy component at 1116.4 eV confirms GaN bondings. The results are consistent with previously reported XPS spectra of GaN samples [100 –102].

Considering the N 1s - Ga LM1 range (Figure 2.22-b), the depth shift of the main peak from 397.8 eV to 397.1 eV can assess the presence of N 1s nitride bonding in the sub-surface as well as the component around 392 eV, characteristic of the Ga LM1 Auger line in the nitride form. In conclusion, from the XPS characterization study, it can be concluded that GaN QDs with many unsatisfied dangling bonds are synthesized. These unpassivated surface states act as bonding sites for contaminants, especially oxygen during the post processing technique.

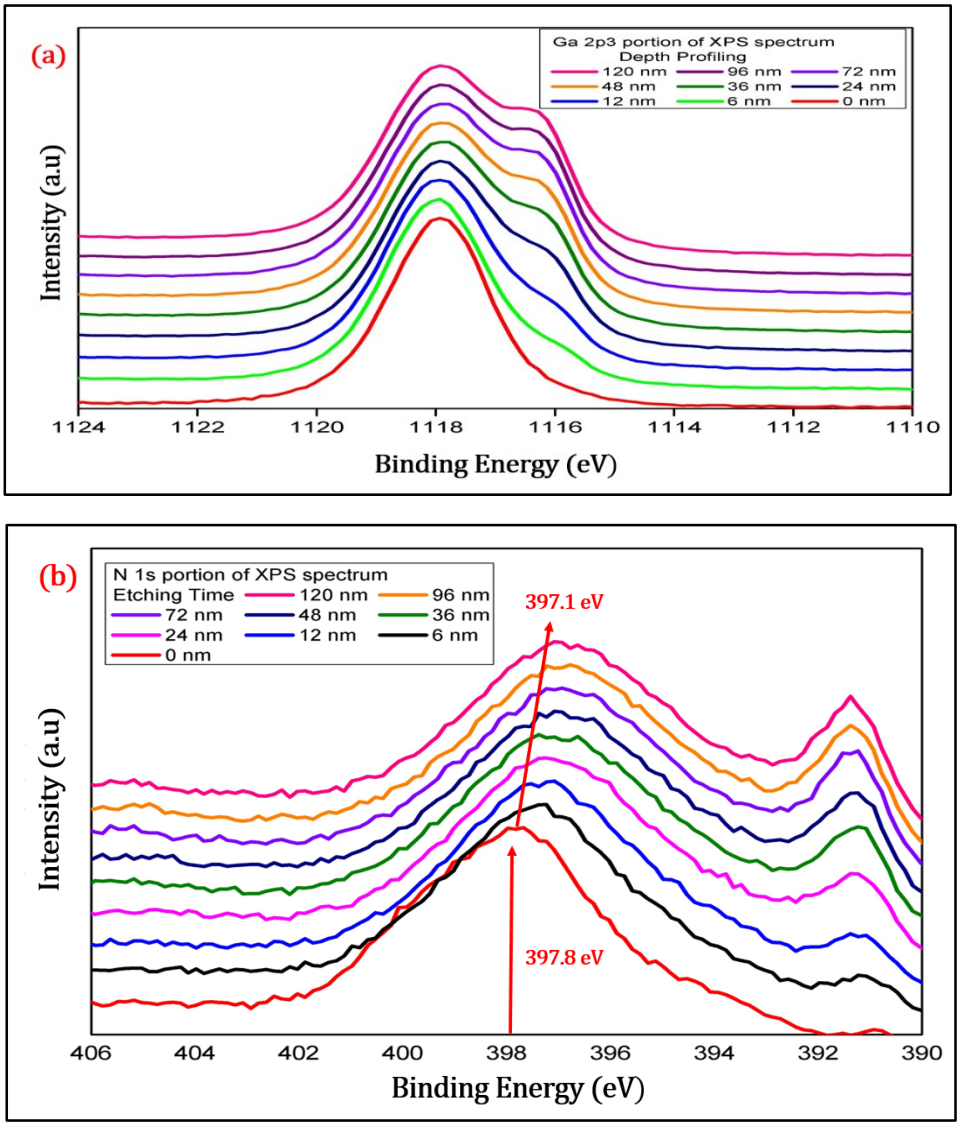

Figure 2.22. *XPS sputtered spectra of GaN nanomaterials (0s to 120 nm in depth). a. Ga 2p3 spectra; b. N 1s spectra.*

2.5.2.3. Optical characterization

The electromagnetic radiation's interaction with the synthesized nanomaterials were characterized through their optical properties. UV-VIS liquid absorption and room temperature PL emission were performed on the GaN nanomaterials.

GaN nanomaterials synthesized from the pre-heater millireactor were washed by centrifugation and dispersed in anhydrous acetonitrile for the optical study. Compared to other organic solvents like hexane, cyclohexane and toluene etc., the acetonitrile solvent allows for better dispersion of particles and less settling was seen. The liquid absorption study was performed on the GaN samples dispersed in acetonitrile solvent, resulting in an absorption spectrum depicted in Figure 2.23. The GaN nanomaterials synthesized from the pre-heater exhibited highly intense well defined peak at 302 nm. This characteristic blue shifted peak (85 nm, in Figure 2.23) compared to the bulk cubic GaN (387 nm), specifies that highly quantum confined GaN quantum dots are synthesized by this continuous flow process.

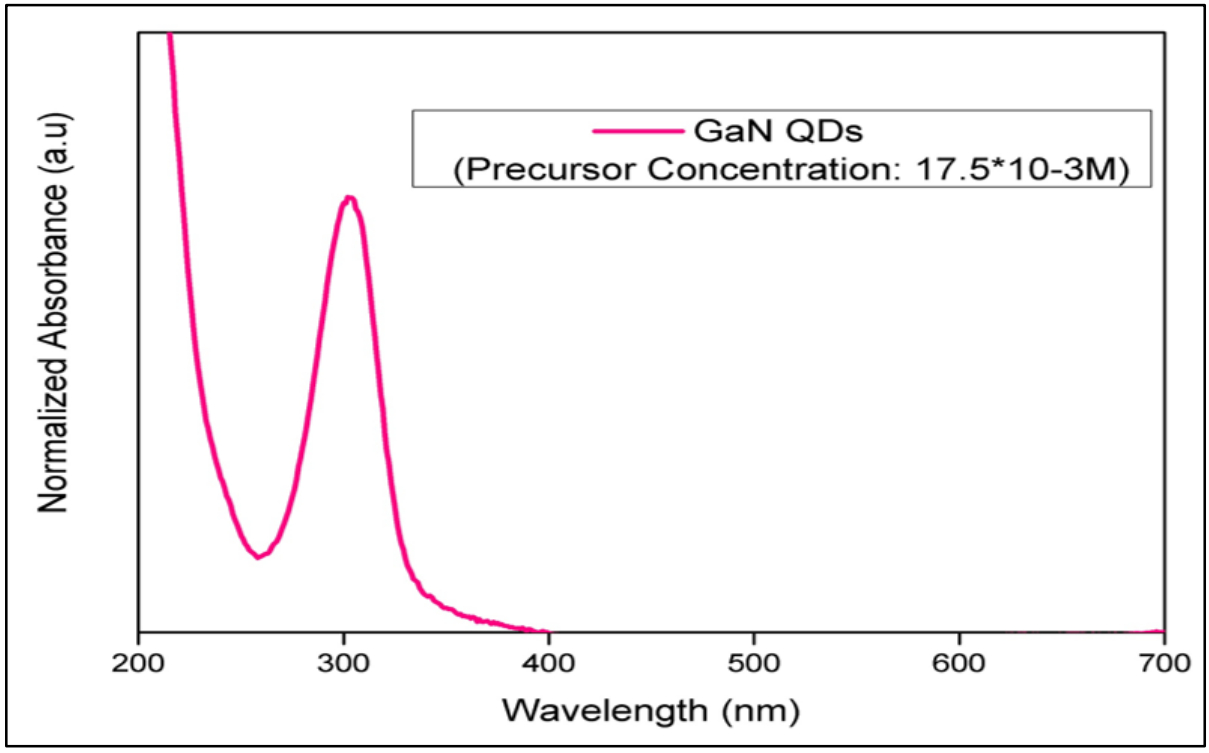

Figure 2.23. *UV-Visible absorption spectrum of the GaN nanomaterials synthesized from pre-heater fixed supercritical millireactor with precursor concentration of* $17.5 * 10^{-3} M$ *in the millireactor, dispersed in acetonitrile.*

The optical direct energy band gap of the GaN QDs was calculated by using the relationship between the absorption coefficient of the sample and the energy of the incident photon [99]:

$$\alpha hv = A(hv - E_{sample})^{n} \quad \textbf{(2.4)}$$

Where A = constant, $\boldsymbol{hv}$ = energy of the incident photon, $\boldsymbol{E_{sample}}$ = optical energy gap of the sample measured and the value of n is determined by the disposition of the electronic transition

accountable for the optical absorption. 'n' = 1/2, 2, 3/2 and 3 for direct allowed, indirect allowed, direct forbidden and indirect forbidden transitions, respectively [100]. Here in this study, n = 1/2 will be used, since GaN is a direct band gap semiconductor.

α = absorption coefficient, which can be determined from Beer lambert's law:

$$\alpha = \frac{(2.303 * \text{Absorbance})}{l} \quad \textbf{(2.4)}$$

Where 'Absorbance' values are obtained from room temperature UV-VIS absorption study of the GaN QDs. l refers to the path length (l = 1cm) in this study.

Figure 2.24, represents the plot of $(\alpha hv)^2$ vs $hv\ (eV)$ for the GaN QDs (Tauc's Plot). The optical band gap was obtained by the linear extrapolation of the Tauc's curve at the intercept of the zero y-axis ($(\alpha hv)^2 \rightarrow 0$). The optical band gap obtained using the Tauc's plot was 3.8 eV. The obtained value indicates that, highly quantum confined GaN was synthesized using the pre-heater supercritical millireactor, where the QDs are 0.6 eV and 0.4 eV blue shifted compared to the β-GaN (cubic – zinc blende) and α-GaN (hexagonal -wurtzite) with a bulk band gap of 3.2 eV and 3.4 eV, respectively [74]. This value is quite close to the band gap obtained for the GaN QDs synthesized using the co-flow system (3.77 eV).

The shift of the band energy gap is due to the size dependent quantization effect, where the relationship between the shift of the band gap, $\Delta E = (E_{QD} - E_{bulk})$ and the quantum dot size can be related under certain circumstances and assumptions. The model which proposes such a relationship is called Brus' active mass model [101 –105].

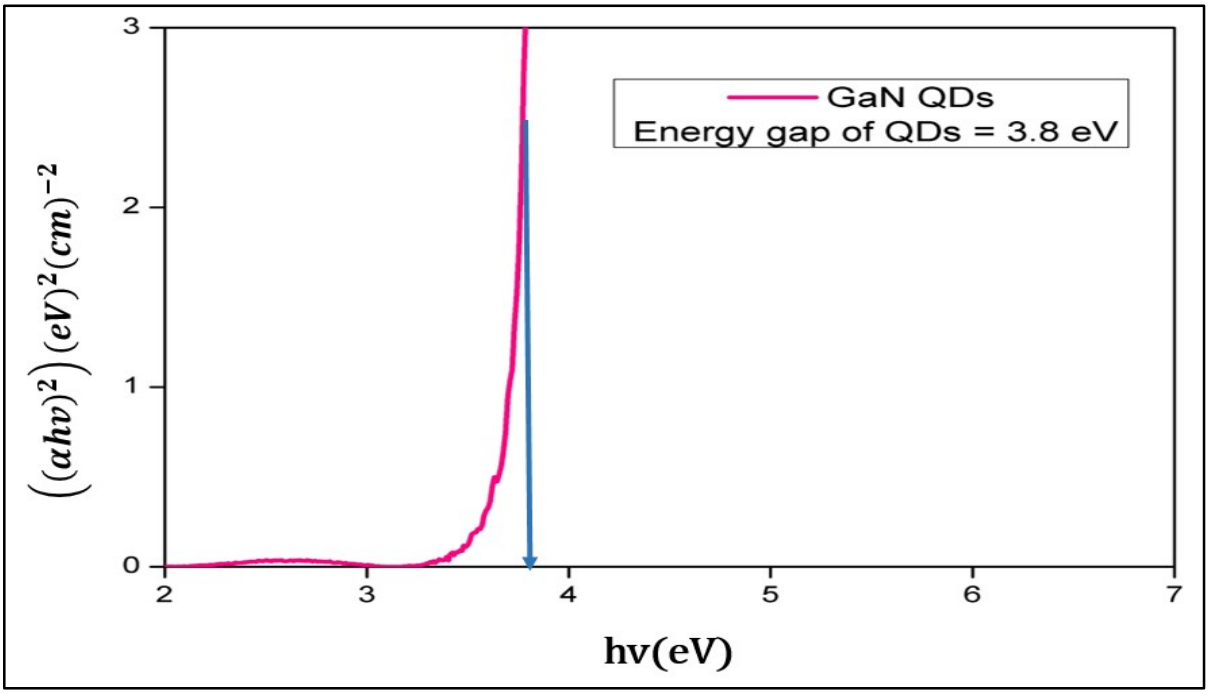

Figure 2.24. *Tauc spectrum of GaN QDs calculated from the absorption spectrum depicted in Figure 2.23.*

The radius of the spherical GaN QDs can be determined using the relationship mentioned in equation (3) [74].

$$\Delta E = \frac{h^2}{8\mu R^2} - \frac{1.786e^2}{4\pi\varepsilon_{QD}\varepsilon_O R} \quad \textbf{(2.5)}$$

Where ΔE → Energy shift in joules = 0.6*1.6021*10^{-19} J = 0.96*10^{-19} J,

h → Planck's constant = 6.626*10^{-34}J.s,

R → estimated radius of the GaN QD,

e → electron's charge = 1.602*10^{-19}C and

ε_o → Vacuum dielectric constant = 8.854*10^{-12} Fm^{-1}.

The size dependent static dielectric constant expression was used, since the $\boldsymbol{\varepsilon_{QD}}$ varies significantly for the GaN QD compared to three dimensional bulk GaN materials. ε_{QD} is calculated using equation (4) [74]:

$$\varepsilon_{QD} = 1 + \frac{\varepsilon_{3D}-1}{1+\left[\Delta E^2 / E_{QD}^2\right]} \quad \textbf{(2.6)}$$

Where, $E_{QD} = 3.8\ eV$, $\Delta E =$ 0.6 eV for zinc blende and 0.4 eV for wurtzite GaN, and ε_{3D} = 9.7 for cubic zinc blende GaN and 8.9 for hexagonal wurtzite GaN.

Here, both the zinc blende and wurtzite crystallite structure GaN QDs were considered because the powder XRD and HRTEM confirmed that GaN QDs possessed a non-uniform mixture of monocrystallites. The calculated $\boldsymbol{\varepsilon_{QD}}$ are 9.488 for zinc blende and 8.813 for wurtzite, respectively . Similarly, the μ value are calculated for the zinc blende and the wurtzite QDs, from active electron mass and active mass of hole using m_O. The m_O here refers to the electron rest mass, whose value is equal to 9.1095*10^{-31} kg. Substituting these values and solving the quadratic equation (3), the radius of GaN QDs was 14 Å. and 19.8 Å for zinc blende and wurtzite structures of GaN QDs, respectively. The values obtained here falls below the Bohr exciton radius of 2.8 nm [55, 56, 106], denoting that well quantum confined colloidal nanomaterials are synthesized. Besides these values are fitting well with the size of the crystalline coherent domains of GaN observed in the HR-TEM analysis.

Room temperature photoluminescence study was performed on the colloidal dispersion of the GaN QDs in acetonitrile solvent. Figure 2.25 depicts the PL spectra of GaN QDs excited at 300 nm with a maximum emission peak at 388 nm. The emission peak has FWHM of around 1.1 eV. The emission peak obtained here has the aslant protuberance (bump) at 331 nm near the onset of the peak and a similar sloppy bump at 463 nm. These protrusions can be attributed to surface defects present or may be due to a non-homogeneous passivation of the surface by ligands. In pre-heater study, no external ligands were added and ligands are generated from the thermolysis of the amido complex precursor itself during synthesis.

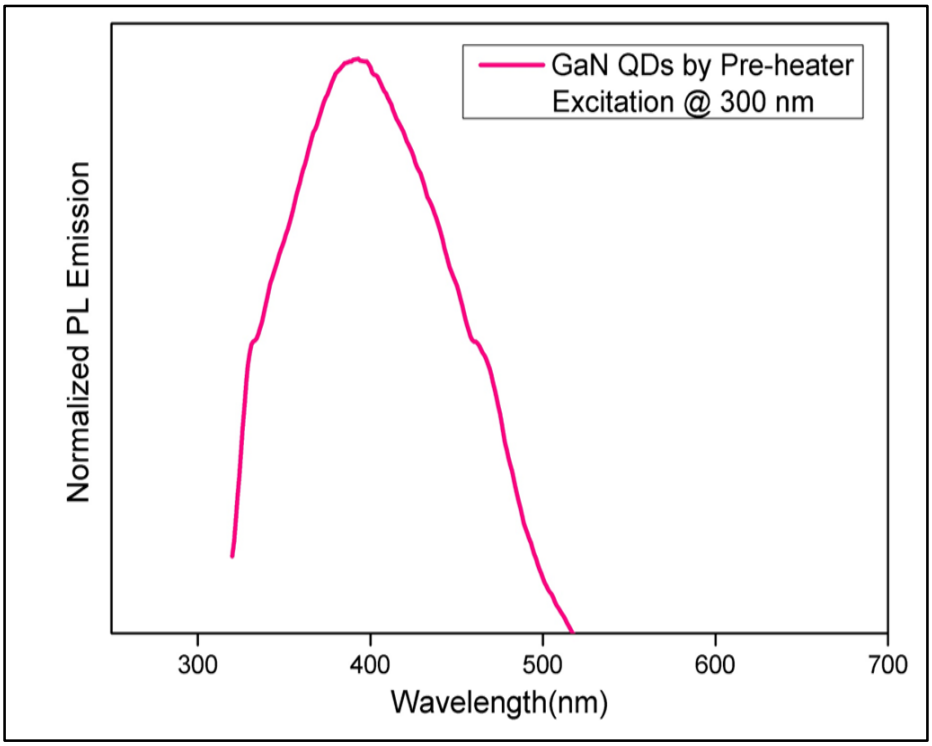

Figure 2.25. *PL emission spectra of GaN QDs (dispersed in acetonitrile) synthesized using pre-heater supercritical millireactor with precursor concentration of* $17.5 * 10^{-3} M$.

2.5.3. Conclusion

To conclude, the pre-heater supercritical millireactor yielded GaN QDs with enhanced reproducibility and increased rector's lifetime. Highly quantum confined GaN QDs are synthesized, which possessed an intense blue shift of about 0.6 eV and 0.4 eV compared to the bulk cubic zinc blende and hexagonal wurtzite GaN structure. Regarding the size distribution and the particle dispersion, compared to the co-flow technique, well dispersed GaN nanomaterials are obtained from the pre-heater setup along with spherical aggregates. More interestingly, in one set of synthesis, up to 150 mg of GaN (yield of 62%) can be synthesized continuously. The GaN QDs obtained from the pre-heater supercritical setup were employed in direct photochemical excitation study concerning the degradation of dye in the next section of the chapter.

2.6. Application of GaN in heterogeneous photocatalysis

2.6.1. Introduction

As mentioned in chapter 1, heterogeneous photocatalysis can be defined as an accelerated photoreaction in the presence of a catalyst (semiconductor material) and differs from the traditional mode of catalysis by its photonic activation instead of thermal activation. The science of heterogeneous photocatalysis involves the dual capacity of the semiconductor molecule to absorb the energy (photons or electrons) and the reactants on its surface concurrently [107]. The photons prompted chemical reactions occurs on the surface of the photocatalyst in heterogeneous photocatalysis, which discloses it into two distinct processes. Upon illumination of light on a semiconductor material dispersed in a gas or a liquid, if the reactive adsorbed substrate on the photocatalyst surface absorbs the photons and then interacts with the semiconductor material by transferring the electron, it is called catalyzed photoreaction. On the other hand, if the photocatalyst absorbs the photons and transfers the electrons to the adsorbed reactive substrate, then it called sensitized photoreaction [108, 109]. This domain consists of multitude of chemical reactions, molecular transformations and designates itself as an advanced oxidation technologies (AOT) for refining air and water processes [110, 111].

2.6.2. Heterogeneous photocatalysis for the degradation of pollutants (organic dye)

Heterogeneous photocatalytic systems employ the Advanced Oxidation Process (AOPs), which has the ability to decompose the environmental pollutants rapidly and non-selectively. AOPs are highly advantageous and attractive due to their inherent ability to completely mineralize the targeted pollutants. AOPs is completely banked on the *in situ* generation of highly reactive hydroxyl radicals ($OH^{\cdot}$), which can practically oxidize any compound present in the system. In heterogeneous photocatalytic processes, such radicals have been successfully produced upon interaction of light with the photocatalysts dispersed in the fluid matrix [107, 112 –115]. Concerning the heterogeneous photocatalytic applications in environmental remediation processes, the major studies have been carried out on the photocatalytic degradation of organic dyes in waste water streams. Such focus of the heterogeneous photocatalytic field on dye degradation is mostly due to the fact that world's water pollution is caused by the effluents of textile and dyeing industries. Around 0.1 million ton of non-biodegradable dyes are released within the ground water bodies [116]. Hence, the persistent development of heterogeneous photocatalytic processes with high efficiency is still required to address this issue of dye pollution,

Within the various heterogeneous photocatalytic systems, studied over last two decades, titanium dioxide (TiO_2) photocatalysts has been intensively used due to their potential to degrade a wide range of organic dyes. The process of the photocatalytic degradation of organic dyes in water streams employing TiO_2 or any semiconductor photocatalytic materials can be carried out by indirect or direct methods. In the former case of a direct dye degradation process,

a visible light source (λ > 390 nm) is employed for the excitation of the dye molecule from its ground state to its excited (triplet, DYE^*) state. The later interaction of excited (triplet) state of the dye with the ground state of the (TiO_2) photocatalyst results in the transfer of the electrons to the CB of the semiconductor materials. Upon electron injection, the excited dye molecule is converted to cationic dye radical (semi-oxidized form).

The electrons transferred to the CB of the photocatalysts react further to form oxidizing species like O_2^-, H_2O_2 and $OH^·$, which oxidize (degrade) the dye molecules [117 – 120], as depicted in Figure 2.26. The direct degradation process is very complex and not many researches have been carried out in this regime, especially concerning the mechanism of degradation of cationic dye molecules toward their complete demineralization. Additionally, this system doesn't involve the role of holes in the oxidation process as seen in conventional indirect process.

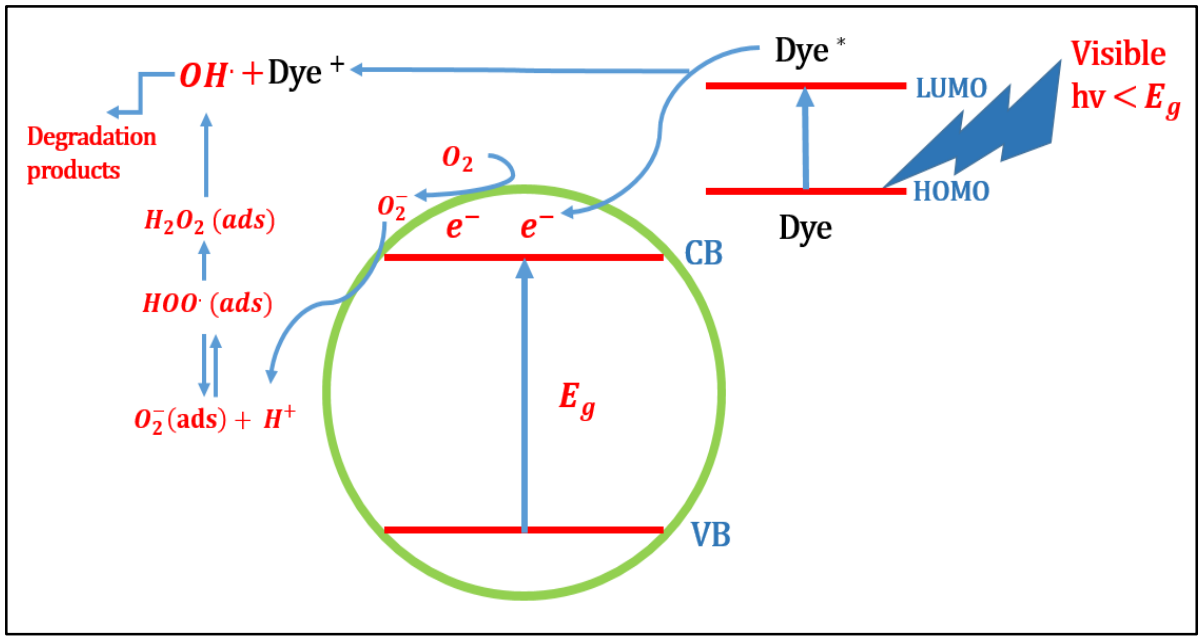

Figure 2.26. *Schematic representation of direct dye degradation process under the visible light irradiation, re-drawn based on the articles [116, 120].*

Analogously, in the latter case of indirect dye degradation, the process is activated by the photoexcitation step (mostly by UV irradiation). The photoexcitation occurs in the semiconductor photocatalyst and electrons and holes are generated in the CB and VB of the semiconductor. For instance, in the case of water, the photogenerated holes reacts with the surface bounded water molecules, resulting in the formation of radicals and this process is called ionization of water. The photogenerated electrons of the CB react with surface adsorbed oxygen molecules forming superoxide anionic (O_2^-) radicals. These get protonated, resulting in the formation of highly active hydroxyl radicals, which later reacts with dye molecules and results in produces the oxidation products [121 – 123], as depicted in Figure 2.27.

To conclude regarding the researches carried out in the dye degradation processes applied to the heterogeneous photocatalysis, the so far reported articles have concerned only in the indirect degradation process. Some researchers have found that direct degradation processes employing the TiO_2 under visible light activity is slow and more activity is being attained under UV light involving the indirect degradation process.

Galindo *et al.* carried out the photocatalytic degradation of methyl orange using powder of TiO_2 under visible and UV irradiation and found that visible light (direct) degradation is less kinetically active than UV degradation (indirect) [118]. The other remaining notable works in direct degradation process were the degradation of Orange II, Red acid and Fluorescein dye under visible light using powder $TiO_2/SiO_2/magnetic$ nanocomposite photocatalysts reported by Zhang *et al.* [117] and photocatalytic degradation of Rhodamine B (RhB) dye by TiO_2 films under visible light, reported by Ma *et al.* [119].

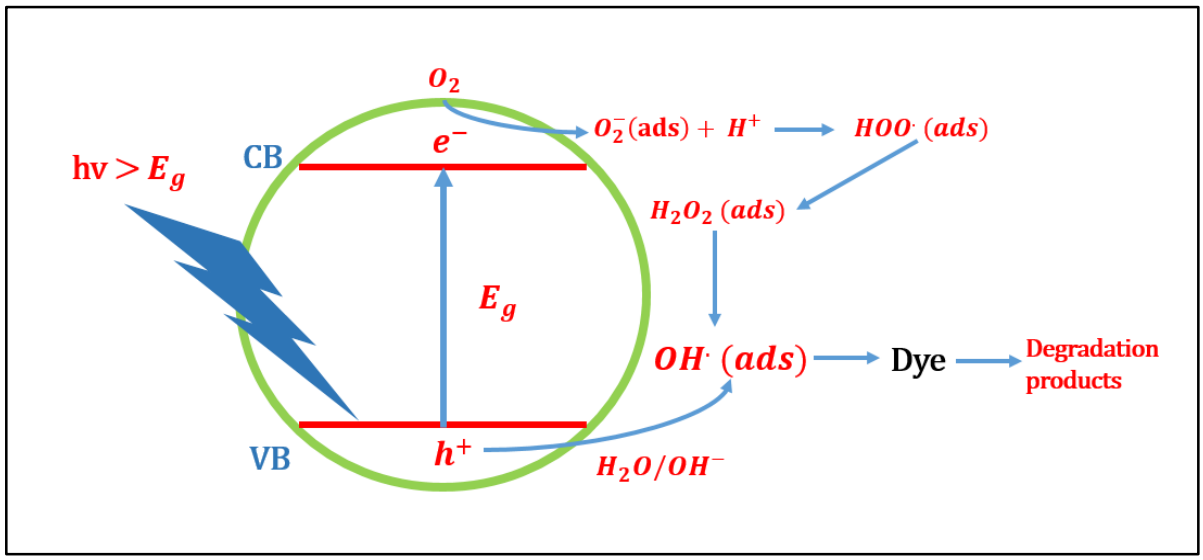

Figure 2.27. *Schematic representation of indirect dye degradation process under the UV irradiation, re-drawn based on the articles [116, 120].*

2.6.3. Direct photocatalytic degradation of Methyl Orange using GaN QDS

In this research work, the main motive of performing the direct degradation of a model dye with GaN QDs as photocatalysts is to know how effective are the GaN QDs (especially its surface) synthesized from supercritical conditions as a photocatalysts in degrading the organic dyes compared to conventional commercial available titania (Degussa P25, TiO_2) photocatalysts under visible light irradiation. This study can give insights into how the surface and surface area of the GaN QDs can render the degradation process viable under visible light irradiation, which will be useful for developing and employing solar irradiated degradation of toxic dyes.

Here, we report the photocatalytic degradation of 4-[4-(Dimethylamino) phenylazo] benzene sulfonic acid sodium salt (Orange *III* or Methyl Orange), with molecular formula $C_{14}H_{14}N_3NaO_3S$, under visible light (395 – 405 nm) using GaN QDs as photocatalysts. The structure of methyl orange is depicted in Figure 2.28.

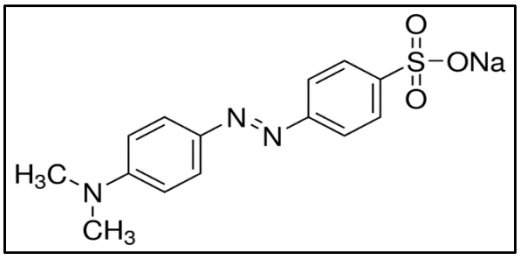

Figure 2.28. *Pictorial representation of the structure of the methyl orange dye, drawn based on the article [124].*

The crucial reason for opting the methyl orange dye as a model compound is because it belongs to the azo dye family. The azo dye constitutes the largest group of colorants used in the current dyeing and textile industry. Azo dyes are characterized by a double bond of nitrogen ($-N = N -$), where at least one of the nitrogen atom is bonded to an aromatic group, as depicted in Figure 2.28.

The activity of the GaN QDs was compared with the one of commercially available TiO_2, for the catalyzed photodegradation of dye compound. The photodegradation study was monitored using UV-Visible absorption study, where the maximum absorbance peak of the dye compound is measured.

2.6.3.1. Analytical techniques

The photocatalytic activities of the GaN QDs and the commercially available TiO_2 photocatalysts were evaluated through the direct photodegradation of Methyl Orange (MO) dye molecules. The photodegradation study is analysed through the UV-VIS absorption measurement. The concentration of the targeted dye during the photocatalytic experiment was obtained using the absorbance calibration curve.

The calibration curve was plotted by varying the concentration of the MO dye in the aqueous solution within the range 10^{-4} – 10^{-6} M, and then the absorbance values were recorded for each concentration using UV-VIS spectroscopy. The concentration of the dye was maintained in such way that the intensity of the absorption peaks varies linearly with the concentration of the solution, indicating that the absorption study follows a Beer Lambert's law. The absorption spectrum of the dye exhibited two distinctive peaks at 270 nm and 463 nm. I used the variation of intensity of the peak at 463 nm during the photocatalysis investigations. The schematic variation of the absorbance of the aqueous dye solution with varying concentration is depicted in Figure 2.29-a and the corresponding calibration curve is plotted and schematically depicted in Figure 2.29-b.

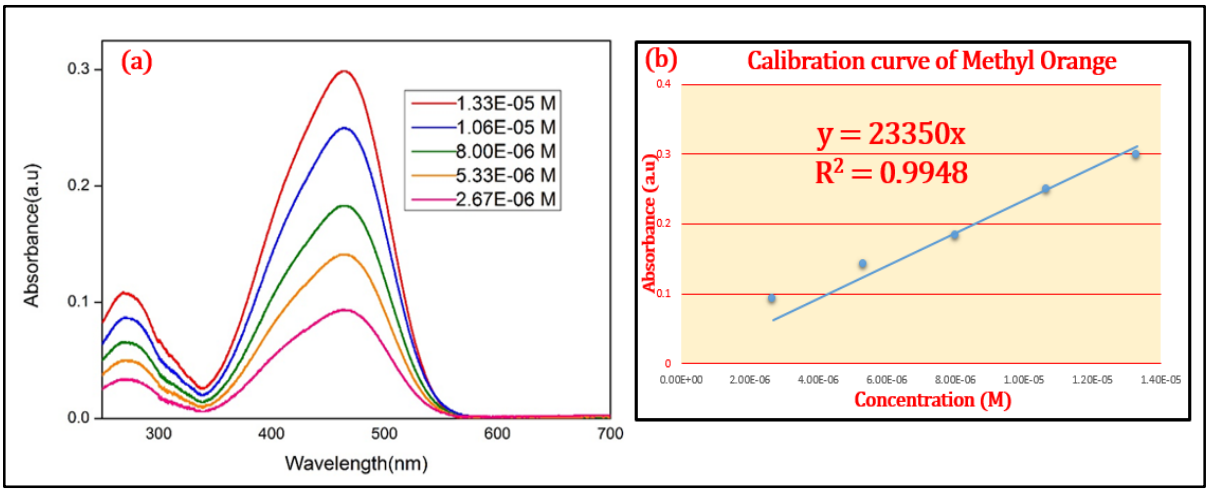

Figure 2.29. *a. Absorption spectrum of the MO dye at various concentration; b. Calibration curve plotted using the data from the corresponding absorption spectra in Figure (2.28.a).*

2.6.3.2. Photoreactor setup

The heterogeneous photocatalytic process of direct dye degradation is a triphasic system consisting of solid-liquid-gas interface. The solid is the semiconductor (GaN QDs or TiO_2 (Degussa P25)), liquid is the aqueous deionized water and the gas phase is atmospheric air used as the gas source in this study. The utilization of the photocatalyst in such a triphasic system can be achieved only in two ways: (i) suspended or (ii) immobilized in the reactor system. Suspended (slurry) photoreactor was employed in this study, as it provides high photocatalytic activity by furnishing high surface area per unit volume of photocatalysts. Thus, the suspended slurry photoreactor consists in a cylindrical glass tube fitted with a rubber septum. The suspension of photocatalyst within the photoreactor is achieved with the aid of a magnetic stirrer.

Effective illumination of visible light to such system is achieved by orienting the light source parallel to the cylindrical photoreactor in the radial direction. The orientation of the LED lamps is parallel to the vertical cylindrical reactor, it is placed external to the reactor system and provides uniform and radial illumination. This kind of radial arrangement was found to be an effective one for operating such small volumes of slurry photoreactor. The effective uniform, radial and parallel illumination attained in our work can be visualized in Figure 2.30.

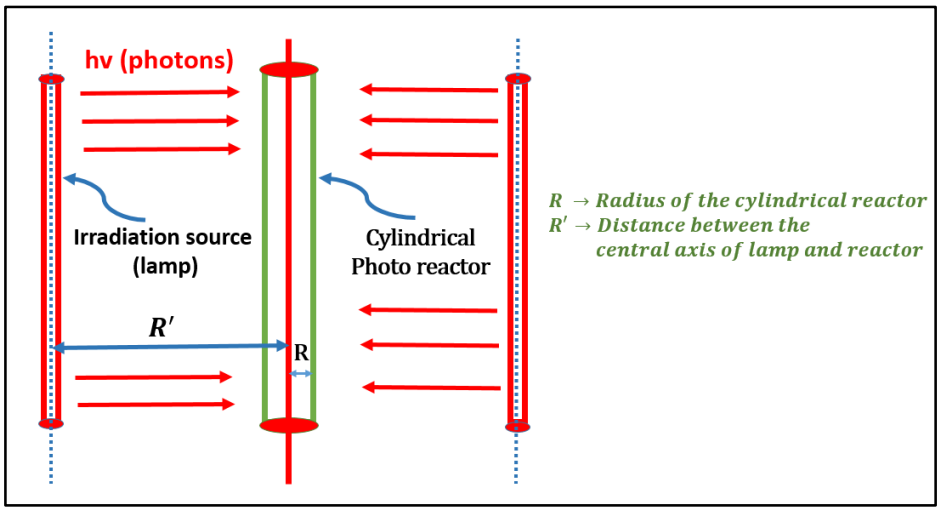

Figure 2.30. *Schematic representation of orientation of parallel and radial arrangement of light source (LED) with respect to cylindrical photoreactor, where the light source is placed external to the system. This diagram was redrawn based on the articles [125, 126].*

The photoreactor consists of a hallow cylindrical (outer) vessel of 9 cm inner diameter and 10.5 cm in height. The inner surface of the vessel is coated with a highly reflective aluminium tape and LED strips are used as visible light source here (24 W, 3.5 m long LED strips) by coiling (radially) on the inner side of the cylindrical box consisting of around 200 LEDs. The LEDs emit a purple light with a maximum intensity at 400 nm (395 – 405 nm).

Photoreactor was made up cylindrical glass vessel fitted with rubber spectrum. The reaction vessel was 9 cm in height and 1 cm in diameter. It is positioned in the centre of the hollow cylindrical vessel in such way that LEDs are equidistant from the cylindrical glass reactor (4 cm). The top of the system is covered with non-attachable lid, through which the photoreactor can be fixed. A gas balloon is fitted to the rubber septum and depending on the type of reaction, gas in the balloon can be varied. Here, for the photocatalytic degradation process, the balloon is filled with air.

The entire alignment of the photoreactor and the LEDs are made in such a way that cylindrical photoreactor with parallel light source arrangement is attained. This way, the cylindrical reactor is exposed to equivalent quantity of photons in all directions. A schematic and pictorial representation of the photocatalytic setup is depicted in Figures 2.31-a and 2.31-b. In the bottom of photocatalytic setup, an airline (air flow at 4 - 6 bar pressure) is connected to ensure maintaining the constant temperature during the experiment.

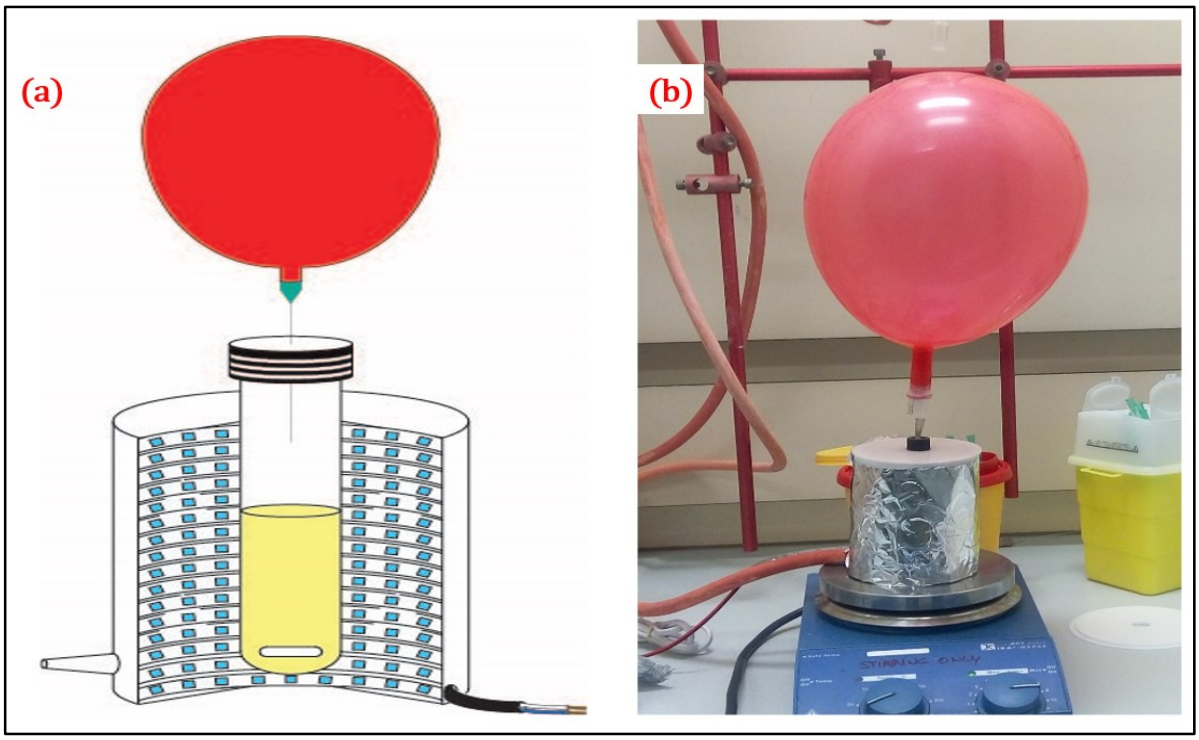

Figure 2.31. *a. Schematic depiction of the heterogeneous photocatalytic setup, illustrating the parallel and radial orientation of LED strips; b. Pictorial representation of the photocatalytic setup, placed on the magnetic stirrer for attaining effective suspension of the nanophotocatalysts.*

2.6.3.3. Experimental section of the photocatalytic experiments

In each typical experiment, 3 mg of photocatalysts were added to a 5 mL aqueous solution of Methyl orange (MO) ($8.3 * 10^{-5} M$) and placed within a magnetically stirred photoreactor vessel. The system is little bit pressurized by installing a balloon of air at the top of the reactor through a syringe needle. The system was first stirred for 10 minutes in the dark so that the adsorption-desorption equilibrium of the reactive molecules on the catalysts surfaces is attained. The LEDs are then switched on and the degradation of the dye is visualized through the decolouration of the solution, rate of which is determined by measuring the absorbance of the dye at λ_{max} = 463 nm, through UV-visible spectroscopy. In order to systematically evaluate the degradation efficiency, aliquots are taken from the reactive system at regular intervals. They are centrifuged at 10,000 RPM for 10 minutes twice and the photocatalyst is removed. The resulting supernatant solution is subjected to UV-Vis absorption spectroscopy.

2.6.3.4. Results and discussion

As mentioned before, aliquots were taken at specified time intervals, after the LEDs were turned on. The corresponding UV-VIS absorption spectra were obtained after centrifugation (Figure 2.32). The MO dye displays two distinctive absorption peaks at 273 nm and 463 nm. The peak at 463 nm is due to the chromophore azo group ($-N = N -$) and at 273 nm is due to the $\pi \rightarrow \pi^*$ transitions occurring in the aromatic ring [127].

In the GaN photocatalytic study, the degradation of the dye happens through the destruction of this azo group resulting in the decolourization of the aqueous photocatalytic suspension during the photocatalytic process. The complete decolourization of the sample happens within one-hour illumination of visible light. This photocatalytic degradation process can be visualized in Figure 2.32. Where the absorbance at 463 nm gets decreased with increase illumination time. From this photocatalytic degradation study involving highly quantum confined GaN QDs (absorption band edge at 302 nm), the heterogeneous photocatalytic process has occurred completely through direct degradation process, as the illumination source emit photons at (λ_{max} = 400 nm) smaller than the band gap of the photocatalysts (302 nm).

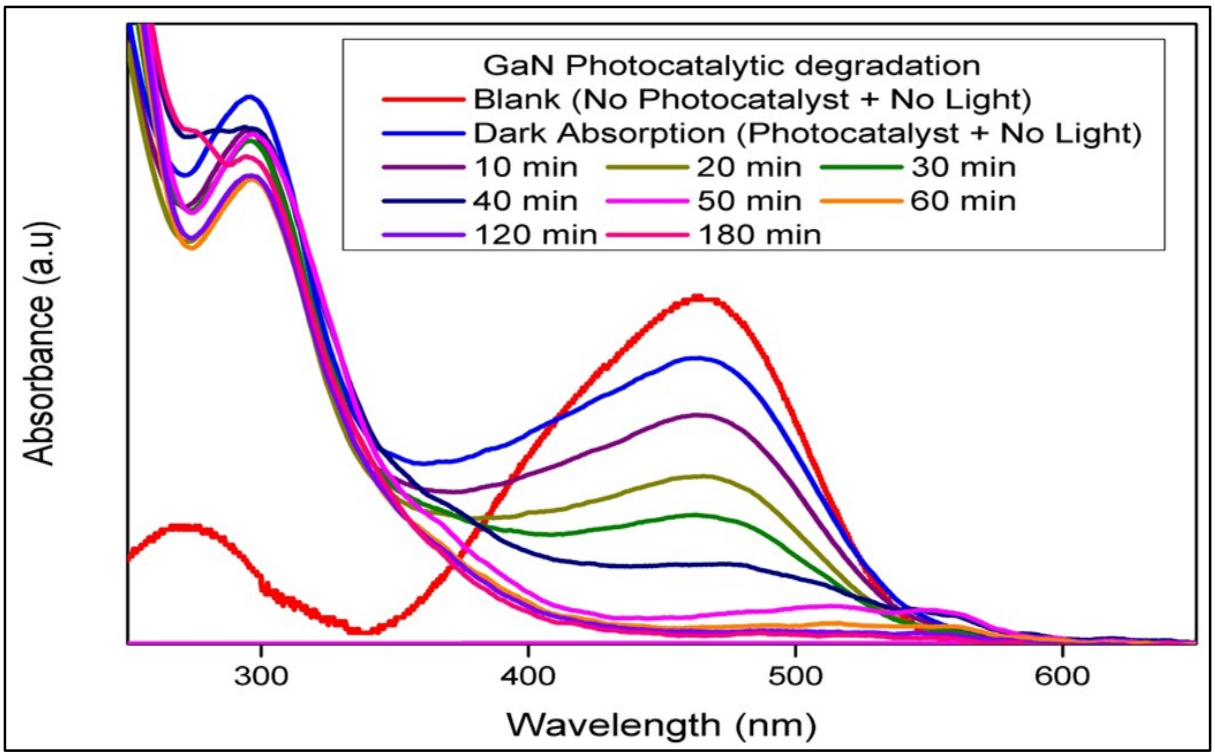

Figure 2.32. *UV/VIS absorbance spectrum of aliquots of aqueous MO dye suspension taken at different times during the GaN photocatalytic degradation of MO.*

The chromophore azo group is completely degraded (confirmed by decreases of absorbance of dye at 463 nm). Contrastingly, the absorbance around 273 nm has not decreased and has been constantly increasing with illumination time. This is because the illumination source is in the visible region ($\lambda_{max} = 400nm$) and no absorption has occurred in that region (around 273 nm), which could have resulted in no electron injection into the semiconductor particles from the degraded smaller aromatic group.

The same photo catalytic study was carried with commercial TiO_2 (Degussa P25) photocatalysts and the corresponding absorption spectrum are depicted in Figure 2.33. Compared to GaN heterogeneous photocatalytic degradation of MO dye, the photocatalytic activity of commercial TiO_2 was very slow and even after 3 h of illumination to light source, no complete degradation of the dye was noticed. This was visually observable as the suspension still exhibited an orange-yellow color (at the end of 3 h of photocatalytic process), which can

also be inferred from the absorbance spectrum of TiO_2 photocatalyzed MO degradation aliquots taken at different times, as depicted in Figure 2.33. Interestingly, in the heterogeneous photocatalysis employing TiO_2 photocatalyst, the concurrent decrease of both the MO peaks at 273 nm and 463 nm was observed indicating that oxidation (destruction) of both ($-N=N-$) group and the π bonds in the aromatic rings is also happening in the photocatalytic process. The probable reason for such a degradation is because in TiO_2 photocatalysis both the direct and indirect degradation mechanism occurs. The commercial TiO_2 photocatalysts has a crystalline mixture of 78% anatase and 14% rutile phase of TiO_2 and the remaining corresponds to amorphous titania. The anatase crystalline particles exhibit absorption in the near visible region (3.2 eV or 387 nm) while the Rutile ones have a band gap in the visible region (3 eV or 413 nm). Since our light source has maximum emission at 400 nm, the rutile phase has the tendency to perform the indirect degradation process but on an overall picture direct degradation is more prevalent in this case due to the large amount of anatase TiO_2 nanomaterials. Even though both the mechanisms of dye degradation occurs within the TiO_2 photocatalysis, its activity is very low compared to GaN QDs, which degrade the dye through direct degradation method.

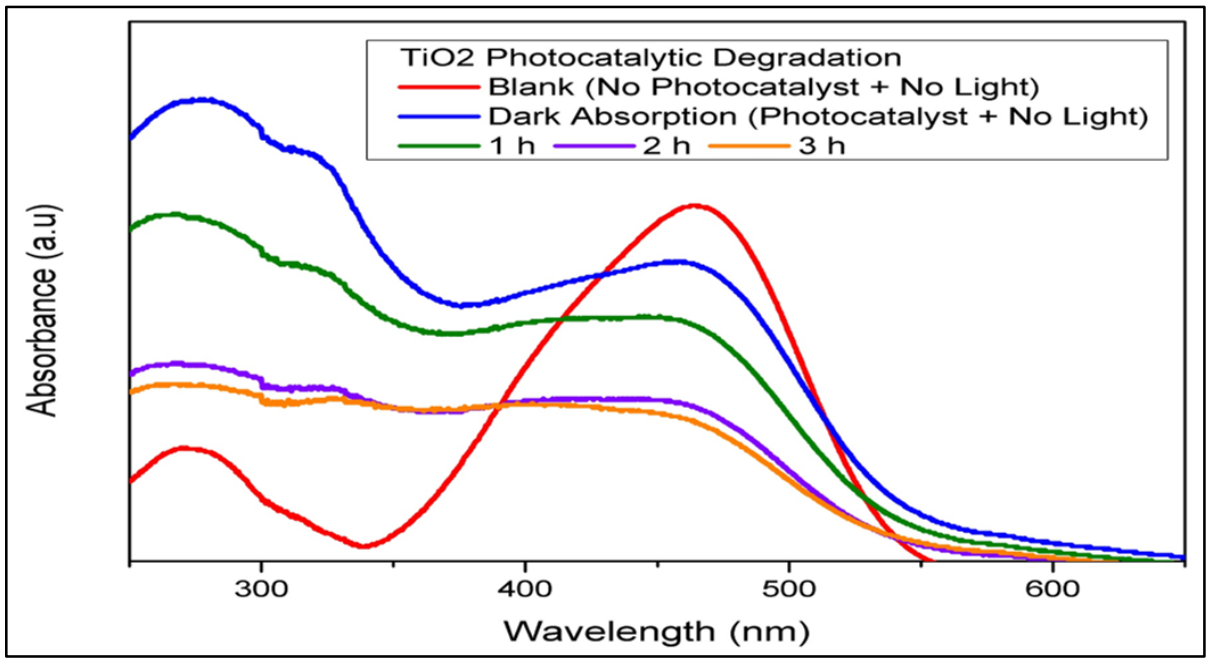

Figure 2.33. *UV/VIS absorbance spectrum of aliquots of aqueous MO dye suspension taken at different times during the TiO_2 photocatalytic degradation of MO.*

The photocatalytic experiment for blank samples was also carried out for the total period of three hours, for blank samples (without photocatalysts and light) no degradation of dyes was observed. The photocatalytic mixture with (Dye + photocatalysts (GaN or TiO_2)) negligible degradation (5 -10%) was observed without light after a period of 3 h. The degradation efficiency of the MO dye in this heterogeneous photocatalytic process can be calculated using Equation 2.8 [128].

$$\text{Degradation efficiency (\%)} = \frac{C_O - C}{C_O} * 100 \qquad \textbf{(2.8)}$$

Where C_O is the equilibrium concentration and C is the concentration of the dye molecule (aliquot) taken at time, t. In this study, it was found that the GaN QDs system exhibited 94% of dye degradation after one hour of illumination, which is 18 times higher than the degradation efficiency exhibited by commercial TiO_2 photocatalysts (18% for one hour illumination). Meanwhile the titania reached a maximum 50% degradation efficiency after 3 hours of illumination, as depicted in Figure 2.34. This dye degradation efficiency, confirms that GaN QDs synthesized by supercritical pre-heater method have excellent photocatalytic properties.

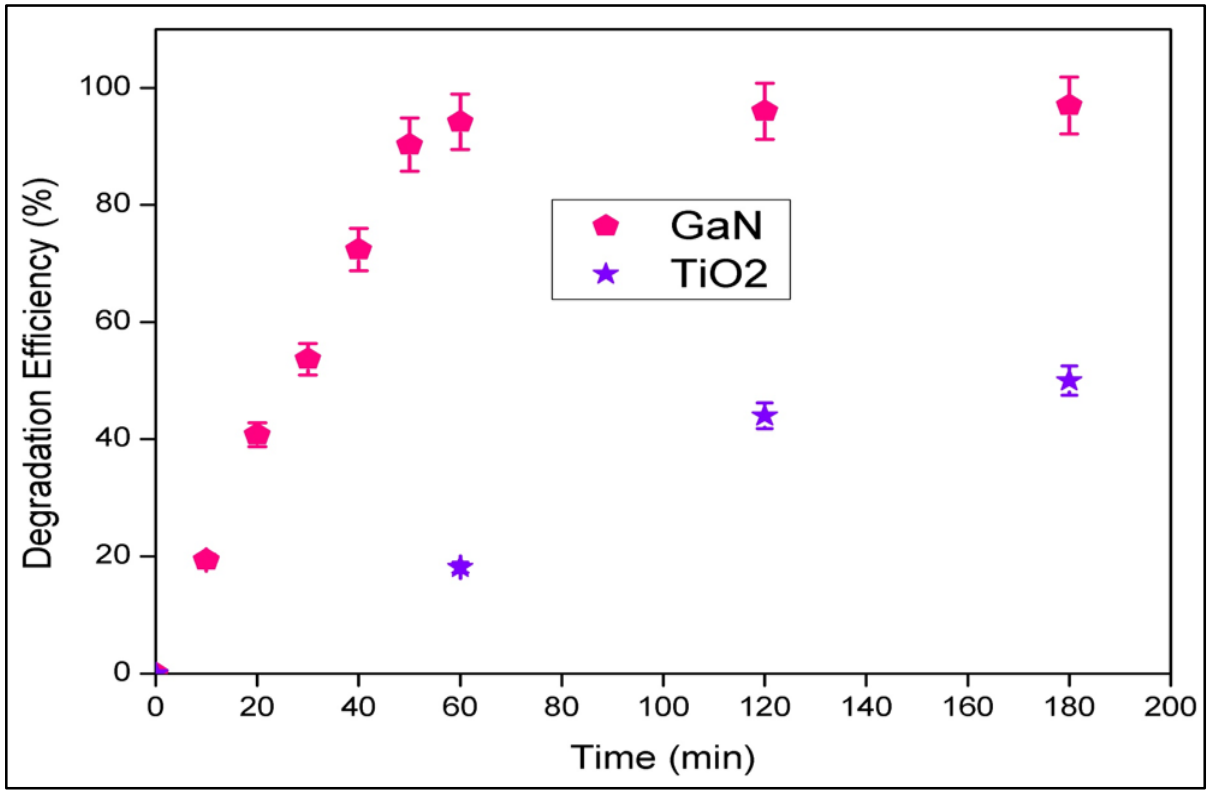

Figure 2.34. *Photocatalytic degradation of MO dye for GaN or TiO_2 photocatalysts (MO = 8.3 $*$ $10^{-5}M$, photocatalysts dosage = 3 mg and illumination duration = 180 min).*

2.6.4. Conclusion of the photocatalytic study

To conclude, there can be several reasons attributed to the enhanced photocatalytic behaviour of GaN QDs compared to the commercially available TiO_2 (Degussa, P25) nanomaterial photocatalysts. Since the degradation of the dye takes place through direct photochemical excitation or catalyzed photoreaction, where the primary process is the electron injection from the dye molecule to the semiconductor material, the superior photocatalytic behaviour of the GaN QDs is predominantly due to the higher or faster electron injection process from the dye to the GaN photocatalysts compared to the TiO_2 systems.

The reasons for the occurrence of faster electron injection in GaN QDs are:

- The GaN QDs size is small (2.8 ± 0.7nm) compared to the TiO_2 (Degussa, P25) (21 nm). Due to this small size, the GaN QDs possess more surface area than TiO_2, resulting in more adsorption of reactant molecules per unit time.

- Since the number of active sites (vacant sites) directly depends on the surface area, as GaN QDs possess more surface area it has more active sites for enhanced electron injection and photocatalytic process.

- The unique distinctive set of size alignment of GaN QDs (spherical aggregates + well dispersed small colloidal nanocrystals) could favour effective photon absorption or photon entrapment and enhanced light scattering (Mie Theory) resulting in enhanced excitation of the surface-bounded dyes. The Mie scattering effect can happen in a large scale in this ensemble of GaN QDs, as the conglomeration of spherical aggregates of one or two spherical aggregates size are in the order of magnitude of the wavelength of the light source used in this photocatalytic study. Such a phenomenon scatters light in the forward direction in the form of an antenna lobe with higher intensity, resulting in the decrease of path length of light between the neighbour particles, thus boosting the effective light utilization over the spheres.

- Another major reason for the effective electron injection into the GaN QDs is due to the reduced band bending effect compared to the TiO_2 photocatalysts. As explained before in this chapter, GaN is intrinsically a n-type semiconductor without any doping, likewise TiO_2 photocatalysts is also intrinsically a n-type semiconductor at ambient conditions [130]. Due to the n-type behaviour, both the semiconductor exhibit upward band bending phenomenon on interaction with dye molecules. Due to this band bending, tunnelling of electrons in the space charge layer on the semiconductor surface occurs, resulting in quenching the electrons from the excited dye molecule by recombination into its ground state instead of getting transferred to the reactant molecules. Since GaN QDs has a small size, the band bending effect is reduced compared to the titania molecules. Thus promoting the effective electron injection from dye to semiconductor, resulting in enhanced photocatalytic activity.

Finally, GaN QDs consist of a mixture of hexagonal-wurtzite, cubic-zinc blende/rocksalt structured nanocrystalline particles. Due to this characteristic, the entire ensemble of suspension possesses anisotropic properties resulting in enhanced transport of electrons from the GaN's surface to surface-bounded oxygen for forming the reactive radical species. Therefore, the GaN QDs synthesized at supercritical conditions possess better photocatalytic behaviour than the commercial photocatalysts due their novel shape, size, interesting structural orientation or arrangement in the liquid phase and mixture of GaN nanomaterials crystallized in different crystal structures (wurtzite, zinc blende and rocksalt). These highly beneficial novel features are achieved by the successful synthetic conjunction of single source tris (dimethyl amido)-gallium(III) precursor and pre-heater continuous supercritical millireactor.

2.7. Conclusion

To summarize, the entire research work of this chapter was concentrated on synthesizing highly active GaN QDs photocatalysts. The research accomplishments done in this chapter include:

(i) The identification of drawbacks in the previously reported co-flow supercritical continuous millireactor system,
(ii) The evolution of a new novel continuous system through the simulation of supercritical conditions in millireactors hinged with different mixers (co-flow or pre-heater),
(iii) The fabrication of a novel pre-heater supercritical millireactor for the synthesis of GaN QDs,
(iv) The successful synthesis of GaN QDs with higher throughput (100 -150 mg of GaN QDs per synthesis produced in 33 s of residence time),
(v) The newly designed millireactor system furnished enhanced reproducibility and long reactor's lifetime than the previously reported systems,
(vi) The designed system can be up scaled to a precursor concentration of 10^{-2} M or mole/L in the millireactor,
(vii) Regarding the photocatalytic research regime, a direct dye degradation study was performed on GaN QDs,
(viii) The as-synthesized GaN QDs exhibited better photocatalytic performance than the commercially available TiO_2 (Degussa, P25),
(ix) The GaN QDs exhibited enhanced degradation of organic pollutants with 94% degradation efficiency within one hour irradiation, which is 18 times higher in efficiency than the TiO_2 (Degussa, P25) system.

Eventhough the GaN QDs possess such an advantageous feature for direct photochemical excitation in heterogeneous photocatalysis, it is not photocatalytically active in the visible region to perform indirect photochemical excitation or photosensitized reaction involving the synthesis of organic molecules or general C-C bond formation, due to its wide band gap (3.8 eV). This binary GaN QDs can be rendered visible active by engineering its band gap by combining it with narrow group-III nitrides resulting in the formation of ternary solid solution photocatalysts. The next chapter will elaborately deal with the synthesis of visible light active GaN based solution nanomaterials and its applications in heterogeneous photocatalysis involving indirect excitation method for the synthesis of organic molecules.

References

[1] A. Cruz-López *et al.*, “Synthesis and characterization of gallium nitride nanoparticles by using solvothermal-soft-chemical methodology,” *Mater. Sci. Semicond. Process.*, vol. 30, pp. 435–441, 2015.

[2] D. Andiwijayakusuma, M. Saito, and A. Purqon, “Density functional theory study : Electronic structures of RE:GaN in wurtzite G $_{\alpha 15}$ RE $_{1}$ N $_{16}$,” *J. Phys. Conf. Ser.*, vol. 739, p. 12027, 2016.

[3] T. Lei, T. D. Moustakas, R. J. Graham, Y. He, and S. J. Berkowitz, “Epitaxial growth and characterization of zinc-blende gallium nitride on (001) silicon,” *J. Appl. Phys.*, vol. 71, no. 10, pp. 4933–4943, 1992.

[4] I. Vurgaftman, J. R. Meyer, and L. R. Ram-Mohan, “Band parameters for III-V compound semiconductors and their alloys,” *J. Appl. Phys.*, vol. 89, no. 11 I, pp. 5815–5875, 2001.

[5] P. Review, T. Van Vechten, and V. Vechten, “High pressure structure of gallium nitride: Wurtzite to rocksalt phase transition,” vol. 47, no. 19, pp. 925–928, 1993.

[6] E. V Dirote, *Nanotechnology at the leading edge*. 2006.

[7] Y. Xie, Y. Qian, S. Zhang, W. Wang, X. Liu, and Y. Zhang, “Coexistence of wurtzite GaN with zinc blende and rocksalt studied by x-ray power diffraction and high-resolution transmission electron microscopy,” *Appl. Phys. Lett.*, vol. 69, no. 3, pp. 334–336, 1996.

[8] C. H. Hong, D. Pavlidis, S. W. Brown, and S. C. Rand, “Photoluminescence investigation of GaN films grown by metalorganic chemical vapor deposition on (100) GaAs,” *J. Appl. Phys.*, vol. 77, no. 4, pp. 1705–1709, 1995.

[9] P. Das and D. K. Ferry, “Hot electron microwave conductivity of wide bandgap semiconductors,” *Solid State Electron.*, vol. 19, no. 10, pp. 851–855, 1976.

[10] P. E. Van Camp, V. E. Van Doren, and J. T. Devreese, “High pressure structural phase transformation in gallium nitride,” *Solid State Commun.*, vol. 81, no. 1, pp. 23–26, 1992.

[11] H. Amano, M. Kito, K. Hiramatsu, and I. Akasaki, “P-Type Conduction in Mg-Doped GaN Treated with Low-Energy Electron Beam Irradiation (LEEBI)\n,” *Jpn. J. Appl. Phys.*, vol. 28, no. Part 2, No. 12, pp. L2112–L2114, 1989.

[12] W. Kim *et al.*, “Mg-doped p-type GaN grown by reactive molecular beam epitaxy Mg-doped p -type GaN grown by reactive molecular beam epitaxy,” vol. 559, no. 1996, pp. 1–4, 2015.

[13] S. Lany and A. Zunger, “Dual nature of acceptors in GaN and ZnO: The curious case of the shallow MgGadeep state,” *Appl. Phys. Lett.*, vol. 96, no. 14, 2010.

[14] B. Monemar *et al.*, “Evidence for two Mg related acceptors in GaN,” *Phys. Rev. Lett.*, vol. 102, no. 23, pp. 10–13, 2009.

[15] J. L. Lyons, A. Janotti, and C. G. Van De Walle, “Shallow versus deep nature of Mg acceptors in nitride semiconductors,” *Phys. Rev. Lett.*, vol. 108, no. 15, pp. 1–5, 2012.

[16] Z. Liu *et al.*, “Impurity resonant states p-type doping in wide-band-gap nitrides,” *Sci. Rep.*, vol. 6, no. January, pp. 1–8, 2016.

[17] D. Bisi *et al.*, “Kinetics of Buffer-Related R ON -Increase in GaN-on-Silicon MIS-HEMTs,” *IEEE Electron Device Lett.*, vol. 35, no. 10, pp. 1–3, 2014.

[18] C. Ostermaier *et al.*, “Reliability investigation of the degradation of the surface passivation of InAlN/GaN HEMTs using a dual gate structure,” *Microelectron. Reliab.*, vol. 52, no. 9–10, pp. 1812–1815, 2012.

[19] B. H. Chu *et al.*, “Aluminum gallium nitride (GaN)/GaN high electron mobility transistor-based sensors for glucose detection in exhaled breath condensate,” *J. Diabetes Sci. Technol.*, vol. 4, no. 1, pp. 171–179, 2010.

[20] S. J. Pearton and F. Ren, “Gallium nitride-based gas, chemical and biomedical sensors,” *IEEE Instrum. Meas. Mag.*, vol. 15, no. 1, pp. 16–21, 2012.

[21] J. Schalwig, G. Müller, O. Ambacher, and M. Stutzmann, “Group-III-Nitride Based Gas Sensing Devices,” *Phys. Status Solidi Appl. Res.*, vol. 185, no. 1, pp. 39–45, 2001.

[22] D. S. Lee, J. H. Lee, Y. H. Lee, and D. D. Lee, “GaN thin films as gas sensors,” *Sensors Actuators, B Chem.*, vol. 89, no. 3, pp. 305–310, 2003.

[23] N. Ghazali, M. Mahmood, K. Yasui, and A. Hashim, “Electrochemically deposited gallium oxide nanostructures on silicon substrates,” *Nanoscale Res. Lett.*, vol. 9, no. 1, p. 120, 2014.

[24] M. S. Z. Abidin, A. M. Hashim, M. E. Sharifabad, S. F. Abd Rahman, and T. Sadoh, “Open-gated pH sensor fabricated on an undoped-AlGaN/GaN HEMT structure,” *Sensors*, vol. 11, no. 3, pp. 3067–3077, 2011.

[25] M. S. Z. Abidin, Shahjahan, and A. M. Hashim, “Surface reaction of undoped AlGaN/GaN HEMT based two terminal device in H+and OH ion-contained aqueous solution,” *Sains Malaysiana*, vol. 42, no. 2, pp. 197–203, 2013.

[26] B. Chitara, D. J. Late, S. B. Krupanidhi, and C. N. R. Rao, “Room-temperature gas sensors based on gallium nitride nanoparticles,” *Solid State Commun.*, vol. 150, no. 41–42, pp. 2053–2056, 2010.

[27] M. Mohamad *et al.*, “The sensing performance of hydrogen gas sensor utilizing undoped-AlGaN/GaN HEMT,” *IEEE Int. Conf. Semicond. Electron. Proceedings, ICSE*, pp. 301–304, 2010.

[28] M. E. Levinshtein, S. L. Rumyantsev, and M. S. Shur, *Properties of Advanced Semiconductor Materials: GaN, AIN, InN, BN, SiC, SiGe*. John Wiley & Sons, 2001.

[29] C. M. Balkaş and R. F. Davis, “Synthesis routes and characterization of high-purity, single-phase gallium nitride powders,” *Journal of the American Ceramic Society*, vol. 79, no. 9. pp. 2309–2312, 1996.

[30] M. A. Qaeed, K. Ibrahim, K. M. A. Saron, and A. Salhin, “Cubic and hexagonal GaN nanoparticles synthesized at low temperature,” *Superlattices Microstruct.*, vol. 64, pp. 70–77, 2013.

[31] S. Nakamura, M. Senoh, N. Iwasa, and S. I. Nagahama, “High-power InGaN single-quantum-well-structure blue and violet light-emitting diodes,” *Applied Physics Letters*, vol. 67. p. 1868, 1995.

[32] “Candela-class high-brightness InGaN AlGaN double-heterostructure blue-light-emitting diodes.pdf.” .

[33] S. Nakamura, M. Senoh, and T. Mukai, “High-power InGaN/GaN double-heterostructure violet light emitting diodes,” *Appl. Phys. Lett.*, vol. 62, no. 19, pp. 2390–2392, 1993.

[34] H. Morkoç, S. Strite, G. B. Gao, M. E. Lin, B. Sverdlov, and M. Burns, “Large-band-gap SiC, III-V nitride, and II-VI ZnSe-based semiconductor device technologies,” *J. Appl. Phys.*, vol. 76, no. 3, pp. 1363–1398, 1994.

[35] J. C. Johnson, H. J. Choi, K. P. Knutsen, R. D. Schaller, P. Yang, and R. J. Saykally, “Single gallium nitride nanowire lasers,” *Nat. Mater.*, vol. 1, no. 2, pp. 106–110, 2002.

[36] V. D. Bondar, T. E. Felter, C. E. Hunt, and I. Y. Kucharsky, “Synthesis and Luminescent Properties of GaN and GaN-Mn Blue Nanocrystalline Thin-Film Phosphor for FED,” *MRS Proc.*, vol. 685, p. D17.1.1, 2001.

[37] T.-H. Kim, S. Choi, and D.-W. Park, “Thermal Plasma Synthesis of Crystalline Gallium Nitride Nanopowder from Gallium Nitrate Hydrate and Melamine,” *Nanomaterials*, vol. 6, no. 3, p. 38, 2016.

[38] Y. Huang, X. Duan, Y. Cui, and C. M. Lieber, “Gallium Nitride Nanowire Nanodevices,” *Nano Lett.*, vol. 2, no. 2, pp. 101–104, 2002.

[39] J. D. Holmes, K. P. Johnston, R. C. Doty, and B. A. Korgel, “Control Orientation of of Thickness and Solution-Grown Nanowires Silicon,” *Adv. Sci.*, vol. 287, no. 5457, pp. 1471–1473, 2010.

[40] H.-J. Choi *et al.*, “Self-Organized GaN Quantum Wire UV Lasers,” *J. Phys. Chem. B*, vol. 107, no. 34, pp. 8721–8725, 2003.

[41] J. Goldberger *et al.*, “Single-crystal gallium nitride nanotubes,” *Nature*, vol. 422, no. 6932, pp. 599–602, 2003.

[42] M. S. Shur, a D. Bykhovski, and R. Gaska, “PYROELECTRIC AND PIEZOELECTRIC PROPERTIES OF GAN-BASED Pyroelectricity in gallium nitride thin films,” vol. 6, pp. 1–12, 1999.

[43] S. S. Kocha, M. W. Peterson, D. J. Arent, J. M. Redwing, M. A. Tischler, and J. A. Turner, “Electrochemical Investigation of the Gallium Nitride-Aqueous Electrolyte Interface,” *J. Electrochem. Soc.*, vol. 142, no. 12, p. L238, 1995.

[44] K. F. and K. Ohkawa, “Photoelectrochemical Properties of p-Type GaN in Comparison with n-Type GaN,” *Jpn. J. Appl. Phys.*, vol. 44, no. 7L, p. L909, 2005.

[45] K. F. and T. K. and K. Ohkawa, “Hydrogen Gas Generation by Splitting Aqueous Water Using n-Type GaN Photoelectrode with Anodic Oxidation,” *Jpn. J. Appl. Phys.*, vol. 44, no. 4L, p. L543, 2005.

[46] M. Ono *et al.*, “Photoelectrochemical reaction and H2generation at zero bias optimized by carrier concentration of n -type GaN,” *J. Chem. Phys.*, vol. 126, no. 5, 2007.

[47] B. A. and M. H. and S. F. and S. Z. and H. P. T. N. and M. G. K. and Z. Mi, “High efficiency photoelectrochemical water splitting and hydrogen generation using GaN nanowire photoelectrode,” *Nanotechnology*, vol. 24, no. 17, p. 175401, 2013.

[48] H. Xu, S. Ouyang, L. Liu, P. Reunchan, N. Umezawa, and J. Ye, “Recent advances in TiO $_2$ -based photocatalysis,” *J. Mater. Chem. A*, vol. 2, no. 32, p. 12642, 2014.

[49] M. G. Kibria *et al.*, “Visible light-driven efficient overall water splitting using p-type metal-nitride nanowire arrays,” *Nat. Commun.*, vol. 6, pp. 1–8, 2015.

[50] H. Pang, L. Liu, S. Ouyang, H. Xu, Y. Li, and D. Wang, “Structure , Optical Properties , and Photocatalytic Activity towards H 2 Generation and CO 2 Reduction of GaN Nanowires via Vapor-Liquid-Solid Process,” vol. 2014, pp. 1–7, 2014.

[51] and G.-C. Y. Hye Seong Jung, Young Joon Hong, Yirui Li, Jeonghui Cho, Yong-Jin Kim, “Photocatalysis Using GaN Nanowires,” vol. 2, no. 4, pp. 1–21, 2008.

[52] S. Munusamy *et al.*, “Synthesis and characterization of GaN/PEDOT-PPY nanocomposites and its photocatalytic activity and electrochemical detection of mebendazole,” *Arab. J. Chem.*, 2015.

[53] M. G. Kibria and Z. Mi, “Artificial photosynthesis using metal/nonmetal-nitride semiconductors: Current status, prospects, and challenges,” *J. Mater. Chem. A*, vol. 4, no. 8, pp. 2801–2820, 2016.

[54] O. I. Mićić, S. P. Ahrenkiel, D. Bertram, and A. J. Nozik, “Synthesis, structure, and optical properties of colloidal GaN quantum dots,” *Appl. Phys. Lett.*, vol. 75, no. 4, pp. 478–480, 1999.

[55] S. F. (CEA-C. F.Rol, “Probing exciton localization in non-polar GaN/AlN Quantum Dots by si,gle dot optical spectroscopy,” no. c, pp. 1–4.

[56] P. Ramvall, P. Riblet, S. Nomura, Y. Aoyagi, and S. Tanaka, “Optical properties of GaN quantum dots,” *J. Appl. Phys.*, vol. 87, no. 8, pp. 3883–3890, 2000.

[57] Y. Tokuda, Y. Matsuoka, H. Ueda, O. Ishiguro, N. Soejima, and T. Kachi, “DLTS study of n-type GaN grown by MOCVD on GaN substrates,” *Superlattices*

Microstruct., vol. 40, no. 4–6 SPEC. ISS., pp. 268–273, 2006.

[58] K. Al-Heuseen, M. R. Hashim, and N. K. Ali, "Synthesis of hexagonal and cubic GaN thin film on Si (111) using a low-cost electrochemical deposition technique," *Mater. Lett.*, vol. 64, no. 14, pp. 1604–1606, 2010.

[59] L. A. Hernández-Hernández *et al.*, "Synthesis of gallium nitride and related oxides via ammonobasic reactive sublimation (ARS)," *Mater. Res.*, vol. 20, no. 6, pp. 1707–1712, 2017.

[60] Y. B. Tang *et al.*, "Vertically aligned p-type single-crystalline GaN nanorod arrays on n-type Si for heterojunction photovoltaic cells," *Nano Lett.*, vol. 8, no. 12, pp. 4191–4195, 2008.

[61] Y. S. P. and T. W. K. and R. A. Taylor, "Abnormal photoluminescence properties of GaN nanorods grown on Si(111) by molecular-beam epitaxy," *Nanotechnology*, vol. 19, no. 47, p. 475402, 2008.

[62] W. Han, F. S., Q. Li, and Y. Hu, "Synthesis of gallium nitride nanorodes through a carbon nanotube-confined reaction," *Science (80-.).*, vol. 277, no. August, p. 1287, 1997.

[63] W. Q. Han and A. Zettl, "Pyrolysis approach to the synthesis of gallium nitride nanorods," *Appl. Phys. Lett.*, vol. 80, no. 2, pp. 303–305, 2002.

[64] W.-G. J. and S.-H. J. and P. K. and M. Razeghi, "Fabrication of GaN nanotubular material using MOCVD with an aluminium oxide membrane," *Nanotechnology*, vol. 17, no. 1, p. 54, 2006.

[65] C. H. and G. P. and S. K. and B. Monemar, "Growth of GaN nanotubes by halide vapor phase epitaxy," *Nanotechnology*, vol. 22, no. 8, p. 85602, 2011.

[66] S. Y. Bae, H. W. Seo, J. Park, H. Yang, and S. A. Song, "Synthesis and structure of gallium nitride nanobelts," *Chem. Phys. Lett.*, vol. 365, no. 5–6, pp. 525–529, 2002.

[67] S. Xue, X. Zhang, R. Huang, D. Tian, H. Zhuang, and C. Xue, "A study on self-assembled GaN nanobelts by a new method: Structure, morphology, composition, and luminescence," *Cryst. Growth Des.*, vol. 8, no. 7, pp. 2177–2181, 2008.

[68] K. M. A. Saron and M. R. Hashim, "Study of using aqueous NH3to synthesize GaN nanowires on Si(1 1 1) by thermal chemical vapor deposition," *Mater. Sci. Eng. B Solid-State Mater. Adv. Technol.*, vol. 178, no. 5, pp. 330–335, 2013.

[69] K. M. A. Saron and M. R. Hashim, "Broad visible emission from GaN nanowires grown on n-Si (1 1 1) substrate by PVD for solar cell application," *Superlattices Microstruct.*, vol. 56, pp. 55–63, 2013.

[70] W. S. Jung, "Preparation of Gallium Nitride Powders and Nanowires from a Gallium(III) Nitrate Salt in Flowing Ammonia," *Bull. Korean Chem. Soc.*, vol. 25, no. 1, pp. 51–54, 2004.

[71] R. Kudrawiec, M. Nyk, M. Syperek, A. Podhorodecki, J. Misiewicz, and W. Strek, "Photoluminescence from GaN nanopowder: The size effect associated with the surface-to-volume ratio," *Appl. Phys. Lett.*, vol. 88, no. 18, pp. 1–4, 2006.

[72] A. Podhorodecki, M. Nyk, R. Kudrawiec, J. Misiewicz, J. C. Pivin, and W. Strek, "Optical properties of GaN nanocrystals embedded into silica matrices," *Superlattices Microstruct.*, vol. 40, no. 4–6 SPEC. ISS., pp. 533–536, 2006.

[73] G. Pan, M. E. Kordesch, and P. G. Van Patten, "Room-temperature synthesis of GaN nanopowder," *Chem. Mater.*, vol. 18, no. 23, pp. 5392–5394, 2006.

[74] K. Dimos, L. Jankovič, I. B. Koutselas, M. A. Karakassides, R. Zbořil, and P. Komadel, "Low-Temperature Synthesis and Characterization of Gallium Nitride Quantum Dots in Ordered Mesoporous Silica," *J. Phys. Chem. C*, vol. 116, no. 1, pp. 1185–1194, 2012.

[75] B. Giroire, S. Marre, A. Garcia, T. Cardinal, and C. Aymonier, "Continuous supercritical route for quantum-confined GaN nanoparticles," *React. Chem. Eng.*, vol. 1, no. 2, pp. 151–155, 2016.

[76] H. R. Rajabi, "Photocatalytic Activity of Quantum Dots," 2016.

[77] Z. Zhang and J. T. Yates, "Band bending in semiconductors: Chemical and physical consequences at surfaces and interfaces," *Chem. Rev.*, vol. 112, no. 10, pp. 5520–5551, 2012.

[78] P. E. Averill, Bruce A., *Principles of General Chemistry*. 2012.

[79] C. Aymonier and A. Loppinet-serani, "Review on materials science and supercritical fluids Franc," vol. V, no. 2003, pp. 331–340, 2004.

[80] T. No, *Organometallic Flow Chemistry*, vol. 57. 2016.

[81] V. Hessel, "Novel process windows–gate to maximizing process intensification via flow chemistry," *Chem. Eng. Technol.*, vol. 32, no. 11, pp. 1655–1681, 2009.

[82] K. F. Jensen, "Microreaction engineering — is small better?," *Chem. Eng. Sci.*, vol. 56, no. 2, pp. 293–303, 2001.

[83] V. Hessel, H. Löwe, and F. Schönfeld, "Micromixers - A review on passive and active mixing principles," *Chem. Eng. Sci.*, vol. 60, no. 8–9 SPEC. ISS., pp. 2479–2501, 2005.

[84] S. R. L. Gobert, S. Kuhn, L. Braeken, and L. C. J. Thomassen, "Characterization of Milli- and Microflow Reactors: Mixing Efficiency and Residence Time Distribution," *Org. Process Res. Dev.*, vol. 21, no. 4, pp. 531–542, 2017.

[85] C. J. Carmalt, "Amido compounds of gallium and indium," *Coord. Chem. Rev.*, vol. 223, no. 1, pp. 217–264, 2001.

[86] D. M. Hoffman, "Chemical vapour deposition of nitride thin films," *Polyhedron*, vol.

13, no. 8, pp. 1169–1179, 1994.

[87] "2D digramatic representation of Tris(dimethylamido)-gallium(III)." [Online]. Available: https://www.sigmaaldrich.com/catalog/product/aldrich/546534?lang=fr&region=FR.

[88] K. M. Waggoner, M. M. Olmstead, and P. P. Power, "Structural and spectroscopic characterization of the compounds [Al(NMe2)3]2, [Ga(NMe2)3]2, [(Me2N)2Al{μ-N(H)1-Ad}]2(1-Ad = 1-adamantanyl) and [{Me(μ-NPh2)Al}2NPh(μ-C6H4)]," *Polyhedron*, vol. 9, no. 2–3, pp. 257–263, 1990.

[89] J. F. Janik and R. L. Wells, "Gallium Imide, {Ga(NH) 3/2 } n , a New Polymeric Precursor for Gallium Nitride Powders," *Chem. Mater.*, vol. 8, no. 12, pp. 2708–2711, 1996.

[90] J. L. Coffer, M. A. Johnson, L. Zhang, R. L. Wells, and J. F. Janik, "Influence of Precursor Route on the Photoluminescence of Bulk Nanocrystalline Gallium Nitride," *Chem. Mater.*, vol. 9, no. 12, pp. 2671–2673, 1997.

[91] P. Guiquan, M. E. Kordesch, and P. G. Van Patten, "Pyrolysis route to GaN quantum dots," *Chem. Mater.*, vol. 18, no. 17, pp. 3915–3917, 2006.

[92] "Critical temperature and pressure data of cyclohexane," *NIST*.

[93] J. W. Hwang, J. P. Campbell, J. Kozubowski, S. A. Hanson, J. F. Evans, and W. L. Gladfelter, "Topochemical Control in the Solid-State Conversion of Cyclotrigallazane into Nanocrystalline Gallium Nitride," *Chem. Mater.*, vol. 7, no. 3, pp. 517–525, 1995.

[94] S. Amiroudine, J. P. Caltagirone, and A. Erriguible, "A Lagrangian-Eulerian compressible model for the trans-critical path of near-critical fluids," *Int. J. Multiph. Flow*, vol. 59, pp. 15–23, 2014.

[95] C. Aymonier, G. Philippot, A. Erriguible, and S. Marre, "Playing with chemistry in supercritical solvents and the associated technologies for advanced materials by design," *J. Supercrit. Fluids*, vol. 134, no. December 2017, pp. 184–196, 2018.

[96] Y. Yang, V. J. Leppert, S. H. Risbud, B. Twamley, P. P. Power, and H. W. H. Lee, "Blue luminescence from amorphous GaN nanoparticles synthesized in situ in a polymer," *Appl. Phys. Lett.*, vol. 74, no. 16, pp. 2262–2264, 1999.

[97] R. Carin, "An XPS study of GaN thin films on GaAs," *Surf. Interface …*, vol. 16, pp. 65–69, 1990.

[98] S. D. Wolter, B. P. Luther, D. L. Waltemyer, C. Önneby, S. E. Mohney, and R. J. Molnar, "X-ray photoelectron spectroscopy and x-ray diffraction study of the thermal oxide on gallium nitride," *Appl. Phys. Lett.*, vol. 70, no. 16, pp. 2156–2158, 1997.

[99] N. Ghobadi, "Band gap determination using absorption spectrum fitting procedure," *Int. Nano Lett.*, vol. 3, no. 1, p. 2, 2013.

[100] P. Chand, A. Gaur, and A. Kumar, "Structural and optical properties of ZnO

nanoparticles synthesized at different pH values," *J. Alloys Compd.*, vol. 539, pp. 174–178, 2012.

[101] L. E. Brus, "Electron-electron and electron-hole interactions in small semiconductor crystallites: The size dependence of the lowest excited electronic state," *J. Chem. Phys.*, vol. 80, no. 9, pp. 4403–4409, 1984.

[102] L. Brus, "Electronic wave functions in semiconductor clusters: Experiment and theory," *J. Phys. Chem.*, vol. 90, no. 12, pp. 2555–2560, 1986.

[103] Y. Kayanuma, "Quantum-size effects of interacting electrons and holes in semiconductor microcrystals with spherical shape," *Phys. Rev. B*, vol. 38, no. 14, pp. 9797–9805, 1988.

[104] D. Denzler, M. Olschewski, and K. Sattler, "Luminescence studies of localized gap states in colloidal ZnS nanocrystals," *J. Appl. Phys.*, vol. 84, no. 5, pp. 2841–2845, 1998.

[105] J. Xue-yin, J. Yan, Z. Zhi-lin, and X. Shao-hong, "Mn-doped nanometer-size ZnS clusters in chitosan film matrix prepared by ion-coordination reaction," *J. Cryst. Growth*, vol. 191, no. 4, pp. 692–696, 1998.

[106] G. Steude *et al.*, "Optical investigations of AlGaN on GaN epitaxial films," *Appl. Phys. Lett.*, vol. 74, no. 17, pp. 2456–2458, 1999.

[107] J.-M. Herrmann, "Heterogeneous photocatalysis: fundamentals and applications to the removal of various types of aqueous pollutants," *Catal. Today*, vol. 53, no. 1, pp. 115–129, Oct. 1999.

[108] A. L. Linsebigler, G. Lu, and J. T. Yates, "Photocatalysis on TiO2Surfaces: Principles, Mechanisms, and Selected Results," *Chem. Rev.*, vol. 95, no. 3, pp. 735–758, 1995.

[109] M. A. Fox and M. T. Dulay, "Heterogeneous Photocatalysis," *Chem. Rev.*, vol. 93, no. 1, pp. 341–357, 1993.

[110] J.-M. Herrmann, C. Guillard, and P. Pichat, "Heterogeneous photocatalysis : an emerging technology for water treatment," *Catal. Today Elsevier Sci. Publ. B.V*, vol. 17, pp. 7–20, 1993.

[111] O. Legrini, E. Oliveros, and A. M. Braun, "Photochemical Processes for Water Treatment," *Chem. Rev.*, vol. 93, no. 2, pp. 671–698, 1993.

[112] M. Sleiman, D. Vildozo, C. Ferronato, and J. M. Chovelon, "Photocatalytic degradation of azo dye Metanil Yellow: Optimization and kinetic modeling using a chemometric approach," *Appl. Catal. B Environ.*, vol. 77, no. 1–2, pp. 1–11, 2007.

[113] M. Stylidi, D. I. Kondarides, and X. E. Verykios, "Visible light-induced photocatalytic degradation of Acid Orange 7 in aqueous TiO2suspensions," *Appl. Catal. B Environ.*, vol. 47, no. 3, pp. 189–201, 2004.

[114] C. G. Silva, W. Wang, and J. L. Faria, "Photocatalytic and photochemical degradation

of mono-, di- and tri-azo dyes in aqueous solution under UV irradiation," *J. Photochem. Photobiol. A Chem.*, vol. 181, no. 2–3, pp. 314–324, 2006.

[115] J. Madhavan, P. Maruthamuthu, S. Murugesan, and S. Anandan, "Kinetic studies on visible light-assisted degradation of acid red 88 in presence of metal-ion coupled oxone reagent," *Appl. Catal. B Environ.*, vol. 83, no. 1–2, pp. 8–14, 2008.

[116] A. Ajmal, I. Majeed, R. N. Malik, H. Idriss, and M. A. Nadeem, "Principles and mechanisms of photocatalytic dye degradation on TiO $_2$ based photocatalysts: a comparative overview," *RSC Adv.*, vol. 4, no. 70, pp. 37003–37026, 2014.

[117] F. Chen, Y. Xie, J. Zhao, and G. Lu, "Photocatalytic degradation of dyes on a magnetically separated photocatalyst under visible and UV irradiation," *Chemosphere*, vol. 44, no. 5, pp. 1159–1168, 2001.

[118] C. Galindo, P. Jacques, and A. Kalt, "Photodegradation of the aminoazobenzene acid orange 52 by three advanced oxidation processes: UV/H2O2, UV/TiO2 and VIS/TiO2," *J. Photochem. Photobiol. A Chem.*, vol. 130, no. 1, pp. 35–47, 2000.

[119] Y. Ma and J.-N. Yao, "Photodegradation of Rhodamine B catalyzed by Ti02 thin films," *J. Photoc+Fmistry Photobiol. AChemistry J. Photochem. Photobiol. A Chem.*, vol. 116, no. 7 ml, pp. 167–170, 1998.

[120] J. Zhao, C. Chen, and W. Ma, "Photocatalytic Degradation of Organic Pollutants Under Visible Light Irradiation," *Top. Catal.*, vol. 35, no. 3–4, pp. 269–278, 2005.

[121] J. Saien and A. R. Soleymani, "Feasibility of using a slurry falling film photo-reactor for individual and hybridized AOPs," *J. Ind. Eng. Chem.*, vol. 18, no. 5, pp. 1683–1688, 2012.

[122] M. R. Hoffmann, S. T. Martin, W. Choi, and D. W. Bahnemann, "Environmental Applications of Semiconductor Photocatalysis," *Chem. Rev.*, vol. 95, no. 1, pp. 69–96, 1995.

[123] J. Peral, X. Domènech, and D. F. Ollis, "Heterogeneous photocatalysis for purification, decontamination and deodorization of air," *J. Chem. Technol. Biotechnol.*, vol. 70, no. 2, pp. 117–140, 1997.

[124] S. C. Yan, Z. S. Li, and Z. G. Zou, "Photodegradation of Rhodamine B and Methyl Orange over Boron-Doped g-C $_3$ N $_4$ under Visible Light Irradiation," *Langmuir*, vol. 26, no. 6, pp. 3894–3901, 2010.

[125] Y. Su, N. J. W. Straathof, V. Hessel, and T. Noël, "Photochemical transformations accelerated in continuous-flow reactors: Basic concepts and applications," *Chem. - A Eur. J.*, vol. 20, no. 34, pp. 10562–10589, 2014.

[126] A. E. Cassano, P. L. Silveston, and J. M. Smith, "Photochemical Reaction Engineering," *Ind. Eng. Chem.*, vol. 59, no. 1, pp. 18–38, 1967.

[127] N. Panda, H. Sahoo, and S. Mohapatra, "Decolourization of Methyl Orange using

Fenton-like mesoporous Fe2O3-SiO2 composite," *J. Hazard. Mater.*, vol. 185, no. 1, pp. 359–365, 2011.

[128] J. Liao, S. Lin, L. Zhang, N. Pan, X. Cao, and J. Li, "Photocatalytic degradation of methyl orange using a TiO2/Ti mesh electrode with 3D nanotube arrays," *ACS Appl. Mater. Interfaces*, vol. 4, no. 1, pp. 171–177, 2012.

[129] W. Xu *et al.*, "Nanoporous CuS with excellent photocatalytic property," *Sci. Rep.*, vol. 5, pp. 1–11, 2015.

[130] M. K. Nowotny, P. Bogdanoff, T. Dittrich, S. Fiechter, A. Fujishima, and H. Tributsch, "Observations of p-type semiconductivity in titanium dioxide at room temperature," *Mater. Lett.*, vol. 64, no. 8, pp. 928–930, 2010.

Chapter 3

Continuous synthesis of visible light active $Ga_xIn_{1-x}N$ solid solution photocatalysts

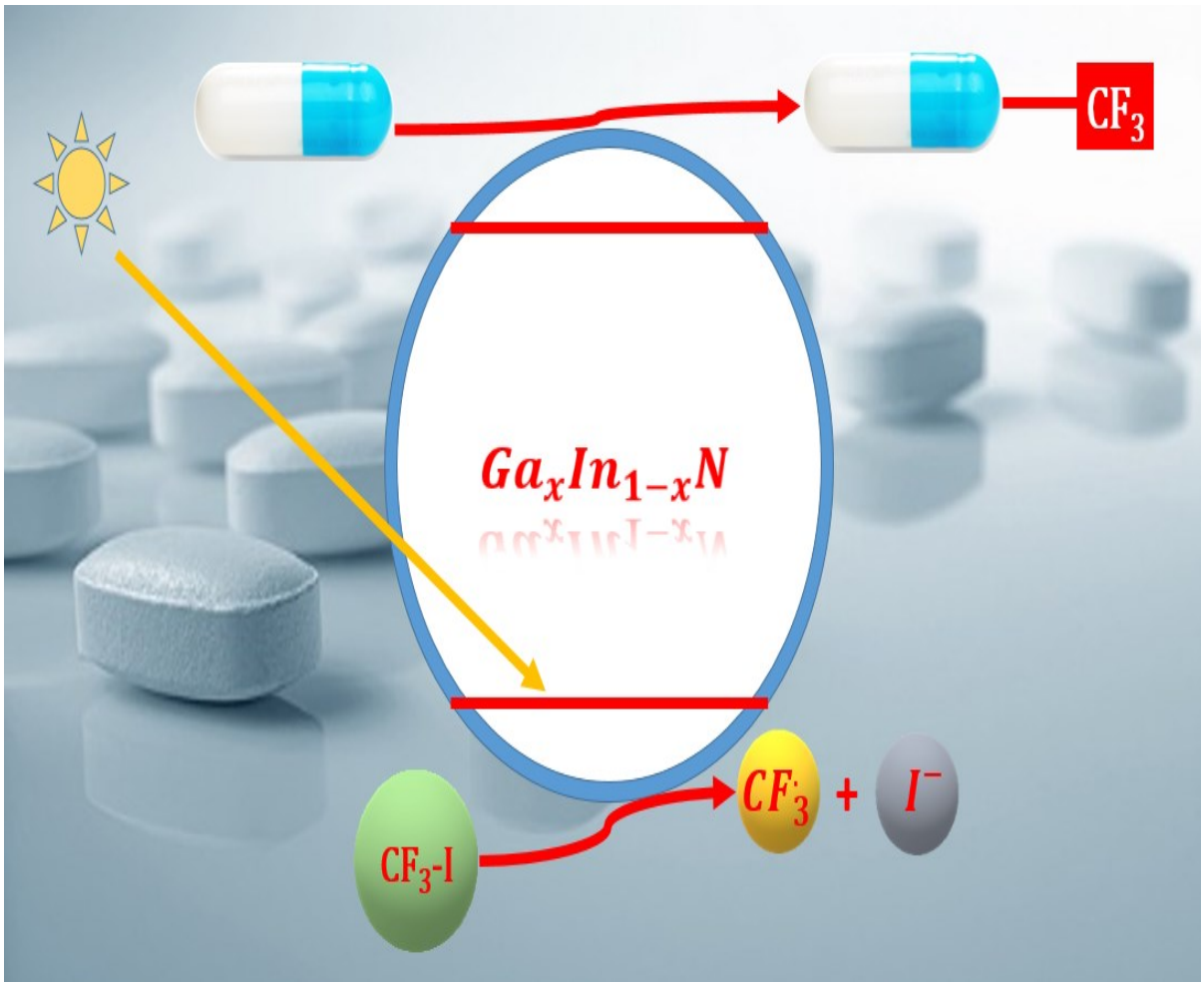

Contents

3. Continuous synthesis of visible light active $Ga_xIn_{1-x}N$ solid solution photocatalysts 171

3.1. Introduction 175

3.1.1. Motivation of the research work 175

3.1.2. Introduction to InGaN ternary material 175

3.1.3. Synthetic methodologies and difficulties in attaining $Ga_xIn_{1-x}N$ ($0 \leq x \leq 1$) solid solution 177

3.1.4. Conclusion 179

3.2. Experimental Section 180

3.2.1. Introduction of the synthetic strategy developed for obtaining GaxIn1-xN ($0 \leq x \leq 1$) solid solutions 180

3.2.2. Continuous supercritical synthesis of the $Ga_xIn_{1-x}N$ ($0 \leq x \leq 1$) solid solution in toluene 181

3.2.3. Characterization of the $Ga_xIn_{1-x}N$ ($0 \leq x \leq 1$) solid solutions from supercritical toluene 184

3.2.4. Reasons for opting dual solvent system 193

3.3. Tunability of $Ga_xIn_{1-x}N$ solid solution using toluene and methanol supercritical mixture 195

3.3.1. Introduction to the synthesis 195

3.3.2. Characterization of $Ga_xIn_{1-x}N$ solid solution synthesized in toluene and methanol supercritical mixtures 195

3.3.3. Conclusion 215

3.4. Efficient trifluoromethylation of heteroarenes by visible light photoredox catalysis over $Ga_xIn_{1-x}N$ solid solutions semiconductor system 216

3.4.1. Introduction 216

3.4.2. State-of-the-art methods for CF_3 incorporation or C-CF_3 bond formation 218

3.4.3. Photocatalyzed trifluoromethylation in batch mode using $Ga_{0.53}In_{0.47}N$ nanophotocatalysts 221

3.4.4. Continuous flow heterogeneous photocatalysis for direct radical trifluoromethylation of heteroarenes 227

3.4.5. Conclusion of photocatalytic studies 236

3.5. Conclusion 236

General Conclusion 245

3.1. Introduction

3.1.1. Motivation of the research work

The objective of this chapter is to synthesize visible light active photocatalysts to be employed in indirect photochemical excitation processes for conventional heterogeneous photocatalytic study. In particular, the incorporation of fluorinated functional groups into chemical compounds, especially drug molecules, was the application implemented in this research work through heterogeneous photocatalysis. The necessity of this fluorinated moieties (CF_3) incorporation stems from the protection offered to the drug molecule against metabolic oxidations (*in vivo*) induced by proteins of the organisms, in which the drugs are injected for imparting their biological activity. As discussed in the previous chapter, GaN is active in the UV region and is rendered active under visible light irradiation in this chapter by the fabrication of $Ga_xIn_{1-x}N$ solid solution nanomaterials. The first part of the research work focuses on developing a suitable chemical methodology for the continuous supercritical synthesis of $Ga_xIn_{1-x}N$ solid solution and the second part concentrates on the heterogeneous photocatalytic study.

3.1.2. Introduction to InGaN ternary materials

Semiconductor materials have become essential constituents of devices used in our daily activities. Optoelectronic devices involve the interaction of electrons and photons and require semiconductors with strong emission and absorption characteristics. Direct band gap group III-nitride semiconductors suffice this requirement and disposes itself as propitious materials for blue, green light emitting devices (optoelectronic devices), photovoltaics and electronics due to their high physical hardness, exceptionally substantial heterojunction offsets, elevated melting temperature and thermal conductivity. Especially within group III nitrides, hexagonal wurtzite structure are intensively employed for the above applications because their alloys exhibit direct band gap energy resulting in enhanced emission in optoelectronic devices[1, 2].

The direct optical band gaps of the group-III nitrides for the hexagonal wurtzite crystal structure are: 6.2 eV (α-AlN), 3.4 eV (α-GaN) and 1.9 eV (α-InN). In contrast to other III-V semiconductors, which possess stable cubic zinc blende structure like GaAs and InP, the group III-nitrides possess thermodynamically stable wurtzite hexagonal structure [3]. Among these group III-V materials, InGaN (Indium Gallium Nitride) ternary alloys or Quasi-Binary system of GaN and InN compounds was focused as one of the contender for solid state lighting (SSL) devices, especially blue light emission and photovoltaics due to the variation of direct band gap energy from near UV to visible (3.4 to 1.9 eV), as a function of Indium molar ratio [4]. The band gap of group-III nitrides and their corresponding crystal structures are depicted in Figure 3.1.

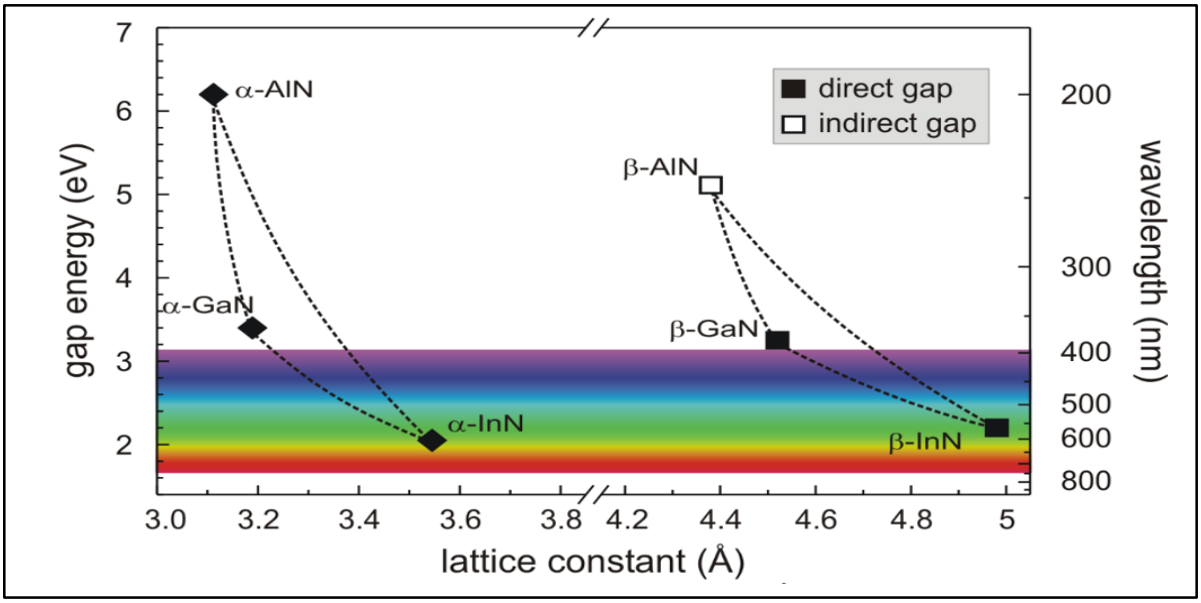

Figure 3.1. *Schematic depiction of band gap vs lattice constant for group III-nitride semiconductors possessing hexagonal wurtzite (α) and cubic zinc-blende (β) crystal structures, with band gaps measured at 300K [5].*

The rapid progress of InGaN in the SSL research have successfully rendered scientists to conceive single quantum well (SQW) of InGaN for light emitting diodes (LED) [6], laser diodes (LDs) [7] especially blue, green and yellow LEDS with high brightness using SQW structures and multi quantum well (MQW) structures of InGaN for LDs [8]. Now a day InGaN quantum well based LEDs with emission wavelength ranging in the wavelength of blue/violet light or in combination with phosphors for white light source are commercially available [9]. Compared to quantum well structures, quantum dots (QDs) of InGaN exhibit eminent properties like enhanced exciton location and had found applications in LEDs [10] and single photon source photoelectric devices [11, 12]. Currently several research groups have focused on QDs rather than other structures. Besides quantum wells and dots, walls and wires of InGaN nanomaterials are used effectively in SSL. The emission wavelength is the ultimate parameter that determines the implementation of InGaN solid solution nanostructures or InGaN based heterostructures in various light emitting devices. Exciton binding energy and quantum confinement properties dictate the value of emission wavelength.

Parallelly, like for optoelectronics, InGaN Quasi-Binary systems have grabbed an intensive focus in the photovoltaics field because of the highest overlap of the system's bandgap with the solar spectrum [13 – 15]. Besides, they possess propitious photovoltaic properties like large absorption co-efficient and high carrier mobility [16, 17]. Latterly it was also found that InGaN-based solar cells exhibited predominant resistance to strident atmosphere consisting of high temperature and acute energy radiations [18]. Besides possessing such interesting properties, the commercialization of InGaN-based solar cells is in sluggish state due to its low conversion efficiencies compared to the other solar cells available on the market [18].

In the perspective of heterogeneous photocatalysis InGaN systems as photocatalysts were reported only in the last few years and mostly for water splitting reactions.

The exploration of InGaN in photocatalytic water splitting and as photoactive catalytic materials in photoelectrochemical (PEC) cells for the water splitting reaction into molecular hydrogen and oxygen has emerged recently because of the successful synthesis of 1-D nanostructures of InGaN systems [19, 20]. Currently, the successful demonstration of InGaN-based photo-electrolysis system with single and dual photo-electrodes have been reported [21].

The notable InGaN-based photocatalytic materials reported in heterogeneous photocatalysis are: p-type GaN/$Ga_{0.8}In_{0.2}N$ nanowire array reported by Kibria *et al.* for water splitting reaction [22] and InGaN nanodots grown on GaN/sapphire template by metal organic vapour phase epitaxy for the degradation of methylene orange dye under visible light irradiation reported by Lai *et al.* [23]. To conclude the synthetic application of InGaN Quasi-Binary systems, as far as we known, there were no report on the photocatalytic study on InGaN QDs or nanomaterials (powdered materials without any support). The aim of this work is therefore to investigate a trifluoromethylation reaction for the insertion of fluorinated compound using InGaN QDs/nanomaterials as photocatalysts in heterogeneous photocatalysis.

3.1.3. Synthetic methodologies and difficulties in attaining $Ga_xIn_{1-x}N$ ($0 \leq x \leq 1$) solid solution

The isostructural end members of group III Nitrides, InN (Indium Nitride) and GaN (Gallium Nitride) form the $Ga_xIn_{1-x}N$ ($0 \leq x \leq 1$) solid solution. The first synthesis of $Ga_xIn_{1-x}N$ was reported in 1972 as a polycrystalline thin film through electron beam plasma technique by Osamura *et al.* [24]. Since then, several techniques were established for the synthesis of InGaN systems in the form of films with high quality. These techniques are metal organic vapour phase epitaxy (MOVPE) [25 – 28], molecular beam epitaxy (MBE) [29, 30] and hydride vapour phase epitaxy (HVPE) [31].

Irrespective of the synthetic approach, the attainment of full composition ranges of $Ga_xIn_{1-x}N$ ($0 < x \leq 1$) is very difficult and primarily challenging due to (i) the large difference in the ionic radii of gallium (Ga^{3+}: 0.47 Å) and indium (In^{3+}: 0.79 Å) [32], (ii) large lattice mismatch (11%) existing between GaN and InN due to this very different tetrahedral radii and finally the (iii) high equilibrium vapour pressure (EVP) of N_2 over InN [33].

$Ga_xIn_{1-x}N$ alloys possess the same crystal structure as their end constituents but the lattice constant of the alloy (solid solution) changes due to the large difference in the ionic radius of indium compared to gallium, due to which two different types of strain occurs in the $Ga_xIn_{1-x}N$ based systems: internal and interfacial strains. The internal strains, especially, can lead to phase segregation. Interfacial strains are observed on the InGaN based heterostructues, where strain leads to both defect formation and phase separation.

Explicitly, $Ga_xIn_{1-x}N$ Quasi-Binary systems exhibit a miscibility gap, which means that at a certain composition of the $Ga_xIn_{1-x}N$, the alloy or Quasi-Binary system becomes

thermodynamically more stable if it separates into two co-existing bulk phases, where one phase has more amount of indium and the other has more amount of gallium.

Synthetic methodology developed in this research must address this issue of phase separation due to solid phase miscibility gap, as it has a profound effect on the optical properties of the $Ga_xIn_{1-x}N$ system, which might have a strong influence on the photocatalytic activity.

In the scientific field targeting the $Ga_xIn_{1-x}N$ ($0 \leq x \leq 1$) solid solution system, there is a large number of experimental evidences for the above mentioned phase separation and change in optical properties due to such a behaviour [34]. It is very difficult to characterize this phenomenon quantitatively. The understanding of this behaviour in a quantitative manner was provided by the implementation of molecular-thermodynamic modelling studies. Stringfellow and Ho *et al.* did the pioneering work in this modelling study for providing a quantitative insight of this phase immiscibility issue. They studied the solution thermodynamics by calculating the mixing enthalpy of the solid phase and extent of miscibility gap using a modified valence-force-field (VFF) model [35]. A schematic representation of solid phase miscibility gap in the $Ga_xIn_{1-x}N$ ($0 \leq x \leq 1$) system is depicted in Figure 3.2.

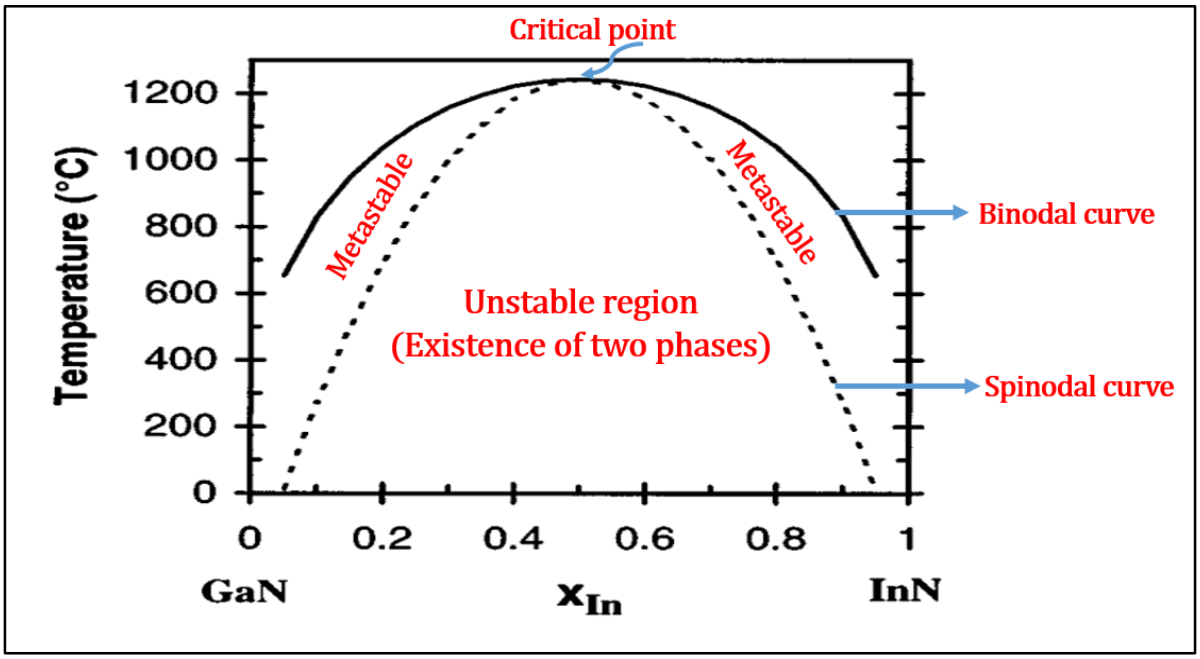

Figure 3.2. *Miscibility diagram for the $Ga_xIn_{1-x}N$ ($0 \leq x \leq 1$) system. The solid lines are binodal curve and dashed line indicate the spinodal curve for the $Ga_xIn_{1-x}N$ system calculated by Stringfellow et al. [35].*

The model has many approximations and the maximum InN solubility in the system achieved at 800°C of growth temperature was less than 6%. Currently, many models have been developed, however, I will not get deep into the models as this is beyond the scope of this research. Experimentally, high solubility of InN is attained in several synthetic strategies. They will be described below and a new synthetic methodology will be developed here for attaining the complete solution tunability of $Ga_xIn_{1-x}N$ ($0 \leq x \leq 1$).

The synthesis of non-planar nanosized $Ga_xIn_{1-x}N$ ($0 \leq x \leq 1$) solid solutions has demonstrated the reduction of the strain to certain extent, leading to very less phase separation phenomenon. Synthesis of nanowires of $Ga_xIn_{1-x}N$ solid solution with a composition covering most of the range from (x = 0 to 1) with very few phase segregation, through HVPE technique, was recently reported by Kuykendall *et al*. [36] in the last decade. Highly crystalline $Ga_{0.5}In_{0.5}N$ solid solution with small particle size (micro-size) was reported by Garcia *et al*. [37]. The corresponding solid solution was synthesized by pyrolyzing complex salt solid solution precursor containing gallium and indium with ammonia gas in tubular reactor.

Recently, in the solution based synthetic strategy, 5% and 10% indium incorporation into $Ga_xIn_{1-x}N$ solid solution was successfully attained by Bhat *et al.* [38] using a solvothermal method. They pyrolyzed a single source precursor gallium and indium cupferronate with 1,1,1,3,3,3-Hexamethyldisilazane (HMDS) as a nitrogen source in a toluene solvent inside an autoclave. The decomposition was carried out at 300°C for 24 h.

3.1.4. Conclusion

The primary motivation is to synthesize visible light active photocatalysts based on the $Ga_xIn_{1-x}N$ ($0 \leq x \leq 1$) Quasi-Binary system. So far, there has been no report on the synthesis of this $In_xGa_{1-x}N$ in supercritical millireactor. The elementary idea of this chapter targets the transposition of the synthetic methodology involving wet chemical synthesis for producing $Ga_xIn_{1-x}N$ solid solution to a continuous supercritical process. Bhat *et al.* pioneered the work in incorporating (5 -10%) InN into $In_xGa_{1-x}N$ system successfully using the solution based technique. Their methodology (reaction of single source cupferronate precursor and HMDS) will be transposed into the continuous supercritical millireactor and correspondingly a new reactive environment or supercritical condition will be developed for the synthesis of the full range of composition of $Ga_xIn_{1-x}N$ ($0 \leq x \leq 1$) solid solution.

3.2. Experimental Section

3.2.1. Introduction of the synthetic strategy developed for obtaining GaxIn1-xN ($0 \leq x \leq 1$) solid solutions

The synthesis of visible light active $Ga_xIn_{1-x}N$ solid solutions in nano-size was successfully achieved in both solutions based and non-solution based synthesis in batch mode only. This section of the chapter initially explains the background of the precursor chemistry and the mechanism of the nitride formation.

To attain the full compositional range of the $Ga_xIn_{1-x}N$ system, especially with high indium content, solution based or pyrolysis based synthetic methodology is the facile route due to the thermodynamic properties of indium and nitrogen (N_2). The high bonding energy of the N_2 molecule and the relatively low bonding energy of InN makes the direct growth of InN from their constituents (In + N_2) extremely difficult. The most successful method for synthesizing InN or high content of indium in the $Ga_xIn_{1-x}N$ system is the chemical reduction method [39].

In the realm of solution based synthesis, Rao and Sardar developed a new solvothermal route for attaining quantum confined GaN nanocrystals crystallized in hexagonal wurtzite crystal structure by attempting a reaction between organometallic precursor, gallium cupferronate ($Ga(C_6H_5N_2O_2)_3$) or gallium (III) chloride ($GaCl_3$) as gallium source and 1,1,1,3,3,3-Hexamethyldisilazane, HMDS [$\{(CH_3)_3Si\}_2NH$] as the nitriding agent in toluene [40]. Through thermogravimetric analysis it was found that ($Ga(C_6H_5N_2O_2)_3$) decomposes in a N_2 environment sharply at 230°C under ambient pressure. The mechanism of the GaN formation in this solvothermal method occurs initially through the generation of nascent gallium oxide (Ga_2O_3) molecules from the pyrolysis of ($Ga(C_6H_5N_2O_2)_3$), as shown in Equation 3.1, this reactive route was confirmed through the NMR analysis.

$$\{Ga(C_6H_5N_2O_2)_3\} \xrightarrow[(Toluene)]{\Delta\,(240°C)} Ga_2O_3 \qquad \textbf{(3.1)}$$

Subsequently, GaN formation takes place through the nitridation reaction between the formed nascent gallium oxide nanoparticles and the nitrogen precursor (HMDS), as depicted in Equation 3.2, observed and confirmed by NMR studies.

$$Ga_2O_3 + 2[(CH)_3Si]_2NH \xrightarrow[Toluene]{\Delta\,(240°C)} 2GaN + 2[(CH)_3Si]_2O + H_2O \qquad \textbf{(3.2)}$$

This method extended the similar strategy of cupferron and HMDS chemistry for other group-III nitride (InN and AlN) [41]. Based on this strategy, they developed a simple solvothermal route for obtaining $Ga_xIn_{1-x}N$ (x = 0.9) solid solution nanocrystals. The Quasi-Binary system was attained by pyrolyzing the solid solution of gallium (III) and indium (III) cupferronate precursor ($Ga_xIn_{1-x}(C_6H_5N_2O_2)_3$) with HMDS in toluene [38, 41] as shown in Equation 3.3.

$$2(Ga_xIn_{1-x}(C_6H_5N_2O_2)_3) + 2[(CH)_3Si]_2NH \xrightarrow[Toluene]{\Delta\,(300°C)\ 24h} 2Ga_xIn_{1-x}N + 2[(CH)_3Si]_2O + H_2O \qquad \textbf{(3.3)}$$

Through the reactive route of Equation 3.3, they successfully able to achieve 'x' compositions up to 90% only, indicating that only 10% of indium was incorporated into GaN lattice. Similarly, using the same solvent (Toluene), but at superheated condition, Choi *et al.* synthesized InN (Indium nitride) nanomaterials through the metathesis reaction between indium (III) bromide ($InBr_3$) and sodium azide (NaN_3) with refluxing hexadecane solvent at 280 °C. They developed the same metathesis route in toluene solvent and synthesized $Ga_xIn_{1-x}N$ (x = 0.5 and 0.75) solid solution with high Indium amount in the solid solution [42].

Initially, prior to the adaptation of these solvothermal synthetic routes of $Ga_xIn_{1-x}N$ ($0 \leq x \leq 1$) solid solution at continuous supercritical conditions, certain key factors have to be considered. The design of the continuous supercritical millireactor with operating temperature and pressure should be opted in such a way that the decomposition of InN doesn't take place, resulting in the formation metallic indium. The solvent opted for the synthetic methodology should ensure the reactivity at supercritical conditions so that the phase segregation is minimized or completely eliminated in the $Ga_xIn_{1-x}N$ solid solution. Usually, InN decomposition begins about 650 °C, 1 bar under N_2 pressure [39]. In general, for obtaining high InN amount in the ternary solid solution, the pyrolyzing temperature of the precursor should be below 650 °C. Hence, the solvent chosen in the supercritical domain should possess a critical temperature well below 650 °C and it should provide the necessary polarity and reactivity for obtaining homogeneously distributed cations.

3.2.2. Continuous supercritical synthesis of the $Ga_xIn_{1-x}N$ ($0 \leq x \leq 1$) solid solution in toluene

The pyrolysis of gallium (III) and indium (III) cupferronate solid solution precursor with the presence of HMDS as a nitriding agent in supercritical toluene was chosen as the primary chemical reactive pathway for the synthesis of $Ga_xIn_{1-x}N$ solid solution. The general scheme of this synthetic route is depicted in Figure 3.3.

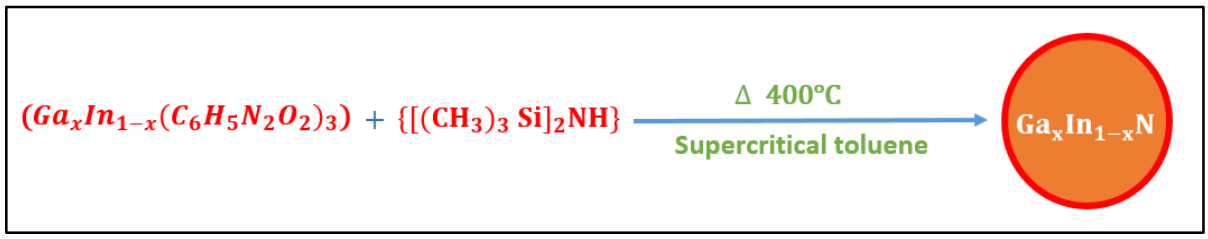

Figure 3.3. *Cupferron and HMDS chemistry attempted in supercritical toluene for the synthesis of the full range of $Ga_xIn_{1-x}N$ ($0 \leq x \leq 1$) solid solution nanomaterials.*

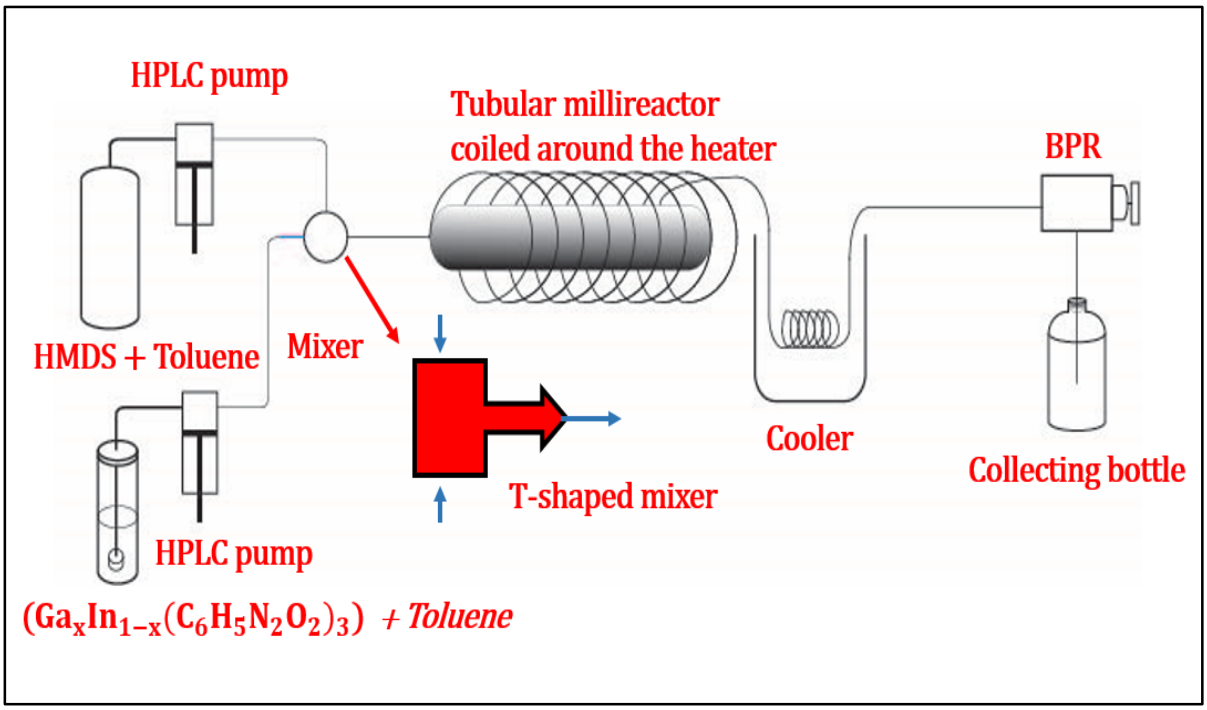

Figure 3.4. *Schematic diagram of the continuous flow supercritical millireactor set-up for the $Ga_xIn_{1-x}N$ ($0 \leq x \leq 1$) solid solution synthesis.*

3.2.2.1. Experimental set-up

We used a similar reactor set-up as the one developed for GaN QDs (See Chapter II). The continuous flow setup used here for the synthesis of $Ga_xIn_{1-x}N$ ($0 \leq x \leq 1$) solid solution is depicted in Figure 3.4. Since the synthetic pathway consists of dual precursor chemistry for the generation of nanomaterials of $Ga_xIn_{1-x}N$ ($0 \leq x \leq 1$), the process set-up was designed such a way that on the upstream side, the set-up consists of a t-shaped elementary mixer for the uniform mixing of the complex solid solution of cupferronate precursor and the nitriding source at ambient room temperature. The dual precursors: solid solution cupferronate and HMDS (nitriding agent) were both dissolved in anhydrous toluene in two separate vessels leading to two precursor solutions: (1) gallium/indium cupferronate and (2) HMDS solution. Each precursor solution is pumped using separate JASCO high pressure (HPLC) pumps.

The downstream portion of the set-up consists of a cooling section made up of a water bath in order to reduce the temperature and to quench the reaction. The pressure of the flow system (150 bar) is maintained and controlled by a back pressure regulator (BPR). The tubular millireactor was made up of three-meter long 1/16``of an inch, 1 mm inner diameter stainless steel tube. The millireactor is made by manually coiling the stainless steel tube around a heating cartridge (Acim Jouanin, 800 W and 230 V). The heating cartridge is fitted with feedback responsive thermostat, where both the heating cartridge and the thermostat are connected to the temperature control system for varying or maintaining the temperature of the process medium during the synthesis.

3.2.2.2. Reagents & solvents used

The reagents used in the synthesis of the ternary solid solutions are: (1) gallium (III) iodide (GaI_3) powder, anhydrous with 99.999% trace metal basis, indium (III) iodide (InI_3) powder, anhydrous with 99.998% trace metal basis, N-Nitroso-N-phenyl hydroxylamine ammonium salt (Cupferron), 97% reagent grade and nitriding gent (HMDS). All these precursors were purchased from sigma-aldrich. They were received in inert gas filled sealed packages and stored in an argon gas circulating glove box. The precursors were used directly as received without any post processing or further modifications. Deionized water, anhydrous toluene (99.8%) and anhydrous methanol (99.8%) were the solvents used in this synthesis. Toluene and methanol were purchased from sigma-aldrich and de-ionized water was prepared from the water distilling equipment in our lab.

3.2.2.3. Synthetic procedure of the cupferronate precursors

The next two sections will deal with (i) the synthesis of gallium (III) indium (III) cupferronate solid solution from the GaI_3 and InI_3 precursors and (ii) the continuous supercritical synthesis of $Ga_xIn_{1-x}N$ ($0 \leq x \leq 1$) solid solution.

GaI_3 and InI_3 salts were used as sources of gallium (III) and indium (III), respectively for the synthesis of the complex solid solution cupferronate precursor. Based on the size and volume of the precursor bottle and the glass bottle that can be taken inside the glove box, the total maximum amount of both GaI_3 and InI_3 taken was 1.2 mmol. Both salts are added together in a glass bottle within the glove box. In another separate bottle, 4.8 mmol of cupferron was added, within the glove box. A 3:1 (cupferron: mixture of GaI_3 + InI_3) ratio is necessary to be in the stoichiometric conditions. To ensure this, cupferron was put in excess with a 4:1 ratio. Both these bottles were closed with tight septum fitted cap and taken outside the glove box and placed in ice cubes filled water bath in the lab. Through the septum, 20 mL of cold deionized water (4 – 7 °C) was added to each bottle separately.

The mixture of GaI_3 and InI_3 dissolves in the cold water within few minutes, if the salts are fine as powders. The cupferron's dissolution in cold water takes around 10 to 15 minutes, sometimes depending on the size of the cupferron particles taken, the mixture of cold water and cupferron was ultrasonicated for few minutes in higher power ultrasonicator bath filled with water and ice. After the complete dissolution of cupferron in water, it forms a yellow colour solution. Then, the transparent gallium and indium salt solution and the cupferron solution are mixed quickly in a separate argon filled bottle, through the septum of the glass bottle. During this process, the argon filled bottle is immersed in the ice filled bath as the reaction with the salt is exothermic. This reaction leads to the formation of a cupferronate solid solution precursor, as depicted in Equation 3.4.

$$(C_6H_9N_3O_2)_3 + 3NH_4^+ + x(GaI_3) + (1-x)(InI_3) \xrightarrow[\text{Ice bath}]{0°C} Ga_xIn_{1-x}(C_6H_5N_2O_2)_3 + 3NH_4I \quad \textbf{(3.4)}$$

The solid solution cupferronate complex precipitates as a white-light yellowish compound. The precipitate is separated and centrifuged with fresh de-ionized water at 10000 RPM for 10 minutes. After centrifugation, the supernatant was removed and the precipitate was again dispersed in fresh deionized water and the procedure was repeated twice. Consecutively, the precipitate is dried in vacuum for several hours to remove the water molecules present at ambient temperature. The dried cupferronate precursor is later used for the synthesis of the solid solution nanomaterials without any further treatment.

3.2.2.4. Synthesis of $Ga_xIn_{1-x}N$ ($0 \leq x \leq 1$) solid solution nanomaterials

The dried cupferronate solid solution is dissolved in 60 mL of anhydrous toluene, resulting in a concentration of 0.02 M. A light yellowish solution is obtained after complete dissolution. The solution is transferred to the precursor bottle, depicted in Figure 3.4 for the continuous injection. In another precursor bottle, 2 mL of nitriding agent (HMDS) was added to 58 mL of toluene inside the glove box, resulting in a concentration of 0.1645 M. The HMDS and toluene solutions are taken outside the glove box and fitted to the supercritical setup for the continuous injection for synthesis.

The supercritical set-up was operated at 150 bar pressure using the BPR (the critical conditions of toluene are: T_c = 320 °C and P_c = 41 bar). Both the cupferronate solution and the nitriding agent solution were injected at the same time using HPLC pumps. Each precursor was injected at 1mL/min, and temperature of the system was maintained at 400 °C. The combined total flow rate was 2mL/min, resulting in a residence time of 33 s. The particles were collected in the collection bottle. The colour of the colloidal solution obtained depended on the composition of the solid solution targeted in the synthesis. The particles were washed twice by centrifugation and after each centrifugation, the particles were collected and redispersed in fresh anhydrous toluene. The dispersed particles were used for characterization without any further treatment.

3.2.3. Characterization of the $Ga_xIn_{1-x}N$ ($0 \leq x \leq 1$) solid solutions from supercritical toluene

Different compositions of the cupferronate precursor $Ga_xIn_{1-x}(C_6H_5N_2O_2)_3$ were prepared. Here, 'x' in the precursor compound was increased by 10% systematically for each cupferron precursor ($x = 0,0.1,0.2,0.3,0.4,0.5,0.6,0.7,0.8,0.9$ and 1) to attain the complete range of the solid solution. The very important factor observed in the synthesis of $Ga_xIn_{1-x}N$ ($0 \leq x \leq 1$) in supercritical toluene is that the solubility of the cupferronate precursor for the composition range of $x \leq 0.4$ decreases even though the concentration taken for all the precursors in toluene was the same. The insolubility of the precursor in toluene was observed for high indium contents. Hence, this toluene solvent was favourable only for the dissolution of precursor with high gallium content. Therefore, our approach was only tested for the composition ranging between x = 0.3 and x = 1, as indicated by the theoretical stoichiometric column in Table 3.1. The obtained nanoparticles were characterized by various techniques listed in the next sections.

3.2.3.1. Elemental analysis

To estimate the stoichiometric amount of gallium/indium present in the as-synthesized solid solution nanomaterials (experimental/actual values). Subsequently, compare the experimental

values to the theoretical stoichiometric amount of gallium/indium taken for the cupferronate precursor preparation, inductively couple plasma-mass spectrometry (ICP-MS) was carried out.

Nanomaterials of different compositions of gallium and indium obtained after synthesis were centrifuged at 10,000 RPM for 10 minutes. After centrifugation, the supernatant was removed and the particles were dispersed in fresh anhydrous toluene. The centrifugation procedure was repeated twice and the particles were dispersed and stored in known quantities of toluene solvent. For the ICP-MS analysis, the particles were recovered from the dispersed solvent and dried in open atmosphere. To the known quantity (usually 1 - 10 mg) of dried particles, 1 ml of concentrated hydrochloric acid (HCl), 1 ml of sulphuric acid (H_2SO_4) and 1 ml of nitric acid (HNO_3) was added to ensure a complete dissolution of the nanomaterials. Then, 25 mL of deionized water was added to this solution. This solution was kept undisturbed for 24 h and then taken for ICP-MS measurement. The obtained results are provided in Table 3.1.

From the ICP results, it is obvious that the experimental stoichiometric amount of gallium/indium in the solid solution nanomaterials were more or less similar to the theoretical gallium/indium amount taken for their corresponding cupferronate precursor preparation. Especially, when the gallium content is high in the solid solution, like the solid solutions mentioned in entries 1, 2 and 3 of Table 3.1.

Table 3.1. *ICP-MS results for the composition of $Ga_xIn_{1-x}N$ solid solution nanomaterials synthesized in supercritical toluene.*

S.No	Stoichiometric amount of gallium and indium in the cupferronate precursor (mole basis) (theoretical)	Stoichiometric amount obtained in the $Ga_xIn_{1-x}N$ solid solution nanomaterials (mole basis) (experimental)
1.	$Ga_{0.8}In_{0.2}$	$Ga_{0.92}In_{0.08}$
2.	$Ga_{0.8}In_{0.2}$	$Ga_{0.88}In_{0.12}$
3.	$Ga_{0.8}In_{0.2}$	$Ga_{0.84}In_{0.16}$
4.	$Ga_{0.7}In_{0.3}$	$Ga_{0.74}In_{0.26}$
5.	$Ga_{0.6}In_{0.4}$	$Ga_{0.74}In_{0.26}$
6.	$Ga_{0.5}In_{0.5}$	$Ga_{0.58}In_{0.42}$
7.	$Ga_{0.4}In_{0.6}$	$Ga_{0.51}In_{0.49}$
8.	$Ga_{0.3}In_{0.7}$	$Ga_{0.54}In_{0.46}$

As the indium content is increased, some significant dissimilarities between the obtained experimental values of gallium/indium amount and the theoretical amount gallium/indium amount taken for precursor preparation begins to appear, as shown in Table 3.1. In the continuous supercritical toluene synthesis, the maximum indium incorporation attained was 49% (mole basis) based on ICP results, as shown entry 7 of Table 3.1. Following ICP analysis, the structure of these nanomaterials were characterized through powder XRD study.

3.2.3.2. Structural characterization

The particles obtained after the synthesis were centrifuged twice. After centrifugation, they were dispersed in a fresh anhydrous solvent. For XRD measurements, the particles were recovered from the dispersed solvent and deposited on a silicon substrate with zero background and X-ray powder diffraction study was performed for each solid solution nanomaterial mentioned in Table 3.1. The obtained powder XRD results are plotted and schematically depicted for various $Ga_xIn_{1-x}N$ solid solutions in Figure 3.5.

The XRD spectrum of the various $Ga_xIn_{1-x}N$ solid solutions with different contents of gallium and indium in Figure 3.5 are wide in nature, without any distinguishing peaks of a particular crystallite structure. These featureless broad peaks are conventional XRD pattern of nanocrystalline materials found on GaN and InN. This kind of similar peaks was also observed in the chapter II, when studying the GaN nanomaterials.

When observing each XRD pattern corresponding to the solid solution nanomaterials in Figure 3.5, it is obvious that there are two bumpy regions in each spectrum. The big bump region is from 25 - 40° and the small protuberance region is from 45 - 67°. From the XRD, it can be seen that the uniform bumpy region from 25 - 40° becomes wider with decreasing indium content and for the composition of $Ga_{0.88}In_{0.12}N$ with high gallium content, the uniform shape is completely lost and the bump region (25 - 40°) starts exhibiting shift to the higher 2θ values with a growing contribution at 36°, corresponding to the (101) plane of GaN hexagonal wurtzite crystal structure.

Additionally, the width of the small protuberance ranging from 45 - 67° starts to shrink in the protrusion range with increasing gallium content and reaches a limit of 54 - 68° for the XRD pattern of GaN nanomaterial. This small bumpy region also shifts with an increasing gallium content in the solid solution. From the XRD pattern, it is difficult to clearly conclude about the crystal structure(s). Further investigations regarding the crystal structure and d-spacing analysis will be carried out through HR-TEM analysis and electron diffraction study.

The morphology and size of the $Ga_xIn_{1-x}N$ ($0.5 \leq x \leq 1$) nanomaterials were studied using Transmission Electron Microscopy (TEM). The synthesized nanomaterials obtained immediately from synthesis are centrifuged twice and dispersed in anhydrous toluene and stored. From this dispersed solution, particles were recovered for TEM analysis and dispersed in anhydrous ethanol. These ethanol solutions with particles were ultrasonicated for few minutes and the resultant concentrated solutions are drop casted on carbon (formvar) covered 200 mesh copper grid for TEM analysis. This drop casting procedure is done in open atmosphere and the grids are dried for 5 -10 min and then installed directly into the equipment for measurement. The studied images are schematically depicted in Figures 3.6-a – 3.6-d.

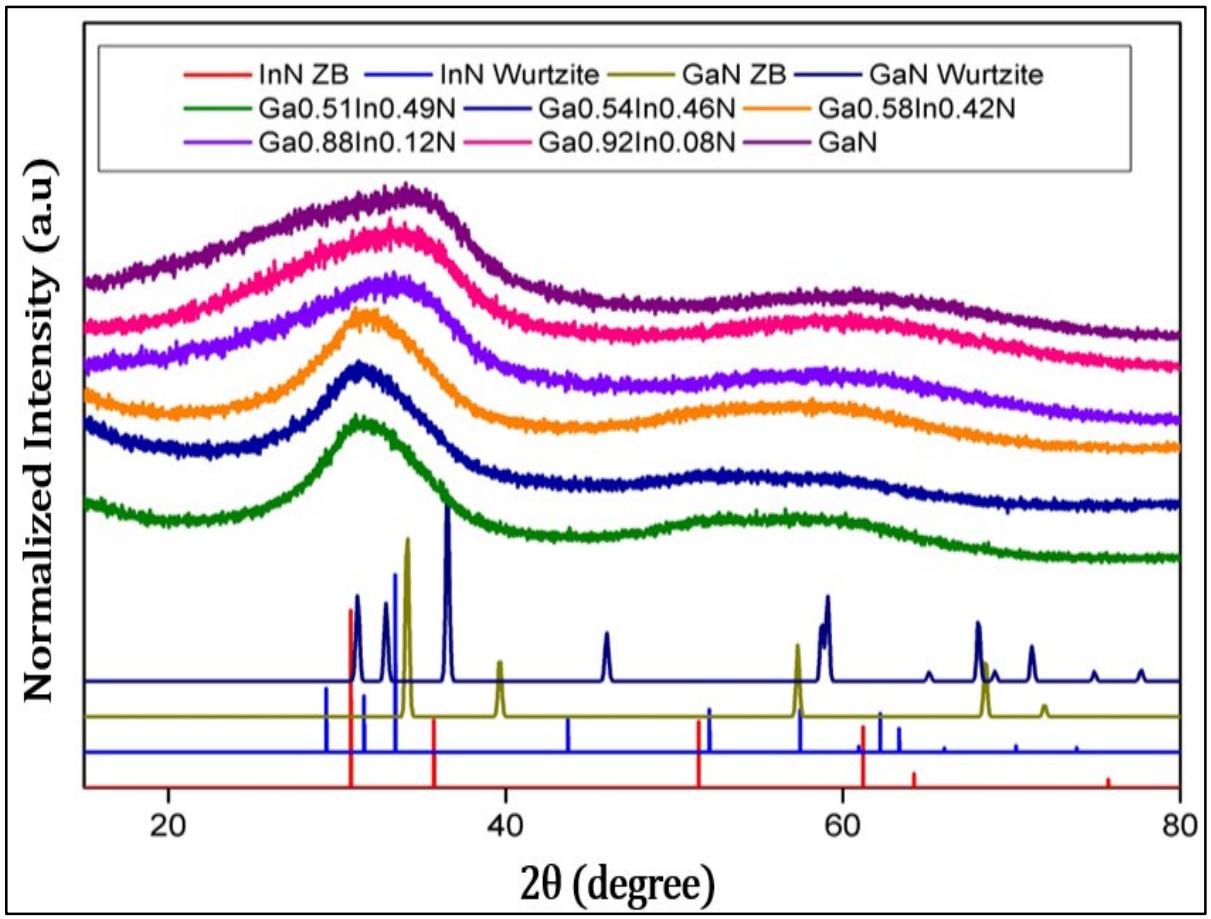

Figure 3.5. *XRD pattern of the various $Ga_xIn_{1-x}N$ ($0.5 \leq x \leq 1$) solid solution nanomaterials synthesized continuously in supercritical toluene. The values of gallium/indium amount mentioned in each solid solution nanomaterials are experimental obtained values from the ICP-MS analysis.*

From the TEM characterization of the $Ga_xIn_{1-x}N$ ($0.5 \leq x \leq 1$) nanomaterials, it appears that irrespective of the amount of gallium/indium in the solid solution. The samples exhibit two distinctly set of nanoparticles, as illustrated through the TEM images depicted schematically in Figure 3.6. The first set of nanoparticles are well dispersed particles with average sizes of about 2.5 ± 0.5 nm. These small particles present in all the places of ensemble of nanomaterials analysed, as shown exclusively in the TEM image of Figure 3.6-c. The size range of these particles are pretty much in agreement with the size of the GaN QDs obtained in batch mode through cupferron and HMDS chemistry [40]. The Bohr exciton radius of bulk GaN at room temperature is 2.8 nm [43, 44] and that of InN was 8 nm [45]. As the size of the low dimensional particles in the $Ga_xIn_{1-x}N$ nanomaterials are well below the exciton radius of GaN and InN material, quantum confinement is expected in these systems. Besides these low dimensional particles, larger spherical aggregates are observed in all the solid solutions studied. This is clearly depicted in the all image of Figure 3.6. These big spherical aggregates possess an average size of 67 ± 13 nm. In order to further investigate these large aggregates, HR-TEM measurements were performed.

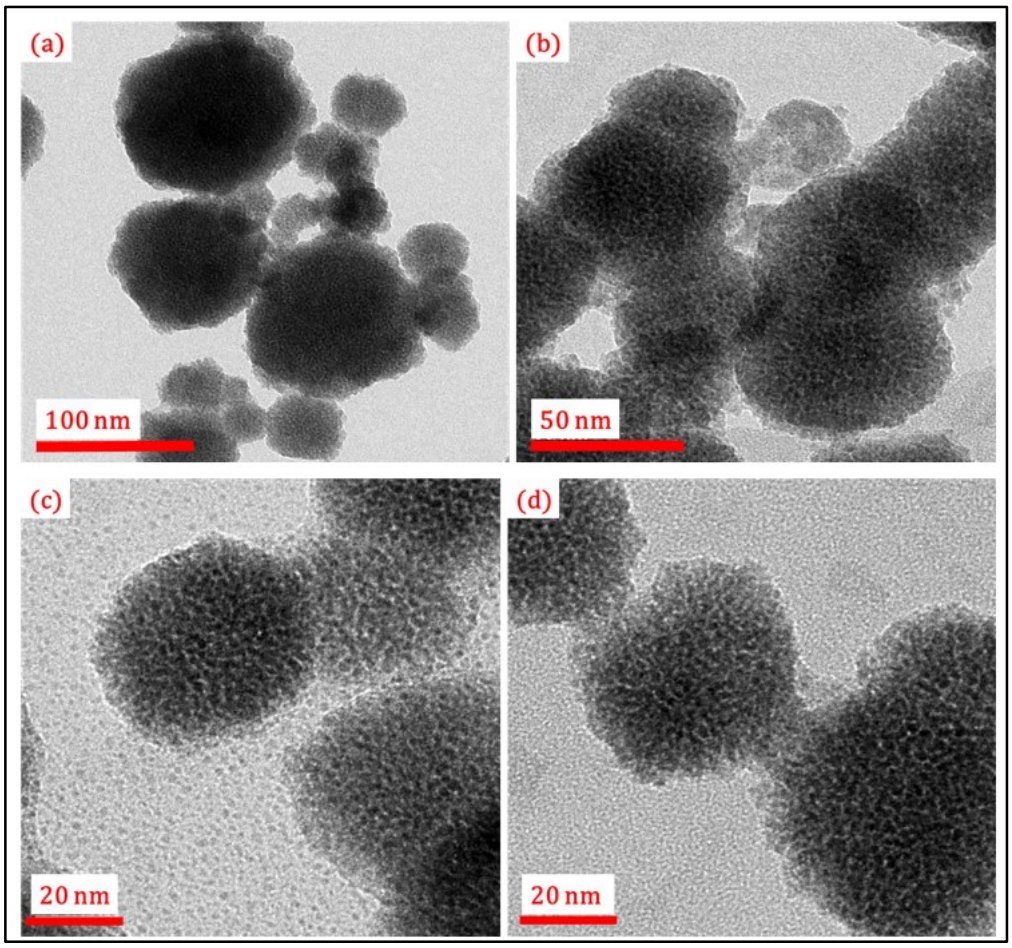

Figure 3.6. *a, b, c and d. TEM images of* $Ga_{0..84}In_{0.16}N$, $Ga_{0.74}In_{0.26}N$, $Ga_{0.58}In_{0.42}N$ *and* $Ga_{0.54}In_{0.42}N$ *solid solution nanomaterials, respectively, synthesized with the continuous flow millireactor using supercritical toluene as the reactive medium.*

For the HR-TEM characterization, the nanoparticles (NPs) of $Ga_xIn_{1-x}N$ ($0.5 \leq x \leq 1$) were dispersed in anhydrous ethanol and ultrasonicated for few minutes. Subsequently, the resultant concentrated colloidal solution were drop casted on LACEY carbon covered 300 mesh copper grid, following the completion of drop casting technique. The grids are dried in open atmosphere and then installed directly into the equipment for HR-TEM study. When observing the spherical aggregates with the HR-TEM technique no lattice fringes were seen. To reveal further information and to identify whether phase segregation of GaN and InN has occurred in this quasi-binary $Ga_xIn_{1-x}N$ solid solution, elemental mapping was performed. The same HR-TEM equipment was used for this study, the particular region of ensemble of nanomaterials on which elemental mapping studied was photographed through STEM (scanning transmission electron microscope) mode. The as obtained STEM images are depicted in Figures 3.7-a and 3.7-b.

The elemental mapping of $Ga_xIn_{1-x}N$ solid solutions is obtained through energy dispersive X-ray spectroscopy (EDS). The mapped image mentioned in Figures 3.8 and 3.9 corresponds to the nanomaterial region depicted in Figures 3.7-a and 3.7-b, respectively. From the elemental mapping images mentioned in Figures 3.8 and 3.9, it can be seen that a homogeneous

distribution of the cations in the $Ga_xIn_{1-x}N$ Quasi-Binary system has not been achieved in the nanomaterials synthesized in supercritical toluene. Phase segregation has occurred and this has resulted in regions possessing more GaN nanoparticles and other region with more InN nanoparticles. This kind of phase segregation is seen in solid solution with low Indium content 16% (atom%) as depicted for $Ga_{0.84}In_{0.16}N$ solid solution in both Figures 3.8 and 3.9. From the STEM and elemental mapping images, it can be concluded that such kind of phase segregation has resulted in some sort of nanocomposite core/shell system instead of solid solution nanomaterials. To further understand the impact of this phase segregation on the optical properties and to ensure the ability of these nanomaterials to function as visible light

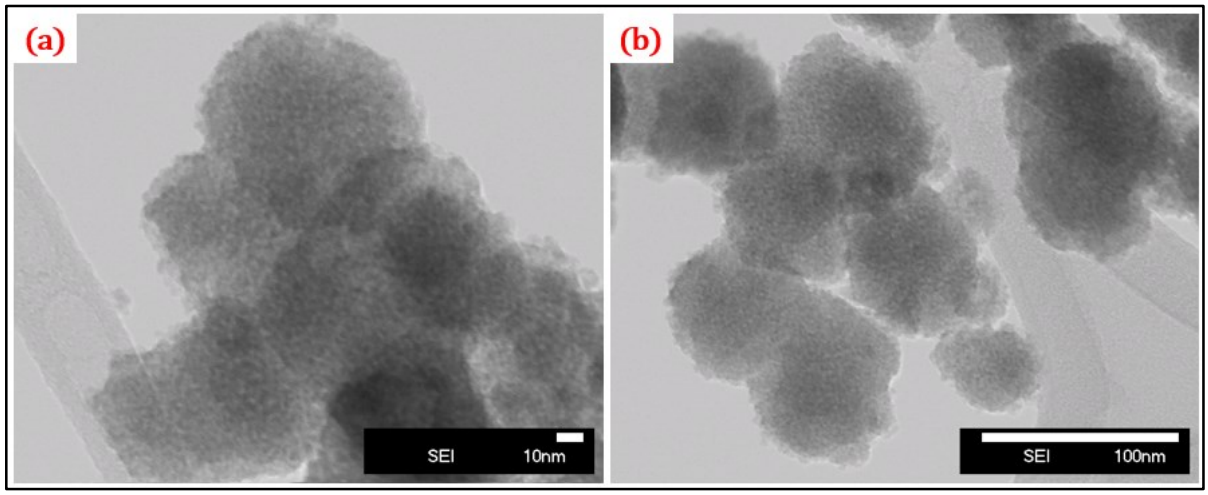

active photocatalysts UV-VIS absorption study was performed.

Figure 3.7. *a and b. STEM images of* $Ga_{0.84}In_{0.16}N$ *solid solution nanomaterials synthesized through continuous flow millireactor in supercritical toluene.*

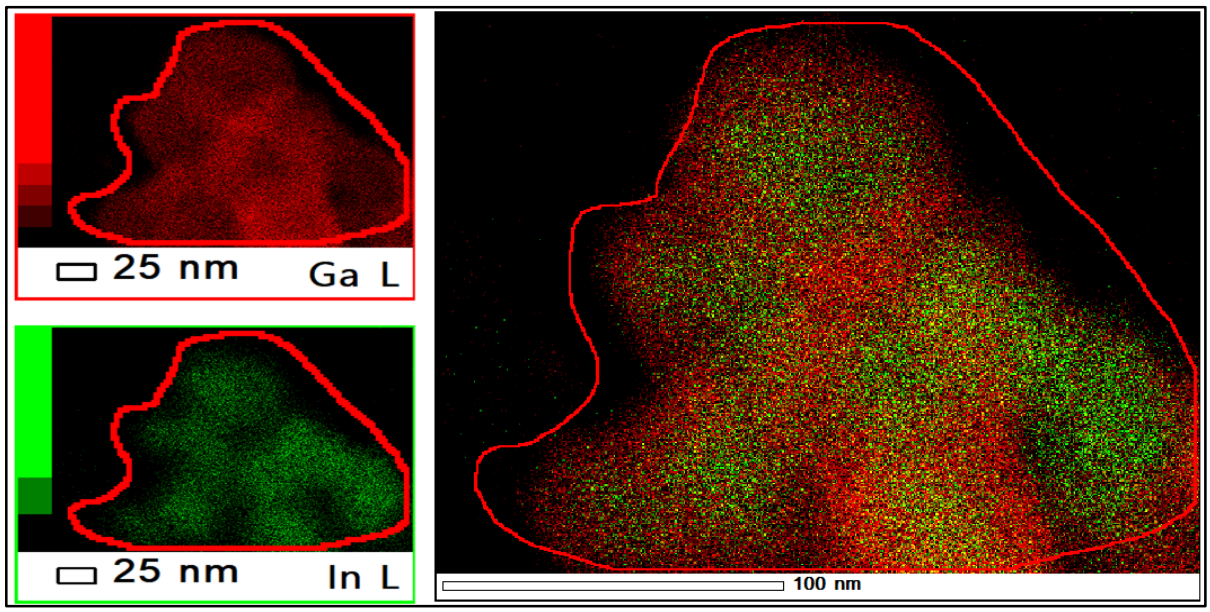

Figure 3.8. *Elemental mapping of $Ga_{0.84}In_{0.16}N$ solid solution nanomaterial synthesized through continuous flow millireactor in supercritical toluene, this particular image corresponds to region depicted in STEM image of Figure 3.7.a.*

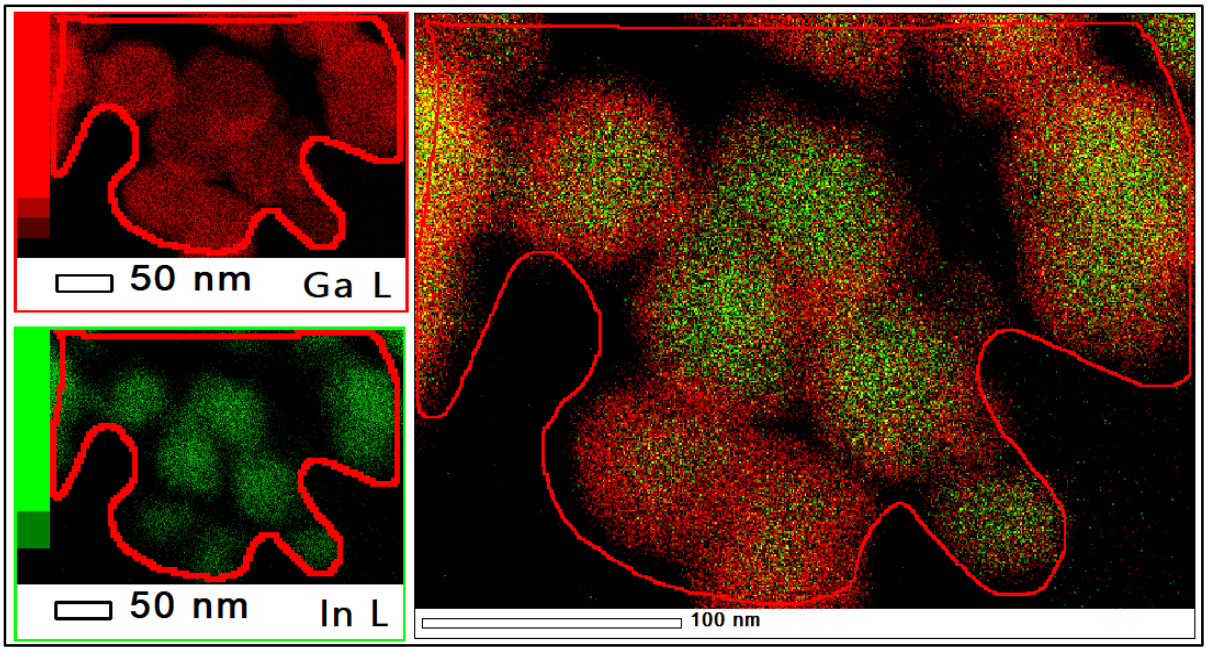

Figure 3.9. *Elemental mapping of $Ga_{0.84}In_{0.16}N$ solid solution nanomaterial synthesized through continuous flow millireactor in supercritical toluene, this particular image corresponds to region depicted in STEM image of Figure 3.7.b.*

3.2.3.3. Optical characterization

The interaction of light (electromagnetic waves) with nanomaterials are studied through the characterization of the optical properties of the nanomaterials. UV-VIS absorption spectroscopy is performed on the $Ga_xIn_{1-x}N$ ($0.5 \leq x \leq 1$) nanomaterials to estimate their optical band gap and the shift of band gap with the indium incorporation into the $Ga_xIn_{1-x}N$ Quasi-Binary system. The $Ga_xIn_{1-x}N$ nanoparticles are washed through centrifugation twice at 10,000

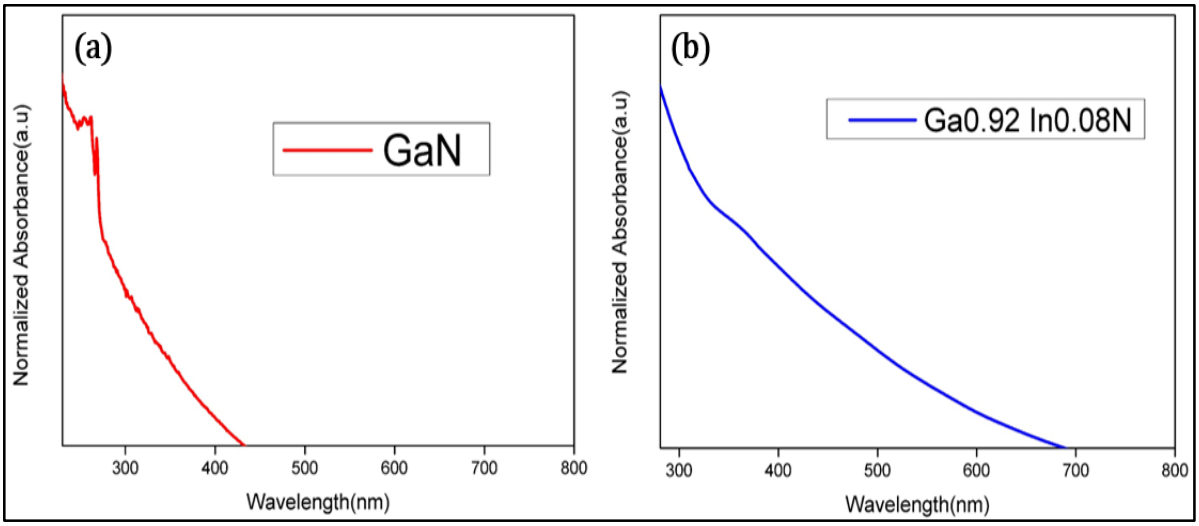

RPM for a period of ten minutes. For the UV-VIS absorption study, the particles were dispersed in acetonitrile solvent. As the acetonitrile provided an ideal solvation effect on the particles compared to the other solvents (ethanol, toluene, etc.). On these colloidal solutions absorption was performed and resulting spectra are plotted and illustrated in Figures 3.10-a – 3.10-f.

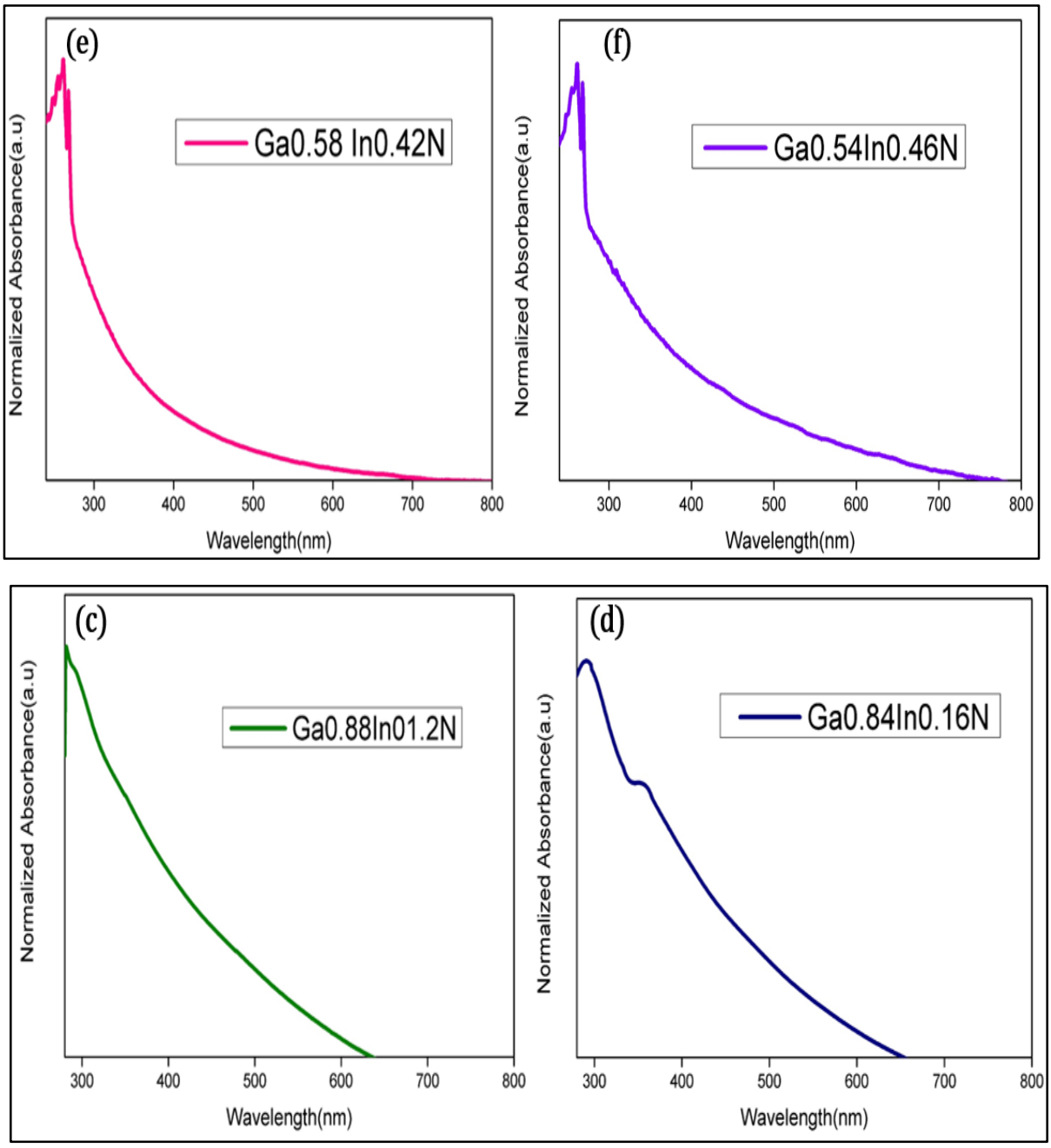

Figure 3.10. *a, b, c, d, e and f. UV-VIS absorption spectrum of GaN, $Ga_{0.92}In_{0.08}N$, $Ga_{0.88}In_{0.12}N$, $Ga_{0.84}In_{0.16}N$, $Ga_{0.58}In_{0.42}N$ and $Ga_{0.54}In_{0.46}N$ nanomaterials, respectively, synthesized through cupferronate and HMDS chemistry in supercritical toluene*

For an ideal solid solution system formed between a wide band gap and narrow band gap semiconductor materials, the continuous red shift of the absorption spectrum with an increasing

content of narrow band gap semiconductor indicates that a perfect solid solution has formed with a precise tuning of the band gaps. Here, in the $Ga_xIn_{1-x}N$ nanomaterials synthesized in supercritical toluene such continuous red shift with increasing InN content was not observed, as depicted in the absorption spectra in Figure 3.10. The phase segregation phenomenon effect on the nano spheres (avg size 67 nm) has resulted in a nanocomposite core/shell system (see Figures 3.8 and 3.9). Such a formation of nanocomposite sphere has detrimental effect on the red shift of the absorption spectrum. Therefore, a precisely tunable visible light active photocatalysts is unachievable through the supercritical synthesis in toluene. In order to clearly visualize the absorption pattern of each solid solution nanomaterials and the extent to which the phase segregation has effected the band edge absorption, some absorption spectrum of some compositions are plotted individually (see Figure 3.10) and discussed below.

In this continuous flow supercritical synthesis in toluene using cupferronate and HDMS, GaN was synthesized and its UV-VIS absorption spectrum is depicted in Figure 3.10-a. From the absorption spectrum, it is obvious that quantum confined GaN nanomaterials are produced, as the steep absorption region onset on 274 nm with intense band gap at 264 nm are present. As InN is incorporated into the GaN lattice, a band shift and the reduction of the band edge at 264 nm is observed as depicted in Figure 3.10-b for UV-VIS absorption of the $Ga_{0.92}In_{0.08}N$ solid solution. The tail end of the continuous absorption spectra of $Ga_{0.92}In_{0.08}N$ spans up to 685 nm with just 8% (atom%) of indium incorporation.

On the further successive increment of indium content into the $Ga_xIn_{1-x}N$ solid solution system, a continuous shift was not observed, as depicted in Figures 3.10-c and 3.10-d. The UV-VIS absorption spectrum of $Ga_{0.88}In_{0.12}N$ (Figure 3.10-c) and $Ga_{0.84}In_{0.16}N$ (Figure 3.10-d), the extent of absorption ranges in both these spectra falls behind the absorption spectrum of $Ga_{0.92}In_{0.08}N$ sample even though more amount of indium is present in these solid solutions. The phase segregation phenomenon, as depicted in Figures 3.8 and 3.9 for $Ga_{0.84}In_{0.16}N$ solid solution, was the main reason for this decrement in the red shift of the absorption spectrum even though more amount of indium is incorporated into the system. The phase segregation behaviour obviously changes the nature of the system from a solid solution to a nanocomposite behaviour, depending on the morphology and the composition of the Quasi-Binary system. When further increasing the indium content in this $Ga_xIn_{1-x}N$ solid system synthesized in toluene, the red shift of absorption is completely lost and distinct appearance of band edge of GaN quantum confined peak is more obvious as seen in Figures 3.10-e and 3.10-f.

Eventually, for an indium content up to 50% (atom%) in the solid solution, no significant red shift into deep visible or near IR was seen. Analogously, the sharp quantum confined band edge of GaN distinctly appears for both $Ga_{0.58}In_{0.42}N$ and $Ga_{0.54}In_{0.46}N$ at 264 nm with a sharp onset of steep region at 280 nm. These results clearly indicate that core/shell kind of nanocomposite system has been formed all around the ensemble of nanomaterials with shell consisting of GaN and inside a core of InN, as depicted for a particular region of ensemble of nanomaterials in Figure 3.9.

3.2.3.4. Conclusion

The strains present in the $Ga_xIn_{1-x}N$ ternary alloy system due to the large lattice mismatch (11%) between the GaN and InN are the main reasons for the phase segregation effect in this particular solid solution. Nevertheless, synthesis in nanomaterial (powder) form with non-planar structure can successfully insert indium content of more than 50% into the $Ga_xIn_{1-x}N$ solid solution system without any phase segregation, resulting in continuous red shift of the absorption band edge of the nanomaterials so that a novel visible light photocatalysts can be realized from this system.

The appropriate methodology to succeed in synthesizing the full $Ga_xIn_{1-x}N$ ($0 \leq x \leq 1$) solid solution is to play with the reactive medium because toluene not only yielded phase segregation in high indium content, but it was also unable to dissolve the solid solution precursor with more than 70% (atom%) of indium. The first criteria was to choose a solvent system which could dissolve the complete range of the $Ga_xIn_{1-x}N$ solid solution ($0 \leq x \leq 1$) precursor and would function as a proper medium for attaining homogenous well distributed solid solution with negligible phase segregation. In the next section, I will describe the use of a combined toluene and methanol mixture to reach this goal.

3.2.4. Reasons for opting for dual solvent system

For attaining the complete tunability of the solid solution, appropriate solvent was needed to dissolve all the precursor pertaining to the complete range of the system. The indium rich cupferronate ($Ga_xIn_{1-x}(C_6H_5N_2O_2)_3$) precursor ($x<0.3$) or the indium cupferronate precursor ($In(C_6H_5N_2O_2)_3$) was not soluble in anhydrous toluene solvent. The solvent opted for the dissolution of the cupferronate precursor should also be compatible with HMDS precursor. It was already reported that HMDS (Hexamethyldisilazane, $[\{(CH_3)_3Si\}_2NH]$) is a non-nucleophilic base, aminating reagent and selective silylating reagent [46]. The solvent opted shouldn't be extremely reactive with HMDS resulting in the formation of other by-products. Additionally, HMDS is very sensitive to air and moisture and it decomposes rapidly on exposure to the air & water at ambient conditions. HMDS is highly preferred by the organic chemist for the synthesis of trimethylsilyl ethers. Alcohols, amines and thiols reacts rapidly with the HMDS resulting in the trimethylsilylation of their corresponding aliphatic or aromatic group of the compound reacting with HMDS with the evolution of ammonia, as shown in Equation 3.5 [46].

$$\{(CH_3)_3Si\}_2NH + 2ROH \rightarrow 2RO(\{(CH_3)_3Si\}_2) + NH_3 \quad \textbf{(3.5)}$$

The ultimate prerequisite reaction required for the generation of solid solution is given by Equation 3.3

$$2(Ga_xIn_{1-x}(C_6H_5N_2O_2)_3) + 2[(CH)_3Si]_2NH \xrightarrow[\text{Toluene}]{\Delta\,(300°C)\ 24h} 2Ga_xIn_{1-x}N + 2[(CH)_3Si]_2O + H_2O \quad \textbf{(3.3)}$$

On systematic analysis of the solubility of $(In(C_6H_5N_2O_2)_3)$ or indium rich $(Ga_xIn_{1-x}(C_6H_5N_2O_2)_3)$ ($x \leq 0.3$) solid precursor it was found that both these precursors were easily soluble in anhydrous methanol, anhydrous 1,4-Dioxane and hexylamine. In order to avoid the reaction occurring in Equation 3.5, which can happen when the HMDS is dissolved in these solvent systems in the precursor bottle outside the continuous flow supercritical millireactor at ambient conditions. Hence dual solvent system was opted for the synthesis of $Ga_xIn_{1-x}N$ ($0 \leq x \leq 1$) solid solution, where HMDS will be dissolved in the solvent like toluene or cyclohexane and solid solution cupferronate will be dissolved in methanol or amine. Systematically solubility of the precursor, facile operation in the synthesis and reactor lifetime was checked for the dual solvent system mentioned below. One system among these which satisfied all the above conditions was adopted for the synthesis of the entire composition of the solid solution.

Table 2. Dual solvent system in which the cupferronate and HMDS chemistry were attempted for the effective and facile synthesis of InN and $Ga_xIn_{1-x}N$ ($0 \leq x \leq 1$) solid solution

S.No	Solvent opted for the cupferronate precursor	Solvent for the N_2 source (HMDS)
1.	Methanol	Cyclohexane
2.	Hexylamine	Cyclohexane
3.	Hexylamine	Toluene
4.	1,4-Dioxane	1,4-Dioxane
5.	Methanol	Toluene

The indium rich $Ga_xIn_{1-x}(C_6H_5N_2O_2)_3)$ solid solution and $(In(C_6H_5N_2O_2)_3)$ precursors were synthesized and found to be soluble in the solvents mentioned in Table 3.2, entries 1 – 5. Out of these solvents both the Indium cupferronate and the entire range of solid solution precursor $(Ga_xIn_{1-x}(C_6H_5N_2O_2)_3)$ was easily soluble in methanol compared to the other solvents. Hence the dual solvent system of methanol and toluene was seeming to be an appropriate solvent system for the synthesis of the complete range of solid solutions.

3.3. Tunability of $Ga_xIn_{1-x}N$ solid solution using toluene and methanol supercritical mixtures

3.3.1. Introduction to the synthesis

The complete range of composition in $Ga_xIn_{1-x}N$ ($0 \leq x \leq 1$) solid solution was successfully achieved using supercritical toluene and methanol mixture from solid solution cupferronate dissolved in methanol and HMDS precursor dissolved in toluene. The synthesis was done in such way that for each individual continuous synthesis of solid solution, the indium percentage was varied by step of 10% (atom%) and consecutive successive increment of indium in GaN was accomplished. Indium molar percentage in solid solution is varied by varying the molar amount of InI_3 taken for the solid solution cupferronate synthesis. The synthesis was carried out in the same set-up used for the synthesis of $GaxIn_{1-x}N$ solid solution in toluene (see Figure 3.4).

The synthesis was carried out at 400°C and 150 bar well above the critical temperature (T_c) and pressure (P_c) of both toluene (T_c = 320 °C and P_c = 41 bar) [47] and methanol (T_c = 240 °C and P_c = 81 bar) [48] and their critical mixtures. A 4 m long stainless steel tubular millireactor with 1 mm inner diameter (volume = 3.14 mL) was employed in this synthesis. The amount of $(Ga_xIn_{1-x}(C_6H_5N_2O_2)_3)$ precursor dissolved in 60 mL of methanol was taken in such a way that a 0.02 M concentration was maintained. 5 ML of HMDS was added to 55 mL methanol in another precursor bottle. The ratio of HMDS to cupferronate $(Ga_xIn_{1-x}(C_6H_5N_2O_2)_3)$ precursor was 20. Such a high amount of nitrogen precursor was taken for the effective incorporation of higher indium content in the solid solution system. The solutions were injected separately through two different pumps at a flow rate of 1mL/min for each pump, resulting in a residence time of 19 s.

3.3.2. Characterization of $Ga_xIn_{1-x}N$ solid solution synthesized in toluene and methanol supercritical mixtures

The particles obtained after each synthesis were recovered from the collection bottle and centrifuged at 10000 RPM for 10 min. Centrifugation was done twice and after each centrifugation, the supernatant was removed and the recovered particles were dispersed in fresh anhydrous toluene. The particles of diverse range of colours were obtained. The colour range spans from orange color for $Ga_{0.53}In_{0.47}N$ & $Ga_{0.49}In_{0.51}N$ solid solution to dark brownish for GaN rich side and darkish grey color for the Indium rich side. The divergent range of colours for solid solution with different composition are depicted in Figure 3.11. Similarly, like the previous synthesis, the samples were characterized with various techniques detailed below.

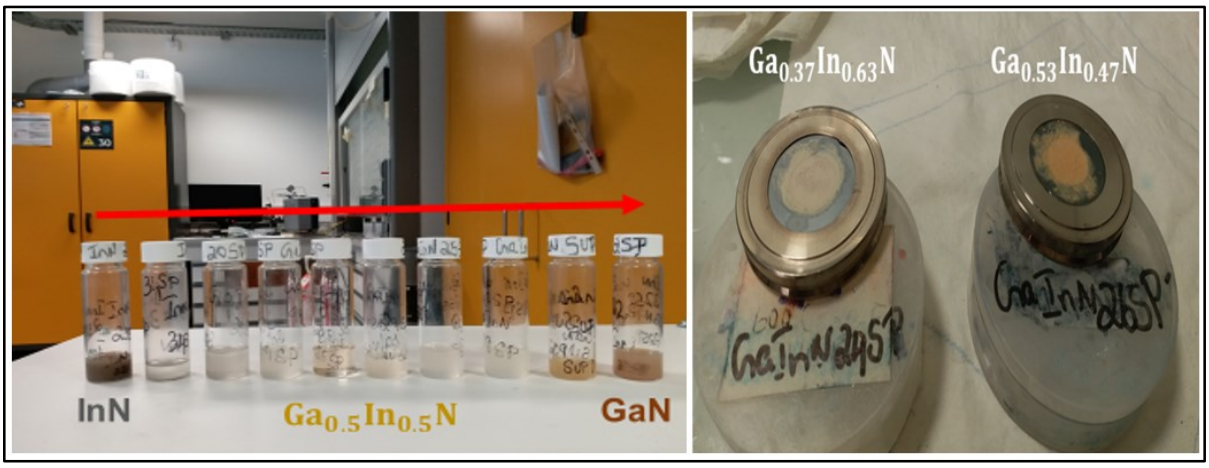

Figure 3.11. *Manifold of $Ga_xIn_{1-x}N$ ($0 \leq x \leq 1$) solid solution particles with divergent colours depending upon the composition.*

3.3.2.1. Elemental analysis

The actual amount or ratio of gallium and indium present in the various solid solutions of quasi-binary $Ga_xIn_{1-x}N$ ($0 < x < 1$) are determined through ICP-MS analysis of the prepared liquid samples of solid solutions. The $Ga_xIn_{1-x}N$ ($0 < x < 1$) materials with different contents of gallium and indium obtained after synthesis are washed through centrifugation twice and then dispersed in fresh anhydrous toluene. For ICP analysis, these particles are recovered from the dispersed solvent and dried in open atmosphere. The samples are prepared for ICP for each of the material by taking small quantities (usually 1 – 10 mg) of dried particles from each composition in a separate plastic vessel, to which 1 ml of concentrated hydrochloric acid (HCl), 1 ml of sulphuric acid (H_2SO_4) and 1 ml of nitric acid (HNO_3) was added for ensuring a complete dissolution of the nanomaterials. This mixture was mixed with 25 mL of deionized water and was kept undisturbed for 24 hours and then taken for ICP-MS measurements. The obtained results for each sample and the stoichiometric ratio of their corresponding cupferronate precursors are provided in Table 3.3.

From the ICP results, it can be seen that the difference between the amount of gallium/ indium elements in the prepared precursors (theoretical value) and the amount obtained in the final solid solution nanomaterials were not much deviating, oppositely to the case of the solid solution synthesized in toluene. This proves that the dual solvent system at supercritical conditions coupled with the optimized parameters, have provided the complete range of the compositions. Previously, the maximum Indium content that was attained in the solid solution nanomaterials synthesized in toluene was (49%, atom%) that is much lower than the one obtained within the toluene and methanol system (to 86%, atom%). Hereafter, the ICP obtained values will be used to designate the particular solid solution studied, especially for photocatalysis investigations or the other characterization techniques.

Table 3. ICP-MS results of $Ga_xIn_{1-x}N$ solid solution synthesized in toluene & methanol dual solvent system. The values mentioned for the $(Ga_xIn_{1-x}(C_6H_5N_2O_2)_3)$ are the actual amount of gallium and indium taken for the preparation of the precursor.

S.No	Stoichiometric amount of gallium and indium in the $(Ga_xIn_{1-x}(C_6H_5N_2O_2)_3)$ Precursor (theoretical)	Stoichiometric amount of gallium and indium in the $Ga_xIn_{1-x}N$ solid solution synthesized (experimental)
1.	$In_{0.9}Ga_{0.1}$	$In_{0.86}Ga_{0.14}$
2.	$In_{0.8}Ga_{0.2}$	$In_{0.78}Ga_{0.22}$
3.	$In_{0.7}Ga_{0.3}$	$In_{0.70}Ga_{0.30}$
4.	$In_{0.6}Ga_{0.4}$	$In_{0.63}Ga_{0.37}$
5.	$In_{0.5}Ga_{0.5}$	$In_{0.51}Ga_{0.49}$
6.	$In_{0.5}Ga_{0.5}$	$In_{0.47}Ga_{0.53}$
7.	$In_{0.4}Ga_{0.6}$	$In_{0.45}Ga_{0.55}$
8.	$In_{0.3}Ga_{0.7}$	$In_{0.32}Ga_{0.68}$
9.	$In_{0.2}Ga_{0.8}$	$In_{0.23}Ga_{0.77}$

3.3.2.2. Structural characterization

The solid solution nanoparticles were deposited on a silicon substrate with zero background for powder X-ray diffraction study. The powder diffraction spectrum of the solid solutions for the entire composition range resulted in two different kinds of diffraction patterns. On the indium rich side, distinctive, definite peaks corresponding to various crystal structures are clearly seen. This resultant XRD pattern for the indium rich $Ga_xIn_{1-x}N$ ($0 < x < 0.4$) solid solution is depicted in Figure 3.12.

In the solid solution of $Ga_xIn_{1-x}N$ synthesized here, as the gallium content is increased in a continuous step wise manner, the crystallite peak's gets broader. For $Ga_{0.37}In_{0.63}N$ solid solution possessing 37% (atom%) of gallium, the XRD pattern becomes a wider and featureless spectrum with only one distinctive peak on the sloppy bump, as depicted in Figure 3.12.

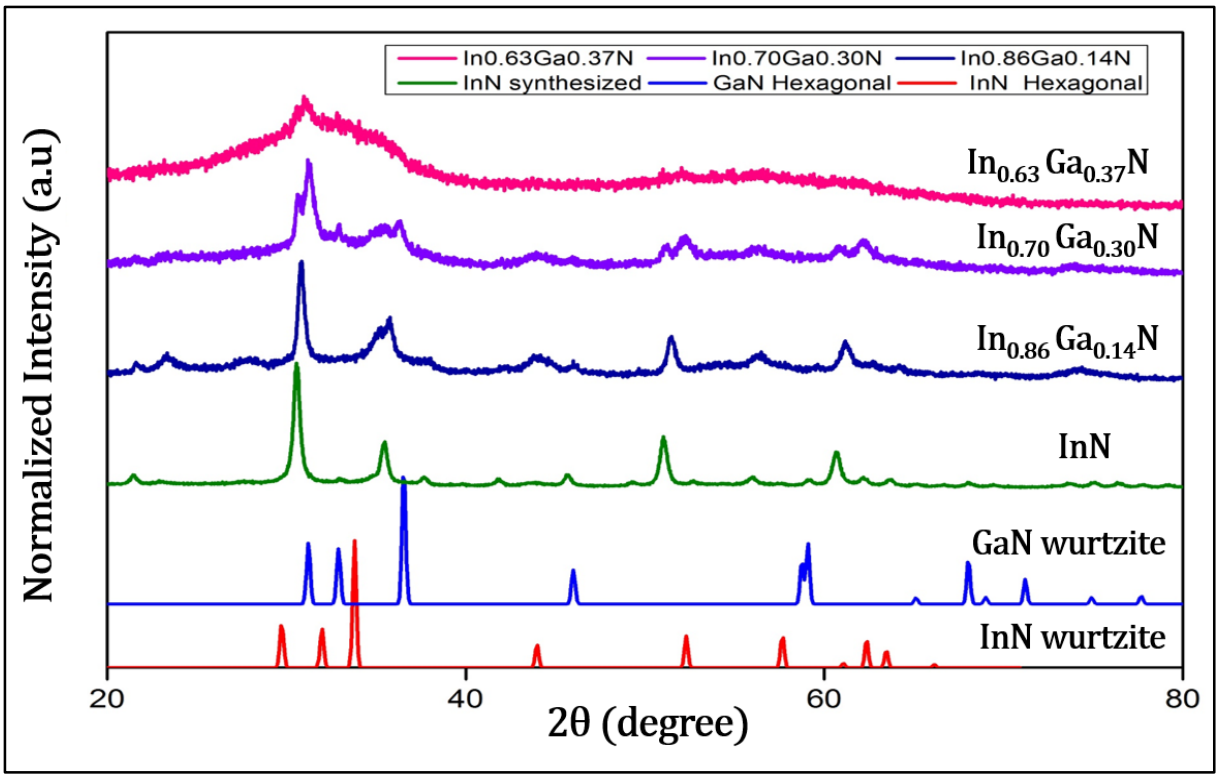

Figure 3.12. *Powder XRD patterns of the $Ga_xIn_{1-x}N$ ($0 < x < 0.4$) solid solution nanomaterials with high indium content.*

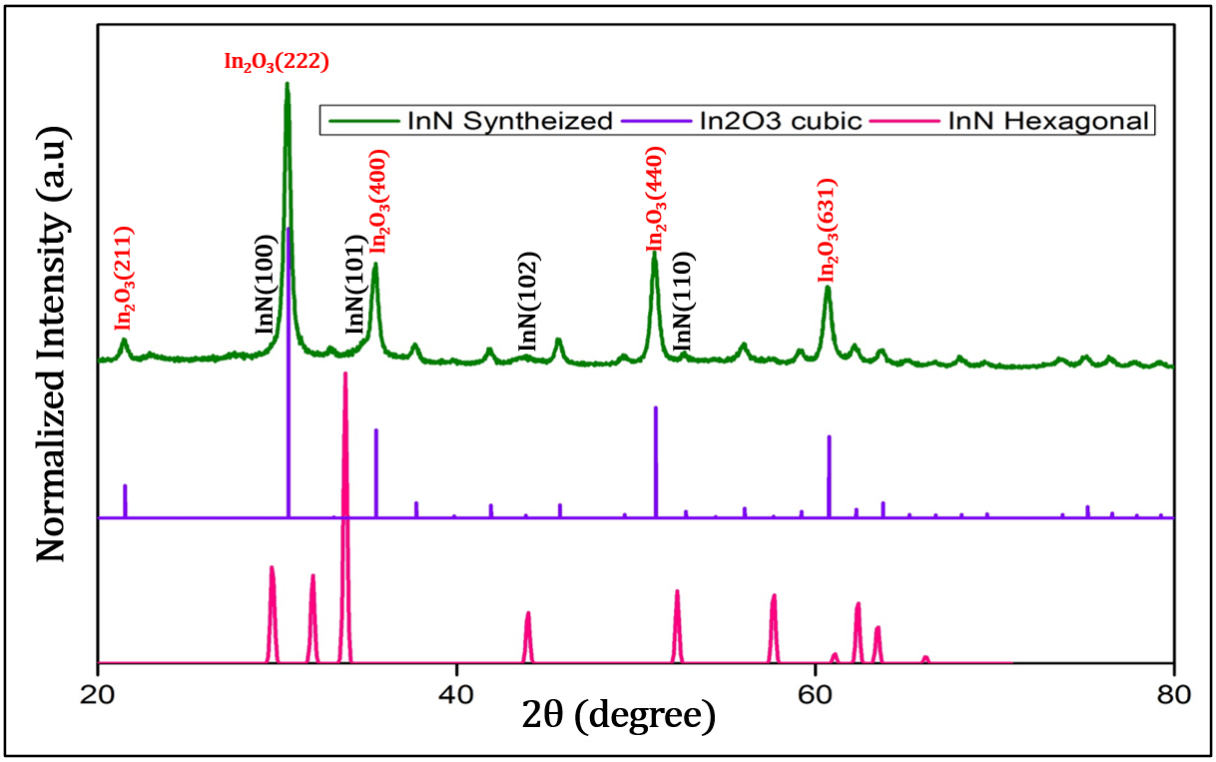

Figure 3.13. *XRD pattern of the as-synthesized InN material in a supercritical mixture of toluene and methanol.*

For the InN material synthesized here, the powder diffraction pattern depicted in Figures 3.12 and 3.13, clearly indicates that the sample is composed of a mixture of InN and In_2O_3 phases. The distinctive reflections of InN phases were found to be peaks corresponding to (100), (101), (102) and (110) planes of InN hexagonal wurtzite crystal structure. The crystallite reflections of In_2O_3 consists of distinctive peaks corresponding to the (211), (400), (440) and (631) planes of cubic crystal structure, systematically depicted in Figure 3.13. Such similar XRD pattern consisting of hexagonal InN and cubic In_2O_3 was reported by Zhang *et al.* for InN/In_2O_3 coaxial nanocables [49]. Similar kind of core/shell system with InN core and In_2O_3 shell would have also occurred in this InN nanomaterial synthesized, the detailed bonding nature of oxygen with indium nitride or other materials will be discussed in the later part of the section, especially thanks to XPS investigations.

As the GaN is incorporate into this InN binary material, ternary solid solution is formed and this is confirmed by the peak shift of the crystallite planes. Both the GaN and InN group III semiconductors are isostructural binary compounds, for which peak at 29.11° corresponds to the (100) plane of hexagonal crystal structure for InN, where as in case of GaN, XRD peak at 32.37° corresponds to the (100) plane of the hexagonal structure. As the GaN molecule is introduced into the host InN crystal lattice, the shift of the (100) plane towards 32.37° confirms that (100) plane of $Ga_xIn_{1-x}N$ is formed. The red shift of (100) is more obvious and it is inching more towards the GaN (100) crystallite phase. This shift of the peak corresponding to (100) plane is systematically depicted in Figure 3.14.

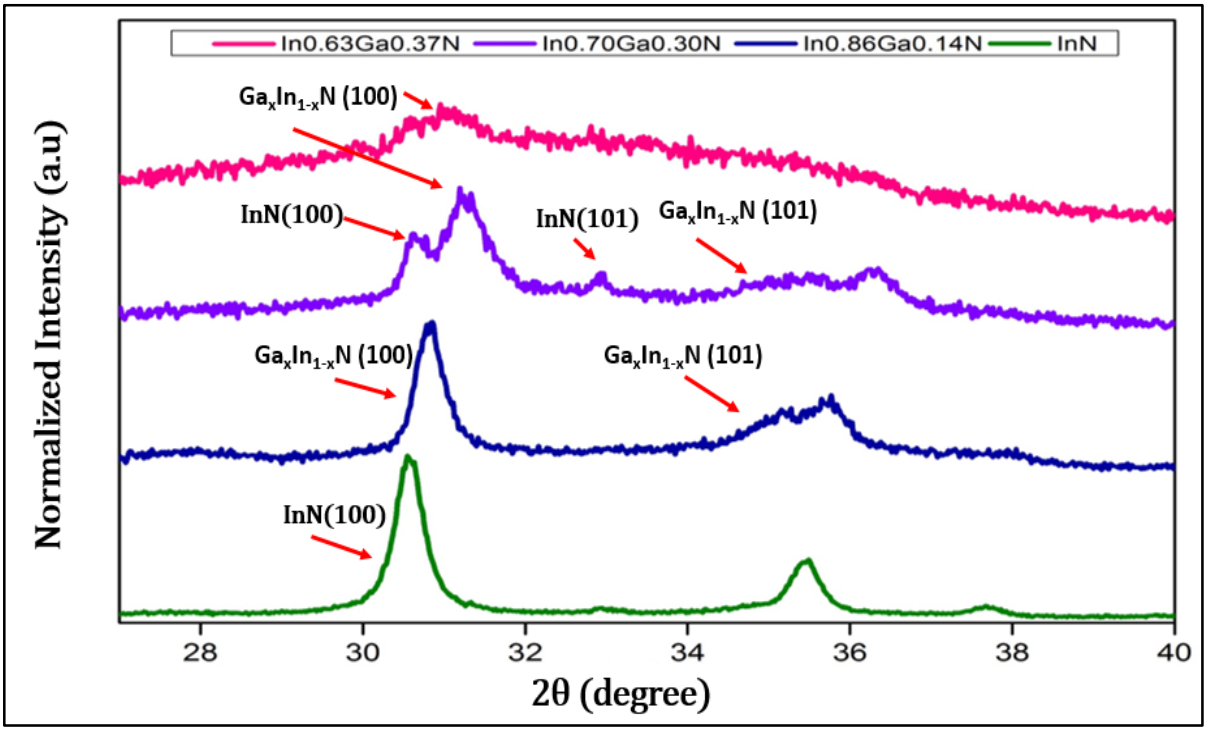

Figure 3.14. *XRD pattern of InN and $Ga_xIn_{1-x}N$ ($0 < x < 0.4$) solid solutions with high Indium content.*

The appearance of plane corresponding to solid solution was also seen for (101) plane, whose peak intensity is fixed between the range of 33.16° to 36.83°, spanning from InN to GaN, corresponding to (101) plane of wurtzite crystal structure respectively, this phase was evidently seen for XRD pattern of $In_{0.86}Ga_{0.14}N$ and $In_{0.70}Ga_{0.30}N$ solid solutions.

Interestingly in the $In_{0.70}Ga_{0.30}N$ solid solution, composition fluctuation (due to phase segregation) has occurred. This is evident from the appearance of InN (101) at 33° and an aslant projection from the onset of 33.16° to 36.83°. Similarly, appearance of the separate peak corresponding to (100) plane of InN along with (100) plane of $Ga_xIn_{1-x}N$, indicates that phase segregation has resulted in this solution with 70% (atom%) indium content. As the Gallium amount in the solid solution is increased continuously, the intensity of the peaks decreases with successive shift towards the GaN domain. Beyond 30% (atom%) of gallium content, the diffraction pattern becomes wide and featureless without any distinctive peaks. This broadening can be seen for the diffraction pattern of $In_{0.67}Ga_{0.33}N$ solid solution in Figure 3.12 and 3.14. The extent of broadening depends completely on the gallium content in the solid solution.

The XRD pattern of $Ga_xIn_{1-x}N$ ($x \geq 0.53$) systems display a broad curve without any individual representation of definite peaks. These unique broad spectra are systematically depicted in Figure 3.15 and are a typical characteristics of materials in the nanosize. The feature of these wide spectrum is the uniform bell shaped portion, spanning from 28° to 41°. Furthermore, the same XRD pattern contains a uniform region like an aslant protuberance with smaller height spanning from 50° to 70°. These two uniform regions of the XRD pattern can be clearly seen for the diffraction pattern of the $In_{0.47}Ga_{0.53}N$ solid solution nanomaterials, as depicted in Figure 3.15. As the compositional gradient of the solid solution is shifted towards more gallium rich region, two observations can be noticed in the powder XRD pattern.

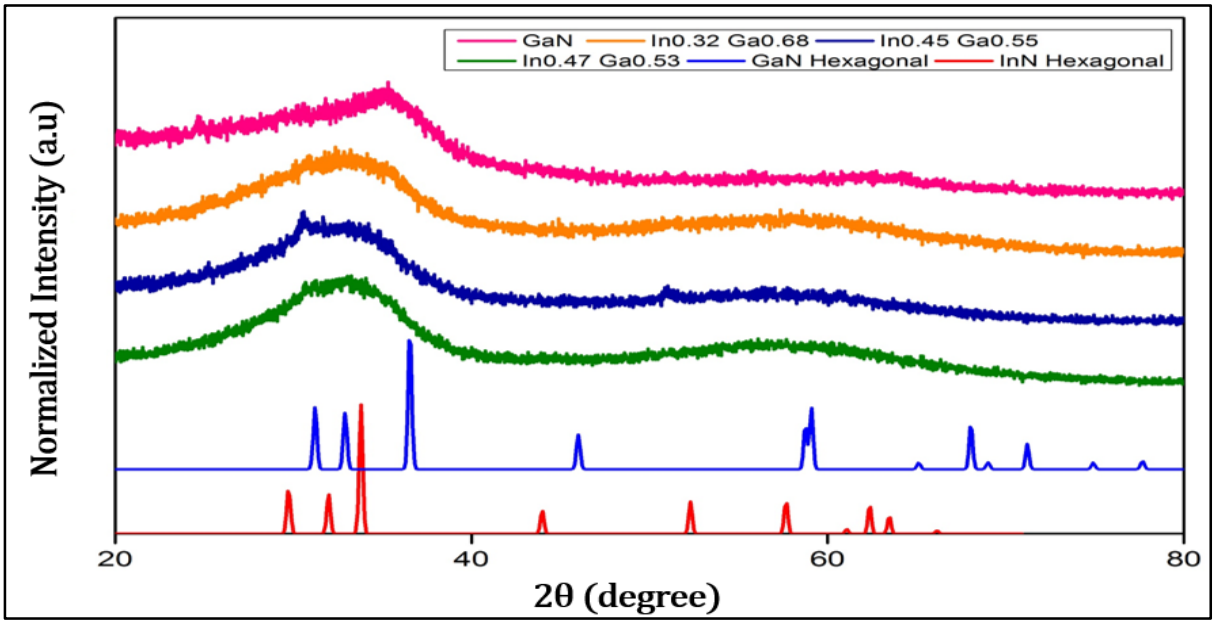

Figure 3.15. *XRD pattern of GaN and $Ga_xIn_{1-x}N$ ($x \geq 0.53$) solid solution with high gallium content.*

Firstly, the height of uniform region from 50° to 70° decreases and the aslant protuberance completely disappears when GaN has formed. Most distinctively, the peak maximum of the bell shaped uniform curve red shifts as the gallium amount is increased. The peak maximum is 36° when there is no indium amount, besides the uniformity of this region also diminishes as the compositional gradient is completely hinged toward GaN nanomaterial. Thus to conclude, the powder XRD pattern clearly depict that ternary solid solution of GaInN nanomaterial was synthesized by continuous supercritical technique using the cupferronate chemistry in dual solvent system. The red shift of the peaks for the solid solutions with increasing gallium gradient was also stood in agreement with the previously reported shift for the $Ga_xIn_{1-x}N$ solid solution synthesized in toluene solvent alone. Similar diffraction trend was observed in the $Ga_xIn_{1-x}N$ solid solution nanowires synthesized by halide chemical vapour deposition technique [36]. Inspection of phase segregation through elemental mapping and study about the size morphology of these solid solutions are carried through HR-TEM analysis.

In order to investigate the crystallinity of the $Ga_xIn_{1-x}N$ ($x \geq 0.5$) solid solutions with high gallium content and to identify the phase segregation phenomenon in the complete range of the $Ga_xIn_{1-x}N$ ($0 < x < 1$) solid solutions, high resolution (HR) imagining mode transmission electron microscopy (TEM) studies were performed.

In this section we have focus mostly on the $In_{0.7}Ga_{0.3}N$ and $In_{0.47}Ga_{0.53}N$ compositions. The solid solution was dispersed in anhydrous ethanol, and was ultrasonicated for few minutes. The resultant solution was drop casted on lacey carbon covered 300 mesh copper grid. The grid containing the solution droplets was dried for few minutes in open atmosphere and then directly inserted into the equipment for HR-TEM study.

The $In_{0.7}Ga_{0.3}N$ composition

The HR-TEM study of $In_{0.7}Ga_{0.3}N$ solid solution nanomaterials reveals that the particles analysed consist of aggregates of crystallized coherent domains (nanocrystalline particles). The average size of these nanocrystalline particles was 7.1 ± 2 nm, where the minimum size of these crystalline domain was 5.1 nm and maximum was 12.8 nm. These crystallized nanomaterials particularly refer to the low dimensional particles with lattice fringes, as depicted in Figure 3.16-a. Besides these crystallized domains with lattice fringes, there were several low dimensional particles without lattice fringes possessing an average size of 8.3 ± 2.4 nm. Supplementary aggregates of spherical particles with an average size of 37.5 ± 6.7 nm, were observed as seen in the HR-TEM image of Figure 3.16-b.

These low dimensional nanoparticles (including the nano crystallized coherent domains) were aggregates into big spherical shaped structures, as depicted in Figures 3.17-a, 3.17-b and 3.17-c. Figure 3.17-a specifically focuses on the one big spherical structure indicating that it is made up by the aggregation of several low dimensional particles, especially nanoparticles with an average size of 7 - 8 nm. These spherical aggregates or spherical structures possess an average diameter of 169 ± 70 nm with maximum size around 272 nm and minimum of about 71 nm, as depicted in Figures 3.17-b and 3.17-c.

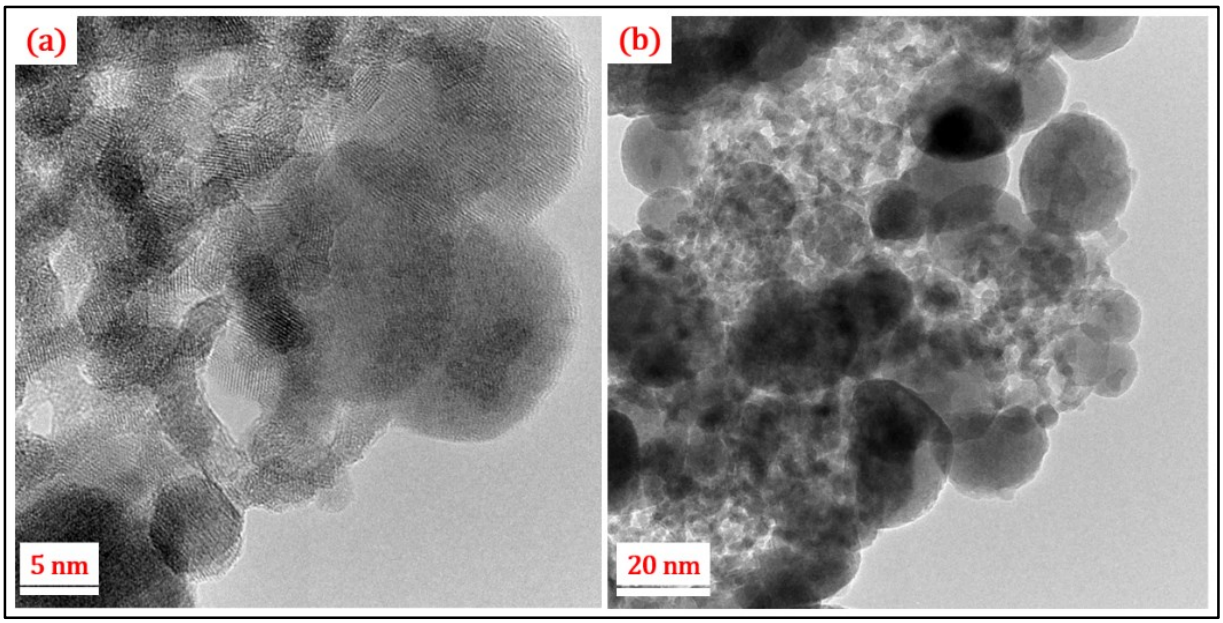

Figure 3.16. *a and b. HR-TEM images of the $In_{0.7}Ga_{0.3}N$ solid solution nanomaterials synthesized in methanol and toluene supercritical mixture.*

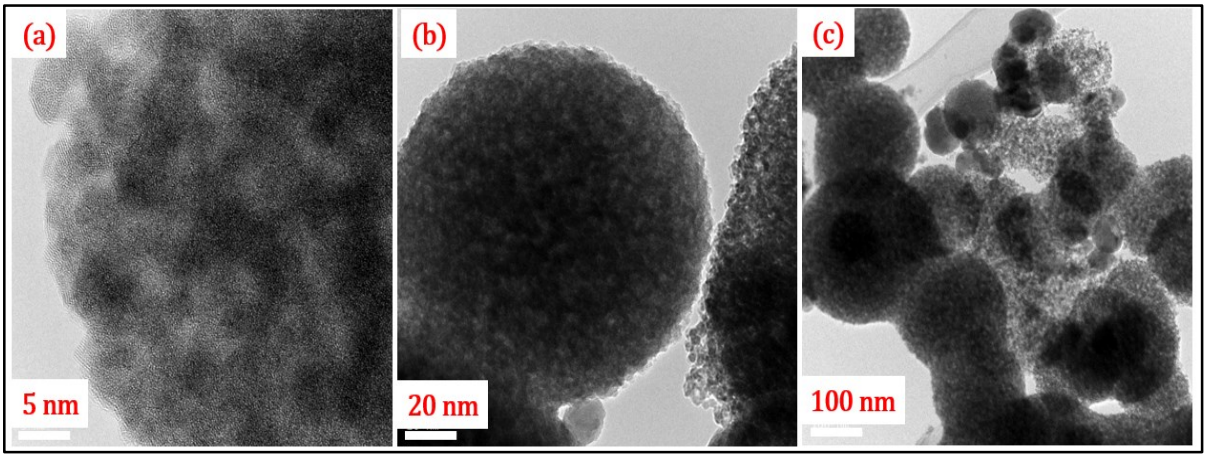

Figure 3.17. *a, b and c. HR-TEM image depicting the spherical structured aggregates for the $In_{0.7}Ga_{0.3}N$ solid solution synthesized.*

These spherical structured aggregates were also observed for the GaN QDs synthesized through different precursor systems, as seen in chapter 2. On closer observation of the crystallized coherent domains, the d-spacing values for most of the nanoparticles were in the range of 2.98 – 3.06 Å. These measured d-spacing indicate that the synthesized solid solution has a wurtzite crystal structure with hexagonal symmetry. The d-spacing values obtained here are within the range of d-spacing of the (100) plane of wurtzite InN (3.08 Å) and GaN (2.76 Å) crystal structure. A schematic depiction of these measured d-spacing is illustrated in Figure 3.18.

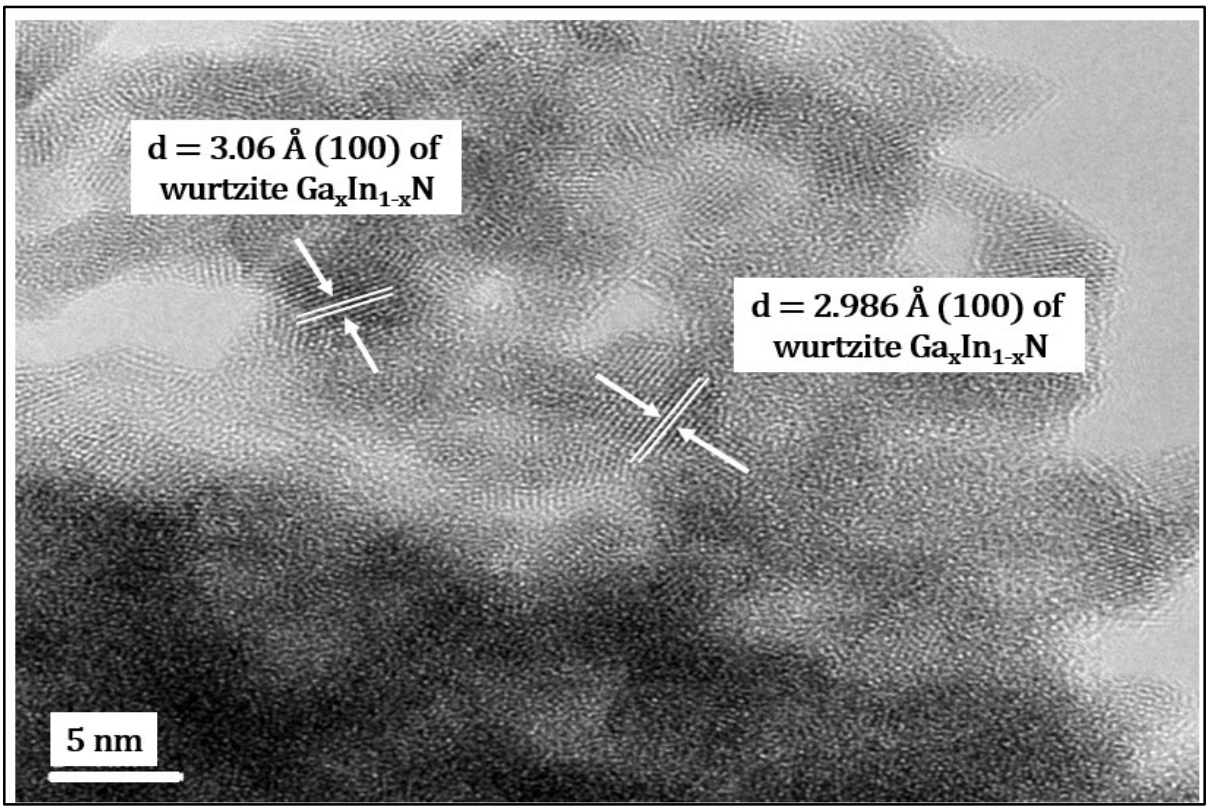

Figure 3.18. *HR-TEM image of $In_{0.7}Ga_{0.3}N$ solid solution illustrating the measured d-spacing values for the crystallized domains present in the system.*

The histogram of lattice periodicity for the corresponding lattice fringes measured in Figure 3.18 are depicted in figure 3.19.

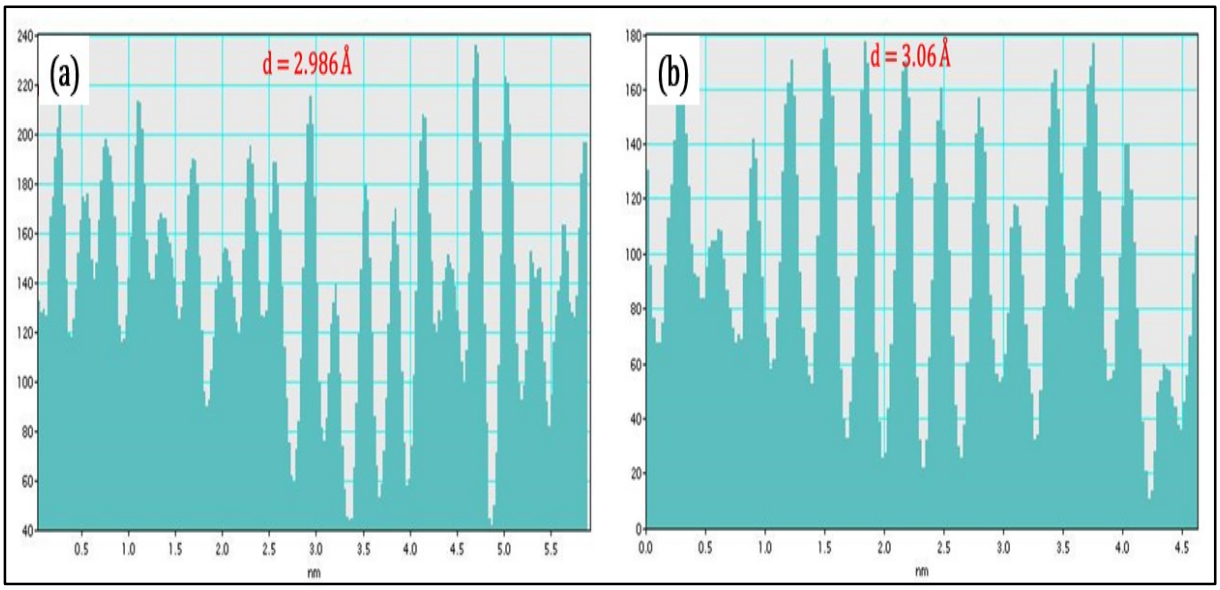

Figure 3.19. *a and b. Histogram of lattice periodicity of the lattice fringes measured in Figure 3.18.*

In order to visualize the spatial distribution of the elements and quantitatively identify the occurrence of any phase segregation between GaN and InN in this $Ga_xIn_{1-x}N$ solid solution, elemental mapping was carried out. Using the same HR-TEM equipment and the same grid used for measuring HR-TEM images, the elemental mapping study was performed. The area consisting of ensemble of nanomaterials selected for elemental mapping was pictured though scanning transmission electron microscope (STEM) mode, as depicted in Figure 3.20.

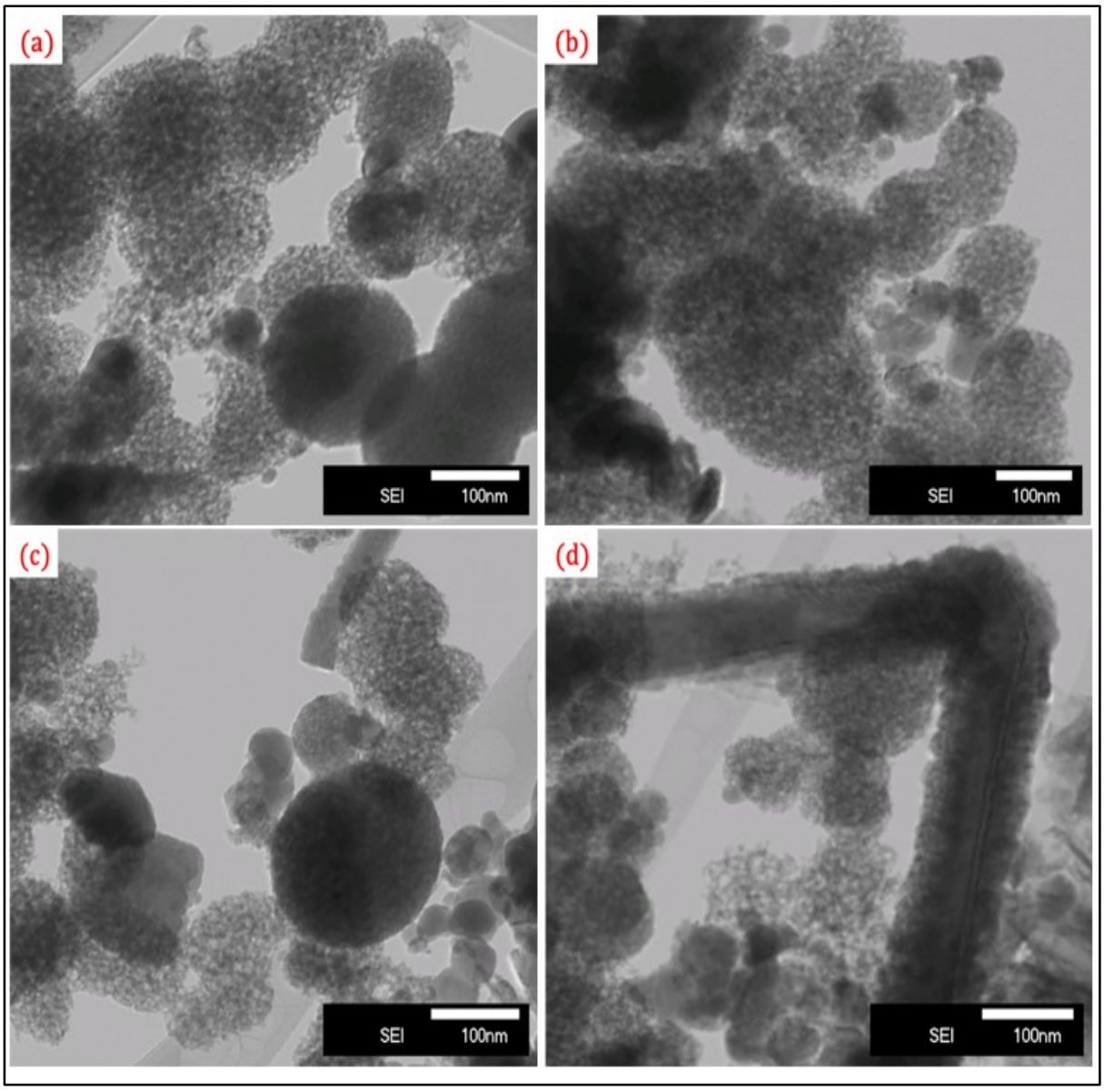

Figure 3.20. *a, b, c and d. STEM images of* $In_{0.7}Ga_{0.3}N$ *solid solution.*

The elemental mapping of the indium and gallium atoms was obtained through energy dispersive X-ray spectroscopy (EDS). From figure 3.21, it can be noticed that a uniform distribution of indium and gallium elements is observed in the most parts of the image, especially homogenous distribution occurred in the spherical aggregates. The quantitative mass percentage of gallium and indium obtained through STEM-EDX for the particles analyzed in Figure 3.21 was 71% of In and 29% of Ga (mass basis), closely in accordance with the ratio of gallium and indium obtained for this solid solution through ICP (70% of In and 30% of Ga

(molar basis), 78% of In and 22% of Ga (mass basis)). Interestingly, nanoflakes, along with spherical aggregates were observed in both STEM image of Figures 3.20-c and 3.20-d. There was very small piece of nanoflakes was observed in Figure 3.20-c, analogously in Figure 3.20-d a big nanoflake in the form of elongated rod structure was seen. The corresponding elemental mapping of Figure 3.20-d is shown in Figure 3.22.

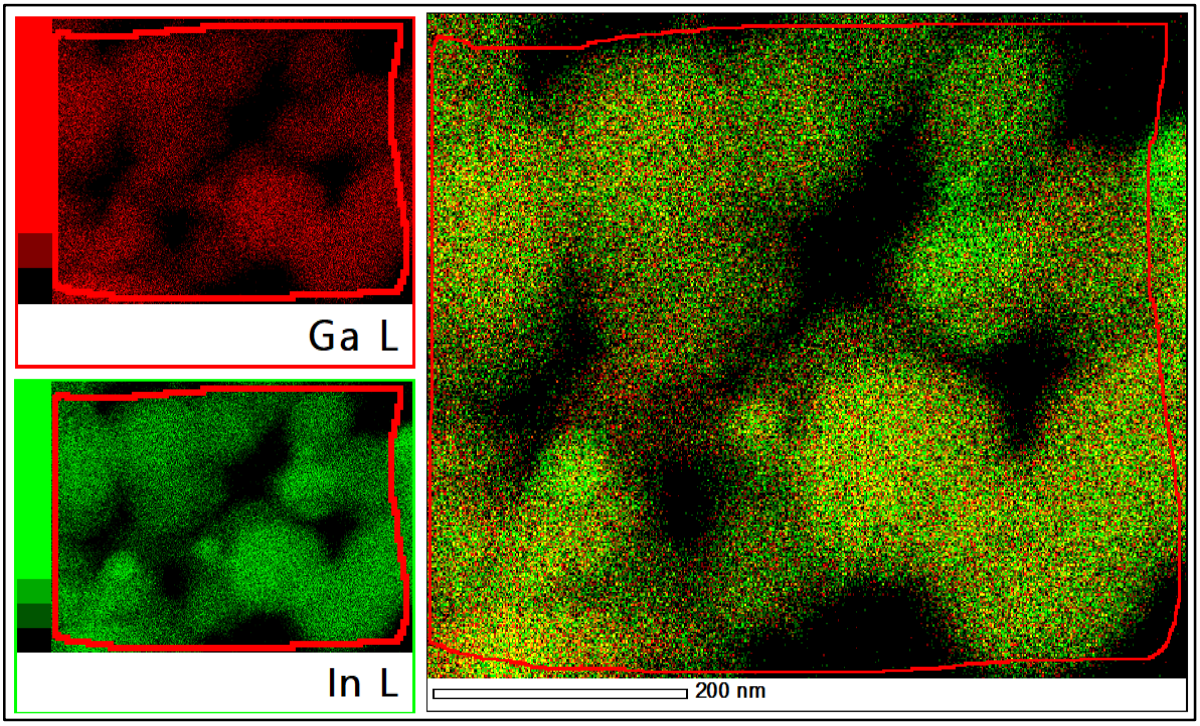

Figure 3.21. *Elemental mapping of $In_{0.7}Ga_{0.3}N$ solid solution nanomaterials depicted in the STEM image of Figure 3.20.a, obtained through EDS technique.*

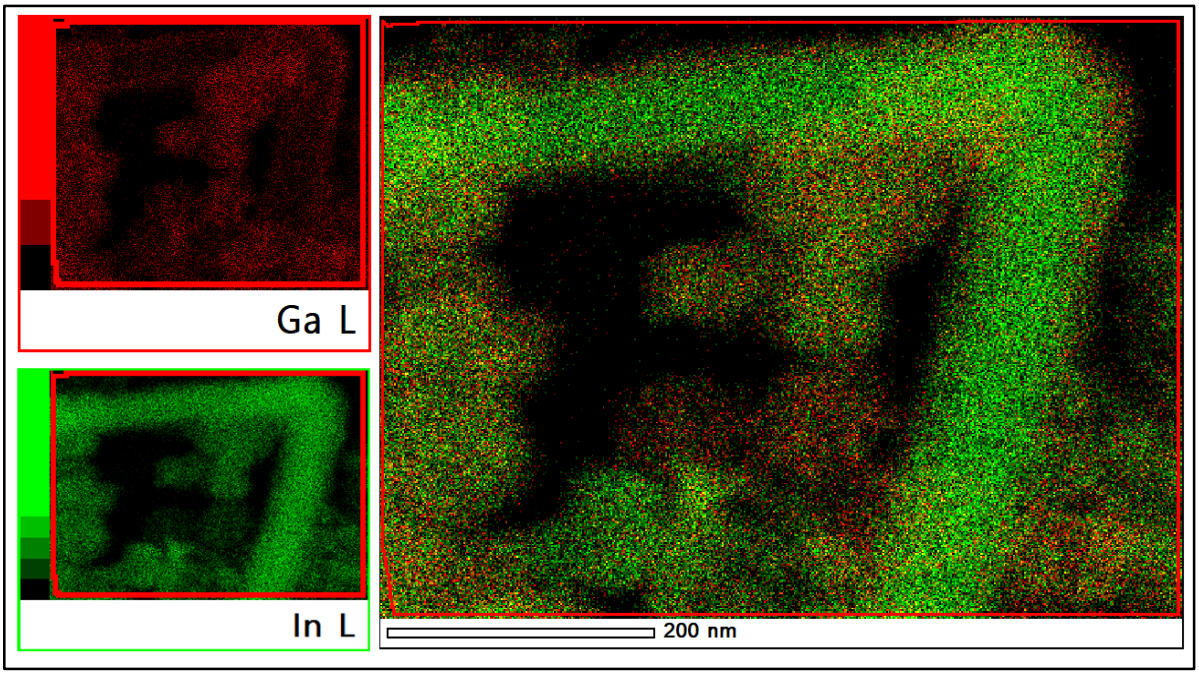

Figure 3.22. *Elemental mapping of $In_{0.7}Ga_{0.3}N$ solid solution nanomaterials depicted in the STEM image of Figure 3.20.d, obtained through EDS technique.*

The elemental mapping image shown in Figure 3.22, indicates that the big nanoflake in the form of a boomerang is composed of mostly Indium nitride nanoparticles. This explains the reason for the phase segregation phenomenon inferred through the powder XRD measurement of this $In_{0.7}Ga_{0.3}N$ solid solution**.** Similar kind of small nanoflakes were also observed in the STEM image of Figure 3.20-c. The generation of these kind of nanostructured InN nanomaterials was the reason for the appearance of the peak in the powder XRD corresponding to the (100) plane of InN wurtzite hexagonal crystal structure. The mass ratio of indium and gallium in Figure 3.22 obtained through STEM-EDX was 81% of In and 19% of Ga.

To conclude in the system of $In_{0.7}Ga_{0.3}N$, a phase segregation has occurred through the formation of elongated nanoflakes containing mostly InN. At the same time, a homogeneous distribution of gallium and indium was observed in the other aggregates of nanoparticles and especially in the spherical aggregates. The dual system of toluene and methanol has provided homogeneous distribution of binary elements in spherical aggregates here. The phase segregation in certain regions of this solid solution can be due to the high indium content. In the next part, a similar kind of characterizations was performed on the solid solution system with 47% (mole basis) of indium to check how successfully InN is incorporated into the GaN binary system, without phase segregation.

The $In_{0.47}Ga_{0.53}N$ composition

The HR-TEM analysis of the $In_{0.47}Ga_{0.53}N$ solid solution reveals that the as-synthesized ternary alloy material consists of crystallized coherent domains (crystallized nanoparticles) in the nanosize regime. As seen in the previous solid solution system, these crystallized nanoparticles refer to low dimensional particle displaying with well-defined lattice fringes. The average size of the low dimensional particles (including both nanoparticles with lattice fringes and the ones in which lattice fringes were not observed) were found to be 4.5 ± 0.8 nm, with a maximum of around 6.4 nm and minimum of about 3.6 nm. They are schematically depicted in HR-TEM images in Figure 3.23.

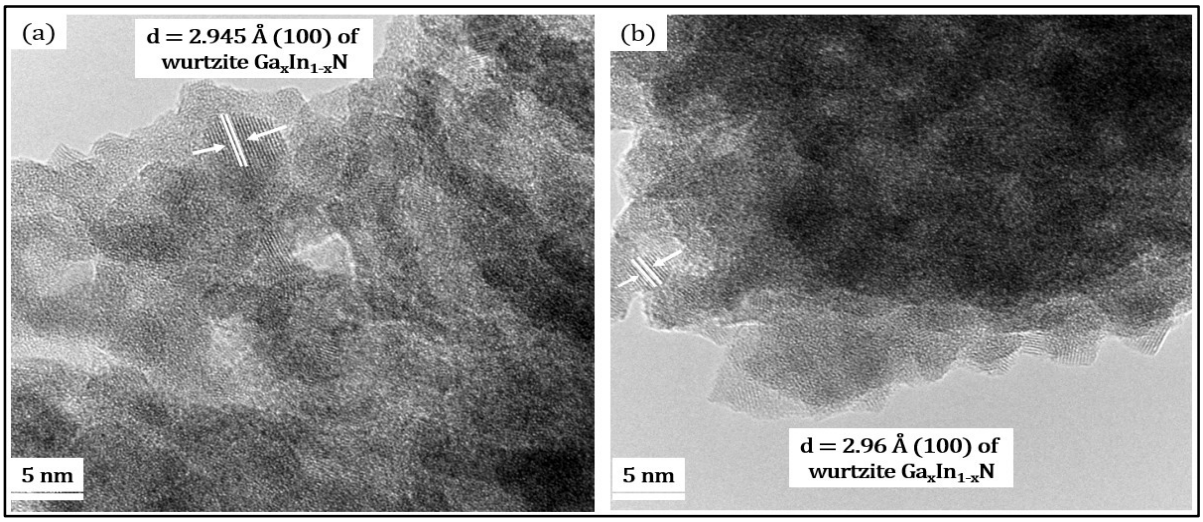

Figure 3.23. *a and b. HR-TEM images of the $In_{0.47}Ga_{0.53}N$ solid solution nanoparticles illustrating the measured d-spacing values for the crystallized domains present in the system.*

Thanks to the d-spacing measurements on the well-defined lattice fringes, it was demonstrated that the synthesized $In_{0.47}Ga_{0.53}N$ solid solution has crystallized in the wurtzite hexagonal crystal structure. The obtained d-spacing values for most of the particles were in the range of 2.94 to 2.96 Å. This values falls within the range of (100) plane of hexagonal wurtzite GaN (d = 2.76 Å) and the same (100) plane of hexagonal wurtzite InN (d = 3.08 Å). The identification of lattice fringe and measured d-spacing values are systematically depicted in Figure 3.23-a and 3.23-b. The corresponding histogram of lattice periodicity of the lattice fringes measures in Figures 3.23-a and 3.23-b are systematically depicted in Figures 3.24-a and 3.24-b, respectively.

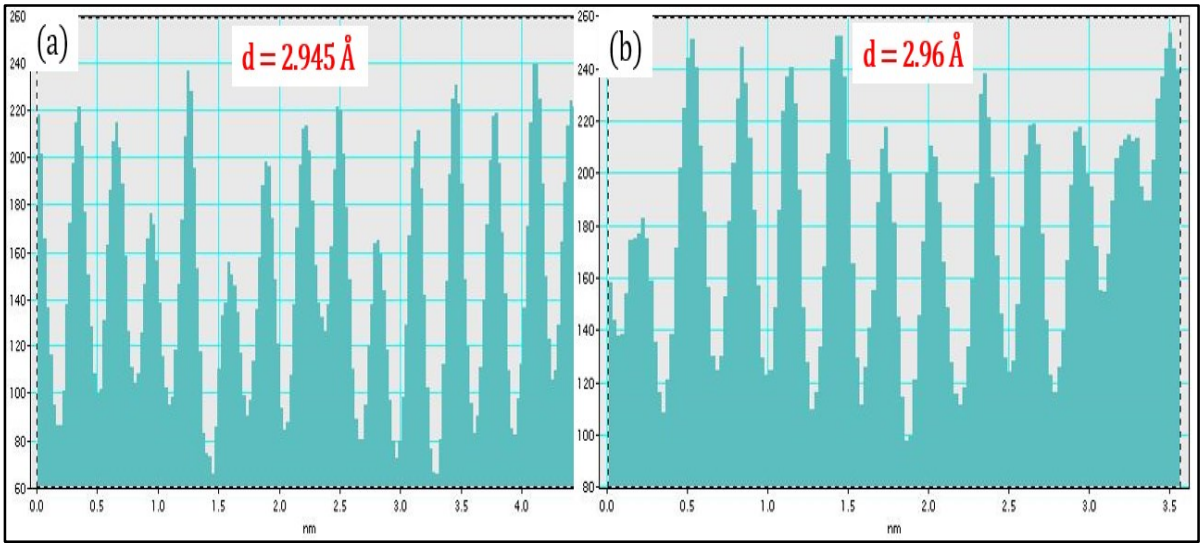

Figure 3.24. *a and b. Histogram of lattice periodicity of the lattice fringes measured in Figures 3.23.a and 3.23.b, respectively.*

The nanoparticles of the $In_{0.47}Ga_{0.53}N$ solid solution were aggregated into two differently shaped structures: (i) big spherical structures and (ii) irregularly shaped structures on most of the ensemble of particles analysed under HR-TEM

The quantitative estimation of gallium and indium content ratio in the solid solution and the study of the spatial distribution of the elements in the solid solutions were done using STEM-EDX analysis. The region consisting of an ensemble of nanomaterials for elemental mapping studies was pictured in the STEM mode and the as-obtained images are depicted in Figure 3.25.

In the $In_{0.47}Ga_{0.53}N$ solid solution, more amount of irregularly shaped aggregates were present compared to spherical aggregates. A complete homogeneous distribution of gallium and indium in this ternary alloy system was achieved in this $In_{0.47}Ga_{0.53}N$ solid solution sample. The schematic illustration of such homogeneous distribution through elemental mapping is shown in Figure 3.26. In this elemental mapping, there was a complete homogeneous distribution of gallium and indium elements in the irregularly shaped aggregates. The ratio of gallium and indium obtained in mass % through STEM-EDX analysis for their region mentioned in Figure 3.26 was 51% of Ga and 49% of In.

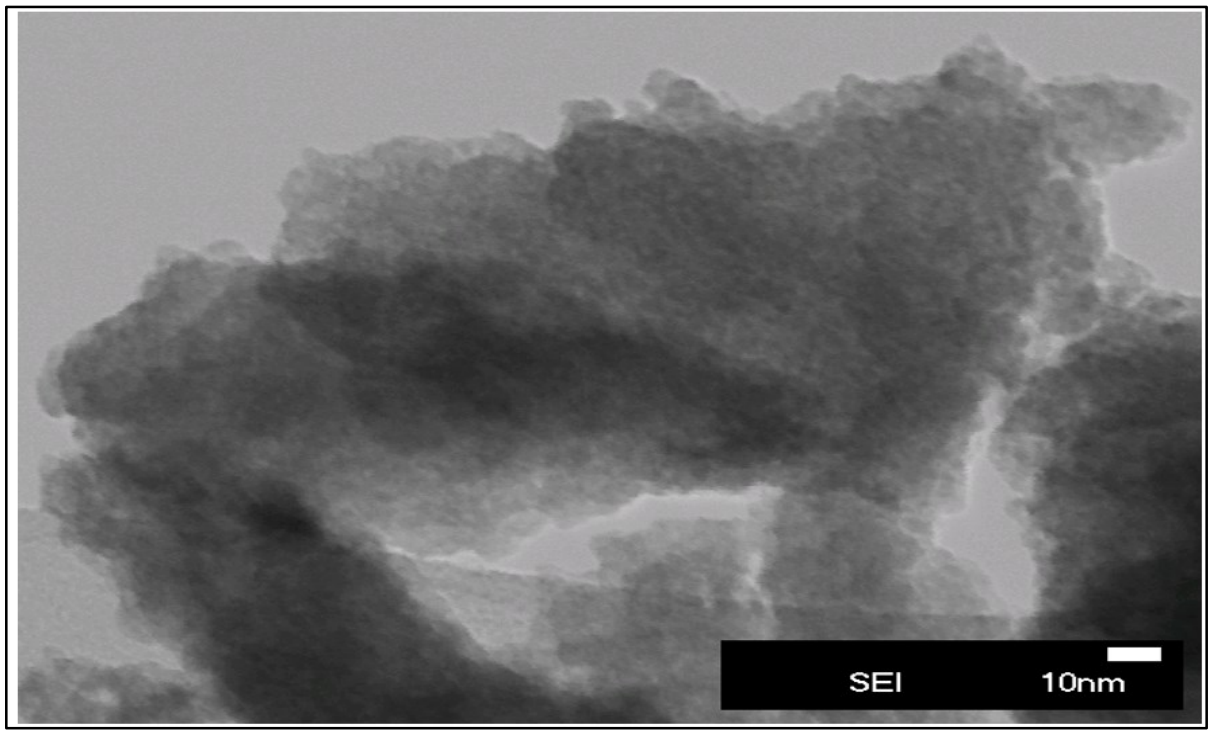

Figure 3.25. *STEM images of the* $In_{0.47}Ga_{0.53}N$ *solid solution.*

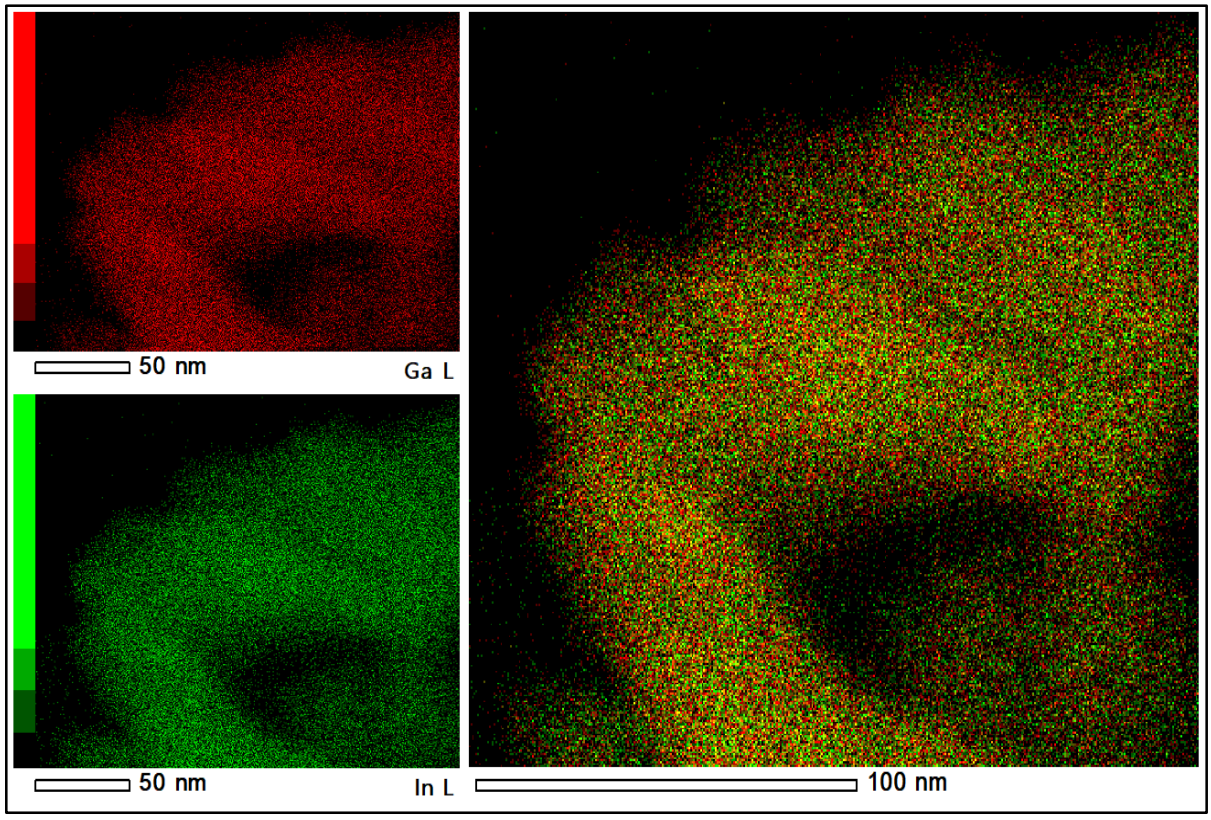

Figure 3.26. *Elemental mapping of the region depicted in the STEM image of Figure 3.25.*

To conclude, there was no phase segregation or separation appearance of InN or GaN nanomaterials in the form of flakes in this $In_{0.47}Ga_{0.53}N$ solid solution. The composition modulation of the solid solution was also not seen as the ratio of the gallium and indium was same for all the regions analysed in this solid solutions. Thus, the implementation of dual solvent system of toluene and methanol played a strong role in attaining $In_{0.47}Ga_{0.53}N$ solid solution where 47% of Indium was successfully incorporated without any phase segregation. This content was very high compared to the previously studied supercritical synthesis of $Ga_xIn_{1-x}N$ solid solution in toluene alone, where above a maximum of 12% (mole basis) of indium incorporation, the phase segregation has started to occur. These kind of solid solution will be implemented for heterogeneous photocatalysis in the coming sections of this chapter.

3.3.2.3. Surface characterization

The $In_{0.47}Ga_{0.53}N$ solid solution nanomaterial was subjected to XPS characterization to understand this materials' surface composition.

For the XPS analytical study, the nanomaterials were recovered from the dispersed toluene solution and dried in open atmosphere prior to measurement. The recorded XPS survey for the $In_{0.47}Ga_{0.53}N$ solid solution is depicted in Figure 3.27.

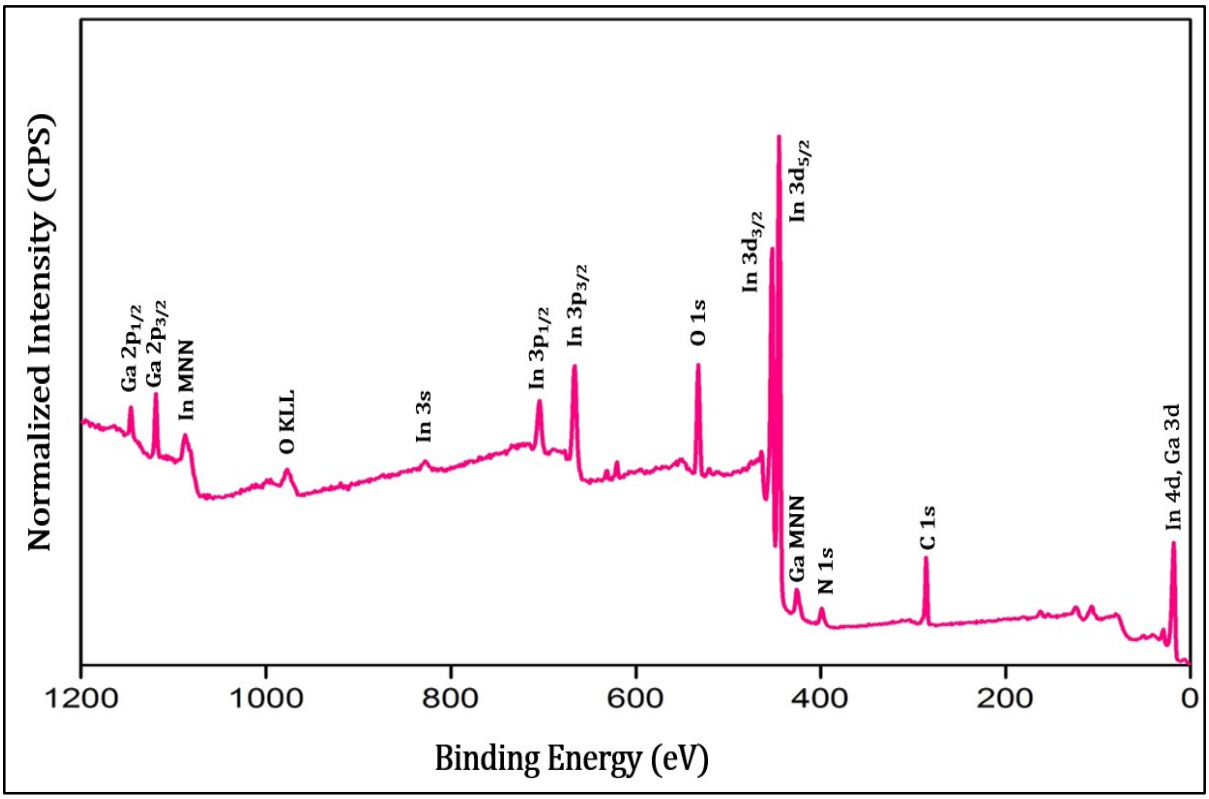

Figure 3.27. *XPS full survey for the $In_{0.47}Ga_{0.53}N$ synthesized by continuous supercritical millireactor using the toluene and methanol dual solvent system.*

All the signals of the expected elements (Ga, In, N, C and O) are present on the survey. The XPS survey quantitatively indicates that the surface of the as-synthesized $In_{0.47}Ga_{0.53}N$ solid solution nanomaterials is contaminated with oxygen and carbon.

The chemical analysis of the $In_{0.47}Ga_{0.53}N$ solid solution's surface is elucidated here by selectively studying the In $3d_{5/2}$, Ga $2p_{3/2}$, N 1s, C 1s and O 1s photoelectron peaks.

The chemical state of indium in the solid solution can be evaluated from the In $3d_{5/2}$ peak (Figure 3.28). The peak maximum position of In $3d_{5/2}$ at 445.2 eV corresponds to the Indium bonded to nitrogen and more specifically it represents the bond existing in InN_xO_y compound. Should In_2O_3 be present in the sample, the In $3d_{5/2}$ would have rather corresponded to 444.6 or 444.7 eV [50, 51]. Significantly, the absence of In 3d peak maximum at 444 eV [51] confirms that no metallic Indium was present in the sample.

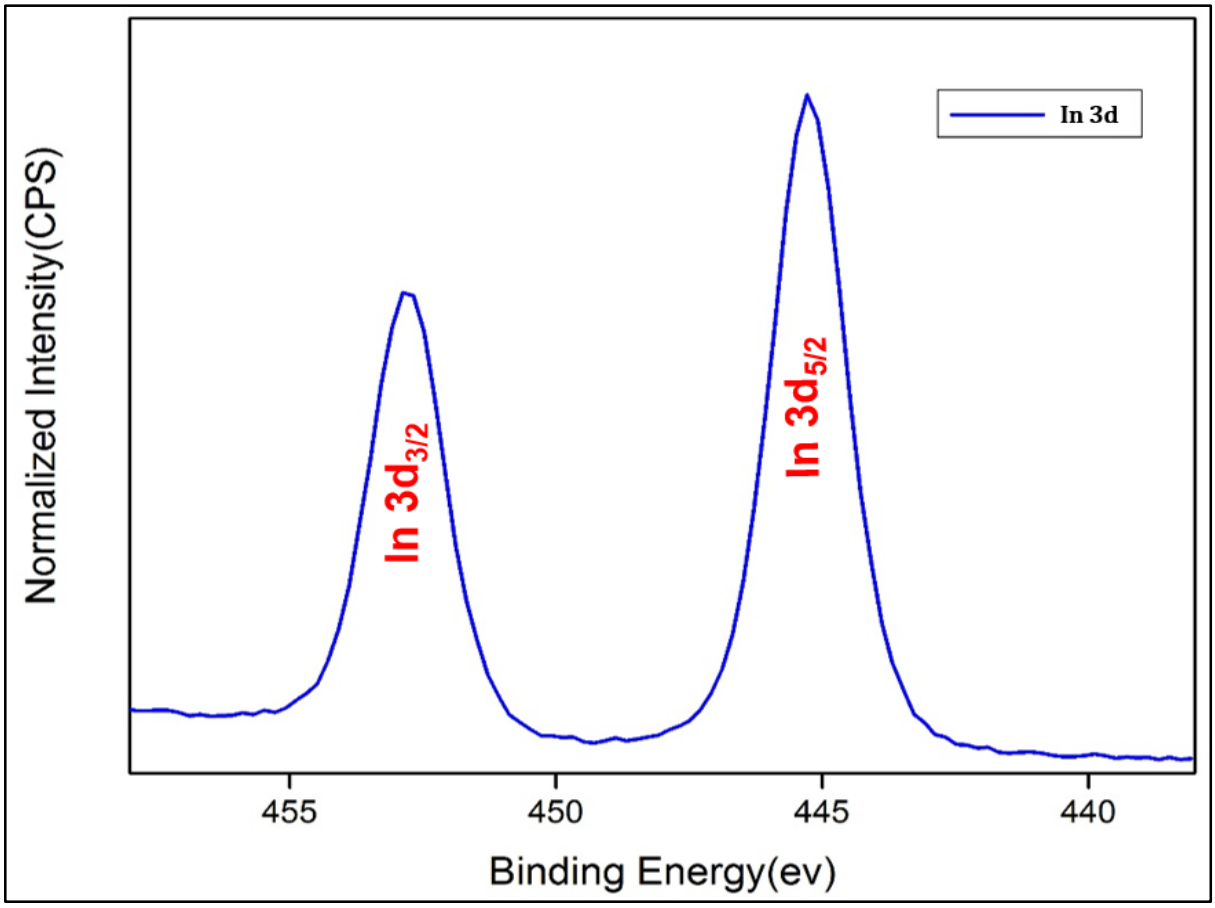

Figure 3.28. *In 3d portion of the XPS spectra depicted in figure 3.27*

The observation of oxidized indium nitride forming the complex InN_xO_y compound in the perspective of indium's nature in the solid solution indicates some surface contamination of the nanomaterial by oxygen atoms due to the exposure to ambient atmosphere for preparing the sample for XPS characterization. Concurrently, the prominent photoelectron peak of O 1s at 532 eV confirms that oxygen is bonded to nitrogen. The non-appearance of O 1s peak at 530.5 and 531.3eV binding energy have confirmed the absence of In_2O_3 or Ga_2O_3 at the surface of the nanomaterials.

The chemical state of gallium on the surface of the solid solution can be interpreted from Ga 3d photoemission line (Figure 3.29). The peak of Ga 3d at 19.17 eV [52] binding energy

confirms that gallium is bonded to nitrogen atoms for GaN compound. The onset of the adjacent spectra at binding energy 16.10 eV is due to the contribution from In 4d orbitals, confirming the bonding between indium and nitrogen resulting in InN compound [53]. The overlap of the contributions from the In 4d orbitals is the main reason for the shift of Ga3d peak from 19.5 eV to 19.17 eV.

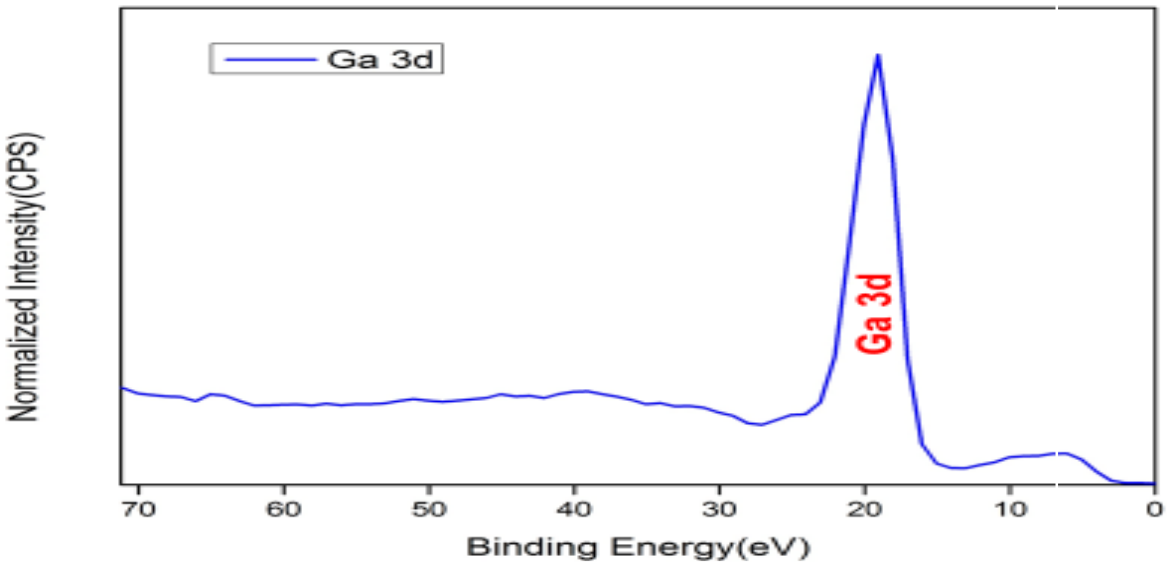

Figure 3.29. *Ga 3d portion of the XPS spectrum depicted in Figure 3.27.*

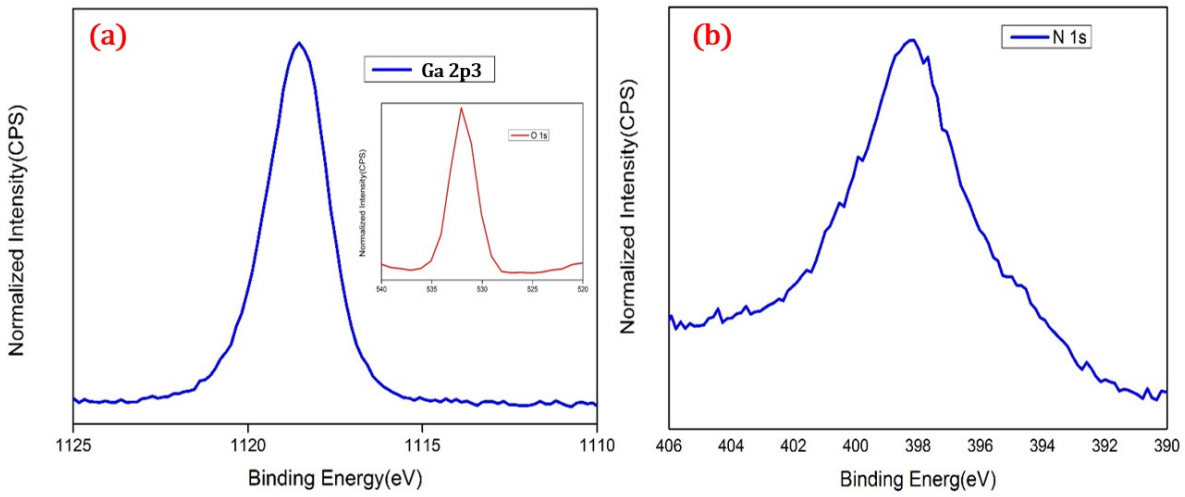

Figure 30. *a. Ga 2p3 portion of the XPS spectrum depicted in Figure 3.27; b. N 1s portion of the XPS spectrum depicted in Figure 3.27.*

The analysis of the Ga 2p3 peak has revealed the chemical state of gallium present on the surface of the solid solution. The binding energy peaks of Ga 2p3 and N 1s were spotted at 1118.514 eV and 398.18 eV instead of 1117 eV and 397.3 eV, respectively. Such a concurrent shift confirms the bonding between gallium and nitrogen atoms resulting in GaN compound. The overlap of auger lines of gallium can also be the primary reason for the shift of the binding

energy, with respect to gallium and nitrogen. Here Ga 2p3 peak can't be assigned to Gallium 2p orbital in Ga_2O_3 compound because the peak of O 1s spectra doesn't exhibit the peak at 531 eV, which corresponds to the Ga_2O_3 compound. The O 1s portion of GaInN XPS spectra is depicted in the inset of Figure 3.30-a. The O 1s spectra exhibits a peak at 532.07 eV corresponding to the bonding of oxygen to Indium Nitride.

3.3.2.4. Optical characterization of the $Ga_xIn_{1-x}N$ ($0 \leq x \leq 1$) solid solution

UV-VIS absorption spectroscopy was performed on the completed range of the $Ga_xIn_{1-x}N$ ($0 \leq x \leq 1$) solid solution synthesized through cupferron and HMDS chemistry, using the dual solvent system of methanol and toluene at supercritical conditions. From the liquid absorption spectrum, their corresponding energy gap is determined and depending on their optical characteristics, the appropriate solid solution nanomaterials is opted for visible light heterogeneous photocatalysis.

The as-synthesized solid solutions were washed through centrifugation, twice and then dispersed into fresh anhydrous toluene. Liquid absorption was performed on these dispersed solutions containing the nanomaterials. From the UV-VIS absorption study, the obtained absorption spectra are depicted in Figure 3.31.

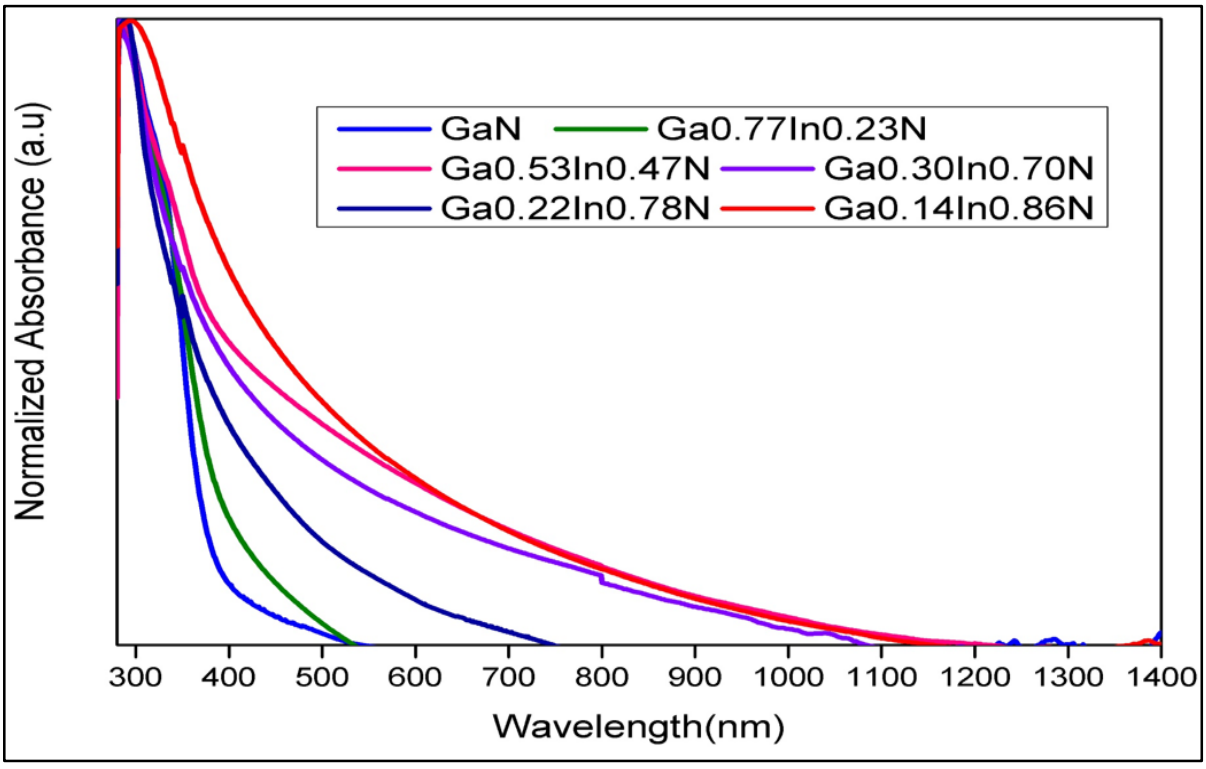

Figure 3.31. *UV-VIS absorption spectra of the $Ga_xIn_{1-x}N$ (x = 0.77, 0.53, 0.30, 0.22 and 0.14) solid solution nanomaterials synthesized in continuous flow millireactor in supercritical medium of toluene & methanol.*

From the absorption spectra it is obvious that the GaN exhibits steep onset of absorption at 353 nm. As the InN incorporated into the host GaN lattice, the onset of absorption shifts continuously as seen in the case of $Ga_{0.77}In_{0.23}N$ solid solution possessing a steep absorption at 375 nm. The shift towards to InN band edge absorption (1.9 eV or 652 nm) is found continuously even when 47% (mole basis) of indium is incorporated into the GaN lattice forming $Ga_{0.53}In_{0.47}N$ solid solution, whose strong steep absorption onset is seen from 477 nm. This solid solution is researched extremely in this chapter and it doesn't possess any phase segregation or composition modulation. The continuous shift of the steep absorption edge is seen maximum for $Ga_{0.14}In_{0.86}N$ solid solution of about 550 nm.

Interestingly, in the absorption spectra depicted in Figure 3.31, for the two solid solutions $Ga_{0.22}In_{0.78}N$ and $Ga_{0.30}In_{0.70}N$, the onset of steep absorption was observed at lower wavelength compared to the other solid solutions. Typically, $Ga_{0.30}In_{0.70}N$ solid solution exhibits steep absorption at 473 nm, which is less than the absorption of the $Ga_{0.53}In_{0.43}N$ solid solution, eventhough 70% of indium (mole basis) is present in this system. This is could be primarily due to the formation of nanoflakes of InN in the system and compositional modulation of the solid solution, as explained in the HR-TEM section for the $Ga_{0.30}In_{0.70}N$. The similar sort of phase segregation and thus a compositional modulation could be also the reasons for the low steep absorption at 402 nm for the $Ga_{0.22}In_{0.78}N$ solid solution. To conclude, the synthesis of $Ga_xIn_{1-x}N$ ($0 \leq x \leq 1$) solid solution in dual solvent system of methanol and toluene has yielded nanomaterials exhibiting continuous shift in the absorption edge from the UV region for GaN up to near IR for InN. The continuous shift is obvious even though composition modulation was observed in certain solid solutions.

The absorption edge due to the interbands transition in these direct band gap solid solution semiconductors can be determined through Equation 3.6, which provides the relationship between the absorption coefficient of the solid solution and the incident photonic energy [54 – 56].

$$\alpha h\nu = A(E - E_{sample})^n \qquad \textbf{(3.6)}$$

Here, A = constant, E = energy of the incident photon, E_{sample} = optical energy gap of the sample measured and the value of n is determined by the disposition of the electronic transition accountable for the optical absorption. 'n' = 1/2, 2, 3/2 and 3 for direct allowed, indirect allowed, direct forbidden and indirect forbidden transitions, respectively [55]. In this study, n = 1/2 will be used, since $Ga_xIn_{1-x}N$ is a direct band gap semiconductor material. Using Equation 3.6, the optical band gap between the conduction and the valence band of the solid solution is determined through the Tauc's plot, which is the squared absorption coefficient (α^2) versus the photon energy (hv). The absorption coefficient (α) is calculated here using the Beer Lambert's law and the equation depicting the relationship for obtaining, α is given by Equation 3.7.

$$\alpha = \frac{(2.303 * \text{Absorbance})}{l} \qquad \textbf{(3.7)}$$

Here, the absorbance values for the $Ga_xIn_{1-x}N$ solid solutions within the entire composition range ($0 \leq x \leq 1$) synthesized are obtained from the room temperature UV-VIS liquid

absorption spectra depicted in Figure 3.31. In Equation 3.7, l refers to the path length, since liquid cell was used in the absorption study, l = 1cm.

Figure 3.32 systematically depicts the Tauc's plot of (α^2) vs (hv) for the $Ga_xIn_{1-x}N$ solid solution nanomaterials. The continuous shift of the band gap energy with successive increment of indium content within the material confirms that perfect solid solutions have formed between GaN and InN materials. From this Tauc's plot depicted in Figure 3.32, the optical energy gap of the solid solutions' semiconductor was obtained through the linear extrapolation of the Tauc's curve at the intercept of zero y-axis ($\alpha^2 \rightarrow 0$). The obtained band gap values for all the solid solution are indicated in Table 3.4. The systematic plot of the energy gap versus the composition of the $Ga_xIn_{1-x}N$ solid solution is depicted in Figure 3.33. The composition modulation in the region of Indium 50 - 70% (mole basis), especially for the $Ga_{0.30}In_{70}N$ solid solution, explains the reason for the minor deviation of the plot (in Figure 3.33) from the linear variation of energy gap with respect to composition of the solid solution.

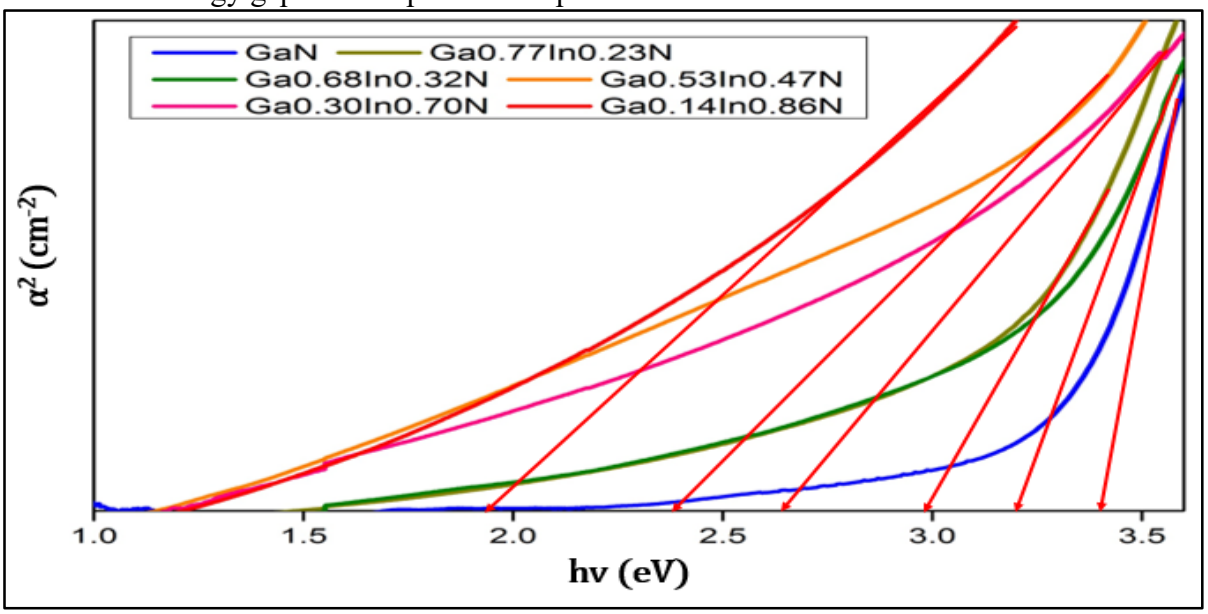

Figure 3.32. *Tauc plot of the $Ga_xIn_{1-x}N$ (x = 1, 0.77, 0.68, 0.53, 0.30 and 0.14) solid solution nanomaterials synthesized in continuous flow millireactor in supercritical medium of toluene & methanol.*

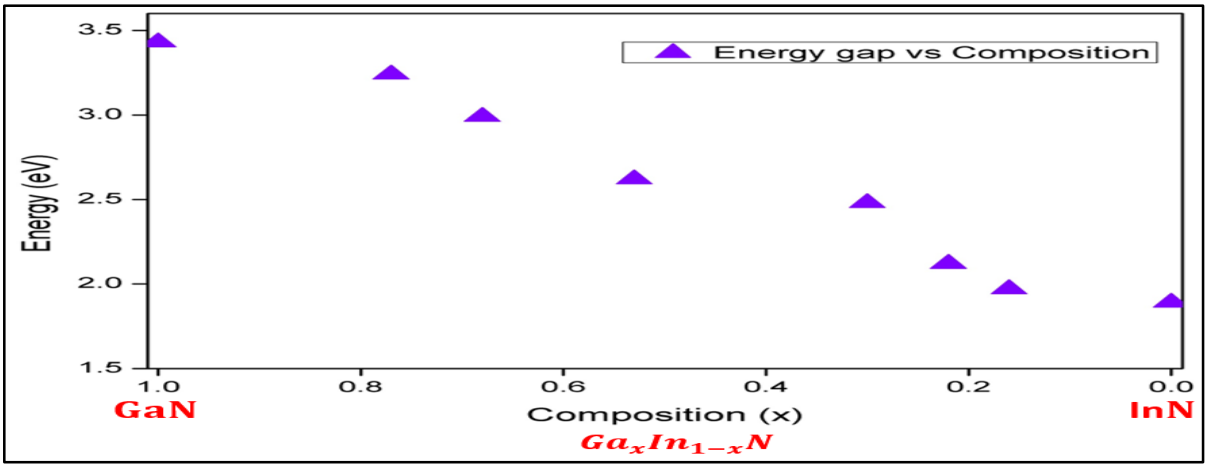

Figure 3.33. *Energy gap plotted as a function of the Indium concentration, determined through ICP analysis.*

Table 3.4. *Energy gap values for the $Ga_xIn_{1-x}N$ (x = 1, 0.77, 0.68, 0.53, 0.30, 0.22, 0.16 and 0) solid solution synthesized using supercritical mixture of toluene & methanol, estimated through the Tauc's plot.*

S.No	$Ga_xIn_{1-x}N$ Solid solution	Energy gap (eV)
1	*GaN*	*3.43*
2	$Ga_{0.77}In_{0.23}N$	*3.24*
3	$Ga_{0.68}In_{0.32}N$	*2.99*
4	$Ga_{0.53}In_{0.47}N$	*2.62*
5	$Ga_{0.30}In_{0.70}N$	*2.48*
6	$Ga_{0.22}In_{0.78}N$	*2.12*
7	$Ga_{0.16}In_{0.84}N$	*1.97*
8	*InN*	*1.89*

3.3.3. Conclusion

A supercritical millireactor was developed and a dual solvent system of methanol & toluene was successfully employed, utilizing cupferronate and HMDS chemistry, for synthesizing $Ga_xIn_{1-x}N$ solid solutions where maximum 47% (mole basis) of indium incorporation was done successfully without any phase segregation or composition modulation. The as-synthesized $Ga_{0.53}In_{0.47}N$ solid solution possessing a band gap of 2.62 eV, it didn't exhibit any phase segregation or composition modulation confirmed through HR-TEM – EDX characterization study. A composition modulation was observed on the solid solution samples possessing indium concentration higher than 47% (mole basis), along with the appearance of InN nanoflakes as seen in the case of the $Ga_{0.30}In_{0.70}N$ sample. This explains the reasons for the minor deviation in the linear variation of the band gap, as the indium content is increased in the sample. The continuous red shift of the steep absorption band edges from 353 nm (GaN) to 652 nm (InN) in this $Ga_xIn_{1-x}N$ system has confirmed the precise engineering of the band gap in this solid solution rendering it active from UV region to near IR region. These solid solutions are synthesized using a continuous flow supercritical millireactor with a residence time of 19 s. The next section of this chapter will focus on the heterogeneous photocatalysis under visible light for synthesis of novel moieties required for the pharmaceutical industries using $Ga_xIn_{1-x}N$ nanophotocatalysts.

3.4. Efficient trifluoromethylation of heteroarenes by visible light photoredox catalysis over $Ga_xIn_{1-x}N$ solid solutions semiconductor systems

3.4.1. Introduction

Cytochrome 450 (CYP450) is a biological term categorized to a family of *heme-thiolate* enzymes produced by the hepatocytes (a typical functional unit of liver, a liver cell) and epithelial cells of the small intestines in human beings. The intrinsic role of such enzymes is the oxidative metabolism (catalysis) of various exogenous and endogenous substances found in the human body [57]. In the allopathy medical field, drugs are consumed by human beings to cure various diseases occurring to them. Since drug is an exogenous chemical compound, they are biological transformed (oxidized) by the CYP450 proteins to small molecules, which are easily eliminated by the human body through excretion. The metabolism of most of the drugs (xenobiotic metabolism) usually occurs in the liver cells, where lipophilic chemical compounds (drugs molecules) are converted into highly polar derivatives, hydrophilic compounds [58], which are easily excreted from the body.

This drug metabolism process can be divided into three different phases:

1. Phase I consists of the oxidative reactions catalyzed by the CYP450 alone,

2. Phase II, where the converted hydrophilic compounds are further conjugated to polar compounds,

3. Phase III in which the conjugated drug molecules are excreted out of the system by efflux transporters.

CYP450 are responsible for the 'Phase I' metabolism of 80% of the drugs molecules currently in use for various diseases. The various oxidative reactions catalyzed by the CPY450 in 'Phase I' include hydroxylation, epoxidation, dealkylation, deamination and dehalogenation [57]. The schematic depiction of phase I metabolism implicated by heme-thiolate CPY450 is shown in Figure 3.34. In order to protect the drug molecules from these in vivo enzymatic reactions and to efficiently increase the exertion of its medicinal value, several strategies have been developed in the pharmaceutical industry.

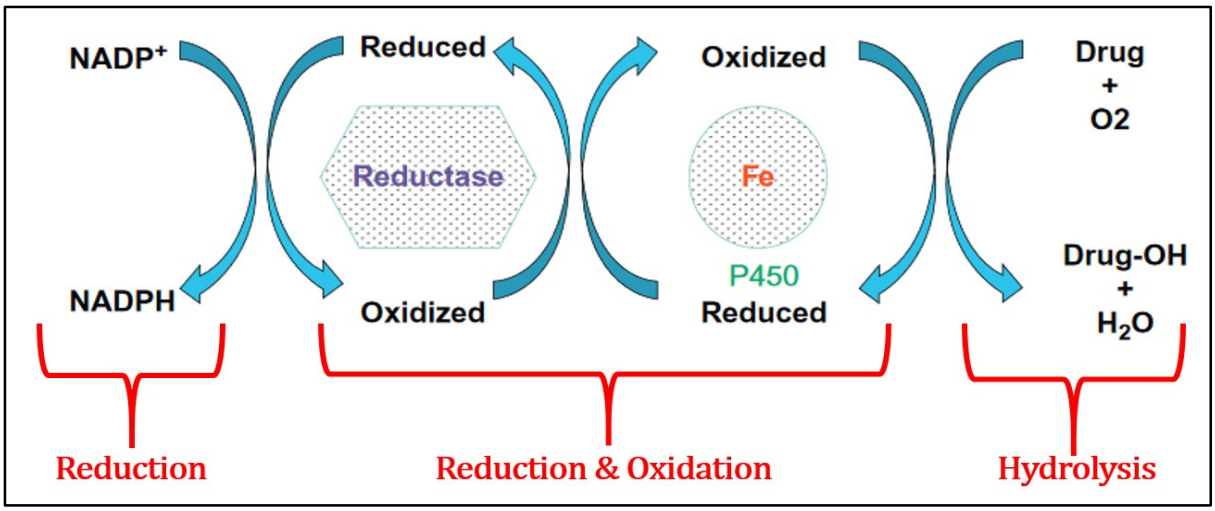

Figure 3.34. *Sequential events in the CYP450-catalyzed 'Phase I' metabolism of drug molecules (redrawn based on the diagram from article [57])*

Regularly, the deployed synthetic strategies of drug molecules include the incorporation of electron withdrawing, trifluoromethyl (CF_3) moieties into the drug substrates. CF_3 groups are staple synthon that alter the physical and chemical properties of the organic molecules in which they are incorporated [59]. The drug molecules possessing CF_3 groups exhibit a declining effect on the 'Phase I' metabolism by the CYP450 enzymes. Simultaneously, CF_3 groups enhance the efficacy of the drug molecules by promoting the electrostatic interactions with the targeted molecules and improve the cellular membrane permeability [60]. Thus the trifluoromethylated drugs are distinguished as compounds possessing a robust metabolic stability, predominant lipophilicity, enhanced bioavailability and binding selectivity compared to their non trifluoromethylated drug analogues [61]. Some examples of the currently available trifluromethylated drug molecules are: (i) 'Fluoxetine', sold under the name 'Prozac', an antidepressant drug molecule possessing the CF_3 group in one of its aryl rings, as depicted in Figure 3.35-a, (ii) 'Efavirenz', marketed under the trade name 'Sustiva', a non-nucleoside reverse transcriptase inhibitor used especially for the treatment of the HIV affected AIDS patient [61]. In the Efavirenz drug molecule, the CF_3 group is incorporated to the tertiary stereogenic centre in a heteroaliphatic ring, as shown in Figure 3.35-b.

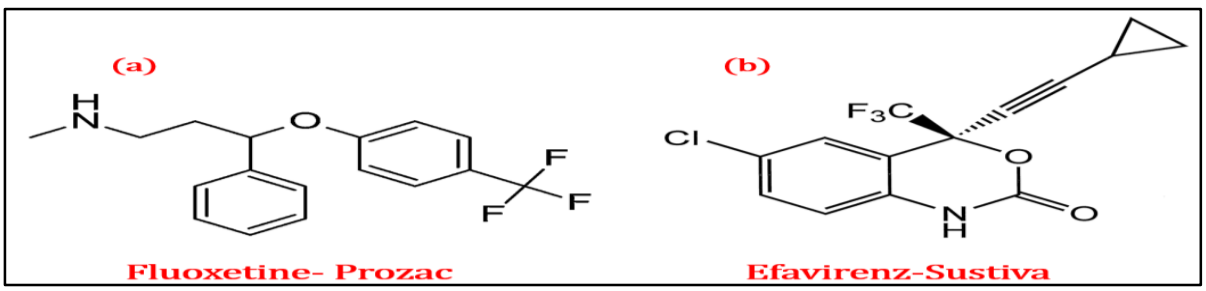

Figure 3.35. *a. Chemical structure of the Fluoxetine, an anti-depressant drug molecule [62]; b. Chemical structure of Efavirenz, a drug employed for the treatment of HIV affected AIDs patient [63].*

3.4.2. State-of-the-art methods for CF_3 incorporation or C-CF_3 bond formation

In the perspective of trifluoromethyl moiety's chemistry, there are three ways by which CF_3 can be incorporated into the organic compounds, resulting in the formation of C-CF_3 bond [64]. They are:

(i) Nucleophilic trifluoromethylation reaction

$$R^+ + [CF_3]^- \rightarrow R - CF_3 \quad \textbf{(3.8)}$$

(ii) Electrophilic trifluoromethylation reaction

$$R^- + [CF_3]^+ \rightarrow R - CF_3 \quad \textbf{(3.9)}$$

(iii) Radical trifluoromethylation reaction

$$R^{\cdot} + [CF_3]^{\cdot} \rightarrow R - CF_3 \quad \textbf{(3.10)}$$

Here the 'R' corresponds mostly to aryl and sometimes to aliphatic substrates to which the CF_3 group is incorporated. Initially the trifluoromethylation reactions were carried out through transition metal catalyzed cross coupling reactions involving a nucleophilic or an electrophilic addition, as depicted in Equations 3.8 and 3.9 [65, 66]. These methods suffered from several drawbacks like the requirement of stoichiometric amount of the metal catalysts and the pre-functionalized arene molecules as reactants and harsh conditions.

Additionally, they also provide very low yield under thermal activation. However, the replacement of aromatic halide by a CF_3 group through copper mediated coupling reactions occurs under milder conditions and works effectively only for aromatic iodides [67 – 69]. The copper catalysts' limitations for effectively incorporating the CF_3 group in other aromatic halides were subdued by the use of palladium as a catalyst material [70]. In order to perform tamed trifluoromethylations reaction through cross coupling reactions, several sources of CF_3 groups were developed. The nucleophilic source of CF_3 is provided by the Ruppert-Prakash reagent (Me_3SiCF_3), whereas the trifluoromethyl chalcogen salts (Umemoto's reagents) and hypervalent iodine (III)-CF_3 reagents (Togni's reagents) were used as electrophilic source of CF_3 groups. The schematic depiction of such cross coupling reactions involving transition metal catalysis is shown in Figure 3.36.

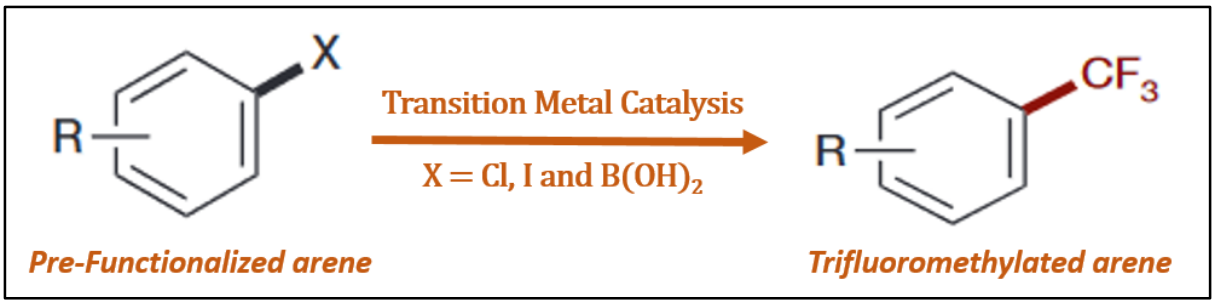

Figure 3.36. *Trifluoromethylation of arene through cross coupling reactions catalyzed by transition metals employing the Ruppert-Prakash or the Umemoto's reagent as CF_3 source (diagram redrawn based on the equation in the article [60].*

To conclude, the cross coupling reactions have furnished a simplified route for the synthesis of diverse range of CF_3 group-incorporated organic molecules without the dependence of fluorinated groups on the substrate. However, an ideal position for the incorporation of CF_3 into the drug molecule are achieved through parallel and multiple synthetic pathways involving aryl precursors possessing activated groups at different positions of the aromatic rings. Therefore, the challenge associated with cross coupling reactions for attaining CF_3-incorporated drug molecules is the dependence on the substituted precursors and their varying reactivity with respect to the catalysts and other parameters of the reactive medium.

3.4.2.1. Direct Incorporation of CF_3 group by photoredox catalysis

An efficient synthetic route for the synthesis of CF_3-incorporated drugs requires the complete elimination of the pre-functionalization route and (mainly) direct installation of the CF_3 group into the drug molecule, preferably at the positions of the metabolic susceptibility. To address this challenge and to perform direct installation of the CF_3 group into non-activated arene (non-pre-functionalized arene), Nagib & MacMillan *et al.* proposed a single electron pathway by taking advantage of photoredox catalysis, for generating electrophilic radicals ($CF_3^{\cdot}$).

Through a radical addition method, as shown in Equation 3.10, these $CF_3^{\cdot}$ radicals are site-specifically incorporated at metabolically susceptible positions of arenes and heteroarenes. The key ideas that intuited these techniques was that the generation of $CF_3^{\cdot}$ radicals, inspired from redox chemistry photosynthesis [71 – 73]. They proposed a strategy for the direct installation of CF_3 through electrophilic addition, which was in analogy to the single electron modifications of the drugs by the CYP450 enzymes. This sort of similarity can be visualized in Figure 3.37. Nagib & MacMillan *et al.* employed triflyl chloride (CF_3SO_2Cl) as the CF_3 source and polypyridyl organometallic complex, $Ru(phen)_3Cl_2$ (Tris(1,10-phenanthroline) ruthenium(II) chloride hydrate) as visible light photocatalyst.

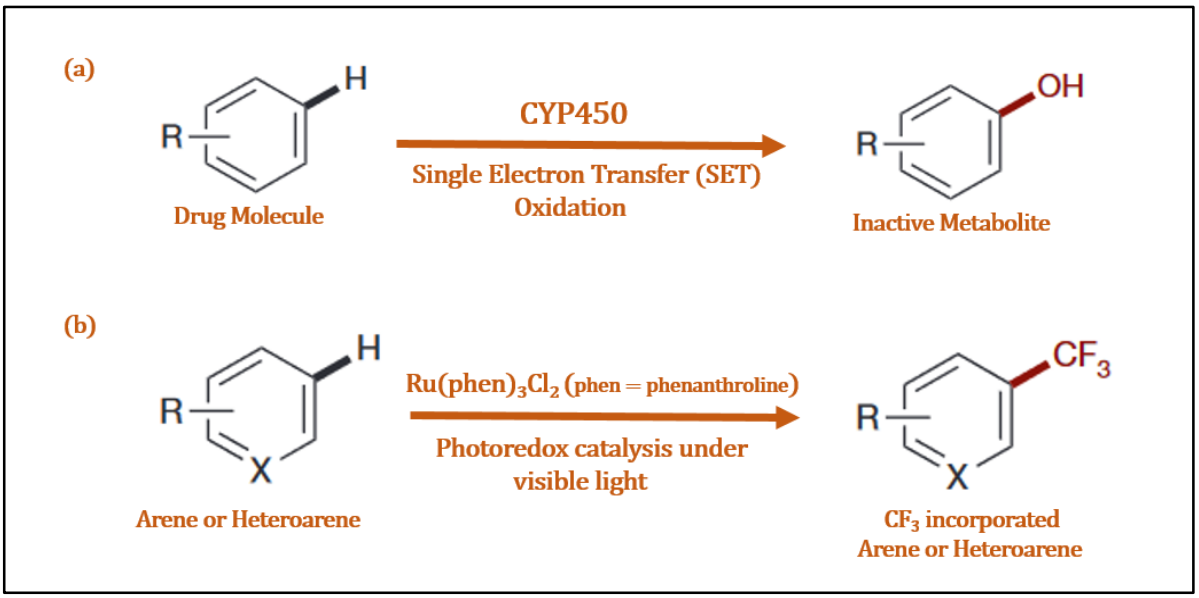

Figure 3.37. *a. In vivo metabolism of drug molecules by CYP450 through single electron transfer; b. Analogy to the enzymatic process, the direct installation of CF_3 group by functionalization of un-functionalized arenes through electrophilic addition (diagram redrawn based on the article [60]).*

Following this successful installation of CF_3 group to arene & heteroarenes in batch mode (24 h) by MacMillan *et al.* [60], Cho & Iqbal *et al.* further developed this trifluoromethylation reaction through a radical addition (in batch mode :16 - 24 h) and reported the synthesis of trifluoromethylated products by using trifluoroiodomethane (CF_3-I) as the trifluoromethyl radical source and tris(bipyridine)ruthenium(II) chloride ($[Ru(bpy)_3]Cl_2$) as a visible light active photocatalysts [74].

Both these above mentioned synthetic strategies used visible light active homogeneous photocatalytic materials in batch mode and required long reaction time to achieve the appropriate yields. Since continuous microreactors offer several advantages features like enhanced control over heat & mass transfer and residence time distribution with safe handling of hazardous reactants, Natan & Noel *et al.* fabricated microreactor systems and performed the mentioned radical based direct trifluoromethylation reactions. Their continuous flow photocatalytic diphasic system consisting of gaseous CF_3I reactant and liquid heteroarene substrates yielded the required CF_3 incorporated heteroarenes within minutes' time scale [74], as depicted in Figure 3.38.

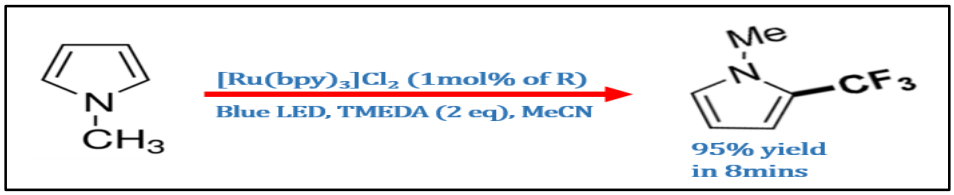

Figure 3.38. *Accelerated trifluoromethylation of heteroarenes by continuous flow photocatalysis using organometallic complex $[Ru(bpy)_3]Cl_2$ as photocatalyst, as reported by Natan & Noel et al. [74].*

3.4.2.2. Switching from homogeneous to heterogeneous photocatalyzed trifluoromethylation reactions

The ultimate motivation of this research work is to synthesize a visible light active semiconductor photocatalyst to replace the homogeneous complex organometallic, $[Ru(bpy)_3]Cl_2$ photocatalyst. Principally, the presence of highly toxic transition-metal contaminant like Ru (Ruthenium) in the drug molecule causes adverse effects to human health. $[Ru(bpy)_3]Cl_2$, is a coordination compound, whose cation performs the role of the sensitizer in the photocatalytic process. The complex tris(2,2′-bipyridine) ruthenium(II), $Ru(bpy)_3^{2+}$ absorbs light in the visible region (452 nm) of the electromagnetic spectrum and produces stable long lived photo excited states with life time of 1100 ns. These excited species are involved in the bimolecular electron transfer reactions, in competition with its deactivation pathways [75]. The main limitations associated with this material is the difficulty of recovery after the completion of the reaction and its reusability. Currently, there is an outburst of research in finding a suitable replacement for these homogeneous photocatalysts. Cho & Choi *et al.* have reported very recently an inorganic electride (dicalcium nitride) as a replacement for the $Ru(bpy)_3^{2+}$-based system for the direct trifluoromethylation of alkenes and alkynes [59].

In this research work an effective replacement for $Ru(bpy)_3^{2+}$ photocatalysts could be provided by the $Ga_xIn_{1-x}N$ solid solution semiconductor heterogeneous photocatalysts for the direct trifluoromethylation of heteroarenes. In the continuous series of solid solution synthesized, $Ga_{0.53}In_{0.47}N$ solid solution semiconductor possessing the appropriate band gap (2.62 eV) in the visible region was used here for carrying the trifluoromethylation through heterogeneous photocatalysis.

3.4.3. Photocatalyzed trifluoromethylation in batch mode using $Ga_{0.53}In_{0.47}N$ nanophotocatalysts

Initially, the trifluoromethylation reaction using the solid solution semiconductor $Ga_{0.53}In_{0.47}N$ will be carried out in a batch system. Then, flow reactors will be fabricated and experimented in this chapter to perform the continuous flow trifluoromethylation of substrates under visible light.

The study of this photocatalytic process in batch mode falls under the category of solid-liquid diphasic system, where all the reactants, including the CF_3 source, are present in the liquid phase. In order to achieve the efficient implementation of the solid semiconductor photocatalytic materials in the photoredox process, two systems can be realized. The first consists in immobilizing the photocatalysts, the second consists in using a slurry photoreactor. In the former case, the photocatalytic material is immobilized on some inert surface and in the latter case the solid semiconductor is suspended in the liquid phase. The suspension system is called slurry system and provides higher total surface area for the photocatalyst per unit volume than the immobilized system. Here, a suspended slurry photoreactor is fabricated and made up of a cylindrical glass tube, where suspension of the solid photocatalysts is achieved through

magnetic stirring with the aid of magnetic pellets present within the reaction medium. The schematic depiction of the batch photoreactor is depicted in Figure 3.39.

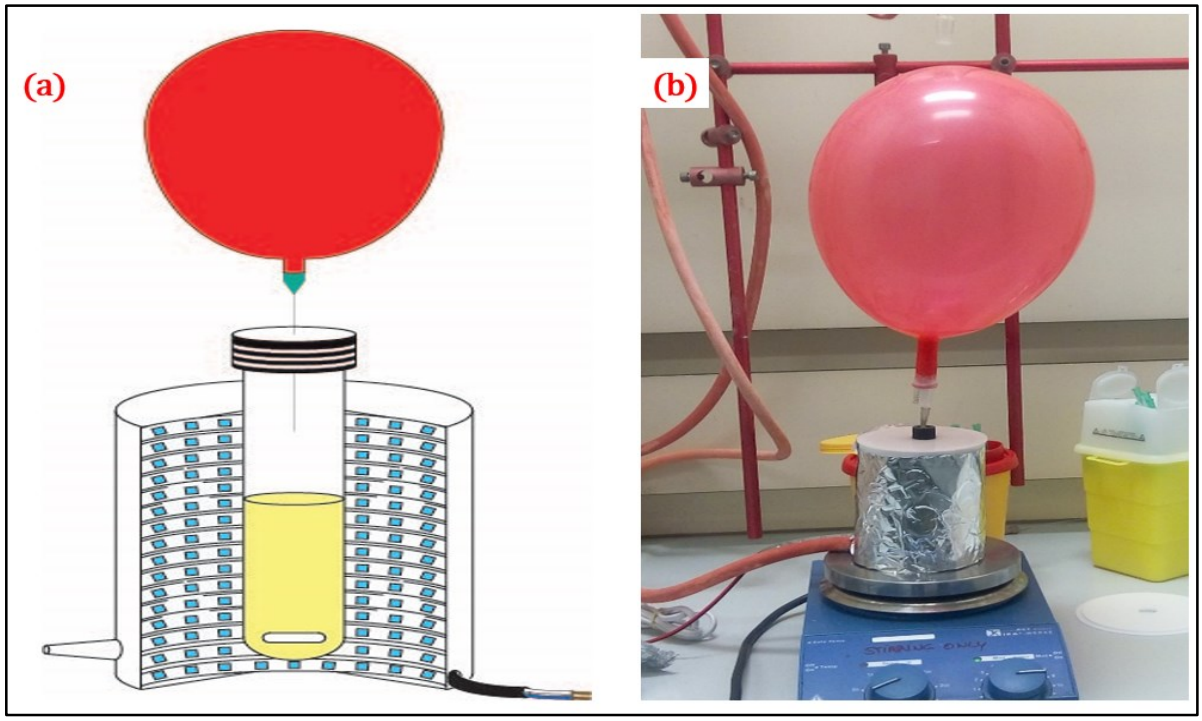

Figure 3.39. *a. Schematic depiction of the heterogeneous photocatalytic set-up, illustrating the attainment of a suspension with the aid of small magnetic pellet with the parallel and radial orientation of LED strips; b. Photograph of photocatalytic set-up, placed on the magnetic stirrer for attaining effective suspension.*

Effective illumination of visible light to such system is achieved by the parallel orientation of the LED strips to the cylindrical photoreactor in radial direction. The position of the LED lamps is external to the reactor system and provides uniform and radial illumination. This kind of radial arrangement was found to be an effective one for operating such small volumes of slurry photoreactor, as depicted in Figure 3.39. The photo reactor consists of a hallow cylindrical (outer) vessel of 9 cm inner diameter and 10.5 cm height and the inner surface of the vessel is coated with a highly reflective aluminium taps. 24 W, 3.5 m long LED strips (around 200 LEDs) are integrated in the system by coiling (radially) on the inner side of the cylindrical box. Two different visible light LEDs were used in this study. One emits purple light with a maximum intensity at 400 nm (395 – 405 nm) and the other emits intense bright light blue light in the wavelength range 450 - 460 nm, with a maximum intensity at 455 nm. The reaction vessel was made up cylindrical glass vessel fitted with rubber spectrum, which was 9 cm in height and 1 cm in diameter. It was positioned in the centre of the hollow cylindrical vessel in such way that LEDs are equidistant from the cylindrical glass reactor, at distance of 4 cm. The top of the system is covered with non-attachable lid, through which the photoreactor can be fixed. A gas balloon is fitted to the rubber septum and it is filled with argon gas. The entire setup was placed on the magnetic stirrer and at the bottom of the photoreactor, there provision

for the continuous flow of air (4 – 6 bar) for maintaining the temperature of the photocatalytic process constant throughout the study.

3.4.3.1. Experimental Section

Chemical used

In this heterogeneous photocatalytic study, N-Methylpyrrole (99%) was chosen as the substrate for the CF_3 incorporation. Trifluoroiodomethane (CF_3I) (99%) compound was used as the trifluoromethyl source. *N*,*N*,*N*′,*N*′-Tetramethylethylenediamine (TMEDA) (99.5%) was used as a base and anhydrous α,α,α-Trifluorotoluene (≥ 99%), anhydrous acetonitrile (99.8%), anhydrous Dimethyl Sulfoxide (DMSO) (≥ 99.9%) and deuterated dimethyl sulfoxide-d_6 (DMSO-d_6) (99.96 atom%) were used as solvents. All chemicals were purchased from sigma aldrich, except the CF_3I bottle, everything was stored inside the glove box. The CF_3I bottle was stored in the cylindrical storage place near the fume hood fitted with air circulation and cool atmosphere. They were used directly for the synthesis without further purification.

Trifluoromethylation of N-Methylpyrrole in batch mode

The cylindrical glass vessel used for the batch study was cleaned and dried in the oven prior to use. To this vessel, 1 mmol of N-Methylpyrrole (0.2 M), 2 mmol of TMEDA (2 eq), 4 mmol CF_3I (4 eq), 1 mmol of Internal standard (1 eq), $Ga_{0.53}In_{0.47}N$ nanophotocatalysts (4 mol% of reactant) and acetonitrile (MeCN) were added. Prior to this, the CF_3I was bubbled in an anhydrous acetonitrile solvent and its concentration was measured (4 mmol/ml). The CF_3I added to the system was dissolved in the acetonitrile solvent. Fresh acetonitrile was added to this mixture so that concentration of the reactant substrate (N-Methylpyrrole) was maintained at 0.2 M in the resultant mixture.

To this mixture, a small magnetic pellet was added and subsequently the cylindrical vessel was closed with rubber septum and flushed several times with argon gas. A balloon filled with argon was fitted to the top of the rubber septum and the rubber septum was completely sealed with paraffin tape. This entire mixture was stirred, using magnetic stirrer at 1000 RPM in dark for one hour prior to the photocatalytic process. After this step, resulting in the attainment of the absorption and desorption equilibrium of the reactant molecules on the photocatalysts surface. The LEDs were switched on and the batch photocatalysis was carried for several hours. During the reaction, the photocatalytic reactor system was maintained at ambient temperature by constant flow of air at 6 bar from the central air flow system, as the photocatalytic process is an exothermic process.

Either at the end or during the photocatalytic process, aliquots of the reaction mixture were taken and 19-F NMR analysis was directly performed to determine the yield of the product obtained (^{19}F NMR (300 MHz, DMSO): - 57.12 ppm for the product).

3.4.3.2. Results and discussion of batch trifluoromethylation reaction

The schematic depiction of the heterogeneous photocatalysis for the direct installation of the CF_3 into the N-Methylpyrrole substrate through sensitized photoreaction is depicted in Figure 3.40.

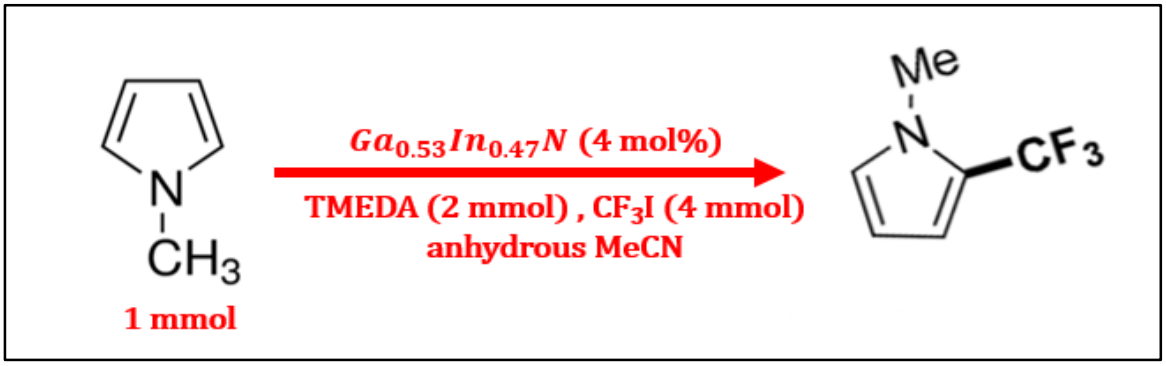

Figure 3.40. *Heterogeneous photocatalysis for the direct radical CF_3 installation to heteroarene under visible light irradiation.*

In this heterogeneous photocatalytic study, when utilizing the $Ga_{0.53}In_{0.47}N$ solid solution semiconductor as photocatalysts, the photoredox catalysis of the CF_3 incorporation process takes place through an indirect photochemical excitation mode. Here, the semiconductor material ($Ga_{0.53}In_{0.47}N$) possessing a band gap of 2.62 eV (477 nm), absorbs the visible light and produces the electron and hole in its conduction band (CB) and valence band (VB), respectively. Then, these photogenerated species interact with the ground state of the reactants adsorbed on the surface of the photocatalysts through the charge transfer process basically involving a single electron transfer (SET).

Initially, the batch study was carried out under bright light blue light having, $\lambda_{max} = 455\ nm$, 19-F NMR yield of 77% of was attained after 60 h of illumination for the product 1-methyl-2-(trifluoromethyl)-1H-pyrrole, as depicted in Figure 3.40. The same batch photocatalysis then was carried on using violet light possessing, $\lambda_{max} = 400\ nm$, in this case the similar yield of about 70% was attained within 7 h of illumination. The batch study in both these different illuminations was repeated and the similar trend was reproducible.

The violet light illumination was found to produce higher photocatalytic activity than the lower energy blue light. Since $Ga_xIn_{1-x}N$ solid solution is used as the photocatalytic material, and it formed an alloy between GaN and InN, the localized states in these semiconductors become hybridized and dispersed in the solid solution. The high energy violet light provides the possibility of exciting electrons into higher density of states.

Due to the dispersed nature of the valence and conduction band, more time is taken by the higher energy excited species to recombine, as result of which higher activity is furnished by the violet light compared to the blue light. The schematic representation of batch photocatalytic

study at a time interval of 1 h under violet light irradiation and the corresponding emission spectrum of the violet and blue light is depicted in Figure 3.41.

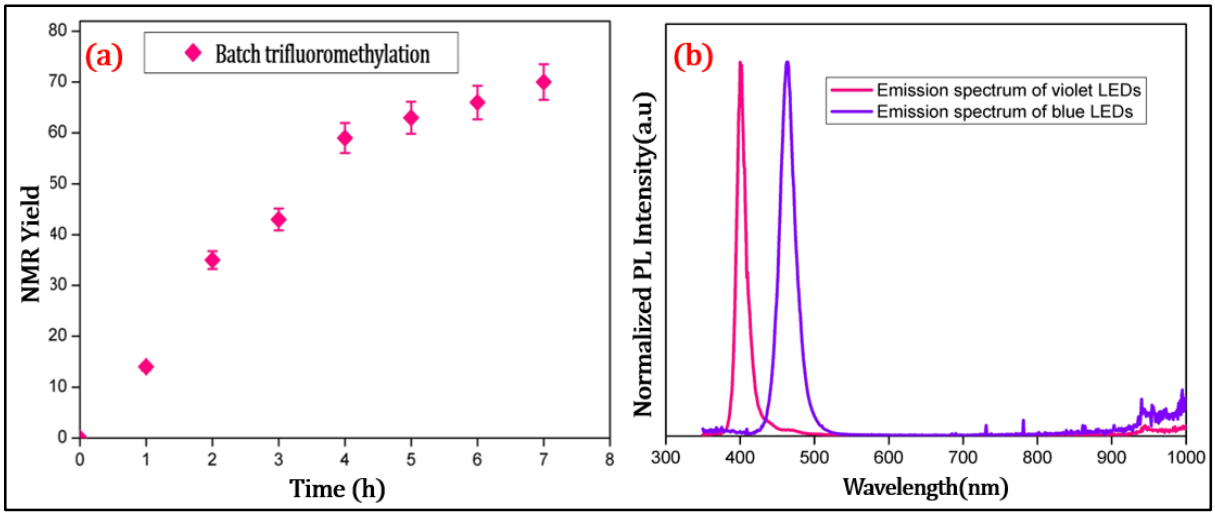

Figure 3.41. *a. Batch photocatalytic trifluoromethylation of N-Methylpyrrole by* $Ga_{0.53}In_{0.47}N$ *semiconductor photocatalyst under violet light irradiation* ($\lambda_{max} = 400\ nm$) *in batch mode; b. Emission spectrum of the violet and blue LEDs used in this heterogeneous batch photocatalytic study.*

Importantly, without any light, no trifluoromethylation reaction was observed, in the NMR analysis of the sample. Based on this observation and on the difference of photocatalytic activity with respect to the wavelength of the illumination source, it can be concluded that this trifluoromethylation reaction occurs through an indirect photochemical excitation type, where only the photocatalysts behave like a sensitizers and absorbs the visible light, while the other constituents of the reaction do not absorb the light but interact with the excited photocatalysts through charge transfer by SET pathway.

Based on the mechanism proposed by Cho *et al.* [74] and Noel *et al.* [76] for the direct radical incorporation of CF_3 radicals into the heteroarene substrate by $Ru(bpy)_3^{2+}$-based homogeneous photocatalysts, the possible mechanistic pathway that can occur in the semiconductor solid solution-based heterogeneous photocatalysis is depicted in Figure 3.42. Upon the excitation of the $Ga_{0.53}In_{0.47}N$ solid solution semiconductor by visible light, the following events occur, that sums up to be the mechanism involved in this trifluoromethylation reaction. The possible events are:

1. Upon exposure of the reaction mixture to visible light ($\lambda_{max} = 400\ or\ 455\ nm$), the $Ga_{0.53}In_{0.47}N$ solid solution is excited and electrons are promoted from its valence band (VB) to conduction band (CB) and hole is formed in the VB,

2. The excited high energy electron in the CB interacts with the surface-bounded trifluoroiodomethane (CF_3-I) in the ground state through single electron transfer (SET), resulting in the single electron reduction of the CF_3-I bond,

3. Due to step 2, electrophilic carbon centered $CF_3^{\cdot}$ radicals and iodide ions (I^-) are generated,

4. The holes formed in the VB are quenched by the electrons provided by the base (TMEDA) (amine molecule) molecules through SET, resulting in the formation of base radical or ammonium radical cation,

5. The electron deficient carbon centered ($CF_3^{\cdot}$) radicals couples with the surface- bounded heteroarene (N-Methylpyrrole) electron rich heterocycle, resulting in a complex radical,

6. This complex radical undergoes oxidation on combining with the $TMEDA^+$, ammonium radical cation through a SET route, resulting in the regeneration of the base (TMEDA) molecules,

7. The oxidized complex radical further undergoes re-aromatization resulting in the formation of the trifluoromethylated product.

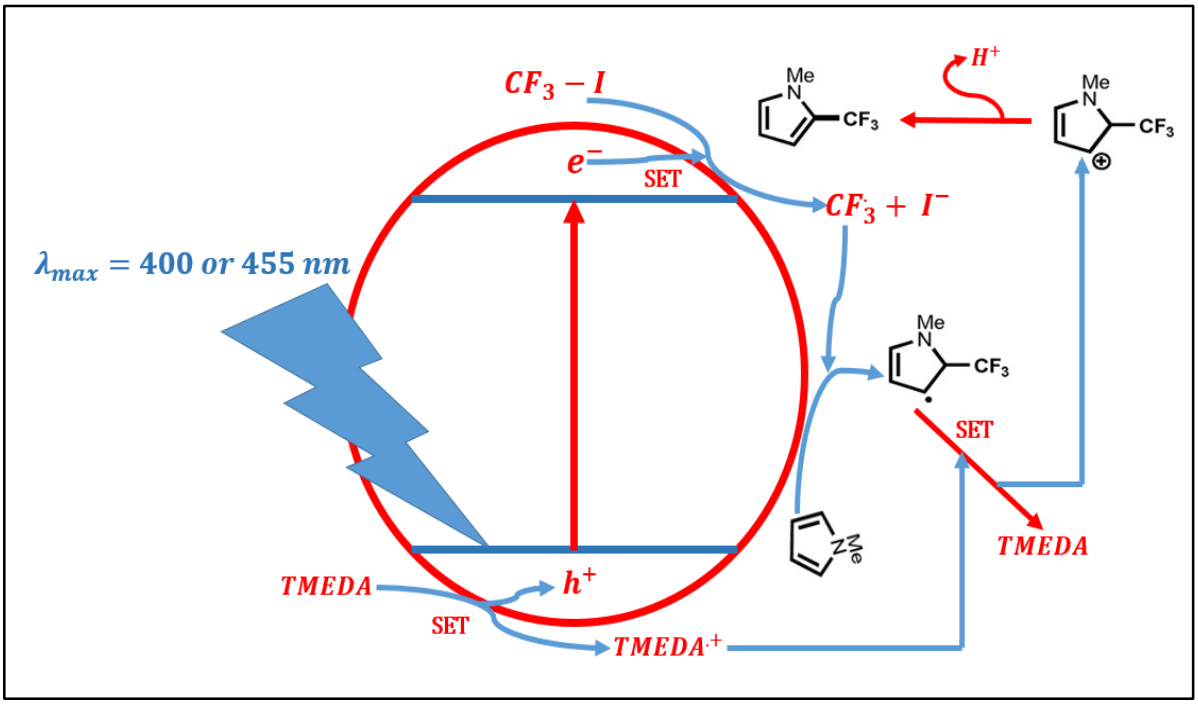

Figure 3.42. *Mechanism of trifluoromethylation of heteroarene through heterogeneous photoredox catalysis by semiconductor $Ga_{0.53}In_{0.47}N$ solid solution photocatalysts.*

To conclude the direct trifluoromethylation of heteroarenes was successfully performed under visible light through heterogeneous photocatalysis using solid solution nanomaterials synthesized through the continuous flow supercritical millireactor.

3.4.4. Continuous flow heterogeneous photocatalysis for direct radical trifluoromethylation of heteroarenes

Eventhough batch process was successfully carried out for the trifluoromethylation reaction at mild conditions, it suffers from several drawbacks like: (i) limitations in the scale up of the reaction medium, (ii) inefficiency in the homogeneous light distribution in the batch reactor system due to light attenuation effect (Beer- Lambert's Law), (iii) long reaction time due to inefficient mass transfer rate to the surface of the photocatalytic materials and (iv) also due to inefficient heat transfer rate (for cooling the system). In order to overcome these issues and to perform facile trifluoromethylation reaction, continuous flow system is an effective choice, as they provide an increased control over the various parameters of the reactive medium like: mass transfer, heat transfer, residence time, gas-liquid characteristics and enhanced light penetration in the case of micro, milli-reactor (short distances for photon to cross).

3.4.4.1. Design of a continuous flow photoreactor

Typically, in a multiphasic system consisting of a liquid and a gaseous reactant, the mass transfer of such diphasic systems can be studied through the 'Two-Film' model, as depicted in Figure 3.43.

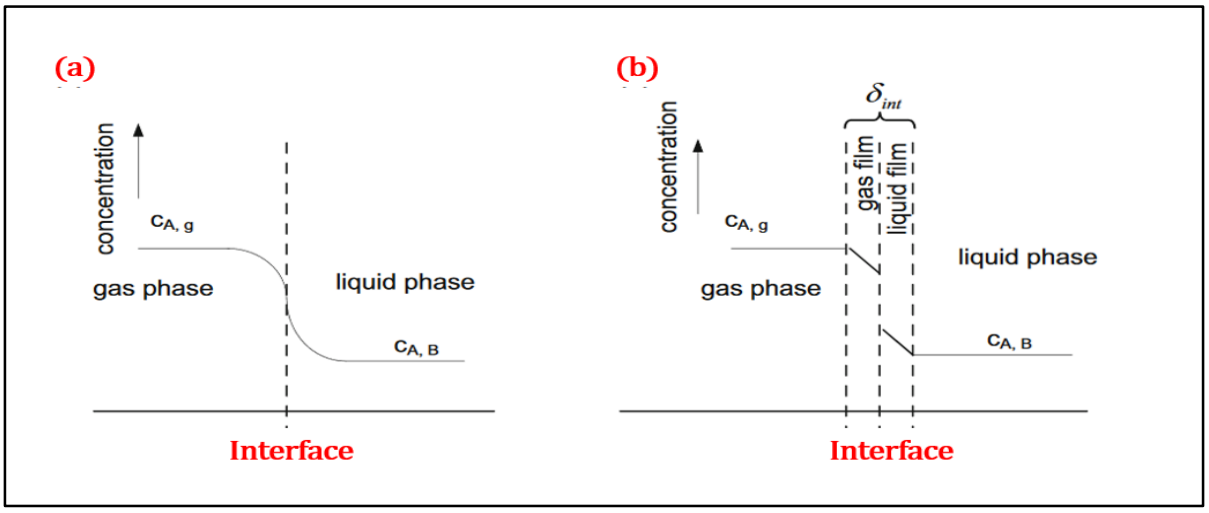

Figure 3.43. *a. Schematic illustration of diffusion and reaction of gas reactant into the liquid phase; b. Schematic depiction of the 'Two-film' model for liquid-gas diphasic system [77].*

In this liquid-gas diphasic system, the gaseous reactant is diffusing from the gaseous phase into the liquid phase and the reaction is taking place in the liquid phase. The driving force for mass transfer and chemical reaction to occur is the concentration gradient. Thus the 'Two-Film' model consists of two stagnant zones, where the gas-liquid equilibrium is reached. This system allows for calculating the mass transfer co-efficient (k_L) for segmented flow regimes in various reactors. The mass transfer efficiency for these systems are often represented by the liquid side volumetric mass transfer co-efficient (k_La), which is a product of mass transfer co-efficient (k_L) and the interfacial area (a). The calculated values of these mass transfer parameters are indicated in Table 3.5.

Table 3.5. *Comparison of mass transfer coefficient, efficiency and interfacial area for conventionally available reactor systems (data adapted from [77]).*

Type of reactor/contactor	$k_L a \times 10^2$ (s^{-1})	$k_L \times 10^2$ (m s^{-1})	a (m^2/m^3)
Bubble column	0.5–24	10–40	50–600
Couette–Taylor flow reactor	3–21	9–20	200–1,200
Impinging jet absorber	2.5–122	29–66	90–2,050
Packed column	0.04–102	4–60	10–1,700
Spray column	1.5–2.2	12–19	75–170
Static mixer	10–250	100–450	100–1,000
Stirred tank	3–40	0.3–80	100–2,000
Tube reactor	0.5–70	10–100	50–700
Microreactor	30–2,100	40–160	3,400–9,000

From the data provided in the previous table, it is pretty much obvious that high mass transfer rate is provided by the microreactor and it was therefore opted here for continuous flow photocatalysis. The critical criteria for opting this microreactor is because for the gas-liquid segmented flow in microchannel with diameter in micro regime (diameter < 1 μm), the internal circulation within the liquid phase is intensified [77] and since in our case it involves the use of nanoparticle solid solution semiconductor material as photocatalysts, the effective suspension of the photocatalysts in the liquid phase (internal circulation) is promoted by the toroidal or non-toroidal agitation of the gas phase. In order to investigate the effect of the flow on the photocatalytic reaction efficiency, we have considered two systems: (i) using a single phase liquid flow and (ii) a gas-liquid segmented flow, which are both detailed in the next sections.

3.4.4.2. Single phase continuous flow for the heterogeneous photocatalysis for trifluoromethylation reaction

Continuous flow single phase study of heterogeneous photocatalysis targeting the trifluoromethylation reaction was first carried out here. In this study, all the reactants and the solid photocatalysts are premixed in DMSO solvent (Figure 3.45) and successfully used for the continuous flow heterogeneous photocatalysis. The gaseous reactant CF_3I is dissolved in anhydrous DMSO (4 mmol of CF_3I in DMSO reaching a concentration of 0.2 M) and is combined with N-Methyl pyrrole (1 mmol with a concentration of 0.2M in DMSO), TMEDA (2 mmol, 2 eq of pyrrole precursor) and 4 mol% of $Ga_{0.53}In_{0.47}N$ nanomaterials. The reaction mixture is purged with argon gas continuously. Subsequently, dark absorption is carried out during 1 h by stirring the mixture using a magnetic stirrer at 1000 RPM. After reaching adsorption-desorption equilibrium of the reactant molecules on the photocatalysts surface, the mixture is loaded into the continuous flow photoreactor, as depicted in Figure 3.44.

The fundamental idea that went behind the design of this continuous flow tubular reactor with micro dimensional channel is that no settling or clogging of the solid photocatalysts is observed at any part of the system. After dark absorption, the resultant mixture appeared as light brown suspension with no particle settling. This mixture was loaded into the specially designed

syringe as depicted in Figure 3.44. Internally, the syringe is loaded with a small (0.25 - 0.5 cm in length) cylindrical magnetic pellets. These pellets are set into a magnetic stirring with help of external magnetic field controlled using the ADUM programmed control system. Once the mixture is loaded, even when the injection operation is going on, the magnetic pellets are continuously stirring, maintaining the homogeneous suspension and pumping this uniform suspension into the photoreactor. The outlet from the syringe is connected immediately to a T-shaped mixer immersed under a high power ultra sonicator. One end of the T-mixer is connected here to argon line for cleaning and purging the system. While in continuous flow process, the ultrasonicator is on and as the suspension enters the mixer, immersed below the liquid level in the sonicator, the suspension is tremendously sonicated. Irradiation of this suspension with ultrasonic waves (> 20 kHz) resulted in the generation of vacuum bubbles or voids within the liquid samples. This constantly provided the presence of irregular voids within the liquid samples resulting more or less like a perfectly segmented gas-liquid flow. As a result of which there was no settling or deposition of solid photocatalytic materials within the photoreactor tubes with micro dimensions.

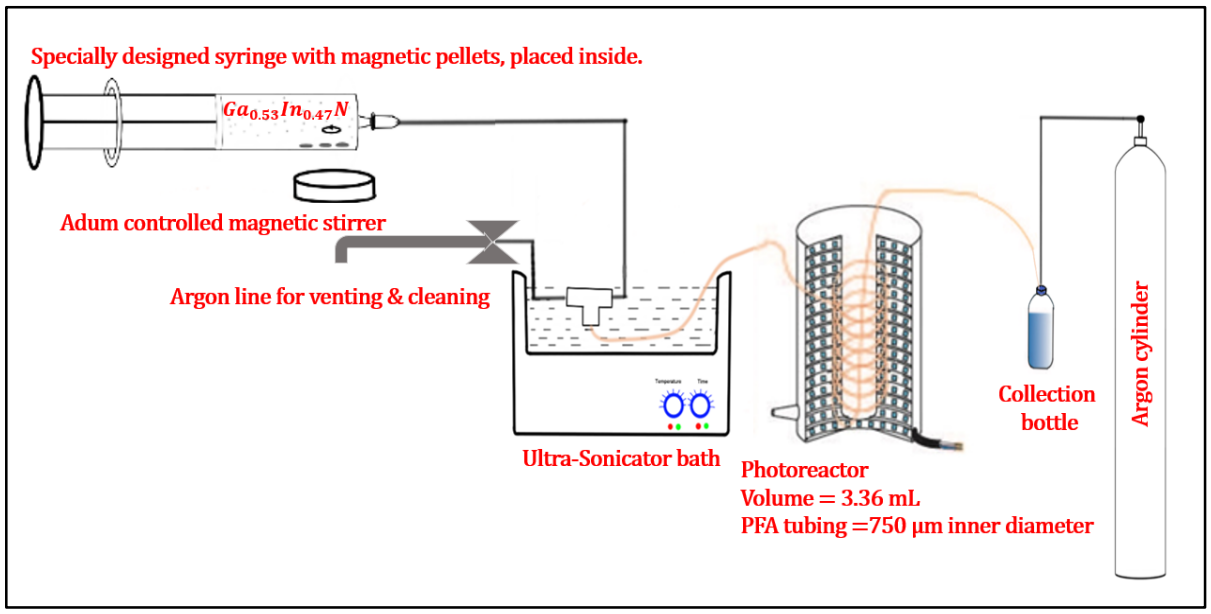

Figure 3.44. *Continuous flow photoreactor fabricated for the heterogeneous photocatalysis of trifluoromethylation in single phase.*

The photo reactor consists of a hallow cylindrical (outer) vessel of 9 cm inner diameter and 10.5 cm height and inner cylindrical vessel with 2 cm diameter and 10 cm height. The inner surface of the cylinder and outer surface of the internal cylinder is coated with a highly reflective aluminium taps. A 24 W, 3.5 m (400 nm (395 – 405 nm)) long LED strips is fabricated in the system, by coiling (radially) on the inner side of the hallow cylinder (200 LEDs). The reaction system or vessel is made up of a perfluoroalkoxy alkane (PFA) capillary tubing with an internal diameter of 750 µm. This PFA tubing of length 7.6 m was coiled around the outer surface of the internal cylinder, resulting in a total volume of 3.97 mL, where 3.6 mL volume was successfully exposed to illumination of photons. The internal cylindrical vessel with PFA tubing is placed in such way that the LEDs are equidistant from external cylinder, at

distance of 4 cm. The top of the system is covered with non-attachable lid, through which internal cylinder can be fixed or removed. After the continuous flow, the suspension is collected in the separate specially designed collection bottle fitted with an argon recirculation line. The obtained suspension is eventually taken for NMR analysis.

3.4.4.2.1. Results and discussion

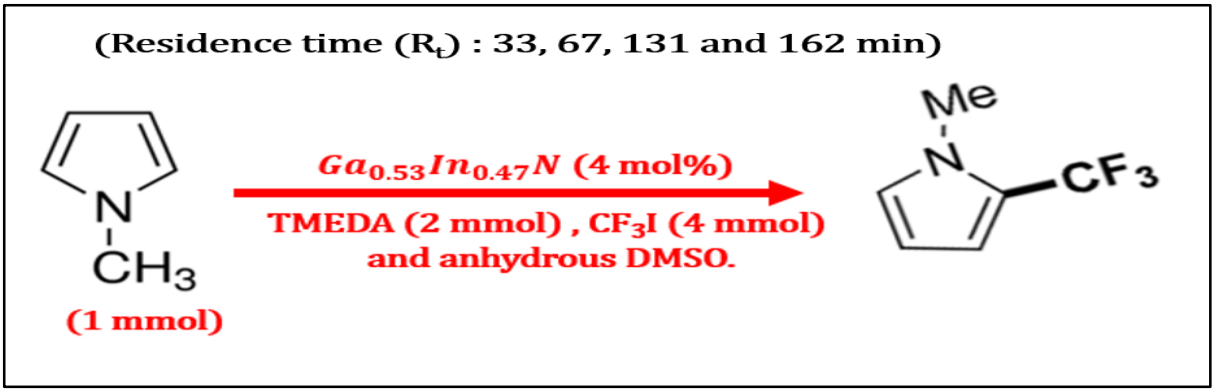

Figure 3.45. *Schematic depiction of the reactive medium used in the continuous single phase flow heterogeneous photocatalytic process.*

The key important difference between the study performed here and in the batch system is that anhydrous DMSO was used as solvent here (Figure 3.45), as it provided better solvation effect for attaining a uniform suspension of the solid solution photocatalysts in the flow process without any settling.

The perfect synchronization of the solvation effect coupled with the ultrasonic waves (> 20 KHz) and the magnetic stirring within the injection syringe provided a novel continuous flow single phase system without any deposition of the photocatalytic material or clogging of the system. The continuous single phase flow offered better results than the batch process for trifluoromethylation of heteroarenes. The 19F-NMR yields were calculated for various residence times and systematically plotted in Figure 3.46. For each residence time, the continuous flow synthesis was repeated twice to check the reproducibility of the results and thus the results of both trial 1 and trial 2 are depicted in Figure 3.46.

The continuous single phase flow provided better results than the batch process. Here, the maximum yield of 84% was attained within 162 min (Table 3.6) but in the batch process it took up to 7 h to reach a yield of 70%. The as-designed system with uniform and efficient illumination of the micro dimensional channel has provided uniform suspension without settling of particles leading to enhanced charge and mass transfer from the photocatalytic surface. In this system, there was some difference in the NMR yields for low residence times, but similar yields were observed at longer residence times. After each synthesis carried out here, the system was purged with fresh solvent of DMSO and cleaned thrice by continuously purging argon gas into the system. The minor discrepancies in the lower residence times could be attributed to the purging issues in the system, which later identified and rectified.

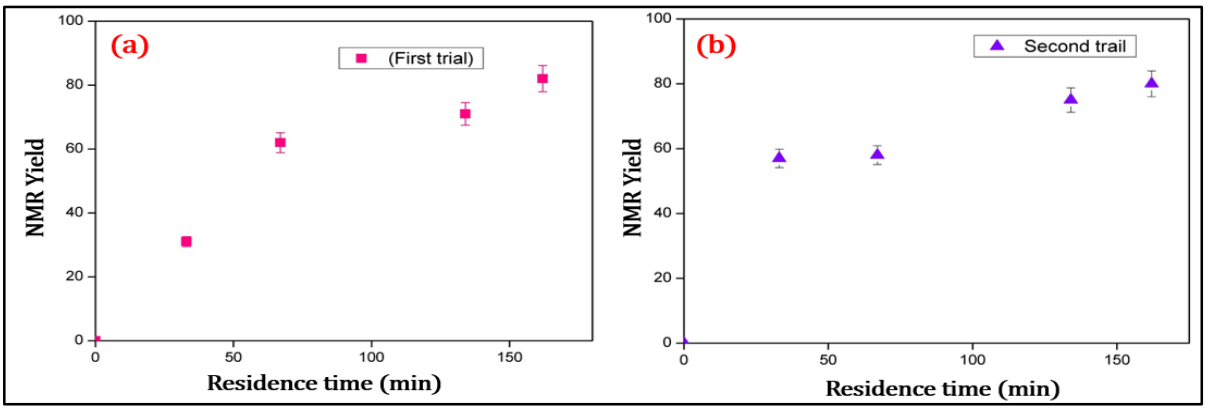

Figure 3.46. *Trifluoromethylation of N-Methylpyrrole at various residences times; a and b. Trial one and trail two, performed to check the reproducibility of the process*

Table 3.6. *Continuous single phase trifluoromethylation by $Ga_{0.53}In_{0.47}N$ photocatalytic material*

S.No	Residence time (R_t) (min)	NMR Yield (Trial One)	NMR Yield (Trial Two)
1	*33*	*31%*	*57%*
2	*67*	*62%*	*58%*
3	*131*	*72%*	*75%*
4	*162*	*80%*	*84%*

3.4.4.2.2. Recyclability of the ($Ga_{0.53}In_{0.47}N$) heterogeneous photocatalyst for continuous single phase trifluoromethylation reaction

In order to check the recyclability of the photocatalysts for the trifluoromethylation reaction in continuous single phase flow, the semiconductor material was recovered from the final solution by centrifuging at 10,000 rpm for 10 min. Then, the supernatant was removed and the resultant parties were dispersed in fresh DMSO solvent. The centrifugation procedure was repeated twice and the particles were dried in open atmosphere.

The obtained results are systematically depicted in Figure 3.47. The recyclability study indicates that the photocatalyst works effectively for three consecutive runs without much reduction of the photocatalytic activity. The significant decrease in the yield at higher residence time could be attributed to the competitive reaction existing between the required CF_3 incorporated heteroarene and the iodide ion coupling reaction to hydrogen cation of the solvent molecule. As the heterogeneous photocatalysis is a surface-bounded process occurring on the surface of the photocatalysts. There exists the competition between the various reactions occurring on the surface. The spectroscopic study interpreting the other chemical reactions

occurring on the surface of the photocatalysts is beyond the scope of this research and will be dealt in the future. To conclude, we were successfully able to reuse the photocatalysts and a similar photocatalytic activity was exhibited by the solid solution photocatalysts. There was no depreciation in the photocatalytic activity even after the three consecutive runs of continuous single phase heterogeneous photocatalysis. The separation of this solid semiconductor photocatalysts is very facile and do not require costly separation equipment as needed by homogeneous photocatalysts.

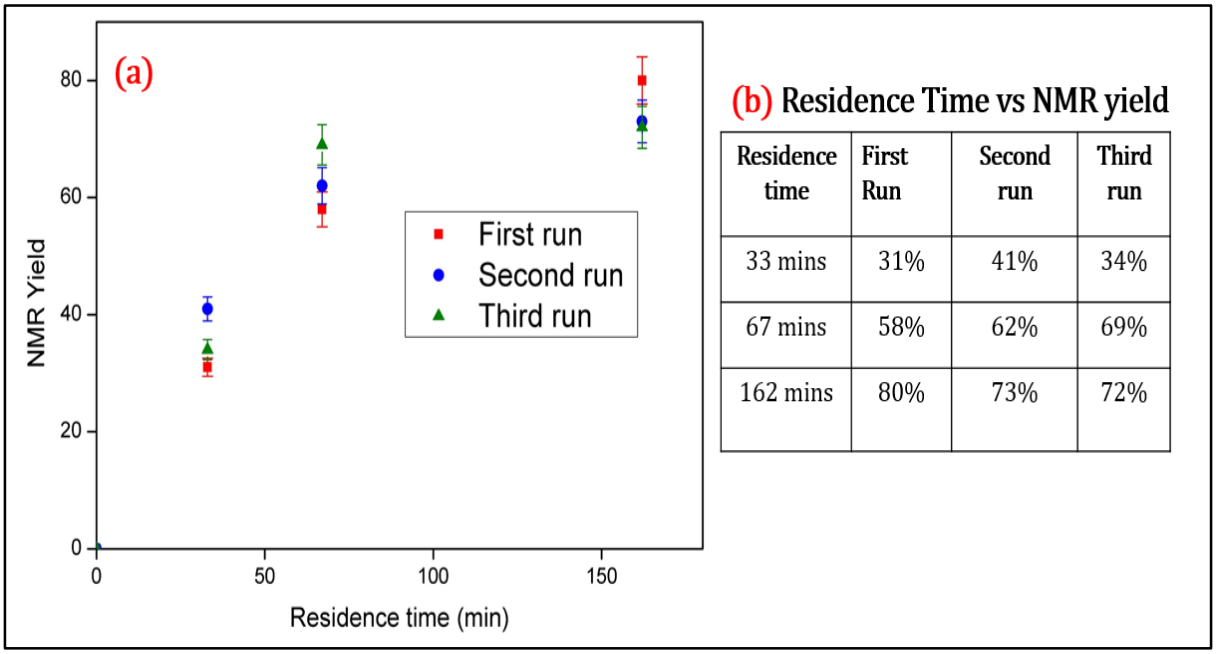

(b) Residence Time vs NMR yield

Residence time	First Run	Second run	Third run
33 mins	31%	41%	34%
67 mins	58%	62%	69%
162 mins	80%	73%	72%

Figure 3.47. *a. Systematic depiction of graphical plot of residence time (R_t) vs NMR yield; b. Table summarizing the data points used for plotting the graph mentioned in Figure 3.47.a.*

3.4.4.3. Continuous segmented flow heterogeneous photocatalysis for trifluoromethylation reaction

To further optimize the continuous trifluoromethylation of heteroarene process, a continuous segmented flow synthetic procedure was adopted for the direct radical incorporation of CF_3 group into the N-Methylpyrrole substrate. Here, the trifluoromethyl source, trifluoroiodomethane (CF_3I) was used directly as the gaseous reactant with the aid of a mass flow controller (MFC) and the heteroarene substrate was kept in the liquid phase.

The N-Methylpyrrole (1 mmol), TMEDA (2 mmol, 2 eq) and $Ga_{0.53}In_{0.47}N$ nanophotocatalysts (4 mol% of pyrrole substrate) were added to a dried cylindrical vial with magnetic pellets. The suspension with the photocatalysts was continuously stirred using a magnetic stirrer at 1000 RPM for one hour in the dark, so that absorption-desorption equilibrium of the heteroarene substrate on the photocatalysts was attained. Subsequently, this resultant suspension was loaded into the specially designed syringe, as depicted in Figure 3.48.

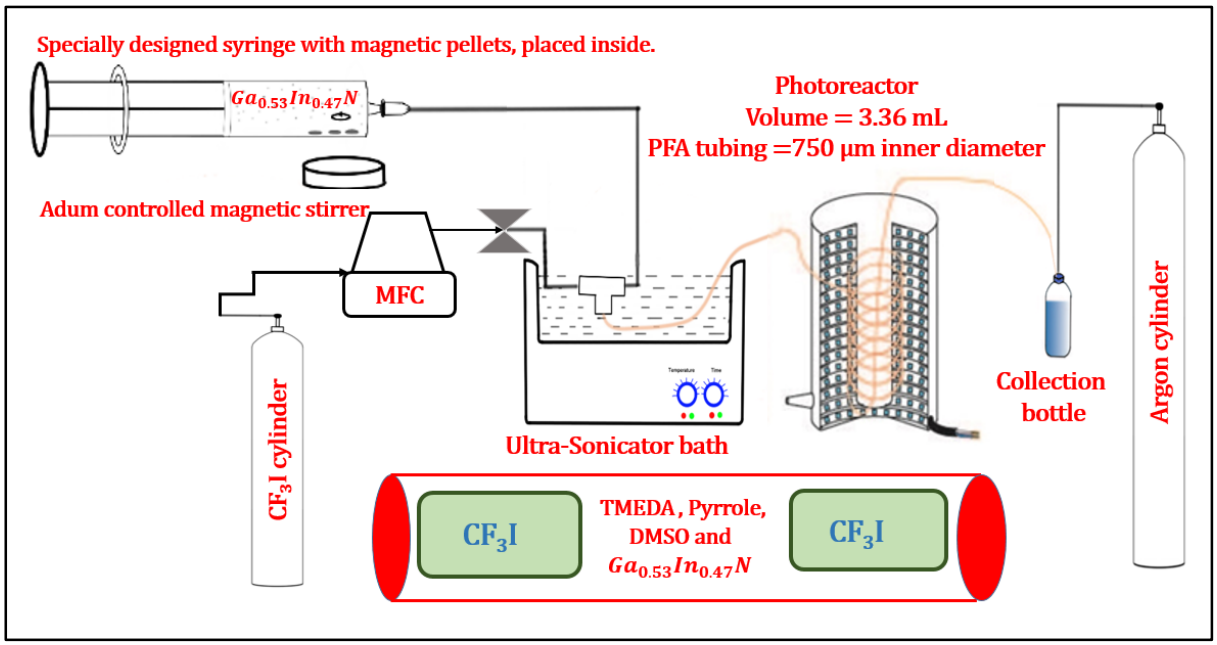

Figure 3.48. *Schematic depiction of the continuous segmented flow photoreactor set-up for the trifluoromethylation reaction by heterogeneous photocatalysis using $Ga_{0.53}In_{0.47}N$ as photocatalysts, with gas-liquid segmented flow.*

In this segmented continuous flow study, a precise variation of the residence time is attained through the tuning of the liquid flow rate (modulation through syringe pump) and gas flow by using the MFC. The obtained results are systematically depicted in Figure 3.49.

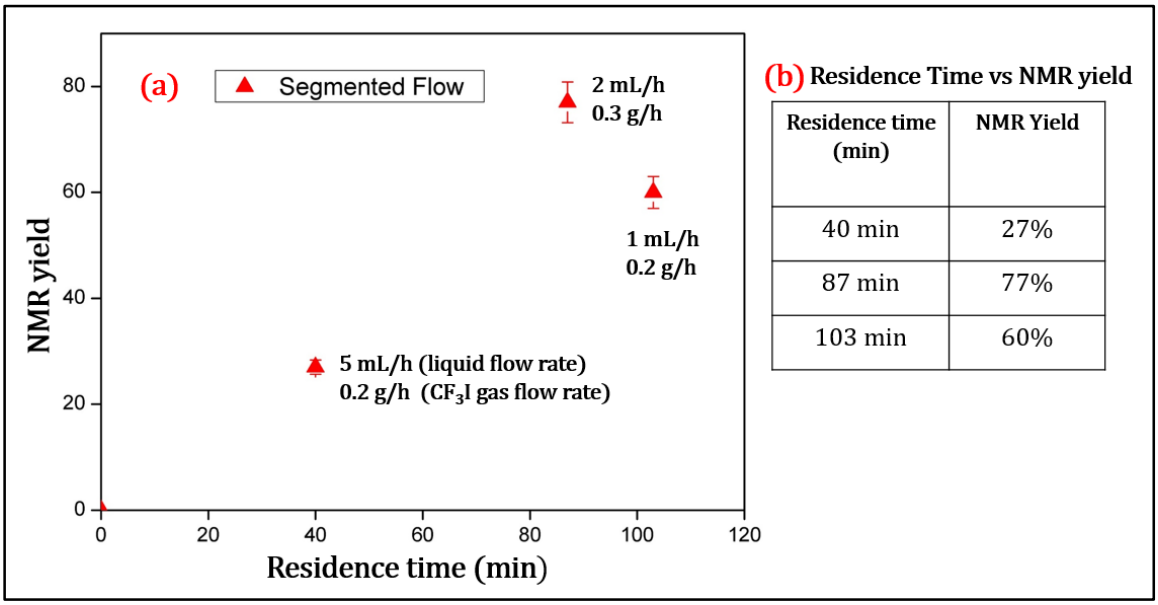

(b) Residence Time vs NMR yield

Residence time (min)	NMR Yield
40 min	27%
87 min	77%
103 min	60%

Figure 3.49. *a. Systematic depiction of the graphical plot of NMR yield vs residence time (R_t) for the segmented flow of (CF_3I + Methylpyrrole); b. Table summarizing the data points used for plotting the graph mentioned in Figure 3.49.a.*

During the continuous segmented flow process, the ultrasonication system was kept on to ensure perfect mixing of the gas and liquid phase in the mixer region. The resultant suspension on combining with CF_3I gas forms perfectly homogenised gas-liquid segmented flow. This segmented flow gave more optimized trifluoromethylated product yield of 77% with 87 min of residence time, this is half of the time taken by the continuous single phase flow process for attaining such yield. This can be attributed to the perfectly balanced segmented flow. Indeed, the internal circulation within the bulk liquid phase allow higher mass transfer rate compared to the continuous single phase flow. Additionally, the reflection of light by the gas bubbles is also observed in this system, which further increases the penetration of photons within the suspension of nanoparticles, thus increasing the photocatalytic yield. Generally, in gas-liquid diphasic systems, the increase of liquid flow rate, increases the mass transfer efficiency and additionally, internal circulation is also intensified. These phenomena led to the increase in the yield of the product obtained, this was observed in this segmented flow study for the residence time of 87 and 103 min, where the high liquid flow rate led to an increase in the photocatalytic yield (flow rate values are shown in Figure 3.49-a. At the same time for very low residence time possessing a very high liquid flow rate, there would have enhanced mass transfer but the system wouldn't have acquired enough photons for achieving high photocatalytic yield. This is seen for the case of the 27% yield obtained for a 40 min residence time.

3.4.4.4. Continuous segmented flow by non-reactant argon gas and the reactive mixture for heterogeneous photocatalysis of trifluoromethylation reaction

To further investigate the effect of reflections of photons on the gas-liquid interface and their impact on the continuous segmented flow heterogeneous photocatalysis of trifluoromethylation reaction, a segmented flow with argon gas was studied. Here, the CF_3I was dissolved in the solvent prior to the synthesis and kept in the liquid phase along with heteroarene substrate. Meanwhile, argon (non-reactive) gas was used only to generate a perfectly homogenised gas-liquid segmented flow, as attained in the previous segmented flow with CF_3I gas. Through this study, the mass transfer of CF_3I gas is eliminated as it is already dissolved in the liquid solvent and only the effect of reflections of light by the interfaces and its influence on the photocatalytic activity of trifluromethylated product was studied. The schematic description of the setup developed for the argon generated gas-liquid segmented flow is shown in Figure 3.50.

In this study, all the reactants and the solid photocatalysts are premixed in DMSO solvent and successfully used for the argon generated segmented flow heterogeneous photocatalysis. The gaseous reactant CF_3I is dissolved in anhydrous DMSO (4 mmol of CF_3I in DMSO with concentration of 0.2 M) is combined with N-Methyl pyrrole (1 mmol with concentration of 0.2 M in DMSO), TMEDA (2 mmol, 2 eq of pyrrole precursor) and 4 mol% of $Ga_{0.53}In_{0.47}N$ nanophotocatalysts. Subsequently dark absorption is carried out on the mixture for 1 h by stirring the mixture using a magnetic stirrer at 1000 RPM. After reaching adsorption-desorption equilibrium of the reactant molecules on the photocatalysts surface, the mixture is loaded into the continuous syringe, as depicted in Figure 3.50. Here, the perfect segmented flow is reached

by precisely tuning the suspension flow rate by modulating the syringe pump and flow rate of argon gas is varied with the aid of MFC.

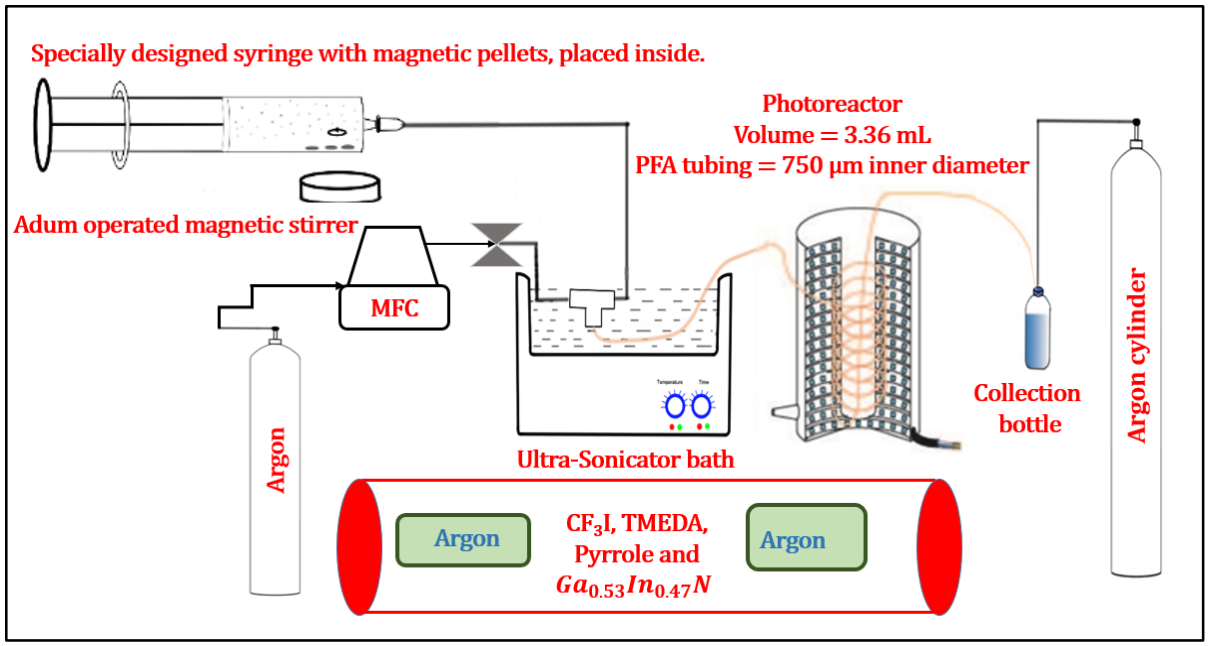

Figure 3.50. *Schematic depiction of the continuous argon generated segmented flow photoreactor set-up for the trifluoromethylation reaction by heterogeneous photocatalysis using* $Ga_{0.53}In_{0.47}N$ *nanophotocatalysts.*

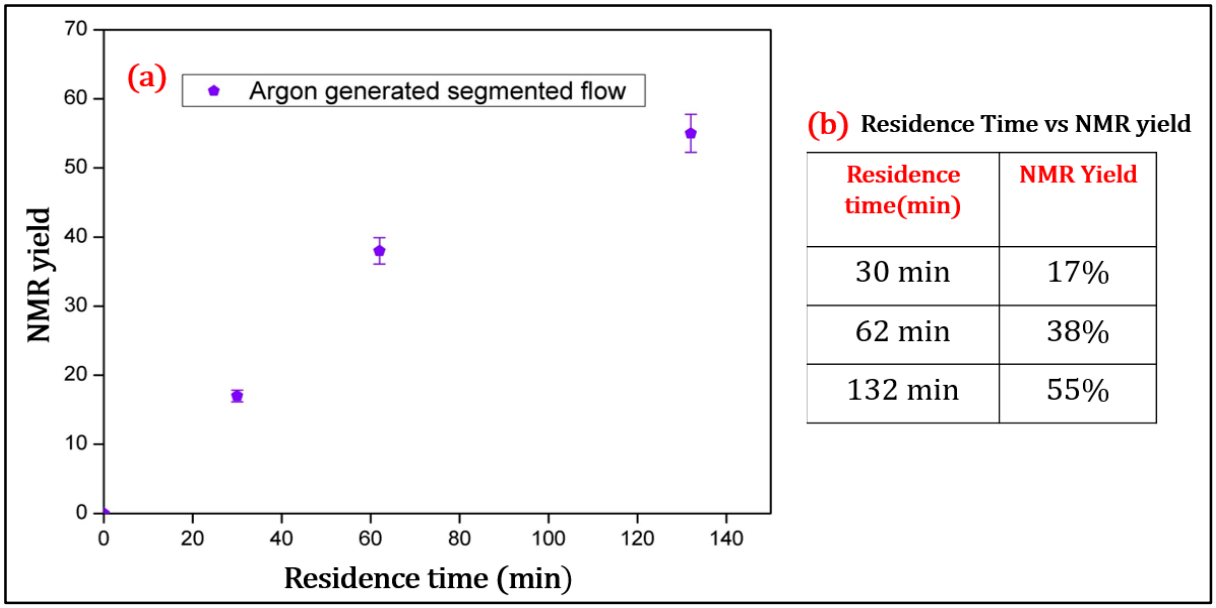

(b) **Residence Time vs NMR yield**

Residence time(min)	NMR Yield
30 min	17%
62 min	38%
132 min	55%

Figure 3.51. *a. Systematic depiction of graphical plot of the NMR yield vs residence time* (R_t) *for segmented flow of (Argon + Reacting mixture of suspension); b. Table summarizing the data points used for plotting the graph mentioned in Figure 3.51.b.*

The obtained results are plotted and systematically depicted on Figure 3.51. Argon gas generated continuous segmented flow was not as efficient has the segmented flow generated with the CF_3I gas nor with the continuous single phase flow process. This indicates that in such a continuous flow, the reflections of light by the gas bubbles doesn't have profound effect on the heterogeneous photocatalysis, since the dimension of the microchannel is small, efficient illumination by transmission itself using a single phase flow system is attained and the reflection has no specific beneficial effect. The reasons for the very low activity of the argon gas generated segmented flow compared to single phase continuous flow, the increased diffusion of argon gas into the liquid phase, secondary circulations within the bulk liquid phase would have affected the surface-bounded reactions on the photocatalysts surface as both the CF_3I and N-Methylpyrrole are already adsorbed on the particle surface during the dark absorption process.

3.4.5. Conclusion of photocatalytic studies

The direct radical CF_3 incorporation into the heteroarene (drug model of substrate) was achieved here by heterogeneous photocatalysis, which was not performed so far using semiconductor photocatalysis. The trifluoromethylation reaction was successfully carried out in both batch and flow reactors. Comparing the various flow reactors reported in this research work, segmented flow system with CF_3I was highly efficient in achieving enhanced yield within short time compared to other systems. Here, in this research work the perfect synchronization of ultrasonication and magnetic stirring within the syringe has allowed to reach a flow of nanoparticles in micro channels without any clogging or settling of the particles.

3.5. Conclusion

In this chapter, there has been two significant research advancements reported. The first one corresponds to the continuous flow supercritical synthesis of direct band gap $Ga_xIn_{1-x}N$ ($0 \leq x \leq 1$) solid solution nanomaterials. Here, significant exploration for the synthesis of this solid solution with high indium incorporation and small phase segregation was done. Successfully, a dual solvent system of toluene and methanol was found to be an optimum system allowing the incorporation up to 47% (mole%) of Indium into the solid solution without any phase segregation through cupferronate and HMDS precursor chemistry. This is the highest attained so far in this nanoscale solid solution using this precursor methodology. The as-synthesized $Ga_{0.53}In_{0.47}N$ solid solution was successfully proposed as a replacement for complex expensive transition metal homogeneous photocatalysts used for in the field photocatalysis for drug synthesis.

In the second part of the chapter, the $Ga_{0.53}In_{0.47}N$ solid solution nanophotocatalysts effectively performed the direct radical trifluoromethylation reaction process both in batch and flow mode. The heterogeneous photocatalysis was carried out through indirect photochemical excitation process or sensitized photoreaction where the photonic energy is effectively converted for the CF_3 incorporation into heteroarene. From the resultant solution, the photocatalysts were easily recovered through centrifugation process and didn't require any other down streaming process for recovery.

In this chapter, a continuous flow photoreactor in microscale dimension (capillary PFA tube) was fabricated and combined with a specially designed syringe with magnetic pellets and ultrasonication system for executing the continuous flow using nanoparticles suspension without any settlement or clogging. Through these flow systems, the photocatalytic material exhibited enhanced activity due to efficient homogeneous distribution of the photons and the gas promoted agitation, which maintained the suspension of nanoparticles within the system. The $Ga_{0.53}In_{0.47}N$ photocatalysts material exhibited enhanced recyclability without much decrease in its photocatalytic activity even after three consecutive runs. Such recyclability is impossible to achieve in the previously employed transition metal based homogeneous photocatalysts.

Finally, this $Ga_{0.53}In_{0.47}N$ solid solution nanomaterials are currently effective replacement for complex organometallic visible light active homogeneous photocatalysts. Implementation of this semiconductor for drug production will effectively reduce the cost of the drug and will obviate the costly downstream process which are usually used to remove the transition metal contaminates present in the drug molecules. Since CF_3 incorporation is highly required for drugs used to cure AIDS and cancer, the implementation of this solid solution has a huge potential commercial value in the coming years.

References

[1] S. Mokkapati and C. Jagadish, "III-V compound SC for optoelectronic devices," *Mater. Today*, vol. 12, no. 4, pp. 22–32, 2009.

[2] V. R. Murthy, A. Srivani, and G. Veera, "Physical Studies in III-Nitride Semiconductor Alloys," *Int. J. Thin. Fil. Sci. Tec.*, vol. 27, no. 1, pp. 15–27, 2017.

[3] S. Nakamura, M. Senoh, N. Iwasa, and S. I. Nagahama, "High-brightness InGaN blue, green and yellow light-emitting diodes with quantum well structures," *Jpn. J. Appl. Phys.*, vol. 34, no. 7, pp. L797–L799, 1995.

[4] "Candela-class high-brightness InGaN AlGaN double-heterostructure blue-light-emitting diodes.pdf." .

[5] A. Rizzi, "Band gap vs Lattice parameter for Group-III nitrides," *Private communications, 2001*. .

[6] S. Nakamura, M. Senoh, N. Iwasa, S. Nagahama, T. Yamada, and T. Mukai, "Superbright Green InGaN Single-Quantum-Well-Structure Light-Emitting Diodes," *Jpn. J. Appl. Phys.*, vol. 34, no. Part 2, No. 10B, pp. L1332–L1335, Oct. 1995.

[7] S. Sota, "Shortest wavelength semiconductor laser diode Shortest wavelength semiconductor laser diode," vol. 32, no. 12, pp. 1105–1106, 1996.

[8] J. Journal and A. P. Related, "Related content InGaN-Based Multi-Quantum-Well-Structure Laser Diodes," 1996.

[9] G. F. Yang *et al.*, "InGaN/GaN multiple quantum wells on selectively grown GaN microfacets and the applications for phosphor-free white light-emitting diodes," *Rev. Phys.*, vol. 1, no. 1800, pp. 101–119, 2016.

[10] Q. Wang, T. Wang, J. Bai, A. G. Cullis, P. J. Parbrook, and F. Ranalli, "Influence of annealing temperature on optical properties of InGaN quantum dot based light emitting diodes," *Appl. Phys. Lett.*, vol. 93, no. 8, pp. 1–4, 2008.

[11] A. F. Jarjour, R. A. Taylor, R. A. Oliver, M. J. Kappers, C. J. Humphreys, and A. Tahraoui, "Cavity-enhanced blue single-photon emission from a single InGaNGaN quantum dot," *Appl. Phys. Lett.*, vol. 91, no. 5, pp. 2005–2008, 2007.

[12] L. Wang, W. Lv, Z. Hao, and Y. Luo, "Recent progresses on InGaN quantum dot light-emitting diodes," *Front. Optoelectron.*, vol. 7, no. 3, pp. 293–299, 2014.

[13] K. Y. Lai, G. J. Lin, Y. L. Lai, Y. F. Chen, and J. H. He, "Effect of indium fluctuation on the photovoltaic characteristics of InGaN/GaN multiple quantum well solar cells," *Appl. Phys. Lett.*, vol. 96, no. 8, pp. 2008–2011, 2010.

[14] K. Y. Lai, G. J. Lin, C. Y. Chen, Y. L. Lai, and J. H. He, "Origin of hot carriers in InGaN-based quantum-well solar cells," *IEEE Electron Device Lett.*, vol. 32, no. 2, pp.

179–181, 2011.

[15] J. Wu *et al.*, “Small band gap bowing in In1-xGaxN alloys,” *Appl. Phys. Lett.*, vol. 80, no. 25, pp. 4741–4743, 2002.

[16] Y. Nanishi, Y. Saito, and T. Yamaguchi, “RF-molecular beam epitaxy growth and properties of InN and related alloys,” *Japanese J. Appl. Physics, Part 1 Regul. Pap. Short Notes Rev. Pap.*, vol. 42, no. 5 A, pp. 2549–2559, 2003.

[17] O. Jani, I. Ferguson, C. Honsberg, and S. Kurtz, “Design and characterization of GaNInGaN solar cells,” *Appl. Phys. Lett.*, vol. 91, no. 13, pp. 89–92, 2007.

[18] D. H. Lien *et al.*, “Harsh photovoltaics using InGaN/GaN multiple quantum well schemes,” *Nano Energy*, vol. 11, pp. 104–109, 2015.

[19] M. Ebaid *et al.*, “Enhanced solar hydrogen generation of high density, high aspect ratio, coaxial InGaN/GaN multi-quantum well nanowires,” *Nano Energy*, vol. 12, pp. 215–223, 2015.

[20] M. Ebaid *et al.*, “Unbiased photocatalytic hydrogen generation from pure water on stable Ir-treated In0.33Ga0.67N nanorods,” *Nano Energy*, vol. 37, no. May, pp. 158–167, 2017.

[21] M. Ebaid, J. W. Min, C. Zhao, T. K. Ng, H. Idriss, and B. S. Ooi, “Correction: Water splitting to hydrogen over epitaxially grown InGaN nanowires on a metallic titanium/silicon template: Reduced interfacial transfer resistance and improved stability to hydrogen (Journal of Materials Chemistry A (2018) 6 (6922-6930) DOI: ,” *J. Mater. Chem. A*, vol. 6, no. 26, p. 12794, 2018.

[22] M. G. Kibria *et al.*, “Visible light-driven efficient overall water splitting using p-type metal-nitride nanowire arrays,” *Nat. Commun.*, vol. 6, pp. 1–8, 2015.

[23] L. Wang, W. Zhao, Z.-B. Hao, and Y. Luo, “Photocatalysis of InGaN Nanodots Responsive to Visible Light,” *Chinese Phys. Lett.*, vol. 28, no. 5, p. 57301, May 2011.

[24] K. Osamura, K. Nakajima, Y. Murakami, P. H. Shingu, and A. Ohtsuki, “Fundamental absorption edge in GaN, InN and their alloys,” *Solid State Commun.*, vol. 11, no. 5, pp. 617–621, 1972.

[25] H. P. D. Schenk *et al.*, “Indium incorporation above 800 °C during metalorganic vapor phase epitaxy of InGaN,” *Appl. Phys. Lett.*, vol. 75, no. 17, pp. 2587–2589, 1999.

[26] M. Shimizu, K. Hiramatsu, and N. Sawaki, “Metalorganic vapor phase epitaxy growth of (InxGa1-xN/GaN)n layered structures and reduction of indium droplets,” *J. Cryst. Growth*, vol. 145, no. 1–4, pp. 209–213, 1994.

[27] W. Shan *et al.*, “Optical properties of InxGa1-xN alloys grown by metalorganic chemical vapor deposition,” *J. Appl. Phys.*, vol. 84, no. 8, pp. 4452–4458, 1998.

[28] N. Yoshimoto, T. Matsuoka, T. Sasaki, and A. Katsui, “Photoluminescence of InGaN films grown at high temperature by metalorganic vapor phase epitaxy,” *Appl. Phys.*

Lett., vol. 59, no. 18, pp. 2251–2253, 1991.

[29] Z. Liliental-Weber *et al.*, "Compositional modulation in InxGa1-xN," *Phys. B Condens. Matter*, vol. 376–377, no. 1, pp. 468–472, 2006.

[30] "Unknown - Unknown - Small band gap bowing in In1xGaxN alloys.pdf." .

[31] D. Lu *et al.*, "Dynamic scaling of the growth process of GaN thin films deposited on sapphire substrates by HVPE," *Phys. Lett. Sect. A Gen. At. Solid State Phys.*, vol. 327, no. 1, pp. 78–82, 2004.

[32] O. Ambacher, "Growth and applications of group III-nitrides," *J. Phys. D. Appl. Phys.*, vol. 31, no. 20, pp. 2653–2710, 1998.

[33] D. Doppalapudi, S. N. Basu, K. F. Ludwig, and T. D. Moustakas, "Phase separation and ordering in InGaN alloys grown by molecular beam epitaxy," *J. Appl. Phys.*, vol. 84, no. 3, pp. 1389–1395, 1998.

[34] S. Chichibu, T. Azuhata, T. Sota, and S. Nakamura, "Luminescences from localized states in InGaN epilayers," *Appl. Phys. Lett.*, vol. 70, no. 21, pp. 2822–2824, 1997.

[35] I. H. Ho and G. B. Stringfellow, "Solid phase immiscibility in GaInN," *Appl. Phys. Lett.*, vol. 69, no. 18, pp. 2701–2703, 1996.

[36] T. Kuykendall, P. Ulrich, S. Aloni, and P. Yang, "Complete composition tunability of InGaN nanowires using a combinatorial approach," *Nat. Mater.*, vol. 6, no. 12, pp. 951–956, 2007.

[37] R. García, G. A. Hirata, M. H. Farías, and J. McKittrick, "A novel method for the synthesis of sub-microcrystalline wurtzite-type InxGa1-xN powders," *Mater. Sci. Eng. B Solid-State Mater. Adv. Technol.*, vol. 90, no. 1–2, pp. 7–12, 2002.

[38] S. V. Bhat, K. Biswas, and C. N. R. Rao, "Synthesis and optical properties of In-doped GaN nanocrystals," *Solid State Commun.*, vol. 141, no. 6, pp. 325–328, 2007.

[39] S. Krukowski *et al.*, "Thermal properties of indium nitride," *J. Phys. Chem. Solids*, vol. 59, no. 3, pp. 289–295, 1998.

[40] K. Sardar and C. N. R. Rao, "New Solvothermal Routes for GaN Nanocrystals," *Adv. Mater.*, vol. 16, no. 5, pp. 425–429, 2004.

[41] C. N. R. Rao, S. R. C. Vivekchand, K. Biswas, and A. Govindaraj, "Synthesis of inorganic nanomaterials," *J. Chem. Soc. Dalt. Trans.*, no. 34, pp. 3728–3749, 2006.

[42] J. Choi and E. G. Gillan, "Low-temperature solvothermal synthesis of nanocrystalline indium nitride and Ga-In-N composites from the decomposition of metal azides," *J. Mater. Chem.*, vol. 16, no. 38, pp. 3774–3784, 2006.

[43] S. F. (CEA-C. F.Rol, "Probing exciton localization in non-polar GaN/AlN Quantum Dots by si,gle dot optical spectroscopy," no. c, pp. 1–4.

[44] P. Ramvall, P. Riblet, S. Nomura, Y. Aoyagi, and S. Tanaka, "Optical properties of

GaN quantum dots," *J. Appl. Phys.*, vol. 87, no. 8, pp. 3883–3890, 2000.

[45] P. K. B. Palomaki, E. M. Miller, and N. R. Neale, "Control of plasmonic and interband transitions in colloidal indium nitride nanocrystals," *J. Am. Chem. Soc.*, vol. 135, no. 38, pp. 14142–14150, 2013.

[46] U. Anderson, Benjamin A. (Lilly Research Laboratories, Indianapolis, IN, "Hexamethyldisilazane," *John Wiley & Sons, Ltd*. [Online]. Available: http://reag.paperplane.io/00001483.htm#3.

[47] "Critical Pressure & Temperature of Toluene," *NIST*. [Online]. Available: https://webbook.nist.gov/cgi/cbook.cgi?ID=C108883&Mask=4#Thermo-Phase.

[48] "Critical Temperature & Pressire of Methanol," *NIST*. [Online]. Available: https://webbook.nist.gov/cgi/cbook.cgi?ID=C67561&Mask=4#Thermo-Phase.

[49] J. Zhang *et al.*, "Growth and structural characterization of InN/In2O3coaxial nanocables," *Mater. Lett.*, vol. 60, no. 17–18, pp. 2153–2157, 2006.

[50] M. Krawczyk *et al.*, "Surface and in-depth characterization of InGaN compounds synthesized by plasma-assisted molecular beam epitaxy," *J. Alloys Compd.*, vol. 509, no. 40, pp. 9565–9571, 2011.

[51] G. Hollinger and M. Gendry, "Hollinger'94 Oxides on GaAs and InAs surfaces An x-ray-photoelectron-spectroscopy study of reference compounds.pdf," vol. 49, no. 16, 1994.

[52] T. L. Duan, J. S. Pan, and D. S. Ang, "Investigation of Surface Band Bending of Ga-Face GaN by Angle-Resolved X-ray Photoelectron Spectroscopy," *ECS J. Solid State Sci. Technol.*, vol. 5, no. 9, pp. P514–P517, 2016.

[53] M. Lozac'h *et al.*, "Determination of the surface band bending in InxGa1-xN films by hard x-ray photoemission spectroscopy," *Sci. Technol. Adv. Mater.*, vol. 14, no. 1, pp. 1–6, 2013.

[54] N. Ghobadi, "Band gap determination using absorption spectrum fitting procedure," *Int. Nano Lett.*, vol. 3, no. 1, p. 2, 2013.

[55] P. Chand, A. Gaur, and A. Kumar, "Structural and optical properties of ZnO nanoparticles synthesized at different pH values," *J. Alloys Compd.*, vol. 539, pp. 174–178, 2012.

[56] D. Mandal and T. W. Hamann, "Band energies of nanoparticle semiconductor electrodes determined by spectroelectrochemical measurements of free electrons," *Phys. Chem. Chem. Phys.*, vol. 17, no. 17, pp. 11156–11160, 2015.

[57] B. Mittal, S. Tulsyan, S. Kumar, R. D. Mittal, and G. Agarwal, "Cytochrome P450 in Cancer Susceptibility and Treatment," *Adv. Clin. Chem.*, vol. 71, pp. 77–139, Jan. 2015.

[58] N. Taxak and P. V Bharatam, "Drug Metabolism," *J. Clin. Pharmacol.*, no. January,

pp. 259–282, 2004.

[59] S. Choi, Y. J. Kim, S. M. Kim, J. W. Yang, S. W. Kim, and E. J. Cho, "Hydrotrifluoromethylation and iodotrifluoromethylation of alkenes and alkynes using an inorganic electride as a radical generator," *Nat. Commun.*, vol. 5, pp. 1–7, 2014.

[60] D. A. Nagib and D. W. C. Macmillan, "Trifluoromethylation of arenes and heteroarenes by means of photoredox catalysis," *Nature*, vol. 480, no. 7376, pp. 224–228, 2011.

[61] W. K. Hagmann, "Perspecti V e The Many Roles for Fluorine in Medicinal Chemistry," *J. Med. Chem.*, vol. 51, no. 15, pp. 4359–4368, 2008.

[62] D. Bigdelifam *et al.*, "Sensitive spectrophotometric determination of fluoxetine from urine samples using charge transfer complex formation after solid phase extraction by magnetic multiwalled carbon nanotubes," *Anal. Methods*, vol. 6, no. 21, pp. 8633–8639, 2014.

[63] S. K. Balani, L. R. Kauffman, F. A. Deluna, and J. H. Lin, "Nonlinear pharmacokinetics of efavirenz (DMP-266), a potent HIV-1 reverse transcriptase inhibitor, in rats and monkeys," *Drug Metab. Dispos.*, vol. 27, no. 1, pp. 41–45, 1999.

[64] H. Song, "Research progress on trifluoromethyl-based radical reaction process," *IOP Conf. Ser. Earth Environ. Sci.*, 2017.

[65] A. Studer, "A 'renaissance' in radical trifluoromethylation," *Angew. Chemie - Int. Ed.*, vol. 51, no. 36, pp. 8950–8958, 2012.

[66] O. A. Tomashenko and V. V. Grushin, "Aromatic trifluoromethylation with metal complexes," *Chem. Rev.*, vol. 111, no. 8, pp. 4475–4521, 2011.

[67] Y. Kobayashi and I. Kumadaki, "Trifluoromethylation of aromatic compounds," *Tetrahedron Lett.*, vol. 10, no. 47, pp. 4095–4096, 1969.

[68] V. C. R. Mcloughlin and J. Thrower, "A route to fluoroalkyl-substituted aromatic compounds involving fluoroalkylcopper intermediates," *Tetrahedron*, vol. 25, no. 24, pp. 5921–5940, 1969.

[69] M. Oishi, H. Kondo, and H. Amii, "Aromatic trifluoromethylation catalytic in copper," *Chem. Commun.*, no. 14, pp. 1909–1911, 2009.

[70] E. J. Cho, T. D. Senecal, T. Kinzel, Y. Zhang, D. a Watson, and S. L. Buchwald, "Trifluoromethylation of Aryl Chlorides," *Science (80-.).*, vol. 328, no. June, pp. 4–6, 2010.

[71] J. M. R. Narayanam and C. R. J. Stephenson, "Visible light photoredox catalysis: Applications in organic synthesis," *Chem. Soc. Rev.*, vol. 40, no. 1, pp. 102–113, 2011.

[72] D. A. Nicewicz and D. W. C. Macmillan, "Merging Photoredox Catalysis with Organocatalysis," *Science (80-.).*, vol. 322, no. October, pp. 77–80, 2008.

[73] T. P. Yoon, M. A. Ischay, and J. Du, “Visible light photocatalysis as a greener approach to photochemical synthesis,” *Nat. Chem.*, vol. 2, no. 7, pp. 527–532, 2010.

[74] N. Iqbal, S. Choi, E. Ko, and E. J. Cho, “Trifluoromethylation of heterocycles via visible light photoredox catalysis,” *Tetrahedron Lett.*, vol. 53, no. 15, pp. 2005–2008, 2012.

[75] C. K. Prier, D. A. Rankic, and D. W. C. MacMillan, “Visible Light Photoredox Catalysis with Transition Metal Complexes: Applications in Organic Synthesis,” *Chem. Rev.*, vol. 113, no. 7, pp. 5322–5363, 2013.

[76] Y. Su, K. P. L. Kuijpers, N. König, M. Shang, V. Hessel, and T. Noël, “A Mechanistic Investigation of the Visible-Light Photocatalytic Trifluoromethylation of Heterocycles Using CF3I in Flow,” *Chem. - A Eur. J.*, vol. 22, no. 35, pp. 12295–12300, 2016.

[77] T. Noël, *Organometallic Flow Chemistry*, vol. 57. 2016.

General Conclusion

In this PhD research, the motif is based completely on the synthesis and development of novel heterogeneous photocatalysts, I have first addressed the rationale behind the design for achieving the essential criteria of an advanced photocatalytic systems, along with their corresponding synthetic strategies. This was done through briefly addressing the currently developed semiconductor materials and their corresponding applications in the photochemical fields. This was done for most of the notable semiconductor materials reported all across the globe in the last four decades. Such a distinctive immense study has led me to classify the various available semiconductor materials into the four different families of heterogeneous photocatalysts belonging to one-step excitation (conventional) system. This literature survey of chapter one, provided the insights in photocatalysts design parallelly furnished a way for successfully realizing promising systems among each family for performing several photochemical reactions. Additionally, literature review was also provided for the successful current implementations of various heterogeneous photocatalysts in diverse photoreactor systems. The entire work done here is completely relied on the currently developing one-step photoexcitation semiconductor photocatalysts. The successful and facile development of nanophotocatalysts within the four classified families of heterogeneous photocatalysts would pave way for developing photocatalysts for the unconventional two-step photoexcitation (z-scheme process) process in the upcoming decades.

Based on the various literature surveys performed, group-III nitride system was chosen as base semiconductor material in this research work. Since group-III materials (especially GaN and InN) exhibits the propensity to form semiconductor photocatalysts belonging to the four different families of heterogeneous photocatalysts, they were opted in this PhD study. The initial synthetic target of chapter two focused on the synthesis of GaN nanoparticles using the reactive, facile homoleptic amido complex single source precursor in a continuous supercritical millireactor.

Here, the thermolysis of the precursor was studied in previously reported flow injection (co-flow) strategy and reproducibility was checked. The drawbacks associated with the co-flow set-up was identified through mathematical simulation study. This simulation coupled with numerical analysis provided deep insights into the temperature and density fields of the supercritical millireactor hinged with co-flow injection technique. The results of the simulation study provided the complete overview of the flow process and the influence of injection strategy on the heat transfer with flow streams. This provided me the idea to develop a novel pre-heater injection based millireactor set-up, which eliminated the drawbacks associated with co-flow system. The as-developed pre-heater system experimentally exhibited the beneficial similar process conditions observed in the simulation studies. The continuous thermolysis of single source precursor in pre-heater hinged millireactor yielded continuous production of highly quantum confined GaN QDs (3.8 eV) at a higher throughput of 100 - 150 mg pre synthesis, in 33 s residence time. The as-designed pre-heater system exhibited the potential for scaling the precursor concentration from 10^{-3} to 10^{-2} M or mole/L in the millireactor. Parallelly, high reactor life time was exhibited by the pre-heater hinged system, where no clogging was

observed even after 30 individual continuous syntheses of GaN QDs with $1.7*10^{-2}$ M precursor concentration in the millireactor for each individual synthesis. Regarding the research in the photochemistry, as this PhD under the Photo4Future project focuses also on effectively utilising the visible light. The as-synthesized QDs were successfully implemented in the direct photochemical excitation (catalyzed photoreaction) phenomenon involving the advanced oxidation process (AOPs) for degrading an organic azo dye (methyl orange) under visible light irradiation. In the heterogeneous photocatalytic field, exploration in direct photochemical excitation was not addressed for a long time due to the lack of development of nanophotocatalysts, which effectively exhibits high electron injection efficiency from the surface adsorbed dye molecule and concurrently provide high surface area for dye adsorption. The as-synthesized GaN QDs from the pre-heater hinged continuous supercritical millireactor exhibited the above mentioned unique qualities of high electron injection efficiency and high surface area and supplementarily provided enhanced light trapping ability through Mie scattering phenomenon, arising from its unique spherical aggregate morphology.

This novel GaN QDs nanophotocatalysts exhibited enhanced direct dye degradation of methyl orange dye, exhibiting 94% degradation efficiency within one-hour irradiation. This photocatalytic activity of GaN QDs is 18 times higher in performance compared to the commercially available TiO_2 (Degussa P25) nanophotocatalysts. This study provided a pathway for effectively utilizing visible light through binary nanophotocatalysts for photochemical reactions involved in the environmental remediation processes.

Analogously for the photochemical reactions involving the conversion of photonic energy into chemical energy, like the carbon-carbon bond formation and reduction of carbon di-oxide, the conventional indirect photoexcitation process is the prerequisite. The wide band gap binary nanophotocatalysts (GaN QDs) do not possesses the potential for such indirect heterogeneous photocatalytic phenomenon under visible light irradiation. To render a nanophotocatalysts for sensitized photoreaction (indirect photoexcitation process), narrow band gap semiconductor system is required. GaN QDs' band gap is precisely engineered within the narrow visible range of the electromagnetic spectrum when combined with InN semiconductor through the formation of ternary solid solution $Ga_xIn_{1-x}N$ system. So far in the material science field the complete tunability of $Ga_xIn_{1-x}N$ system in nanoparticles domain has not addressed due to the lattice mismatch of 11% existing between the isostructural GaN and InN binary semiconductors. This lattice mismatch arises from the differences in the tetrahedral radius of the gallium and indium cations resulting in the formation of phase segregation and compositional modulation of the $Ga_xIn_{1-x}N$ solid solution.

In this research work, through systematic evaluation of the cupferronate and HMDS chemistry for the synthesis of $GaxIn_{1-x}N$ system in various solvent systems, a novel dual solvent system was identified, developed, optimized and implemented in continuous flow supercritical millireactor. Through this dual solvent system (toluene + methanol) complete tunability of $Ga_xIn_{1-x}N$ solid solution with very less phase segregation was achieved. Maximum up to 47% indium (mole basis) was successfully incorporated into the GaN lattice of $Ga_xIn_{1-x}N$ solid solution without any phase segregation. This is the first and highest attained incorporation of indium in $Ga_xIn_{1-x}N$ solid solution using the cupferronate and HMDS precursor chemistry.

The as-synthesized $Ga_{0.53}In_{0.47}N$ solid solution was successfully applied as a replacement for complex expensive transition metal homogeneous photocatalysts for efficient drug synthesis. Here $Ga_{0.53}In_{0.47}N$ solid solution nanophotocatalysts (2.6 eV) was used in photoredox catalysis for the direct trifluoromethylation of heteroarenes. Heteroarenes was experimented as a reactive substrate for trifluoromethylation, as they form the fundamental structural unit of drug molecules currently targeted in the pharmaceutical industry. These nanophotocatalysts exhibited enhanced activity in single phase continuous flow photocatalytic process under visible light irradiation, where a maximum of 84% NMR yield was attained in 162 min compared to batch process (70% MNR yield in 7 h). Among the various continuous process like single phase flow and gas-solid-liquid segmented flow, the segmented flow exhibited the enhanced activity. Thus to conclude in the regime of indirect photochemical excitation process used for direct trifluoromethylation reaction, effective heterogeneous photocatalysis process in flow conditions was successfully attained in this research work. This $Ga_{0.53}In_{0.47}N$ solid solution exhibited facile separation from the product stream and its photocatalytic activity was not depreciated, even after three consecutive heterogeneous photocatalysis in flow.

In conclusion, in this research work several research advancements in the synthesis of nanophotocatalysts belonging to families of binary and ternary solid solution was successfully accomplished using continuous flow millireactor. These nanophotocatalysts was efficiently implemented in both catalyzed photoreaction (direct photoexcitation) and sensitized photoreaction (indirect photoexcitation) processes pf heterogeneous photocatalysis. These two process are highly favourable in the future, among these two the indirect photoexcitation involving the CF_3 incorporation would be highly required in the recent times, as efficient CF_3 incorporation is highly required for drugs used to cure AIDS and cancer. Implementation of $Ga_{0.53}In_{0.47}N$ nanophotocatalysts in drug production will effectively reduce the drug production cost as they obviate the costly downstream process used in the current pharmaceutical industries for removing the homogenous photocatalysts from the product stream.